Giovanna Bertolini *Editor*

Body MDCT in Small Animals

Basic Principles, Technology, and Clinical Applications

Springer

Body MDCT in Small Animals

Giovanna Bertolini
Editor

Body MDCT in Small Animals

Basic Principles, Technology, and Clinical Applications

Springer

Editor
Giovanna Bertolini
San Marco Veterinary Clinic
Padua, Italy

ISBN 978-3-319-46902-7 ISBN 978-3-319-46904-1 (eBook)
DOI 10.1007/978-3-319-46904-1

Library of Congress Control Number: 2017951501

Printed on acid-free paper

This Springer imprint is published by Springer Nature
The registered company is Springer International Publishing AG
The registered company address is: Gewerbestrasse 11, 6330 Cham, Switzerland

You see a block, think about the image.
It's inside; you only have to undress it.
(*Michelangelo Buonarroti*)

This book is dedicated to Marco,
my love and a constant inspiration to me.

Preface

MDCT represents a tremendous technological evolution of CT technology, which is increasing in importance in the diagnostic standards for various conditions. Although MDCT is now widely accessible in veterinary medicine, there is scant informational literature for MDCT users, and no book on this topic has been published before now.

This book was developed based on my 14 years of experience with MDCT in dogs and cats. I started employing MDCT in my practice in 2003 with a 16-MDCT, the most advanced MDCT scanner technology available at that time. I realized that a revolution in medical imaging and in small animal medicine had begun, leading us to a new diagnostic world. I developed scan protocols and designed new CT approaches for various clinical scenarios. I decided to write this book in 2014, when my group started to work with a dual-source technology and thus realized that practices were evolving once again and that those changes would bring new challenges.

To date, my group has performed more than 13,000 MDCT examinations in dogs and cats at our center. My colleagues and I, all veterinarians, perform all examinations ourselves, day and night. This experience has made it possible to tailor scan protocols to a great variety of clinical situations, thereby maximizing the diagnostic value of the procedure. The cases presented in this book are supported by anamnestic, clinical, clinicopathological, surgical, endoscopic, and pathological results. The images were selected directly from our report database and reflect our daily work.

I hope this book will be useful for other MDCT users. Because of the general similarities between the human and veterinary medicine paradigms and the lack of veterinary literature on certain subjects, some observations in this book were based in part on the human radiology literature and personal experience. I expect that some information in this book will require revision in the future. I would be delighted if this book would serve as an inspiration to my critical and knowledgeable readers to contribute their own research findings on this topic.

The book has seven sections, divided into 21 chapters, and over 600 images. The first chapter introduces the MDCT technique and its technological evolution. This knowledge is essential for understanding the notable differences among various MDCT scanners in terms of their capabilities and possible applications. Nowadays, with the availability of rapid MDCT scanners, standard MDCT examinations have the potential to serve as CT angiographies. For this reason, the second chapter describes the general principles of MDCT angiography in dogs and cats. The rest of the book encompasses major pathological conditions seen within abdominal and thoracic structures in dogs and cats and includes the most recent MDCT applications, such as cardiac CT and the potential for dual-energy CT.

Padua, Italy Giovanna Bertolini

Acknowledgments

I am grateful to Dr. Sebastian Faby and Dr. Thomas Flohr, top CT experts, for their considerable contributions to the first chapter of this book. They have strived for a balanced description of the basic principles and evolution of MDCT and DSCT technologies, employing ample supporting references and illustrations. I have gratitude for Dr. Randi Drees for her critical contributions in the chapters on cardiac MDCT and pulmonary vasculature.

I am grateful to all those who have contributed knowingly and unknowingly to my professional growth. In particular, I thank the "human" radiologist Dr. Stefano Cesari, my first mentor. I will be forever indebted to Prof. Mathias Prokop, my advisor during my rewarding PhD research fellowship in the Netherlands. My indebtedness extends to my colleagues in the CT and MRI division of the San Marco Veterinary Clinic. I would like to express my special thanks to Dr. Luca Angeloni, friend and colleague, for his continuous, enthusiastic, and competent work and also to Dr. Arianna Costa and Dr. Chiara Briola, talented colleagues and friends. I love working with all of them and I could not have completed this book without their support. The collegiality and expertise of internists, surgeons and other specialists of the San Marco Clinic contribute every day to the adoption and acceptance of MDCT in various clinical circumstances. In particular, I am grateful to Dr. Tommaso Furlanello for his constant faith in and professional support of our work. I thank the anesthesiologists, whose work is essential for patient safety and for the quality of images we obtain. In particular, I thank Dr. Cristiano Stefanello for our 10-year collaboration and friendship.

I extend a special thank you to my husband, Dr. Marco Caldin, founder of the San Marco Veterinary Clinic and Laboratory. He has my constant, enduring admiration and my gratitude for enlightening me with a greater curiosity and love for medicine. I thank him, my family, and my friends for their patience and forbearance during my time of neglect while preparing this book.

Contents

Editor and Contributors

Editor

Giovanna Bertolini Diagnostic and Interventional Radiology Division, San Marco Veterinary Clinic, Padova, Italy

Contributors

Randi Drees QMHA Diagnostic Imaging Section, Royal Veterinary College, University of London, London, UK

Sebastian Faby Siemens Healthcare GmbH, Diagnostic Imaging, Computed Tomography, Forchheim, Germany

Thomas Flohr Siemens Healthcare, Erlangen, Germany

Eberhard Karls Universität, Tübingen, Germany

Part I
Technics and Technology

Multidetector-Row CT Basics, Technological Evolution, and Current Technology

Sebastian Faby and Thomas Flohr

1 MDCT Basics

Computed tomography (CT) is a cross-sectional imaging modality based on the absorption of X-rays in the patient. The cross-sectional images are reconstructed from multiple X-ray projections acquired from different views, i.e., different angular positions of the measurement system relative to the patient. Today's multidetector-row CT (MDCT) systems comprise an X-ray tube and a detector array mounted on opposite sides of the patient in a continuously rotating gantry (see Fig. 1). The power supply between the rotating inner part of the gantry (rotor) and the fixed outer part (stator) is typically realized by slip rings, the same applies to data transmission. Lately, with increasingly fast rotation times, also contactless transmission technology has become available. The high voltage necessary for the X-ray tube is supplied by a generator that is mounted in the rotating part of the gantry as well. Depending on the system and the required power reserves (consider, e.g., rotation time and scan speed), these generators typically provide between 30 kW and up to 120 kW power. The available tube voltage ranges usually from 80 to 140 kV; this range has recently been extended from 70 to 150 kV. The X-ray tube emits a fan beam of about 50° fan angle, allowing covering a circular scan field of view (SFOV) with a diameter of typically 50 cm. The detector array usually

S. Faby (✉)
Siemens Healthcare GmbH, Diagnostic Imaging, Computed Tomography, Forchheim, Germany
e-mail: sebastian.faby@siemens.com

T. Flohr
Siemens Healthcare GmbH, Diagnostic Imaging, Computed Tomography, Forchheim, Germany

Eberhard-Karls-University, Tübingen, Germany
e-mail: thomas.flohr@siemens.com

G. Bertolini (ed.), *Body MDCT in Small Animals*, DOI 10.1007/978-3-319-46904-1_1

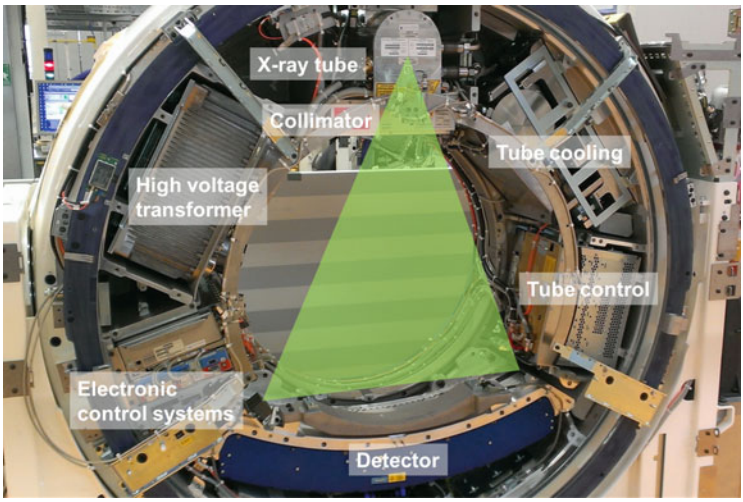

Fig. 1 Basic CT components arranged in a gantry. The fan beam emitted by the X-ray tube toward the detector is shown in *green*

consists of 16 or more detector rows and about 700 or more detector elements per row. Over a full gantry rotation, about 1000–2000 projections are acquired by the detector. The X-ray detection is today based on a scintillator material (e.g., Siemens UFC) converting the incoming X-ray photons into optical light, which is then detected by silicon photodiodes. The resulting analog signal is subsequently processed and converted into a digital signal using analog-to-digital converters (ADC). Classically, all this signal processing takes place on a separate circuit board. Recently, detectors with fully integrated electronics have been introduced (e.g., Siemens Stellar detector). In these detectors, the signal processing and ADC electronics are directly integrated with the photodiode situated underneath the scintillator. This results in much shorter analog signal paths with the goal to reduce electronic noise and detector cross talk. Electronic noise plays a role in low-signal scenarios, e.g., when bigger patients are scanned or in examinations at low radiation dose levels. A study with a 30 cm water phantom scanned at 80 kV showed a significant noise reduction for the detector with integrated electronics compared to a conventional detector (Duan et al. 2013).

The detector may provide different collimations, i.e., using either a different number of detector rows or different collimated slice widths. The collimated slice width is always measured at the isocenter, which is the center of the gantry rotation. Depending on the vendor and the system, the minimal collimated slice width is typically 0.5 mm, 0.6 mm, or 0.625 mm. By combining data from multiple rows, it is also straightforward to generate thicker slices, e.g., 2×0.6 mm $= 1.2$ mm. A conventional 16-slice scanner provides, for example, a 16×0.6 mm collimation. By closing the collimator leaves at the X-ray tube further, narrowing the emitted X-ray beam, the system may also provide a 4×0.6 mm collimation. If the detector

only features detector elements of the same size, e.g., 0.6 mm, it is called a fixed array detector. Most of the 64-row detectors are fixed array detectors, e.g., having 64 rows with 0.6 mm detector elements providing a 64 × 0.6 mm collimation. Some of the smaller detectors use a concept called adaptive array detector. This is the case for many 16-slice systems. They do not only provide a 16 × 0.6 mm collimation but also the possibility of using a 16 × 1.2 mm collimation. This is achieved by electronically combining the data of two of the 0.6 mm detector rows each, leading to 8 × 1.2 mm, and using four additional detector rows with 1.2 mm element size on each side. The detector in this example has thus not only 0.6 mm detector elements but also larger 1.2 mm detector elements at the outside. This concept is illustrated in Fig. 2.

Today, the predominant acquisition mode is spiral scanning—using a continuous gantry rotation and table movement—succeeding the sequence (axial or step-and-shoot) acquisition mode, which remains only in usage for special applications like cardiac imaging. Spiral image acquisition allows the reconstruction of images at

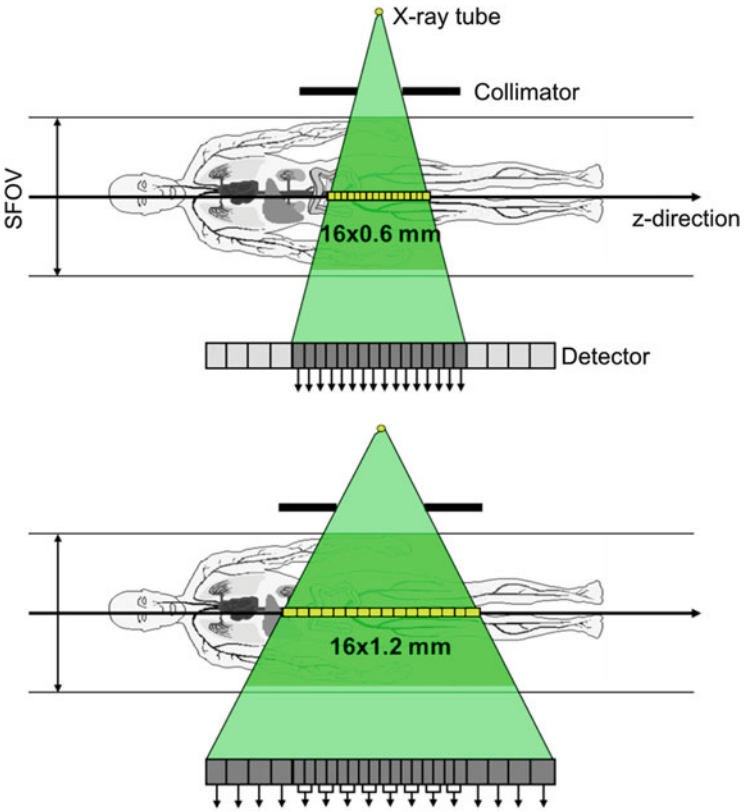

Fig. 2 Illustration of the working principle of an adaptive array detector with 24 detector rows that can either provide a 16 × 0.6 mm collimation (*top*) or a 16 × 1.2 mm collimation by a pairwise combination of the thinner inner detector elements (*bottom*)

any position in the acquired volume, also allowing, for example, overlapping slices by choosing the reconstruction interval accordingly. It is also possible to reconstruct thicker slices than the acquired collimated slice thickness from the same dataset. A very central parameter in spiral scanning is the so-called spiral pitch factor, which is defined as

$$\text{Pitch} = \text{table feed per rotation}/\text{collimated detector width}. \quad (1)$$

Consider the following example: a detector with 64 detector rows and 0.6 mm collimated slice width has a collimated detector width of 64×0.6 mm $= 38.4$ mm. If the table feed is 38.4 mm per rotation, this results in a pitch of 1. The pitch can be interpreted as a measure of the density of data sampling, with a pitch <1 meaning overlapping acquisition and a pitch >1 leading to sparser data acquisition. In the isocenter, a pitch of 0.5 leads to a 50% overlap between the beam profiles (see Fig. 3). In MDCT, the maximum available pitch is about 1.5.

Many CT parameters depend on the pitch, like the scan speed:

$$\text{Scan speed} = \text{collimated detector width} \times \text{pitch}/\text{rotation time}. \quad (2)$$

The scan speed is describing the volume coverage per time in a CT scan. This is relevant, for example, in thoracic imaging, determining the time required to scan the whole lung. The shorter the required acquisition time, the less likely are motion artifacts to occur, e.g., due to breathing. The acquisition time can roughly be estimated by dividing the scan range by the scan speed. Using the above example, with a collimated detector width of 64×0.6 mm $= 38.4$ mm together with a

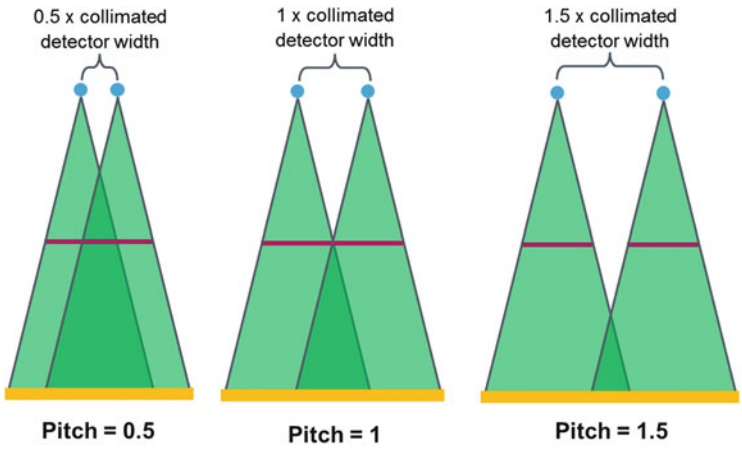

Fig. 3 Influence of the pitch factor on the data overlap. At a pitch of 0.5, there is an overlap in the isocenter of half the collimated detector width after a full rotation. At pitch 1 after a full rotation, the table has moved by exactly the collimated detector width. A pitch of 1.5 leads to a gap of half the collimated detector width

rotation time of 0.3 s and a pitch of 1.5 yields a scan speed of 38.4 mm × 1.5/0.3 s = 192 mm/s, using Eq. (2). The 300 mm scan range of a lung can thus be acquired in roughly 300 mm/192 mm/s = 1.6 s. This scan time is much shorter than the time a human can usually hold his breath. Please note that this estimation of the scan time is a best-case assumption neglecting pre- and post-scan rotations that are required in spiral scanning to be able to fully reconstruct also the borders at the beginning and end of the scan range. It is also important to consider that fast scanning inherently requires high tube power.

Not only is the scan speed important to avoid motion artifacts in the direction of the patient's long axis but also the in-plane temporal resolution (or axial temporal resolution). This is the temporal resolution of a respective single axial image. The in-plane temporal resolution depends on acquisition parameters like pitch and rotation time but also on the reconstruction algorithm. In parallel beam geometry, 180° of projection data are necessary to reconstruct an image of the full field of view (FOV) that has been acquired. In fan beam geometry—as used in today's CT systems—the minimum required data are typically 180° + the fan angle of the desired FOV, i.e., the area to be reconstructed. For a full 50 cm FOV, at least about 180° + 50° = 230° of data are required. Going to smaller FOVs, the required fan angle is decreasing. Close to the isocenter (e.g., in cardiac imaging), thus only about 180° coverage are necessary. This corresponds to half a rotation of the gantry, and therefore the in-plane temporal resolution is directly related to the rotation time. In the best case, the temporal resolution in a sequence scan is therefore rotation time/2. However, many sequence scan modes use data from a full rotation, and in this case, the temporal resolution is a full rotation time. In spiral scanning the situation is more complex and the pitch value also plays a role. As described, the pitch determines the data overlap. At a pitch of 1, data from a full rotation are available for reconstruction, so the temporal resolution is roughly equal to the rotation time. Operating the scanner at the maximum pitch value (~1.5) yields no redundant data, and in this case, the temporal resolution is ~rotation time/2. Lowering the pitch to 0.5 leads to data from two rotations being available due to the overlap, and the temporal resolution is consequently ~rotation time × 2. The temporal resolution could thus be defined as the time necessary to collect the data used for reconstruction of the image. With the concept of Dual Source CT, featuring two X-ray sources and detectors, a significantly better temporal resolution (~rotation time/4) can be achieved. This concept will be described in more detail in the next section together with the evolution of MDCT.

Also the effective tube current time product ("effective mAs") depends on the pitch:

$$\text{Effective mAs} = \text{tube current} \times \text{rotation time}/\text{pitch}. \tag{3}$$

The "effective mAs"-concept takes the abovementioned overlap for different pitch factors into account. The tube current is adjusted such that the effective mAs are the same as in a sequence scan (tube current × rotation time). Benefits of this approach are a constant image noise level independent of pitch or rotation time and

a decoupling of radiation dose and pitch for the user. The effective mAs are directly proportional to the X-ray tube output and thus to the dose and the $CTDI_{vol}$. Using a sequence scan with a tube current of, e.g., 200 mA at a rotation time of, e.g., 0.5 s as reference (200 mA × 0.5 s = 100 mAs), the variation of different parameters illustrates the dependencies. The following examples all result in the same effective mAs and the same dose (assuming of course the same tube voltage, geometry, etc.) as the above reference sequence scan with 100 mAs:

- A spiral scan with the same tube current and rotation time at a pitch of 1:
  200 mA × 0.5 s/1 = 100 eff. mAs.
- Decreasing the pitch to 0.5 (50% overlap) requires only half the tube current:
  100 mA × 0.5 s/0.5 = 100 eff. mAs.
- Increasing the pitch to 1.5 requires an increase of the tube current by 50%:
  300 mA × 0.5 s/1.5 = 100 eff. mAs.
- Additionally decreasing the rotation time to 0.25 s at a pitch of 1.5 requires a high tube current:
  600 mA × 0.25 s/1.5 = 100 eff. mAs.

  This is a fast scanning example (fast rotation time, high pitch), highlighting the high tube power requirements. This is especially an issue at low tube voltages.

2 Evolution of MDCT

Since the first clinical CT scan of a patient in October 1971—back then, CT was only available for the head (EMI Mark I head CT scanner)—the CT technology has made substantial improvements over the years, which is also owned to its fast acceptance due to the obvious benefits of noninvasive tomographic imaging. One of the most significant steps in the evolution of CT was the introduction of MDCT in 1998, initializing the transition of CT from a cross-sectional slice-by-slice acquisition to a true volume acquisition modality. The key innovations enabling MDCT were the introduction of spiral scanning (Kalender et al. 1990) with continuous tube-detector rotation and table movement and the construction of detector arrays with multiple detector rows in z-direction (i.e., table movement direction/caudo-cranial direction).

The first step in the direction of MDCT was the introduction of the first two-slice CT scanner (Elscint CT Twin) in 1992 (Liang and Kruger 1996). In 1998, all major vendors introduced the first true multi-slice systems, acquiring four slices simultaneously (4 × 1 mm or 4 × 1.25 mm collimation) at gantry rotation times down to 0.5 s (Klingenbeck-Regn et al. 1999). The benefits resulting from these MDCT systems compared to previous generations, especially single-slice systems operated in sequential step-and-shoot mode, are shorter scan times and a substantially improved z-axis spatial resolution. The scan time aspect is relevant because it is desirable to scan whole organs in one breath-hold of the patient, thus avoiding

motion artifacts. The *z*-axis resolution is not just important for the visualization of small features, but an isotropic spatial resolution, i.e., one that is equal in all directions, is one of the prerequisites for three-dimensional image post-processing, which will be discussed later. The four-slice systems had still some limitations regarding scan times. This also resulted in the fact that for many routine applications, still no fully isotropic resolution could be achieved. A human thorax examination with 4 × 1 mm collimation and 0.5 s rotation time took 25–30 s. Nevertheless, CT was quickly recognized as gold standard for its usefulness in the diagnosis of pulmonary embolism (PE), to a subsegmental artery level (Remy-Jardin et al. 2002). ECG-gating functionality was introduced at this time as well to enable the evaluation of the coronary arteries with CT (Ohnesorge et al. 2000). However, the temporal resolution was limited, and therefore coronary CT angiography was only suitable for human patients with lower heart rates (Achenbach et al. 2000).

In 2000 an eight-slice CT scanner was introduced, which brought improvements regarding scan time: however, the spatial resolution in *z*-direction did not improve (8 × 1.25 mm collimation).

This only changed with the advent of 16-slice CT scanners, which have been commercially available since 2001. With these systems now, MDCT could for the first time unfold all its benefits, allowing routine scanning with true isotropic submillimeter spatial resolution (Flohr et al. 2002). These systems featured a thinnest collimation of 16 × 0.5 mm, 16 × 0.625 mm, or 16 × 0.75 mm, depending on the manufacturer. The fastest gantry rotation time was 0.42 s, later reduced to 0.375 s. This allowed the coverage of the human thorax in 8–10 s with isotropic resolution, a significant improvement over the four-slice systems' performance. This had an impact on several clinical applications, e.g., allowing CT angiography (CTA) of the entire thorax and abdomen at once. Cardiac CTA benefitted from the improved temporal (~rotation time/2) and spatial resolution (Nieman et al. 2002), allowing an evaluation of the cardiac function in one scan (Coche et al. 2005). For thorax diagnostics, the detection of central and peripheral PE became reliably possible even in dyspneic patients (Schoepf et al. 2003).

CT technology evolution did not stop at 16 slices, but only 3 years later—in 2004—all major vendors presented CT scanners acquiring 64 slices, quadrupling thus the number of acquired slices. The gantry rotation time was also improved, now performing a full rotation in down to 0.33 s. The 64 slices are acquired manufacturer-dependent at 0.5 mm, 0.6 mm, or 0.625 mm collimated width. One of the vendors used a 32-row detector in combination with a double sampling technique in *z*-direction to acquire 64 overlapping slices. This double sampling is enabled by a so-called *z*-flying focal spot (*z*-FFS) technique in the X-ray tube, where the focal spot is deflected between two alternating *z*-positions on the anode, allowing to acquire 64 overlapping 0.6 mm slices (see Fig. 4). The benefits of this approach are an increased isotropic spatial resolution of 0.33 mm, independent of the pitch. Additionally, spiral artifacts are strongly reduced by the *z*-FFS approach (Flohr et al. 2005). Clinically, the 64-slice systems further increased the anatomical range coverable at submillimeter resolution. The acquisition of a human thorax

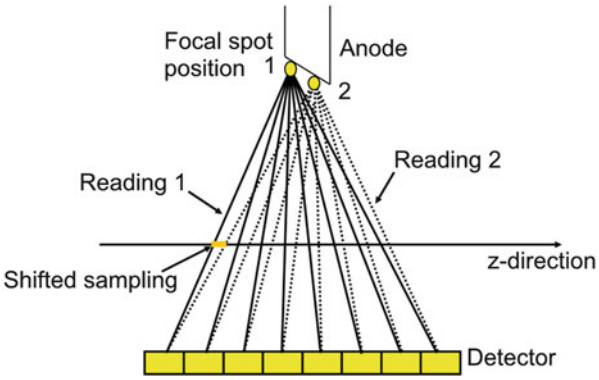

Fig. 4 The *z*-flying focal spot concept (*z*-Sharp, Siemens Healthcare). Due to alternating focal spot positions between two readings, the sampling in *z*-direction is improved. The focal spot positions are chosen such that the sampling is shifted by half a collimated slice width in the isocenter. The data of the two readings are interleaved to form one projection of double the slice number at half the *z*-sampling distance

requires now less than 5 s, improving imaging of uncooperative and emergency patients. Coronary CTA became more robust due to the increase in temporal resolution (Leber et al. 2005), facilitating its way into clinical routine protocols. Cardiac morphology and function could be evaluated in a comprehensive scan, including high-resolution imaging of the coronary arteries (Salem et al. 2006). The so-called triple rule out with a single scan for patients with acute chest pain was introduced with 64-slice scanners (Johnson et al. 2007). The goal of this kind of examination is to distinguish between PE, aortic dissection/aneurysm, or coronary artery disease (CAD). Although these systems were a significant improvement of the previous 16-slice scanners, still some challenges remained, especially motion artifacts in cardiothoracic imaging.

While so far the evolution had always been going to more and more slices, CT stood now at a crossroads. Most vendors continued adding more slices, and in 2007 different manufacturers launched a 128-slice system (64 × 0.6 mm × 2 (double sampling by *z*-FFS), 0.3 s rotation time, Siemens Definition AS+), a 256-slice system (128 × 0.625 mm × 2 (*z*-FFS), 0.27 s rotation time, Philips Brilliance iCT), and even a 320-slice system (320 × 0.5 mm collimation = 16 cm coverage at isocenter, 0.35 s rotation time, Toshiba Aquilion ONE), after a long prototype evaluation phase using a system with 256 × 0.5 mm collimation and 0.5 s rotation time (Mori et al. 2004). The idea behind this wide 16 cm detector approach is the potential to cover certain organs—like the heart, the brain, or the kidneys—in a single rotation without table movement (Rybicki et al. 2008), especially in perfusion imaging. One vendor, however, introduced in 2005 a new concept to CT imaging: Dual Source CT (DSCT). DSCT features two X-ray tubes and two detectors mounted in one gantry in the same imaging plane at an angle of 90° between the two source-detector systems (Flohr et al. 2006) (see Fig. 5). The most

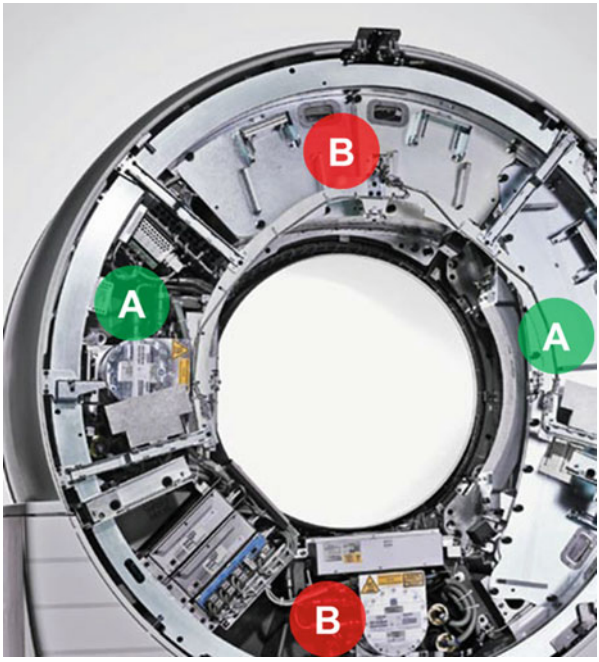

Fig. 5 A Dual Source CT system with two X-ray tubes and two detectors mounted at an angle of 90° (source-detector system A and B)

obvious benefit from such an approach is the significantly improved hardware-based temporal resolution of 83 ms (~rotation time/4), which is relevant in cardiac imaging. This value is independent of the patient's heart rate. Comparable single source MDCT systems back then had a temporal resolution of 165–190 ms.

The wide detector approach was much later also adopted by a second vendor, introducing in 2013 a system with 256 × 0.625 mm collimation and 0.28 s rotation time (GE Revolution CT) (Raju et al. 2016). The original DSCT from 2005 acquiring 2 × 64 slices (2 × 32 × 0.6 mm × 2 (*z*-FFS), 0.33 s rotation time, Siemens SOMATOM Definition) was further improved in 2008 to a 2 × 128-slice system (2 × 64 × 0.6 mm × 2 (*z*-FFS), 0.28 s rotation time, Siemens SOMATOM Definition Flash) and later again in 2013 to 2 × 192 acquired slices (2 × 96 × 0.6 mm × 2 (*z*-FFS), 0.25 s rotation time, Siemens SOMATOM Force). The temporal resolution of these three DSCT systems has improved from 83 ms (Petersilka et al. 2008), to 75 ms (Flohr et al. 2009), and down to 66 ms (Flohr et al. 2015).

Apparently, there are now two different philosophies of cardiac CT imaging: wide 16 cm detectors and DSCT. This is the current state of the art in CT in 2016. The advantages and disadvantages of these two approaches will now be discussed. Classically, cardiac acquisitions controlled by an ECG signal are composed of multiple image stacks from consecutive heartbeats. The different stacks are stitched to obtain the complete volume. The number of required image stacks depends on the detector width. For 4 cm detectors, four stacks may be required, while this

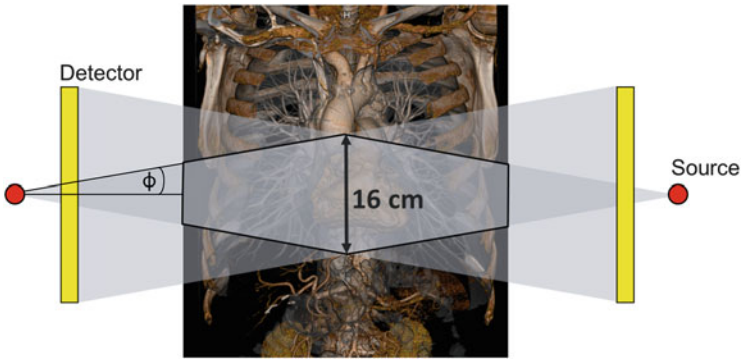

Fig. 6 Axial scanning with a wide detector that allows covering the heart without table movement. The acquired SFOV is decreasing going outward according to the cone angle ϕ

number is reduced to two stacks for 8 cm detectors. These stacks may be shifted with respect to each other due to differences in the heart motion from beat to beat. This will be visible as stair step or banding artifacts. These artifacts can be avoided by 16 cm detectors since the heart can be covered in a single axial scan (see Fig. 6). At the same time this possible advantage has the disadvantage that consequently all images will be affected when arrhythmia or ectopic heartbeats interfere with the data acquisition. The successful usage of wide detectors for cardiac imaging has been shown (Dewey et al. 2009), also for first-pass perfusion evaluation (George et al. 2014). A newer generation of the 320-slice system is reported to require less dose for coronary CTA studies than the initial system did (Tomizawa et al. 2013). For the 256-slice CT scanner, recently a first phantom and pig study on dynamic myocardial perfusion was published (So et al. 2016); this publication also discusses all the necessary corrections that are required for the data from the 16 cm detector. This is related to the fact that technically, these wide detectors require a large cone angle of the X-ray beam in *z*-direction for the data acquisition, meaning that the acquired planes are strongly inclined. This poses a problem for image reconstruction (Li et al. 2012). The cone beam also causes a cone-shaped SFOV that covers 16 cm in the isocenter and that decreases to only about 10 cm going to the outside of a 50 cm axial FOV (see Fig. 6). The X-ray spectrum is affected as well from the large cone angle by the so-called heel effect, which leads to a different shape of the spectrum depending on the *z*-position due to a varying inherent anode pre-filtration, potentially resulting in inhomogeneous CT values across the 16 cm. 16 cm systems have the benefit of being able to cover a limited anatomical area without table movement by repeated scanning. This is especially of interest for studies of the brain, e.g., regarding vessel malformations (Willems et al. 2012) or perfusion (Manniesing et al. 2015). In the thorax, first-pass perfusion studies for the differentiation of pulmonary nodules have been reported (Ohno et al. 2011).

Dual Source CT relies on two independent source-detector systems, as mentioned above, with the benefit of obtaining double the detector coverage of a comparable single source system without having to resort to large cone angles

and a high temporal resolution down to 66 ms at 0.25 s rotation time by combining the data from the two detectors. At least 180° of scan data are required to reconstruct an image close to the isocenter, also referred to as partial scan or quick scan. If the cone angle becomes too large, however, this is no longer true for the outer slices. By combining two 90° segments of the two measurement systems of a DSCT, the temporal resolution is about the time required to acquire 90° of data, i.e., ~rotation time/4. It is important to note that the temporal resolution here is independent of the patient's heart rate because only data from one cardiac cycle contributes to the reconstruction of one image. Single source systems are able to achieve similar temporal resolution values well below 100 ms by employing so-called multi-segment reconstruction where data from multiple heart cycles contributes to an image. In this case the temporal resolution strongly depends on heart rate and rotation time. There are many clinical studies on DSCT showing that it can reliably perform coronary CTA in human patients with high and also irregular heart rates (Sun et al. 2011). Even in difficult-to-image patients, DSCT can diagnose clinically significant CAD (Westwood et al. 2013). The high temporal resolution of DSCT is also beneficial in cardiothoracic studies (Sandfort et al. 2016). The DSCT concept has another important advantage: by combining the data from the two measurement systems, it cannot only provide a high temporal resolution but also very high scan speeds (Petersilka et al. 2008; Flohr et al. 2009). While the maximum pitch in single source MDCT is usually about 1.5, DSCT can be operated at double this value (128-slice DSCT pitch 3.4, 192-slice DSCT pitch 3.2). The resulting maximum scan speed for 128-slice DSCT is 458 mm/s and even 737 mm/s for 192-slice DSCT. At the maximum pitch, this scan mode delivers a temporal resolution of ~rotation time/4 since no redundant data are acquired. Lowering the pitch also lowers the temporal resolution. At a pitch of two, the temporal resolution is ~rotation time $\times$ 0.4, which equals 100 ms at 0.25 s rotation time (Flohr et al. 2009). This high-pitch scan mode is well suited to cover large anatomical ranges in very short scan times and at a high temporal resolution, minimizing thus motion artifacts. Possible applications are chest CTA (Sabel et al. 2016), triple rule out (Hou et al. 2013), and fast CTA of the aorta at low radiation and contrast agent dose (Zhang et al. 2015) or in uncooperative or pediatric patients (Bridoux et al. 2015). This high-pitch mode can also be employed with ECG triggering for cardiac imaging. Table positioning and acceleration are calculated and positioned such that the table arrives at full speed at the prescribed z-position in the requested cardiac phase. This scan mode has the potential to scan the entire heart in one beat at very low radiation dose (Gordic et al. 2014). This is also one way to avoid the abovementioned composition of the heart of multiple image stacks. For the planning of transcatheter aortic valve implantation (TAVI) or comprehensive thorax examinations in the emergency room, the ECG-triggered high-pitch scan mode of DSCT can be used because the coronary arteries, aorta, and iliac arteries can be visualized in a single scan at low radiation dose. The very short scan times may potentially allow for the reduction of contrast agent (Bittner et al. 2016). DSCT also enables quantitative dynamic myocardial perfusion imaging at full temporal resolution by using the two measurement systems and a shuttle movement of the table to

cover about twice the detector width (Caruso et al. 2016). Dynamic imaging of larger anatomical structures or organs way beyond the detector width is possible as well by a continuously oscillating back-and-forth table movement. 192-slice DSCT can dynamically cover up to 80 cm, e.g., for dynamic CTA studies, in 128-slice DSCT, it is 48 cm (Haubenreisser et al. 2015). For quantitative dynamic perfusion studies, e.g., of the brain or the liver, 22 cm coverage is provided by 192-slice DSCT and 14 cm by 128-slice DSCT at a temporal sampling of 1.5 s (Morsbach et al. 2014). The DSCT concept with two X-ray tubes allows operating them at two different tube voltages to acquire dual-energy data. Dual-energy CT will be discussed in more detail in the next section. The DSCT concept also has some challenges to overcome. One issue is cross-scattering of scattered radiation between the two measurement systems (Engel et al. 2008), i.e., photons emitted by tube A that are scattered by the patient and detected by detector B or vice versa. The effect of scatter radiation is a reduced CNR. Cross-scatter can be reduced by anti-scatter grids and can efficiently be corrected by algorithms (Petersilka et al. 2010; Petersilka et al. 2014). A further challenge is the limited space in the gantry, leading to a smaller SFOV of the second detector (35 cm for 192-slice DSCT), which can lead to incomplete information outside the smaller SFOV in all Dual Source scan modes. This may be an issue for larger patients.

Another technology trend that should be mentioned here is low kV imaging. The motivation of low kV imaging, i.e., using tube voltages well below the conventional 120 kV, is the potential to save radiation and/or contrast agent dose in contrast-enhanced CT studies. The rationale behind this is the fact that the iodine in the contrast agent shows a strongly increasing contrast toward lower energies due to its K-edge at 33 keV (see Fig. 7). At a constant radiation and contrast agent dose, this

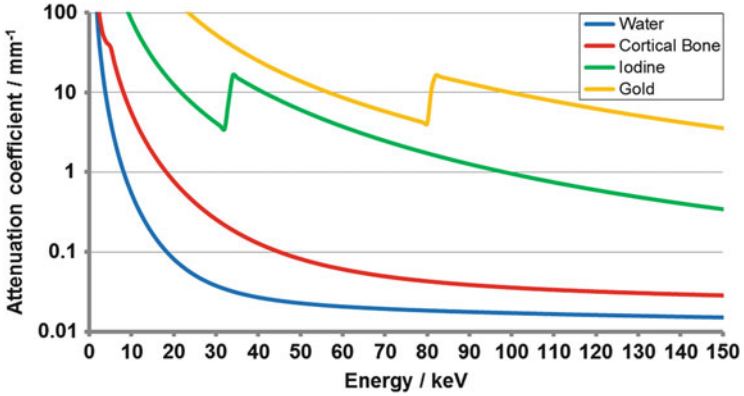

Fig. 7 X-ray attenuation coefficient for different materials at different energies. Water and bone behave differently, especially at low energies where the photoelectric effect dominates. The photoelectric effect is also responsible for the discontinuities in the absorption coefficient here visible for the elements iodine and gold, the so-called K-edges. The reason for the increased attenuation above the K-edge (I, 33.2 keV; Au, 80.7 keV) is that by exceeding this energy, the X-ray photons become able to remove electrons from the innermost shell, the K-shell. The position of the K-edge depends on the atomic number (Z) of the element

leads to an increasing iodine contrast-to-noise ratio (CNR) toward lower tube voltages. Keeping the iodine CNR constant with respect to 120 kV allows turning the CNR increase at lower tube voltages into radiation and/or contrast agent dose savings (Lell et al. 2015). While the increasingly faster CT scanners require more and more powerful tubes to generate a certain tube output in shorter time frames, low kV imaging even puts additional requirements on the generator and X-ray tube. To be able to use low tube voltages like 90 kV, 80 kV, or even 70 kV not only in small patients but also in normal or even larger adults, high tube power is required at these tube voltages. Siemens' Vectron tube (120 kW, available in 192-slice DSCT) has been designed to deliver 1300 mA tube current (per tube) at 70, 80, and 90 kV, enabling low kV imaging in routine. This tube can provide all tube voltages between 70 and 150 kV in 10 kV steps to better adapt to the patient (Winklehner et al. 2015). Also Siemens' Straton tube has been redesigned (Straton MX Sigma, 100 kW, available in 128-slice DSCT, Siemens SOMATOM Drive) for the requirements of low kV imaging, delivering 650 mA at 70 kV and 750 mA at 80 kV and 90 kV, as well as 10 kV steps between 70 and 140 kV.

3 Dual-Energy CT

The idea of dual-energy CT (DECT) dates back to the beginning of CT itself (Alvarez and Macovski 1976). The basic principle behind this idea is the fact that the X-ray absorption behavior of different materials at different energies is not the same (see Fig. 7). Additionally, in the relevant energy range used for CT imaging, the X-ray absorption process is governed physically by two processes: the photoelectric effect and Compton scattering. Scanning an object with two different energies will therefore provide information on the energy dependence of the object's absorption coefficient and thus on its material. The X-ray spectra emitted from today's X-ray tubes are far from being monoenergetic, but they typically start at around 30 keV and go up to the maximum energy provided by the tube voltage, e.g., 120 keV for 120 kV tube voltage. Nevertheless, depending on the tube voltage, every X-ray spectrum has a different average energy, leading to a different image contrast (see Fig. 8). It is thus possible to scan the patient with two different spectra generated by different tube voltages to obtain the desired two energy information (=dual energy). Some vendors may refer to dual-energy CT as spectral CT. Clinical benefits of DECT may come from the possibility of material characterization. In a conventional single-energy CT scan, the CT value in Hounsfield units (HU) can be the same for a bony structure and a vessel containing iodine contrast agent. DECT can differentiate bone (calcium) from iodine, allowing a bone removal in CTA studies for a clear view at the vessels. DECT applications will be discussed at the end of this section.

To be able to do DECT in an effective manner, there are some criteria that should be considered, like the spectral separation, the temporal coherence, the temporal resolution, and the dose efficiency. These criteria are of varying importance

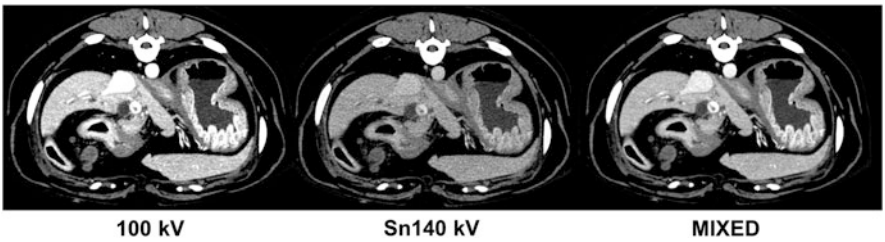

Fig. 8 Example of a DECT dataset. Please note the different soft tissue contrast for the low energy dataset (100 kV) and the high energy dataset (Sn140 kV = 140 kV + tin filter), especially of the contrast agent-filled structures. With better spectral separation, this difference becomes more pronounced, which is important for the DECT post-processing. The mixed image on the right is generated as a combination of the low and the high energy image, containing thus the full information. The image impression of the mixed image is similar to a 120 kV image (Data courtesy of San Marco Veterinary Clinic, Padova, Italy)

depending on the desired DECT application, and also the different available DECT techniques perform differently in these aspects. The spectral separation describes how different the low and high energy information are, i.e., how large is the overlap between the two detected spectra. It is a measure for the separability of two materials. This is especially important for a reliable and quantitative material decomposition. With a better spectral separation, less dose is needed to obtain the same material image quality (Faby et al. 2015). The temporal coherence describes how well correlated in time the acquired low and high energy projections are. This is important due to contrast agent dynamics and in the context of motion. Contrast agent dynamics lead to different iodine concentrations in the vessels and organs at two different points in time; therefore, the low and high energy data should be acquired without significant delay in between. The same is true for motion in general. The temporal resolution is referring to the temporal resolution of the low and high energy images themselves and is defined as the time necessary to collect the data for reconstruction (see above). A high temporal resolution is especially important in cardiac or thorax imaging. The dose efficiency is important as well. DECT should be dose neutral compared to a conventional 120 kV scan to be acceptable. All the established dose reduction techniques should also be applicable for DECT scanning, like tube current modulation and iterative reconstruction. The next paragraph describes the history and the different technological approaches of DECT.

Already in the 1980s, DECT was implemented in the commercially available Siemens SOMATOM DRH (Kalender et al. 1986) by using a fast kV-switching technique, alternating the tube voltage from projection to projection. At that time the main application was vertebral bone mineral analysis, but due to limited clinical benefits, the availability of dual-energy X-ray absorptiometry, and patient dose penalties, the fast kV-switching approach was discontinued. DECT had a revival starting in 2005 with the introduction of DSCT (Siemens SOMATOM Definition), allowing to operate the two X-ray tubes simultaneously at two different tube

voltages (80 kV/140 kV) while scanning the patient (Flohr et al. 2006). The low and high energy projections are acquired simultaneously with a 90° offset, leading to a good temporal coherence. Both detector systems acquire the full number of projections per rotation. In 2008 an improved version of the Dual Source DECT concept was introduced (Siemens SOMATOM Definition Flash). This system features a tin filter—an additional filter at the X-ray tube that removes low energy photons from the high energy 140 kV spectrum (Sn140 kV) to improve the spectral separation between the low and the high energy spectrum (see Fig. 9) (Primak et al. 2009). With this approach DSCT can provide the best available spectral separation. The tube current can be modulated independently for the two tubes, allowing adaptation to the patient's anatomy for optimal results. The dual-energy data is only available inside the smaller FOV defined by the second detector (up to 35 cm, depending on the system), which may be a problem for large or obese patients. Fast kV-switching DECT was reintroduced by a different vendor and launched in 2009 as Gemstone Spectral Imaging (Discovery CT750 HD, GE Healthcare), rapidly alternating the tube voltage from 80 kV to 140 kV from projection to projection (Zhang et al. 2011). With this approach the low and high energy projections are acquired nearly simultaneously (one projection offset), so the temporal coherence is high. A drawback of the fast switching of the tube voltage is the fact that the tube current cannot be switched this fast between projections for technical reasons. The tube current is therefore fixed and also has to stay at a relatively high level to allow stable switching of the tube voltage. This leads to the problem that the tube current cannot be modulated according to the patient's anatomy and that the tube current is either too low for 80 kV or too high for 140 kV. Equal dose levels in the 80 and 140 kV projections can then only be achieved if each 80 kV projection is 2–4 times as long as the corresponding 140 kV projection. The fast switching between nominally 80 and 140 kV also leads to blurred spectra due to the imperfect transition, resulting in a reduced spectral separation. In 2013 Philips introduced a DECT system equipped with a dual-layer detector (Philips IQon Spectral CT) (Gabbai et al. 2015), after this approach has been studied for some time (Carmi et al. 2005). This approach uses a fixed kV setting of the tube (120 or 140 kV) and a special detector consisting of two layers of scintillators one above the other. The upper layer absorbs rather the low energy part of the incident X-ray spectrum, while the lower layer absorbs the high energy photons that have penetrated the upper scintillator. Since absorption is a statistical process, there is a strong overlap between the spectra detected by the two layers, leading to only a moderate spectral separation (Tkaczyk et al. 2007). The low and high energy projections are perfectly registered since the one detector layer is situated directly above the other, leading to an optimal temporal coherence. In 2013, Dual Source DECT was again improved (Siemens SOMATOM Force) for even better spectral separation by extending the available tube voltage range from 70 to 150 kV and by employing an even thicker tin filter (see Fig. 9) (Krauss et al. 2015).

In 2014 a new approach to dual-energy imaging was introduced: TwinBeam Dual Energy (Siemens Healthcare) (Euler et al. 2016), which is available for selected single source CT systems. This technique generates two different X-ray

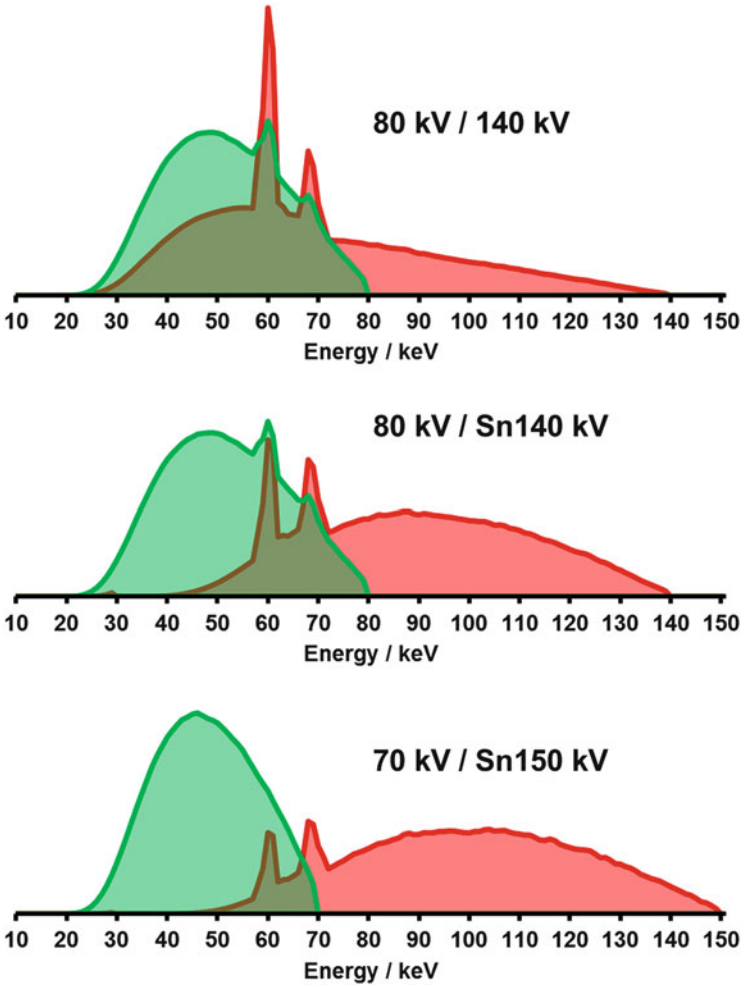

Fig. 9 Illustration of the spectral overlap between two different X-ray spectra as used for dual-energy imaging. The first situation applies to Dual Source DECT without additional tin filter for the high energy spectrum and also to a switching of the tube voltage either between two scans ("Dual Spiral" DECT) or between rotations (slow kV-switching DECT). However, the first scenario does not apply to fast kV-switching DECT, where the tube voltage is alternated between projections, with the fast switching leading to a blurring of the spectra and thus to an inferior spectral separation. Current X-ray tube technology also does not allow adjusting the tube current for the two tube voltages in fast kV-switching. The spectra shown in the middle represent the situation for Dual Source DECT with additional tin filter for the high energy spectrum. Compared to the 140 kV spectrum above, the tin filter shifts the spectrum to higher energies reducing the spectral overlap. The two spectra shown at the bottom are currently only available for 192-slice Dual Source DECT using Siemens' Vectron tube. The increased thickness of the tin filter and the higher tube voltage together with a low kV spectrum lead to an excellent spectral separation for high-accuracy dual-energy imaging

Fig. 10 The principle behind TwinBeam Dual Energy (Siemens Healthcare). Two different prefilters at the X-ray tube shift the spectrum to lower (Au120 kV) and higher energies (Sn120 kV), respectively. The two different spectra are incident simultaneously on the patient, being detected by either the first or second half of the detector

spectra from a 120 kV spectrum by using two different types of prefilters next to each other in *z*-direction at the X-ray tube: gold and tin, leading to an Au120 kV low energy and a Sn120 kV high energy spectrum. The tin removes the low energy photons from the spectrum and works in the same way as the tin filter employed in Dual Source DECT for the high energy spectrum. The gold filter shifts the incident 120 kV spectrum to lower energies due to its K-edge at 80.7 keV. The key is the higher absorption above the K-edge than below (see Fig. 7). The TwinBeam technology is also referred to as split filter. The filter generates two different X-ray spectra in *z*-direction that are simultaneously incident on the detector (see Fig. 10): Assuming a 64-row detector, basically the first 32 rows see the low energy spectrum and the second 32 rows the high energy spectrum. Since the low and high energy spectra are based on the same 120 kV spectrum, the resulting spectral separation is moderate. The TwinBeam DECT approach uses a spiral acquisition mode, and the temporal coherence can be as good as one rotation time offset. Another DECT technique is slow kV switching (currently available in Toshiba systems at 80 kV/135 kV, e.g., Aquilion ONE) (Cai et al. 2015), where the tube voltage is switched from rotation to rotation, as opposed to from projection to projection in fast kV-switching. The benefit of this approach over fast kV-switching is that the tube current can be modulated due to the slower switching. The slower switching of the tube voltage also leads to a better spectral separation since there is no more blurring in the transition time. The drawback over fast kV-switching is that the temporal coherence is at least one rotation offset, plus potential overlay times. Dual-energy data can of course also be generated by simply scanning the patient two times subsequently with two different X-ray spectra ("Dual Spiral" DECT). Each of the two scans uses approximately half of the dose of a comparable conventional single-energy scan. The problem with this method is the possible time delay between the two scans that can lead to a misalignment between the low and high energy datasets, i.e., having a low temporal coherence. While the misalignment can be corrected by employing an image registration algorithm, a more severe problem of the time delay is the fact that contrast agent dynamics lead to different iodine concentrations in the vessels and organs in the two scans. The

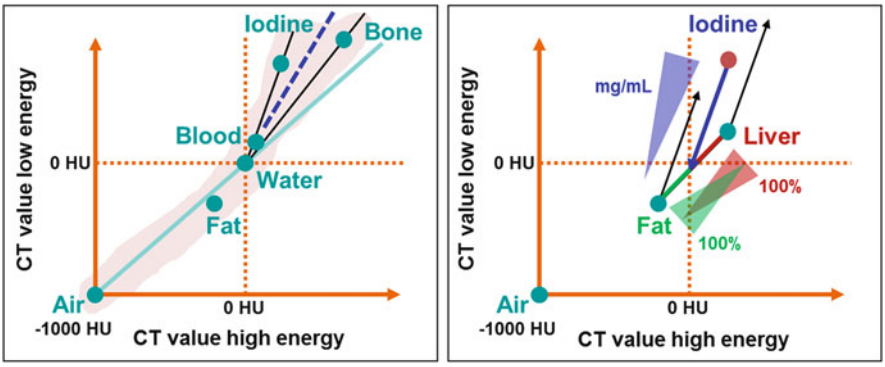

Fig. 11 Dual-energy data processing techniques illustrated in the dual-energy diagram. The approach on the left is referred to as material labeling, separating different types of materials based on their characteristic slope, e.g., iodine from bone by the *dashed blue line*. The graph on the right shows a material decomposition. In this case it is a three-material decomposition approach. The *brown dot* represents a hypothetical example voxel consisting of 50% fat and 50% liver tissue. By adding an iodinated contrast agent, the voxel is shifted in the direction of the iodine vector (*black arrows*) to its shown position. The three-material decomposition algorithm projects each voxel onto the soft tissue vector (defined by a fat and a liver reference point). The length of the displacement in iodine vector direction is proportional to the iodine concentration (*blue arrow*). The position on the soft tissue vector gives the relative fat (*green*) and liver tissue (*red*) contributions

severity of the time delay depends on the scan speed of the scanner and the scan range. Therefore, this "Dual Spiral" DECT method is not recommended, for example, for CTA applications or thorax imaging due to breathing and cardiac motion but applications where static structures are imaged. The spectral separation is good if 80 and 140 kV spectra are used, and in this case, it would be the same spectral separation as for slow kV switching at the same tube voltages (see Fig. 9).

As mentioned above, the power of DECT lies in its ability to characterize materials. Most DECT applications can be categorized as belonging to one of the two general dual-energy data processing classes: (quantitative) material decomposition and (qualitative) material labeling. Depending on the application additional segmentation, threshold, filtering, or other post-processing may be employed. The additional information derived from the dual-energy data is often displayed using a color-coded overlay on the grayscale images. Figure 11 shows the basic principle of the material decomposition and material labeling technique. The dual-energy data are presented in the dual-energy diagram, plotting the low energy CT value of an image voxel versus the high energy CT value of the same voxel. All voxels containing materials that behave like water regarding their energy dependence can be found on the diagonal in this diagram, i.e., having the same low and high energy CT value (slope of 1). Their exact position on this line depends on their density. This behavior is due to the water calibration of the CT system. Pure water should always have a CT value of 0 HU, independent of the applied spectrum. This is not true for other materials however. They may have different CT values in the

low and high energy images, which leads to a different behavior in this diagram, exhibiting a material characteristic slope. The spectral separation that was mentioned above has a large impact on this slope (Krauss et al. 2015), and a better spectral separation leads to a larger angle between two materials, e.g., water and iodine or bone and iodine, making them more reliably distinguishable. The material labeling technique (on the left in Fig. 11) makes use of this material slope and the position of a certain voxel in the dual-energy diagram to separate iodine from bone voxels for a bone removal or to separate different types of kidney stones. The material decomposition technique (on the right in Fig. 11) can be interpreted as a change of basis transformation to express the dual-energy information not in low energy/high energy CT value dimensions but as basis material concentrations. The dual-energy data is thus decomposed into the contributions of two basis materials, like water and iodine or water and bone. In contrast to material labeling, this decomposition can provide quantitative material information, e.g., an iodine concentration in mg/mL. In the dual-energy diagram, the new basis is given by the material vectors of the chosen basis materials. By employing a volume conservation constraint, material decomposition in three materials is possible. The situation shown on the right in Fig. 11 is a three-material decomposition using first an iodine vector and a soft tissue vector (defined by fat and liver tissue) to obtain an iodine image and a so-called virtual non-contrast (VNC or virtual unenhanced) image where the contrast agent has been removed as a surrogate for a native CT scan without contrast agent (Johnson 2012). Additionally, the relative contributions of fat and liver are identified. Another important type of application is monoenergetic (or monochromatic) imaging (Yu et al. 2011), where an image set at a user-selectable energy is generated, typically in the energy range from 40 to 190 keV. This is possible by using the polychromatic low and high energy data for a material decomposition into two basis materials or into the photoelectric effect and Compton scattering component of the absorption coefficient. From this information, it can be calculated how the attenuation would look like at different energies since the energy dependence of the chosen basis materials, or the photoelectric effect and Compton scattering, is known. This technique is also referred to as pseudo-monoenergetic or virtual monoenergetic imaging since the monoenergetic images are calculated from dual-energy data but have not actually been acquired at these energies using a truly monoenergetic X-ray source. In the following, a selection of today's DECT applications will be described.

Monoenergetic imaging is clinically employed to improve the iodine CNR in CTA studies or generally in contrast-enhanced examinations (Sudarski et al. 2014) by choosing low keV levels. Another application is the reduction of beam-hardening artifacts (Secchi et al. 2014) or even metal artifacts if the metal is not too dense or too abundant (Winklhofer et al. 2014). In this case rather high keV levels will be used. Monoenergetic imaging also has the potential to improve the soft tissue contrast, e.g., for gray-white matter differentiation (Postma et al. 2015). Conventional monoenergetic imaging generates a high contrast at low keV levels, but also the noise level increases, which can lead to a decreasing CNR at the lowest energy levels. The performance at low and high keV can be improved by using a novel frequency split approach (Monoenergetic Plus, Siemens Healthcare). This

algorithm uses the low spatial frequencies (containing mostly the object structures) from the target keV level and the high spatial frequencies (that represent mostly the image noise) from a keV level with optimal noise properties for mixing the final image. Benefits of this algorithm have been shown in several publications (Grant et al. 2014), and also contrast agent dose savings have been reported in this context (Meier et al. 2016).

In virtual unenhanced imaging, the iodine is subtracted from a contrast-enhanced scan, yielding a VNC image with the potential to replace the native scan, saving radiation dose and time. This application provides at the same time a quantitative iodine map showing the contrast agent distribution. The "Liver VNC" three-material decomposition algorithm (Siemens Healthcare) that was described in more detail above is designed for abdominal applications, like liver, kidney, or pancreas imaging (De Cecco et al. 2016) (see Fig. 12). The possibility to quantitatively measure the iodine uptake of lesions can be especially interesting for oncological applications, like treatment response monitoring (Uhrig et al. 2013). A similar algorithm—replacing fat and liver tissue as basis materials by air and soft tissue—may be applied in lung imaging, e.g., for the diagnosis of PE. The iodine content may be used as a surrogate for the perfused lung volume (Meinel et al. 2013).

Another widely used DECT application is urinary stone characterization. This is a material labeling application separating uric acid-based stones from non-uric acid stones (see Fig. 13), which is relevant for the treatment decision: dissolve uric acid stones using medication versus shock wave lithotripsy or even interventions (Jepperson et al. 2013).

There is another prominent material labeling application that is looking at monosodium urate (MSU) crystal deposits. The gout application visualizes the

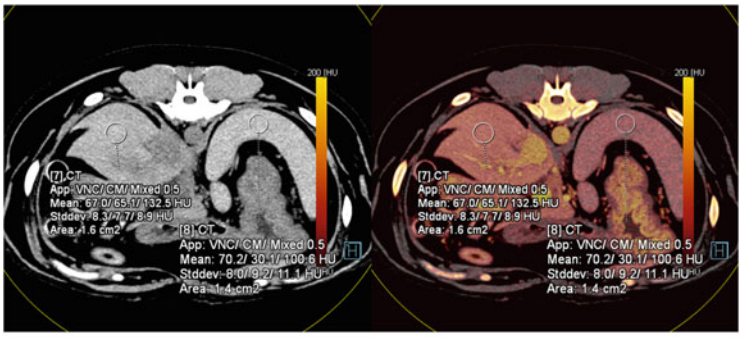

Fig. 12 The Liver VNC application (Siemens Healthcare) uses DECT data to calculate a virtual non-contrast image (VNC, on the *left*) where the contrast agent has been removed as a surrogate for a native scan. The image on the *right* shows the iodine distribution using a *color* coding as an overlay on the VNC image. The ROI measurement directly shows the mean CT value and the standard deviation for the VNC image, the enhancement due to contrast agent (CM), and the mixed image (Data courtesy of San Marco Veterinary Clinic, Padova, Italy)

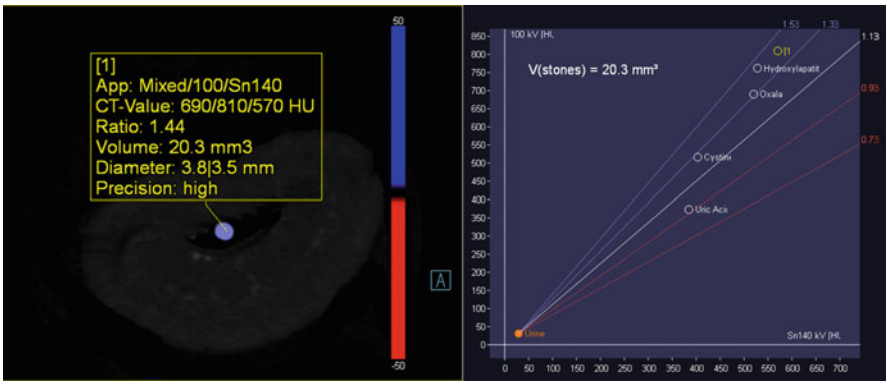

Fig. 13 Images from the Calculi Characterization application (Siemens Healthcare). The material labeling uses a red color for uric acid stones and a *blue color* for non-uric acid stones. The stone ROI does not only show the CT value in the low energy, high energy, and mixed image, as well as volume and dimension information, but also the dual-energy ratio, which corresponds to the material characteristic slope in the dual-energy diagram as shown in Fig. 11. This information is shown in more detail in the graph on the right. Combined with different reference points of stone materials, this allows a more specific stone characterization (Data courtesy of San Marco Veterinary Clinic, Padova, Italy)

distribution and quantity of MSU crystals, helping in the differential diagnosis of gout, possibly avoiding joint aspirations (Melzer et al. 2014).

Bone removal is supported by dual-energy information, separating bone from iodine using a material labeling approach (see Fig. 14), e.g., for better vessel visualization in CTA studies of the trunk (Schulz et al. 2012).

Lately, a new DECT application has become commercially available for bone marrow imaging. It is three-material decomposition-based "virtual non-calcium" imaging, where the calcium is removed allowing assessing differences in the density of the underlying bone marrow. This application may be used in cases of traumatic or compression fractures (Kaup et al. 2016) or multiple myeloma lesions (Thomas et al. 2015).

Another recently available application is a material decomposition to yield the electron density (rho) and the effective atomic number (Z) distribution (rho/Z, Siemens Healthcare). These two physical parameters are material-specific and relevant for the absorption properties of a material and may therefore be used for general material characterization and may be of future interest for radiation therapy treatment planning, especially for the treatment with ions.

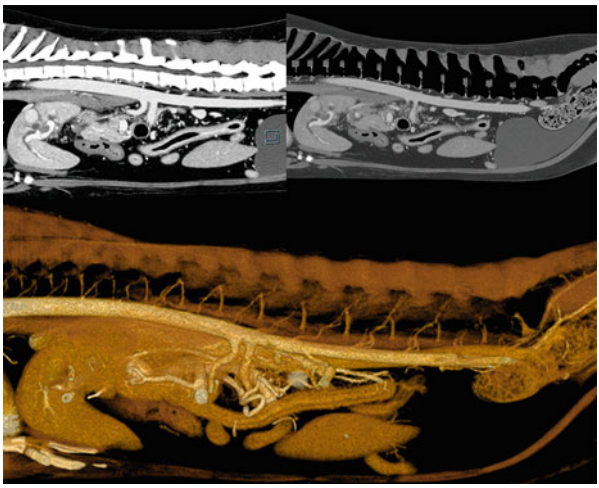

Fig. 14 Illustration of a bone removal. The sagittal image on the *top left* still contains all bony structures. In the image on the *top right*, the bones have been removed, allowing a better view on the vasculature as shown at the *bottom* (Data courtesy of San Marco Veterinary Clinic, Padova, Italy)

4 Post-processing Applications

CT data are not always read in their natural axial slices; today there are many different types of post-processing applications available that may either be conducted at the scanner console (manually or even automatically), a separate workstation, or also at a console of the picture archiving and communication system (PACS), depending on the type of application, its availability, and the working environment. Standardization becomes more and more important with the increasing amount of information available to the physician. Intelligent reading and post-processing software supports the reader in handling the data efficiently and in a standardized way with less and less manual interaction. Some software is already able to recognize the required post-processing on a case-by-case basis, automatically conduct the desired post-processing steps, and send the resulting images to PACS (e.g., *syngo*.via with Rapid Results Technology, Siemens Healthcare).

Nevertheless, the axial slice images are the basis for all further processing, and their reconstruction parameters should thus carefully be considered. While in many cases thin slices are always acquired (e.g., 0.6 mm collimated slice width), the reconstruction of the raw data allows selecting a wide range of slice thicknesses (e.g., 0.6–10 mm) and slice increments. Thicker slices are often used for primary viewing and PACS archiving and thin submillimeter slices for evaluation and post-processing. Choosing the slice increment smaller than the slice thickness improves the resolution in z-direction of the image volume but generates more image slices. Using an increment that is 0.5–0.7 times the slice thickness, object sizes down to 0.7–0.9 times the reconstructed slice thickness may be resolved. The image slices are typically reconstructed on a 512×512 matrix; some vendors provide up to 1024×1024 matrices for reconstruction. The choice of the FOV defines the in-plane voxel size according to the equation FOV/matrix size, e.g., 500 mm/$512 \approx 0.98$ mm voxel size or 300 mm/$512 \approx 0.59$ mm voxel size. The voxel size

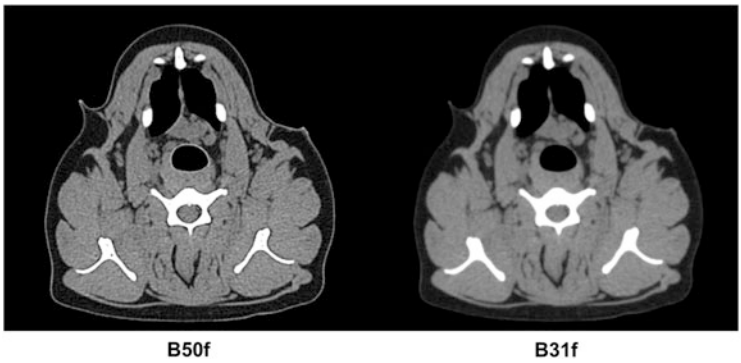

Fig. 15 Comparison of two different reconstruction kernels. The kernel on the *left* is a sharper kernel for lung or bone imaging. The one on the *right* is a smoother soft tissue kernel. With the higher sharpness comes a higher image noise level (Data courtesy of San Marco Veterinary Clinic, Padova, Italy)

in *z*-direction is defined by the reconstructed slice thickness. It is important to note that the voxel size is not necessarily equivalent to the spatial resolution. Another important parameter in image reconstruction with a large impact on the in-plane spatial resolution is the choice of the reconstruction kernel (see Fig. 15). The kernels typically used for soft tissue applications limit the spatial resolution to around 0.6 mm object size. This matches the voxel size of a conventional FOV (30 cm) and also the minimum available slice thickness of 0.6 mm for many systems, leading to an isotropic spatial resolution. Only the sharpest kernels, e.g., for bone evaluation, may provide an in-plane spatial resolution of around 0.3 mm (limited by the scanner hardware, like sampling, focal spot size, detector element size). In this case, a smaller FOV must be chosen to be able to benefit from the high spatial resolution (e.g., 150 mm/512 $\approx$ 0.29 mm). The reconstruction kernel has no impact on the resolution in *z*-direction. This is governed by the reconstructed slice thickness. Thicker slices show less image noise but at the expense of less spatial resolution. This problem can be avoided to some extent by using thin reconstructed slices and view them as slab maximum intensity projection of a few millimeter slab thickness. Such viewing concepts will be discussed in the following.

The axial images are building up a three-dimensional image volume; a multiplanar reformation (MPR) lets the user interact with this volume by placing an image plane with the desired orientation in this volume. All voxels that are cut by this plane are visualized in a planar image. The spatial resolution of the MPR is thus defined by both the in-plane spatial resolution and the one in *z*-direction, with the relative contribution depending on the plane's orientation. MPR quality benefits from an isotropic spatial resolution, by choosing appropriate reconstruction parameters as discussed above. Considering axial images as an MPR parallel to the *x*-*y*-plane (transverse plane in veterinary patients), two other perpendicular imaging planes are often chosen for reconstruction as well, e.g., in thoracic imaging: the sagittal MPRs (parallel to *y*-*z*-plane) and coronal MPRs (parallel to *x*-*z*-plane; dorsal plane in veterinary patients) (Fig. 16). While these orthogonal planes are

Fig. 16 MPR showing the three orthogonal imaging planes: an axial (transverse), a coronal (dorsal), and a sagittal plane of a lung (Data courtesy of San Marco Veterinary Clinic, Padova, Italy)

quite suitable for lung imaging, other organs may benefit from using oblique MPRs, i.e., inclined planes in arbitrary orientation. To image the coronary arteries with their tortuous course, for example, oblique MPRs along the left anterior descending artery or the right coronary artery may be useful. It is also possible to generate so-called curved MPRs, calculated on a curved plane but displayed as a flat two-dimensional image. Such curved planes can either be manually defined by the user, or they can be the result of an automatic centerline tracing through a vessel. In this way, curved MPRs allow to follow the course of a winding vessel. Advanced post-processing software does this automatically for the coronary arteries, for example, to facilitate stenosis assessment. The slab thickness of the MPR can be modified as well. The slab thickness is defined as the range in which the voxel values are averaged orthogonal to the chosen view plane, i.e., it is the "slice thickness" of the MPR. This allows trading off resolution for less image noise. MPRs maintain the same full information as the axial images; no information is discarded. However, the positioning of the view planes depends on the operator if done manually, and improper positioning may have a negative impact on the diagnosis.

Another way of looking at the three-dimensional image volume is using a maximum intensity projection (MIP). Like for MPRs the user may select arbitrary viewing planes in the volume, and the MIP algorithm searches for the maximum CT values along parallel rays in viewing direction and displays these values. The rays are cast orthogonally to the viewing plane through the volume. A MIP preserves the grayscale and the visual perception of image sharpness while lowering the perceived noise level. However, MIPs do not maintain the full information of the axial images since they are rather projection images where the depth information is lost and high-density structures obscure structures of lower attenuation. MIPs allow for a good differentiation between contrast agent-enhanced structures and background, e.g., in vascular imaging. High-contrast structures like calcifications and bones are well visualized. A bone removal may be required to avoid the bone superimposing the vasculature. The missing depth information can be disadvantageous for visualizing complex structures like the thoracic vasculature. This situation can be improved by using so-called thin-slap MIPs (Napel et al. 1993). This type of MIP

does not display the maximum CT value along the complete ray through the whole volume but only in a user-selectable distance perpendicular to the viewing plane. This distance is the slab thickness, the same concept as for slab MPRs. For visualizing the coronary arteries, typical slab thicknesses are ranging from 3 to 10 mm. Interactive software allows scrolling through the volume using thin-slab MIPs; this is referred to as sliding thin-slab MIP. The calculation can be done on the fly. Also curved thin-slab MIPs are available (Raman et al. 2003), like there are curved MPRs, with the same advantage of being able to follow curved structures like vessels. Although thin-slab MIPs show the maximum CT value of only a limited range, they are, for example, not suitable for visualizing the in-stent lumen due to their projection nature. Also the display of blood clots in the pulmonary arteries for the diagnosis of PE is not recommended with MIPs. However, the visualization of plaques, e.g., in the coronary arteries, is excellent when an appropriate slap thickness is used. There exists also the contrary concept of minimum intensity projection (MinIP) that displays the minimum CT value, which can be used to visualize air in the body or the airways.

Three-dimensional data can also be animated by using computer graphics technology to generate a so-called shaded surface display (SSD) (Calhoun et al. 1999). The origin of this technology is nearly as old as CT itself and uses a threshold-based surface definition. Starting at the point of view along rays, all the first voxels exceeding the preset threshold value define the surface by making these voxels totally opaque; all succeeding voxels behind are not considered. Virtual light sources are used to generate shading effects and improve the three-dimensional impression of the SSD. This type of processing discards the original CT values and only shows the information on the defined surface but nothing behind, dismissing a lot of information from the dataset. The threshold must thus be chosen with care. If the threshold is set to a very low CT value, only the patient's skin or clothes will form the surface, and everything inside is not visible. The displayed object can be interactively turned and viewed from all directions. Applications of SSDs can be found, for example, in surgical planning (Franca et al. 2000).

The next step in the evolution of computer-rendered three-dimensional volumes is the volume rendering (VR) technique (Calhoun et al. 1999). Unlike SSDs, which only consider the first voxel that exceeds the defined threshold along the viewing rays, VRs can make use of all the voxels along the viewing rays. All these voxels contribute according to their opacity, which is defined by a transfer function assigning a certain opacity to a certain CT value. The opacity describes the absorption of light. A voxel with opacity 1 is fully absorbing and thus completely opaque, while opacity 0 means a fully transparent and thus invisible voxel. When a ray hits a voxel of opacity 1, only this voxel will be shown, and the contribution of all other voxels of lower opacity is set to 0. The user can adjust the transfer function according to the needs, making certain structures more or less transparent. Transfer functions are usually of linear, triangular, or trapezoidal shape over a range of CT values. VRs that only use the opacity as a parameter are still grayscale images since the resulting image is a weighted sum of CT values. The user can additionally apply a color lookup table to the CT values, e.g., a brownish red to CT values in the range

of soft tissue and white to the higher CT values of bone. VR software may have additional features like transfer functions that take the local CT value gradient into account. A homogeneous region with small CT value changes, and thus a low gradient will be assigned a reduced opacity (higher transparency), and regions with strong changes of the CT value (high gradient) will have an increased opacity (lower transparency) to enhance the visualization of boundaries. To improve the three-dimensional appearance of the VR images, different lighting and shading techniques can be applied, calculating from the ambient light the diffuse and specular reflections in the direction of the point of view. VRs may require a lot of user interaction for good image results. Segmentation of surrounding or overlapping structures may be necessary if not done automatically, e.g., to isolate the heart. VRs should be used with caution due to the various parameters and potential pitfalls if applied incorrectly. However, VRs are helpful to display anatomical structures in an interactive and three-dimensional way, e.g., to communicate findings to patients or to visualize anomalous anatomy. VRs can also be used

Fig. 17 Example for Cinematic Rendering in a canine trauma case. The *top* image shows a rendering using a soft tissue window setting; the image below uses a bone window, revealing fractures of the transverse processes of several vertebrae and fractures of the pelvis. The image at the *bottom* gives a detailed view of the situation in the pelvis (Data courtesy of San Marco Veterinary Clinic, Padova, Italy)

for noninvasive virtual endoscopy (Rubin et al. 1996), like CT colonoscopy (Macari et al. 2002).

Recently, a new type of volume rendering technique has been introduced that simulates the interaction of photons with the anatomy to generate a very realistic image impression (Cinematic Rendering, *syngo*.via VB20, Siemens Healthcare) (Dappa et al. 2016). The incident photons are simulated in a Monte Carlo approach, allowing a much more realistic simulation of the physical effects influencing the behavior of the optical photons than what is done in conventional VRs (see Fig. 17). This approach was inspired by technology that is used to render animated movies. Applications may go beyond the ones of VRs, e.g., to virtual anatomy teaching.

There are also many other advanced applications supporting the reader, e.g., a bone unfolding (an unfolding of the rips or the skull onto a flat plane) that facilitates the detection of lesions like fractures (Bier et al. 2016) or an automatic spine labeling.

References

Achenbach S, Ulzheimer S, Baum U, et al. Noninvasive coronary angiography by retrospectively ECG-gated multislice spiral CT. Circulation. 2000;102:2823–8.

Alvarez RE, Macovski A. Energy-selective reconstructions in x-ray computerised tomography. Phys Med Biol. 1976;21:733.

Bier G, Mustafa DF, Kloth C, et al. Improved follow-up and response monitoring of thoracic cage involvement in multiple myeloma using a novel CT postprocessing software: the lessons we learned. Am J Roentgenol. 2016;206:57–63.

Bittner DO, Arnold M, Klinghammer L, et al. Contrast volume reduction using third generation dual source computed tomography for the evaluation of patients prior to transcatheter aortic valve implantation. Eur Radiol. 2016;26:4497–504.

Bridoux A, Hutt A, Faivre J-B, et al. Coronary artery visibility in free-breathing young children on non-gated chest CT: impact of temporal resolution. Pediatr Radiol. 2015;45:1761–70.

Cai X-R, Feng Y-Z, Qiu L, et al. Iodine distribution map in dual-energy computed tomography pulmonary artery imaging with rapid kVp switching for the diagnostic analysis and quantitative evaluation of acute pulmonary embolism. Acad Radiol. 2015;22:743–51.

Calhoun PS, Kuszyk BS, Heath DG, et al. Three-dimensional volume rendering of spiral CT Data: theory and method 1. Radiographics. 1999;19:745–64.

Carmi R, Naveh G, Altman A. Material separation with dual-layer CT. IEEE; 2005, 3 pp.

Caruso D, Eid M, Schoepf UJ, et al. Dynamic CT myocardial perfusion imaging. Eur J Radiol. 2016;85:1893–9.

Coche E, Vlassenbroek A, Roelants V, et al. Evaluation of biventricular ejection fraction with ECG-gated 16-slice CT: preliminary findings in acute pulmonary embolism in comparison with radionuclide ventriculography. Eur Radiol. 2005;15:1432–40.

Dappa E, Higashigaito K, Fornaro J, et al. Cinematic rendering–an alternative to volume rendering for 3D computed tomography imaging. Insights Imaging. 2016;7:849–56.

De Cecco CN, Muscogiuri G, Schoepf UJ, et al. Virtual unenhanced imaging of the liver with third-generation dual-source dual-energy CT and advanced modeled iterative reconstruction. Eur J Radiol. 2016;85:1257–64.

Dewey M, Zimmermann E, Deissenrieder F, et al. Noninvasive coronary angiography by 320-row computed tomography with lower radiation exposure and maintained diagnostic accuracy. Circulation. 2009;120:867–75.

Duan X, Wang J, Leng S, et al. Electronic noise in CT detectors: impact on image noise and artifacts. Am J Roentgenol. 2013;201:W626–32.

Engel KJ, Herrmann C, Zeitler G. X-ray scattering in single-and dual-source CT. Med Phys. 2008;35:318–32.

Euler A, Parakh A, Falkowski AL, et al. Initial results of a single-source dual-energy computed tomography technique using a split-filter: assessment of image quality, radiation dose, and accuracy of dual-energy applications in an in vitro and in vivo study. Investig Radiol. 2016;51:491–8.

Faby S, Kuchenbecker S, Sawall S, et al. Performance of today's dual energy CT and future multi energy CT in virtual non-contrast imaging and in iodine quantification: a simulation study. Med Phys. 2015;42:4349–66.

Flohr T, Stierstorfer K, Bruder H, et al. New technical developments in multislice CT – Part 1: approaching isotropic resolution with sub-millimeter 16-slice scanning. ROFO Fortschr Geb Rontgenstr Nuklearmed. 2002;174:839–45.

Flohr T, Stierstorfer K, Ulzheimer S, et al. Image reconstruction and image quality evaluation for a 64-slice CT scanner with z-flying focal spot. Med Phys. 2005;32:2536–47.

Flohr TG, McCollough CH, Bruder H, et al. First performance evaluation of a dual-source CT (DSCT) system. Eur Radiol. 2006;16:256–68.

Flohr TG, Leng S, Yu L, et al. Dual-source spiral CT with pitch up to 3.2 and 75 ms temporal resolution: Image reconstruction and assessment of image quality. Med Phys. 2009;36:5641–53.

Flohr TG, De Cecco CN, Schmidt B, et al. Computed tomographic assessment of coronary artery disease: state-of-the-art imaging techniques. Radiol Clin N Am. 2015;53:271–85.

Franca C, Levin-Plotnik D, Sehgal V, et al. Use of three-dimensional spiral computed tomography imaging for staging and surgical planning of head and neck cancer. J Digit Imaging. 2000;13:24–32.

Gabbai M, Leichter I, Mahgerefteh S, Sosna J. Spectral material characterization with dual-energy CT: comparison of commercial and investigative technologies in phantoms. Acta Radiol. 2015;56:960–9.

George RT, Mehra VC, Chen MY, et al. Myocardial CT perfusion imaging and SPECT for the diagnosis of coronary artery disease: a head-to-head comparison from the CORE320 multi-center diagnostic performance study. Radiology. 2014;272:407–16.

Gordic S, Husarik DB, Desbiolles L, et al. High-pitch coronary CT angiography with third generation dual-source CT: limits of heart rate. Int J Cardiovasc Imaging. 2014;30:1173–9.

Grant KL, Flohr TG, Krauss B, et al. Assessment of an advanced image-based technique to calculate virtual monoenergetic computed tomographic images from a dual-energy examination to improve contrast-to-noise ratio in examinations using iodinated contrast media. Investig Radiol. 2014;49:586–92.

Haubenreisser H, Bigdeli A, Meyer M, et al. From 3D to 4D: Integration of temporal information into CT angiography studies. Eur J Radiol. 2015;84:2421–4.

Hou DJ, Tso DK, Davison C, et al. Clinical utility of ultra high pitch dual source thoracic CT imaging of acute pulmonary embolism in the emergency department: are we one step closer towards a non-gated triple rule out? Eur J Radiol. 2013;82:1793–8.

Jepperson MA, Cernigliaro JG, Sella D, et al. Dual-energy CT for the evaluation of urinary calculi: image interpretation, pitfalls and stone mimics. Clin Radiol. 2013;68:e707–14.

Johnson TR. Dual-energy CT: general principles. Am J Roentgenol. 2012;199:S3–8.

Johnson TR, Nikolaou K, Wintersperger BJ, et al. ECG-gated 64-MDCT angiography in the differential diagnosis of acute chest pain. Am J Roentgenol. 2007;188:76–82.

Kalender WA, Perman W, Vetter J, Klotz E. Evaluation of a prototype dual-energy computed tomographic apparatus. I. Phantom studies. Med Phys. 1986;13:334–9.

Kalender WA, Seissler W, Klotz E, Vock P. Spiral volumetric CT with single-breath-hold technique, continuous transport, and continuous scanner rotation. Radiology. 1990;176:181–3.

Kaup M, Wichmann JL, Scholtz J-E, et al. Dual-energy CT–based display of bone marrow edema in osteoporotic vertebral compression fractures: impact on diagnostic accuracy of radiologists with varying levels of experience in correlation to MR imaging. Radiology. 2016;280:510–9.
Klingenbeck-Regn K, Schaller S, Flohr T, et al. Subsecond multi-slice computed tomography: basics and applications. Eur J Radiol. 1999;31:110–24.
Krauss B, Grant KL, Schmidt BT, Flohr TG. The importance of spectral separation: an assessment of dual-energy spectral separation for quantitative ability and dose efficiency. Investig Radiol. 2015;50:114–8.
Leber AW, Knez A, von Ziegler F, et al. Quantification of obstructive and nonobstructive coronary lesions by 64-slice computed tomography: a comparative study with quantitative coronary angiography and intravascular ultrasound. J Am Coll Cardiol. 2005;46:147–54.
Lell MM, Jost G, Korporaal JG, et al. Optimizing contrast media injection protocols in state-of-the art computed tomographic angiography. Investig Radiol. 2015;50:161–7.
Li B, Toth TL, Hsieh J, Tang X. Simulation and analysis of image quality impacts from single source, ultra-wide coverage CT scanner. J X-Ray Sci Technol. 2012;20:395–404.
Liang Y, Kruger RA. Dual-slice spiral versus single-slice spiral scanning: comparison of the physical performance of two computed tomography scanners. Med Phys. 1996;23:205–20.
Macari M, Bini EJ, Xue X, et al. Colorectal neoplasms: prospective comparison of thin-section low-dose multi–detector row CT colonography and conventional colonoscopy for detection 1. Radiology. 2002;224:383–92.
Manniesing R, Oei MT, van Ginneken B, Prokop M. Quantitative dose dependency analysis of whole-brain CT perfusion imaging. Radiology. 2015;278:190–7.
Meier A, Higashigaito K, Martini K, et al. Dual energy CT pulmonary angiography with 6g iodine—a propensity score-matched study. PLoS One. 2016;11:e0167214.
Meinel FG, Graef A, Bamberg F, et al. Effectiveness of automated quantification of pulmonary perfused blood volume using dual-energy CTPA for the severity assessment of acute pulmonary embolism. Investig Radiol. 2013;48:563–9.
Melzer R, Pauli C, Treumann T, Krauss B. Gout tophus detection—a comparison of dual-energy CT (DECT) and histology. Semin Arthritis Rheum. 2014;43:662–5.
Mori S, Endo M, Tsunoo T, et al. Physical performance evaluation of a 256-slice CT-scanner for four-dimensional imaging. Med Phys. 2004;31:1348–56.
Morsbach F, Sah B-R, Spring L, et al. Perfusion CT best predicts outcome after radioembolization of liver metastases: a comparison of radionuclide and CT imaging techniques. Eur Radiol. 2014;24:1455–65.
Napel S, Rubin GD, Jeffrey RB. STS-MIP: a new reconstruction technique for CT of the chest. J Comput Assist Tomogr. 1993;17:832–8.
Nieman K, Cademartiri F, Lemos PA, et al. Reliable noninvasive coronary angiography with fast submillimeter multislice spiral computed tomography. Circulation. 2002;106:2051–4.
Ohnesorge B, Flohr T, Becker C, et al. Cardiac imaging by means of electrocardiographically gated multisection spiral CT: initial experience 1. Radiology. 2000;217:564–71.
Ohno Y, Koyama H, Matsumoto K, et al. Differentiation of malignant and benign pulmonary nodules with quantitative first-pass 320–detector row perfusion CT versus FDG PET/CT. Radiology. 2011;258:599–609.
Petersilka M, Bruder H, Krauss B, et al. Technical principles of dual source CT. Eur J Radiol. 2008;68:362–8.
Petersilka M, Stierstorfer K, Bruder H, Flohr T. Strategies for scatter correction in dual source CT. Med Phys. 2010;37:5971–92.
Petersilka M, Allmendinger T, Stierstorfer K. 3D image-based scatter estimation and correction for multi-detector CT imaging. International Society for Optics and Photonics; 2014. pp. 903309–903309.
Postma AA, Das M, Stadler AA, Wildberger JE. Dual-energy CT: what the neuroradiologist should know. Curr Radiol Rep. 2015;3:1–16.

Primak A, Ramirez Giraldo J, Liu X, et al. Improved dual-energy material discrimination for dual-source CT by means of additional spectral filtration. Med Phys. 2009;36:1359–69.
Raju R, Cury RC, Precious B, et al. Comparison of image quality, and diagnostic interpretability of a new volumetric high temporal resolution scanner versus 64-slice MDCT. Clin Imaging. 2016;40:205–11.
Raman R, Napel S, Rubin GD. Curved-slab maximum intensity projection: method and evaluation. Radiology. 2003;229(1):255–60.
Remy-Jardin M, Tillie-Leblond I, Szapiro D, et al. Spiral CT angiography (SCTA) of pulmonary embolism (PE) in patients with underlying respiratory disease: impact of multislice CT (MSCT) on image quality and diagnostic accuracy. Eur Radiol. 2002;12:149.
Rubin GD, Beaulieu CF, Argiro V, et al. Perspective volume rendering of CT and MR images: applications for endoscopic imaging. Radiology. 1996;199:321–30.
Rybicki FJ, Otero HJ, Steigner ML, et al. Initial evaluation of coronary images from 320-detector row computed tomography. Int J Cardiovasc Imaging. 2008;24:535–46.
Sabel BO, Buric K, Karara N, et al. High-pitch CT pulmonary angiography in third generation dual-source CT: image quality in an unselected patient population. PLoS One. 2016;11:e0146949.
Salem R, Remy-Jardin M, Delhaye D, et al. Integrated cardio-thoracic imaging with ECG-gated 64-slice multidetector-row CT: initial findings in 133 patients. Eur Radiol. 2006;16:1973–81.
Sandfort V, Ahlman MA, Jones EC, et al. High pitch third generation dual-source CT: coronary and cardiac visualization on routine chest CT. J Cardiovasc Comput Tomogr. 2016;10:282–8.
Schoepf UJ, Becker CR, Hofmann LK, et al. Multislice CT angiography. Eur Radiol. 2003;13:1946–61.
Schulz B, Kuehling K, Kromen W, et al. Automatic bone removal technique in whole-body dual-energy CT angiography: performance and image quality. Am J Roentgenol. 2012;199:W646–50.
Secchi F, De Cecco CN, Spearman JV, et al. Monoenergetic extrapolation of cardiac dual energy CT for artifact reduction. Acta Radiol. 2014. doi:10.1177/0284185114527867.
So A, Imai Y, Nett B, et al. Technical note: evaluation of a 160-mm/256-row CT scanner for whole-heart quantitative myocardial perfusion imaging. Med Phys. 2016;43:4821–32.
Sudarski S, Apfaltrer P, Nance JW, et al. Objective and subjective image quality of liver parenchyma and hepatic metastases with virtual monoenergetic dual-source dual-energy CT reconstructions: an analysis in patients with gastrointestinal stromal tumor. Acad Radiol. 2014;21:514–22.
Sun M, Lu B, Wu R, et al. Diagnostic accuracy of dual-source CT coronary angiography with prospective ECG-triggering on different heart rate patients. Eur Radiol. 2011;21:1635–42.
Thomas C, Schabel C, Krauss B, et al. Dual-energy CT: virtual calcium subtraction for assessment of bone marrow involvement of the spine in multiple myeloma. Am J Roentgenol. 2015;204:W324–31.
Tkaczyk JE, Rodrigues R, Shaw J, et al. Atomic number resolution for three spectral CT imaging systems. International Society for Optics and Photonics; 2007. pp. 651009–651009.
Tomizawa N, Maeda E, Akahane M, et al. Coronary CT angiography using the second-generation 320-detector row CT: assessment of image quality and radiation dose in various heart rates compared with the first-generation scanner. Int J Cardiovasc Imaging. 2013;29:1613–8.
Uhrig M, Sedlmair M, Schlemmer H, et al. Monitoring targeted therapy using dual-energy CT: semi-automatic RECIST plus supplementary functional information by quantifying iodine uptake of melanoma metastases. Cancer Imaging. 2013;13:306.
Westwood ME, Raatz HD, Misso K, et al. Systematic review of the accuracy of dual-source cardiac CT for detection of arterial stenosis in difficult to image patient groups. Radiology. 2013;267:387–95.
Willems PW, Taeshineetanakul P, Schenk B, et al. The use of 4D-CTA in the diagnostic work-up of brain arteriovenous malformations. Neuroradiology. 2012;54:123–31.

Winklehner A, Gordic S, Lauk E, et al. Automated attenuation-based tube voltage selection for body CTA: Performance evaluation of 192-slice dual-source CT. Eur Radiol. 2015;25:2346–53.

Winklhofer S, Benninger E, Spross C, et al. CT metal artefact reduction for internal fixation of the proximal humerus: value of mono-energetic extrapolation from dual-energy and iterative reconstructions. Clin Radiol. 2014;69:e199–206.

Yu L, Christner JA, Leng S, et al. Virtual monochromatic imaging in dual-source dual-energy CT: radiation dose and image quality. Med Phys. 2011;38:6371–9.

Zhang D, Li X, Liu B. Objective characterization of GE discovery CT750 HD scanner: gemstone spectral imaging mode. Med Phys. 2011;38:1178–88.

Zhang LJ, Zhao YE, Schoepf UJ, et al. Seventy–peak kilovoltage high-pitch thoracic aortic CT angiography without ECG gating: evaluation of image quality and radiation dose. Acad Radiol. 2015;22:890–7.

Part II
MDCT Angiography

Basic Principles of MDCT Angiography

Giovanna Bertolini

1 Introduction

Computed tomography angiography (CTA) is among the most impressive achievements in diagnostic imaging. CTA was developed in the early 1990s, with the advent of spiral CT. The continuous gantry rotation and table movement of spiral CT enabled the coverage of limited body regions so rapidly that the transient enhancement of vascular structures after contrast medium injection could be visualized with a single scan. In 1998, most manufacturers introduced four-detector row scanners with rotation times of 0.5 s, which substantially enhanced scanning performance compared with single-slice CT.

Multidetector-row computed tomography angiography (MDCTA) was first used for dogs and cats in the early 2000s. Although this modality immediately showed tremendous potential for a variety of clinical applications in small animals, its diffusion in veterinary practice took 10 years. Initially, veterinary radiologists did not understand that a revolution was occurring in the field of advanced imaging. The initial cost of MDCT scanners was another likely reason for the delay in MDCT diffusion. Over the past few years, with the worldwide distribution of new and refurbished scanners in many university radiology departments and private practices, MDCT has gained a tremendous boost and MDCTA is now accepted widely as the standard technique for vascular imaging.

MDCTA is a highly standardizable imaging technique. It provides three-dimensional (3D) information about the vasculature and enables simultaneous evaluation of the vascular lumen, as well as the vessel wall and surrounding structures. However, continuous advances in CT technology often exceed radiologists' ability to use these advanced scanners in an optimal or appropriate manner. An

G. Bertolini (✉)
San Marco Veterinary Clinic, Padua, Italy
e-mail: bertolini@sanmarcovet.it

G. Bertolini (ed.), *Body MDCT in Small Animals*, DOI 10.1007/978-3-319-46904-1_2

understanding of the principal technical factors for MDCTA is essential to achieve consistently high-quality results, especially in veterinary patients.

2 Contrast Medium Distribution

The use of contrast medium (CM) for MDCTA is essential. CM is generally injected through an intravenous catheter placed in a peripheral vein. When injected into a cephalic vein, CM reaches the heart and then travels throughout the body in the cardiovascular circulation.

The intravascular, interstitial, and intracellular spaces are the three main fluid compartments in the body. CM is transported exclusively in the plasma and does not interact with the organism, as it does not penetrate the membranes of cells, with the exception of hepatocytes.

Thus, CM distribution consists of two phases: an initial intravascular phase and a second extravascular phase, in which the CM redistributes from the vascular to the interstitial spaces of the organs (Fig. 1).

The *first phase (intravascular)* of CM distribution within the body is useful for MDCTA. CM delivery during this phase depends on circulatory dynamics. The *second phase (interstitial)* is useful for tissue-perfusion studies. In the second phase, CM enhancement depends on blood volume and the permeability of each specific tissue or organ. During the first phase, hemodynamic physiological and physiopathological changes direct the distribution of CM within the body in the same way as for blood.

Organs with exclusively arterial blood supplies, such as the lungs, spleen, and kidneys, enhance rapidly during the first pass in the right atrium. In the second phase, CM mixed in the blood is transported to the periphery of the circulatory system, where it passes through the pores of the capillary endothelium into the interstitium. Regulatory factors for CM distribution during this phase are the

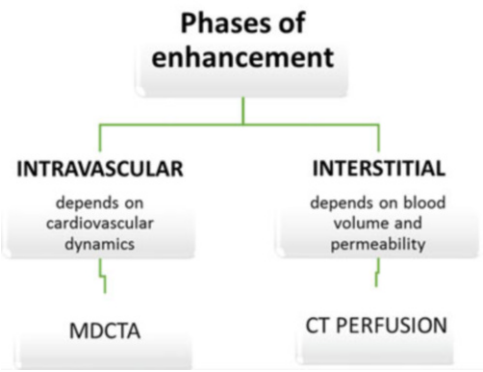

Fig. 1 Phases of CM distribution in the body. The first, or intravascular, phase is useful for vascular studies. The second, or interstitial, phase is an extravascular phase that is useful for tissue perfusion studies

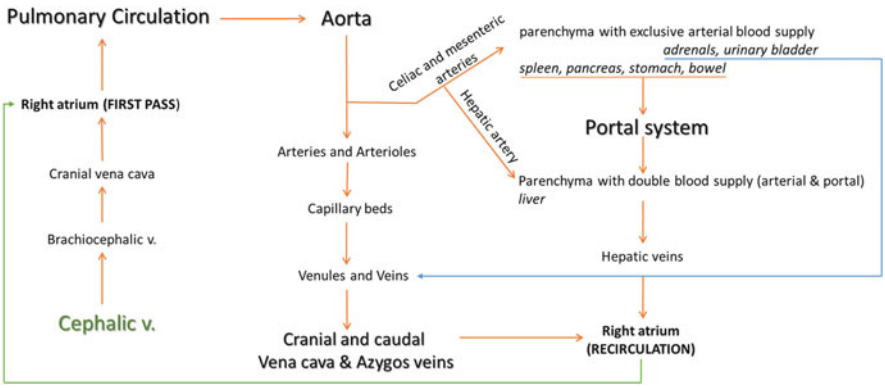

Fig. 2 Schematization of CM distribution in the vascular system following peripheral injection (via the cephalic vein)

osmotic pressure of plasma, hydrostatic pressure, and permeability of the capillary wall. CM dynamics within the body are summarized in Fig. 2.

2.1 Contrast Enhancement

Anatomic coverage, CM protocol, acquisition and reconstruction parameters, and post-processing techniques are all important factors to be considered when designing an MDCTA protocol. The goal in practice is to achieve adequate opacification of the vascular territory of interest (*magnitude of contrast enhancement*), within a certain time (*timing of contrast enhancement*), and to maintain a consistent level of enhancement throughout scanning (*shaping of contrast medium*).

Vascular contrast enhancement is influenced by various factors that may be divided into three groups: (1) patient-related factors, (2) CM-related factors, and (3) MDCT scanner-related factors (Fig. 3). Patient- and CM-related factors are highly interrelated and determine CM pharmacokinetics and thereby the dynamics of contrast enhancement. They can influence the temporal pattern (timing) and magnitude of contrast enhancement to variable degrees. The scanning technique does not directly influence enhancement, but some scanner-dependent factors play a critical role by enabling the acquisition of data at a specific enhancement time point and providing high-quality volume data (in terms of temporal and spatial resolution).

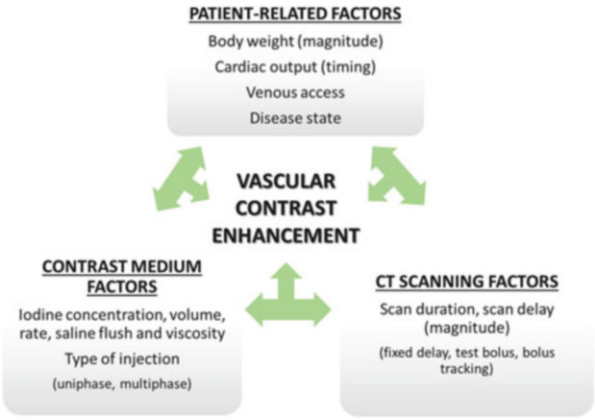

Fig. 3 Factors influencing CM distribution in the body

2.2 *Patient-Related Factors Influencing Contrast Enhancement*

Physiological patient characteristics that affect vascular enhancement include cardiac output (heart rate and stroke volume) and body weight. Both of these characteristics are extremely variable in veterinary patients, which have wide ranges of size and heartbeat. Moreover, time to peak enhancement differs from different target vessel (aorta, pulmonary artery, iliac arteries, etc.) depending on various factors such as the distance from the venous access site and underlying pathological condition. Other factors, such as the patient positioning, anesthetic protocols, and vascular anomalies, may also influence CM distribution.

Body weight is the most important patient-related factor affecting enhancement magnitude in vascular and parenchymal studies. Body weight and the magnitude of contrast enhancement are inversely related. In larger patients, the administered CM is diluted into larger blood compartments. The timing of contrast enhancement is not affected by body weight. Interindividual differences in vascular contrast enhancement may be reduced by adjusting the overall iodine dose (by increasing CM volume and/or iodine concentration) and by increasing the injection rate proportional to body weight. CM dosages of 300–800 mgI/kg have been reported in the veterinary literature, depending on the vascular district studied and the scanner used.

Cardiac output and cardiovascular circulation are major patient-related factors affecting the temporal pattern (timing) of contrast enhancement. Cardiac output is related inversely to the degree of arterial enhancement (particularly in the first-pass dynamic). In patients with normal cardiac output, peak arterial contrast enhancement is achieved shortly after CM injection. Studies conducted in normal dogs using single-slice CT scanners have shown that the median time of peak enhancement in the cranial abdominal aorta ranges from 2 to 12 s, and the median time of portal peak enhancement ranges from 23 to 46 s. A recent study conducted with a

small group of normal cats using different CM protocols showed that the time to peak aortic enhancement ranged from 11 to 25.5 s. These wide ranges of time to peak aortic enhancement reflect physiological and pathological variations in veterinary patients. The cardiac output of a patient at the time of CT scan initiation is always unknown. This is particularly true for veterinary patients, due to their variable size, cardiovascular changes during CM injection, and the influence of anesthesia on cardiac parameters.

In general, CM is distributed and clears slowly in patients with decreased cardiac output and blood volume, leading to delayed and persistent peak arterial and parenchymal enhancement. This effect must be kept in mind when designing CM protocols for advanced MDCT scanners with more rapid image acquisition, as rapid scans may outpace the CM bolus and acquire data before the peak of contrast enhancement (i.e., more distal vascular regions will not be enhanced). For patients with higher cardiac output (normal in small/toy breeds and cats or associated with various clinical conditions, such as anemia and sepsis), CM distribution is unpredictable. Thus, the use of a fixed injection-to-scan delay is not recommended.

2.3 Injection-to-Scan Delay Individualization

For MDCTA, methods are used to predict how CM will behave in a given patient (e.g., test bolus) or for real-time injection-to-scan delay individualization (e.g., automated bolus triggering, or bolus tracking).

For the *test bolus* method, a small amount of CM is injected and multiple low-dose non-incremental scans are taken over the region of interest (ROI) until the contrast is visualized in the selected vessel. This approach determines the *CM arrival time* in that vessel, enabling determination of the optimal scan delay for that patient. For slow scanners (ranging from single-slice CT to 4-MDCT devices), this time is always used directly as the scanning delay for subsequent CTA. This approach is not applicable when using more advanced MDCT scanners with shorter CM injection times. Additional time must be included to obtain a diagnostic delay (calculated taking into account the scan length), assuring optimal contrast enhancement in the target vessel. Selection of the appropriate scan delay is critical for more rapid MDCT scanners (64-MDCT and above). The time to CM arrival, scan speed, and CM injection duration should be considered when calculating the optimal scan delay (Fig. 4).

In theory, the test bolus technique offers the advantages not only of tailoring the peak of arterial enhancement for an individual subject but also of calculating CM injection parameters using pharmacokinetic simulation. In other words, it can be used to determine not only when but also how CM distributes in the body of a given patient. This technique is preferred for patients with compromised cardiac function, which may have more rapid and variable arterial-to-venous transit times. A disadvantage of the test bolus technique in veterinary practice is that the volume of iodinate CM is often a few milliliters and the test bolus may contain a

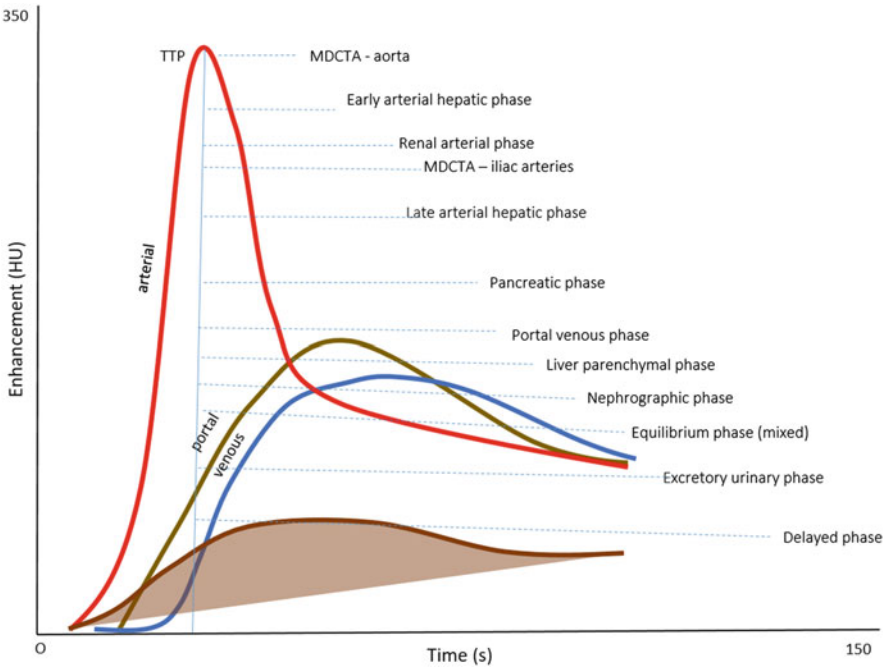

Fig. 4 Schematization of contrast enhancement in vascular and parenchymal territories after a single CM injection. *Red*, *green*, and *blue lines* represent the arterial, portal, and venous phases of the liver, respectively. The *brown line* represents the enhancement curve of the liver parenchyma. TTP, time to peak aortic enhancement. The individual arrival time to reach maximum enhancement in the aorta cannot be used as the scanning delay for most advanced MDCT scanners. *Dotted straight lines* represent the additional delay required between the TTP and the start of scanning. This delay depends on the intrinsic hemodynamics of the organ, the CM protocol, and the scanner characteristics

disproportionately large fraction of the total contrast dose in small patients, due to weight-based CM dosage.

With the *bolus-triggering technique*, test bolus injection is not necessary. All state-of-the-art MDCT systems feature this option. Multiple images are obtained over the ROI in a non-incremental manner during CM injection. The attenuation value within the ROI is monitored constantly and visualized on the monitor. The scan is initiated automatically when the density within the vessel exceeds a predetermined Hounsfield unit (HU) value (e.g., 30 HU in the descending aorta for abdominal studies) or manually (in first-generation MDCT scanners) when a visual threshold is reached (Fig. 5). This technique is less time-consuming than the test bolus technique, and it provides consistently good CTA image quality in most instances.

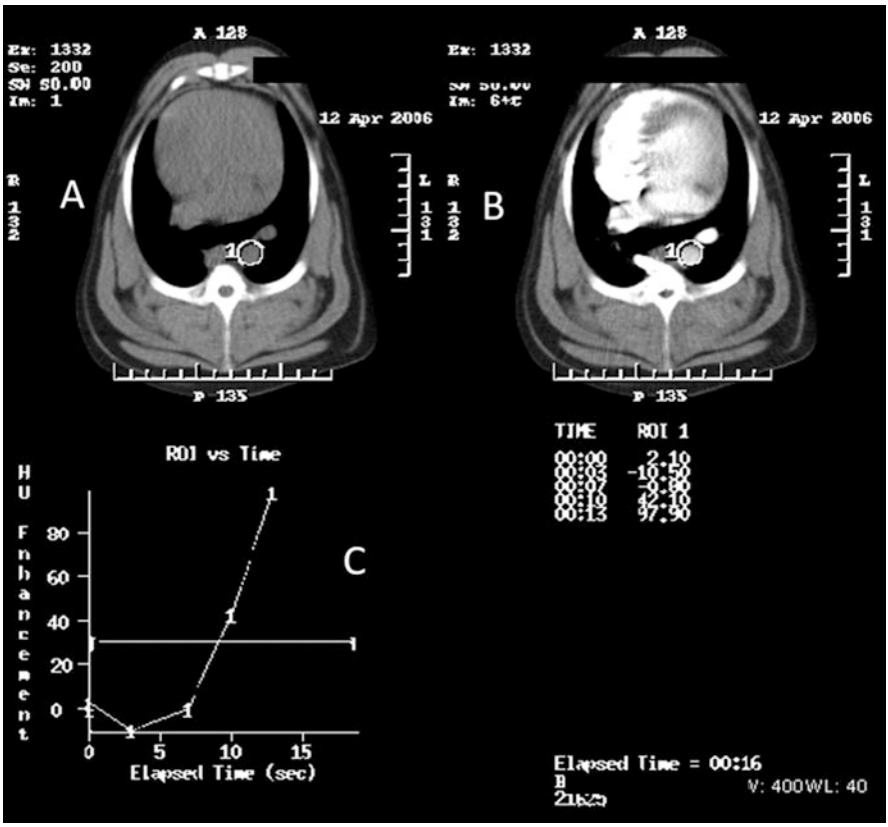

Fig. 5 Example of the monitor appearance on the CT console during bolus tracking (Lightspeed 16; GE Medical Systems). (**a**) Pre-contrast slice through the dome of the diaphragm. Note the round ROI on the descending aorta (1). (**b**) Image of a non-incremental series obtained during CM injection. Note the enhancement of cardiovascular structures. (**c**) Time graph showing the enhancing curve. With this scanner, the scan is started manually when a predetermined threshold (here, 30 HU) is reached within the ROI

2.4 CM-Related Factors Influencing Contrast Enhancement

Iodinate derivatives are the most commonly used injectable CMs for contrast-enhanced CT examinations in dogs and cats. The diagnostic use of these CMs is based on the ability of iodine to absorb X-rays, which increases HU values in plasma and target organs, thereby enhancing vascular structures and hypervascular lesions. CM concentration and injection protocol influence vascular enhancement. The amount of iodine and the X-ray energy level directly influence the degree of contrast enhancement. The increase in opacity in a given tissue after CM injection is directly proportional to the iodine concentration reached in that tissue (e.g., 1 mg iodine/mL = 26 HU increase in contrast enhancement at 120 kVp) and inversely

related to the X-ray energy level (a lower kVp results in more vascular contrast enhancement but also more image noise).

The selection of a CM depends on various factors, including the scanner type, injector system, and cost. Commercially available intravenous CMs have various iodine concentrations, ranging from 240 to 370 mgI/mL. Table 1 summarizes some published protocols for CTA using different scanners in several clinical situations in dogs and cats.

In general, the CM concentration and injection protocol need to be adapted to take advantage of the capabilities of the MDCT scanner used. For instance, CMs with higher iodine concentrations (up to 370 mgI/mL) are preferred for more rapid MDCT scanners (64, 128, or more rows) to achieve a high and rapid iodine delivery rate, thereby maximizing arterial enhancement for MDCTA. The use of a CM with a high iodine concentration is an alternative approach to increasing the CM injection rate to obtain good vascular opacification (Fig. 6). This approach may be indicated in patients in which a high injection rate may be problematic, such as those that are small or have cardiovascular disease or very fragile veins.

Injection protocol parameters that may alter the enhancement of target vessels are the injection duration (volume:rate), rate, and volume (duration × rate). The duration of iodine injection influences the magnitude and timing of contrast enhancement in vascular region. Arterial enhancement depends on the flow rate (mL/s). An increased injection rate shortens the time to vascular arterial enhancement and increases its magnitude (i.e., when a compact bolus is used). Moreover, more rapid injection rates improve the distinction of various vascular phases in multiphase examinations for vascular studies of the liver, pancreas, and gastrointestinal system, thereby improving the detection of hypervascular lesions (Fig. 7). A short, high-rate CM injection, however, is not ideal for parenchymal studies. Peak parenchymal enhancement occurs later than arterial enhancement, necessitating an increased injection duration. A multiphasic (multiple vascular phases) approach is necessary for abdominal studies to enable assessment of both the vascular and parenchymal tissues.

Types of CM injection include uniphasic, biphasic, and multiphasic injections. For uniphasic injection, the whole CM bolus is delivered at a constant injection rate. With this kind of injection, contrast enhancement increases to a peak and then declines. CTA includes the upslope and downslope of the CM distribution curve, and enhancement is not uniform during volume acquisition. This characteristic is less important for short scan ranges (e.g., CTA of the neck or thorax), but may be problematic for larger vascular territories (e.g., in larger patients or peripheral CTA).

Biphasic injection (a rapid first phase, followed by a slower phase) and multiphasic, exponentially decelerating techniques (multiphasic-rate injection bolus with exponentially decreasing rate) provide more uniform enhancement with a longer plateau phase. These techniques are indicated for clinical applications requiring coverage of a larger vascular territory or for slow CT scanners.

A mechanical power injector is an indispensable device for MDCTA. All injectors allow preprogramming of the CM volume and flow rate and the setting

Table 1 Suggested protocols for CTA

Author	Species	Purposes	Type of scanner	Type of CM (mgI/mL)	Dosage (mgI/kg)	Modality of injection	Rate of injection (mL/s)	Saline flush	Target vessel	Threshold (HU)	Method	Tube voltage (kv)
Bertolini et al. (2006) and Bertolini (2010)	Dog	Dual-phase for PSS	16-MDCT	Iodixanol 320	640	Single-barrel power injector	3	–	Descending aorta	30	Bolus tracking	120
Nelson and Nelson (2011)	Dog	Dual-phase for PSS	16-MCDT	Iohexol 300	810	Single-barrel power injector	3	–	Descending aorta	–	Bolus test	120/140
Habing et al. (2012)	Dog	Pulmonary CTA	16-MDCT	Iohexol 300	390	Single-barrel power injector	5	–	Right main pulmonary artery	–	Bolus tracking	–
Henjes et al. (2011)	Dog	Aortic arch anomalies	64-MDCT	Iobitridol 350	640	Single-barrel injector	3	Dilution of CM	Aortic arch	110	Bolus test	120
Drees et al. (2012)	Dog	Coronary arteries	64-MDCT	Iopamidol 370	555–962	Dual-barrel power injector	2	30 mL	Ascending aorta	–	Bolus test	120
Cassel et al. (2013)	Dog	Pulmonary CTA	2-sliceCT	Iohexol 300	600	Single-barrel power injector	3	Manual	Right main pulmonary artery	150	Bolus test	130
May et al (2013)	Cat	Renal CTA	16-MDCT	Iohexol 240	528	Dual-barrel power injector	5	10 mL	Descending aorta	90	Bolus test and bolus tracking	–
Kim et al. (2013)	Dog	Dual-phase for PSS	8-MDCT	Iohexol 350	700	Single-barrel power injector	3	–	Descending aorta	30	Bolus tracking	120
Goggs et al. (2014)	Dog	Pulmonary embolism	16-MDCT	Iohexol 300	600	Dual-barrel power injector	2–3	–	Pulmonary artery	–	Bolus test	120
Brunson et al. (2016)	Dog	Three-phase for PSS	8-MDCT	Iohexol 350	640	Single-barrel power injector	3	–	Not reported	Not reported	Bolus tracking	Not reported

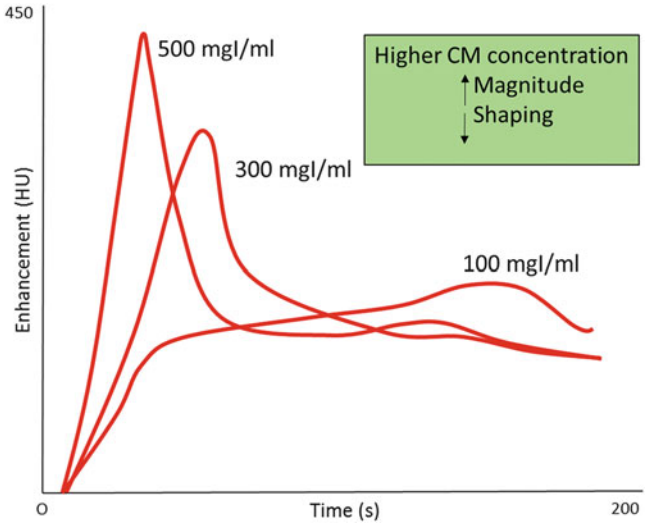

Fig. 6 Schematization of theoretical arterial enhancement behavior using a constant iodine concentration and variable injection rate (mL/s)

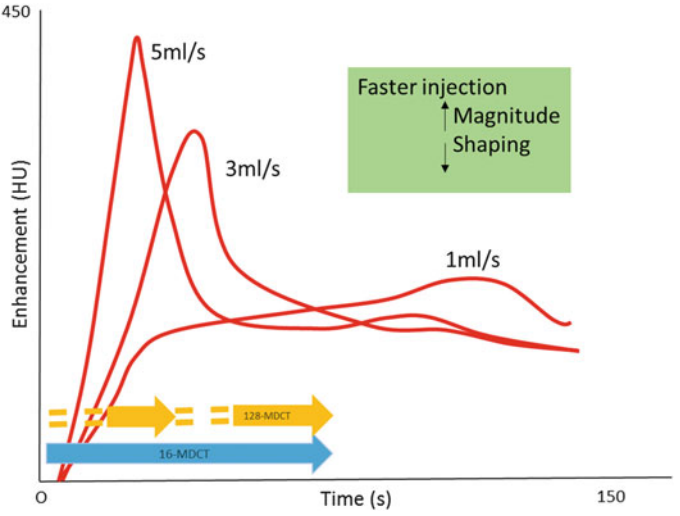

Fig. 7 Schematization of theoretical arterial enhancement behavior using a constant iodine concentration and variable injection rate (mL/s). A faster injection rate shortens the time to vascular arterial enhancement and increases the magnitude of contrast enhancement. Faster injection enables excellent acquisition of multiphasic studies using more rapid scanners, improving the distinction of various vascular phases. *Arrows* represent a comparison of hypothetical scanning protocols for the abdomen using 128-MDCT and 16-MDCT scanners. *Dotted yellow lines* represent the scan delay necessary to avoid outrunning the contrast bolus using the more rapid 128-MDCT

of an injection pressure limit. Most systems permit uniphasic and multiphasic injections. A dual-barrel system with two distinct syringes (one filled with CM and the other with saline solution) can be used to flush the access vein and push the CM bolus. Saline flushing improves arterial opacification and prolongs the arterial enhancement phase. In veterinary patients, high, uniform contrast enhancement in conjunction with high *z*-axis resolution is essential for the diagnosis of thrombosis, embolism, vascular invasion, and vascular anomalies and for adequate segmentation of 3D volume-rendered images.

When saline flushing is not used, some of the injected bolus may remain as a relatively static contrast column in the cranial veins; this CM is cleared very slowly, resulting in significant streak artifacts in the thoracic inlet. Moreover, the residual CM does not contribute to arterial enhancement. In our experience, the use of a saline flush that follows the administered CM bolus at the same rate and of half-to-same volume (using a dual-barrel injector system) effectively improves contrast distribution, allowing delivery of the fully injected bolus to the whole vascular system during acquisition. Saline flushing is particularly useful in small patients when a small total amount of CM is used (i.e., for the assessment of vascular anomalies in toy-breed dogs).

2.5 Scanner-Related Factors Influencing Contrast Enhancement

MDCT scanner technology and protocols may indirectly influence the success of vascular studies by allowing the acquisition of data at a specific time point of contrast enhancement. Differences in scanning parameters are related to the type of scanner available (i.e., 4-, 8-, 16-, 64-, 128-, 256-, or 320-detector row CT scanner) and to scanner performance. Even when the study of a given patient and the CM characteristics are optimized, inadequate CT scanning parameters will lead to unpredictable vascular enhancement results.

Substantial changes in CT protocols are essential as radiologists migrate from single-slice helical CT to MDCT technology and among various MDCT scanner generations. The number of detector rows in MDCT scanners has increased progressively, and the scan time has been dramatically reduced. Scanner performance has roughly doubled every 2 years since the mid-1980s. Compared with 4-MDCT scanners, the performance of 64-MDCT scanners has increased more than 20 times, due to the increase in the number of detector rows and rotation speed. The most recent dual-source CT scanner, which features two tube-detector arrays, can achieve a rotation time of up to 0.25 s and a volume coverage speed of up to 737 mm/s.

The most important factor that determines scanner performance in MDCTA is the relationship between scanning speed and *z*-axis resolution (maximum table speed and thinnest section width that can be reconstructed using that table speed).

Isotropic ($x = y = z$) resolution is mandatory for high-quality vascular studies in veterinary patients. With the first generations of MDCT scanners (with 4, 8, and 16 rows), high-spatial-resolution longitudinal (z-axis) data can be acquired for relatively small volumes but not for extended coverage of the entire abdomen or body. In these cases, strategies to obtain high-quality angiographic studies are to limit the scan range to the vascular territory of interest and to sustain the CM injection throughout scanning. When a larger volume needs to be covered, a possible strategy with slow MDCT scanners is to acquire near-isotropic data with 50% reconstruction overlap. For example, to achieve acceptable results in abdominal MDCTA of larger dogs using a 16-MDCT scanner, a good compromise between volume coverage and image quality might be the following: 0.7 s gantry rotation, 0.938:1 pitch, and 1.2 mm slice thickness with 50% reconstruction overlap.

The acquisition of direct scans prior to angiographic series may result in X-ray tube heating, limiting the current available for high-quality MDCTA series using 4–8–16 MDCT scanners. In most instances, for vascular studies, unenhanced scans do not add significant diagnostic value to enhanced MDCT images and do not need to be acquired.

Most advanced MDCT scanners (with 64, 128, 256, and 320 detector rows) with improved temporal and spatial resolution enable isotropic volumetric acquisition over larger scan ranges in a few seconds, enabling the use of a multiphasic approach to the whole body, thoracic and abdominal regions, or peripheral vasculature without compromise.

3 How to Review MDCTA Datasets

As for most MDCT applications, isotropic abdominal vascular imaging may provide thousands of images for each series. An almost unlimited number of ways to reconstruct and view MDCTA datasets are available, but none are exclusively correct. The review of transverse images is time-consuming and less accurate than 2D multiplanar and 3D visualization, especially for vascular structures. Axial source images remain useful for the analysis of suspected artifacts on 2D MPRs or 3D volume-rendered images. Most 3D reconstructions are now interactive in real time, and the most complex processing techniques, such as automatic bone removal, are immediate or take just seconds to complete (see the chapter "Multidetector-Row CT Basics, Technological Evolution, and Current Technology"). Most common 2D and 3D post-processing techniques used for MDCTA datasets in clinical practice are here briefly resumed:

Multiplanar reformatted reformation (MPR) is a two-dimensional real-time technique (2D) that can simultaneously display multiple views of the same volume, in sagittal, dorsal, transverse, or any oblique plane. The quality of multiplanar reconstructions is directly related to the image slice thickness. When isotropic

resolution is used the quality of a reconstructed image in any plane is virtually identical to the original axial image. Instead of individually viewing hundreds or thousands of transverse slices, MPRs enable the radiologist to interact with the data as a volume.

Maximum Intensity projection (MIP) is a 3D real-time technique that uses a computer algorithm, which evaluates each voxel along a line from the viewer's eye through the image and selects the voxel with the maximum intensity as the value of the corresponding display pixel. It is the most widely used three-dimensional (3D) technique for visualization of blood vessels for CT angiography.

Volume rendering (VR) is the most flexible 3D visualization tool. In contrast to MIP where only the voxel with the highest CT number is used, in VR each voxel is used to calculate the final image. The image is generated by assigning each voxel in the examined volume an opacity value (from 0% to 100%, total transparency to total opacity) based on its attenuation value. Color can be applied to enhance the discrimination between the tissues by selecting image presets or by changing parameters interactively until the desired effect is achieved.

Endoluminal imaging or "virtual endoscopy" is a perspective VR technique that allows users to visualize the lumen of anatomical or pathological structures. Virtual endoscopy is most successful for displaying air-containing structures, such as tracheobronchial tree, but can be also applied to high-density structures, such as enhanced blood vessels.

Our MDCTA data analysis comprises the interactive assessment of 2D orthogonal and multioblique MPR views and 3D thin-slab MIP and volume-rendered maps of the vascular tree. In clinical practice, a slab MIP of 5–20-mm thickness is excellent for the depiction of CM-filled structures. MIP and VR provide excellent 3D vascular maps. Importantly, however, only the voxels within the highest CT number (HU) are projected on MIP maps, and the perception of depth relationships between structures using this 3D technique is compromised. In contrast to MIP, for which only the voxel with the highest CT number is used, in VR each voxel is used to calculate the final image. Volumes can be manipulated in many different ways to visualize the desired anatomy. For instance, the use of 3D VR from isotropic datasets for the assessment of vascular anomalies dramatically simplifies interpretation of the courses of small vessels or complex vascular relationships. The resulting volume-rendered images contain more information and are potentially more useful than source 2D images. Importantly, the quality of VR results depends greatly on the quality of the original dataset and user's skill in optimizing rendering parameters.

Table 2 resumes the criteria for MDCTA optimization.

Table 2 Suggestions for MDCTA optimization

MDCTA optimization
• Avoid unnecessary scans (tube heating)
• Limit the scan range (for slow scanners)
• Use the bolus tracking/test bolus technique
• Calculate an additional scan delay (for faster scanners)
• Use isotropic/near isotropic resolution (with overlap)
• Combine high iodine rate/concentration and fast scanning to optimize the arterial enhancement
• Use a saline flushing to improve vascular opacification
• Use biphasic/multiphasic injection for more uniform opacification and prolonged plateau phase (e.g., peripheral arteries)
• Review MDCT datasets using 2D-MPRs and 3D-VR post-processing techniques

Further Readings

Bae KT. Intravenous contrast medium administration and scan timing at CT: considerations and approaches. Radiology. 2010;256(1):32–61. doi:10.1148/radiol.10090908

Bertolini G, Prokop M. Multidetector-row computed tomography: technical basics and preliminary clinical applications in small animals. Vet J. 2011;189(1):15–26. doi:10.1016/j.tvjl.2010.06.004

Bertolini G, Rolla EC, Zotti A, Caldin M. Three-dimensional multislice helical computed tomography techniques for canine extra-hepatic portosystemic shunt assessment. Vet Radiol Ultrasound. 2006;47(5):439–43.

Cassel N, Carstens A, Becker P. The comparison of bolus tracking and test bolus techniques for computed tomography thoracic angiography in healthy beagles. J S Afr Vet Assoc. 2013;84(1). doi:10.4102/jsava.v84i1.930

Fishman EK, Ney DR, Heath DG, Corl FM, Horton KM, Johnson PT. Volume rendering versus maximum intensity projection in CT angiography: what works best, when, and why. Radiographics. 2006;26:905–22.

Fleischmann D. CT angiography: injection and acquisition technique. Radiol Clin N Am. 2010;48(2):237–47, vii. doi:10.1016/j.rcl.2010.02.002

D F, Kamaya A. Optimal vascular and parenchymal contrast enhancement: the current state of the art. Radiol Clin N Am. 2009;47(1):13–26. doi:10.1016/j.rcl.2008.10.009

Ichikawa T, Erturk SM, Araki T. Multiphasic contrast-enhanced multidetector-row CT of liver: contrast-enhancement theory and practical scan protocol with a combination of fixed injection duration and patients' body-weight-tailored dose of contrast material. Eur J Radiol. 2006;58(2):165–76.

Kim J, Bae Y, Lee G, Jeon S, Choi J. Dynamic computed tomographic determination of scan delay for use in performing cardiac angiography in clinically normal dogs. Am J Vet Res. 2015;76(8):694–701. doi:10.2460/ajvr.76.8.694

Kirberger RM, Cassel N, Carstens A, Goddard A. The effects of repeated intravenous iohexol administration on renal function in healthy beagles – a preliminary report. Acta Vet Scand. 2012;54(1):47. doi:10.1186/1751-0147-54-47

Kishimoto M, Yamada K, Tsuneda R, Shimizu J, Iwasaki T, Miyake Y. Effect of contrast media formulation on computed tomography angiographic contrast enhancement. Vet Radiol Ultrasound. 2008;49(3):233–7.

Hu K-C, Kuo C-J, Chen L-K, Yeh L-S. Effects of body weight and injection rate of contrast medium on 16-row multidetector computed tomography of canine aorta. Taiwan Vet J. 2011;37(2):93–103.

Lee CH, Goo JM, Bae KT, Lee HJ, Kim KG, Chun EJ, Park CM, Im JGCTA. contrast enhancement of the aorta and pulmonary artery: the effect of saline chase injected at two different rates in a canine experimental model. Investig Radiol. 2007;42(7):486–90.

Mai W, Suran JN, Cáceres AV, Reetz JA. Comparison between bolus tracking and timing-bolus techniques for renal computed tomographic angiography in normal cats. Vet Radiol Ultrasound. 2013;54(4):343–50. doi:10.1111/vru.12029

Makara M, Dennler M, Kühn K, Kalchofner K, Kircher P. Effect of contrast medium injection duration on peak enhancement and time to peak enhancement of canine pulmonary arteries. Vet Radiol Ultrasound. 2011;52(6):605–10. doi:10.1111/j.1740-8261.2011.01850.x

Napoli A, Fleischmann D, Chan FP, Catalano C, Hellinger JC, Passariello R, Rubin GD. Computed tomography angiography: state-of-the-art imaging using multidetector-row technology. J Comput Assist Tomogr. 2004;28(Suppl 1):S32–45.

Pannu HK, Thompson RE, Phelps J, Magee CA, Fishman EK. Optimal contrast agents for vascular imaging on computed tomography: iodixanol versus iohexol. Acad Radiol. 2005; 12(5):576–84.

Schoellnast H, Deutschmann HA, Berghold A, Fritz GA, Schaffler GJ, Tillich M. MDCT angiography of the pulmonary arteries: influence of body weight, body mass index, and scan length on arterial enhancement at different iodine flow rates. AJR Am J Roentgenol. 2006;187(4): 1074–8.

Tateishi K, Kishimoto M, Shimizu J, Yamada K. A comparison between injection speed and iodine delivery rate in contrast-enhanced computed tomography (CT) for normal beagles. J Vet Med Sci. 2008;70:1027–30.

Part III
The Abdomen

The Abdominal Vasculature

Giovanna Bertolini

1 Introduction

Adult mammals have three unpaired abdominal vascular systems: the aorta, caudal vena cava, and portal venous system. In normal adult animals, no active connection is present among the three systems (Fig. 1). The ductus venosus, an intrahepatic channel between the left umbilical vein and the left branch of the portal vein, is present in fetuses and closes shortly after birth. Here, a brief anatomical background is given.

1.1 Abdominal Aorta

The abdominal aorta (Ao) begins at the aortic hiatus of the diaphragm and courses ventrally to the vertebral column, giving off branches to supply the stomach, kidneys, intestines, gonads, and other organs through extensive arterial networks. Branches of the abdominal aorta may be divided into three sets: parietal, visceral, and terminal branches. The parietal branches of the aorta develop from the fetal dorsal intersegmental arteries and include the paired and symmetrical phrenic and abdominal arteries, lumbar arteries, and deep circumflex iliac arteries. The visceral branches of the abdominal aorta are the unpaired celiac artery, the cranial and caudal mesenteric arteries, and other paired vessels, i.e., renal, adrenal, and gonadal arteries. The aorta ends by dividing into two major blood vessels, the iliac arteries that supply blood to the pelvic limbs and the pelvis (Fig. 2).

G. Bertolini (✉)
San Marco Veterinary Clinic, Padua, Italy
e-mail: bertolini@sanmarcovet.it

G. Bertolini (ed.), *Body MDCT in Small Animals*, DOI 10.1007/978-3-319-46904-1_3

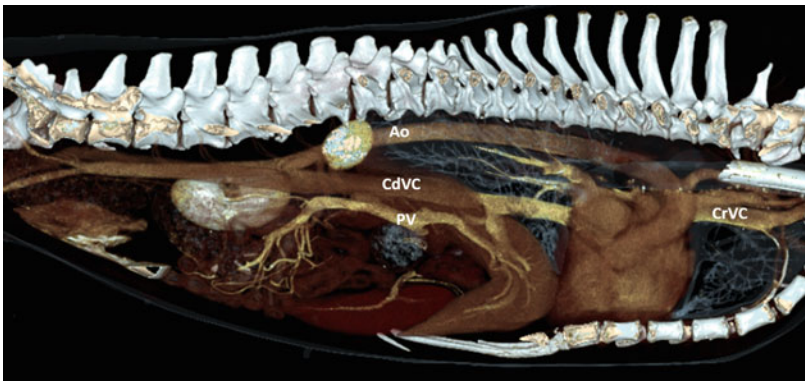

Fig. 1 3D volume-rendered image (*right lateral view*) of the abdominal vessels in a dog, showing the three vascular systems. *Ao* aorta, *CdVC* caudal vena cava, *CrVC* cranial vena cava, *PV* portal vein

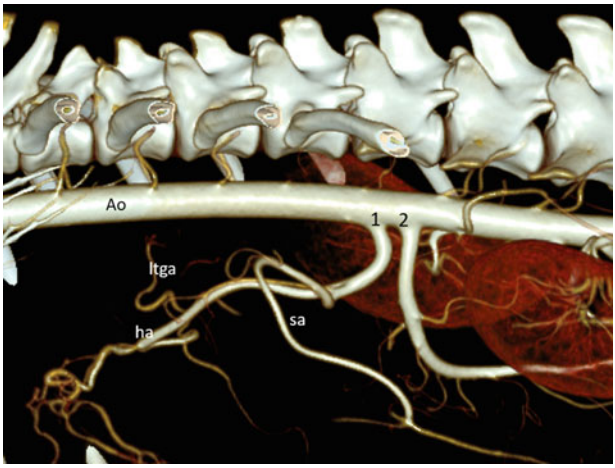

Fig. 2 Volume-rendered images from abdominal MDCTA. *Left lateral view*. *Ao* descending aorta, *1* celiac artery, *2* cranial mesenteric artery, *3 ha* hepatic artery, *sa* splenic artery, *ltga* left gastric artery

Celiac Artery The unpaired celiac artery emerges from the ventral surface of the abdominal aorta at the level of the first lumbar vertebra. It gives off at least three branches: the hepatic artery, the left gastric artery, and the splenic artery. It ends by trifurcating or can give off the hepatic artery and a gastrosplenic trunk. The gastrosplenic trunk subsequently divides to form the left gastric artery and the splenic artery. In its extrahepatic course, the *hepatic artery* runs cranioventrally to the right side next to the portal vein. It gives off three to five branches, which enter the portal area of the liver and accompany the hepatic branches of the portal vein.

The number and course of the hepatic artery branches, as well as the regions supplied by them, vary among individuals.

Mesenteric Arteries The *cranial mesenteric artery* is the largest visceral branch of the abdominal aorta. It arises from the ventral surface of the aorta directly caudal to the celiac artery. It gives off several branches for the pancreas and the small and large intestines. The *caudal mesenteric artery* is a thin vessel that originates from the ventral surface of the abdominal aorta (at approximately the same level as the deep circumflex iliac arteries) and supplies the terminal portion of the intestine.

Renal Arteries Renal arteries are paired lateral visceral branches of the abdominal aorta, which can have extremely variable patterns. Commonly, a single renal artery bifurcates into dorsal and ventral branches, which supply the cranial and caudal portions of the kidney; the site of this duplication is extremely variable. A double renal artery can be present on one or both sides. At the renal hilus, each renal artery branch gives off interlobar end arteries, which continue into the kidney and form the arcuate and interlobular arteries, and the glomerular afferent arterioles.

Terminal Branches At the level of the penultimate or ultimate lumbar vertebra, the abdominal aorta gives off the left and right *external iliac arteries* for the pelvic limbs, which give off the internal iliac arteries and end by diminishing rapidly in size, continuing into the median sacral artery.

1.2 Caudal Vena Cava

The caudal vena cava (CdVC) begins around the penultimate lumbar vertebra or more cranially, near the convergence of the left and right common iliac veins. It is the largest vessel of the abdomen. Based on its embryological origin, the caudal vena cava is customarily divided into four segments: the prerenal, renal, prehepatic, and hepatic segments. The deep circumflex iliac vein is the first tributary of the caudal vena cava (Fig. 3). When the caudal vena begins cranial to the sixth lumbar vertebra, the deep circumflex iliac vein can discharge into the corresponding common iliac vein. The lumbar veins are segmental vessels that accompany the corresponding arteries. The renal veins are paired tributaries of the caudal vena cava. Within the kidney, the arcuate and interlobular veins accompany the corresponding arteries. The left renal vein receives the left gonadal vein, accompanying the corresponding arteries, whereas the contralateral gonadal vein joins the caudal vena cava directly. Hepatic veins are present within the liver parenchyma and join the caudal vena cava (hepatic segment) along its lateral and ventral surfaces. The major hepatic veins include the right hepatic vein for the right liver lobes; the middle hepatic vein, which drains the quadrate lobe of the liver; and the left hepatic vein for the left part of the liver. Each hepatic vein receives numerous tributaries from different parts of the liver (Fig. 4).

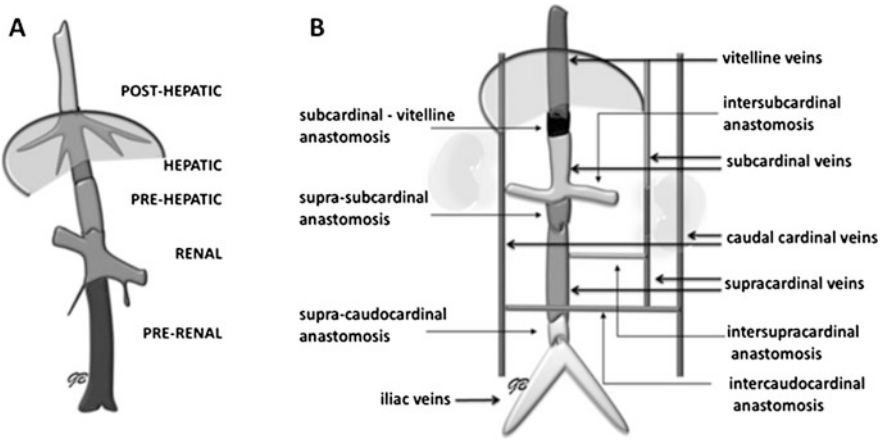

Fig. 3 (**a**) Caudal vena cava segments in adult mammals result from complex vascular anastomoses and regression in the embryo (**b**)

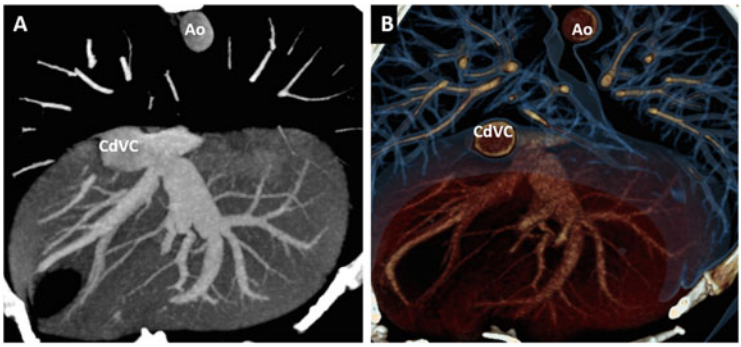

Fig. 4 Hepatic veins. (**a**) Thin-MIP transverse view. (**b**) VR-thin. *CdVC* caudal vena cava

1.3 Portal Venous System

The portal vein (PV) and its branches form the portal venous system, which carries blood from the abdominal viscera to the liver. It collects blood from the gastrointestinal tract (except the caudal segment of the rectum and the anal canal), spleen, and pancreas. Major tributaries of the venous portal system are cranial and caudal mesenteric veins, which drain most of the intestinal tract; the splenic vein, which accompanies the corresponding artery; the left gastric vein, which is a tributary of the splenic vein; the gastroduodenal vein; the right gastric vein; and the gastroepiploic vein. At the hepatic porta, the portal vein divides into right and left branches (Fig. 5). The right branch supplies the right portion of the liver, including the right lateral lobe and the caudate process of the caudate lobe. The left branch of the portal vein supplies the central and left portions of the liver, comprising the right

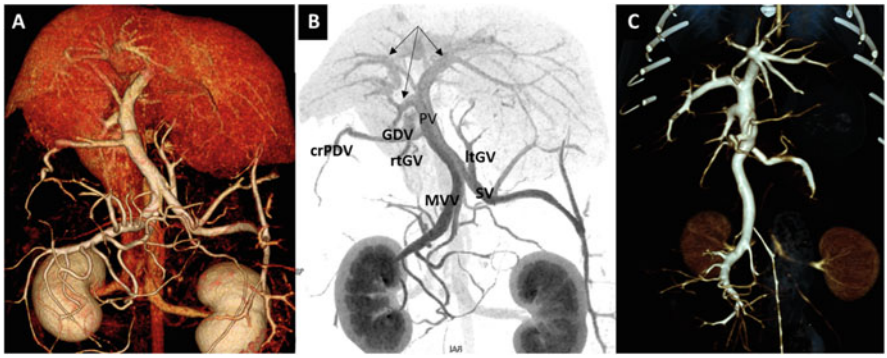

Fig. 5 (**a**) VR of the portal venous system in a dog. (**b**) Thin-slab MIP (inverse video) of the same volume. The portal venous system in mammals forms from the confluence of cranial and caudal mesenteric veins (MVV). It receives the splenic vein (SV) and left gastric vein (ltGV) from the *left* and the gastroduodenal vein, cranial pancreatico-duodenal vein (crPDV), and right gastric vein (rtGV) from the *right* (also the gastroepiploic vein, not visible here). The portal vein (PV) divides into *right* and *left* branches within the liver (*arrows*). (**c**) VR of the normal portal system in a cat

medial, quadrate, left medial, and left lateral lobes. Small branches for the papillary process of the caudate lobe arise from the left branch.

2 MDCT Imaging Strategy

Abdominal MDCTA is indicated in cases of suspected anomalies involving the vascular system of the abdomen. Several important differences exist between spiral CT and the most advanced MDCT technologies. First, MDCT scanners can acquire images much more rapidly (up to 0.25 s rotation time) than can spiral CT scanners. Shorter rotation times improve temporal resolution, which is essential for vascular examinations. MDCT scanners with $\geq$16 rows can acquire true isotropic-volume datasets ($x = y = z$), rather than the individual slice data acquired by spiral CT. With these rapid scanners, isotropic MDCTA can be performed routinely in veterinary patients during dual- or tri-phase examinations of the abdomen. This ability confers a tremendous advantage, as it simultaneously provides information about the vascular and parenchymal structures. With the use of advanced MDCT scanners, all arterial and portal venous phases can serve as respective CTA examinations and can provide information about the enhancement of normal and pathological structures of the abdominal organs. In addition, high-quality vascular image post-processing is a prerequisite for the rapid acquisition of thin-slice data without compromising longitudinal (z-axis) spatial resolution.

Our goals in practice are to reach a certain magnitude of contrast enhancement in the target vascular territory and to maintain a consistent level of enhancement throughout scanning. Intravascular attenuation of at least 250 HU (preferably

300–400 HU) along the full longitudinal extent of the target vasculature and throughout the duration of acquisition is considered to be a prerequisite for CTA. This seemingly simple objective can be very difficult to achieve in practice, especially for veterinary patients, which vary substantially in size and cardiac output (two major factors influencing vascular contrast enhancement). Manual contrast medium (CM) injection according to empirically developed protocols for spiral CT is not applicable when more rapid MDCT scanners are used for CTA. Hence, an injector system and CM injection protocols designed for the technology employed should be used.

In veterinary literature, the peak aortic enhancement of normal dogs varies between 2 and 9.8 s and peak enhancement of the portal vein between 14.6 and 46 s. Vascular anomalies may influence the expected times of CM arrival and peak in the target vessel. In a study we conducted in dogs with congenital portosystemic shunting (CPSS), peak aortic enhancement occurred 2.4–10.2 s after CM injection, and the time to peak portal enhancement (about 250 HU in the portal vein) ranged from 5.5 to 11.1 s. These differences in peak vascular enhancement reported among various papers emphasize the inadequacy of fixed scan delays for vascular assessment, used for many routine nonvascular applications. The scan time must be tailored to each subject using a test bolus or bolus-tracking technique and adapted to the scanner technology available (described in detail in the chapter "Basic Principles of MDCT Angiography").

MDCT imaging strategies for various abdominal vascular territory of the liver, pancreas, kidney, and spleen are reported in the specific chapters of this book.

For *aortoiliac evaluation*, the volume coverage speed varies depending on the length of the imaging field, which in turn depends on individual patient morphology. Given the variability in flow dynamics over this volume, acquisition and CM injection parameters must be selected precisely to synchronize the scan duration (table speed and volume coverage) and CM injection. Circulation time for an individual patient may be determined using a bolus test or bolus-tracking technique to determine the individual CM transit time in the aorta. The arterial inflow and venous outflow anatomies are generally assessed with a single injection. With slower scanners (i.e., those with table speeds of 30–40 mm/s), a biphasic injection (starting before the arrival time in the aorta) may help to improve arterial enhancement. The length of the CM bolus injection should approximate the length of scanning, with the addition of a delay between the aortic arrival time and the beginning of scanning (the scanner delay). Conversely, CM "outrunning" can occur with the use of a more rapid scanner: the table moves faster than the CM in the vascular system, and the scanner may thus outpace the bolus. As a result, the iliac arteries will be unenhanced at the time of acquisition. A possible strategy for aortoiliac MDCTA, if the scanner permits, is to scan the region in the craniocaudal direction and preprogram a second acquisition in the caudocranial direction, in case the distal arteries are not enhanced on the first scan. The CM transit time in the aorta may differ substantially in patients with cardiovascular diseases. Thus, tailored biphasic CM injections with the use of the bolus-tracking technique are recommended in these patients to achieve more predictable aortoiliac enhancement.

A saline flush at the end of injection pushes the CM bolus, leading to uniform and prolonged vascular enhancement.

3 Abdominal Vascular Disorders

A wide spectrum of vascular disorders with different degrees of clinical relevance can involve the abdominal vasculature. The selection of an MDCTA imaging protocol depends on appropriate consideration of the clinical question, including the type of anomaly suspected and the vascular district (arterial, portal, or venous) involved. Abdominal arterial variants and anomalies are relatively rare in small animals. Most common vascular variants and pathological conditions involve the caudal vena cava and the portal system. Caudal vena cava anomalies have no or little clinical significance in themselves, but they are often associated with other vascular anomalies, such as portosystemic shunts, which can have relevant clinical consequences. Congenital and acquired portal-vein and portal-system pathological conditions encompass several patterns that are increasingly recognized with the increased use of advanced imaging modalities in clinical practice. MDCT has brought about dramatic changes in clinical vascular imaging during the past decade, leading to once unimaginable noninvasive diagnostic possibilities.

3.1 Vascular Injuries

MDCTA is certainly the imaging method of choice for the assessment of vascular injuries, most of which are traumatic in veterinary patients. Following blunt abdominal trauma, traumatic vascular injuries of major and minor arteries (e.g., avulsion of the renal artery, mesenteric ischemia) have been reported in dogs.

Traumatic disruption of the aortoiliac vasculature can occur in cases of pelvic fracture and other severe traumatic conditions. A multiphasic approach may be useful in these patients. In a single comprehensive examination, MDCT can provide information about the various organs and tissues involved in the trauma (Fig. 6). Moreover, it aids the distinction of arterial from venous injuries and may guide therapeutic management. Extravascular areas in the retroperitoneum or soft tissues (i.e., muscles) with attenuation values similar to or greater than that in the aorta on early arterial phase scans suggest arterial bleeding. These areas maintain higher attenuation during the portal and delayed vascular phases. The appearance of hyperattenuated areas in the portal venous phase, but not in the arterial phase, suggests active venous bleeding. In cases of severe pelvic trauma, arteries and veins can be lacerated and active bleeding can be revealed by CM extravasation in the arterial and portal venous phases. Hemorrhagic muscular infarction and hemoretroperitoneum can be present. Other MDCT signs of vascular injuries are occlusion, pseudoaneurysm formation, and arteriovenous fistula formation.

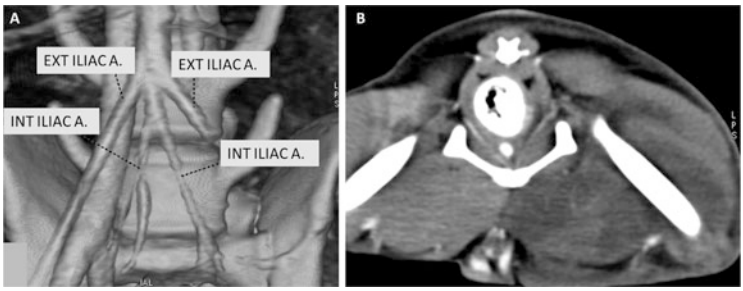

Fig. 6 16-MDCT examination in a 2-year-old male Jack Russell terrier with multiple lacerations of the left external iliac artery and both internal iliac arteries due to a bite injury. (**a**) VR of injured vessels. (**b**) Note the left muscular hypoattenuation (infarction)

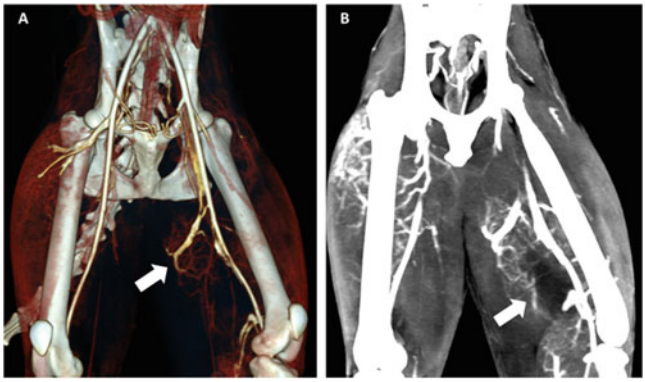

Fig. 7 A 1-year-old domestic shorthair cat with chronic swelling and pain in the left leg. Aortoiliac 128-DSCT image shows early enhancement of the left femoral vein due to multiple arteriovenous fistulas. Note the ipsilateral muscular swelling. Small and tortuous arteries are also present in the contralateral limb

Arteriovenous malformations and fistulas are congenital and acquired high-flow vascular connections. The abnormal vascular communication allows blood to follow the path of least resistance from the high-pressure artery to the low-pressure vein, resulting in increased venous pressure and decreased distal perfusion.

Angiographic studies are necessary for determining the precise location of the fistula. MCDT angiography includes enlarged, tortuous arteries and premature filling of the veins (Fig. 7).

3.2 Anomalies of the Abdominal Aorta and Its Branches

3.2.1 Congenital Anomalies of Abdominal Aorta and its Branches

Congenital anomalies of the abdominal aorta itself are very rare in small animals. Variants or anomalies of its branches are observed more frequently in dogs and cats. Anomalous origin and course of the *lumbar arteries* can be discovered incidentally during MDCTA but do not seem to cause clinical signs. Variations in the number and position of the visceral branches of the abdominal aorta are reported more commonly. About 80% of dogs have single *renal arteries* for each kidney, which divide (in extremely variable ways) into secondary dorsal and ventral branches, providing the interlobar arteries. These latter can have different patterns and close relationships to the collecting system. A small number of dogs have two renal arteries supplying the left and/or right kidneys. Duplication of the renal arteries and variations in the secondary and interlobar branches can easily be studied on MDCT images obtained in the early arterial phase. Variations in the branching patterns of renal arteries have no associated clinical sign. However, knowledge of the individual anatomic vascular variation is of great importance in interventional radiology and the planning of surgical procedures (Fig. 8).

Combined complex vascular anomalies may involve different vascular districts. A *common celiacomesenteric trunk* was visualized using a 4-MDCT scanner in a dog with concomitant acquired portal collaterals and a final diagnosis of portal vein hypoplasia (Fig. 9). Another report described the use of CTA as a noninvasive technique to plan the transarterial coil embolization of *an aortocaval vascular connection* associated with saccular dilatation of the prerenal segment of the caudal vena cava in a dog.

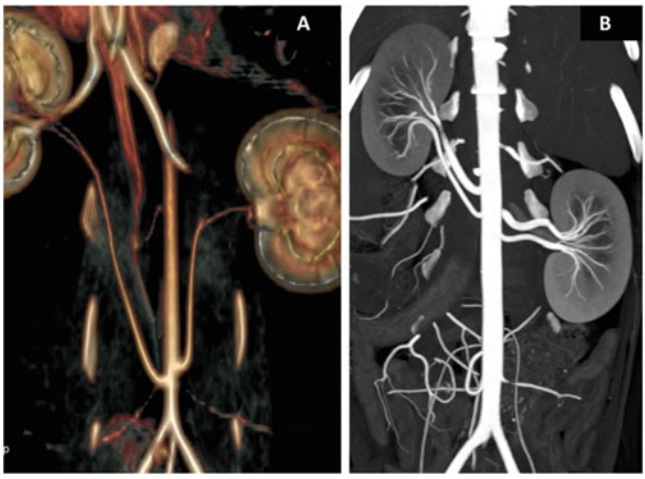

Fig. 8 Variable patterns of renal arteries. (**a**) A 1-year-old male Ragdoll cat with ectopic, caudal origins of both renal arteries. (**b**) A Mongrel dog with bilateral duplication of the renal arteries

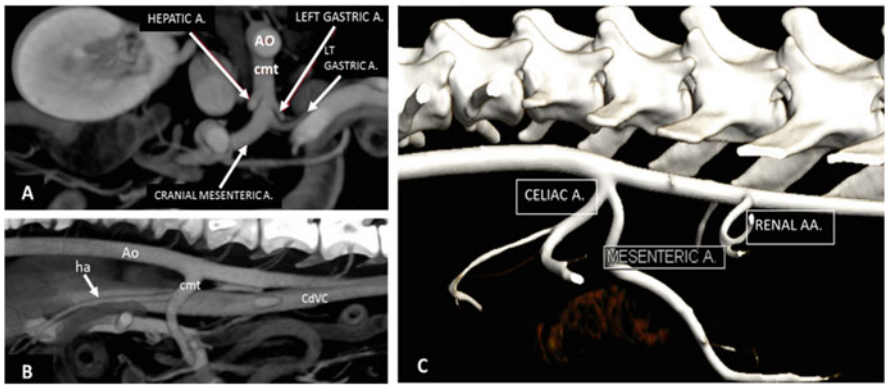

Fig. 9 (**a**) MIP of the mixed vascular abdominal phase (4-MDCT) in a dog with a common celiacomesenteric trunk (cmt). (**b**) Sagittal MIP of the same dog. *Ao* aorta, *CdVC* caudal vena cava, *ha* hepatic artery (**a**, **b** are courtesy of Dr. Mario Ricciardi, Pingry Veterinary Hospital, Bari, Italy). (**c**) Short common celiacomesenteric trunk in a cat

3.2.2 Acquired Anomalies of the Abdominal Aorta and Its Branches

In contrast to those in humans, *aortic aneurysms* in dogs and cats are rarely reported, and most of them involve the thoracic aorta. Segmental dilatation and course deviation of the abdominal aorta are occasionally seen on MDCTA examination, with no associated clinical implication (Fig. 10). In humans, an aortic enlargement with a diameter $\geq$50% larger than expected for that aortic segment is called an aneurysm. A few cases of abdominal aortic segmental dilatation have been reported in association with fungal systemic infection in small animals, but no threshold value for aortic aneurysm in small animals has been established.

Few reports have described *aortic dissection* in small animals, alone or in association with aortic aneurysm. The pathogenesis includes pathological conditions leading to increased aortic wall stress (e.g., systemic hypertension, genetic disorders), in association with intrinsic weakness of the arterial wall. In a recent study, 64-MDCTA was used for the diagnosis and characterization of aortic dissection in a cat. Reported sensitivities and specificities in human patients for the diagnosis of aortic dissection with rapid ($\geq$64 rows) MDCT scanners are as high as 100% and 98%, respectively. In addition, MDCT is useful for the identification of major complications of aortic dissection, such as mediastinal and pericardial hemorrhage, extension of the dissection to other major vessels, and thrombosis.

Aortic thrombosis and thromboembolism are the most common acquired conditions involving the aorta and its branches. Generally, in dogs and cats, thrombi form in morphologically normal arterial vessels of patients with underlying thrombogenic conditions. The visceral and terminal branches are affected much more commonly than are the segmental branches of the aorta. Local thrombosis in the distal aorta with embolization to the iliac and/or femoral artery is the most likely

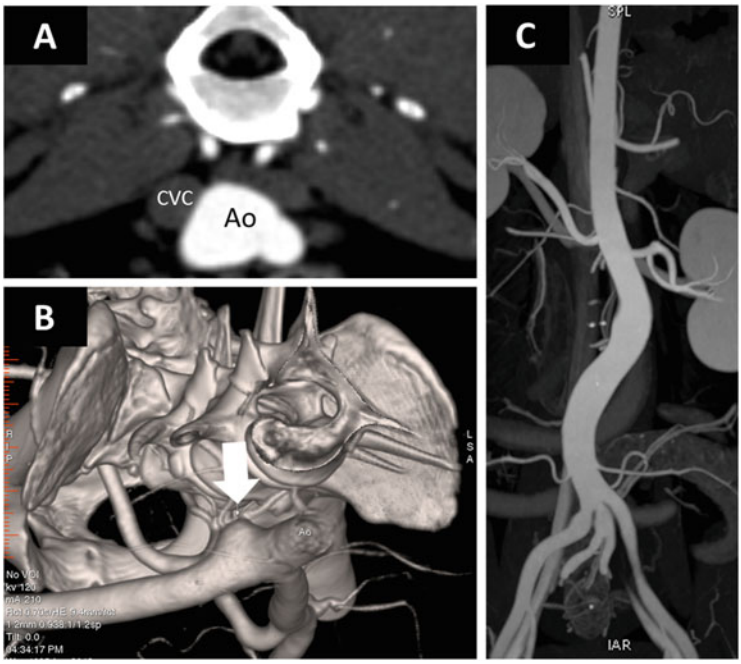

Fig. 10 (**a**) Transverse view from 16-MDCTA of a dog with pseudoaneurysmal dilation at the aortic bifurcation. (**b**) VR, frontal oblique cut, showing the pseudoaneurysm (*arrow*). (**c**) 16-MDCTA image of another dog with a tortuous course of the abdominal tract of the descending aorta

presentation in dogs (Figs. 11 and 12). Aortic thromboembolism is found in cats with preexisting heart disease and other chronic predisposing conditions. MDCTA plays an important role in the definitive diagnosis of aortic thrombosis in dogs and cats, and it aids evaluation of the true extension of vascular occlusion and planning of surgical and interventional radiological procedures. Familial aortic aneurysm with dissecting hemorrhage has been reported in Leonberg dogs. Mural thrombi and/or hematomas, which can lead to spontaneous aortic dissection, can be found in patients with severe systemic diseases (Fig. 13).

3.3 Anomalies of the Caudal Vena Cava

A wide range of congenital variants, anomalies, and pathological conditions can affect the caudal vena cava and the abdominal veins. In adult mammals, the abdominal caudal vena cava is typically a single right-sided vessel developed in five segments: from caudal to cranial, the prerenal, renal, prehepatic, hepatic, and posthepatic segments.

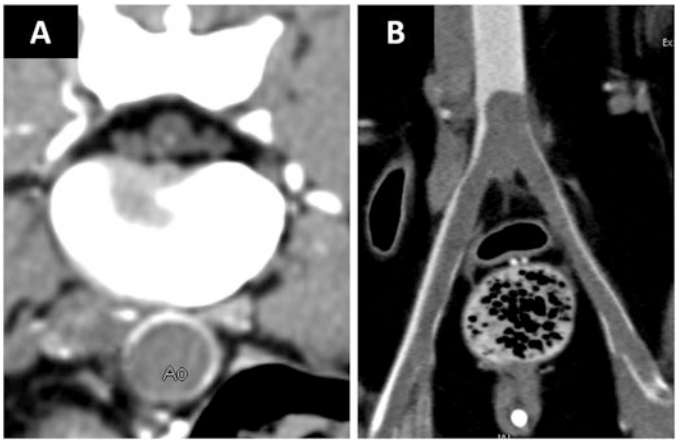

Fig. 11 An 8-year-old dog with extensive aortoiliac thrombosis secondary to nephrotic syndrome due to leishmaniasis. (**a**) Transverse view. Note the filling defect in the aorta (Ao). (**b**) Dorsal MPR view of the same dog, showing the extension of the thrombus into both iliac arteries

3.3.1 Congenital Anomalies of the Caudal Vena Cava

Most caudal segments of the caudal vena cava are more prone to congenital variation, which is generally clinically silent. However, familiarity with these variants is important to avoid misdiagnosis and potential complications during surgery. Moreover, cava variations may affect venous approaches from the femoral vein and should thus be considered before interventional radiological procedures. Again, they are often associated with other vascular and nonvascular anomalies that can be of great clinical relevance (Fig. 14). Knowledge of the developmental mechanisms involved in segmental variation and anomalies in the caudal vena cava is essential for radiological interpretation. However, a full description of normal developmental processes of the venous system in dogs and cats is beyond the scope of this book. Below, we briefly outline possible embryonic mechanisms of each cava variant or anomaly.

The *preureteral vena cava* occurs when the right cardinal vein system fails to develop normally. The genitourinary and vena cava systems develop separately, but spatial relationships between the ureters and the caudal vena cava depend on correct embryonic development of the vessel. A persistent right cardinal vein traps part of the ipsilateral ureter dorsal to it (Fig. 15). This anomaly of the caudal vena cava, also known as "circumcaval ureter" or "retrocaval ureter," can be discovered incidentally during MDCT examination. The ureter may be significantly compressed, resulting in hydroureter and hydronephrosis. In cats, the preureteral vena cava has been associated with various signs in the lower urinary tract, as reported in humans.

The *left-sided caudal vena cava* involves the prerenal segment of the vessel (Fig. 16). The left prerenal cava represents the persistence of the left supracardinal vein with anomalous regression of the right supracardinal vein. In the renal region,

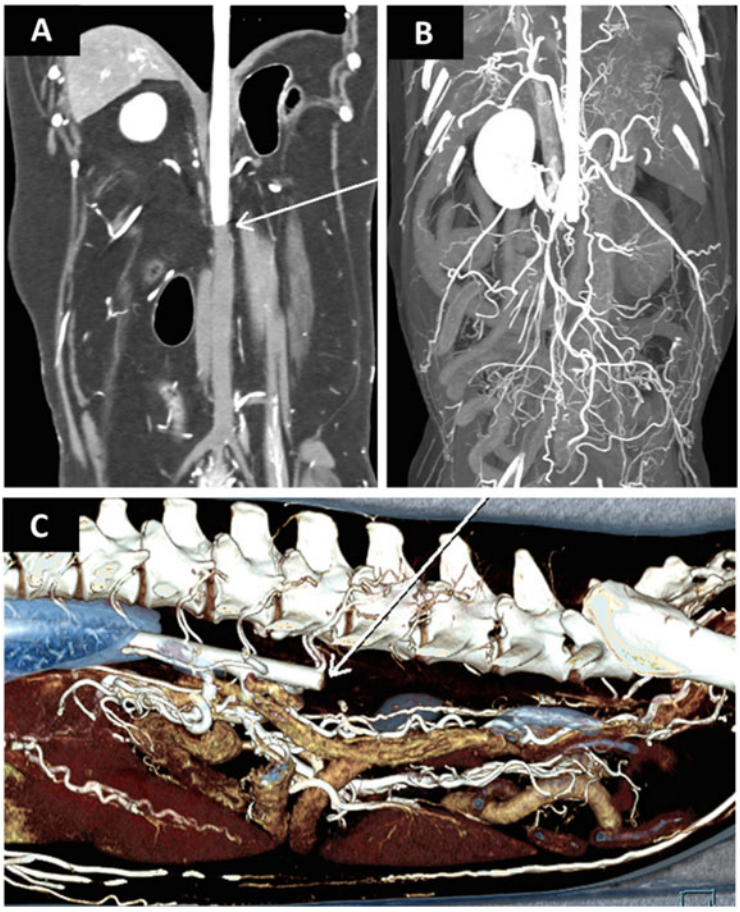

Fig. 12 128-DSCT abdominal angiographic images from a dog with aortic thrombosis involving the left renal artery, caudal mesenteric artery, and iliac arteries. (**a**) Dorsal MPR view showing the interruption of contrast distribution in the descending aorta (*arrow*). (**b**) Dorsal thin-slab MIP view showing numerous collaterals from the abdominal branches of the phrenico-abdominal arteries. (**c**) VR (*left view*) showing the lack of enhancement of the lumbar segment of the descending aorta and lumbar and iliac arteries

the left cava crosses the midline of the abdomen to join the normal right-sided cava. This situation can result in left retrocaval ureter.

Duplication of the caudal vena cava is a not an uncommon MDCT finding in dogs and cats. Two different patterns of duplication are possible in dogs: *complete duplication*, in which the prerenal and renal segments are duplicated; and *partial duplication*, which involves only the prerenal segment of the cava (Fig. 17). The persistence of both supracardinal veins and the intersubcardinal anastomosis and disturbances of the subsupracardinal anastomosis are embryonic mechanisms possibly involved in duplication. In a large-scale study we conducted in dogs in our

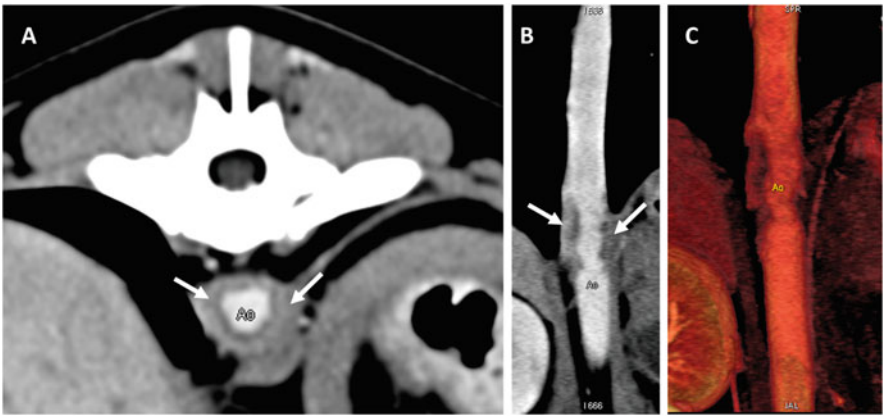

Fig. 13 (**a**) Transverse 2D image from late arterial phase in a dog with systemic micobacteriosis. Note the mural infilatration of the descendig aorta (*arrows*). (**b**, **c**) are 2D MPR dorsal view and 3D VR of the same data, showing the extension of the mural infiltration and the irregular filling defect of the vascular lumen. *Ao* aorta

hospital, the prevalence of caudal vena cava duplication was 2.08%. Small dogs are more likely to have duplication of the cava, and complete duplication is the most common pattern. Certain toy breeds, such as Yorkshire terrier, poodle, and Maltese, seem to have an increased risk of vena cava duplication, and this anomaly is associated significantly with CPSS.

Interruption of the caudal vena cava with azygous continuation occurs when the right subcardinal–hepatic anastomosis fails to form, resulting in right subcardinal vein atrophy. In such cases, the hepatic segment of the caudal vena cava is absent. The caudal vena cava receives the renal veins in its renal segment and then runs dorsally past the diaphragmatic crura to join the right azygous vein in the thorax (Fig. 18). The absence of a normally developed prehepatic segment of the caudal vena cava with azygous continuation can be an incidental finding. However, this vascular variant is often associated with other vascular and nonvascular anomalies with clinical relevance. In dogs, azygous continuation of the caudal vena cava has been described in association with portal vein aplasia and portocaval shunting, with or without situs inversus abdominalis (Fig. 19).

Caudal vena cava aneurysm is a rare condition of local permanent dilatation of the vessel wall. Congenital aneurysm has been reported to be associated with cava interruption with azygous continuation and renal vein aneurysm. Cava thrombosis is present and cava collaterals may form attempting to maintain the venous return to the right heart (Fig. 20).

The caudal vena cava is frequently involved in CPSS and acquired portosystemic shunting (APSS). The prehepatic and hepatic segments of the caudal vena cava are most frequently involved in CPSS. The renal segment of the caudal vena cava is most frequently involved in acquired portosystemic connections, directly or by means of the renal or phrenico-abdominal veins.

Anomaly	Nature	CT signs
Left vena cava	Congenital	Normal shaped, left-sided pre-renal segment of CVC crossing the midline at renal level. It may result in hydrourether and hydronephrosis. Other CVC and portal anomalies can coexist.
Double vena cava	Congenital	Partial (pre-renal) and complete (pre-renal/renal) patterns. The left renal vein joins the unified CVC or the left persistent cava. The two cava veins may have same or different diameter. CVC duplication and PSS may be associated.
Pre-ureteral vena cava	Congenital	The ureter runs dorsal to CVC and may result in hydrourether and hydronephrosis. Other CVC (left CVC or duplication) or portal anomalies can coexist.
Interruption CVC with azygos continuation	Congenital	At renal region, CVC runs dorsally and joins with right azygos (enlarged). Other CVC and portal anomalies can coexist.
CVC aneurysm	Congenital Acquired	Segmental dilatation of the CVC. Associated with azygos continuation in congenital form. Renal vein aneurysm may coexist. Thrombosis and cava collaterals may be present.
CVC thrombosis/invasion	Acquired	Filling defect in contrast-enhanced scans. Neovascularization and collaterals are often present.
CVC collaterals	Acquired	Cavo-cavo collaterals (deep, intermediate, superficial pathways) and cavo-portal collaterals (colic vein, mesenteric vein pathways) are possible. In hepatic/posthepatic CVC obstruction; acquired portocaval shunts may coexist.

Fig. 14 Resumes CdVC variations and concomitant anomalies

3.3.2 Acquired Anomalies of the Caudal Vena Cava

Thrombosis of the caudal vena cava and its tributaries is a persistent filling defect in the vessel that can be visualized by contrast-enhanced examination (Fig. 21). Disturbances of hemostasis and neoplastic states are the most common causes of thrombosis in the caudal vena cava and hepatic veins. Importantly, the mixture of

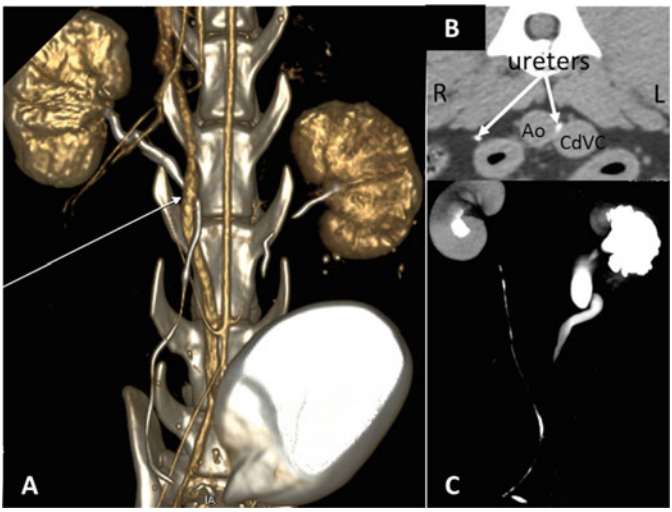

Fig. 15 (**a**) 16-MDCT image (VR, ventral view) of a cat with a right pre-ureteral vena cava trapping the ipsilateral ureter. Note the slight distension proximal to the ureteral entrapment. (**b**) Transverse view of the excretory phase in a Bernese dog with left ureteral entrapment between the aorta (Ao) and left-sided prerenal segment of the caudal vena cava (CdVC). (**c**) Volume-rendered image of the same volume dataset, showing left hydroureter and hydronephrosis

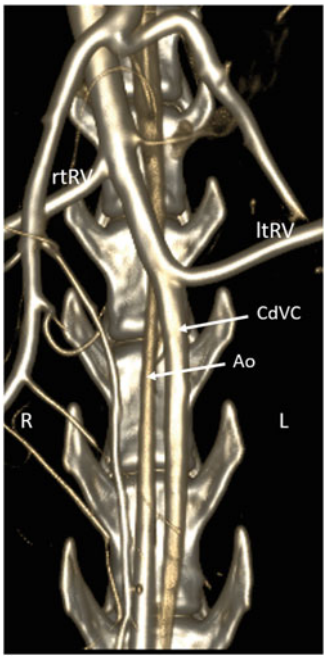

Fig. 16 Left prerenal segment of the caudal vena cava in a cat (16-MDCT volume-rendered image, ventral view). rtRV, right renal vein; ltRV, left renal vein; CdVC, caudal vena cava; Ao, aorta

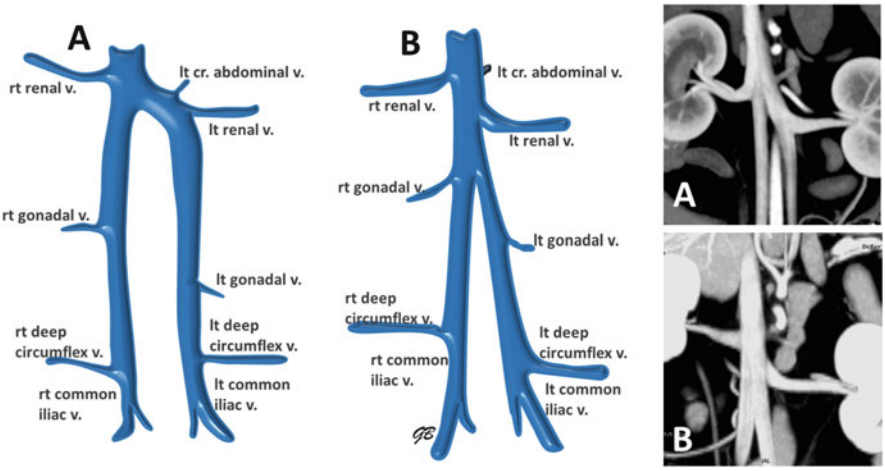

Fig. 17 Patterns of vena cava duplication in dogs (see the text for further explanation)

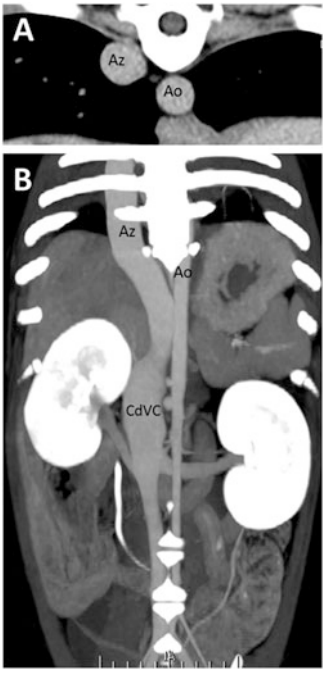

Fig. 18 Azygous continuation of the caudal vena cava. (**a**) Transverse section showing the azygous vein section, which is larger than that of the aorta. (**b**) Dorsal MIP image of another dog with azygos continuation

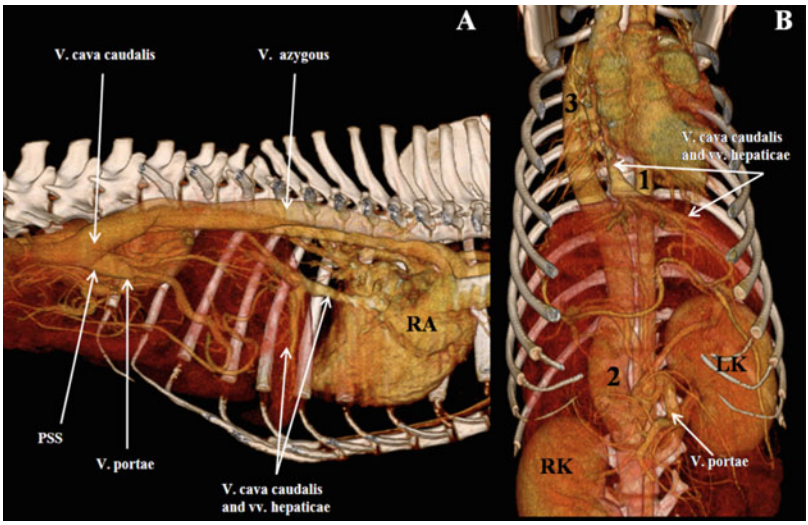

Fig. 19 (**a**) Right lateral view of a volume-rendered image (16-MDCT) of a dog with azygous continuation of the caudal vena cava, and portal atresia with portocaval connection (portosystemic shunt). (**b**) Ventral volume-rendered view of the same dog showing situs inversus abdominalis. The left kidney (LK) is cranial and the right kidney (RK) is caudal. *1* aorta; *2* caudal vena cava; *3* right azygous vein

enhanced blood from the renal veins with unenhanced blood from most caudal regions of the body, which can occur with the use of rapid CM injection rates and early scans, can cause filling artifacts in the caudal vena cava that can mimic thrombosis, leading to misdiagnosis.

Several tumors, especially renal and adrenal neoplasias, can spread into the caudal vena cava. MDCT can be used to easily identify tumor invasion of the caudal vena cava and clearly delineate continuity from the mass and the tumor thrombus within the vessel, aiding the differentiation of malignant thrombosis from a hematic thrombus. This information is essential, as treatment decisions depend on proper assessment of the level and extension of the tumor thrombus.

A thrombus in the caudal vena cava is the principal imaging sign of vascular invasion in oncology patients with retroperitoneal masses. *Malignant thrombosis* can involve one or more segments of the caudal vena cava. Renal tumors may extend directly into the cava or grow into the renal vein and then into the cava's renal segment. Similarly, adrenal tumors can involve the vena cava directly or spread into the phrenico-abdominal and/or renal veins and then into the caudal vena cava (Fig. 22). Depending on the site of tumoral invasion, and the grade and duration of obstruction, other CT signs are expected and should be analyzed. Neovascularization inside and around the tumor thrombus is detectable during the arterial phase and aids the distinction of malignant from nonmalignant obstructions.

With chronic obstructions of the caudal vena cava, independently of the cause of obstruction, *cava collateral pathways* may form to maintain venous drainage to the

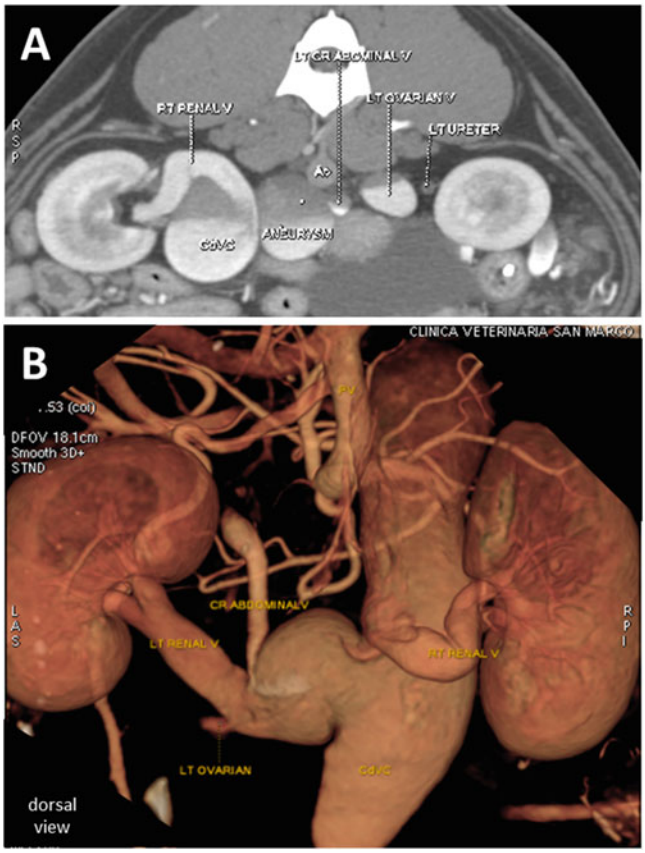

Fig. 20 Congenital caudal vena cava aneurysm in a 1-year-old female Amstaff. (**a**) Transverse view. (**b**) Dorsal volume-rendered image showing the involvement of the renal veins

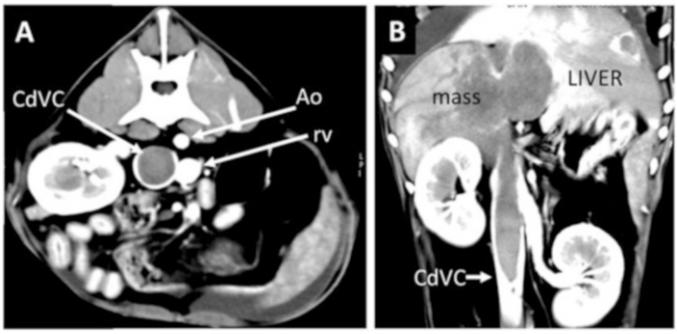

Fig. 21 Caudal vena cava thrombosis in a dog with hepatic sarcoma. *Ao* aorta, *CdVC* caudal vena cava, *rv* renal vein

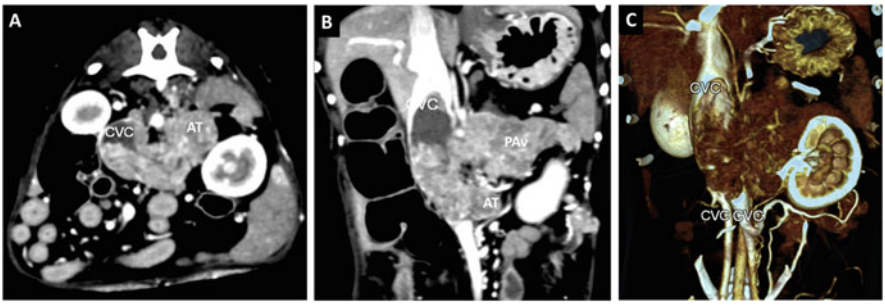

Fig. 22 Malignant thrombosis in a dog with a left adrenal gland tumor (AT). (**a**) Transverse view. The tumor invades the phrenico-abdominal vein (PAV), reaching the renal segment of the caudal vena cava (CVC). Note different components of the thrombus (tumoral and hematic). (**b**) Dorsal MPR view showing the extension of the tumor and hematic thrombi. (**c**) VR of the same volume dataset, showing that the patient also had duplication of the prerenal segment of the caudal vena cava

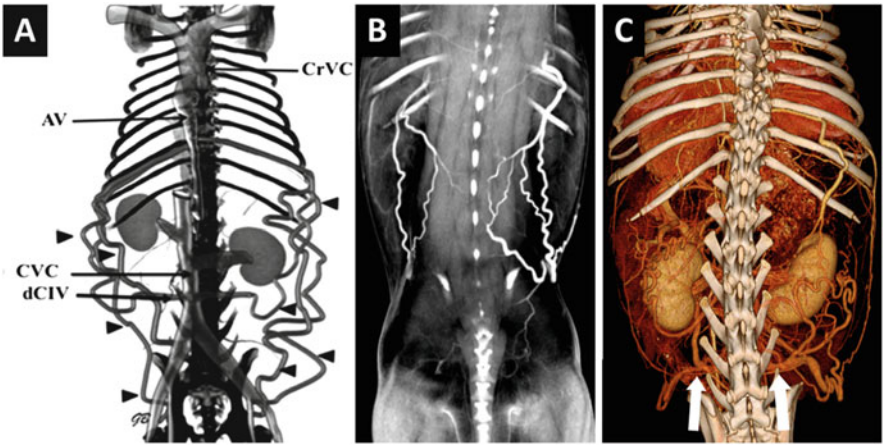

Fig. 23 (**a**) Schematization of superficial pathways. Enlargement of the iliac circumflex veins (dCIV) draining blood from the common iliac veins into the cranial and caudal superficial branches of the iliac circumflex veins, localized in the dorsal abdominal subcutaneous tissues (*arrowheads*), ultimately ending in the azygos vein (AV) through the intercostal veins. (**b**) Dorsal MIP views of a dog with superficial pathways. (**c**) Dorsal volume-rendered view of the same dog. Note the enlarged deep circumflex iliac veins (*arrows*)

right atrium. In a study conducted at our center using 16-MDCT scanner, we identified four main collateral pathways in dogs:

1. *Superficial pathways* draining into the subcutaneous branches of the superficial circumflex veins and then into the azygous vein through the intercostal veins (Fig. 23).
2. *Intermediate pathways* draining into the renal or caval veins, bypassing the obstruction, through the gonadal and periureteric vein (Fig. 24).

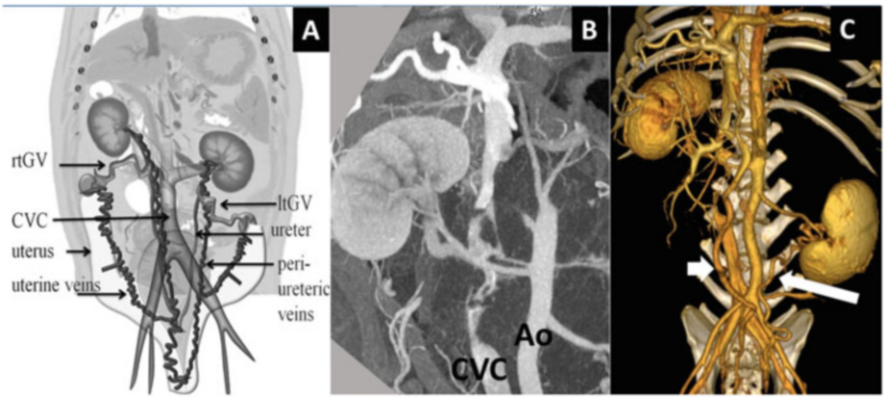

Fig. 24 (**a**) Schematization of intermediated pathways. (**b**) Tumoral invasion of the caudal vena cava (CVC) in a dog. *Ao* aorta. (**c**) Note the enlargement of the periureteric veins (*long arrow*). The left colic vein (*short arrow*) is also enlarged (concomitant cavoportal collateral)

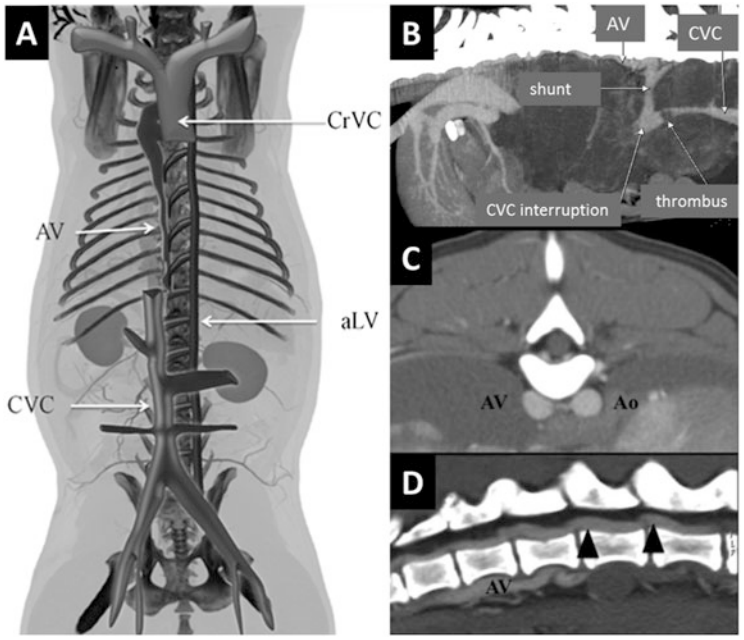

Fig. 25 (**a**) Schematization of deep pathways. (**b**) Cavo-azygos connection in a dog with caudal vena cava interruption due to tumoral invasion. (**c**, **d**) Note the enlargement of the vertebral venous plexus (*arrowheads*) and azygos vein (AV)

3. *Deep pathways* draining into the right azygous vein directly or through the vertebral venous plexus and finally into the azygos vein (Fig. 25).
4. *Portal pathways* draining into the portal vein, also called cavoportal collaterals, due to branches of the mesenteric veins (Fig. 26).

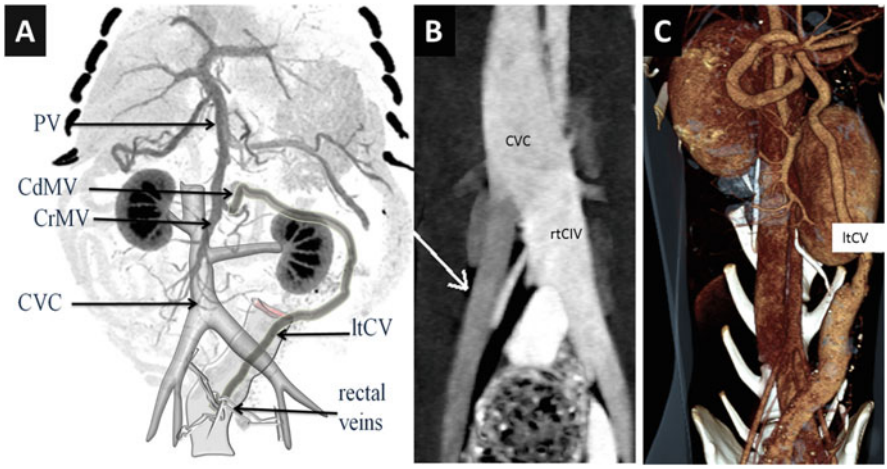

Fig. 26 Portal collateral pathway (cavoportal collateral) in a dog with obstruction of the right common iliac vein. Note the enlargement of the left colic vein. *PV* portal vein, *CdMV* caudal mesenteric vein, *CrMV* cranial mesenteric vein

These pathways should not be confused with other congenital or acquired vascular anomalies having different nature, such as portosystemic shunt. However, acquired portosystemic shunts can occur concomitantly with venous collateral pathways. When a caval thrombus extends cranially, involving the hepatic and/or posthepatic segments of the caudal vena cava, the obstruction of venous flow in the liver can lead to increased portal pressure (post-sinusoidal portal hypertension). In these cases, MDCT shows indirect signs of portal hypertension, such as ascites, varices, and other acquired portosystemic collaterals (Budd–Chiari-like syndrome). Cavoportal collaterals caused by chronic venous obstruction and portosystemic collaterals caused by post-sinusoidal portal hypertension can coexist in patients with hepatic/posthepatic cava obstructions, making imaging analysis difficult. In a multiphasic MDCT evaluation, the opacity of the CM in the collateral vessel matches that of the venous system from which the blood flows: the cava in a case of cavoportal collateral vessels, and the portal system in a case of acquired portosystemic collaterals. High-quality MDCTA data, together with anatomical and physiopathological knowledge, are necessary for accurate image interpretation.

3.4 Anomalies of the Portal Venous System

The portal circulation drains the digestive organs, spleen, and pancreas and delivers blood to the liver via the portal vein and portal branches within the liver. Normally, blood flow in all branches of the portal venous system is hepatopetal (moving in a caudocranial direction), which enables the metabolism of toxic substances absorbed in

the intestine in the liver before they enter the systemic circulation. The detoxified blood is drained by the hepatic veins, which enter the hepatic segment of the caudal vena cava and the right heart through the posthepatic segment of the caudal vena cava.

In normal adult mammals, no apparent vascular connection between the portal system and the systemic venous circulation exists. The systemic venous circulation includes all vascular systems that drain blood directly (bypassing the liver) from the veins of various tissues and organs in the right atrium: the caudal vena cava, azygous vein, and cranial vena cava. Gross anatomic connections between the portal system and systemic venous circulation, at any level, can have serious clinical consequences.

A broad spectrum of congenital and acquired disorders may affect the portal venous system in small animals. Moreover, congenital portal venous system anomalies (PVSA) can cause acquired portal collateral formation. Anomalies of the portal vein and portal system in small animals have been increasingly detected in recent years with the growing availability of advanced imaging techniques in veterinary practice.

Congenital disorders of the portal system reflect a variety of embryonic/fetal disturbances, which may be isolated or combined in complex vascular patterns, and may cause acquired vascular disorders. MDCT is now widely considered to be the method of choice for the diagnosis and monitoring of portal vascular anomalies. MDCTA provides excellent visualization of complex vascular anomalies and a comprehensive overview of the entire portal system and other vascular and nonvascular structures of the abdomen.

Congenital absence of the portal vein (CAPV) refers to the absence of the extrahepatic portal vein, with portal insertion into the caudal vena cava and total diversion of portal blood into the systemic circulation. The extrahepatic portal vein forms from selective involution of the caudal part of the vitelline veins. Portal vein absence is attributed to excessive involution of the periduodenal vitelline veins or failure of the vitelline veins to establish anastomosis with hepatic sinusoids, which leads to partial or complete absence of the portal system. Imaging alone is insufficient to distinguish between these two conditions. Histological confirmation of the presence or absence of portal venules within the portal triad in the liver is mandatory for the final diagnosis of portal agenesis (or aplasia).

The presence or absence of the portal vein (atresia) in an extrahepatic portosystemic shunt (EHPSS) is an important imaging finding that affects therapeutic options and prognosis. However, MDCT features should be interpreted cautiously. Reduced portal blood flow in the portal vein due to flow diversion through the shunt may simulate the absence of the portal vein (Fig. 27). An adequate portal venous vascular phase may reveal a thin, hypoperfused portal vein and branches, which makes the patient a candidate for surgical attenuation of the portosystemic shunt. Catheter angiography and additional histopathological analysis of the liver parenchyma should be performed in patients with suspected congenital absence of the portal vein. When the absence of the portal vein is confirmed, surgical attenuation of the portosystemic connection will result in fatal acute portal hypertension. Other developmental anomalies can occur together with

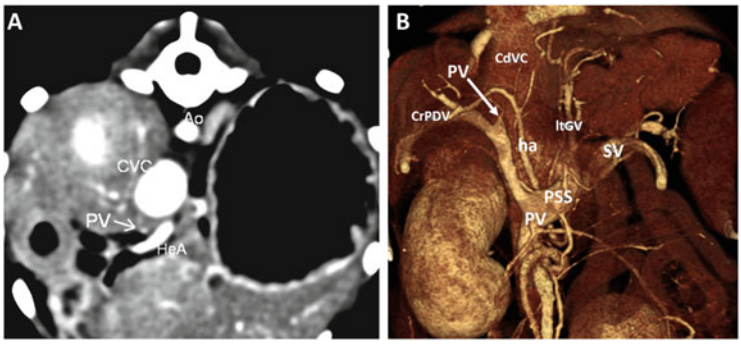

Fig. 27 Portal vein atresia in a dog with an extrahepatic congenital portocaval shunt. (**a**) Transverse view. Note the hypoperfused, thin portal vein and enlarged caudal vena cava. (**b**) VR showing the portosystemic shunt and the apparently interrupted portal vein (*arrow*)

the congenital absence of the portal vein in dogs, and their presence can aid radiological diagnosis. These anomalies include situs inversus, congenital heart diseases, vena cava anomalies, and polysplenia (Fig. 19).

Finally, portal vein stenosis and obstruction may be seen in cases of gradual chronic portal vein thrombosis (PVT) or other chronic conditions (e.g., portal fibrosis, extrinsic neoplastic compression). Portal stenosis and obstruction may cause portal hypertension and can be accompanied by porto-portal collaterals and acquired portosystemic shunt (APSS).

Portal vein hypoplasia (PVH) is a morphological [*primary portal vein hypoplasia (PPVH)*] or functional (*secondary PVH*) disorder in which microscopic portal veins within the liver are underdeveloped. Histopathological diagnosis is thus required; imaging alone cannot be used to diagnose this condition. However, to rule out macroscopic portal system anomalies, the integration of imaging and histological information is mandatory. Macroscopic disorders causing chronic hypoperfusion of the liver, such as portosystemic shunting, arterioportal fistula (APF), and PVT, have the same histological features as PPVH. MDCT features of PPVH are small liver size, hepatic perfusion disorders, and the absence of CPSS. Ascites and acquired portal collaterals may be present, due to hepatic portal hypertension secondary to PPVH.

Portal vein aneurysm (PVA) is a relatively uncommon anomaly in dogs, with a reported prevalence of 0.49%. It can be congenital or acquired in nature. Inherent weakness of the vessel wall or incomplete regression of the distal part of the vitelline vein may give rise to an aneurysm. Larger, male dogs are more frequently affected, and the boxer breed seems to be predisposed to PVA development. On MDCT images, PVA appears as saccular or fusiform dilatation of the portal vein or its branches within the liver. Extrahepatic PVAs are generally located at the insertion of the gastroduodenal vein into the portal vein. Intrahepatic PVAs occur at bifurcations (Fig. 28). Clinical features of PVAs are related to their size and possible complications, such as thrombosis, rupture of the aneurysm, and portal

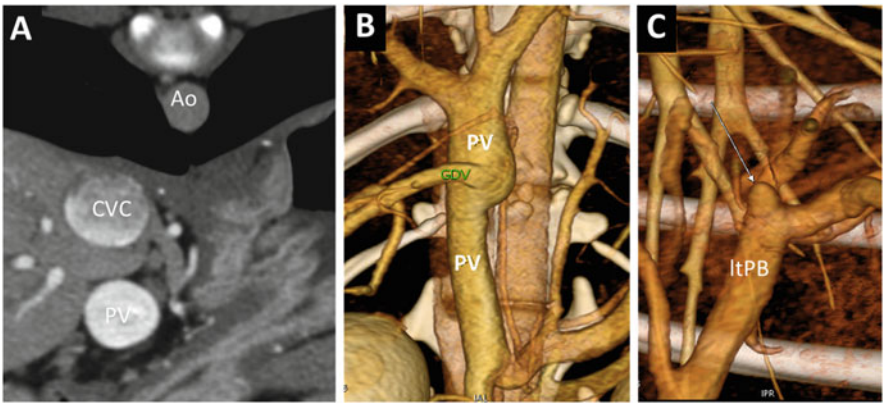

Fig. 28 (**a**) Transverse view at the porta hepatis in a dog with chronic hepatopathy. The portal vein is enlarged. (**b**) Aneurysmatic dilatation of the extrahepatic portal vein. (**c**) In the same dog, small intrahepatic aneurysm of the umbilical portion of the left portal branch (*arrow*)

hypertension. Acquired portal collaterals may coexist with PVA. Focal dilatation of the portal branches can be detected also in cases of intrahepatic CPSS and APF. Mesenteric vein aneurysm can occur in dogs, alone or in combination with PVA (Fig. 29).

3.5 Anomalous Portal Vascular Connections

Anomalous PV connections encompass several congenital and acquired conditions characterized by macroscopic functional connections between the portal and arterial or systemic venous systems. They can be classified broadly as high-flow and low-flow portal connections.

High-flow anomalous portal connections are rare structural or functional communications between a high-pressure hepatic arterial branch and a low-pressure portal branch, which may lead to pre-sinusoidal portal hypertension. They include congenital *hepatic arteriovenous malformation (HAVM)* and acquired *arterioportal fistula (APF)*. HAVM is generally characterized by multiple complex intrahepatic vascular anomalies, which may be accompanied by PVA and are difficult to treat definitively (Fig. 30). Penetrating abdominal trauma, including liver biopsy, and neoplasia are possible etiologies of acquired APF (Fig. 31). These anomalies have been described in dogs and cats. They can be treated by transcatheter embolization alone or, in most serious cases, in combination with surgery (Fig. 32).

MDCT signs of APF include earlier enhancement of the portal vein or its branches in the early arterial phase of a multiphasic thin-slice examination. One or more aneurysmal dilatations of the portal branches can be noted. The surrounding liver may show transient segmental parenchymal enhancement. Indirect signs

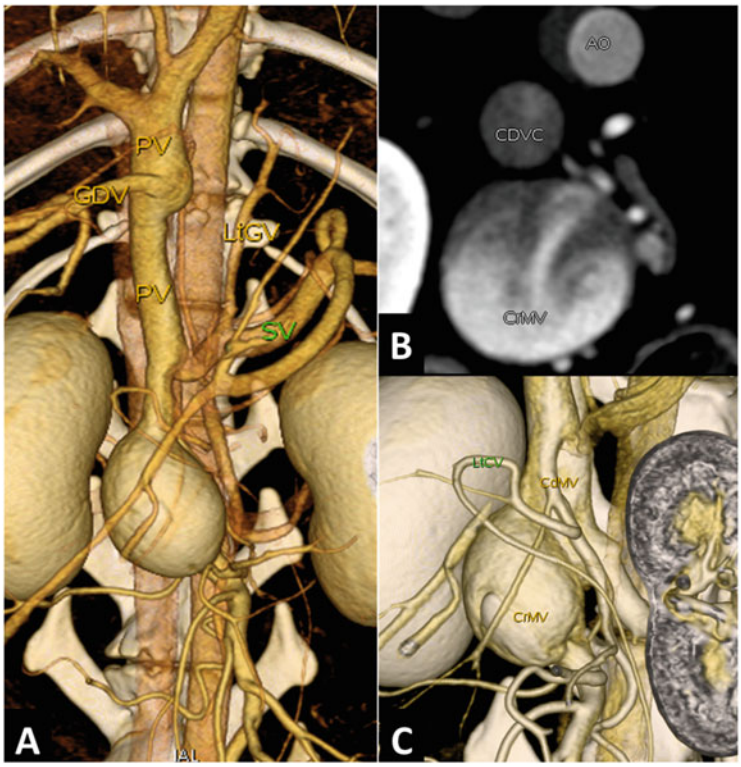

Fig. 29 (**a**) Volume-rendered image of a large aneurysm of the cranial mesenteric vein in a dog. Dilatation of the extrahepatic portal vein is also apparent. *PV* portal vein, *GDV* gastroduodenal vein, *LtGV* left gastric vein, *SV* splenic vein. (**b**) Transverse view showing sections of the aorta and caudal vena cava, and the mesenteric aneurysm (note the turbulent flow, visible during the PVP). (**c**) VR showing the cranial mesenteric vein aneurysm and its relationships with other regional vessels. *CrMV* cranial mesenteric vein, *CdMV* caudal mesenteric vein, *LtCV* left cholic vein

of portal hypertension, such as ascites, varices, and other acquired portosystemic collaterals, may be present. In several pathological conditions of the liver, small acquired peripheral APFs can be detected. These APFs do not require treatment, as they usually resolve spontaneously.

Low-flow anomalous portal connections include congenital and acquired porto-systemic shunts and porto-portal and cavo-portal collaterals. The latter are described earlier in this chapter, with the description of various collateral pathways in cases of chronic obstruction of the caudal vena cava. Porto-portal collaterals may accompany chronic portal vein thrombosis and are described below in this chapter.

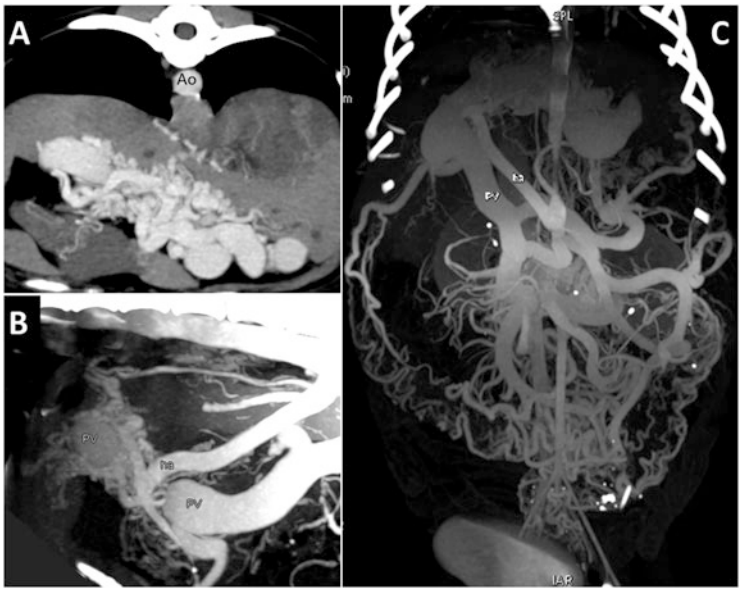

Fig. 30 16-MDCTA image of a dog with congenital HAVM. (**a**) Transverse view at the porta hepatis. (**b**) Sagittal MPR view. (**c**) Dorsal thick-slab MIP image of the same dog, showing multiple collateral pathways

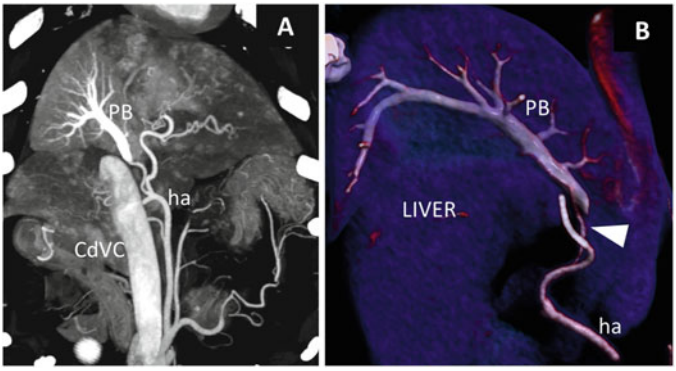

Fig. 31 Multiphasic 128-DSCT study of the liver in a dog with a single acquired intrahepatic APF. (**a**) Dorsal MIP view showing a direct connection between a small artery from the hepatic artery (ha) and a right-sided portal branch (PB) within the liver. Note the early enhancement of the dependent portal vascularization and the surrounding parenchyma. Also note that the caudal vena cava is already enhanced (venous drainage from early perfused liver parenchyma). (**b**) Volume-rendered close-up view of the arterioportal connection within the liver (*arrowhead*)

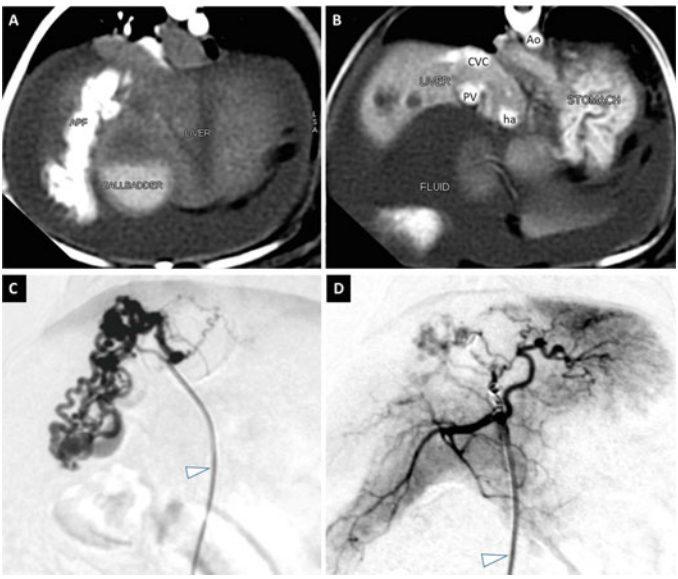

Fig. 32 (**a**, **b**) 16-MDCTA transverse views of the liver of an 8-year-old Chihuahua (2 kg) with an acquired intrahepatic APF and PH. (**c**, **d**) Pre- and post-superselective microcoil embolization angiograms from the same dog. *Arrowhead* indicates the microcatheter in the hepatic artery

3.5.1 Portosystemic Shunts

The advent of MDCT technology has completely changed the diagnostic workup for congenital portosystemic shunt in small animals. MDCT enables simultaneous evaluation of the vascular anomaly and its effects in the body. MDCT data can provide information on liver volume, nephrolithiasis, gastroenteric complications, and brain atrophy secondary to chronic hepatic encephalopathy. The first study of the use of MDCT for the assessment of congenital portosystemic shunt in dogs employed a 16-row scanner and was conducted more than 10 years ago. However, the scientific community did not initially accept this tremendous change, perhaps due to the high cost of the technology at that time. The situation has now changed, with the diffusion of less expensive and refurbished MDCT scanners in veterinary radiology centers worldwide. Nowadays, MDCT is considered the reference method for vascular anomalies in veterinary patients.

Congenital portosystemic shunt (CPSS) refers to the presence of abnormal vascular connections due to embryonic errors or fetal vascular persistence; it connects the portal system directly to a systemic vein (caudal vena cava or azygous system), bypassing the liver. Based on its anatomic location, CPSS may be divided into two main subtypes: intrahepatic and extrahepatic.

An *intrahepatic portosystemic shunt (IHPSS)* represents a patent ductus venosus, which usually closes early after birth. Three phenotypes of IHPSS, depending on the side of insertion into the hepatic caudal vena cava, are commonly

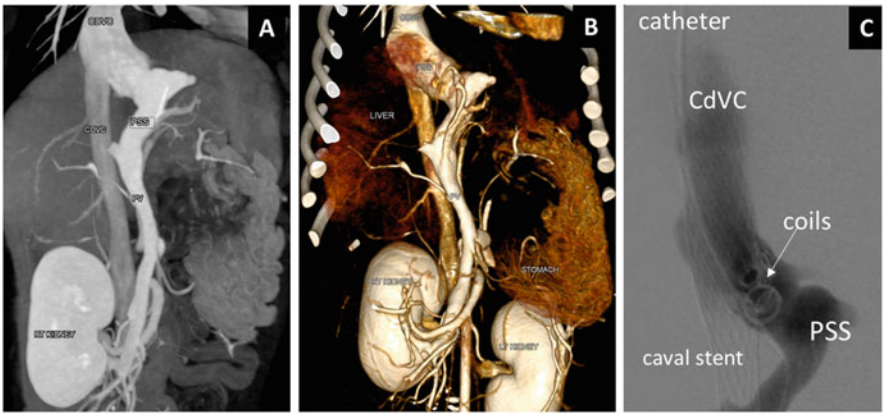

Fig. 33 *Left-sided* IHPSS in a dog. (**a**, **b**) Dorsal MIP and volume-rendered images from a 128-DSCT vascular study. (**c**) Intravascular treatment (caval stenting and coil embolization)

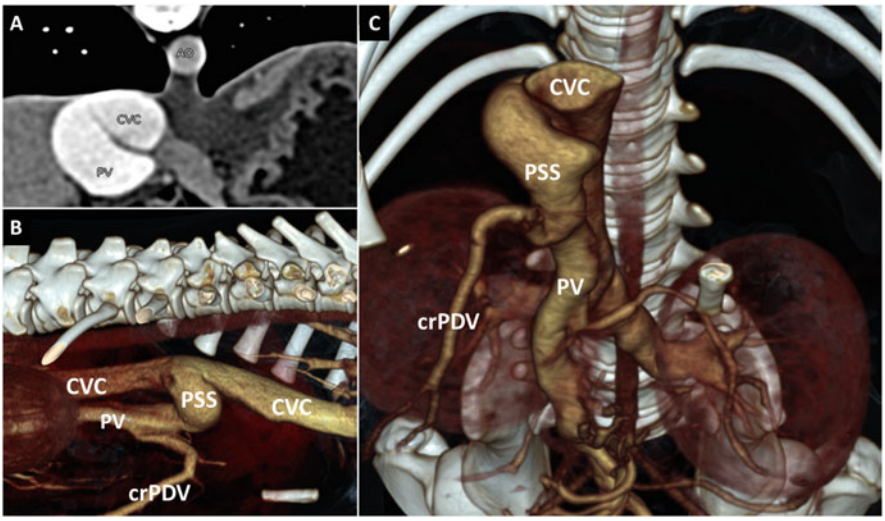

Fig. 34 *Right-sided* IHPSS in a dog (128-DSCT). (**a**) Transverse view. (**b**) Volume-rendered image, *right lateral view*. (**c**) Volume-rendered image, frontal oblique view. *Ao* aorta, *CVC* caudal vena cava, *PV* portal vein, *PSS* portosystemic shunt, *crPDV* cranial pancreaticoduodenal vein

described in the veterinary literature: right-sided, central, and left-sided (or divisional) (Figs. 33, 34, and 35). IHPSS mostly affects large-size dogs. With the widespread use of MDCT in patients with suspected CPSS, we are constantly discovering new IHPSS patterns. Single or multiple peripheral connections between portal branches and hepatic veins, affecting one or more liver lobes, and portosystemic intrahepatic connections through portal aneurysmal dilatations within the liver are possible presentations (Fig. 36). These cases are generally accompanied by critical clinical conditions and are difficult to treat.

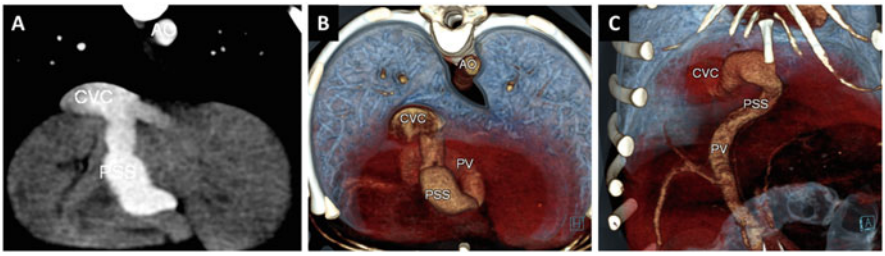

Fig. 35 Central IHPSS in a dog (128-DSCT). (**a**) Transverse view. (**b**) Thin-VR at the porta hepatis. (**c**) VR, ventral view

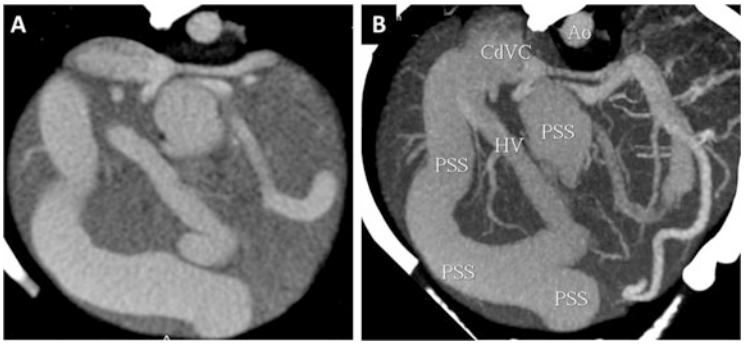

Fig. 36 Complex IHPSS in a puppy

Extrahepatic portosystemic shunts (EHPSSs) are developmental anomalies resulting from anomalous connections between the vitelline veins, which form the portal system, and the cardinal veins, forming the systemic veins. Although the genetic basis of CPSS in dogs has not been clearly established, many studies have demonstrated that this condition occurs more frequently in purebred dogs and that it is inherited in several small and toy breeds. Various repetitive patterns of EHPSS, which reflect a common underlying embryological error, have been described. Several PSS classifications have been proposed so far, based on morphology observed in case series, reports, or review of the literature. Most common types of EHPSSs have been reported in Fig. 37. The shunt can be between the portal vein directly or one of its tributaries (left gastric vein, splenic vein, or right gastric vein) and a systemic vein (caudal vena cava or right azygous vein) (Figs. 27, 38, 39, 40, and 41). Direct connection of the portal vein and a systemic vein may be the result of the congenital absence of the portal vein (described above).

Complex multiple congenital EHPSSs have been reported in dogs. They should not be confused with multiple APSSs, which are sequelae of chronic portal hypertension. Patients with multiple congenital EHPSSs may have other congenital vascular anomalies of the venous system, such as duplication of the caudal vena cava or multiple renal veins. Concomitant ascites and varices suggest an acquired condition.

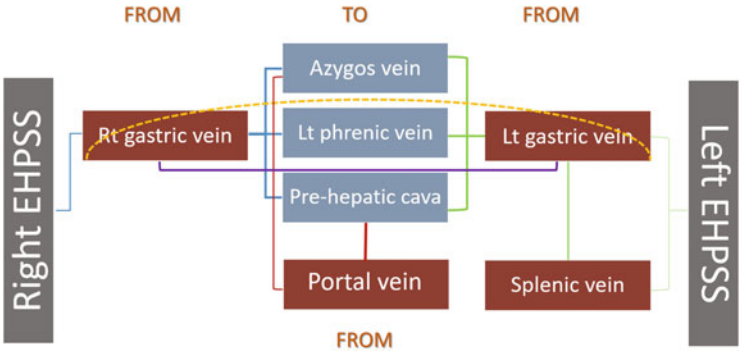

Fig. 37 The most common patterns of EHPSS described in dogs. The portal vein can be interrupted and connected directly with the caudal vena cava or azygos vein (end-to-side shunt with portal vein aplasia). Side-to-side shunts are between a portal vein tributary and a systemic vein. The right gastric vein can emanate shunts joining the caudal vena cava or azygos vein directly or through the phrenic vein or can connect with the left splenogastric veins and then enter the systemic vasculature. From the left, anomalous vessels from splenic and left gastric veins can join the caudal vena cava or azygos vein directly or though the left phrenic vein. The *dotted line* represents the diaphragm

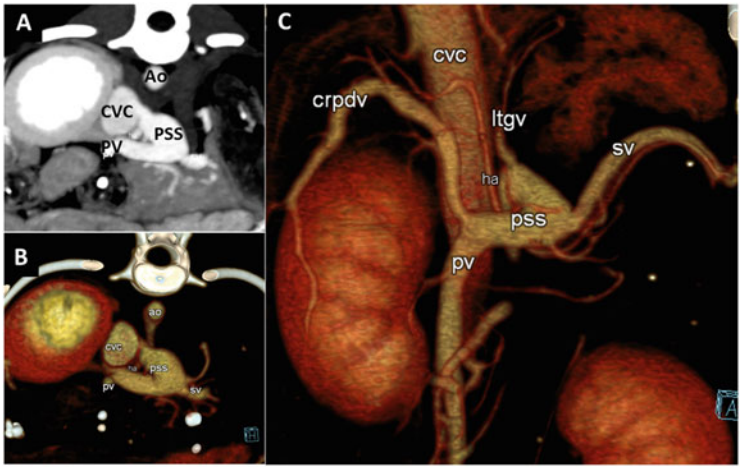

Fig. 38 (**a**) Transverse MIP view of EHPSS between the splenic vein and the prehepatic segment of the caudal vena cava. (**b**) Transverse thin-VR. (**c**) VR, ventral view. *Ao* aorta, *crpdv* cranial pancreatic duodenal vein, *ltgv* left gastric vein, *sv* splenic vein, *ha* hepatic artery, *pv* portal vein, *pss* portosystemic shunt

In patients with CPSS and patent portal veins, the shunting vessel can be closed or attenuated using intravascular or various other surgical techniques. MDCT examinations performed before and after intervention show the degree of attenuation of the shunting vessel, changes in hepatic volume and perfusion, and possible post-attenuation complications.

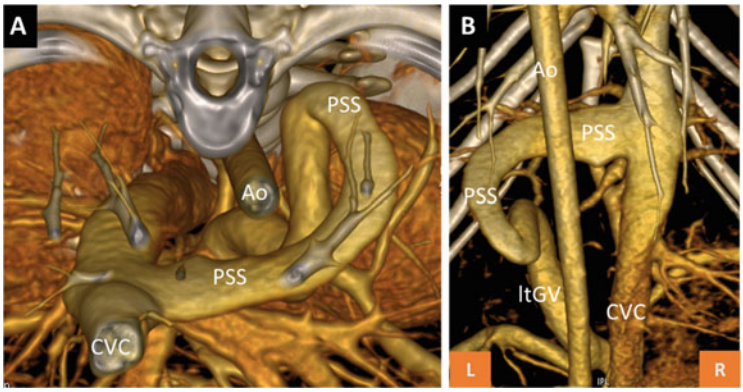

Fig. 39 (**a**, **b**) Transverse and dorsal volume-rendered views of a dog with EHPSS between the left gastric and left phrenic veins

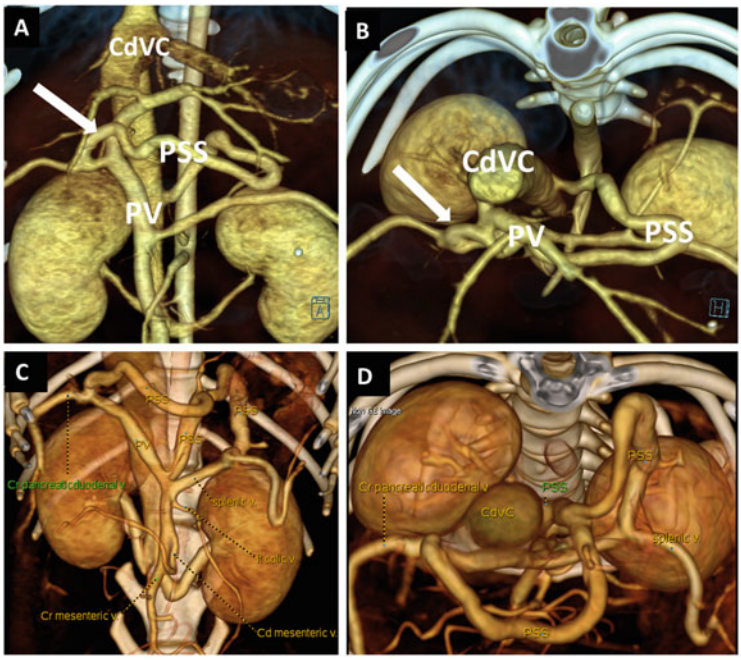

Fig. 40 Two subtypes of EHPSS from the right gastric vein. (**a**, **b**) Ventral and frontal volume-rendered views. The shunting vessel from right gastric vein (*arrow*) crosses the midline of the abdomen and enters the prehepatic segment of the caudal vena cava on its left lateral aspect. (**c**, **d**) Two views of a portosystemic shunt subtype from the right gastric vein. The anomalous vessel starts from the right gastric vein and courses along the lesser curvature of the stomach, where it joins the left gastric vein and enters the prerenal segment of the caudal vena cava

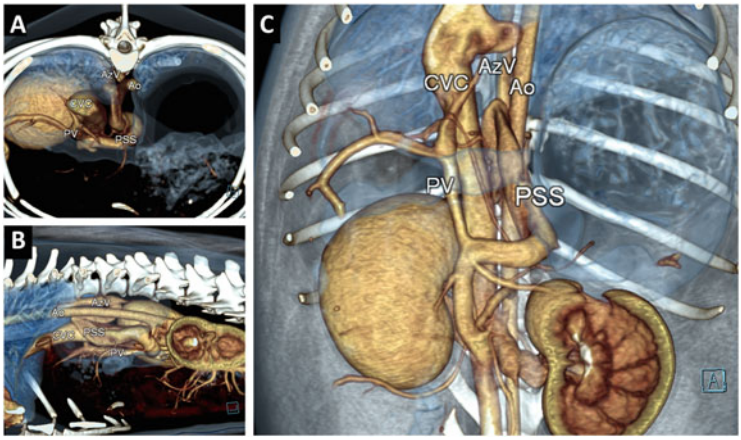

Fig. 41 Left gastro-azygos shunt. (**a**–**c**) Transverse, left, and ventral volume-rendered views from a 128-DSCT vascular study. The shunting vessel originates from the left gastric vein, courses cranially and dorsally, describes a pair of loops, and finally joins the right azygos vein

Acquired portosystemic shunts (APSSs) are characterized by hepatofugal pathways that can be caused by portal hypertension (increased resistance in the portal system) or increased resistance in the cranial vena cava system. In these cases, a combination of hemodynamic, anatomic, and angiogenetic factors leads to neo-angiogenesis and the opening of preexisting vascular connections between the portal and systemic circulations. In normal mammals, no gross connection between these systems is present. In truth, at least three embryonic connections, with no or minimal perfusion, are present in normal animals and may enlarge: the left colic–pudendal vein, left gastric–cardiac esophageal branches, and phrenic–portal vein connections.

Several patterns of APSS have been reported in dogs and cats. They can be divided grossly into large shunts (e.g., left splenogonadal shunt, splenophrenic shunt) and small shunts (e.g., esophageal varices). Large and small APSS often coexist (Fig. 42). Varices may be subdivided according to their anatomic location and pathways into left gastric vein, gastrophrenic, omental, gallbladder, abdominal wall, duodenal, and colic varices (Figs. 43, 44, 45, and 46).

MDCT plays an important role in the diagnostic workup for patients with acquired portal collaterals in cases of portal hypertension or cranial vena cava obstruction. Independent of the cause of portal hypertension, collateral blood flow always bypasses a site of increased resistance or obstruction. On MDCT, the portal vein and portal tributaries caudal to the obstruction are enlarged. One or more collateral pathways may be identified, which enhance to the same degree as does the portal system during the venous portal phase. Ascites and gastroenteric complications of portal hypertension (e.g., superficial hemorrhage, gastric and pancreatic edema) may be identified. Most prehepatic, hepatic, and posthepatic causes of portal hypertension can be easily identified by whole-body MDCT examination.

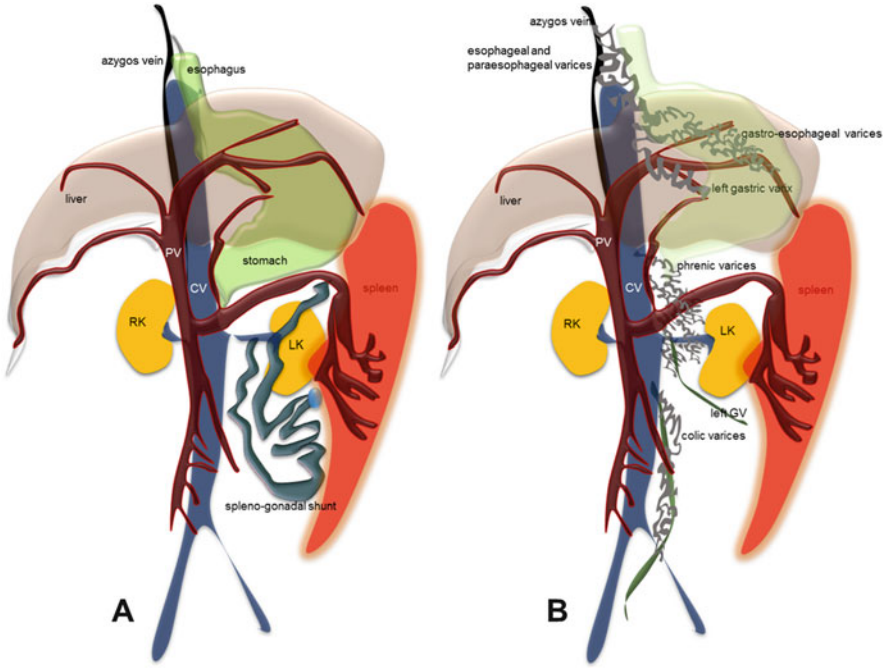

Fig. 42 Schematization of large and small acquired portal collaterals. (**a**) Splenogonadal shunt. (**b**) The most common types of varices and their locations. *GV* gonadal vein, *CV* cava vein, *PV* portal vein

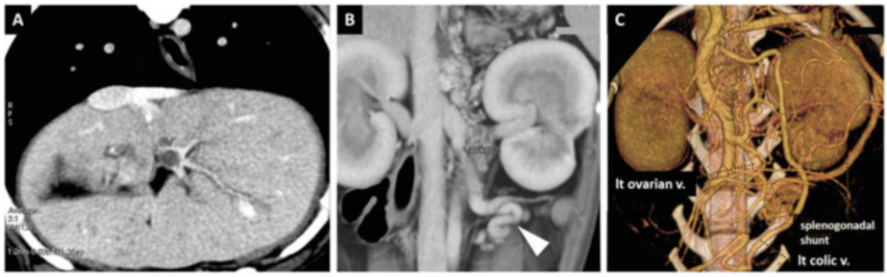

Fig. 43 (**a**) 16-MDCT study in a dog with intrahepatic PVT. (**b**) Dorsal view showing left retroperitoneal (phrenic) varices and simultaneous splenogonadal shunting (*arrowhead*). (**c**) VR from the same dog showing the splenogonadal shunt between the splenic and left ovarian veins and the enlarged left colic vein

MDCT may aid the identification of PVT, portal vein tumoral invasion or extrinsic compression, and portal vein stenosis; intrahepatic parenchymal and biliary diseases; posthepatic caudal vena cava compression or invasion; and right atrial involvement.

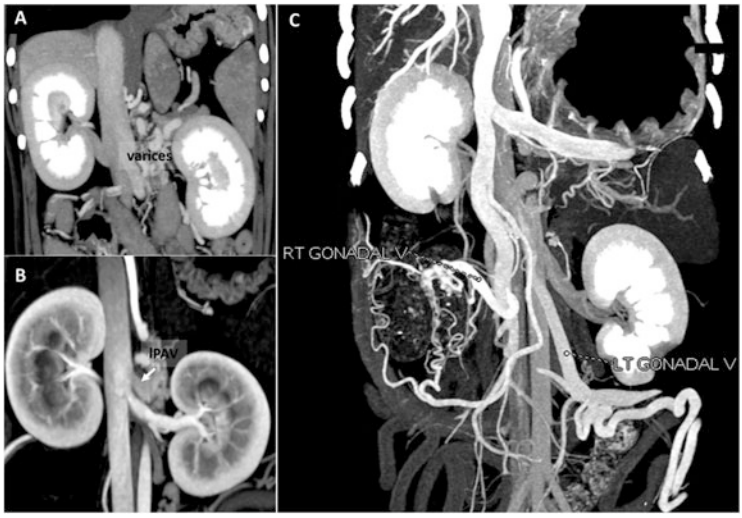

Fig. 44 (**a**) Dorsal view of a dog with left retroperitoneal varices (from the gastrosplenic vein). (**b**) Varices empty into the left phrenico-abdominal vein (lPAV). The enlarged PAV should not be confused with a congenital portosystemic shunt termination. (**c**) MIP image from a female dog showing dilatation of both gonadal veins, which are receiving blood from the splenic vein (left splenogonadal shunt), and caudal mesenteric vein (mesenteric-right gonadal shunt)

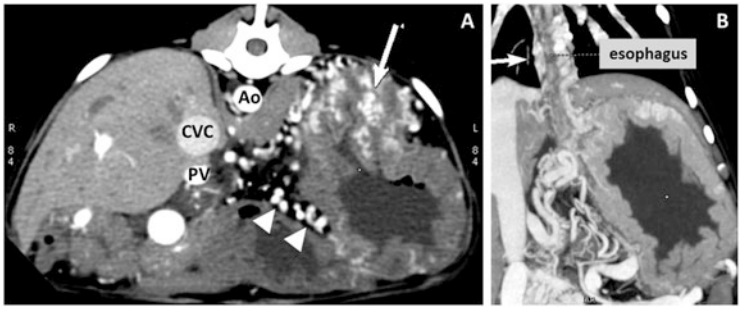

Fig. 45 (**a**) Gastroesophageal varices (*arrowheads*) and submucosal gastric varices (*arrow*) in a puppy with PH due to a congenital intrahepatic APF. (**b**) Dorsal MIP view showing paraesophageal varices (*arrow*)

3.6 Portal Vein Thrombosis

Portal vein thrombosis (PVT) refers to the partial or total luminal obstruction of the portal vein, with or without extension to its portal branches within the liver, the splenic vein, or the mesenteric vein. It has been reported rarely in dogs and cats. One or more risk factors are present in patients with PVT. Hepatobiliary disease,

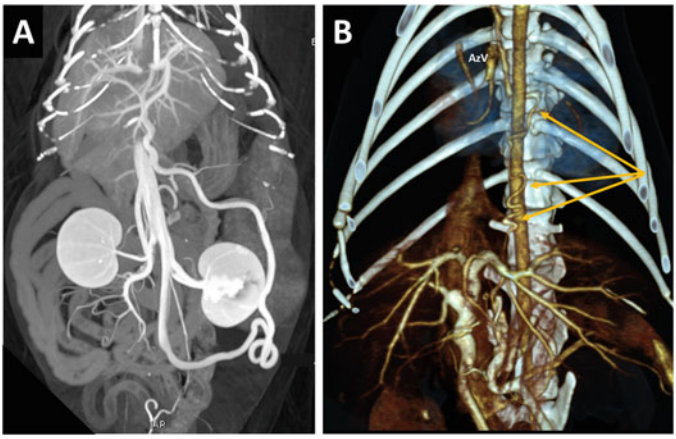

Fig. 46 (**a**) Dorsal MIP view of a cat with left splenogonadal shunting. (**b**) Volume-rendered image of a cat with a left gastric-vein varix (*arrows*) between the left gastric vein and the right azygous vein (AzV)

neoplasia, and other prothrombotic states are predisposing factors for PVT development in both species.

MDCT is an excellent tool for the diagnosis of malignant and nonmalignant PVT and evaluation of its complications. In most cases, MDCT is also indicated to confirm and define the causative conditions of PVT. Local causes, such as PVA and vascular invasion from hepatic or pancreatic neoplasia, are easily identified by MDCT; hepatobiliary diseases, hyperadrenocorticism, myeloproliferative disorders, and other conditions potentially associated with a hypercoagulable state can also be identified.

Laminar flow in the portal vein and its branches during the late arterial phase can mimic a thrombus. During this vascular phase, opacified blood from the splenic vein mixes with unopacified blood from the mesenteric or splenic veins, which creates a transient filling defect in the portal vein. This false thrombus will disappear during the portal venous and late phases. A multiphasic approach is thus necessary for the diagnosis of PVT and associated hepatic perfusion disorders.

Direct and indirect signs of PVT may be identified using MDCT. In cases of acute PVT, unenhanced scans may show slight hyperattenuation of material within the portal lumen, which does not enhance in the portal venous phase. In addition, dependent areas of the liver parenchyma may show increased arterial enhancement and decreased enhancement during the portal venous phase (Fig. 47). PVT can lead to partial or complete obstruction of the portal lumen. Partial and complete PVT may show peripheral enhancement, and these conditions should be distinguished. In cases of partial occlusion, some CM passes around the thrombus. In cases of complete obstruction, enhancement of the peripheral rim of the thrombus is likely due to dilatation of the vasa vasorum in the attempt to recanalize the vessel.

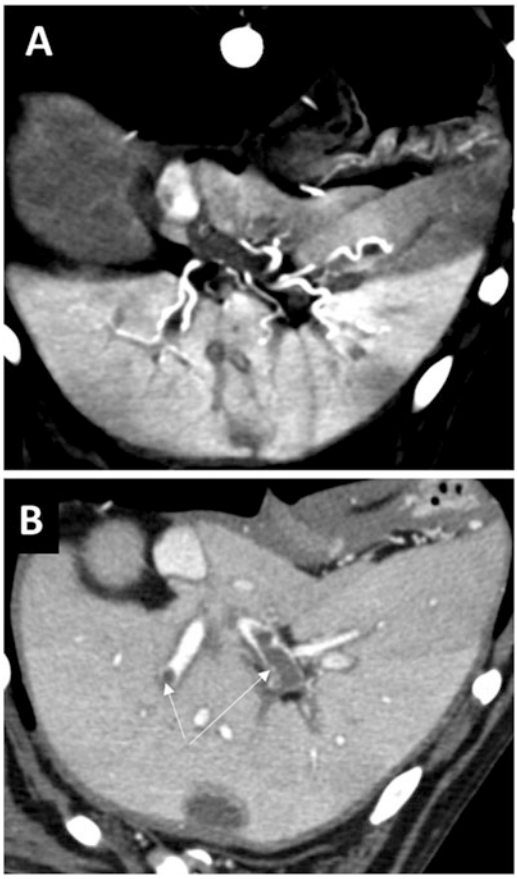

Fig. 47 (**a**) Arterial phase image of the liver in a dog with intrahepatic PVT. The hepatic arterial vessels are tortuous, and some hepatic areas show early enhancement (inappropriate in this vascular phase). (**b**) PVP image from the same dog. Note the filling defects in the portal branches (*arrows*)

Indirect signs of PVT in chronic obstruction are porto-portal collaterals, arterio-portal shunts, and APSS. As a consequence of portal vein obstruction, compensatory mechanisms are immediately activated to reestablish the portal flow to the liver. A first compensatory mechanism is distention of the hepatic artery and its branches within the liver parenchyma, so-called arterialization. Small arterial–portal connections may form within the liver. A second mechanism is the formation of portal venous collaterals. In cases of complete extrahepatic portal vein obstruction, characterized by high pressure in the splanchnic circulation and normal pressure in the hepatic sinusoids, multiple collateral hepatopetal vessels form around the thrombotic segment.

Cavernous transformation of the portal vein (CTPV) refers to the radiological appearance of porto-portal collaterals around a thrombosed portal vein. We recently demonstrated these collaterals in chronic PVT in dogs and cats. Two main types of porto-portal collateral may be found when reviewing MDCT data: short tortuous collaterals developing around/inside the thrombus and long collaterals (Fig. 48).

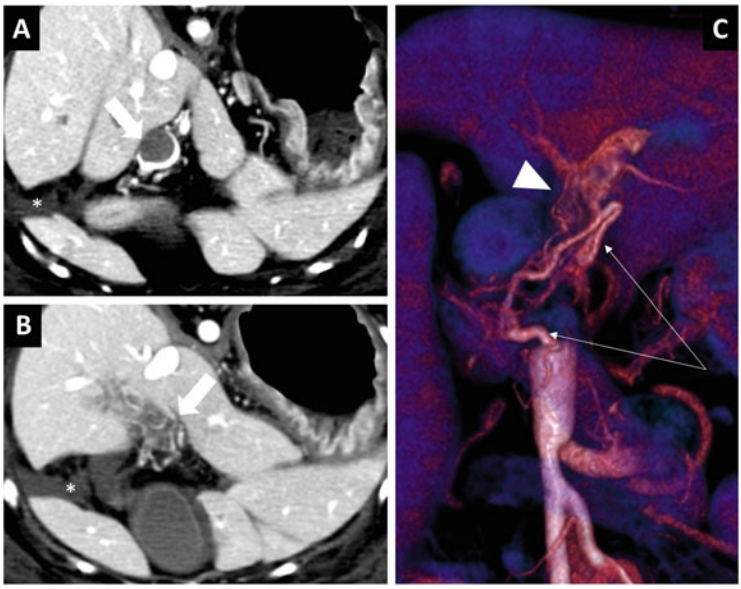

Fig. 48 (**a**) Transverse view at the porta hepatis from a dog with a large filling defect of the portal vein (*arrow*). A small quantity of CM still passes around the thrombus. (**b**) Transverse view just cranial to the previous view, showing the short collaterals around the thrombosed branch (*arrow*). This patient had ascites (*asterisk*) due to portal vein obstruction. (**c**) Long (*arrows*) and short (*arrowhead*) collaterals attempting to recanalize a thrombosed portal vein

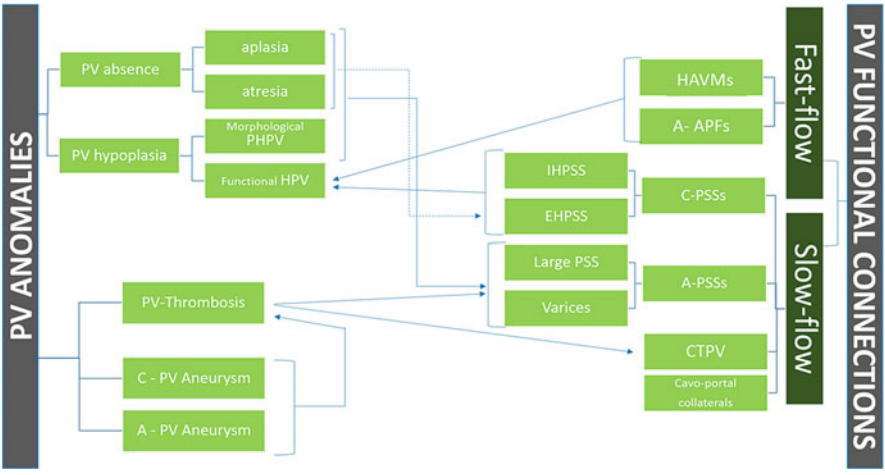

Fig. 49 Portal vein anomalies and functional portal collaterals in dogs and cats. *Arrows* indicate possible coexistence and relationships between congenital and/or acquired conditions (see the text for further explanation)

Long collaterals form a network to overcome the obstructed portal vein, coursing within the hepatoduodenal ligament, around the gallbladder and common biliary and cystic ducts, and terminating in portal branches within the liver. When complete portal vein obstruction persists for some time, portal hypertension can ensue and hepatofugal portosystemic collateral pathways will develop.

Figure 49 resumes the portal venous system anomalies and their relationships.

Further Readings

Bertolini G. Acquired portal collateral circulation in the dog and cat. Vet Radiol Ultrasound. 2010;51(1):25–33.

Bertolini G, Caldin M. Computed tomography findings in portal vein aneurysm of dogs. Vet J. 2012b;193(2):475–80. doi:10.1016/j.tvjl.2011.12.002.

Bertolini G, Prokop M. Multidetector-row computed tomography: technical basics and preliminary clinical applications in small animals. Vet J. 2011;189(1):15–26. doi:10.1016/j.tvjl.2010.06.004.

Bertolini G, Rolla EC, Zotti A, Caldin M. Three-dimensional multislice helical computed tomography techniques for canine extra-hepatic portosystemic shunt assessment. Vet Radiol Ultrasound. 2006;47(5):439–43.

Bertolini G, De Lorenzi D, Ledda G, Caldin M. Esophageal varices due to a probable arteriovenous communication in a dog. J Vet Intern Med. 2007;21(6):1392–5.

Bertolini G, Diana A, Cipone M, Drigo M, Caldin M. Multidetector row computed tomography and ultrasound characteristics of caudal vena cava duplication in dogs. Vet Radiol Ultrasound. 2014;55(5):521–30. doi:10.1111/vru.12162.

De Rycke LM, Kromhout KJ, van Bree HJ, Bosmans T, Gielen IM. Computed tomography atlas of the normal cranial canine abdominal vasculature enhanced by dual-phase angiography. Anat Histol Embryol. 2014;43(6):413–22. doi:10.1111/ahe.12090.

Fukushima K, Kanemoto H, Ohno K, Takahashi M, Fujiwara R, Nishimura R, Tsujimoto H. Computed tomographic morphology and clinical features of extrahepatic portosystemic shunts in 172 dogs in Japan. Vet J. 2014;199(3):376–81. doi:10.1016/j.tvjl.2013.11.013.

Hunt GB, Culp WT, Mayhew KN, Mayhew P, Steffey MA, Zwingenberger A. Evaluation of in vivo behavior of ameroid ring constrictors in dogs with congenital extrahepatic portosystemic shunts using computed tomography. Vet Surg. 2014;43(7):834–42.

Kim SE, Giglio RF, Reese DJ, Reese SL, Bacon NJ, Ellison GW. Comparison of computed tomographic angiography and ultrasonography for the detection and characterization of portosystemic shunts in dogs. Vet Radiol Ultrasound. 2013;54(6):569–74. doi:10.1111/vru.12059.

Kraun MB, Nelson LL, Hauptman JG, Nelson NC. Analysis of the relationship of extrahepatic portosystemic shunt morphology with clinical variables in dogs: 53 cases (2009–2012). J Am Vet Med Assoc. 2014;245(5):540–9. doi:10.2460/javma.245.5.540.

Nelson NC, Nelson LL. Anatomy of extrahepatic portosystemic shunts in dogs as determined by computed tomography angiography. Vet Radiol Ultrasound. 2011;52(5):498–506. doi:10.1111/j.1740-8261.2011.01827.x.

Parry AT, White RN. Portal vein anatomy in the dog: comparison between computed tomographic angiography (CTA) and intraoperative mesenteric portovenography (IOMP). J Small Anim Pract. 2015. doi:10.1111/jsap.12392.

Pey P, Marcon O, Drigo M, Specchi S, Bertolini G. Multidetector-row computed tomographic characteristics of presumed preureteral vena cava in cats. Vet Radiol Ultrasound. 2015;56(4):359–66. doi:10.1111/vru.12251.

Ricciardi M, Martino R, Assad EA. Imaging diagnosis – celiacomesenteric trunk and portal vein hypoplasia in a pit bull terrier. Vet Radiol Ultrasound. 2014;55(2):190–4. doi:10.1111/vru.12062.

Scollan K, Sisson D. Multi-detector computed tomography of an aortic dissection in a cat. J Vet Cardiol. 2014;16(1):67–72. doi:10.1016/j.jvc.2013.11.002.

Specchi S, d'Anjou MA, Carmel EN, Bertolini G. Computed tomographic characteristics of collateral venous pathways in dogs with caudal vena cava obstruction. Vet Radiol Ultrasound. 2014;55(5):531–8. doi:10.1111/vru.12167.

Specchi S, Pey P, Javard R, Caron I, Bertolini G. Mesenteric-reno-caval shunt in an aged dog. J Small Anim Pract. 2015a;56(1):72. doi:10.1111/jsap.12255.

Specchi S, Pey P, Ledda G, Lustgarten M, Thrall D, Bertolini G. Computed tomographic and ultrasonographic characteristics of cavernous transformation of the obstructed portal vein in small animals. Vet Radiol Ultrasound. 2015b. doi:10.1111/Vru.12265.

Weisse C, Berent AC, Todd K, Solomon JA, Cope C. Endovascular evaluation and treatment of intrahepatic portosystemic shunts in dogs: 100 cases (2001–2011). J Am Vet Med Assoc. 2014;244(1):78–94.

White RN, Parry AT. Morphology of congenital portosystemic shunts emanating from the left gastric vein in dogs and cats. J Small Anim Pract. 2013;54(9):459–67. doi:10.1111/jsap.12116.

White RN, Parry AT. Morphology of congenital portosystemic shunts involving the right gastric vein in dogs. J Small Anim Pract. 2015;56(7):430–40. doi:10.1111/jsap.12355.. Epub 2015 Apr 14.

Yoon H, Choi Y, Han H, Kim S, Kim K, Jeong S. Contrast-enhanced computed tomography angiography and volume-rendered imaging for evaluation of cellophane banding in a dog with extrahepatic portosystemic shunt. J S Afr Vet Assoc. 2011;82(2):125–8.

The Liver

Giovanna Bertolini

1 Introduction

Advances in CT imaging have provided unique capabilities for hepatic evaluation in small animals. Imaging of the hepatobiliary system and hepatic vasculature has been affected most by MDCT technology advancement. Diffuse and focal liver disorders, as well as anomalies of the hepatic vasculature, can be evaluated using multiphasic MDCT. The characterization of hepatic masses, presurgical evaluation, and interventional radiology planning are common indications for hepatic MDCT in patients with known liver lesions. Careful evaluation of the liver is also important in oncological staging and in patients with abdominal trauma.

The liver has a dual blood supply; 80% is supplied from the portal system and 20% is supplied from the hepatic artery (Fig. 1). As they enter the liver, the hepatic artery and portal vein divide into several branches that travel parallel to each other into the hepatic parenchyma. The portal system delivers oxygenated, nutrient-rich blood and toxins from the gastrointestinal system. Oxygen also reaches the liver by the hepatic artery and its branches, which normally supply the peribiliary plexus, the portal tract interstitium, and the portal vein wall within the liver. In the intrauterine setting, the hepatic artery and portal vein have approximately equal diameters. As the fetus matures, the portal vein becomes the dominant vessel. The intimate anatomic relationship between the two vessels persists throughout the lifetime. Knowledge of the compensatory relationship between the two sources of blood supply to the liver is important; the arterial flow increases when the portal venous blood supply decreases in many congenital and acquired pathological conditions (e.g., portosystemic shunt, portal vein hypoplasia, portal thrombosis).

G. Bertolini (✉)
San Marco Veterinary Clinic, Padua, Italy
e-mail: bertolini@sanmarcovet.it

G. Bertolini (ed.), *Body MDCT in Small Animals*, DOI 10.1007/978-3-319-46904-1_4

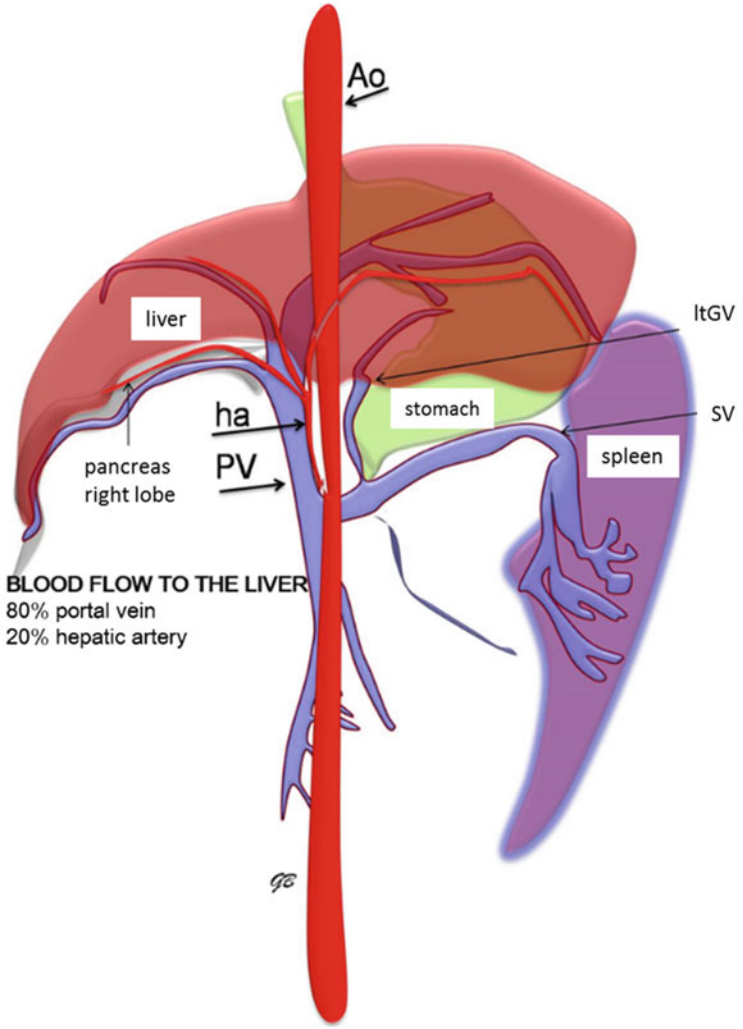

Fig. 1 Schematization of the blood supply to the liver. *Ao* aorta, *PV* portal vein, *ha* hepatic artery, *GV* gastric vein, *SV* splenic vein

2 MDCT Imaging Strategies

Optimal contrast enhancement is crucial for successful MDCT examination of the liver. The goal of contrast-enhanced studies is to detect focal lesions or diffuse changes in the liver parenchyma by enhancing the differences between affected and unaffected liver tissue. Different lesions may appear hyper- or hypovascular to the surrounding tissue in certain vascular phases. Thus, the examiner must consider in

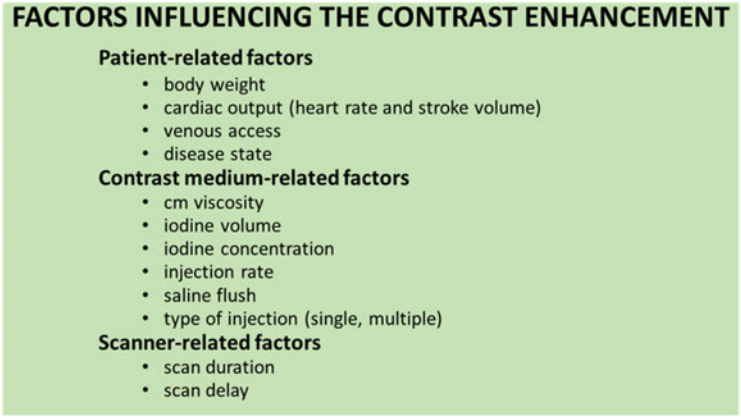

Fig. 2 The most important factors influencing CT contrast enhancement

which phase a CT study has been performed to interpret the data correctly. The various factors influencing CM (contrast medium) dynamics in the body have been treated extensively in chapter "Basic principles of MDCT Angiography" of this book and are here summarized in Fig. 2.

2.1 Multiphase Approach to the Liver

Pre-contrast Series (Non-contrast, Direct, or Unenhanced Series)
A pre-contrast series may be useful in cases of hepatobiliary disorders, but generally is not essential in routine parenchymal liver studies. Pre-contrast scanning is important in two clinical situations: in cases of biliary obstruction, to detect biliary mineralization and stones; and in cases of abdominal trauma, to disclose potential liver hemorrhage (see the chapter "The Body Trauma"). Moreover, pre-contrast scanning may be useful to characterize diffuse parenchymal conditions, such as steatosis and lipidosis.

At our center, with the use of a second-generation dual-source CT (DSCT) scanner, a true pre-contrast series is not always acquired. Images from *virtual non-contrast* series may serve as substitutes for true non-contrast images, eliminating the need to acquire separate pre-contrast datasets. This approach is possible because dual-energy DSCT uses a three-material decomposition algorithm in the image space (after the images have been reconstructed) and relies on the known X-ray absorption properties of three materials (iodine, soft tissue, and fat) at low and high energies. Thus, given the behavior of iodine (the principal CM ingredient) at different energies (80/100 kV and 140 kV), this material may be extracted virtually from a volume to generate a set of simulated unenhanced images. At present, no studies of the effectiveness of material subtraction in routine small-animal clinical practice have been published.

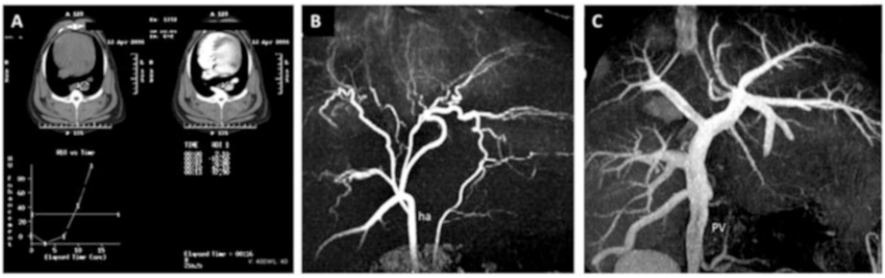

Fig. 3 Image from the monitoring phase of 16-MDCTA examination. The ROI is placed in the lumen of abdominal aorta. The plot of enhancement (*y* axis) versus time (*x* axis) in the lower panel reveals the initial contrast enhancement of the aorta (the threshold is set at 30 HU). For slower (4–16-MDCT) scanners, the arterial phase should also be initiated (manually or automatically) at this time. An additional scan delay is necessary for more rapid scanners

Post-contrast Series (Enhanced Series)

The unique dual blood supply of the liver makes multiphasic MDCT a highly suitable imaging technique for hepatic evaluation in different vascular phases of contrast enhancement. With single- and dual-slice CT scanners, more than 40 s are generally required to scan the liver with acceptable image quality. Thus, some areas of the liver are always scanned too early or too late with these CT technologies, resulting in suboptimal examination. As the number of detectors increases (to 16–64 or more rows), scan protocols using isotropic resolution and larger volume coverage can be performed routinely in a few seconds. A tremendous advantage of shorter scan duration is the ability to precisely time different hepatic vascular phases through the whole liver, thereby improving depiction and enabling differentiation of lesions and other disorders. Scanning of the liver in timed arterial, portal, or late phases maximizes the conspicuity of lesions and hemodynamic changes in the liver parenchyma. Three methods can be used for optimal scan timing after contrast medium injection: the bolus-tracking (or triggering) technique, the bolus test, and the standard delay technique (see the chapter "Basic Principles of MDCT Angiography"). *Dual-phase or three-phase studies* of the liver using all these methods have been described in veterinary literature for portal vascular anomaly studies and to assess hepatic masses. The type of scanner available, the patient's characteristics, the CM protocol, and the pathology studied can strongly influence the success of an MDCT liver study. Given the great diversity of veterinary patients and technology used, the use of automatic bolus-triggering techniques for the individualization of scan delays in multiphasic MDCT examinations is strongly recommended (Fig. 3).

When CM is injected, opacification of the hepatic artery and its branches is encountered first (Fig. 4). Based on contrast distribution, the *hepatic arterial phase (HAP)* can be subdivided into a pure, early arterial phase *(EAP)* and a late arterial phase *(LAP)*, with no or minimal enhancement of the hepatic parenchyma. The EAP (Fig. 5) provides important information in cases of vascular malformation (arteriovenous malformations and arterioportal fistulas). Again, EAP allows rapid and

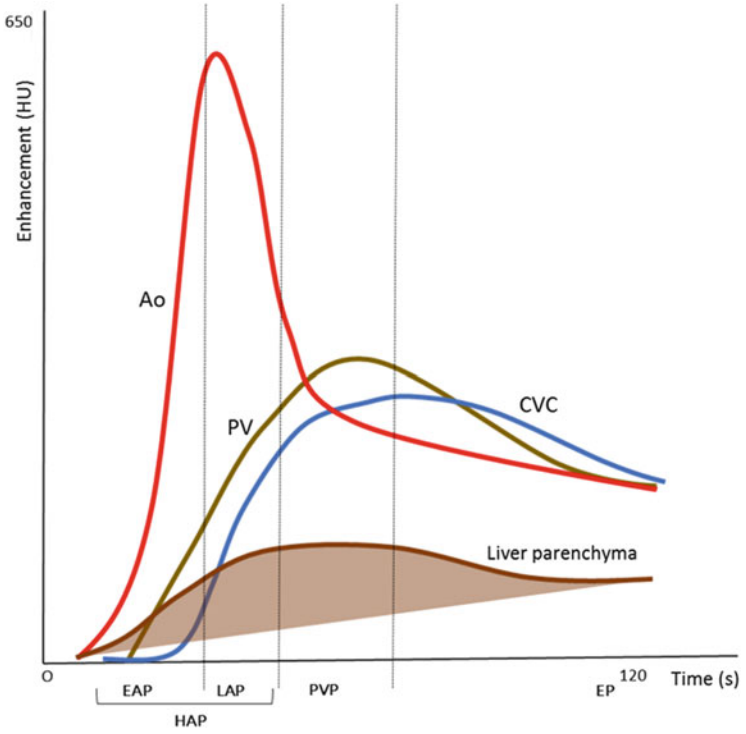

Fig. 4 Schematization of contrast enhancement in the vascular and parenchymal territories after a single CM injection. Different *curves* represent the arterial, portal, and venous phases of the liver. The area below represents the enhancement curve of the liver parenchyma. *Dotted lines* identify different vascular phases. *EAP* early arterial phase, *LAP* late arterial phase (the beginning of portal venous branch enhancement), *PVP* portal venous phase (maximal liver parenchyma enhancement), *EP* equilibrium phase (or, more properly, interstitial hepatic phase)

accurate identification of feeding arteries of focal lesions in patients undergoing endovascular procedures but in general provides little information of focal liver lesions characteristics. In the LAP, inflow in the portal vein can be observed, and the arterial vascular component still shows excellent opacification (Fig. 6a). Benign and malignant hypervascular lesions generally show maximum enhancement during this phase. In a monophasic approach, when multiphasic MDCT is not possible due to scanner limitations or when contrast-enhanced hepatic evaluation is part of a whole-body imaging protocol without suspicion of a specific hepatic pathological condition, the LAP/inflow portal phase is the most effective for the depiction of liver abnormalities and vascular and focal lesions.

The portal *venous phase (PVP)* takes approximately 35–40 s after the start of CM injection (Fig. 6b, c). In normal patients, it corresponds to the maximum enhancement of the liver parenchyma. Canine patients with portovascular

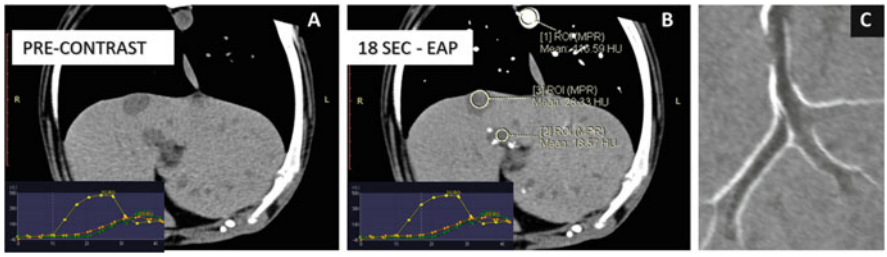

Fig. 5 Multiphasic vascular study of the liver (128-DSCT) in a German Shepherd (38 kg, 700 mg/mL, 4 mL/s, saline flush). (**a**) Transverse pre-contrast (true non-contrast) view. (**b**) Same view during the EAP. Mean opacity in aorta = 416.59 HU. The portal vein and caudal vena cava remain unenhanced (means, 18.57 HU and 28.33 HU, respectively). (**c**) Close-up view of the liver showing great opacification of the arterial branches of the hepatic artery lining unenhanced portal branches

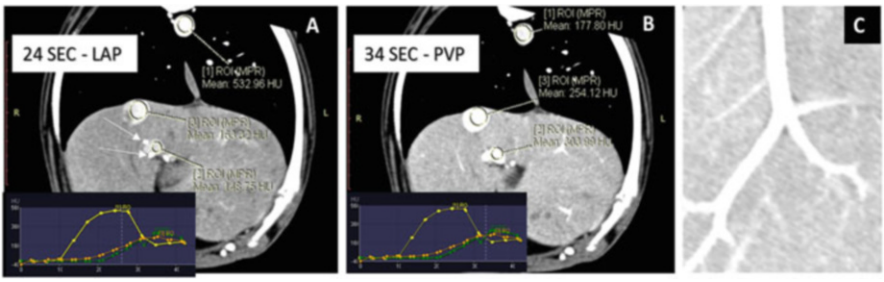

Fig. 6 Multiphasic vascular study of the liver in the same dog as in Fig. 5. (**a**) LAP. The aortic enhancement is greater (532.96 HU), and the parenchymal arteries (*arrows*) are clearly visible. In this phase, the portal vein begins to enhance (inflow portal phase; 148.75 HU). (**b**) PVP. Note that the aortic enhancement is decreased (177.8 HU). The portal vein and its branches have maximum opacification (303.99 HU). The hepatic segment of the caudal vena cava begins to enhance (254.12 HU). (**c**) Close-up view of the liver (same as Fig. 5c) showing great portal branch opacification, which obscures the parallel arterial branches

anomalies may have unpredictable portal vein peaks and hepatic parenchymal enhancement. In this phase, some enhancement of the hepatic veins can be seen.

The *interstitial or equilibrium phase (EP)* can be acquired approximately 120 s after the start of CM injection. When the CM reaches the liver, it immediately begins to diffuse slowly from the vascular district to the interstitium and then back into the central vascular compartment, resulting in a gradual decline in hepatic parenchymal enhancement. In this interstitial phase, the hepatic veins are completely opacified. This phase is important in the assessment of pathological changes with absent or minimal vascular supply, such as hepatic cysts, abscesses, and biliary dilations, as well as in the evaluation of venous thrombosis and tumoral invasion of the hepatic veins and hepatic vena cava.

Different vascular phases and their usefulness are resumed in Fig. 7.

Multiphase study - series			Usefulness
Non-contrast (pre-contrast, direct or unenhnaced)	NC	Normal attenuation value (dog) 59.58 ± 3.34 HU	Liver contusion/fracture/active hemorrhage (trauma) Gallbladder and biliary mineralization and stones Attenuation changes in diffuse storage diseases (glycogen, steatosis, lipidosis etc)
Hepatic arterial phase	HAP		
Early arterial phase	EAP	No parenchymal enhancement	Angiographic studies (arterioportal, arteriovenous fistula, pre-embolization assessment etc.)
Late arterial phase (inflow portal)	LAP	Minimum parenchymal enhancement	Hepatic perfusion disorders, detection of hypervascular focal lesions
Portal venous phase	PVP	Maximum parenchymal enhancement	Parenchymal diseases, hyper/hypovascular focal lesions, portal vascular anomalies
Interstitial phase (equilibrium or hepatic venous phase)	EP		Hepatic cysts, abscess, biliary diseases; venous thrombosis, venous tumoral invasion

Fig. 7 Vascular phases in a multiphasic CT approach to the liver and their clinical applications

2.2 Post-processing and Data Analysis

Quali-quantitative CT assessment of liver data includes the estimation of attenuation values and hepatic volume of the liver parenchyma. In canine and feline patients, the hepatic parenchyma appears homogenous on pre-contrast images. The *CT density of the liver parenchyma* can be assessed quantitatively by comparing hepatic and splenic attenuation. In humans, recent studies have shown that the simple measurement of liver attenuation is less time-consuming and provides similar results to those of liver–spleen comparison. In dogs, the reported liver parenchyma attenuation value is 59.58 ± 3.34 HU, which is 4.69 ± 7.77 HU greater than the value for the splenic parenchyma. In humans, liver steatosis can be diagnosed using CT when the liver attenuation value is <40 HU or ≥10 HU less than that of the spleen. Variations in CT attenuation values for the liver parenchyma have also been reported in experimental and spontaneous conditions in dogs and cats. A significant reduction of liver density can be observed in feline hepatic lipidosis and canine hepatic steatosis (Fig. 8). Increased attenuation values have been described with high dosages of glucocorticoids and steroid-induced hepatopathy (glycogen accumulation).

Liver size is commonly assessed subjectively in routine CT examinations using radiological criteria. However, some conditions require volume quantification to determine the objective parenchymal size. CT has been described as a noninvasive tool for the measurement of liver volume before and after surgical attenuation in dogs with CPSS to evaluate hepatic growth. Liver volume measurements should be corrected for body size (/kilogram body weight). The normal liver CT volume value in dogs, estimated using a manual technique, is 24.5 ± 5.6 cm^3/kg.

CT estimation of liver volume is traditionally performed manually by outlining the liver contour slice by slice on axial images, excluding the major vessels and the gallbladder. The unit's software then calculates the total volume by summing values from the ROIs. The manual technique enables the accurate measurement

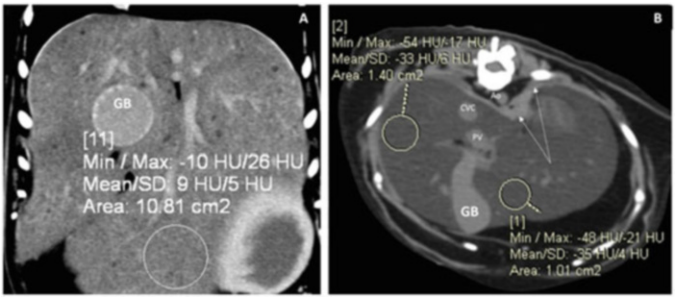

Fig. 8 Pre-contrast images of the liver. (**a**) Dorsal image of the liver in a dog with hepatic steatosis (diabetes). Note the overall hypoattenuation of the liver parenchyma (mean, 9 HU) and relative hyperattenuation of the gallbladder (GB) and vascular structures. (**b**) Pre-contrast transverse image of the liver in a cat with hepatic lipidosis. The liver parenchyma is hypoattenuating (−35 HU and −33 HU in ROIs 1 and 2, respectively). Note the relative hyperattenuation of the gallbladder (GB), vascular structures, and diaphragm (*arrows*). *Ao* aorta, *CVC* caudal vena cava, *PV* portal vein

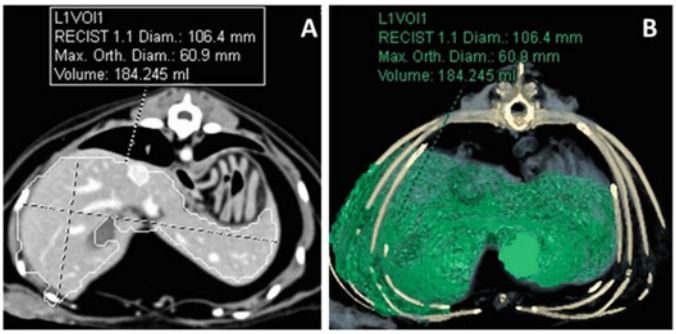

Fig. 9 Hepatic volume estimation in a dog, performed using automatic CT volume software (Syngo.via CT Liver Analysis—Oncology; Siemens Healthcare)

of liver volume, but precise manual outlining of the liver is time-consuming, which discourages the routine CT measurement of liver size. With advanced technology, automated computerized liver volumetry can replace manual liver volumetry, dramatically reducing the time required for this procedure. However, automatic segmentation may fail for certain CT images with low contrast resolution (attenuation values similar to those of adjacent tissue) or due to image noise. Semi-automated methods, with guided automated segmentation of multiplanar reformatted images, have been reported to outperform fully automatic methods. Accurate liver volume estimation relies on precise segmentation of the liver, and more precise results can be obtained using CT images with thinner sections (Fig. 9). Studies in human patients have documented an inverse relationship between section thickness and calculated liver volumes. Liver volumes obtained from the analysis of submillimeter-thick CT sections are typically larger than those calculated from thicker images. Importantly, volumetric assessment depends on the scan phase.

Intuitively, hepatic CT volume is overestimated in the PVP relative to the same volume measured in the pre-contrast phase. Although the latter probably represents the actual size of the liver, the PVP is preferred for liver volume estimation in humans. In this phase, contrast enhancement enables better delineation of the vascular and biliary structures, which should be excluded for the precise calculation of liver volume.

3 MDCT Liver Perfusion: Normal and Abnormal Features

The liver receives approximately 25% of the cardiac output via two inflows: the portal vein and the hepatic artery. Both enter the liver at the porta hepatis (hepatic hilus) and distribute inside the liver parenchyma, accompanied by bile ducts, lymphatics, and nerves. In addition to these two afferent vessels, the liver circulation includes an efferent system involving the hepatic veins, which drains the blood to the right atrium via the hepatic and posthepatic caudal venae cavae.

3.1 Arterialization of the Liver

The portal vein cannot control its blood flow, which is simply the sum of outflows of the extrahepatic splanchnic organs (bowel, spleen, pancreas, and stomach). A compensatory relationship exists between the two blood sources of the liver (the hepatic artery and portal vein), such that the arterial flow increases when the portal venous flow decreases. This mechanism is called the "hepatic arterial buffer response" (HABR) and represents the ability of the hepatic artery to produce compensatory flow changes in response to changes in portal venous flow; it is capable of buffering 25–60% of the decreased portal flow. For instance, a study conducted with dynamic single-slice computed tomography showed that hepatic portal perfusion values were significantly lower in dogs with congenital portosystemic shunt (CPSS) than in clinically normal dogs (0.52 ± 0.47 vs. 1.08 ± 0.45 mL/min mL^{-1}), whereas hepatic arterial perfusion values were significantly higher (0.57 ± 0.27 vs. 0.23 ± 0.11 mL/min mL^{-1}). Other studies have demonstrated that the hepatic arterial fraction is elevated on preoperative evaluation in dogs with CPSS and normalizes in most dogs after successful attenuation of the shunting vessel. The increase in arterial components within the liver can be assessed qualitatively in the HAP in veterinary patients with portosystemic shunting and many other pathological conditions (Fig. 10). Importantly, one must remember that the compensatory relationship between arterial and portal flow into the liver is not reciprocal. Alterations in hepatic arterial perfusion do not induce compensatory changes of the portal vascular flow. Arterial collaterals form rapidly in response to hepatic arterial perfusion impairment. Changes in portal venous flow may have other causes, such as portal hypertension, which should be investigated.

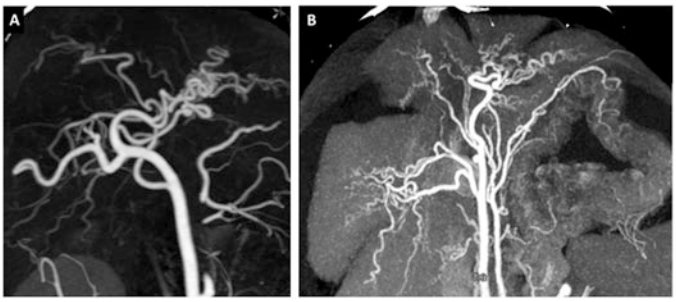

Fig. 10 Arterialization of the liver. (**a**) Dorsal MIP view of the arterial phase in a dog with congenital portosystemic shunting. (**b**) Dorsal view of the arterial phase in a dog with hepatopathy and portal hypertension (PH)

3.2 Qualitative and Quantitative Assessment of Liver Parenchyma Perfusion

In a normal liver, maximal parenchymal enhancement occurs during the PVP. During the arterial phase, opacification of the parenchyma is absent or minimal (Fig. 7). Qualitative changes in hepatic perfusion occur frequently in veterinary patients and can be detected using multiphasic MDCT protocols. Radiologists should be familiar with their appearance, physiopathological mechanisms, and possible causes, most of which are easily recognizable on CT images.

Perfusion CT imaging of the liver includes the qualitative and quantitative assessment of hepatic perfusion. Perfusion CT measures temporal changes in tissue density through a series of dynamically acquired CT images after the intravenous injection of iodinated CM. Functional assessment of the perfusion of normal and pathological tissues in the liver and other organs is performed using quantitative or semiquantitative parameters, such as blood flow, blood volume, mean transit time, portal liver perfusion, arterial liver perfusion, and the hepatic perfusion index. The assessment of hepatic perfusion in dogs using a variety of invasive and noninvasive methods, including single helical CT, has been described. In humans, MDCT liver perfusion imaging is used to further characterize liver disorders, such as hepatic tumors and hepatic fibrosis associated with chronic liver disease, and for the evaluation of treatment response following radiotherapy and chemotherapy and hepatic perfusion changes after radiological and surgical interventions. Initial experiences in veterinary practice have focused on the quantification of hepatic perfusion pre- and postoperatively in dogs with CPSS. MDCT scanners with the ability to obtain 16 or more slices and with extended scan ranges enable the volumetric assessment of liver perfusion and have the potential for use in various other clinical applications.

3.2.1 Hepatic Perfusion Disorder

Hepatic perfusion disorder (HPD) refers to early segmental enhancement of the liver parenchyma, during the HAP. This condition can occur because arterial and portal venous microcirculations into the liver are not independent. Several routes of communication between hepatic arterioles and portal venules normally exist; transsinusoidal, transvasal, and transplexal (or peribiliary) arterioportal communications (shunts) normally open in response to nervous and humoral factors (Fig. 11). In some pathological conditions, organic or functional communication between the arterial and portal vessels increases, resulting in the redistribution of arterial flow into a focal region of portal venous flow due to high pressure in the hepatic arterial bed and low pressure in the portal system. In areas with increased arterioportal shunting, the CM escapes from the arteries to the portal venules, resulting in unexpected parenchymal opacification during the HAP on MDCT images. HPD is typically a transient phenomenon; in the human radiology literature, it is also termed the "transient hepatic parenchymal enhancement pattern." On pre-contrast images, areas affected by hepatic disorders may be isoattenuated or slightly hyperattenuated to the surrounding parenchyma. They show conspicuous hyperattenuation in the hepatic arterial phase (HAP) and iso- to slight hyperattenuation to the liver

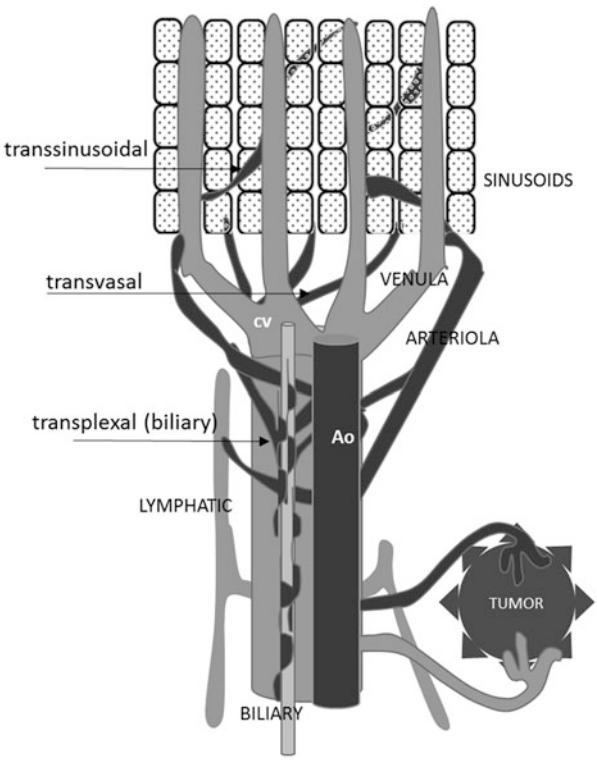

Fig. 11 Schematic representation of routes of communication between hepatic arterioles and portal venules in the liver microcirculation. *Ao* aorta, *cv* central vein

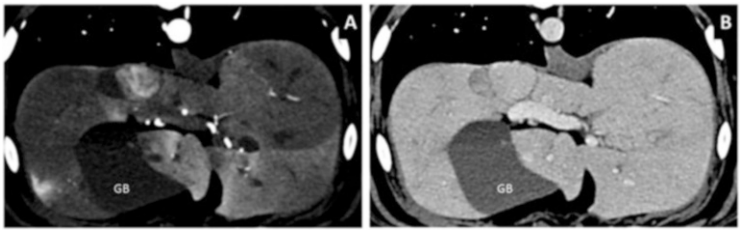

Fig. 12 HPD in a Golden retriever with steroid-induced hepatopathy. (**a**) EAP image shows early enhancement of some parenchymal areas. (**b**) The same slice in the PVP shows homogeneous parenchymal enhancement. *GB* gallbladder

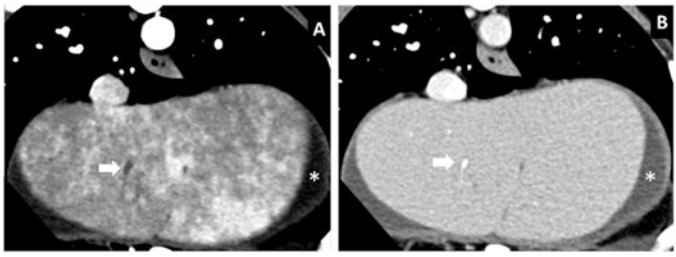

Fig. 13 HPD in a dog with liver cirrhosis. (**a**) EAP image showing diffuse areas of early, transitory parenchymal enhancement. (**b**) The same slice in the PVP. Note the homogenous parenchymal enhancement. *Arrow* indicates a portal branch within the liver. The *asterisk* indicates free fluid due to PH

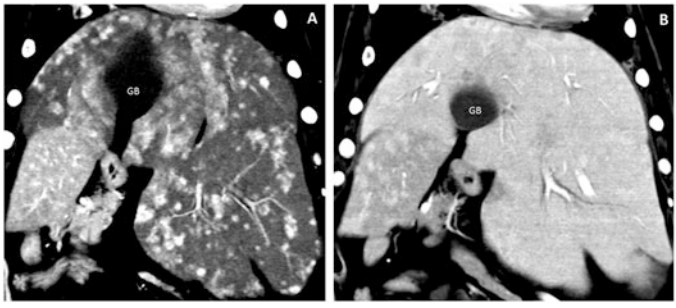

Fig. 14 HPD in a dog with histiocytic sarcoma. (**a**) EAP image shows *spotted* areas of transient parenchymal enhancement, not visible in the PVP (**b**). *GB* gallbladder

parenchyma during the subsequent PVP due to the rapid equilibration of contrast density (complete enhancement of the liver parenchyma).

HPD is a common finding of multiphasic MDCT examination in dogs and cats. Causes of HPD include benign and malignant conditions of the liver, such as diffuse parenchymal diseases (e.g., diffuse liver fibrosis, hepatitis, malignant infiltrative conditions) and focal benign and malignant lesions (Figs. 12, 13, and 14). Intrahepatic

arterioportal shunts can open in response to significant portal blood flow reduction or stoppage (i.e., PVT, stenosis, compression), resulting in a compensatory increase in arterial flow through the corresponding liver lobes. The peribiliary plexus and transvasal plexi are particularly involved in cases of severe portal flow obstruction, such as in chronic portal vein obstruction. Areas of increased arterial perfusion can be detected in dogs with cholecystitis, cholangitis, and other causes of dilation of the intrahepatic biliary ducts, as well as in those with other benign conditions leading to compression and inflammation of the surrounding liver parenchyma.

Importantly, nonpathological hepatic parenchymal compression may result in reversible HPD. Thus, heavy dogs in sternal recumbency, especially those with hepatomegaly or rib anomalies exerting hepatic parenchymal compression, may show perfusion disorders in subcapsular compressed areas. Finally, hepatic parenchymal perfusion should not be assessed using series obtained with a single vascular phase (i.e., LAP/inflow portal phase).

4 MDCT of The Liver Diseases

In 2009, the World Small Animal Veterinary Association's Liver Standardization Group provided a morphological categorization of canine and feline hepatic diseases in the attempt to address inconsistencies and confusion in the existing literature. This morphological approach may aid radiologists' image interpretation and differential diagnosis of hepatobiliary diseases. The classification has four main groups of pathologies: diffuse parenchymal disease, focal liver disease, biliary disorders, and vascular disorders. These categories include benign and malignant conditions and may be combined in advanced disease states.

4.1 MDCT of Diffuse Hepatic Diseases

Depending on the predominant physiopathological mechanism, diffuse parenchymal diseases may be categorized as inflammatory, storage-related (congenital and acquired), or toxic, or degenerative or neoplastic infiltrative diseases. Veterinary studies have focused on the use of multiphasic (dual-phase or tri-phase) MDCT for the characterization of hepatic masses. No report has addressed the usefulness or sensitivity of MDCT for the evaluation of diffuse hepatic disease. Hepatic diseases that lead to infiltration of the liver without disruption of the architecture are difficult to detect on pre-contrast or uniphasic post-contrast CT scans. However, as described earlier in this chapter, the usefulness of pre-contrast CT in the diagnosis of diffuse diseases of the liver, such as steroid-induced hepatopathy in dogs and lipidosis in cats, has been demonstrated (Fig. 8).

Results of a Ph.D.-research study conducted with 175 patients in our center showed that most diffuse hepatic non-tumoral conditions (e.g., swelling, congestion,

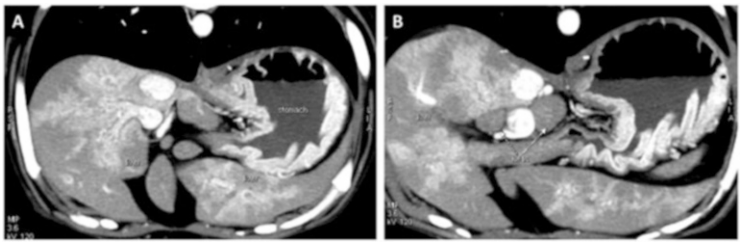

Fig. 15 Suppurative hepatitis in a dog with fever of unknown origin. (**a**) Transverse view from the LAP showing perivascular early parenchymal enhancement. (**b**) Transverse view. Note the hepatic lymph-node enlargement (*arrows*)

hepatitis, steroid-induced hepatopathy, lipidosis, amyloidosis) and infiltrative tumoral diseases (e.g., lymphoma, histiocytic sarcoma, mast cell tumor) are characterized by liver enlargement with segmental or diffuse changes in homogeneity and attenuation. Multiphasic MDCT evaluation of the liver can be used to detect even subtle changes in liver parenchyma perfusion. HPD and inhomogeneous patterns of parenchymal enhancement in the PVP (or parenchymal phase) can be identified easily in several non-neoplastic and neoplastic conditions (Figs. 12, 13, 14, and 15). However, as these changes are nonspecific in most cases, clinical backgrounds and guided needle aspiration or biopsy are necessary for definitive diagnosis.

4.2 MDCT of Focal Hepatic Diseases and Masses

Focal liver lesions include benign and malignant conditions. Small focal lesions in the liver parenchyma are often detected incidentally by MDCT in asymptomatic patients. Hepatic and peribiliary cysts are encountered frequently in routine multiphasic MDCT examination (see also the chapter "The Gallbladder and Biliary System"). They are easy to distinguish from the surrounding parenchyma and other focal lesions, and are generally of little clinical significance, unless they enlarge and impinge upon other organs or structures within the abdomen, or rupture and bleed (Fig. 16). Benign bile duct cystadenomas are the most common primary liver tumor in cats. In contrast to cystic lesions, the incidental detection of solid nodular lesions creates a dilemma in terms of reporting and management of non-oncological patients. In the author's personal experience, hypervascular focal lesions are often encountered in multiphasic examination of the liver of patients undergoing CT for other reasons (Fig. 17). Steroid-induced hepatopathy (excessive hepatocellular glycogen accumulation) as well as hepatic steatosis can appear as single or multiple nodular lesions or mass-like lesions in enlarged liver (Figs. 18 and 19). In humans, strategies for optimizing the management of patients with these incidental hepatic lesions, in terms of deciding which lesions can be ignored or simply monitored over time and which require biopsy, are only beginning to emerge. The veterinary

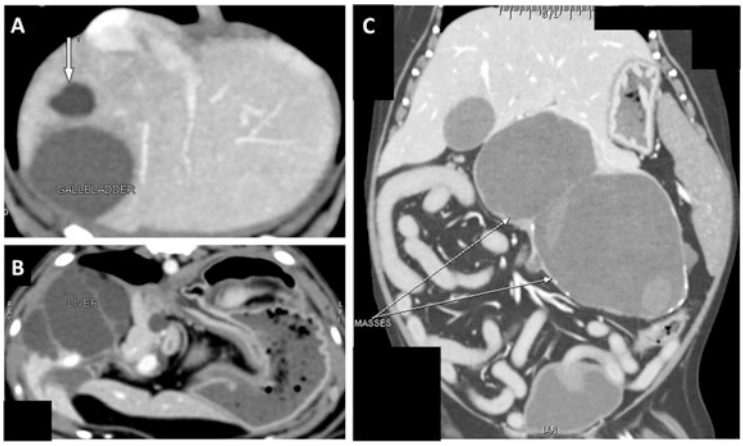

Fig. 16 Cystic hepatic lesions. (**a**) Incidentally discovered hepatic cyst in a dog. (**b**) Cystic hepatic mass in a Persian mix with polycystic kidney disease. (**c**) Large bilobated cystic mass in a Pomeranian with large cystadenoma

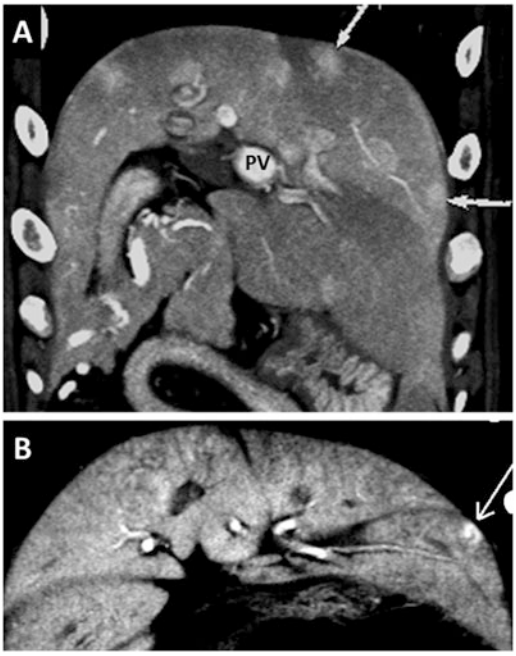

Fig. 17 (**a**) Hepatocellular swelling (vacuolar hepatopathy) in a dog (dorsal view). Note the multiple hypervascular parenchymal areas (*arrows*) in the PVP. (**b**) Nonspecific reactive hepatitis in a dog. Diffuse inhomogeneous enhancement of the liver parenchyma (PVP), with focal hypervascular lesions (*arrow*)

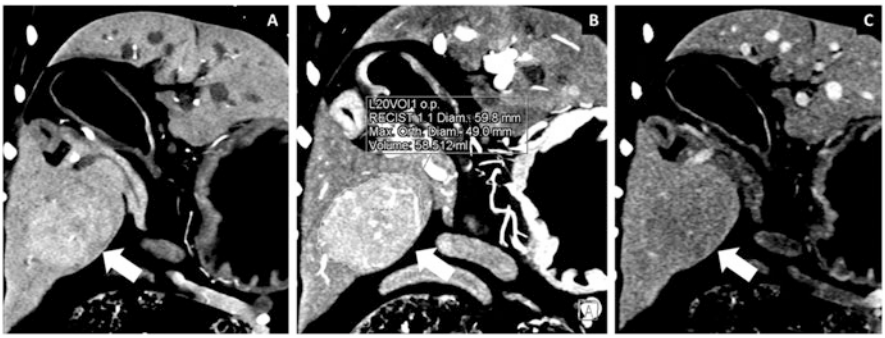

Fig. 18 Steroid-induced hepatopathy in a dog with HAC. (**a**) Dorsal view of the liver from the LAP showing an ovoid mass in the right lateral liver lobe (*arrow*). The mass shows great enhancement in the PVP (**b**) and rapid washout in the EP (**c**)

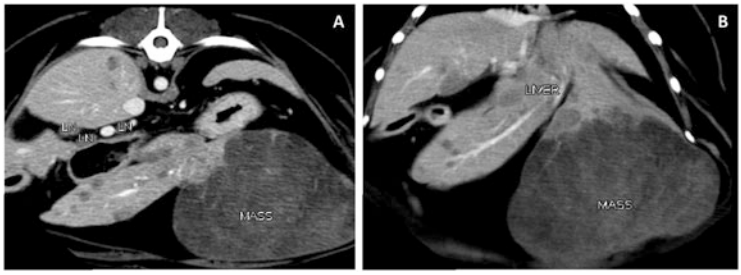

Fig. 19 Hepatic steatosis in a dog with HAC. (**a**, **b**) Transverse and dorsal views from the EP showing a large hypoattenuating mass and several other small hypoattenuating lesions distributed in the liver parenchyma

literature contains no report on the diagnostic criteria or workup for focal hepatic lesions detected incidentally by multiphasic MDCT.

Based on necroscopic studies, the prevalence of primary hepatobiliary neoplasia in dogs ranges from 0.6% to 2.6% and that in cats ranges from 1.5% to 2.3%. *Primary hepatobiliary tumors* can be benign or malignant. They can develop from hepatocytes [hepatocellular adenoma, hepatocellular carcinoma (HCC)], bile duct epithelium [biliary adenoma, biliary carcinoma, or cholangiocellular carcinoma (CCC)], neuroendocrine cells (neuroendocrine carcinoma, carcinoid tumor), or stromal cells (sarcomas). Among these tumors, HCC is the most common, followed by cholangiocellular carcinoma (CCC) and carcinoid tumor (neuroendocrine). Primary vascular and mesenchymal tumors, except for hemangiosarcoma, are rare in dogs and cats. Hemolymphatic tumors (lymphoma, malignant histiocytosis, plasma cell neoplasms, mastocytosis) may involve the liver (Figs. 14, 20 and 21).

Morphologically, a primary hepatic tumor features a single large mass involving one lobe (massive), or it can have a nodular aspect (nodular), involving several lobes, or infiltrate the liver parenchyma (diffuse). In humans, multiphasic MDCT

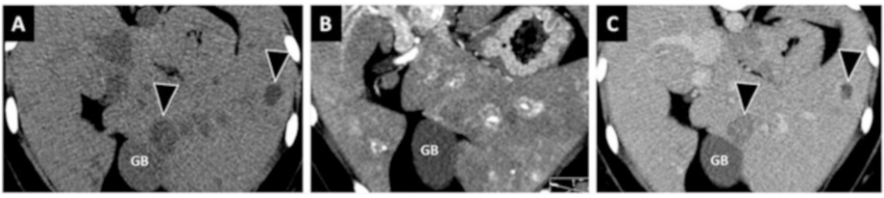

Fig. 20 Waldenstrom's macroglobulinemia in a dog. (**a**) Pre-contrast image showing focal lesions, hypoattenuating to the liver parenchyma. (**b**) LAP image showing perivascular focal enhancement of the liver parenchyma. (**c**) EP image showing the hypoattenuating lesions seen in the pre-contrast phase. *GB* gallbladder

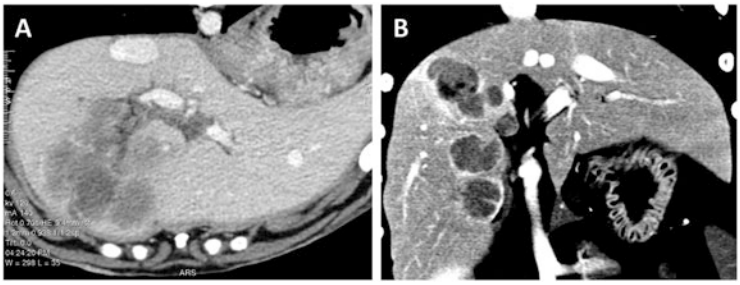

Fig. 21 Lymphoma. (**a**, **b**) Images from two different dogs with focal liver lesions resulting from secondary hepatic involvement of lymphoma

examination is considered to be the method of choice for hepatic mass diagnosis and characterization; it has a particularly important role in the diagnosis of HCC. Major associations for the study of liver disease in humans have stated that the hallmark diagnostic characteristic of HCC on multiphasic MDCT is arterial enhancement followed by PVP and/or delayed phase washout. Veterinary research on this topic is in its infancy, and preliminary findings regarding the MDCT features of primary liver neoplasia show several inconsistencies. The small number of cases studied and differences in disease stage (early detection of a primary hepatic neoplasia may influence its imaging features, size, and enhancement, as well as the number of metastases detected), scan protocols, and CM protocols are major factors leading to these inconsistent results. In all published studies, canine HCC has shown an inhomogeneous hypo-, iso-, or hyperattenuating pattern in the arterial phase and PVP. Figures 22, 23, 24, 25, 26, 27, and 28 show appearance of some primary hepatobiliary tumors in dogs and cats.

MDCT have an important role in presurgical evaluation in patients with known liver lesions. In our experience, three-dimensional MIP and VR from EAP dataset of the liver in patients with HCC or other hepatic neoplasia are also helpful for depiction of arterial feeding vessel/s prior to angiography for trans-arterial chemoembolization/embolization (TACE/TAE) and may have a role in monitoring these patients after treatment (Fig. 29).

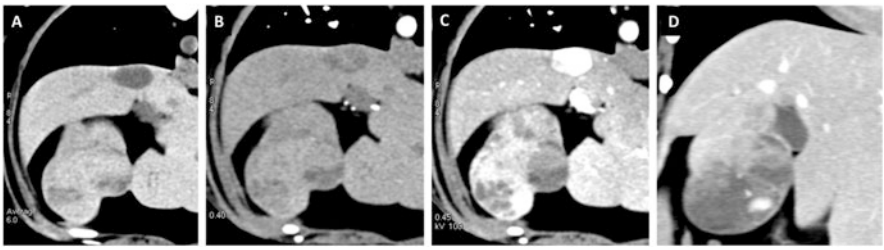

Fig. 22 Hepatic adenoma in a dog. The mass is isoattenuating in pre-contrast series (**a**) and HAP (**b**). It shows great, inhomogeneous enhancement in the PVP (**c**) and hypoattenuation in the EP (**d**)

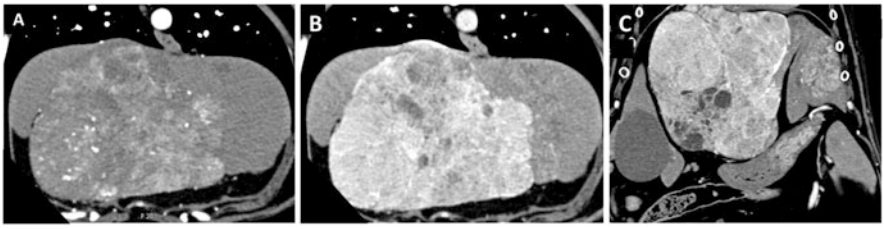

Fig. 23 Hepatic adenoma in a dog. (**a**) The mass is highly vascularized in the HAP (see also Fig. 19), shows greater enhancement in the PVP (**b**), and has an inhomogeneous aspect in the EP, with multiple cystic-like areas (**c**)

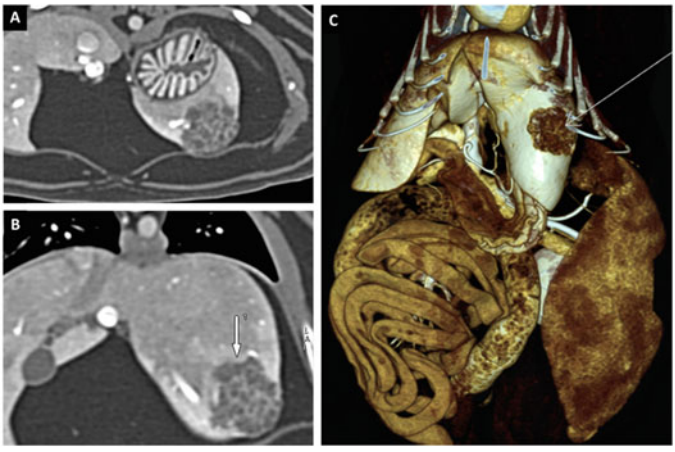

Fig. 24 Biliary adenoma in a cat (*arrow*). (**a**, **b**) PVP transverse views. (**c**) VR of the abdomen

Hepatic metastatic lesions of primary hepatobiliary neoplasia may occur as multiple neoplastic foci of different sizes with characteristics similar to those of the primary mass. A whole-body MDCT should be performed for staging canine and feline patients with primary hepatic tumor. The most common sites of metastasis of

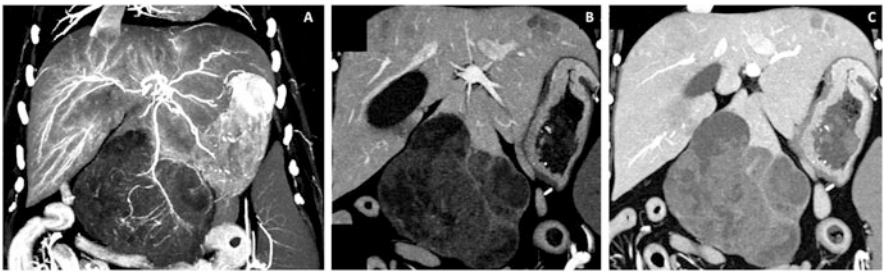

Fig. 25 HCC in a dog. (**a**) EAP, dorsal thin-slab MIP showing a prominent feeding artery. The mass is hypoattenuating in the PVP (**b**) and EP (**c**) with a heterogeneous appearance. Similar lesions are present in other liver lobes

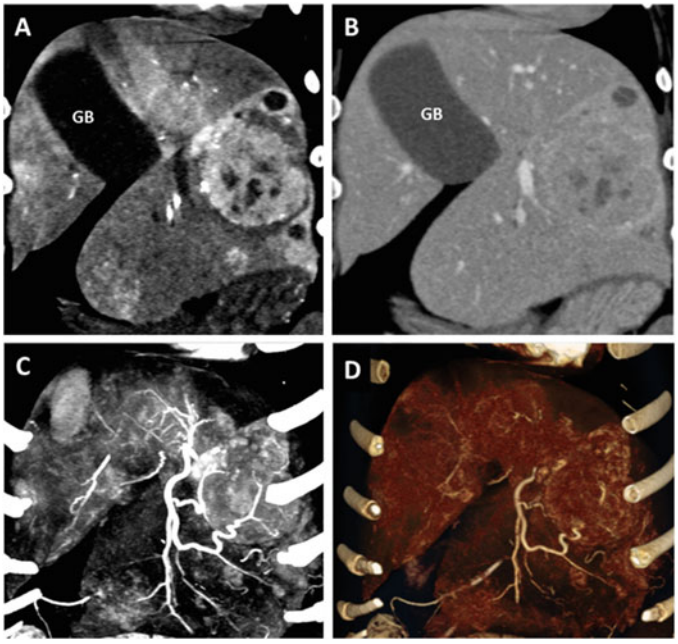

Fig. 26 HCC in a dog. (**a**) HAP, dorsal view. A large left-sided mass with a heterogeneous appearance and areas of early parenchymal enhancement (HPD) are present. *GB* gallbladder. (**b**) The same slice in the PVP. Note the rapid washout of the mass, which is isoattenuating to the liver parenchyma. (**c**) Thin-slab MIP view from the HAP, showing the feeding arteries of the mass. (**d**) Thin-VR of the same volume

primary hepatic neoplasia are local lymph nodes, other liver lobes, the peritoneum, and the lung. Biopsy of the hepatic mass and potential metastasis is necessary to confirm the imaging suspected diagnosis.

Focal hepatic lesions may be detected during oncological staging for non-hepatic tumors. Metastatic liver disease is encountered commonly in practice;

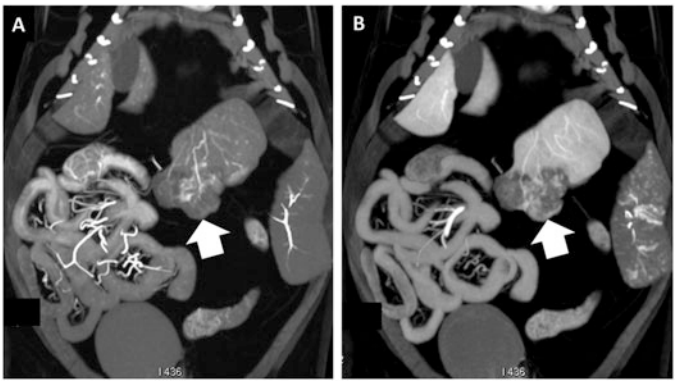

Fig. 27 Cholangiocarcinoma in a cat. (**a**) LAP. (**b**) PVP

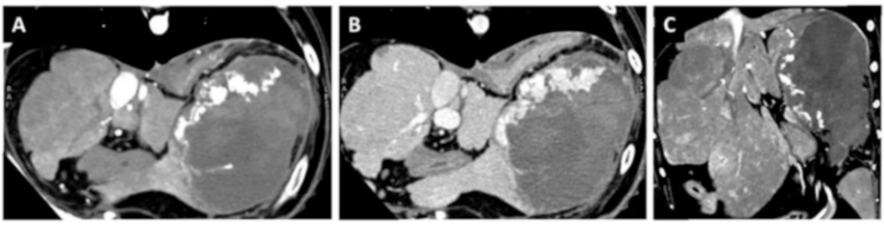

Fig. 28 Hepatic hemangiosarcoma in a dog. (**a**) HAP, transverse view. Large hypoattenuating, hypovascular left-sided mass. (**b**) The same slice in the PVP shows minimal heterogeneous enhancement. (**c**) Dorsal MPR from the same dog showing diffuse hepatic parenchymal abnormalities and perilesional free fluid (ruptured mass)

it occurs in 30.6–36.8% of dogs with primary non-hepatic neoplasia. Most metastatic liver cancer arises from the spleen, pancreas, or intestinal tract. *Metastases from extrahepatic neoplasia* may show different behaviors on multiphasic MDCT, depending on differences in blood supply, cellular differentiation, and the presence of hemorrhage, fibrosis, and necrosis. They may appear as single or multiple parenchymal lesions, iso- to hypoattenuating to the surrounding parenchyma. Most liver metastases are hypovascular (e.g., gastrointestinal tumor) and thus hypoattenuated to the normal liver parenchyma during the PVP (Fig. 30). Nodular regenerative hyperplasia can also appear as hypoattenuating/hypovascular nodules (Fig. 31). However, hypovascular metastasis may sometime show perilesional (ring) enhancement or a target-like appearance, which is particularly evident in the PVP. Hypervascular metastases (e.g., pancreatic insulinoma, pheochromocytoma, carcinoid tumor) have arterial blood supplies and thus enhance earlier and are most conspicuous in the HAP (Figs. 32 and 33).

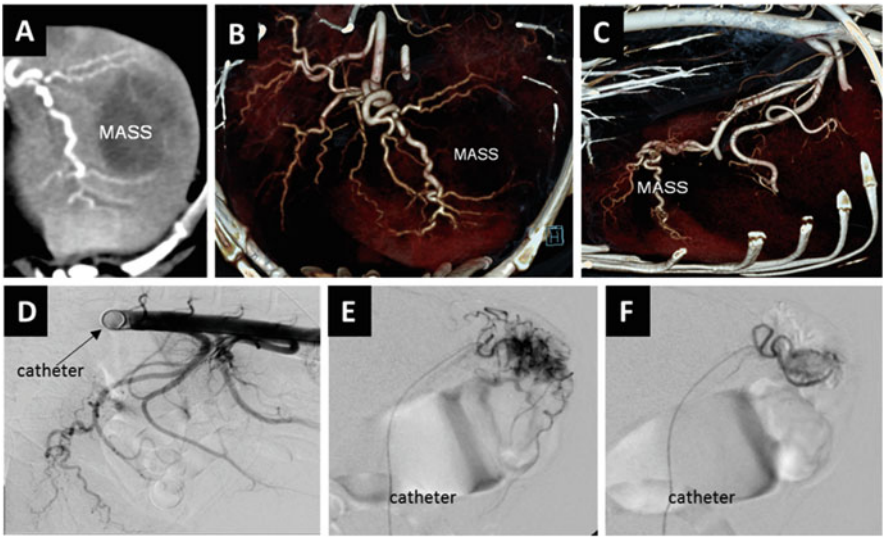

Fig. 29 HCC in a 12-kg dog. (**a**) Transverse view from the EAP showing the mass in the left lateral lobe. 3D-VR from timed EAP. (**b**, **c**) Frontal and left lateral views of volume-rendered reconstructions from the same volume datasets, showing the feeding artery of the mass. (**d**) Image of the same dog from abdominal angiography. The dog was treated with bland superselective TAE (transarterial embolization) using microcoils. (**e**, **f**) Pre- and post-embolization images

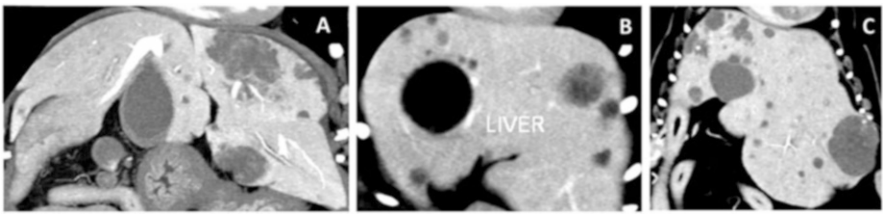

Fig. 30 Hypovascular liver metastases (PVP). (**a**) Dorsal view of a bulldog with metastatic pancreatic carcinoma. (**b**) Dorsal view of the liver in a mongrel dog with liver metastasis of mammary carcinoma. (**c**) Dorsal view of the liver in a dog with metastatic hemangiosarcoma

5 Liver Lobe Torsion

Liver lobe torsion (LLT) is an uncommon condition that has been described in dogs, cats, and rabbits. Although some veterinary radiology sources include this condition among traumatic lesions of the liver, inciting causes for LLT in small animals have not been established and previous abdominal trauma was suspected in only one case reported in the literature (Fig. 34). The left medial and lateral liver lobes are most commonly involved, but caudate lobe and right lateral lobe involvement has also been documented (Fig. 35). To date, the MDCT features of LLT have been described in only one case in a dog, using 4-MDCT examination with an awake patient. Pre-contrast CT showed enlargement and caudoventral deviation of the left

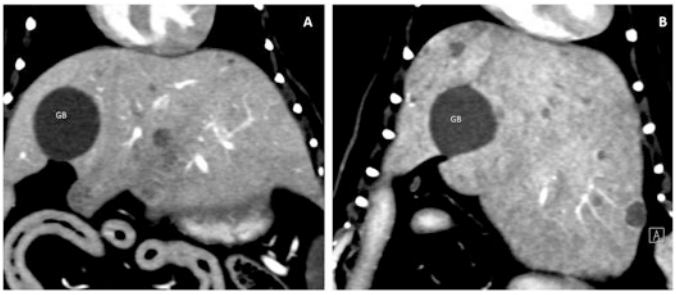

Fig. 31 Focal nodular hyperplasia in two dogs (**a**, **b**) appears as hypovascular nodular lesions

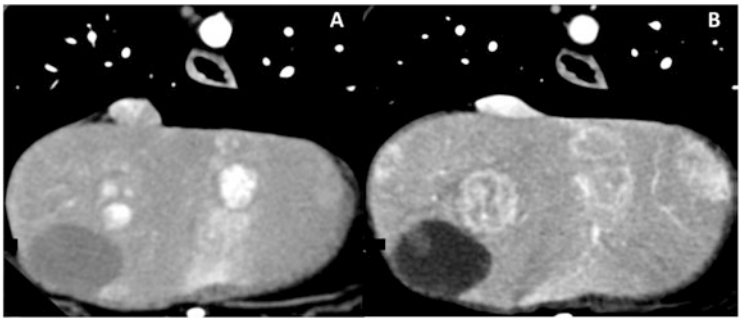

Fig. 32 Hypervascular liver metastasis. Images of the liver in dog with metastatic pancreatic insulinoma. Multiphasic CT examination shows multiple focal lesions in the liver parenchyma, with great enhancement in the LAP (**a**), which decreases in the PVP (**b**)

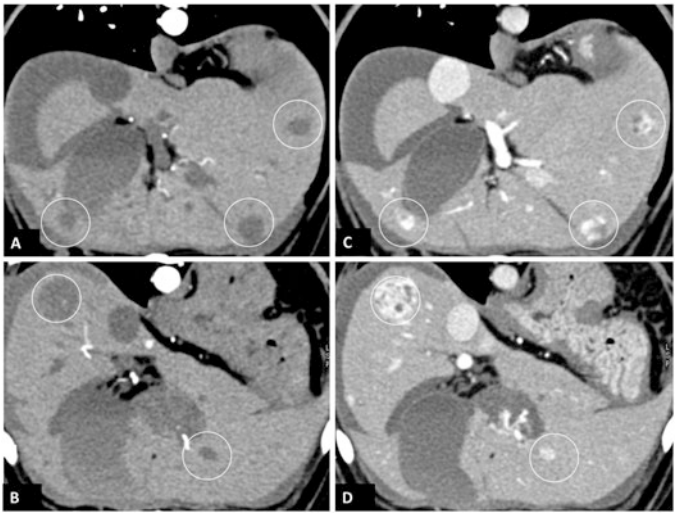

Fig. 33 Arterial-phase (**a**, **b**) and PVP (**c**, **d**) images of the liver in a dog with hemangiosarcoma metastasis to the liver

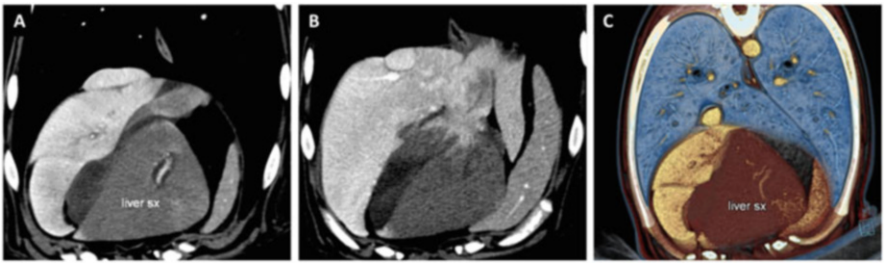

Fig. 34 LLT in a Great Dane. (**a**, **b**) The hypoattenuating, hypovascular left lateral and median lobes do not enhance in the PVP, whereas normal contrast enhancement is visible in unaffected lobes. (**c**) Thin-VR from the same dog. Different *colors* reflect different attenuation of the lobes

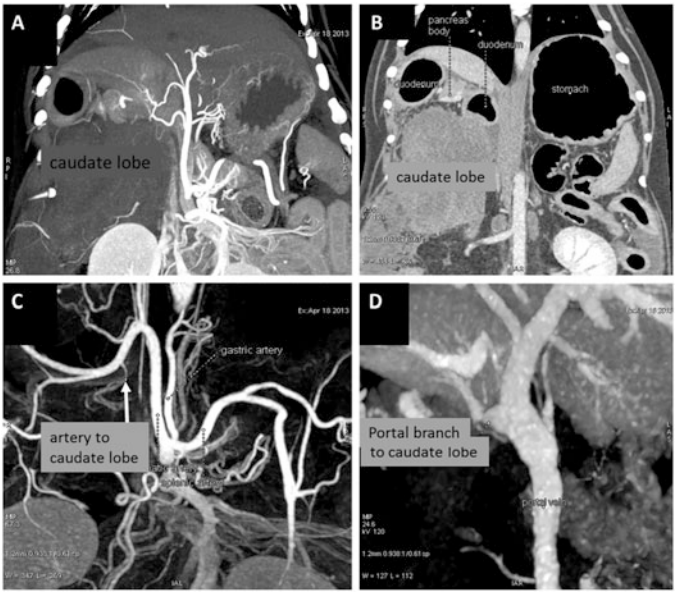

Fig. 35 LLT in a Bernese Mountain dog. (**a**) LAP image of the abdomen showing an enlarged, hypovascular caudate lobe. (**b**) The pancreas and duodenum are dislocated cranially. The duodenum and stomach are distended due to the presence of air. (**c**, **d**) MIP images from the LAP and PVP. Note the thin and hypoperfused artery to the caudate lobe. In (**d**), note the tilted portal branch to the caudate lobe

liver lobe, which had an irregular surface. On post-contrast images, the affected lobe did not enhance (due to torsion of the vascular pedicle), whereas normal contrast enhancement was observed in unaffected liver lobes. In this case, as in the majority of reported cases, LLT was accompanied by peritoneal effusion.

6 MDCT Findings of Portal Hypertension

Portal hypertension (PH) refers to increased resistance and/or blood flow in the portal circulation. MDCT has an important role in the diagnosis of PH. Although it cannot be used to directly measure flow direction and velocity, MDCT can easily detect morphological changes occurring in PH. It can also be used to detect the majority of conditions causing PH.

Physiopathology Background
Blood from the hepatic artery and portal vein enters the hepatic lobule at the portal triad and mixes in the hepatic sinusoids. Each of these circulatory routes provides blood of differing compositions, which allows the liver to perform its unique and vital digestive and metabolic functions. After that, blood drains into the hepatic central vein and then out of the liver through the hepatic veins, eventually reaching the posthepatic caudal vena cava for return to the right atrium. The portal pressure gradient (the difference in pressure in the portal vein and caudal vena cava) is determined by the product of portal blood flow and the vascular resistance opposing that flow. When it increases (to >10–12 mmHg), PH can ensue. The portal vein is a valveless afferent vessel to the liver (hepatopetal flow) that drains blood from the capillary system of the intestine, spleen, pancreas, stomach, omentum, and gallbladder. In cases of PH, blood is redirected caudally, away from the liver (hepatofugal flow). Increased portal pressure is the most important factor leading to the formation of an extensive network of portosystemic collateral vessels. Preexisting embryonic vessels reopen, connecting the portal and systemic circulations, and angiogenic factors then contribute to their maintenance. PH is classified as prehepatic, intrahepatic, or posthepatic according to the anatomic site of increased resistance in the portal system (Fig. 36). Classification of the PH site has clinical relevance because the level of obstruction often suggests possible causes and best treatment.

Causes of PH Detectable on MDCT
Most causes of prehepatic, hepatic, and posthepatic PH are detectable on MDCT images (Fig. 37). PH results in chronic multifactorial diseases. Its causes and consequences may involve abdominal or thoracic structures. Thus, whole-body MDCT scans, including a multiphasic approach to the liver, should be performed in patients with PH.

Prehepatic causes of PH occur in the portal system segment, caudal to the porta hepatis, and include prehepatic portal vein thrombosis (PVT), stenosis, or compression and portal vein anomalies (e.g., atresia, aneurysm) (Fig. 38). *Hepatic causes of PH* may be classified histologically as pre-sinusoidal, sinusoidal, or post-sinusoidal (e.g., venocclusive diseases, which are rarely reported). Most pre-sinusoidal causes, including intrahepatic PVT, portal compression (e.g., by tumors, biliary diseases), and portal vein anomalies (e.g., APF), can be identified by CT. Primary PVH can be suspected based on CT features (small liver, thin portal vein, and absence of macroscopic PSS) and should be confirmed by liver histopathology. Sinusoidal causes of PH are chronic hepatopathies (e.g., cirrhosis,

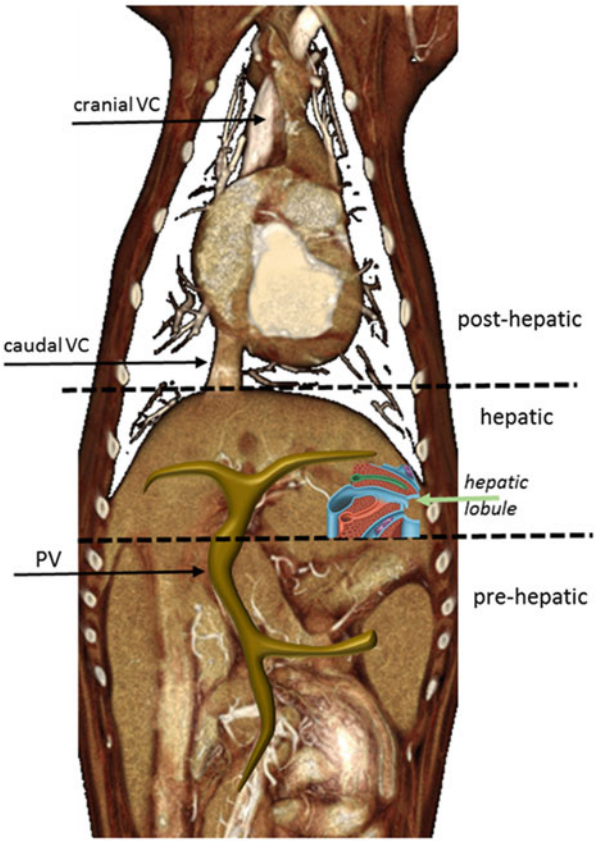

Fig. 36 Anatomy-based classification of PH. Most prehepatic, hepatic, and posthepatic causes can be identified by imaging

Pre-hepatic	Hepatic	Post-hepatic
PV atresia	PHPV (presinusoidal)	Thrombosis/Compression/stenosis of post-hepatic CVC (Budd-Chiari Syndrome)
PVT	APF (presinusoidal)	Thrombosis/Compression/stenosis of the cranial vena cava (Vena Cava Syndrome)
PV stenosis/compression	Congenital/chronic biliary diseases (presinusoidal)	Right heart failure
PV tumoral invasion	Cirrhosis/chronic hepatitis/congenital fibrosis (sinusoidal)	Cardiac neoplasia/anomalies
Surgical/interventional complication (PSS attenuation)	Surgical/interventional complication (PSS attenuation)	Cardiac tamponade
	Veno-occlusive disease (post-sinusoidal)	

Fig. 37 Major prehepatic, hepatic, and posthepatic conditions that are potential causes of PH

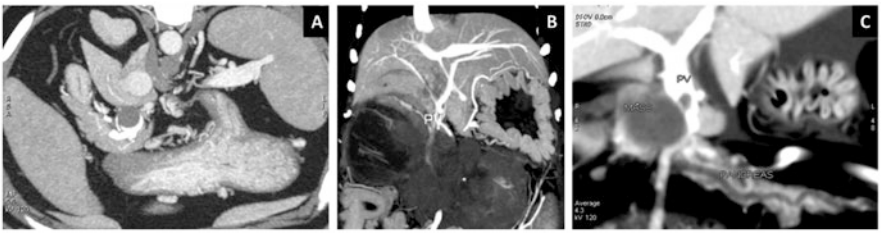

Fig. 38 Prehepatic causes of PH. (**a**) Transverse view at the porta hepatis in a dog with PVT. (**b**) Dorsal thin-MIP view from a dog with pancreatic carcinoma encasing the extrahepatic segment of the portal vein. (**c**) Pancreatic carcinoma, which compresses and invades the extrahepatic portal vein, in a cat

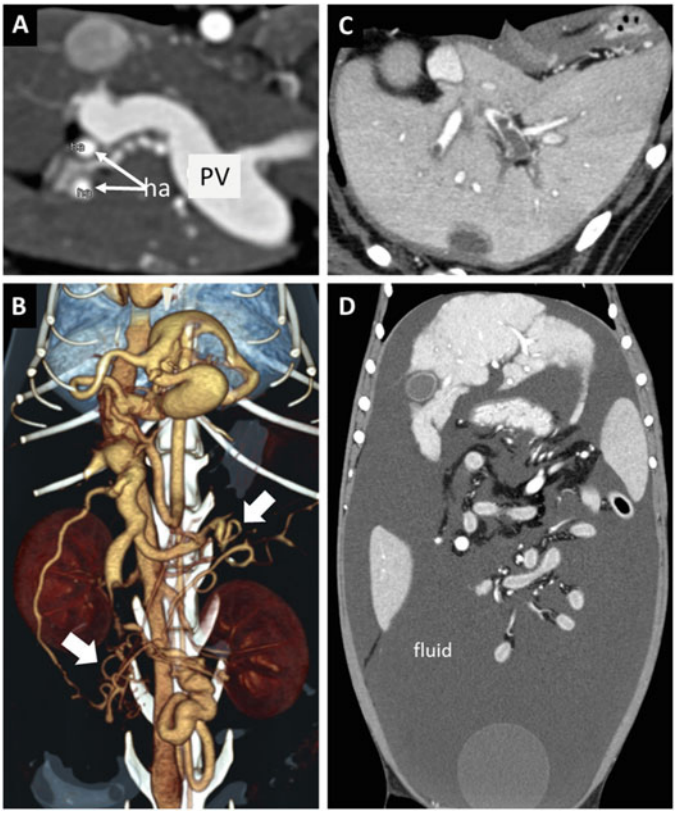

Fig. 39 Hepatic causes of PH. (**a**) Transverse view of the liver in a cat with an intrahepatic APF. (**b**) Volume-rendered image of the abdominal vasculature in the same cat. Note the complex anatomy of the APF, the distended mesenteric veins, and APSS (*arrows*). (**c**) Transverse view of the liver in a dog with intrahepatic PVT. (**d**) Dorsal MPR view of the abdomen in a dog with hepatic cirrhosis and ascites

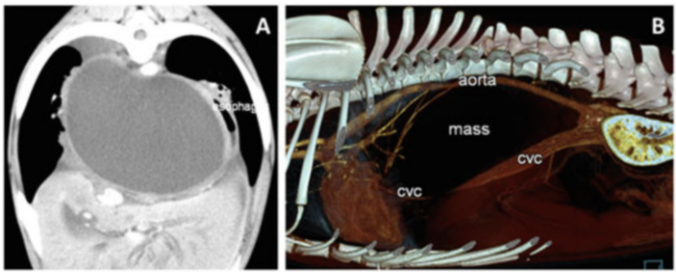

Fig. 40 Posthepatic causes of PH. (**a**) Transverse view showing a large abscess in the caudal-dorsal mediastinum, compressing the posthepatic caudal vena cava. (**b**) VR, left lateral view, from the same dog showing compression of the caudal vena cava

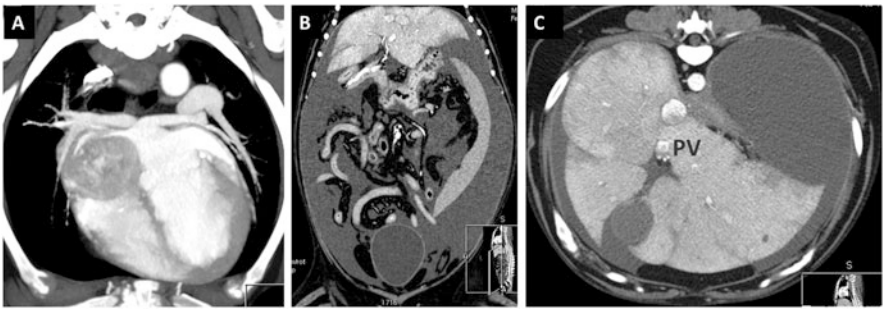

Fig. 41 Posthepatic causes of PH. (**a**) Transverse view of the thorax in a dog with a right atrial mass (non-gated, 16-MDCT image). (**b**) Dorsal MPR view of the same dog, showing abundant ascites. (**c**) Transverse view at the porta hepatis showing liver congestion and portal vein hypoperfusion

fibrosis, dissecting hepatitis, bile duct disorders) (Fig. 39). *Posthepatic causes of PH* include right heart failure, cardiac masses, and increased resistance in the caudal vena cava due to thrombosis, compression, or tumoral invasion (Figs. 40 and 41). When obstruction occurs in the hepatic venous outflow in the caudal vena cava or larger extrahepatic hepatic veins, it is known as Budd–Chiari syndrome.

6.1 MDCT Direct Signs of PH

Hepatic changes depend on the cause of PH. The liver may be enlarged or decreased in size, depending on the primary disease. HPD can be detected in the HAP due to the deficit in portal venous flow to the liver. In cases of PVT, the liver parenchyma shows inhomogeneous enhancement in the hepatic PVP due to the alteration in local portal venous flow. Distention and tortuosity of the portal vein and its tributaries may be direct signs of PH (Fig. 42). Chronic PH may lead to portal vein aneurysm.

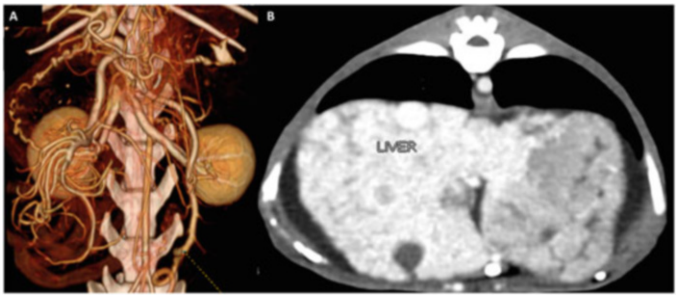

Fig. 42 Direct signs of PH. (**a**) VR of the abdominal vasculature in a cat showing distention of the mesenteric and colic veins due to PH. (**b**) Transverse view of the liver in the same cat (cirrhosis)

6.2 MDCT Indirect Signs of PH

Portal Collateral Circulation

In normal dogs, the portal vein has at least three embryonic connections with the systemic venous system, which are usually unperfused or minimally perfused. These circulatory routes may enlarge and become functional in PH, leading to a repetitive pattern of acquired portosystemic shunt (APSS). In addition, new vessels may develop in patients with PH. Preexisting routes are present between the colic branch of the portal vein and branches of the pudendal vein, between the phrenic vein and small branches of the portal vein, and between the cardiac branches of the left gastric vein and the esophageal branches of the azygos vein. MDCT is an excellent tool for the depiction of large and small portal collaterals, and it enables complete elucidation of their locations and courses. The first comprehensive description and classification of portal collaterals in dogs and cats with PH was made using a 16-MDCT scanner, at our center. With the diffusion of MDCT technology in veterinary practice, other unusual pathways of portosystemic anastomosis are increasingly being recognized. Delineation of these collaterals is important, especially during the consideration of interventional procedures, such as feeding tube placement, biopsy, endosurgery, and conventional surgery, because inadvertent disruption of these vessels can be a significant cause of uncontrollable bleeding. Large collaterals and small tortuous varices can be detected in patients with PH, and they are named according to their anatomic location. Most common large APSS are those involving the gonadal veins. Most common varices are retroperitoneal (renal region), gastric, and esophageal (see the chapter "The Abdominal Vasculature") (Fig. 43).

Importantly, increased resistance in or obstruction of the cranial vena cava (cranial vena cava syndrome) can lead to the formation of esophageal and paraesophageal varices as well (so-called downhill or non-hypertensive varices). In addition, not all forms of PH lead to collateral formation. In posthepatic PH, characterized by the absence of a pressure gradient between the portal and systemic circulations, collaterals do not form. Thus, PH cannot be excluded based on the absence of portal collaterals. Portal collaterals are not always hemodynamically efficient and are often insufficient to normalize portal venous pressure. Therefore, the presence of portal collaterals does not correlate well with the patient's portal pressure level at any given moment.

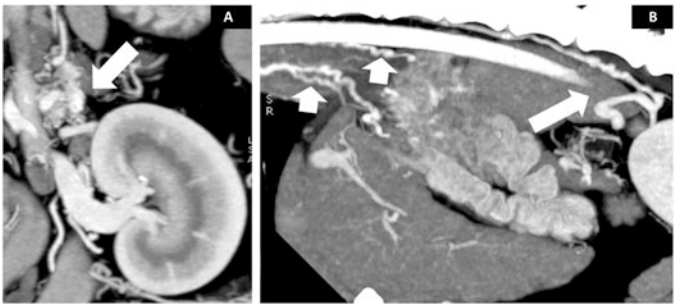

Fig. 43 Indirect signs of PH. (**a**) Dorsal thin-MIP view showing left phrenico-abdominal varices in a dog (*arrow*). (**b**) Sagittal thin-MIP view showing a left gastric vein varix (*long arrow*) and paraesophageal varices (*short arrows*) in a dog with hepatic cirrhosis

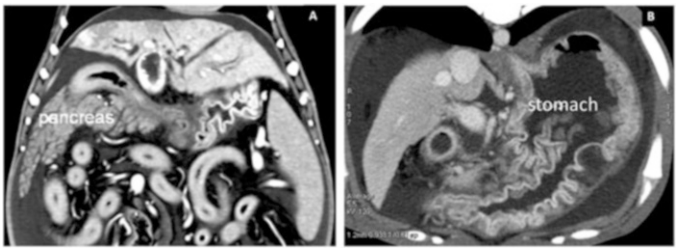

Fig. 44 Indirect signs of PH. (**a**) Pancreatic congestion and ascites in a dog with PH due to cirrhosis. (**b**) Gastric congestion and ascites in a dog with congenital hepatic fibrosis (ductal plate malformation)

Consequently, functional speculations based only on the morphological assessment of collaterals by MDCT should be very cautious.

6.3 MDCT ancillary signs of PH

Ancillary Signs

Increased portal vein pressure drives fluid into the interstitial space. The role of the lymphatic vascular system is to remove interstitial fluid from tissues and return it to the bloodstream. In PH, the lymphatic vascular system reabsorbs excess fluid in the liver and the splanchnic region and helps to prevent ascites formation. When the regional lymphatic capacity is overwhelmed, ascites develops. Initial ascites can be detected in a peripheral perihepatic, gravity-dependent location (based on an attenuation value $<$10 HU). On thin-section MDCT images, other possible indirect signs of PH are engorgement of the abdominal lymphatics and hepatic lymph nodes; gastric, small bowel, and pancreatic congestion; active gastrointestinal hemorrhage; and thickening of the gallbladder wall (Fig. 44).

Further Readings

AK P, AI H, Lieberman PH. Canine hepatic neoplasms: a clinicopathologic study. Vet Pathol. 1980;17:553–64.

Bertolini G. Acquired portal collateral circulation in dog and cat. Vet Radiol Ultrasound. 2010; 51(1):25–33.

Borsetto A. Hepatobiliary diseases in small animals: a comparison of ultrasonography and multidetector-row computed tomography. Dissertation thesis, 2011; http://amsdottorato.unibo.it/id/eprint/3492.

Costa LAVS, Maestri LFP, Júnior JAM, et al. Hepatic radiodensity in healthy dogs by helical computed tomography. Cienc Rural. 2010;40:888–93.

Costa LAVS, et al. Quantitative computed tomography of the liver in dogs submitted to prednisone therapy. Arq Bras Med Vet Zootec. 2013; 65(4):1084–90. ISSN: 1678-4162. doi:10.1590/s0102-09352013000400020.

Cullen JM. Summary of the world small animal veterinary association standardization committee guide to classification of liver disease in dogs and cats. Vet Clin North Am Small Anim Pract. 2009;39(3):395–418. doi:10.1016/j.cvsm.2009.02.003.

Dr S. Clinicopathologic features of primary and metastatic neoplastic disease of the liver in dogs. J Am Vet Med Assoc. 1978;173(3):267–9.

European Association for the Study of the Liver, European Organisation for Research and Treatment of Cancer. Easl-Eortc clinical practice guidelines: management of hepatocellular carcinoma. J Hepatol. 2012;56:908–43.

Fukushima K, Hideyuki K, Ohno K, et al. Ct characteristics of primary hepatic mass lesions in dogs. Vet Radiol Ultrasound. 2012;53:252–7.

Furneaux RW. Liver haemodynamics as they relate to portosystemic shunts in the dog: a review. Res Vet Sci. 2011;91(2):175–80. doi:10.1016/j.rvsc.2010.11.017.

Kodama Y, Ng CS, Wu TT, et al. Comparison of CT methods for determining the fat content of the liver. Am J Roentgenol. 2007;188:1307–21.

Kudo M, Matsui O, Izumi N, Iijima H, Kadoya M, Imai Y, et al. Jsh Consensus-based clinical practice guidelines for the management of hepatocellular carcinoma: 2014 update by the liver cancer study group of Japan. Liver Cancer. 2014;3:458–68.

Kummeling A, Vrakking DJ, Rothuizen J, Gerritsen KM, Van Sluijs FJ. Hepatic volume measurements in dogs with extrahepatic congenital portosystemic shunts before and after surgical attenuation. J Vet Intern Med. 2010;24(1):114–9.

Lee KJ, Yamada K, Hirokawa H, Shimizu J, Kishimoto M, Iwasaki T, Miyake Y. Liver lobe torsion in a Shih-Tzu dog. J Small Anim Pract. 2009;50(3):157. doi:10.1111/J.1748-5827.2009.00733.X.

Liu H, Liu J, Zhang Y, Liao J, Tong Q, Gao F, Hu Y, Wang W. Contrast-enhanced ultrasound and computerized tomography perfusion imaging of a liver fibrosis-early cirrhosis in dogs. J Gastroenterol Hepatol. 2016;31(9):1604–10. doi:10.1111/jgh.13320.

Makara M, Chau J, Hall E, Kloeppel H, Podadera J, Barrs V. Effects of two contrast injection protocols on feline aortic and hepatic enhancement using dynamic computed tomography. Vet Radiol Ultrasound. 2015;56(4):367–73. doi:10.1111/vru.12239. Epub 2015 jan 30.

Nakamura M, Chen HM, Momoi Y, et al. Clinical application of computed tomography for the diagnosis of feline hepatic lipidosis. J Vet Med Sci. 2005;67:1163–5.

Oliveira DC, Costa LSVS, Lopes BF. Computed tomography in the diagnosis of steroidal hepatopathy in a dog: case report. Arq Bras Med Vet Zootec. 2011;63:36–9.

Rockall AG, Sohaib SA, Evans D, et al. Hepatic steatosis in Cushing's syndrome: a radiological assessment using computed tomography. Eur J Endocrinol. 2003;149:543–8.

Rothuizen J, Bunch S, Charles J, et al. Standards for clinical and histological diagnosis of canine and feline liver diseases (WSAVA). Philadelphia: Elsevier Saunders; 2006.

Sg S, Sl M, Keating J, Dl C. Liver lobe torsion in dogs: 13 cases (1995–2004). J Am Vet Med Assoc. 2006;228(2):242–7.

Stieger SM, Zwingenberger A, Pollard RE, Kyles AE, Wisner ER. Hepatic volume estimation using quantitative computed tomography in dogs with portosystemic shunts. Vet Radiol Ultrasound. 2007;48(5):409–13.

Suzuki K, Epstein ML, Kohlbrenner R, Garg S, Hori M, Oto A, Baron RL. Quantitative Radiology: automated CT liver volumetry compared with interactive volumetry and manual volumetry. AJR Am J Roentgenol. 2011;197(4):W706–12. doi:10.2214/Ajr.10.5958.

Swann HM, Brown DC. Hepatic lobe torsion in 3 dogs and a cat. Vet Surg. 2001;30(5):482–6.

Tian J-L, Zhang J-S. Hepatic perfusion disorders: etiopathogenesis and related diseases. World J Gastroenterol: WJG. 2006;12(20):3265–70. doi:10.3748/Wjg.V12.I20.3265.

Trigo FJ, Thompson H, Breeze RG, et al. The pathology of liver tumors in the dog. J Comp Pathol. 1982;92:21–39.

Zwingenberger A, Shofer F. Dynamic computed tomographic quantitation of hepatic perfusion in dogs with and without portal vascular anomalies. Am J Vet Res. 2007;68(9):970–4.

Zwingenberger A, Daniel L, Steffey MA, Mayhew PD, Mayhew KN, Culp WT, Hunt GB. Correlation between liver volume, portal vascular anatomy, and hepatic perfusion in dogs with congenital portosystemic shunt before and after placement of ameroid constrictors. Vet Surg. 2014;43(8):926–34. doi:10.1111/J.1532-950x.2014.12193.X.

The Gallbladder and Biliary System

Giovanna Bertolini

1 Introduction

The biliary system consists of the intrahepatic and extrahepatic structures, which can be affected by various disorders. The canalicular membranes, specialized components of the hepatocyte cell membrane, are the sites of initial bile duct formation into the liver. Bile flows from the hepatic canaliculi (~1 mm in diameter) to the gallbladder along the biliary tree, which includes the bile ductules, intralobular ducts, interlobular ducts, hepatic ducts, and the cystic duct that connects the gallbladder to the common bile duct (Fig. 1). The gallbladder is attached to the liver in a right-sided fossa between the right medial and quadrate liver lobes. The common bile duct (choledochus) is the extrahepatic pathway that directs bile to the duodenum. The sphincter of Oddi, a unidirectional muscular sphincter, prevents retrograde passage of intestinal contents in the biliary system. The communication of the common bile duct and duodenum differs anatomically between dogs and cats, and a great deal of intraspecific variation exists, especially in cats. In dogs, the common bile duct, after a brief intramural course in the duodenum, generally empties into the duodenal lumen at the major duodenal papilla, 1.5–6 cm distal to the pylorus, near the smaller of two pancreatic ducts (the minor duct). The larger (accessory) pancreatic duct opens into the duodenum lumen a few centimeters distally. In cats, the common bile duct and the pancreatic duct join just before entering the duodenal papilla, forming an ampulla, about 3 cm distal to the pylorus.

G. Bertolini (✉)
San Marco Veterinary Clinic, Padua, Italy
e-mail: bertolini@sanmarcovet.it

G. Bertolini (ed.), *Body MDCT in Small Animals*, DOI 10.1007/978-3-319-46904-1_5

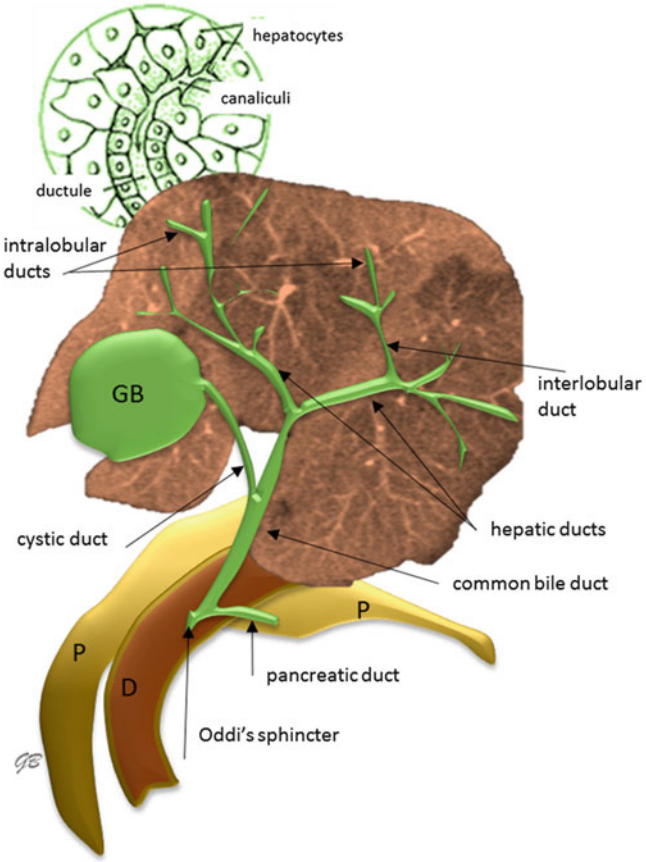

Fig. 1 Macro- and microanatomy of the gallbladder and biliary tree. *GB* gallbladder, *P* pancreas, *D* duodenum

2 MDCT Imaging Strategies

The biliary system should always be evaluated in a CT study of the liver. In patients with known or suspected biliary tract involvement, CT protocols should be designed to optimally image the biliary system, to increase diagnostic accuracy. In particular, thin-section, isotropic (0.6-mm) acquisition is necessary to enhance spatial resolution and minimize partial-volume averaging of small intrahepatic biliary structures. The acquisition of isotropic datasets is also essential for the application of high-quality post-processing techniques, especially in the assessment of the biliary system of small dogs or cats.

In a multiphasic approach, dedicated evaluation of the biliary system should include thin-section *non-contrast series* through the cranial abdomen (including liver, gallbladder, common biliary duct, pancreas, and proximal duodenum) to

identify biliary stones that could be obscured on contrast-enhanced images. Additionally, an initial unenhanced scan provides a baseline for determining whether a possible lesion enhances after CM injection.

Post-contrast series should include various vascular phases, to enhance differences among the liver parenchyma, vessels, and biliary structures. Arterial perfusion of the gallbladder and common bile duct is provided from the cystic artery, which is a branch of the hepatic artery; that of the intrahepatic bile ducts is from the hepatic artery and hepatic portal branches. Thus, a multiphase study of the liver is useful also for the evaluation of the gallbladder and biliary tree.

Arterial enhancement of the walls of biliary structures, which normally do not enhance, can be seen in inflammatory and neoplastic processes. In HAP (hepatic arterial phase), masses involving the biliary system can be easily identified and characterized. Thrombosis of the cystic artery may be found in necrotizing cholecystitis. In the PVP (portal venous phase), the intrahepatic biliary structures are more clearly visible because they are hypoattenuated relative to the liver parenchyma. When not dilated, intrahepatic biliary ducts are barely visible in most dogs and cats. In fasted patients, however, intrahepatic biliary ducts are often visible as thin, low-attenuation channels accompanying the portal branches within the liver (*periportal halo or periportal collar sign*) (Fig. 2). A further delayed CT series may be useful in traumatic/nontraumatic biliary rupture, chronic inflammatory, or neoplastic conditions.

A wide variety of post-processing techniques can be used to evaluate the biliary system. The gallbladder and other biliary structures are not exclusively perpendicular to the transverse plane. Thus, combined interpretation of transverse and high-quality (from isotropic data) multiplanar reformatted (MPR) images strongly improves the diagnostic performance of MDCT in the evaluation of the extent of biliary tract pathologies. Curved multiplanar reconstruction (cMPR) is necessary to depict a duct in a single plane. The use of this technique, however, requires knowledge of the biliary system anatomy and familiarity with post-processing techniques, to avoid the creation of images that could be misinterpreted. Minimum intensity projection (MinIP) with variable slab thickness provides a quick overview of the biliary tree, especially on dorsal-oblique views. The MinIP technique projects the lowest attenuation values along each ray, emphasizing the biliary structures. Importantly, a MinIP slab should not exceed the diameter of the duct being studied, to avoid the inclusion of other hypoattenuating substances (e.g., air, fat) in the projection.

Fig. 2 Periportal halo sign (or collar) in a dog. Thin hypoattenuating tubular structures parallel to/around the major portal branches and their subdivisions represent hepatic biliary ducts (*large arrows*) and interlobular ducts (0.6-mm slice thickness)

3 Disorders of the Gallbladder and Biliary System

A wide spectrum of biliary diseases often show similar imaging characteristics. The assessment requires a multidisciplinary approach to understand possible underlying pathologies. Obstructive and non-obstructive causes lead to *biliary dilatation*, and they can be identified easily with MDCT. Obstructive causes include stones and strictures (inflammatory, post-inflammatory, and neoplastic strictures). Non-obstructive causes include a variety of congenital and acquired conditions (Fig. 3).

3.1 Obstructive Causes of Biliary Dilatation

Biliary Stones (Cholecystolithiasis and Cholelithiasis)
Choleliths and biliary sludge (a mixture of precipitated cholesterol crystals, bile pigments, bile salts, and mucin) are often discovered incidentally in middle-aged and old dogs and cats. Biliary sludge is moderately hyperattenuated relative to normal bile and tends to be in a dependent location when in the gallbladder. In patients with sludge, focal biliary duct wall thickening and contrast enhancement in the late arterial phase can indicate local inflammation of the bile duct. If diffuse, they can be associated with cholangitis or cholecystitis (see below in this chapter).

Most choleliths in companion animals are "stones" of calcium carbonate and bilirubin; they do not contain sufficient mineral for detection on survey radiographs, and they can be missed on ultrasound in the absence of bile duct dilatation. Although asymptomatic in many cases, choleliths can form as a consequence of bile stasis, inflammation, or infection. Conversely, choleliths can injure the bile ducts, leading to bile stasis and inflammation. The detection of biliary cholelithiasis

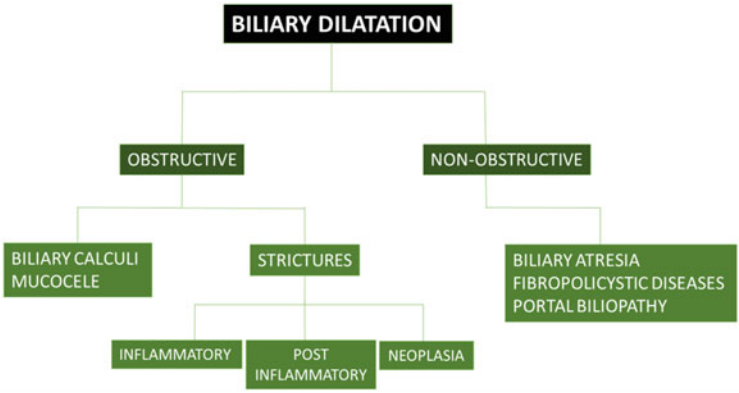

Fig. 3 Flowchart of obstructive and non-obstructive mechanisms leading to segmental and diffuse biliary dilatation

by CT depends on the chemical composition of the cholelith, the CT energy source, and other technical factors. The use of high (140 kVp) tube potential settings can improve the detection of some biliary stones. Thin-section MPR and curved planar reformatted images can greatly aid the diagnosis of biliary tract stones (Figs. 4 and 5). Thick-slab MIP can clearly show hyperattenuating stones, but it should be used cautiously because minerals in the gastrointestinal tract can be superimposed on the liver and mimic biliary tract stones.

Gallbladder mucocele is a non-inflammatory condition characterized by progressive accumulation of gelatinous immobile bile within the gallbladder. From the gallbladder, inspissated bile may also extend into the biliary tree, causing obstruction. Predisposing factors to this condition are middle–old age, decreased bile flow, decreased gallbladder motility, hyperlipidemia/hypercholesterolemia (i.e., endocrinopathies, pancreatitis, nephrotic syndrome), and corticosteroid use. Breed predisposition has been documented in Shetland sheepdogs and other breeds. Gallbladder mucocele is diagnosed readily with abdominal ultrasound. The mucosa

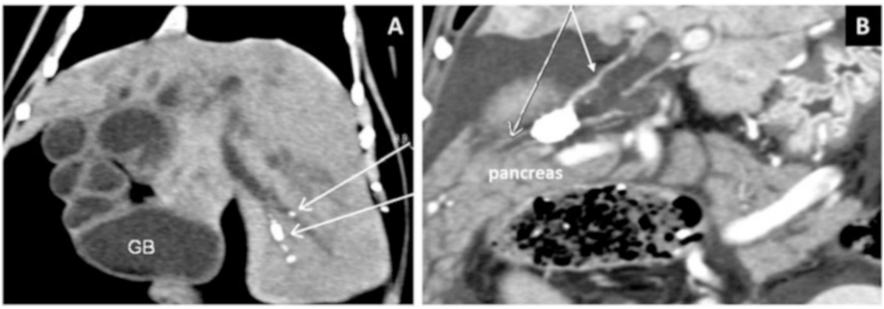

Fig. 4 Biliary dilatation in a cat. (**a**) Dorsal pre-contrast view of the liver. Note the various cholelithes (*arrows*). *GB* gallbladder. (**b**) Obstructive biliary disease in a dog. Dorsal view of the liver (PVP) showing a stone in the common biliary duct (*arrows*)

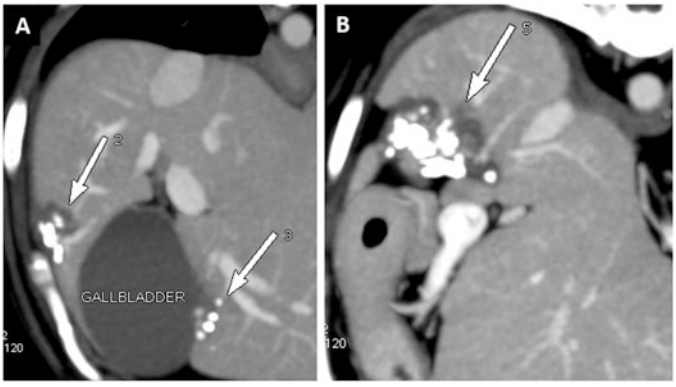

Fig. 5 Intrahepatic biliary stones with ductal dilatation (*arrows*)

shows a variable degree of hyperplasia and the gallbladder lumen has non-gravitationally dependent hyperechoic content, often with a characteristic finely striated or stellate (kiwi fruit-like) appearance. Similar patterns can be recognized on thin-section MDCT images (Fig. 6), although they have not been reported to date in the veterinary literature. Gallbladder mucocele can be asymptomatic but can lead to necrotizing cholecystitis and gallbladder rupture.

Benign and Malignant Biliary Strictures

Benign and malignant stenosis can cause obstruction of the common biliary duct and hepatic ducts [extrahepatic biliary duct obstruction (EHBDO)]. The obstruction of bile flow causes prestenotic enlargement of the biliary duct, clearly visible on MDCT images (Fig. 7). Benign conditions include obstructive sludge,

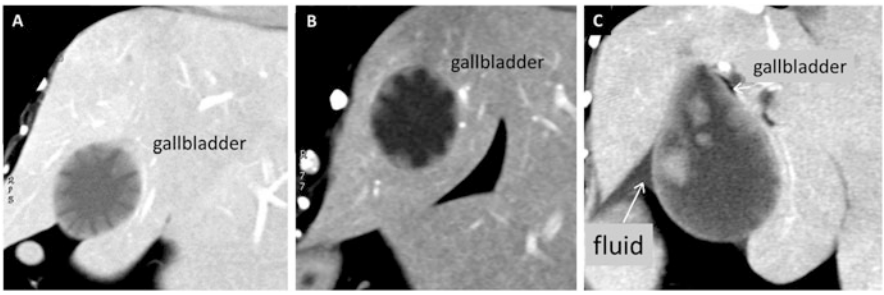

Fig. 6 Gallbladder mucocele in dogs. (**a**, **b**) Dorsal images from two different dogs showing a CT appearance similar to that described for ultrasound. (**c**) Biliary leakage (*arrows*) in a dog with gallbladder mucocele

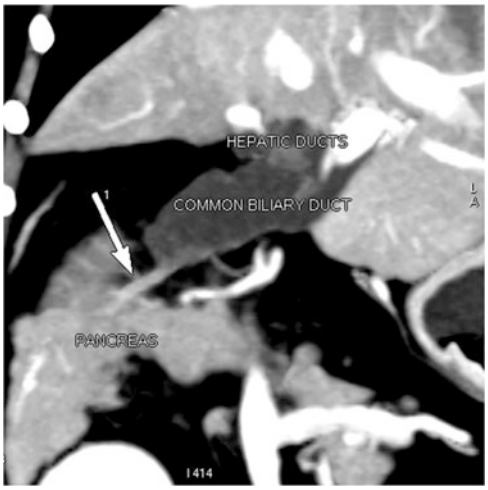

Fig. 7 Benign EHBDO due to post-inflammatory stenosis in a dog. Note the dilatation of the common biliary duct proximal to the stenosis

cholelithiasis, post-inflammatory bile duct or pancreatic entrapment in a diaphragmatic hernia, blunt trauma, and iatrogenic strictures (Figs. 8 and 9). Bile ducts can be affected primarily by hyperplastic and neoplastic conditions (bile duct cystoadenoma, adenocarcinoma) or involved secondarily from pancreatic neoplasia (Figs. 10 and 11). Whatever the cause, obstruction of the biliary ducts can lead to serious hepatobiliary injury within a few weeks. In chronic conditions, irreversible

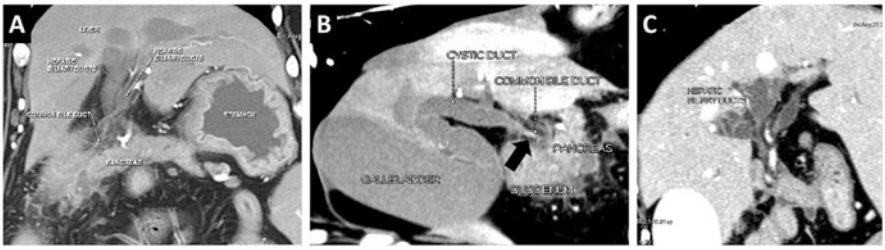

Fig. 8 EHBDO due to benign biliary-duct stricture in a dog with severe pancreatitis. (**a**) Dorsal view showing the enlarged and poorly marginated pancreas. (**b**) Multioblique view. Note the dilatation of the gallbladder, cystic duct, and the proximal part of the common biliary duct. The distal part of the common biliary duct is stenotic (*arrow*). (**c**) Dorsal view showing enlarged hepatic ducts

Fig. 9 Benign EHBDO in a dog. (**a**) Common biliary sludge obstruction. Note the dilatation of the duct proximal to the obstruction. (**b**) Thin-slab MinIP emphasizes the gallbladder and biliary tree dilatation

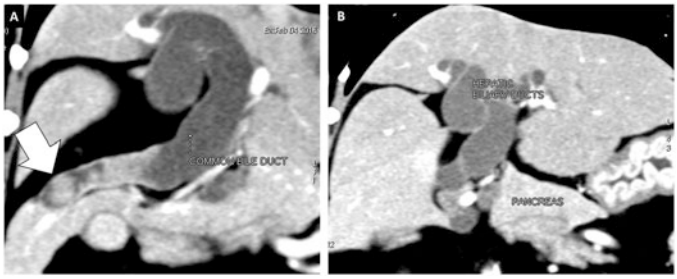

Fig. 10 Benign EHBDO in a dog. (**a**) Dorsal view. *Arrow* indicates a polypoid lesion (hyperplasia) in the distal common bile duct with dilatation of the proximal common bile duct. (**b**) Dorsal view showing dilatation of the hepatic ducts

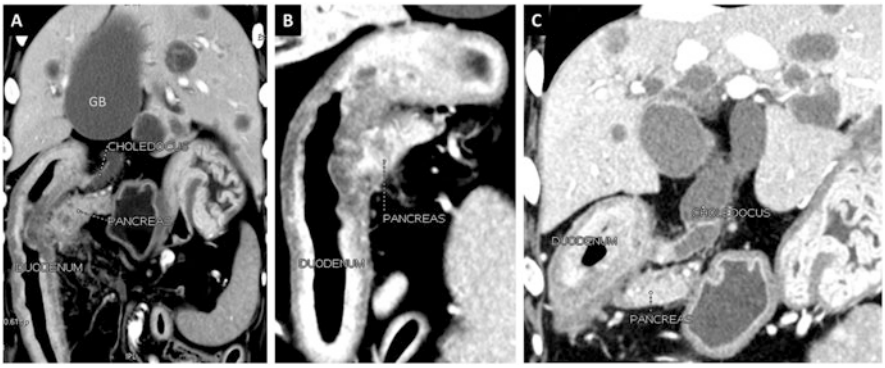

Fig. 11 Malignant EHBDO in a dog. (**a**) Pancreatic carcinoma in a dog (metastatic to the liver). Note the distended gallbladder (GB). (**b**) Malignant involvement of the proximal part of the descending duodenum and distal part of the common biliary duct. (**c**) Dilatation of the biliary hepatic and interlobular ducts within the liver

distention and distortion of major bile ducts develops, accompanied by focal periportal fibrosis. In these cases, signs of portal hypertension, such as ascites and acquired portal collaterals, can be seen on CT images.

3.2 Non-obstructive Causes of Biliary Dilatation

Inflammatory Conditions (Cholecystitis and Cholangitis)
Inflammation of the gallbladder and biliary ducts may be associated with various infectious agents and systemic diseases, or it may occur secondary to bile stasis in cases of chronic benign and malignant bile duct obstruction. Acute and chronic cholangitis/cholangiohepatitis are more common in cats than in dogs. Feline cholangiohepatitis involves the portal triad and surrounding liver parenchyma and is often accompanied by inflammatory processes in the duodenum, pancreas, and kidneys. Ultrasound is the first-level imaging technique used for patients with suspected acute inflammation of the gallbladder and biliary tract. MDCT is generally required when clinical signs are vague and ultrasound findings are equivocal. MDCT evaluation is also indicated in cases of neoplasia (for staging and presurgical planning) and to disclose possible complications (e.g., emphysematous inflammation, perforation), which may indicate the need for exploratory laparotomy and surgical treatment.

Characteristic MDCT findings in *acute biliary inflammation* include slight to moderate enlargement of the bile ducts; reduction of gallbladder volume; pericholecystic free-fluid collection (inflammatory exudate vs. pericholecystic abscess); and thickening of the gallbladder and bile duct walls, which can be enhanced in the late arterial phase (Figs. 12 and 13). Transient focal hepatic perfusion disorders can be seen in the liver parenchyma adjacent to the gallbladder, as a consequence of inflamed gallbladder hyperemia. Uncommonly, the gallbladder

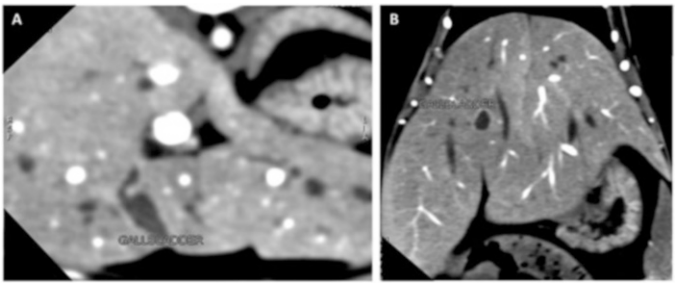

Fig. 12 (**a**, **b**) Transverse and dorsal views of the liver in a cat with acute cholangiohepatitis. The gallbladder is small and has a thickened wall. Note the hepatomegaly (**b**)

Fig. 13 Cholangitis in a cat. (**a**) MinIP image of the liver shows biliary duct dilatation. (**b**) Dorsal MIP image acquired in the arterial phase shows intense enhancement and tortuosity of the hepatic arterial vasculature due to inflammation

and/or bile ducts may contain gas (emphysematous cholecystitis/cholangitis), which is detected easily on MDCT images (Fig. 14). In *chronic biliary inflammation*, the gallbladder is generally increased in volume and may show irregular wall thickening and mineralization (Fig. 15). Wall enhancement might be visualized only on delayed scans.

Biliary ductal narrowing may be associated with chronic portal vein occlusion [portal vein thrombosis (PVT)] or cavernous transformation of the portal vein (CTPV), due to extrinsic compression caused by portal collateral vessels or local ischemia (portal biliopathy) (for further explanation, see the chapter "The Abdominal Vasculature").

Congenital Disorders—Fibropolycystic Diseases and Maldevelopments

Disturbances during embryonic ductal plate development [ductal plate anomalies (DPA)] can lead to various congenital biliary fibropolycystic diseases in dogs and cats, reflecting the developmental stage at which embryogenesis is deranged. These conditions include a complex and poorly understood collection of disorders characterized by dilatation of the biliary tracts and associated congenital liver fibrosis. *Congenital hepatic fibrosis* is a disorder of the smallest part of the ductal plate. It is characterized histologically by various degrees of periportal fibrosis of the small intrahepatic ducts, which appear irregular in shape and are often dilated. Variable

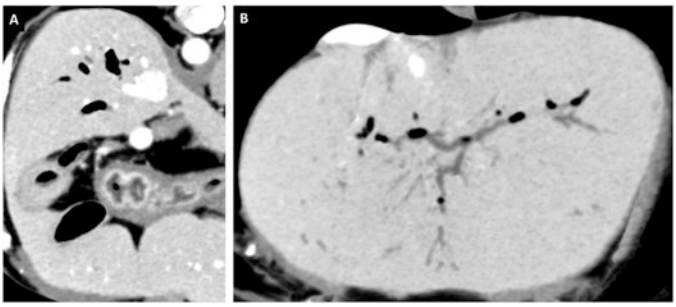

Fig. 14 Pneumobilia in a dog with emphysematous cholangitis

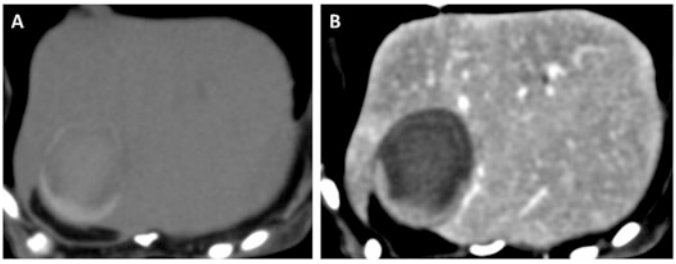

Fig. 15 Cholecystitis. (**a**, **b**) Pre- and post-contrast (PVP) transverse images of the liver in a dog showing gallbladder wall thickening with increased attenuation and enhancement at the fundus

degrees of periportal hepatic fibrosis are also found in other congenital biliary conditions, all of which belong to the same spectrum of ductal plate malformations. In hepatic fibrosis, the liver is small, and a multiphasic MDCT angiographic study of the liver can reveal parenchymal arterialization and diffuse hepatic perfusion disorders during the late arterial phase. Congenital hepatic fibrosis is a dynamic process that can progress to the extent of liver fibrosis over time; thus, other CT features related to portal hypertension, such as abdominal fluid, gastrointestinal bleeding, varices, and other types of acquired portal collateral, may be observed at the time of presentation. *Von Meyenburg complexes* are manifestations of DPA of the smallest intrahepatic bile ducts. In dogs and cats, these complexes appear as isolated or multiple simple round biliary cystic lesions, ranging from a few millimeters to several centimeters in diameter, scattered throughout the liver (Fig. 16a). This condition is usually asymptomatic and discovered incidentally during abdominal imaging examinations. In patients that undergo MDCT for staging of primary neoplasia, these biliary lesions can be mistaken for metastatic disease. Biliary cystic lesions are hypoattenuating on unenhanced scans and do not usually show contrast enhancement, although they may have a peripheral enhancing rim. Simple hepatic solitary cystic lesions, congenital or acquired, can be found in dogs and cats. A solitary cyst appears on CT images as an isolated well-defined cystic-like lesion containing homogeneous and hypoattenuating fluid, which does not enhance on post-contrast scans (Fig. 16b). Autosomal dominant *polycystic disease* has been identified in cats. Biliary and renal tubular malformations are reported frequently in

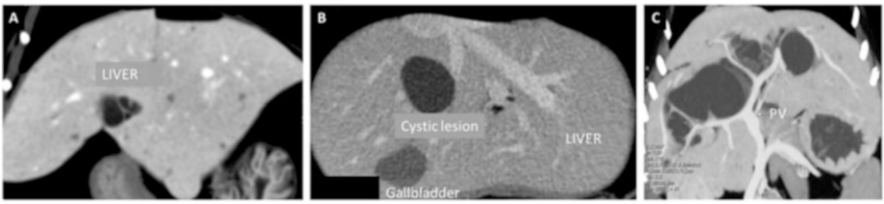

Fig. 16 Fibropolycystic disease (ductal plate maldevelopment) in a cat (**a**) and dogs (**b**, **c**)

Persian cats and other feline breeds. Biliary tract dilatation and concomitant renal cystic malformation have also been reported in young dogs (Cairn and West Highland white terriers and Golden Retriever) (Fig. 16c). This hepatic cystic syndrome may present as a few isolated cysts in the liver, kidney, and pancreas. Most severe patterns show a myriad of submillimetric cystic lesions in these organs. Rarely, larger hepatic cysts can cause hepatomegaly and compression, leading to complications such as infection, bleeding, and rupture. A *Caroli-like syndrome* has been described in a few dogs with multifocal dilatation and calcification of the larger hepatic and segmental biliary ducts, which retain communication with the biliary tree. Mineralization of these ducts reflects bile flow stagnation, which leads to cholangitis, stone formation, and abscess. Variable degrees of periportal fibrosis accompany the biliary dilatation, and polycystic kidney disease can coexist in the same patient. *Choledochal cysts* have been recognized in cats. They are fusiform dilatations of the distal part of the common biliary duct (choledochus) and are associated with severe clinical signs, including abdominal pain, jaundice, fever, and cyst infection. On imaging examinations, obstructive causes of choledochal dilatation should be excluded. Definitive diagnosis may be difficult, but is essential for surgical planning. In general, in the initial setting of choledochal cystic dilation, the intrahepatic ducts can be normal. However, other DPAs can coexist, and choledochal cysts can appear in combination with other intrahepatic and extrahepatic biliary disorders and periportal fibrosis.

Maldevelopment of the gallbladder and biliary tree has been reported rarely in dogs. Abnormal embryonic development of the primitive diverticular bud of the foregut can result in *gallbladder duplication, gallbladder agenesis*, *or atresia* alone or together with DPAs. The diagnosis of gallbladder agenesis is based on the lack of visualization of the gallbladder on images and should be confirmed surgically. Biliary atresia is a disorder in which the extrahepatic biliary system is closed or absent. These developmental anomalies can cause jaundice and severe hepatopathy. The failure of bile excretion into the duodenum may result in biliary dyskinesia and dysfunction of the Oddi sphincter, with subsequent reflux of duodenal contents into the common biliary duct, leading to cholangiohepatitis. MDCT examination can reveal dilatation of the common biliary duct and hepatic ducts (Fig. 17). Hepatic portal hypertension can ensue, and related signs may be identified on CT images.

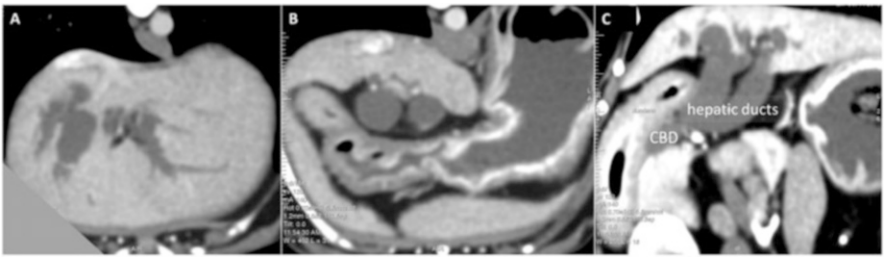

Fig. 17 (**a**) Transverse view of the liver in a 2-year-old miniature poodle showing intrahepatic biliary-duct dilatation. The dog had portal hypertension and collaterals. The gallbladder was not identified on CT examination, and dilated hepatic ducts (**b**, **c**) connected directly to a short and dilated common biliary duct, which apparently did not open into the duodenum. Surgery confirmed agenesis of the gallbladder and papillary stenosis of the sphincter of Oddi

3.3 Rupture of the Gallbladder

Rupture of the gallbladder or common bile duct can occur as a complication of cholelithiasis, cholecystitis, biliary sludge, gallbladder mucocele, impaired vascular supply, or malignancy, or due to blunt trauma. Rupture leads to the leakage of bile into the abdominal cavity and, consequently, to bile peritonitis. This condition is potentially fatal if untreated with surgical cholecystectomy. The CT appearance of acute and chronic gallbladder perforations in small animals has not been described in the veterinary literature so far. In humans, generalized bile peritonitis and free perforation of the gallbladder wall are consistent with an acute process, whereas subacute or chronic gallbladder rupture is accompanied by localized peritonitis or a cholecystoenteric fistula. The "hole sign," described as an ultrasound finding also in small animals, refers to a focal gallbladder defect, which can also be visualized using thin-slice MDCT. This sign is a reliable indicator of gallbladder perforation in dogs (Fig. 18). Other CT signs, such as peritoneal fluid, biliary gas (pneumobilia), and pericholecystic inflammatory changes, are present in cases of nontraumatic gallbladder rupture; hepatic pericholecystic abscess is seen in cases of subacute gallbladder perforation.

3.4 Postoperative Biliary Complications

Several congenital and acquired conditions require gallbladder and/or extrahepatic biliary tract surgery in dogs and cats. MDCT has a great potential to detect early biliary complications in patients that develop new signs or laboratory abnormalities after biliary surgery. Complications such as biliary strictures, anastomotic bile leakage, peritonitis, biloma, and biliary stones are easily detected by MDCT (Figs. 19 and 20).

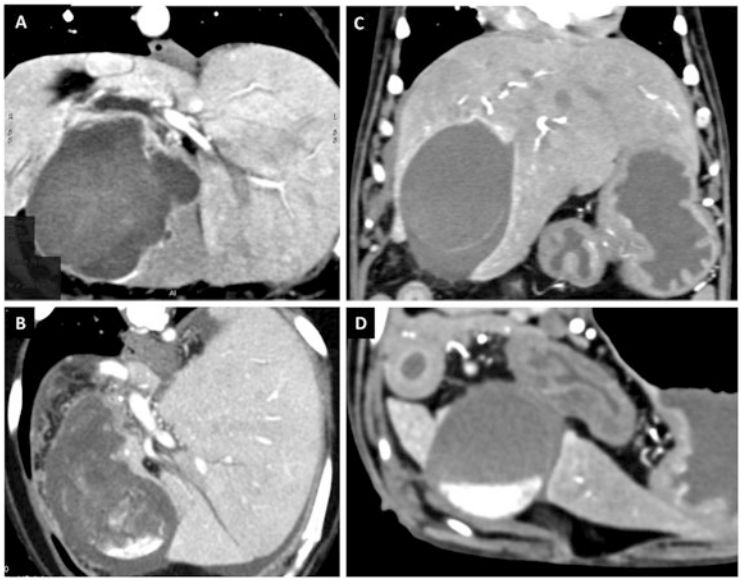

Fig. 18 Rupture of the gallbladder. (**a**) Transverse view of the liver (PVP) in a dog with necrotizing cholecystitis resulting in gallbladder rupture and hepatic pericholecystic fluid collection. (**b**) Transverse view of the liver (PVP) in another dog, with cholelithiasis and cholecystitis. Note the contrast-enhancing fluid inside the gallbladder, consistent with active hemorrhage. Note also the pericholecystic fluid and peritoneal thickening (bile peritonitis). (**c**) Dorsal MPR view of the liver in a dog with cystic mucinous hyperplasia resulting in gallbladder rupture. Note the pericholecystic fluid (*arrow*). (**d**) Another image of the same dog. Note the collection of enhancing material (active hemorrhage) at the fundus of the gallbladder

The collection of detailed clinical information before performing MDCT examination in operated patients is crucial. In cases of early postoperative complications, MDCT findings should be interpreted together with surgeons, as most such complications are iatrogenic (e.g., inadvertent ligation of bile ducts, migration of missed biliary stones, bile peritonitis due to ligature dehiscence). The goals of MDCT examination in these cases are the identification of possible complication sources and planning for re-intervention. MDCT examination performed to assess early postoperative complications can be focalized at the cranial abdomen. Structures that must be examined carefully include the liver parenchyma and ducts, gallbladder, common biliary duct, cranial part of the duodenum, and pancreas, as several surgical procedures involve more than one of these anatomic areas at the same time.

A thin-section unenhanced scan is necessary to exclude biliary stones and hemorrhage, which is a common early complication of biliary tract surgery due to failure to ligate the cystic artery or accidental hepatic parenchyma dissection during surgery. When unenhanced scan findings are negative or unclear, a complete multiphasic examination with enhancement, including the arterial and portal venous phases and late scans of the entire abdomen, is performed. Three-phase MDCT examination should always be performed in cases of late complications of

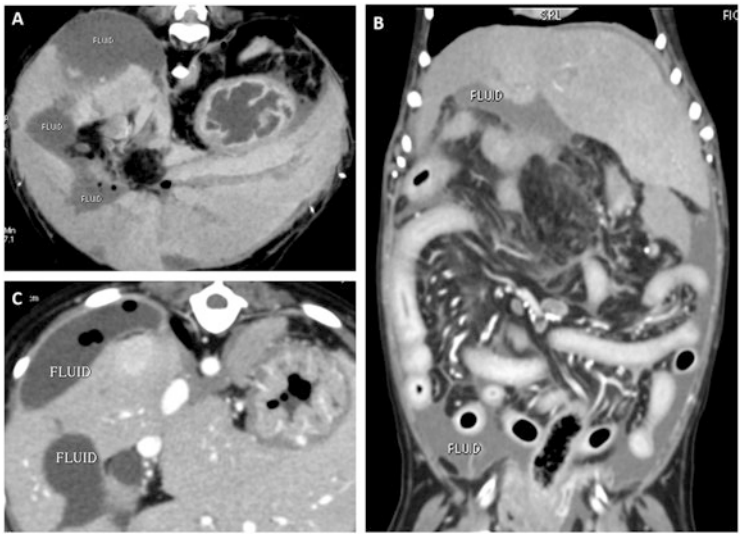

Fig. 19 Postoperative biliary complications. (**a**) Thin-MinIP transverse view of the liver in a dog referred to our center 3 days after cholecystectomy for biliary stones. Note the intrahepatic extrabiliary multiloculated collection of bile (biloma) and gas. (**b**) Dorsal MPR image of the same dog, showing free fluid in the abdominal cavity with thickening and peritoneal stranding (biliary peritonitis). (**c**) Bilomas in a Yorkshire terrier referred to our center a few days after cholecystoduodenostomy

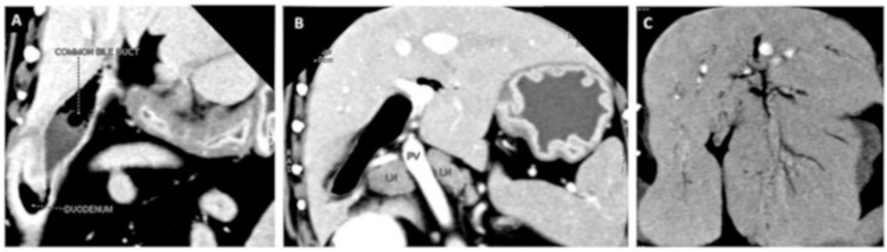

Fig. 20 CT findings 3 years after cholecystoduodenostomy in a dog. (**a**) Dorsal MPR view showing the surgical anastomosis of the gallbladder and the duodenum. Fluid and gas are free to move from the duodenum into the biliary tract. Pneumobilia (gas in the biliary tract) is a common finding in these patients (**b**, **c**). Note the moderate enlargement of the hepatic lymph nodes (**b**)

biliary surgery, which can present days, weeks, or months postoperatively, as in case of biliary strictures. In cases of common biliary-duct stricture, preoperative MDCT examination is necessary to plan biliary stent placement or a new surgical intervention. MDCT enables the accurate measurement of bile duct length and diameter for stent size selection before surgery. Biliary perforation and the presence of intraluminal masses should always be excluded by advanced imaging examination prior to the consideration of biliary stenting.

Further Readings

Austin B, Tillson DM, Kuhnt LA. Gallbladder agenesis in a Maltese dog. J Am Anim Hosp Assoc. 2006;42(4):308–11.

Choi J, Kim A, Keh S, Oh J, Kim H, Yoon J. Comparison between ultrasonographic and clinical findings in 43 dogs with gallbladder mucoceles. Vet Radiol Ultrasound. 2014;55(2):202–7. doi:10.1111/Vru.12120

Görlinger S, Rothuizen J, Bunch S, Van Den Ingh TSGAM. Congenital dilatation of the bile ducts (Caroli's disease) in young dogs. J Vet Intern Med. 2003;17:28–32.

Kamishina H, Katayama M, Okamura Y, Sasaki J, Chiba S, Goryo M, Sato R, Yasuda J. Gallbladder agenesis in a chihuahua. J Vet Med Sci. 2010;72(7):959–62.

Liptak JM. Gallbladder agenesis in a Maltese dog. J Am Anim Hosp Assoc. 2008;44(2):50.

Mehler SJ. Complications of the extrahepatic biliary surgery in companion animals. Vet Clin North Am Small Anim Pract. 2011;41(5):949–67, Vi. doi:10.1016/j.cvsm.2011.05.009

Schulze C, Rothuizen J, Van Sluijs FJ, Hazewinkel HA, Van Den Ingh TS. Extrahepatic biliary atresia in a border collie. Small Anim Pract. 2000;41(1):27–30.

Vasanawala SS, Desser T. Value of delayed imaging in MDCT of the abdomen and pelvis. Am J Roentgenol. 2006;187:154–63.

The Spleen

Giovanna Bertolini

1 Introduction

The spleen is the largest single lymphatic organ in the body and is responsible for central immunological and hematological tasks. Consequently, it is involved primarily or secondarily in a wide range of pathological disorders. The spleen can be explored completely with CT and should be always assessed during abdominal examinations. CT evaluation of the spleen is indicated for the staging of splenic neoplasia and in cases of acute abdomen, hemoabdomen, and trauma (splenic trauma is treated in chapter "The Body Trauma").

The spleen is roughly tongue shaped in dogs and cats and is customarily divided into three segments: the head, body, and tail. Normal spleen size varies substantially among subjects and is influenced by several intrinsic (e.g., contraction) and extrinsic factors. Splenomegaly is a common finding in anesthetized dogs undergoing CT. Some anesthetic drugs used commonly in clinical practice, such as acepromazine, thiopental, and propofol, cause splenomegaly in normal dogs. Hence, the evaluation of spleen size using CT is difficult. Splenomegaly may be found in many benign and malignant conditions in dogs and cats, including non-neoplastic and neoplastic diseases (e.g., splenic congestion, splenic torsion, immune-mediated hemolytic anemia, inflammatory diseases, mastocytoma, lymphoma).

Accessory (or ectopic) spleens are rarely reported in small animals but are not so rarely encountered on whole-body MDCT examinations. They are foci of healthy splenic tissue separated from the main body of the spleen due to the failure of fusion of the initial clustering of embryonic cells from which the spleen develops. Accessory spleens are generally located along the spleno-pancreatic, gastrosplenic, or

G. Bertolini (✉)
San Marco Veterinary Clinic, Padua, Italy
e-mail: bertolini@sanmarcovet.it

G. Bertolini (ed.), *Body MDCT in Small Animals*, DOI 10.1007/978-3-319-46904-1_6

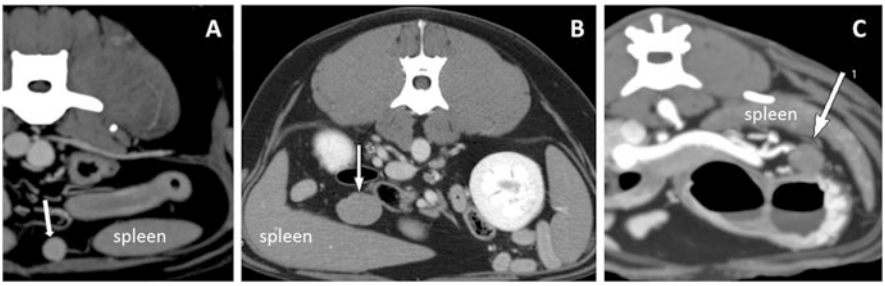

Fig. 1 Accessory spleen. (**a**) Transverse view of the abdomen in a dog, showing a small accessory spleen (*arrow*) supplied by a thin splenic vessel. (**b**) Transverse view from another dog, showing a large accessory spleen (*arrow*). (**c**) Accessory spleen in a cat (*arrow*) with blood supply and drainage by the splenic artery and vein branches

splenorenal ligaments and are supplied by a branch of the splenic artery (Fig. 1). They have same CT appearance as normal splenic tissue and are found most commonly in the proximity of the splenic hilum. These accessory spleens have no clinical significance and should not be removed in non-symptomatic patients. However, ectopic spleens are subject to the same diseases as is eutopic splenic tissue. The presence of ectopic splenic tissue in other organs, such as the liver and the pancreas, has been reported rarely. In the presence of primary splenic cancer, such as hemangiosarcoma, the pancreas should be assessed carefully for metastasis.

The splenic lymph nodes lie along the splenic vessels and are easily detected on thin-section MDCT images. They drain the spleen, as well as the pancreas, esophagus, stomach, and omentum. Thus, they may be enlarged in several pathological conditions.

2 MDCT Imaging Strategies

On pre-contrast CT images, the healthy spleen usually appears to be homogeneous in attenuation and has a density of about 50–60 HU, about 5–10 HU less than that of the liver (Fig. 2). Variations in splenic density can be observed in patients with focal or systemic diseases involving the spleen.

The splenic parenchyma consists of the red and white pulps that form a complex network within the organ. The red pulp is composed of erythrocytes and vascular structures, and the white pulp is formed by lymphatic tissue. With rapid CM injection, the spleen shows inhomogeneous enhancement with variable patterns, reflecting variable blood distribution between the red and white pulps (Fig. 3). These normal inhomogeneous patterns in early contrast-enhanced series vary substantially between dogs and cats and among subjects of the same species. In particular, cats may show a serpentine, cordlike, archiform distribution of splenic

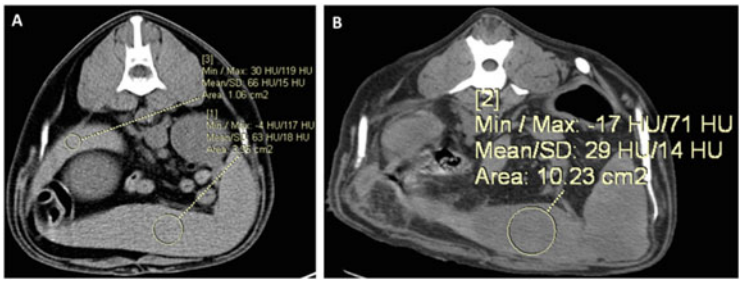

Fig. 2 Splenic attenuation values. (**a**) Non-contrast transverse view in a dog showing a comparison of splenic and hepatic attenuation values. In this patient, the liver has a mean attenuation of 66 HU and the spleen has a mean attenuation value of 63 HU. (**b**) Attenuation value of the spleen in a dog with splenic infarction. The mean value within the ROI at the tail of the spleen is 29 HU (suprafluid)

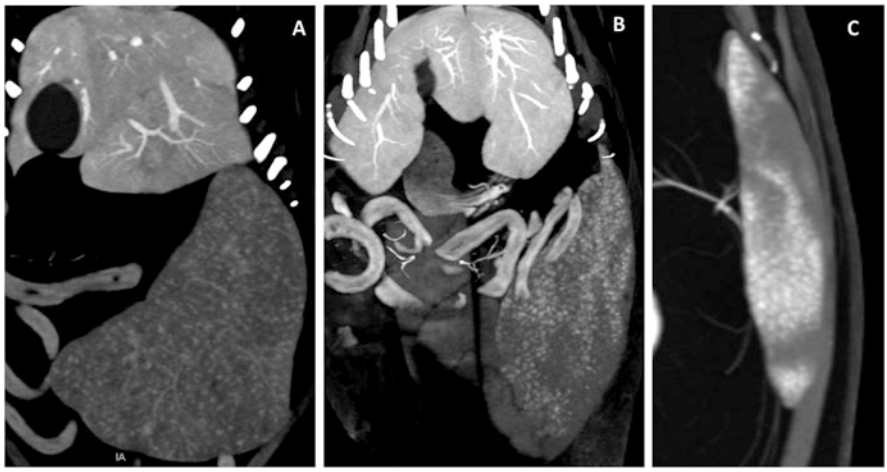

Fig. 3 Normal pattern of enhancement of the spleen in dogs and cats. (**a**) Dorsal MPR view in a dog. (**b**) Dorsal MPR view in a cat. (**c**) Normal pattern of enhancement of the spleen in another cat

parenchymal enhancement, similar to that described in humans. In the delayed phase, the normal spleen parenchyma shows homogeneous enhancement.

Multiphase CT imaging of the spleen is usually obtained during multiphase examination of the liver. Unlike the liver, the spleen has a unique arterial blood supply, from the splenic artery, a branch of the celiac artery. It is drained from the splenic vein, which receives the gastroepiploic and left gastric veins, before entering the portal vein. Thus, complete assessment of the spleen requires dual-phase examination (Fig. 4). The arterial phase provides information about the normal vascularization of the spleen and aids in the diagnosis of splenic torsion and infarction. It may reveal active bleeding (in cases of blunt trauma and benign and

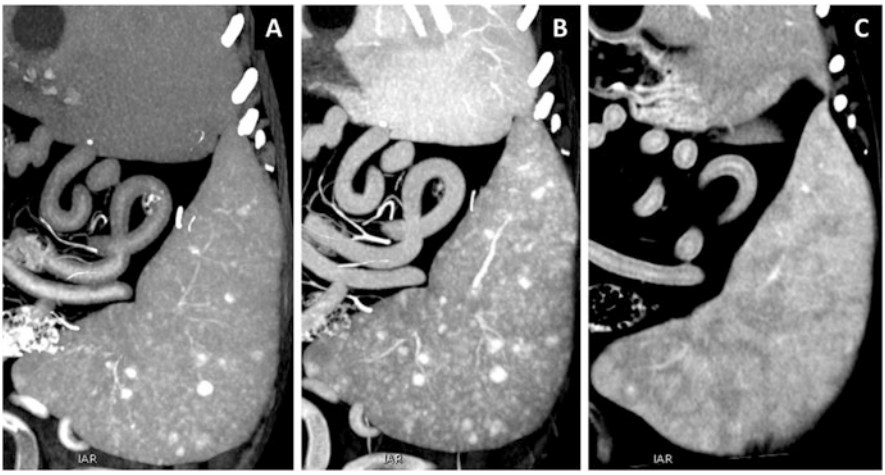

Fig. 4 Multiphasic examination of the abdomen. (**a**) Hepatic arterial phase (HAP). The spleen is enlarged and some hypervascular parenchymal nodules are present (extramedullary hyperplasia). (**b**) Portal venous phase (PVP). The spleen shows maximum parenchymal enhancement. (**c**) Interstitial phase or equilibrium phase (EP) of the liver. The spleen shows more homogeneous enhancement. Hematopoietic nodules are not visible

malignant masses) and may be useful for the detection of benign and malignant hypervascular lesions.

An adequate contrast-enhanced PVP is necessary for the assessment of splenic vein thrombosis and malignant vascular invasion (Fig. 5). Heterogeneous enhancement of the splenic vein is normally seen during the LAP (late arterial phase or inflow portal phase) and should not be confounded with true thrombosis. Multiplanar dorsal views are helpful to show the characteristic pattern of pseudothrombosis (Fig. 6). As it has less viscosity, non-contrasted blood adopts a central laminar flow that can be interpreted mistakenly as thrombosis. Artifactual filling defects of the splenic vein due to its partial opacification represent a time-dependent phenomenon that disappears in subsequent vascular phases. Thus, to avoid misdiagnosis, the examiner should check for complete opacification of the splenic vein in the PVP.

3 Hyperplastic, Reactive, and Inflammatory Splenic Conditions

Hyperattenuating/hypoattenuating lesions of the spleen need to be evaluated in the clinical context, because CT imaging appearances may overlap. Cytologic evaluation may provide a specific diagnosis in most instances.

Splenic extramedullary hematopoiesis (EMH), or the production of hematopoietic cells outside bone marrow, is common in our patients. This may be an

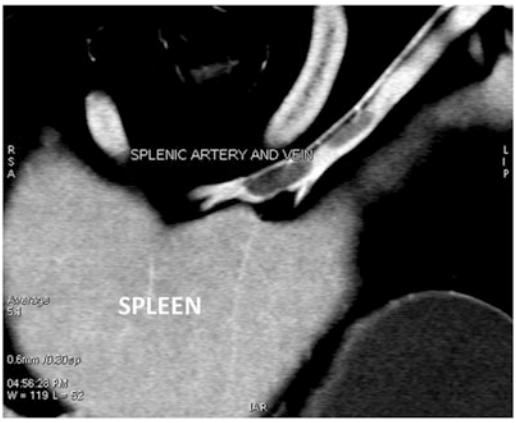

Fig. 5 Splenic vein thrombosis in a dog with lymphoma. Note the filling defects in the splenic vein

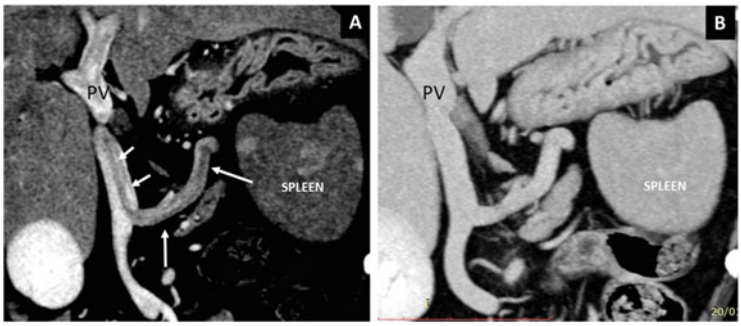

Fig. 6 Pseudothrombosis. (**a**) LAP. Non-contrasted blood of the splenic vein (*long arrows*) adopts a central laminar flow that propagates in the portal vein (*short arrows*). (**b**) In the PVP, the pseudothrombosis disappears, as all vessels are well enhanced

incidental finding, may be found in association with other splenic diseases, or may be a response to bone marrow failure. In personal experience, EMH represents the most common benign lesion of the spleen in dogs. In multiphasic CT examination, EMH appears as multiple hypervascular nodules of same or different sizes (Figs. 7 and 8). *Reactive splenic conditions* refer to generalized hyperplasia with lymphoid hyperplasia and increased hematopoietic precursors. In multiphase CT examination, splenic hyperplasia may have diffuse pattern (miliar or nodular) or may present as single nodule, mimicking a neoplasia (Fig. 9).

Hypoattenuating lesions of the spleen may be seen in case of septic and non-septic inflammatory conditions of the spleen (Fig. 10). These lesions may mimic splenic infarction and need to be evaluated in the clinical context.

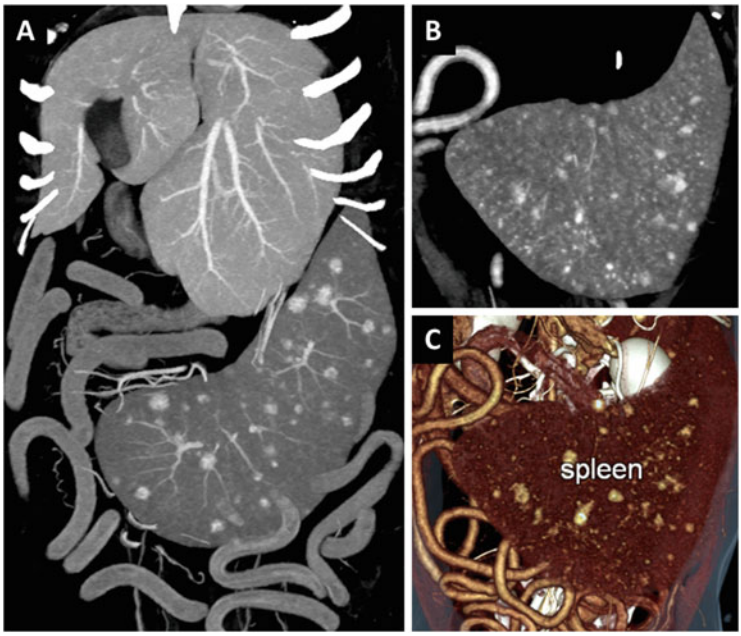

Fig. 7 Extramedullary hematopoiesis of the spleen in three different dogs (**a**–**c**), showing multiple hypervascular nodules

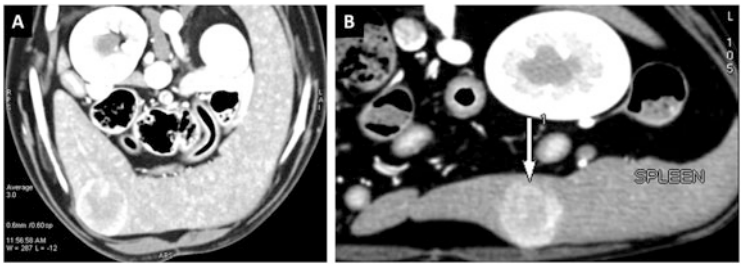

Fig. 8 Extramedullary hematopoiesis of the spleen in two different dogs (**a**, **b**). Extramedullary hematopoiesis presents as a single rounded hypervascular nodule

4 Splenic Infarction and Splenic Vein Thrombosis

Splenic infarction refers to acute occlusion of the arterial blood supply to the spleen, which leads to parenchymal ischemia and subsequent tissue necrosis. Blood enters the spleen at the hilus by way of up to approximately 25 arterial branches. Therefore, small focal splenic infarctions remain generally asymptomatic and can be encountered incidentally during CT examination. In dogs, massive splenic infarction involving the arterial blood supply of the spleen can be observed

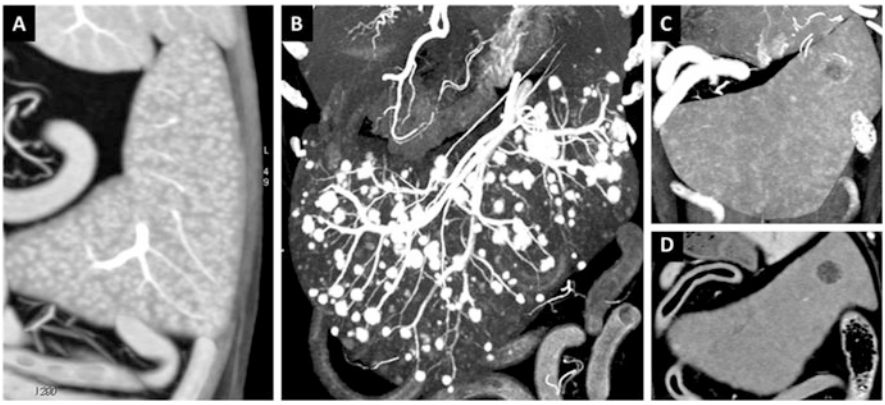

Fig. 9 Splenic hyperplasia in dogs. (**a**, **b**) Diffuse miliary and nodular hypervascular pattern of splenic hyperplasia (PVP and HAP). (**c**, **d**) HAP and PVP in a dog with a single hyperplastic nodule of the spleen

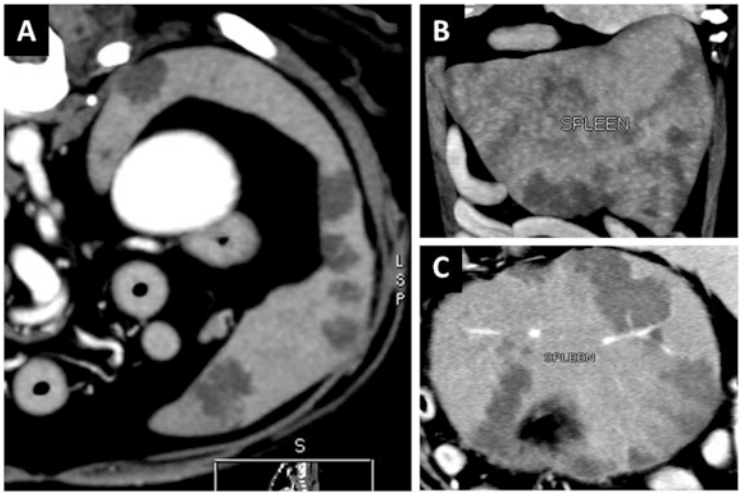

Fig. 10 Splenitis in three different dogs with systemic diseases. (**a**) Multiple hypovascular splenic lesions in a dog with bacterial splenitis and spondylodiscitis (Klebsiella). (**b**) Hypoattenuating/hypovascular lesions in the spleen (suppurative splenitis) of a dog with immunomediated polyarthritis. (**c**) Splenitis in a dog with systemic infection (Mycobacterium avium)

in splenic torsion with or without gastric volvulus, leading to temporary or permanent splenic artery thrombosis. Splenic infarction due to arterial occlusion may have other severe causes, including cardiac diseases and infiltrative hematological tumors. Imaging features of splenic infarction may vary with the cause and stage of the infarct. In splenic torsion, the whole spleen is hypoattenuating and enlarged. Acute infarction with causes other than torsion may present as a typical peripheral,

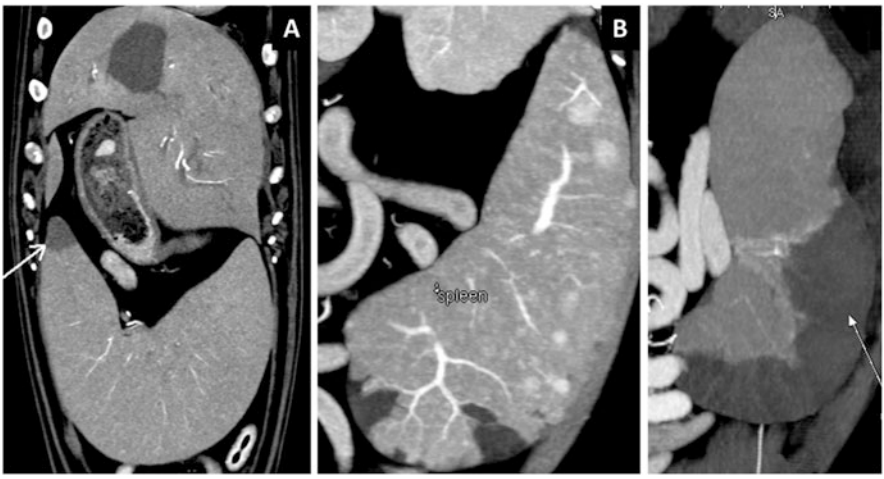

Fig. 11 Splenic infarction. (**a**) Small infarcted marginal areas discovered incidentally in a dog. (**b**) Multiple splenic infarctions in a dog with metastatic lung neoplasia. (**c**) Large chronic infarction in a dog

wedge-shaped hypoenhancing region or multiple, heterogeneous areas of patchy enhancement (Fig. 11). A "rim sign" of high density relative to the parenchyma can be noted on the splenic capsule. In the chronic phase, an infarction may be not detected or may result in progressive volume loss caused by fibrotic contraction, with secondary hypertrophy of the surrounding normal splenic parenchyma.

Splenic vein thrombosis can also result in venous infarction. Local factors, such as splenic masses or infiltration, can cause portal vein occlusion. In addition, systemic risk factors may be involved in the pathogenesis of splenic thrombosis. A hypercoagulable state is the main disorder causing splenic infarction, and it has been associated with a variety of non-neoplastic and neoplastic conditions, including myeloproliferative disorders and prothrombotic conditions, such as pancreatitis, immune-mediated hemolytic anemia, disseminated intravascular coagulation, conditions caused by corticosteroid exposure due to hyperadrenocorticism or exogenous steroid administration, and renal failure with proteinuria (Figs. 5, 12, and 13).

5 Splenic Torsion

Splenic torsion is a relatively uncommon occurrence, and it is usually considered to be secondary to the complex of gastric dilatation and volvulus. Primary or isolated splenic torsion is an uncommon splenic disease, generally occurring in large- or giant-breed, deep-chested dogs, such as Great Danes. Its pathogenesis is not completely clear.

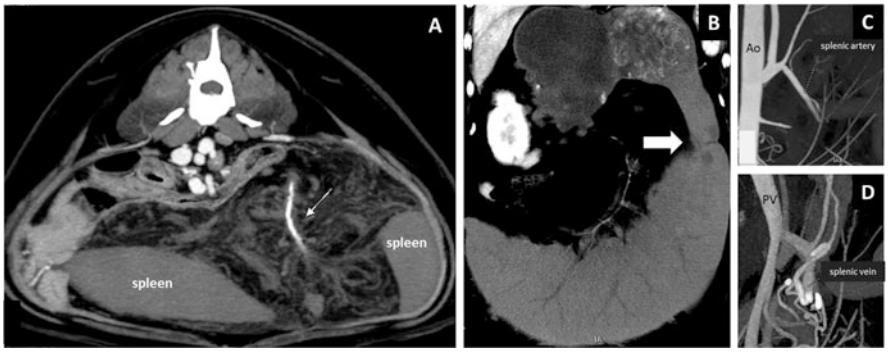

Fig. 12 Splenic infarction in torsion. (**a**) Transverse view in a dog with splenic torsion. The splenic artery (*arrow*) is interrupted and the spleen is not perfused. (**b**) Splenic enlargement and hypoperfusion in a dog with splenic hemangiosarcoma. The dog was referred for suspected splenic torsion. At the time of CT examination, the dog showed a normally positioned spleen, with narrowing at the body (*arrow*) and absent blood flow. (**c**) Interrupted splenic artery. (**d**) Tilted splenic vein (consistent with partial omental torsion)

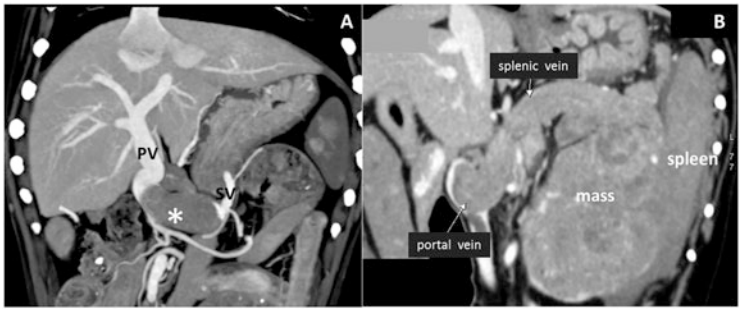

Fig. 13 Splenic vein thrombosis. (**a**) Dorsal MPR view in a dog with a hypercoagulable state and large benign splenic vein thrombosis (*asterisk*). *PV* portal vein, *SV* splenic vein. (**b**) Dorsal MPR view in a dog with a splenic mass (neuroendocrine carcinoma) and tumoral invasion of the splenic vein

Patients with torsion are often evaluated in an emergency setting, where imaging, usually by ultrasonography and CT, plays an important role. MDCT features of splenic torsion include displacement and enlargement of the organ, which shows considerably decreased or heterogeneous attenuation on pre-contrast images (due to infarction). The twisted splenic pedicle containing splenic vessels and surrounding fat produces the "whirl sign," confirming splenic torsion (Figs. 14 and 15). Post-contrast images may show interruption of the vascular blood supply to the spleen. As stated previously, the rim sign (relative capsular hyperdensity) may be noted in cases of massive splenic infarction. Adjacent inflammatory changes and free fluid are generally present.

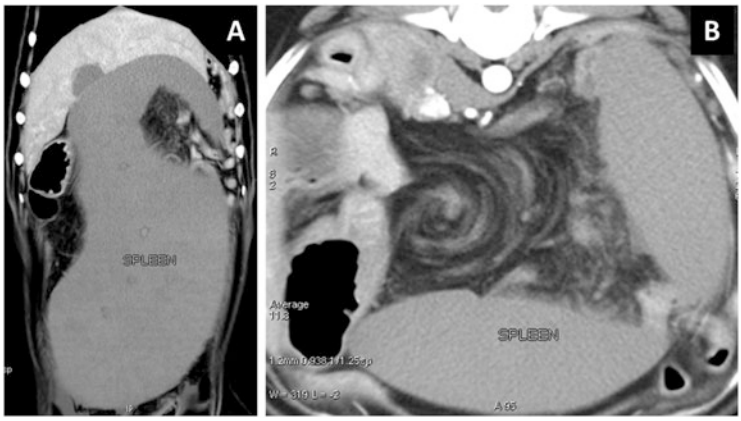

Fig. 14 Splenic torsion. (**a**) Dorsal MPR views from a Great Dane. The spleen is enlarged and avascular. (**b**) Transverse view of the same dog showing a twisted splenic pedicle containing unperfused splenic vessels (*whirl* sign)

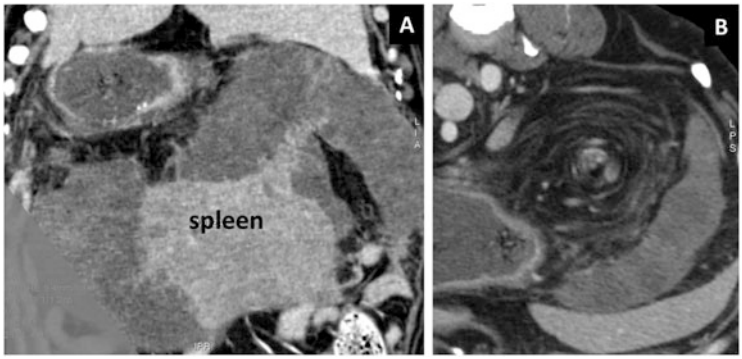

Fig. 15 Splenic torsion and infarction in a Caucasian Mountain dog. (**a**) The spleen is enlarged and some areas of the splenic parenchyma are infarcted. (**b**) *Whirl* sign at the splenic vascular pedicle

6 Splenic Neoplasia

Focal lesions of the spleen are encountered commonly during MDCT examination for various reasons and should be assessed carefully. Although nonmalignant masses have been reported to account for the majority of focal splenic masses in dogs, a recent study of a wide population of dogs showed nearly equal distributions of malignant (53%) and nonmalignant (47%) tumors. Benign lesions encountered commonly on multiphasic MDCT examination of the abdomen include nodular hyperplasia, splenic hematoma, extramedullary hematopoiesis, hemangioma, and myelolipoma (Figs. 8 and 16). Some of these benign lesions can reach considerable

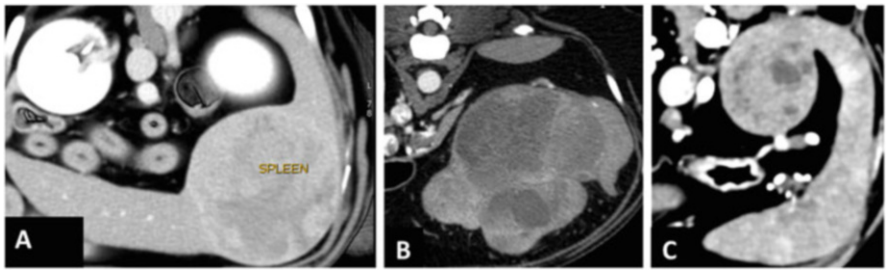

Fig. 16 Benign splenic masses in three different dogs. (**a**) Sagittal thin-MIP image showing a large splenic mass (hematoma). (**b**) Large inhomogeneous mass (hematoma). (**c**) Transverse view of the spleen in a dog with splenic myelolipoma

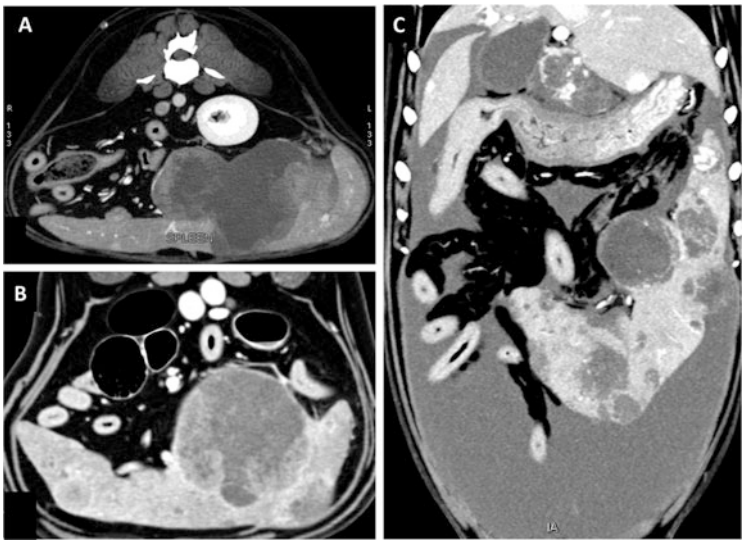

Fig. 17 Splenic hemangiosarcoma in dogs. (**a**, **b**) Transverse view in two dogs with primary splenic hemangiosarcoma. (**c**) Dorsal MPR view in another dog, with hemoabdomen due to ruptured metastatic hemangiosarcoma

dimensions and may be confounded with malignant splenic tumors. Hemangiosarcoma is the most common malignant tumor in the canine spleen, and it is almost indistinguishable from splenic hematoma. In addition, cytology is not always accurate in this case and the two conditions can coexist. Several other histology tumor types are possible in the spleen, such as fibrosarcoma, leiomyosarcoma, undifferentiated sarcoma, osteosarcoma, and histiocytic sarcoma (Figs. 17 and 18).

To ensure accurate interpretation, splenic lesions should be evaluated in the clinical context of the patient's history, as the CT imaging appearances of certain entities overlap and cannot be used to distinguish benign and malignant lesions.

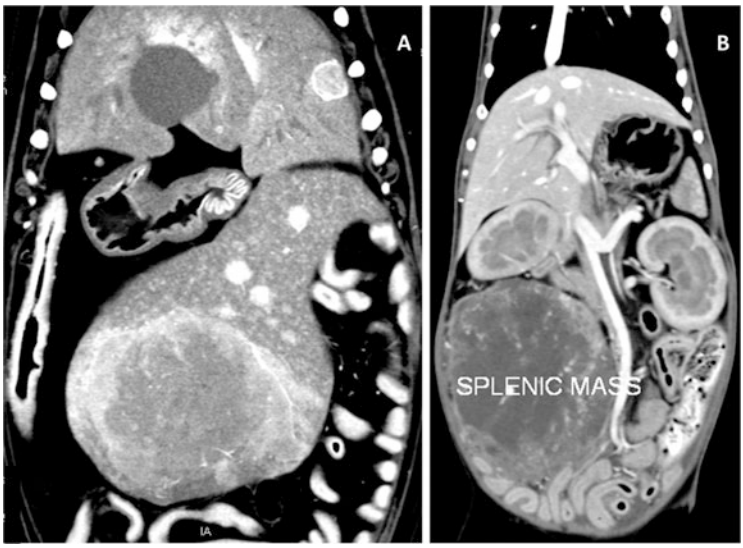

Fig. 18 Malignant splenic neoplasia. (**a**) Dorsal MPR of a dog with histiocytic sarcoma. A large hypervascular mass at the splenic tail and other small hypervascular nodules can be seen. Note the hypervascular nodule in the left lateral hepatic lobe. (**b**) Dorsal MPR of the abdomen in a cat with a large splenic mass (sarcoma)

Benign lesions may assume a mottled pattern or nodular appearance, or may present as large masses, some of which cause organ surface deformation. Thus, size is not a criterion that predicts the malignancy of a splenic lesion. A few studies have explored the CT appearance of various splenic masses in dogs. In a single-phase CT study, with images acquired prior to and approximately 60 s after intravenous CM administration, the malignancy of a splenic mass (i.e., presence of hemangiosarcoma) was associated with hypoattenuation on pre-contrast images and minimal contrast accumulation on post-contrast images. The authors defined a threshold value of 55 HU on post-contrast images to distinguish malignant (<55 HU) from nonmalignant (>55 HU) masses. However, a recent multiphasic MDCT analysis showed that most splenic masses (benign and malignant) were slightly heterogeneous, with median attenuation similar to that of the adjacent parenchyma, in pre-contrast series. Splenic hemangiosarcoma and benign nodular hyperplastic lesions most frequently showed marked, generalized enhancement on early-phase images, with no difference in median enhancement of malignant and nonmalignant masses on delayed-phase images. Independent of their nature, the masses exhibited a wide range of post-contrast attenuation values that spanned 55 HU. The presence of hemoabdomen has been related to the rupture of malignant and benign masses of the spleen. However, it is associated more commonly with hemangiosarcoma and is thus a sign of potential malignancy (Fig. 17c). Lymphoproliferative and myeloproliferative disorders can primary or secondarily involve the spleen (Figs. 19 and 20). Lymphoma of the spleen can present as generalized splenomegaly without focal

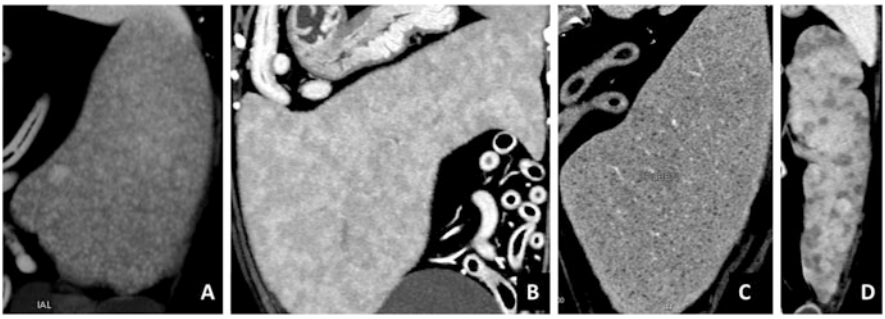

Fig. 19 Different patterns of splenic lymphoma in dogs. (**a**) Miliary diffuse pattern (similar to hyperplastic changes). (**b**) Diffuse infiltrative pattern. (**c**) Diffuse "honeycombing" pattern (B-cell lymphoma). (**d**) Multifocal pattern of lymphoma (B-cell lymphoma) in another dog

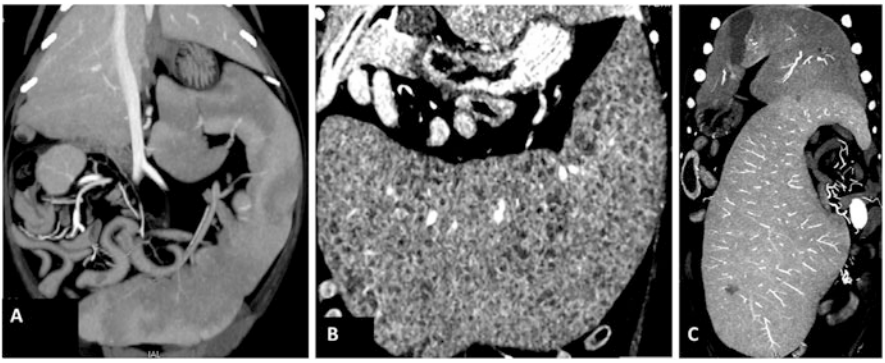

Fig. 20 (**a**) Dorsal MPR view of the abdomen in a cat with multiple myeloma. The spleen is enlarged and diffusely inhomogeneous. (**b**) Dorsal MPR in a dog with Waldenstrom macroglobulinemia. The spleen shows noticeable enlargement with a "honeycombing" pattern. (**c**) Diffuse splenomegaly in myeloid leukemia in a dog

lesions, as multiple focal lesions, or as a single solitary lesion. The presence of hilar lymphadenopathy is suggestive of splenic lymphoma (Fig. 21).

Despite the difficulty of determining the nature of a splenic mass based on its characteristics, MDCT has the advantage of enabling simultaneous assessment of other abdominal parenchyma, the lung, and any other body tissue. Metastatic lesions from primary splenic hemangiosarcoma or other malignancies can be detected easily by whole-body MDCT, aiding in definitive diagnosis.

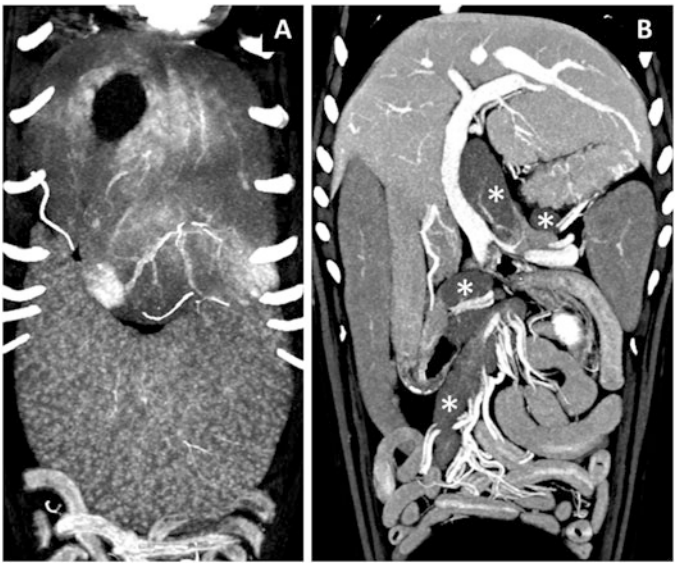

Fig. 21 Multiphasic examination of the abdomen in a dog with T-cell lymphoma. (**a**) EAP. Splenomegaly and diffuse miliary pattern. Note the hepatic perfusion disorders. (**b**) PVP showing abdominal lymph node enlargement (*asterisks*). Note the homogeneous parenchymal enhancement in this vascular phase

Further Readings

Baldo CF, Garcia-Pereira FL, Nelson NC, Hauptman JG, Shih AC. Effects of anesthetic drugs on canine splenic volume determined via computed tomography. Am J Vet Res. 2012;73 (11):1715–9. doi:10.2460/ajvr.73.11.1715.

Fife WD, Samii VF, Drost WT, Mattoon JS, Hoshaw-Woodard S. Comparison between malignant and nonmalignant splenic masses in dogs using contrast-enhanced computed tomography. Vet Radiol Ultrasound. 2004;45(4):289–97.

Irausquin RA, Scavelli TD, Corti L, Stefanacci JD, DeMarco J, Flood S, Rohrbach BW. Comparative evaluation of the liver in dogs with a splenic mass by using ultrasonography and contrast-enhanced computed tomography. Can Vet J. 2008;49(1):46–52.

Jones ID, Lamb CR, Drees R, Priestnall SL, Mantis P. Associations between dual-phase computed tomography features and histopathologic diagnoses in 52 dogs with hepatic or splenic masses. Vet Radiol Ultrasound. 2016;57(2):144–53. doi:10.1111/vru.12336. Epub 2016 Jan 13.

Kim M, Choi S, Choi H, Lee Y, Lee K. Diagnosis of a large splenic tumor in a dog: computed tomography versus magnetic resonance imaging. J Vet Med Sci. 2016;77(12):1685–7. doi:10.1292/jvms.15-0262. Epub 2015 Jul 19.

Laurenson MP, Hopper K, Herrera MA, Johnson EG. Concurrent diseases and conditions in dogs with splenic vein thrombosis. J Vet Intern Med. 2010; 24(6):1298–304. doi:10.1111/j.1939-1676.2010.0593.x. Epub 2010 Sep 14.

Moss AA, Korobkin M, Price D, Brito AC. Computed tomography of splenic subcapsular hematomas: an experimental study in dogs. Investig Radiol. 1979;14(1):60–4.

Ohta H, Takagi S, Murakami M, Sasaki N, Yoshikawa M, Nakamura K, Hwang SJ, Yamasaki M, Takiguchi M. Primary splenic torsion in a Boston terrier. J Vet Med Sci. 2009;71(11):1533–5.

Patsikas MN, Rallis T, Kladakis SE, Dessiris AK. Computed tomography diagnosis of isolated splenic torsion in a dog. Vet Radiol Ultrasound. 2001;42(3):235–7.

Prosser KJ, Webb JA, Hanselman BA. Ectopic spleen presenting with anemia and an abdominal mass in a dog. Can Vet J. 2013;54(11):1071–4.

Ramírez GA, Altimira J, García-González B, Vilafranca M. Intrapancreatic ectopic splenic tissue in dogs and cats. J Comp Pathol. 2013;148(4):361–4. doi:10.1016/j.jcpa.2012.08.006. Epub 2012 Oct 11.

The Gastrointestinal System

Giovanna Bertolini

1 Introduction

The increased temporal and spatial resolution of most modern MDCT scanners enables routine examination of the gastrointestinal tract in small animals. The veterinary literature on this topic is in its infancy, but recent papers have shown the usefulness of contrast-enhanced 16-MDCT as a preliminary screening modality in awake or minimally sedated dogs with acute abdominal signs, including gastrointestinal obstruction and perforation. In patients with neoplastic and nonneoplastic obstructive diseases, MDCT can be used to identify the affected segment and, in most cases, the cause of obstruction. In neoplastic conditions, MDCT is essential for staging and aids intervention planning.

2 MDCT Imaging Strategies

No common strategy for gastrointestinal MDCT has been established for veterinary patients. Patient preparation and scanning protocols can vary, depending on the suspected pathology. At our center, gastrointestinal CT examinations are generally performed with anesthetized patient. This allows performing endoscopy and bioptic procedures under the same anesthesiology episode. In general, adequate distension of the gastrointestinal tract is necessary for the evaluation of wall thickness and integrity, as collapsed intestinal segments can falsely show wall thickening and non-distended gastric plication may conceal small gastric ulcerations. The use of helical hydro-CT for better characterization of gastric tumors has been described in

G. Bertolini (✉)
San Marco Veterinary Clinic, Padua, Italy
e-mail: bertolini@sanmarcovet.it

G. Bertolini (ed.), *Body MDCT in Small Animals*, DOI 10.1007/978-3-319-46904-1_7

dogs with single-slice CT. The recommended dose of water is 30 mL/kg, and the hydro-CT study should be followed by intravenous contrast medium (CM) administration. The use of air/gas contrast is more appropriate with MDCT scanners than the use of water or other neutral fluids, as it allows the acquisition of endoluminal through-flight images from the same volume dataset. In patients with suspected gastrointestinal hemorrhage (i.e., those with hematemesis), no oral CM should be administered; positive CM may mask bleeding, and water or another neutral CM may dilute the extravasated intravenous CM, thereby compromising the ability to identify the site of bleeding. In post-contrast series, moreover, positive oral CM prevents evaluation of the mucosal pattern of enhancement.

Most advanced MDCT scanners can acquire thin-collimated, near-isotropic, or true-isotropic imaging data for the gastrointestinal tract. Multiplanar and 3D views, including endoluminal imaging, can provide detailed information about various pathological conditions. Acquisition of a pre-contrast series is recommended in patients with suspected gastrointestinal hemorrhage. Post-contrast series should include the (late arterial phase) LAP and (portal venous phase) PVP. Properly timed CM injection can reveal even small lesions and subtle changes in mucosal contrast enhancement. In the LAP (or inflow portal phase), the gastrointestinal mucosa shows maximum

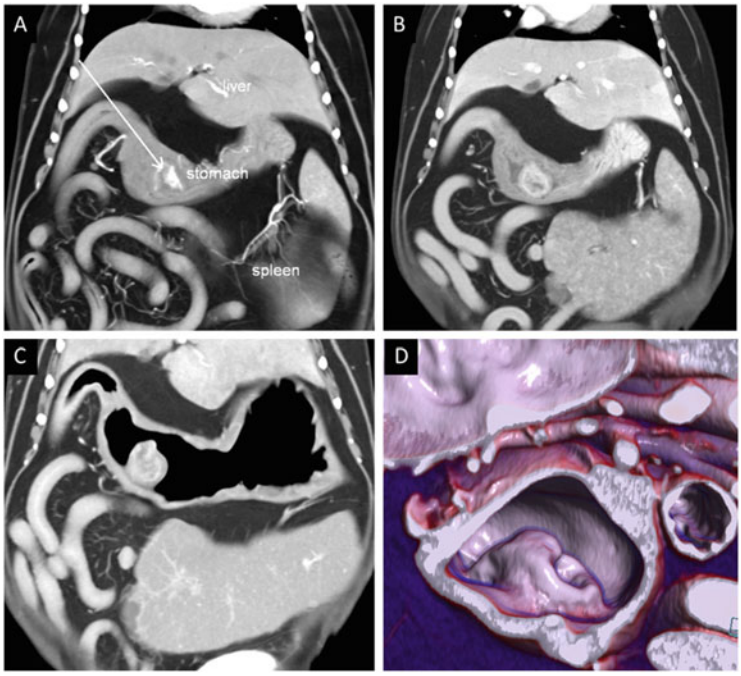

Fig. 1 Multiphasic study in a dog with a gastric mass (leiomyosarcoma). (**a**) Dorsal MPR view of the abdomen (thin slab average) in the HAP. *Arrow* indicates the site of active hemorrhage. (**b**) PVP image from the same dog, with a non-distended stomach. (**c**) Dorsal view obtained after gas insufflation (equilibrium phase). The dimensions and margins of the mass are more appreciable. (**d**) 3D segmentation of the same volume dataset, showing the characteristics of the mass, including large and deep ulceration

enhancement. The arterial phase may show active hemorrhage in patients with benign or malignant gastrointestinal ulceration (Fig. 1). In patients with gastrointestinal tumors, both vascular phases add useful information regarding the vascularity of the mass and the metastasis of lesions to the liver, generally detected in the PVP.

3 Gastrointestinal Thickening

The normal stomach wall thickness is related to the degree of gastric distention, and rugal folds tend to disappear when the stomach is distended. Focal or diffuse gastric wall thickening can be found with inflammatory disease or infiltrative neoplasia, and significant overlap exists between in the imaging features of the two conditions. Gastric wall thickening and thickened folds are common CT sign of gastritis in dogs. Inflammatory polypoid or mass-like folds are difficult to distinguish from gastric lymphoma or other tumors (Figs. 2, 3, 4, and 5).

It has been demonstrated that small intestinal wall thickness varies with weight in the dog, and the duodenal wall is always thicker than the jejunum. In both dogs and cats, the colon wall is generally thinner than the adjacent small intestine, especially when the colon is distended. The gastrointestinal diameter (serosa to serosa) and wall thickness (serosa to mucosa) have been assessed in the non-distended bowels of dogs using single-slice CT. The results (Fig. 6) were

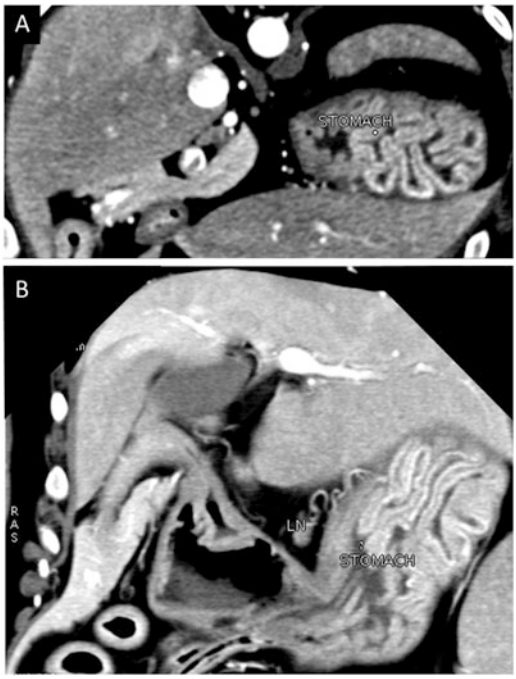

Fig. 2 Gastric rugal fold thickening (chronic lymphoplasmacellular gastroenteritis) in a dog that was referred to our center for suspected gastric neoplasia. Note the conspicuous gastric folds, showing greater enhancement, particularly evident at the gastric fundus. Note also the moderate enlargement of a gastric lymph node (LN), which is normally barely visible

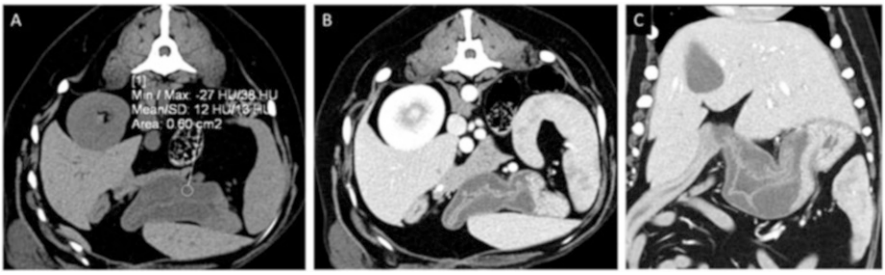

Fig. 3 Gastric wall thickening in a dog with acute gastritis. (**a**) Non-contrast image showing submucosal hypoattenuation at the pyloric antrum and canal, consistent with gastric submucosal edema (12 HU). (**b**, **c**) Transverse and dorsal MPR views of the same dog

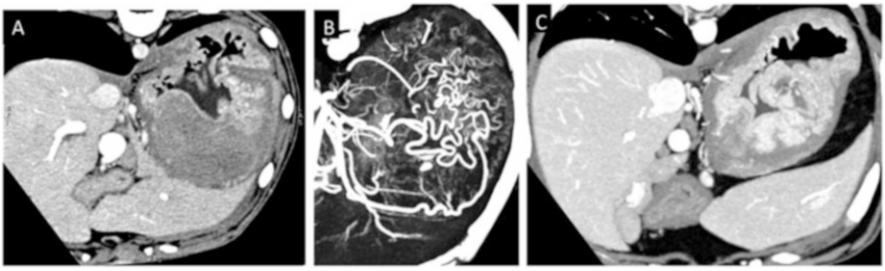

Fig. 4 Gastric wall thickening. (**a**) Transverse view (PVP). Massive mural thickening at the body of the stomach in a dog with aspergillosis. (**b**) MIP view from the HAP showing increased and tortuous arterial vasculature of the stomach due to inflammation. (**c**) CT monitoring image obtained 8 months later. The gastric wall is less thickened and the gastric folds are noticeable, mimicking a mass in the non-distended stomach

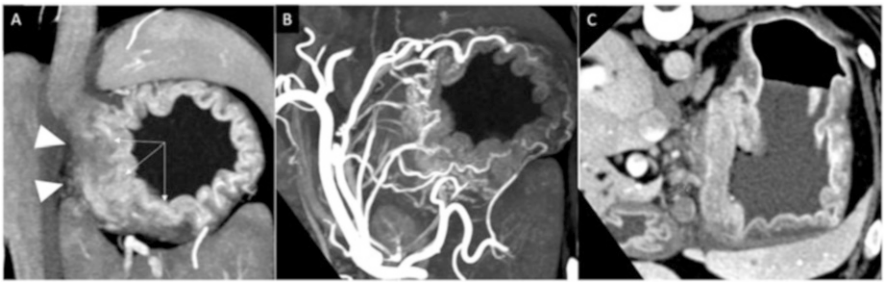

Fig. 5 Gastric wall thickening (gastric carcinoma). (**a**) Dorsal thin-MIP view of the stomach. Note the irregular gastric wall thickening at the lesser curvature (*arrows*). The outer border of the tumor is irregular (*arrowheads*). (**b**) Dorsal MIP from the LAP, showing the blood supply to the neoplastic wall. (**c**) Note the perilesional fat thickening and regional lymph node enlargement

similar to those reported for radiology and ultrasound, which remains the first-line imaging modality for the evaluation of diffuse gastrointestinal disease in small animals. Focal or diffuse gastrointestinal thickening is encountered frequently in veterinary patients, has many causes, and is easily documented by MDCT. As has

Gastrointestinal Regions	Wall thickness (mm)	Segment diameter (mm)
Stomach (fundus, body, pylorus)	0.98 – 2.13 (<9kg); 2 – 3.55	
Pyloric antrum	1.69 -2.74 (<9kg) ; 2.95 – 4.40	9.69 – 12 (<9kg); 13.54 – 16.16
Ascending duodenum	2.59 – 3.30 (< 9 Kg); 4.61 – 5.26	
Descending duodenum		8.79 – 10.46 (<9kg); 11.60 – 16.63
Jejunum	2 – 2.93 (<9kg); 3.31 – 3.87	6.95 – 8.21 (<9kg); 9 – 12.53
Ascending colon	1.05 – 1.45 (<9kg); 1.78 – 2.35	
Transverse colon		9 – 11.93 (<9kg); 12.84 – 21.49

Fig. 6 Wall thickness and segment diameter for various gastrointestinal regions (related to body weight), determined in a group of dogs using a single helical CT unit (Hoey et al. 2013; see the full reference at the end of the chapter)

been said for the stomach, many benign and malignant diseases can lead to gastrointestinal thickening, and considerable overlap exists in the appearance of inflammatory and neoplastic diseases (Figs. 7, 8 and 9). The patient's history and clinical signs are essential in the differential diagnosis. Imaging-guided aspiration, endoscopy, or full thickness biopsies remain necessary for further definition.

4 Gastroduodenal Erosions and Ulcerations

Erosion refers to a defect of the gastric or duodenal mucosa, whereas gastroduodenal ulceration refers to a defect that penetrates the muscularis mucosa. Gastroduodenal ulcerations may develop as the consequence of excessive acid, pepsin, or other harmful substance; they can occur independently or as a complication of many systemic diseases and medical treatments. Inflammatory conditions (gastroenteritis) and the use of steroids and nonsteroidal anti-inflammatory drugs are probably the most common causes of gastrointestinal erosion and ulceration in veterinary patients. Anti-inflammatory drugs decrease local prostaglandin production, thereby reducing mucosal blood flow and limiting the epithelium's capacity to protect itself from the injurious effects of gastric acid. Many other diseases (e.g., mast cell tumor, gastrinoma) are associated with increases in histamine and gastrin levels, which increase gastric acid production, leading to gastrointestinal erosion and ulceration.

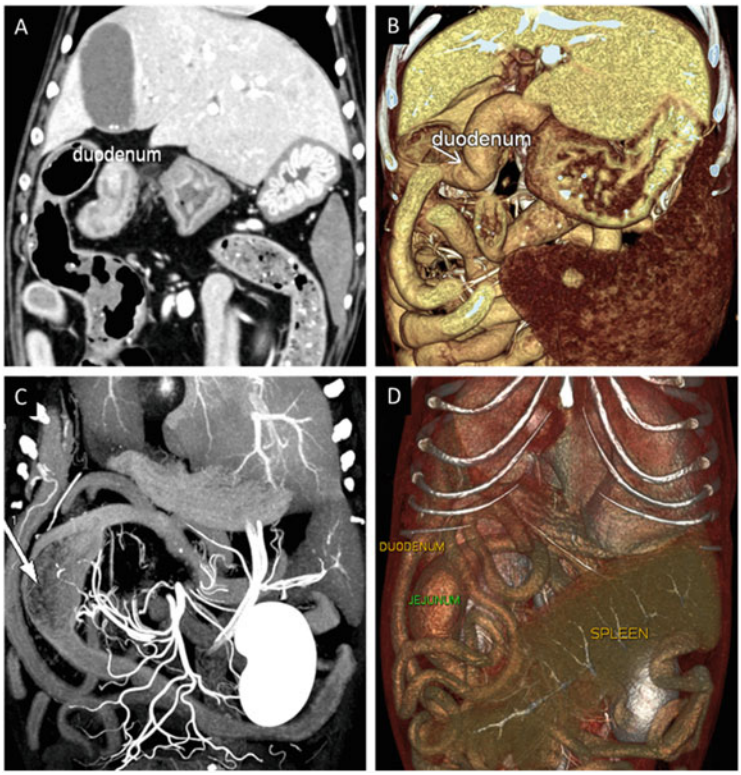

Fig. 7 Intestinal wall thickening. (**a**) Dorsal MPR view of the abdomen in a dog with lymphocytic-plasmacytic enteritis. (**b**) Volume-rendered image of the abdomen in the same dog. Note the diffuse thickening of the intestinal loops. *S* spleen; note a small hypervascular lesion (extramedullary hematopoiesis). (**c**, **d**) Dorsal MIP and volume-rendered images of a dog with segmental jejunal dilatation and focal enteritis due to a subocclusive plastic foreign body (rubber pacifier)

MDCT of *erosion and gastroduodenal ulceration* in small animals has not been described to date. Many MDCT characteristics of gastroduodenal ulceration reported in humans may be observed also in dogs and cats with this condition, with the appropriate use of advanced MDCT technology. Direct and indirect MDCT signs may be encountered in veterinary patients. The disruption of mucosal enhancement (in the LAP) and focal luminal outpouching (ulcer crater development) are the most common direct CT signs of ulceration associated with benign and malignant conditions (Figs. 10, 11, 12, and 13). Indirect signs of erosion or gastric ulceration include gastric fold thickening, mucosal hyperenhancement, and perigastric/periduodenal inflammation (e.g., increased opacity of fat with hazy/ground-glass-like appearance, presence of fluid film). In complicated cases, other CT signs may be present. Complications of gastroduodenal ulceration include active hemorrhage and perforation. Active hemorrhage may not be noted unless a

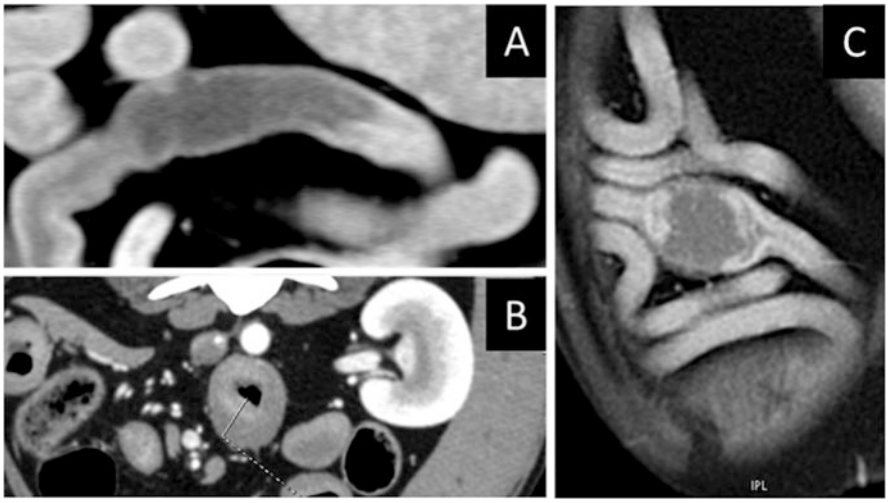

Fig. 8 Focal intestinal thickening. (**a**) Segmental jejunal thickening in a dog with lymphocytic-plasmacytic enteritis. (**b**) Transverse view from a dog (20 kg) with eccentric jejunal segmental thickening (serosa-mucosa diameter, 14 mm), resulting in lymphoma. (**c**) Jejunal focal thickening in a dog with intestinal hemangiosarcoma

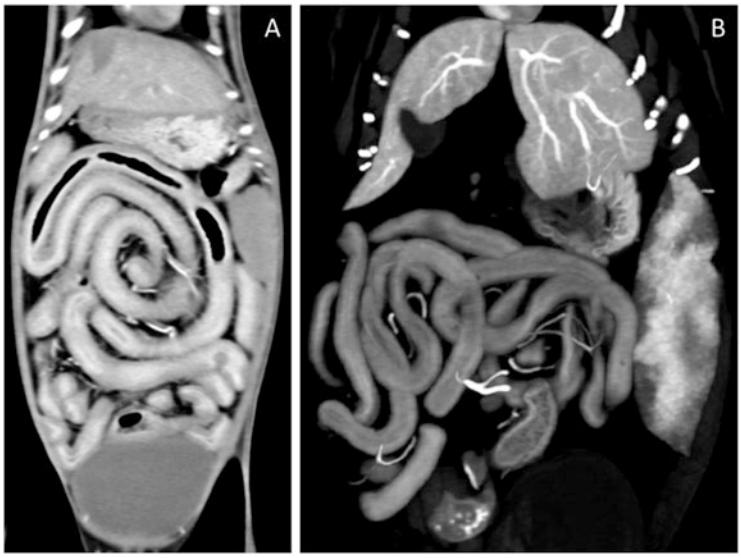

Fig. 9 Diffuse intestinal thickening in two cats with lymphoma

tailored protocol is performed. Direct scans may or may not reveal hyperattenuating material, especially in cases of intermittent bleeding. In the detection of active bleeding with CTA, the greatest sensitivity is achieved by combining findings from the arterial phase and PVP. CM extravasation is observed during the arterial phase,

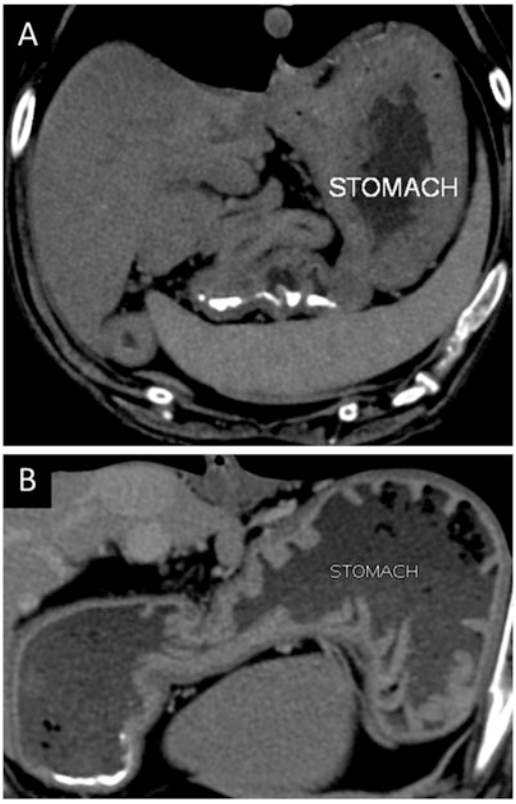

Fig. 10 Gastric erosion. (**a**) Non-contrast transverse view of the stomach in a dog with intestinal sarcoma (not visible here). Note the hyperattenuating material on the gastric mucosal surface, corresponding to ulcerative areas with hemorrhage on endoscopic evaluation. (**b**) Hemorrhagic gastric erosion in a dog due to FANS (nonsteroidal anti-inflammatory drug) therapy

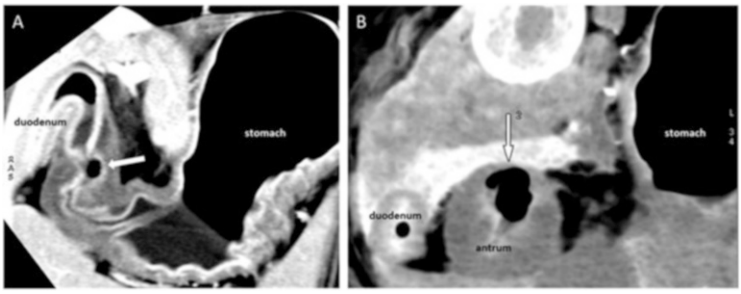

Fig. 11 Ulceration of the stomach in a dog after FANS (nonsteroidal anti-inflammatory drug) overdose. (**a**) Dorsal MPR view. The stomach is distended by gas and fluid. The pyloric antrum shows wall thickening and mucosal interruption, with focal gas collection (*arrow*). (**b**) Transverse MinIP view showing the gas collection expanding into the submucosa. Endoscopic examination confirmed the gastropathy with ulceration

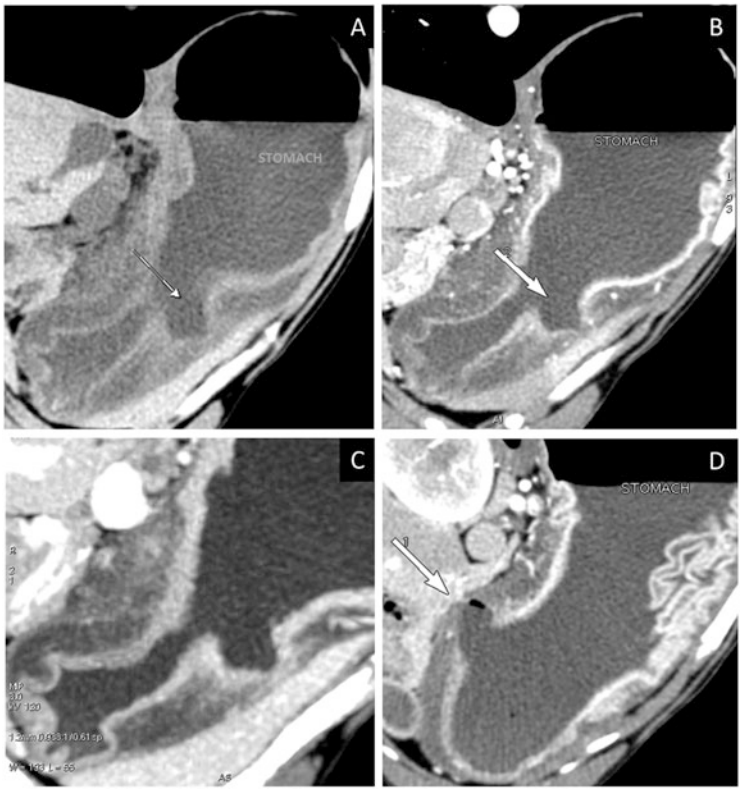

Fig. 12 Complication of a benign ulcer. (**a**) Pre-contrast transverse image of the stomach in a dog with lymphocytic-plasmacytic gastroenteritis. Note the thickened gastric wall. *Arrow* indicates a deep ulcer of the gastric body, with pronounced border having regular margins. (**b**) Same image from the LAP showing the intact mucosal layer. (**c**) MIP from the PVP showing the intact mucosal layer. (**d**) In the same dog, another gastric ulcer at the small curvature, showing interruption of the mucosal layer and the presence of a small gas bubble. These signs are consistent with a perforated ulcer (confirmed by endoscopic examination)

and CM pooling/accumulation is visible during the PVP (Fig. 14). Pre-contrast and dual-phase MDCT of the abdomen should always be performed in patients with histories of hematemesis or hematochezia or laboratory signs of gastrointestinal bleeding.

5 Gastrointestinal Perforation

Gastrointestinal perforation can have various causes in veterinary patients. Most perforations are emergency conditions of the abdomen that require early recognition and timely surgical treatment. Gastrointestinal ulcers, necrotic or ulcerated

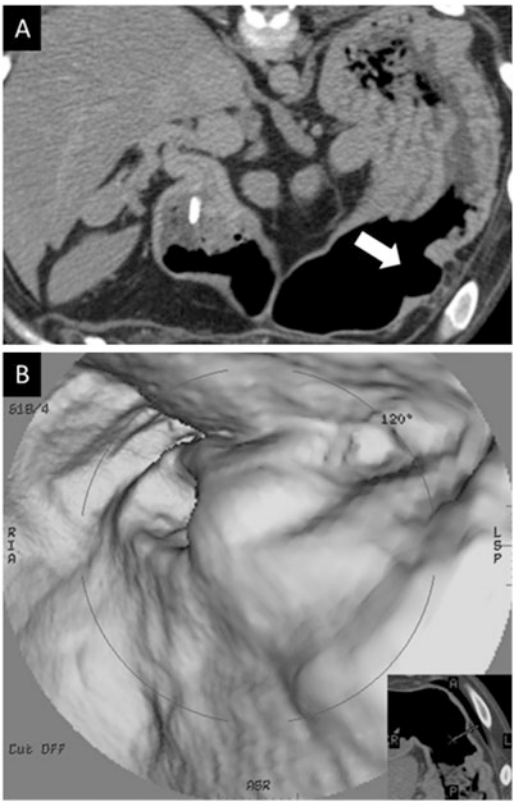

Fig. 13 Malignant gastric ulcer (lymphoma). (**a**) Transverse view of the stomach in a dog showing a profound focal defect at the body of the stomach (*arrow*). (**b**) Endoluminal imaging (virtual endoscopy) of the stomach showed an ulcerative lesion surrounded by prominent, irregular margins

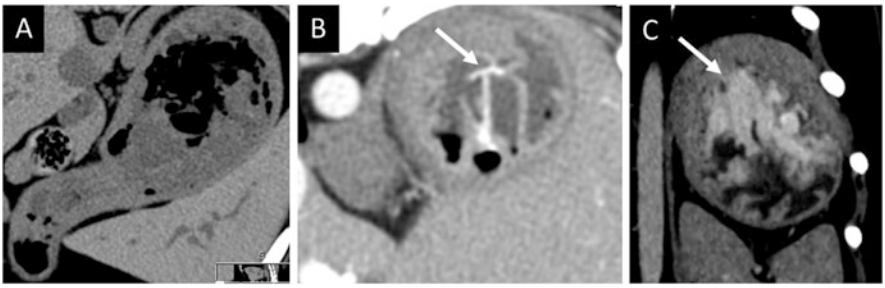

Fig. 14 Active hemorrhage in a dog. (**a**) Pre-contrast image shows no sign of hemorrhage. (**b**) Transverse view from the LAP showing initial extravasation of CM in the stomach (*arrow*). (**c**) CM pooling/accumulation in subsequent scans

malignancies, and iatrogenic and traumatic injuries are the most common causes of GIP. MDCT is very sensitive in GIP detection, and it can also be used to localize the perforation site. In humans, the reported overall accuracy of CT for bowel perforation site prediction ranges from 82 to 90%. The diagnosis of GIP is based on direct and indirect MDCT findings. Direct CT signs are discontinuity of the bowel wall and the presence of extraluminal air. Indirect MDCT findings of GIP include intestinal wall thickening, abnormal wall enhancement, abscess, and the presence of an inflammatory peritoneal mass adjacent to the perforated intestinal segment (Figs. 15 and 16). Depending on the perforation site, free air may be detected in intraperitoneal or retroperitoneal spaces. Gastric and small bowel perforation leads to pneumoperitoneum, whereas large bowel perforation may lead to pneumoretroperitoneum (Fig. 15c). In small bowel perforations, especially when the amount of air is small, concentrated free air bubbles may be seen in close proximity to the intestinal wall. In these cases, MDCT images should be examined thoroughly because free air bubbles tend to stay near the wall from which they arise, and their location may thus aid determination of the perforation site.

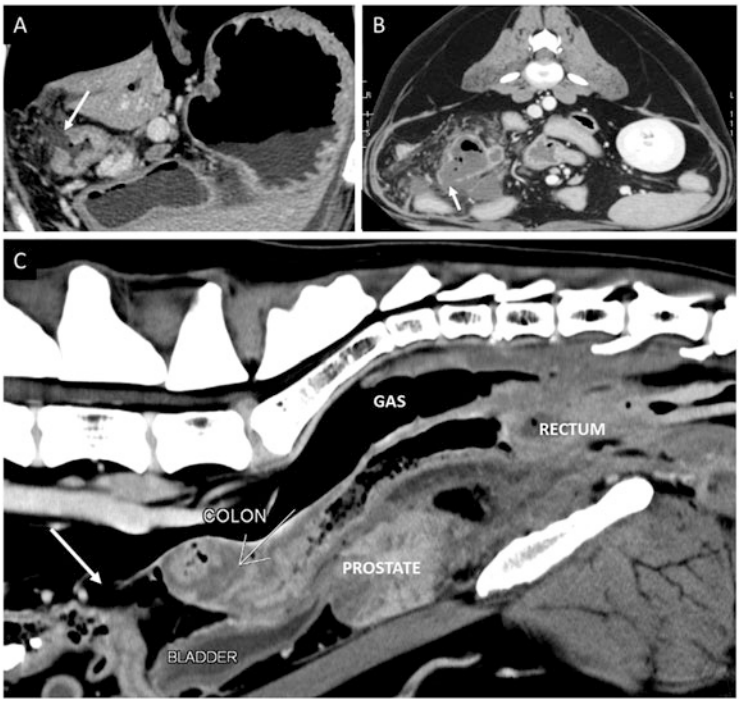

Fig. 15 Intestinal perforation. (**a**) Duodenal perforation in a patient with chronic lymphocytic-plasmacytic enteritis. Note the duodenal discontinuity and intestinal content leakage into the peritoneal cavity (*arrow*). (**b**) Jejunal perforation in a dog with severe mural enteritis. Note the discontinuity of the bowel wall (*arrow*) and surrounding peritoneal thickening and stranding (focal peritonitis). (**c**) Perforation of the descending colon (*arrow*) in a dog with carcinoma, following a biopsy procedure. Note the retropneumoperitoneum (gas)

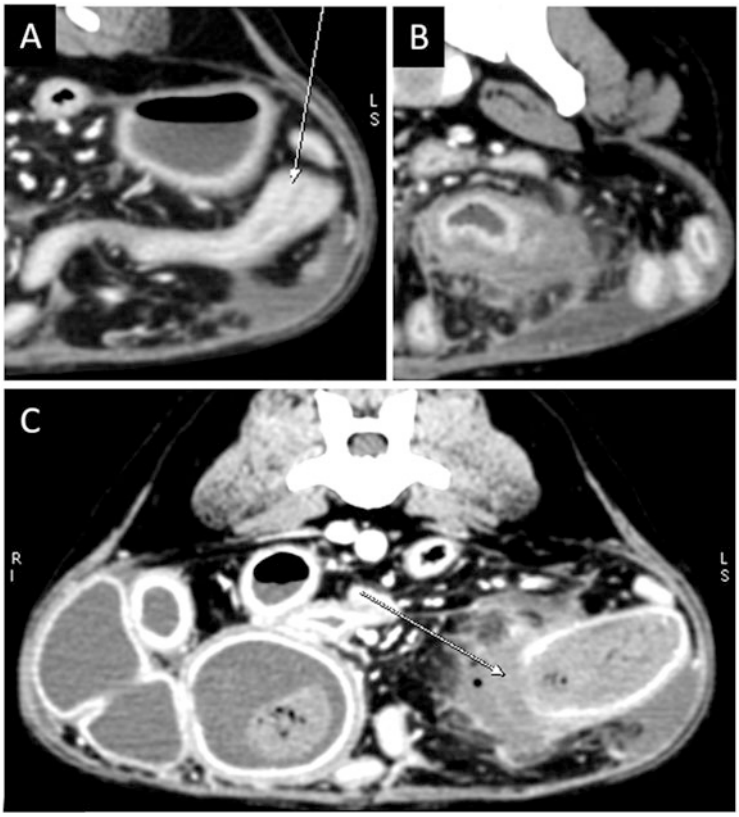

Fig. 16 Intestinal perforation in a dog with obstruction. (**a**) Transverse view of the abdomen showing the narrowing of the jejunal segment. (**b**) Transverse view of the affected segment, showing the thickened intestinal wall and the perilesional peritoneal mass (abscess) adjacent to the perforation site. Note the presence of free fluid in the peritoneal cavity. (**c**) Other intestinal segments are distended by fluid. Note the ruptured intestinal wall (*arrow*), perilesional fluid, and peritoneal thickening and stranding. Surgery confirmed stenosis and prestenotic dilatation and intestinal rupture. Histopathology proved fibrinous purulent enteritis and septic peritonitis

6 Gastrointestinal Obstruction

Gastric outlet obstruction may occur in association with congenital and acquired conditions. Pyloric stenosis refers to congenital benign muscular hypertrophy of the pylorus and is seen in young brachycephalic dogs and Siamese cat. Acquired conditions (e.g., foreign bodies, masses, or infiltrative diseases) can cause hypertrophy of the antral mucosa or a combination of both muscular and mucosal thickening (e.g., chronic hypertrophic pyloric gastropathy) (Figs. 17 and 18). Other nonneoplastic conditions leading to gastric outlet obstruction include intussusception and herniation (hernias are treated in the Chapter "The Peritoneal

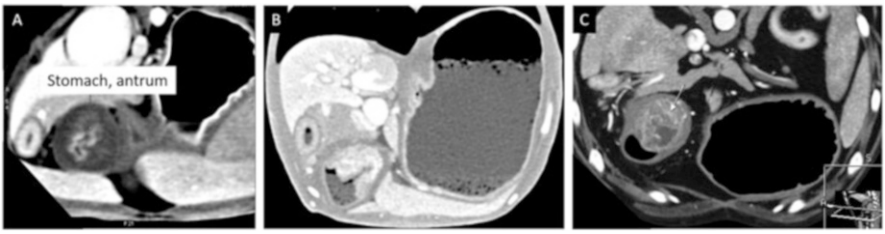

Fig. 17 Pyloric outflow obstruction. (**a**) Benign muscular hypertrophy of the pylorus (congenital pyloric stenosis) in a young bulldog. Note the smooth circumferential pyloric wall thickening involving the muscular component. The mucosa has a normal appearance. The stomach shows moderate dilatation by gas. (**b**) Benign hypertrophy of the pyloric mucosa (chronic antral mucosal hypertrophy) in a mongrel dog, causing outflow obstruction. Note the dilatation of the stomach, which contains fluids and gas. (**c**) Malignant pyloric obstruction in a dog with gastric sarcoma (*arrow*). The stomach is distended by gas

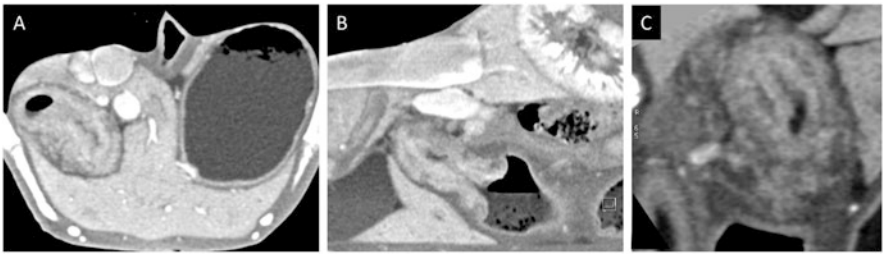

Fig. 18 Malignant hypertrophic pyloric stenosis secondary to gastric carcinoma in a dog. (**a**) Transverse view showing circumferential smooth wall thickening in the antropyloric region of the stomach. The stomach is distended by fluid and gas. (**b**) Midsagittal oblique view showing narrowing and stenosis in the antropyloric region. (**c**) Close-up view of a transverse section of the pyloric region, showing a CT appearance resembling that described in humans (cervix sign, due to indentation of the pylorus into the fluid-filled antrum)

Cavity, Retroperitoneum, and Abdominal Wall"). Intussusception involving the stomach is rarely reported in dogs and cats. A few cases of pylorogastric intussusception have been reported in the veterinary literature to date. Gastro-gastric intussusception not involving the pylorus is also possible (Fig. 19).

Many intrinsic and extrinsic conditions may lead to intestinal narrowing. Common causes of mechanical *small and large bowel obstruction* in dogs and cats are foreign bodies, intussusception, inflammation, neoplasia, abscess, granuloma, and strictures. MDCT examination is generally required in patients with suspected malignant gastrointestinal obstruction or in those with clinical signs of obstruction and unclear results of first-level imaging. In humans, CT evaluation of mechanical intestinal obstruction is highly sensitive, specific, and accurate, allowing identification of the site and cause of obstruction with up to 100% sensitivity. In a recent study, CT outperformed digital radiology in the determination of site and cause of

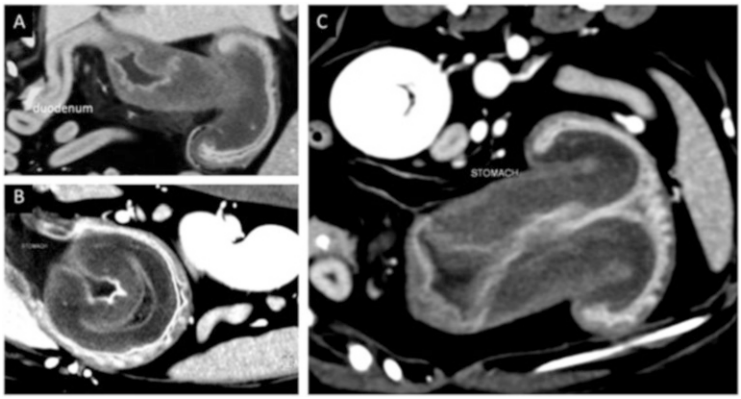

Fig. 19 Gastric outlet obstruction in a young Labrador retriever due to invagination of the antrum into the body of the stomach (gastro-gastric intussusception). (**a**) Note the normal appearance of the pylorus and duodenum, which are not involved in the intussusception. (**b**, **c**) Transverse and sagittal views of the affected part of the stomach

obstruction in 20 dogs, showing greater sensitivity (95.8 vs. 79.2%) and specificity (80.6 vs. 69.4%).

Most CT signs of obstruction reported in humans are encountered also in veterinary patients. Direct CT signs of mechanical intestinal obstruction or strangulation include dilated fluid-filled bowel loops with normal or collapsed distal loops; bowel thickening (mural edema or hemorrhage); U- or C-shaped appearance in cases of volvulus; and hyperattenuation of an intestinal segment on pre-contrast images with absent, reduced, or delayed intestinal wall enhancement on post-contrast images (bowel ischemia or hypoperfusion) (Figs. 20, 21, 22, 23, 24, and 25). Indirect signs include stretched or prominent mesenteric vessels, the "whirl sign" for twisted mesenteric vessels (also seen in torsion of other abdominal organs), and mesenteric fat stranding (Fig. 26). The latter has been described as a feature of mechanical obstruction in dogs, but it is not specific to obstruction and can be found in a broad spectrum of abdominal diseases. However, when detected in patients with suspected gastrointestinal obstruction, it should prompt the examiner to evaluate the regional viscera more rigorously, as it frequently appears adjacent to the obstructed intestinal segment. Other CT signs, such as mesenteric thrombosis and the reticulonodular mesenteric pattern, seen in neoplastic conditions, may accompany mechanical bowel obstruction. Advanced small bowel obstruction leads to bowel dilatation and necrosis or perforation of the intestinal wall (Fig. 16).

Intestinal pseudo-obstruction is a functional disorder of the bowel mimicking clinical and imaging signs of obstruction but in the absence of any mechanical

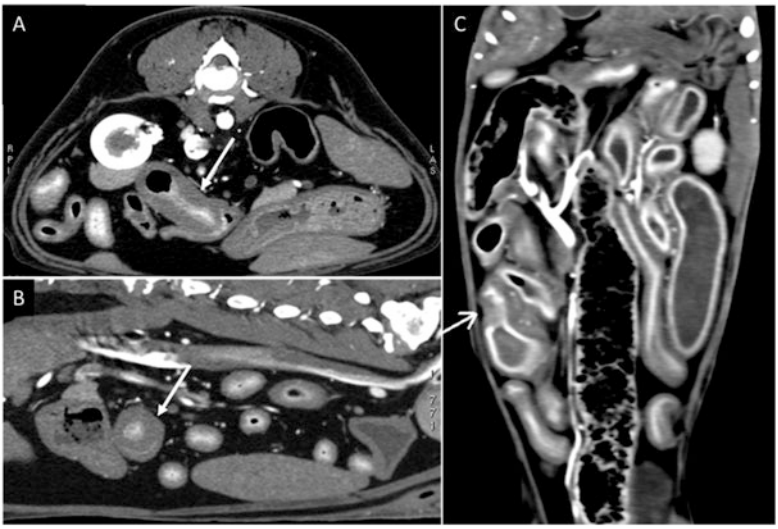

Fig. 20 Intestinal stenosis. (**a**) Ileal narrowing and stenosis in a dog with chronic intestinal inflammatory disease. Transverse view of the abdomen. Moderate prestenotic distention by gas is visible. (**b**) Midsagittal view of the abdomen, showing the transverse section of the affected intestinal segment (*arrow*). (**c**) Jejunal narrowing in a cat with lymphoma (*arrow*). Note the distension of other intestinal loops containing fluid and gas

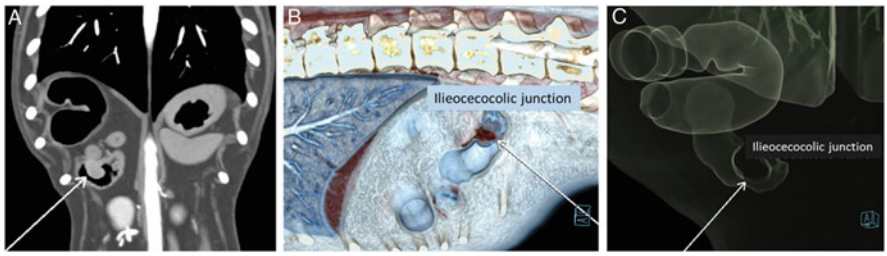

Fig. 21 Partial intestinal stenosis at the ileocecocolic junction in a dog due to a polypoid lesion. (**a**) Dorsal MPR view showing a mass-like lesion protruding into the intestinal lumen at the ileocolic junction. (**b**) Thin-VR of the same volume. (**c**) VR of air-content structure of the body of the stomach, showing the site of the mass and prestenotic bowel dilatation

obstruction. The differentiation between true bowel obstruction and pseudo-obstruction may be problematic using only first-line imaging modalities. MDCT may play an important role in the diagnostic workup of pseudo-obstruction, as it can rule out mechanical causes of obstruction (Fig. 27). However, full thickness intestinal biopsies are the only diagnostic procedure that allows the definitive diagnosis.

Fig. 22 Intestinal strangulation. (**a**) Thin-MinIP transverse view of the abdomen in a dog showing intestinal stenosis (*arrow*). Note the opacification of surrounding omental fat and the distention of other areas of the intestinal tract by fluid and gas. (**b**) Parasagittal view in the same dog showing the stenotic intestinal tract, involving the distal jejunum and ileum. (**c**) Dorsal MPR view showing intestinal loop strangulation (*arrow*). (**d**) Thin-average dorsal MPR view which better defines the strangulation and the absence of an endoluminal or extraluminal mass. Based on CT, intestinal strangulation due to an internal hernia was suspected. Surgery confirmed that parts of the jejunum and ileum were incarcerated in an unusual gap in the greater omentum. Intestinal histopathology revealed severe fibrosis and mild lymphocytic-plasmacytic enteritis

7 Gastrointestinal Masses

Primary gastric and small bowel tumors are rare in small animals. Canine gastric cancer is diagnosed rarely and is reported to account for approximately 0.1–0.5% of canine neoplasias. MDCT characteristics of various tumor types have not been

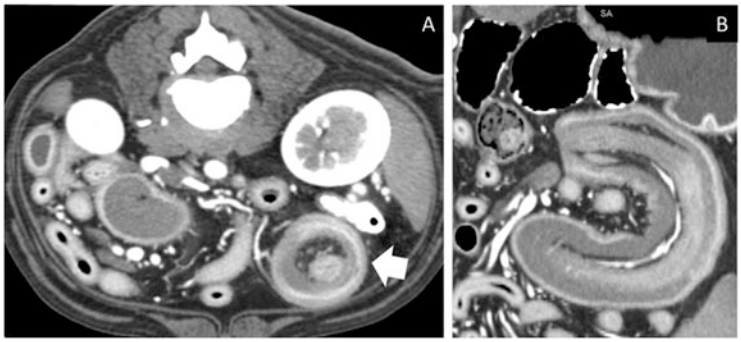

Fig. 23 Intestinal intussusception in dog that underwent CT for staging of hepatic carcinoma. (**a**) Transverse view of the abdomen showing a typical target-shaped lesion resulting from the pulling of the bowel into a neighboring (ileo-jejunal) segment. Note that part of the omentum is also intussuscepted. Other segments are distended by fluid or air. (**b**) Dorsal MPR view showing the multilayered, C- or U-shaped intestinal appearance, the thickened intestinal wall, hypoattenuation due to ischemia, and consequent wall edema. Note the mesenteric vessels inside the intussuscepted segment

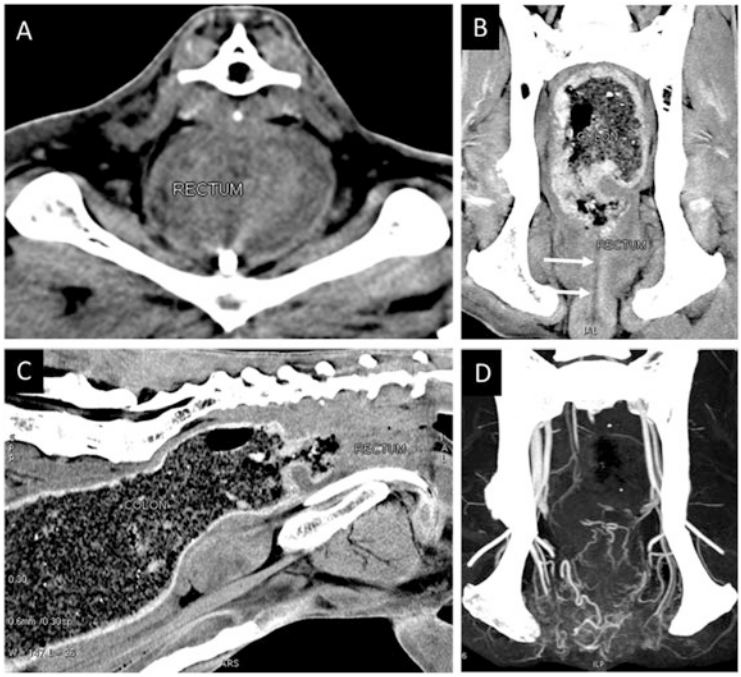

Fig. 24 Benign rectal stenosis due to severe rectal inflammation and proctitis in a German shepherd. (**a**) Pre-contrast transverse image through the pelvis, showing stenosis of the rectum with a mass-like appearance. (**b**) Pre-contrast dorsal MPR view shows a thin, straight hypoattenuating line (*arrows*) indicating the rectal lumen. (**c**) Pre-contrast sagittal view showing stenosis of the rectum and distension of the colon by fecal material. (**d**) Post-contrast dorsal thin-MIP view shows the intense blood supply to the rectal and anal segments due to inflammation

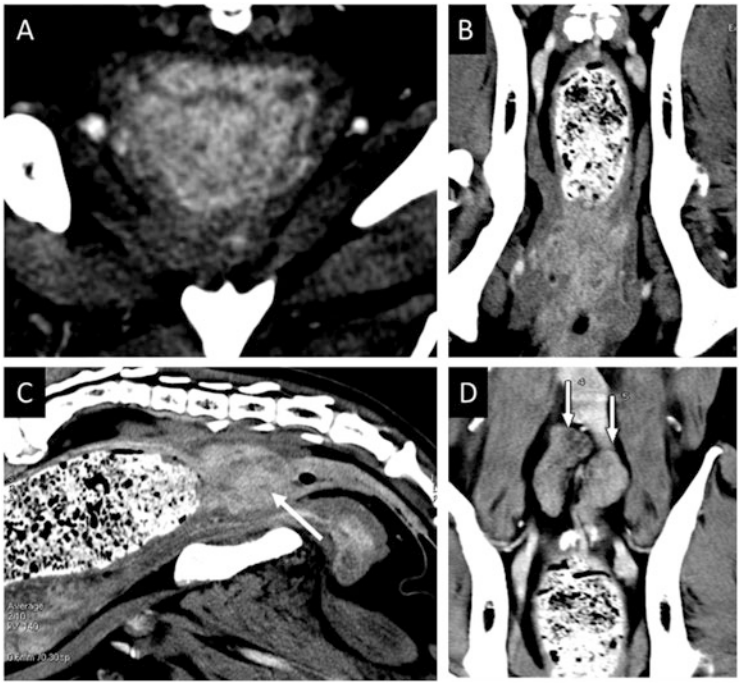

Fig. 25 Malignant stenosis due to colon carcinoma in a dog. (**a**) Transverse view through the pelvis, showing distension and mass-like appearance of the distal part of the descending colon. (**b**) Dorsal MPR view showing moderate contrast enhancement of the colonic mucosa. (**c**) Sagittal view showing a mass obstructing the colon (*arrow*). The rectum is empty and not involved. (**d**) Dorsal MPR view shows only enlargement of the median sacral lymph nodes (*arrows*), resulting in lymph node metastasis

reported in the veterinary literature, and the definitive diagnosis of gastrointestinal tumors is based on cytological or histological demonstration of neoplastic cells.

The main advantage of MDCT over other imaging techniques and endoscopy is that it enables tumor detection and staging during the same procedure. Advanced MDCT scanners can acquire datasets with near-isotropic voxels, with the high resolution needed for diagnostic multiplanar reconstruction and 3D endoluminal imaging. Dorsal, sagittal, and multioblique views of small bowel tumors demonstrate signs of small bowel obstruction, perforation, as well as the mural and extramural extent of small bowel malignancies. Such visualization aids the planning of further diagnostic steps and surgical resection. In addition, regional extent and metastases or peritoneal seeding can be detected with whole-body MDCT.

Benign gastrointestinal tumors (leiomyoma, adenoma) are often discovered incidentally in middle-aged or older patients. Benign gastric tumors may be located submucosally, intramurally, or subserosally and appear on CT as nodular eccentric mural thickening, generally well circumscribed, covered by intact mucosa, with a homogenous appearance and uniform contrast enhancement (Fig. 28). Carcinomas

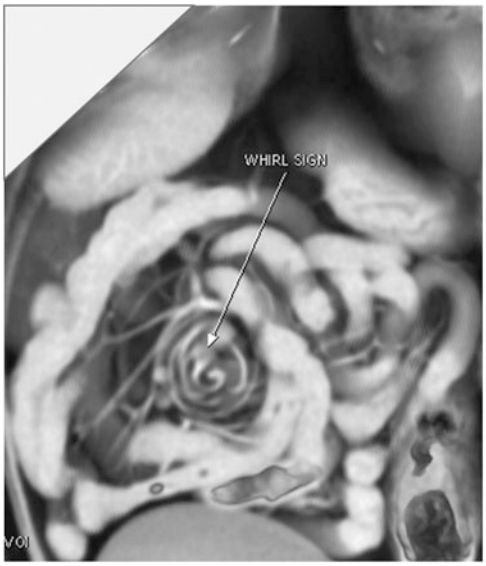

Fig. 26 The "whirl sign" (twisting of the mesenteric vessels) in a cat with lymphoma

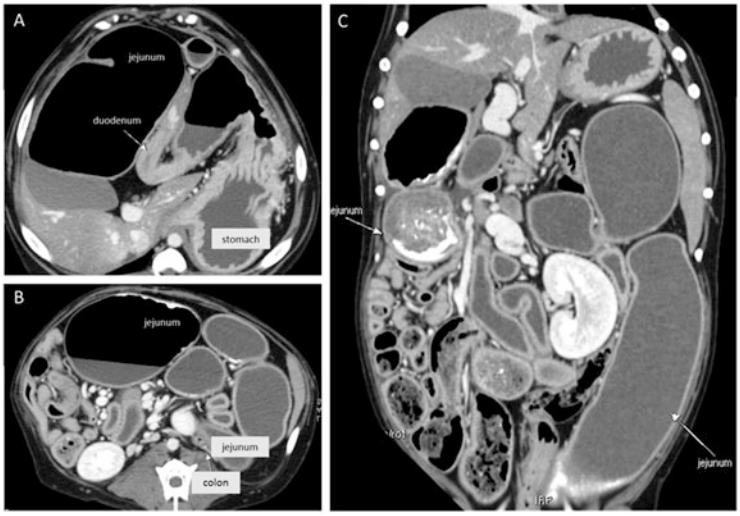

Fig. 27 Pseudo-obstruction in a dog with intestinal leiomyositis. (**a**, **b**) Transverse views of the abdomen showing multiple dilated, fluid-filled intestinal loops. (**c**) Dorsal MPR view showing intestinal distension in the absence of mechanical obstructive causes (consistent with functional ileus)

(adenocarcinoma and other subtypes) are the most common *gastric tumors* in dogs, accounting for 50–90% of cases, followed by leiomyosarcomas and lymphoma (Figs. 1, 5, 13, 17c, 18, and 29). The Tervuren, Bouvier des Flandres, Groenendael, Collie, standard Poodle, and Norwegian Elkhound breeds have been found to have a

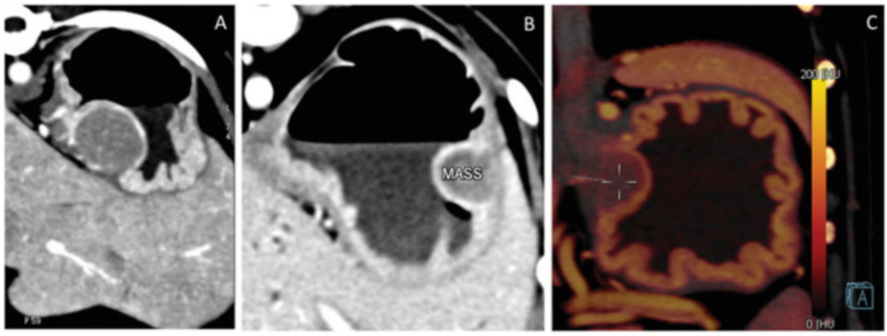

Fig. 28 Benign gastric tumors in dogs. Nodular eccentric lesions covered by intact mucosa. (**a**, **b**) Leiomyomas. (**c**) Adenoma (color-coded iodine map of dual-energy series)

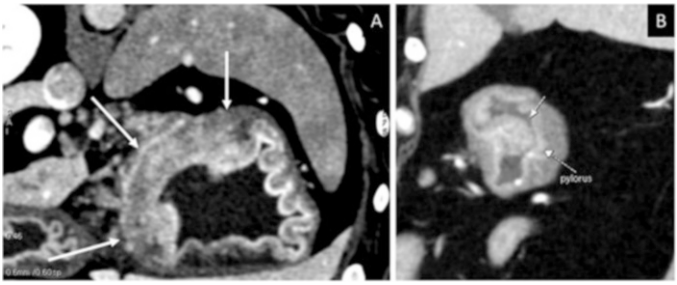

Fig. 29 Gastric carcinomas. (**a**) Eccentric thickening of the gastric wall. The rugal folds are not visible and the mucosa is disrupted. (**b**) Polypoid aspect of pyloric adenocarcinoma, partially obstructing the gastric outflow, in a dog

significantly increased risk of gastric carcinoma. Lymphosarcoma (isolated or as part of a more diffuse gastrointestinal tumor) is the most commonly reported primary gastric tumor in cats. It has a diverse array of appearances, ranging from infiltrative to polypoid lesions. Gastric adenocarcinomas are rare in cats. Extramedullary plasmacytomas have been described as primary gastric or bowel tumors in dogs and cats. Primary histiocytic sarcoma of the stomach has also been documented in dogs.

Adenocarcinoma and lymphosarcoma are the most common *intestinal tumors* in dogs and cats. Other bowel tumor types include leiomyomas, leiomyosarcomas, gastrointestinal stromal tumors, plasma cell tumors, mast cell tumors, carcinoids (tumors of neuroendocrine origin), and extraskeletal osteosarcomas (Figs. 8b, c, 9, 20c, 30, 31, and 32). Active gastrointestinal hemorrhage can accompany gastrointestinal cancer with mucosal ulceration, as well as benign ulcers (Fig. 1). Benign polyps and adenomas can be found in the feline duodenum and canine rectum. The

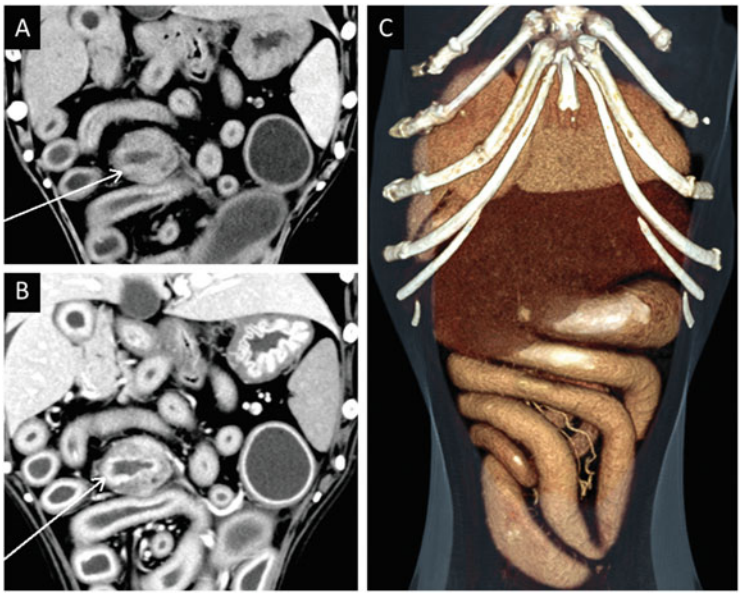

Fig. 30 Intestinal carcinoma in a dog. (**a**, **b**) Dorsal MPR views of the abdomen showing segmental thickening of the ileum (*arrow*). (**c**) Other intestinal loops are distended by fluid

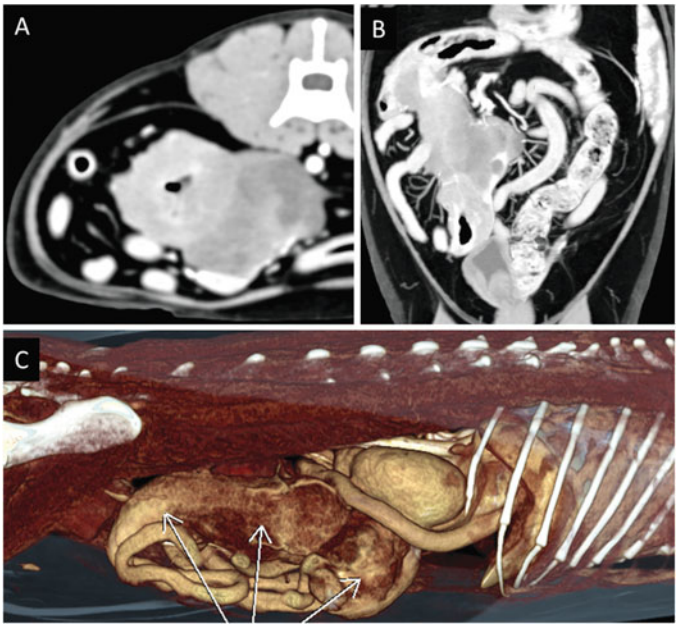

Fig. 31 Intestinal lymphoma in a cat. (**a**) Transverse view showing marked intestinal wall thickening, perilesional omental infiltration, and regional lymph node enlargement. (**b**, **c**) Dorsal MPR and right lateral volume-rendered images show the extension of the intestinal mass

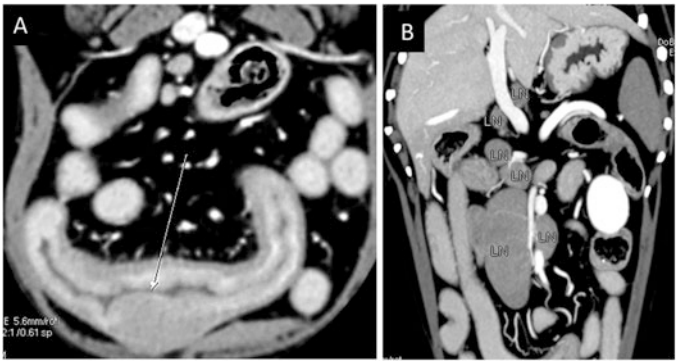

Fig. 32 Intestinal mastocytoma in a dog. (**a**) Transverse view showing segmental, eccentric intestinal thickening. (**b**) Dorsal MPR view of the same dog, showing marked enlargement of the regional lymph nodes (metastasis)

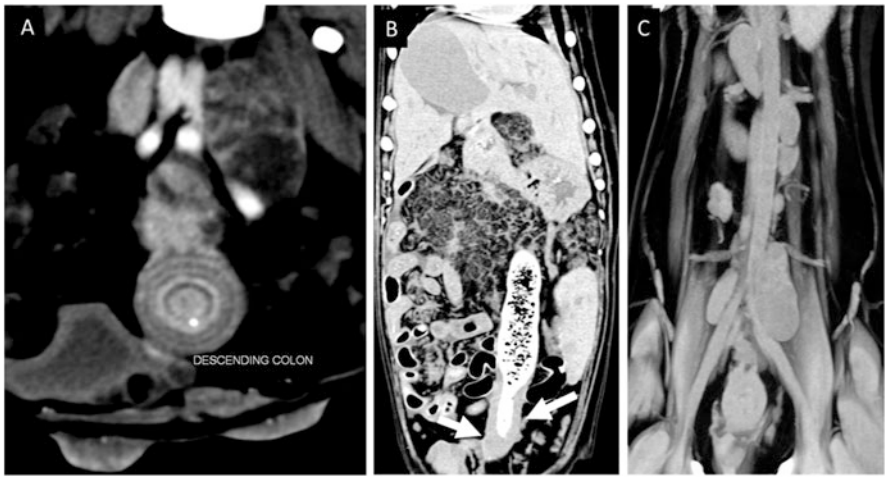

Fig. 33 Colon carcinoma in a dog. (**a**) Transverse view through the pelvis, showing the colon obstruction with a "target sign" appearance. (**b**) Dorsal MPR view showing colic wall thickening (*arrows*) and stenosis. Note the reticulonodular pattern of the peritoneum (carcinomatosis). (**c**) Dorsal MPR view of the retroperitoneal region shows secondary lymph node involvement (metastasis)

absence of mesenteric change and metastasis aids the diagnosis and rules out most malignancies. Malignant tumors of the rectum may show local infiltration, and the definition of the tumoral boundaries based on MDCT images only may be difficult (Figs. 14, 25, 33, 34).

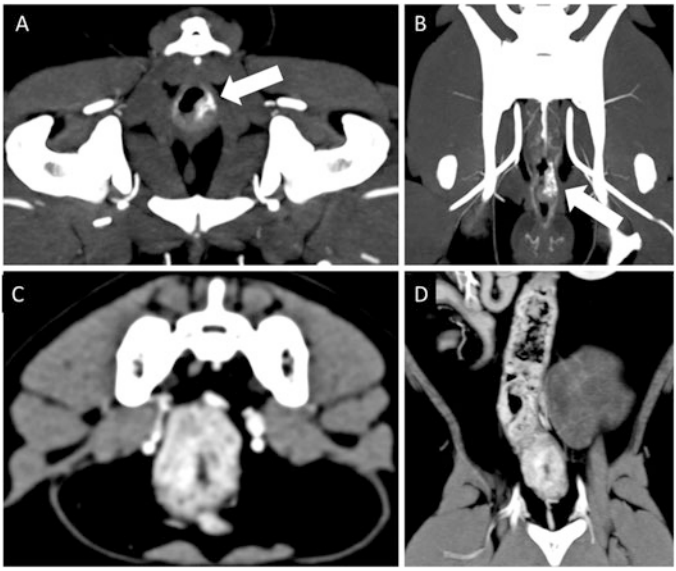

Fig. 34 Colon and rectal carcinomas. (**a**, **b**) Transverse and dorsal MPR views of the pelvis in a dog with small rectal carcinoma. Note the small hypervascular eccentric lesion (*arrow*). (**c**, **d**) Transverse and dorsal MPR images of the pelvis in a cat, showing circumferential wall thickening in the distal colon with marked post-contrast enhancement

Further Readings

Applewhite A, Cornell K, Selcer B. Pylorogastric intussusception in the dog: a case report and literature review. J Am Anim Hosp Assoc. 2001;37:238–43.

Bertolini G, Prokop M. Multidetector-row computed tomography: technical basics and preliminary clinical applications in small animals. Vet J. 2011;189(1):15–26. doi:10.1016/j.tvjl.2010.06.004.

Drost WT, Green EM, Zekas LJ, Aarnes TK, Su L, Habing GG. Comparison of computed tomography and abdominal radiography for detection of canine mechanical intestinal obstruction. Vet Radiol Ultrasound. 2016;57(4):366–75. doi:10.1111/vru.12353.

Fant P, Caldin M, Furlanello T, De Lorenzi D, Bertolini G, Bettini G, Morini M, Masserdotti C. Primary gastric histiocytic sarcoma in a dog – a case report. J Vet Med A Physiol Pathol Clin Med. 2004;51:358–62.

Fields EL, Robertson ID, Osborne JA, Brown JC Jr. Comparison of abdominal computed tomography and abdominal ultrasound in sedated dogs. Vet Radiol Ultrasound. 2012a;53(5):513–7. doi:10.1111/j.1740-8261.2012.01949.x.

Fields EL, Robertson ID, Brown JC Jr. Optimization of contrast-enhanced multidetector abdominal computed tomography in sedated canine patients. Vet Radiol Ultrasound. 2012b;53(5):507–12. doi:10.1111/j.1740-8261.2012.01950.x.

Fitzgerald E, Lam R, Drees R. Improving conspicuity of the canine gastrointestinal wall using dual phase contrast-enhanced computed tomography: a retrospective cross-sectional study. Vet Radiol Ultrasound. 2017 Jan 5. doi:10.1111/vru.12467.

Hoey S, Drees R, Hetzel S. Evaluation of the gastrointestinal tract in dogs using computed tomography. Vet Radiol Ultrasound. 2013;54(1):25–30. doi:10.1111/j.1740-8261.2012.01969.x.

Rivero MA, Vázquez JM, Gil F, Ramírez JA, Vilar JM, De Miguel A, Arencibia A. CT-soft tissue window of the cranial abdomen in clinically normal dogs: an anatomical description using macroscopic cross-sections with vascular injection. Anat Histol Embryol. 2009;38(1):18–22. doi:10.1111/j.1439-0264.2008.00886.x.

Seim-Wikse T, Jörundsson E, Nødtvedt A, et al. Breed predisposition to canine gastric carcinoma – a study based on the Norwegian canine cancer register. Acta Vet Scand. 2013;55(1):25. doi:10.1186/1751-0147-55-25.

Shanaman MM, Hartman SK, O'Brien RT. Feasibility for using dual-phase contrast-enhanced multi-detector helical computed tomography to evaluate awake and sedated dogs with acute abdominal signs. Vet Radiol Ultrasound. 2012;53(6):605–12. doi:10.1111/j.1740-8261.2012.01973.x.

Shanaman MM, Schwarz T, Gal A, O'Brien RT. Comparison between survey radiography, B-mode ultrasonography, contrast-enhanced ultrasonography and contrast-enhanced multi-detector computed tomography findings in dogs with acute abdominal signs. Vet Radiol Ultrasound. 2013;54(6):591–604. doi:10.1111/vru.12079.

Teixeira M, Gil F, Vazquez JM, Cardoso L, Arencibia A, Ramirez-Zarzosa G, Agut A. Helical computed tomographic anatomy of the canine abdomen. Vet J. 2007;174(1):133–8.

Terragni R, Vignoli M, Rossi F, Laganga P, Leone VF, Graham JP, Russo M, Saunders JH. Stomach wall evaluation using helical hydro-computed tomography. Vet Radiol Ultrasound. 2012;53(4):402–5. doi:10.1111/j.1740-8261.2012.01928.x.

Yamada K, Morimoto M, Kishimoto M, Wisner ER. Virtual endoscopy of dogs using multi-detector row CT. Vet Radiol Ultrasound. 2007;48(4):318–22.

Zacuto AC, Pesavento PA, Hill S, McAlister A, Rosenthal K, Cherbinsky O, Marks SL. Intestinal leiomyositis: a cause of chronic intestinal pseudo-obstruction in 6 dogs. J Vet Intern Med. 2016;30(1):132–40. doi:10.1111/jvim.13652. Epub 2015 Nov 26.

The Exocrine Pancreas

Giovanna Bertolini

1 Introduction

The pancreas is a unique abdominal organ in that it is classified as having endocrine and exocrine functions. The exocrine pancreas is constituted by lobules of acinar cells, which produce digestive enzymes and zymogens. Between these lobules are isles of neuroendocrine cells (islets of Langerhans), which synthesize and secrete various peptides, such as insulin and glucagon (endocrine pancreas). Both components of the pancreas can be affected by various pathological processes. Pancreatitis and pancreatic tumors are the most important pancreatic diseases in dogs and cats. Multidetector-row computed tomography (MDCT) can provide unique contributions to the evaluation of the pancreas and peripancreatic structures and has a primary role in the diagnosis and staging of pancreatic neoplasms or pancreatic diffuse diseases, as well documented in the human radiology literature. CT examination is considered to be a very sensitive method for the assessment of diffuse and focal pancreatic changes also in small animals, although veterinary research on this topic is still in its beginning.

2 Anatomy Background

In small animals, the pancreas is a long, narrow organ in the form of a V, with the apex pointing cranially and to the right of the abdomen. This apex forms an angle between two long and narrow limbs, the left and right pancreatic lobes. The right lobe lies in the mesoduodenum, close to the duodenum. The left lobe is wider. It begins at

G. Bertolini (✉)
San Marco Veterinary Clinic, Padua, Italy
e-mail: bertolini@sanmarcovet.it

G. Bertolini (ed.), *Body MDCT in Small Animals*, DOI 10.1007/978-3-319-46904-1_8

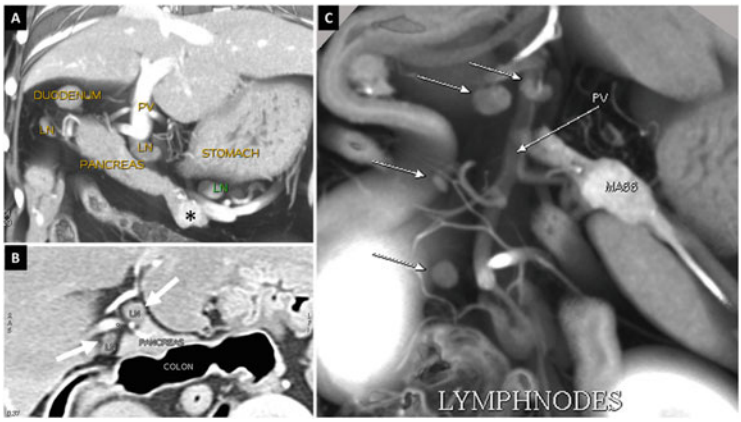

Fig. 1 Lymph nodes draining the pancreas. (**a**) Dorsal MPR image (PVP) showing the left pancreatic lobe in a dog with pancreatic insulinoma (*asterisk*). The image shows moderate enlargement (reactive/metastatic) of the surrounding lymph nodes. (**b**) Transverse view showing lymph nodes at the pancreatic body (*arrows*). (**c**) Thin volume-rendered image of the abdomen in a dog with pancreatic insulinoma of the left lobe

the pancreatic body and crosses the midline of the abdomen, lying in the greater omentum. Since its anatomy, a wide scan range (cranial and middle abdomen) is necessary to examine the whole pancreas. The pancreas is perfused exclusively by the arterial system and drained by the portal system. The *arterial blood supply to the pancreas* is provided by the cranial and caudal pancreaticoduodenal arteries, which anastomose in the gland. The organ also receives pancreatic branches from the splenic and hepatic arteries. In addition, the left lobe receives branches from the gastroduodenal artery and supply directly from the celiac artery.

The *pancreaticoduodenal veins* are satellites of the arteries and drain the blood from the pancreatic lobes to the liver through portal tributaries. The caudal pancreaticoduodenal vein is the most caudal tributary of the cranial mesenteric vein, and the cranial pancreaticoduodenal vein drains into the portal vein through the gastroduodenal vein. The splenic vein receives several branches directly from the left pancreatic lobe. Lymphatics from the pancreas drain into the duodenal, hepatic, splenic, and jejunal lymph nodes. Because they are potential sites of metastasis, all of these lymph nodes should be assessed thoroughly when staging patients with pancreatic neoplasia (Fig. 1).

3 MDCT Imaging Strategies

Recommended patient positioning for scanning of the pancreas varies among reports. The pancreas is located in the dorsal, right-cranial abdomen and is freely mobile, suspended in the duodenal mesentery. In a study on healthy beagles, the

pancreas has demonstrated less displacement in dorsal recumbency. In the author's personal experience, distension and filling of the transverse colon most affects the "readability" of pancreatic scans. In dorsal recumbency, the pancreas may be compacted between the colon and the liver parenchyma, which may complicate the detection of small parenchymal nodules, such as insulinomas. Thus, sternal recumbency is preferred in our center, particularly for dogs. As said in the MDCT angiography chapter, the tissue enhancement achieved after intravenous CM (contrast medium) injection is determined by a combination of factors, including the tissue's vascular blood supply, delay from the start of CM injection, CM dose and injection rate, injection duration, and patient characteristics such as body weight, which affects the magnitude of vascular and parenchymal contrast enhancement (see the chapter "Basic Principles of MDCT Angiography").

Debate regarding the optimal temporal window for evaluation of the pancreas in small animals is in the initial stage. Routinely, the pancreas is evaluated in a multiphasic CT examination including hepatic arterial and portal venous phase. The arterial phase has been reported to be an optimal vascular phase for the detection of canine insulinoma in some studies. However, some tumors are hypovascular and therefore enhance poorly compared to the surrounding pancreatic parenchyma in the arterial phase of dual-phase CT. As a result, they may occasionally be isoattenuating to the surrounding normal parenchyma, thereby leading to misdiagnosis. As said before, unlike that of the liver, the blood supply of the pancreas is uniquely arterial. The hepatic portal venous phase, which is the phase of maximum enhancement of the liver parenchyma, is not the phase of maximum pancreatic parenchyma enhancement. In dynamic CT study, three stages of pancreatic enhancement occur: (1) the EAP (early arterial phase), (2) the parenchymal or pancreatic phase, and (3) the PVP (portal venous phase). The first and third phases are those phases obtained routinely during dual- and three-phase MDCT examinations of the liver. The pancreatic phase, in which the parenchyma of the pancreas shows its maximal enhancement, falls between the arterial and portal hepatic phases (about 5–10 s after the aortic peak enhancement) (Figs. 2 and 3). Which CT phase is the most useful depends on the diagnostic task. Pancreatic hypovascular tumors that are missed in hepatic arterial phase (because they are isoattenuating to the pancreas) might be detected during the pancreatic phase, when the surrounding parenchyma has its maximum enhancement. The veterinary literature on this subject is limited, and results published to date are inconsistent, probably due to differences in scan protocol and tumor stage evaluated and the small numbers of patients included in various studies.

Regarding the scan time, with slower scanners (those with one to four detectors) and longer scan times (20–40 s), the start of the arterial phase coincides with the arrival of CM in the aorta. The time required for the CM to appear in the arterial territory varies substantially among patients (according to cardiac output) and should be individualized using a bolus test or bolus-tracking technique. The use of a fixed scan delay is suboptimal and may produce inconsistent results. The use of the test bolus technique presumes a relationship between the geometries of the test bolus and the main bolus, which is not always the case. In small patients, the

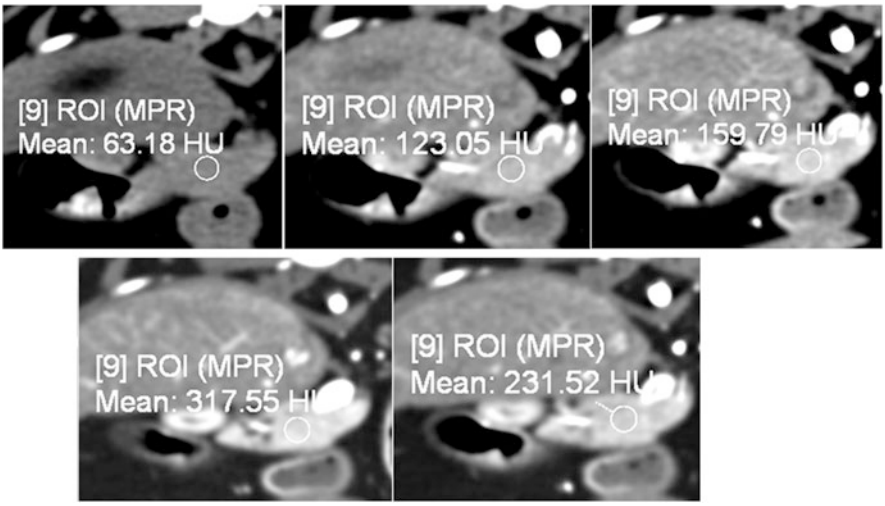

Fig. 2 Dynamic perfusion study of the pancreas in a cat (128-dual source CT). Dorsal multiplanar (MPR) views through the pancreatic body: non-enhanced, EAP, LAP (late arterial phase), pancreatic phase, and PVP

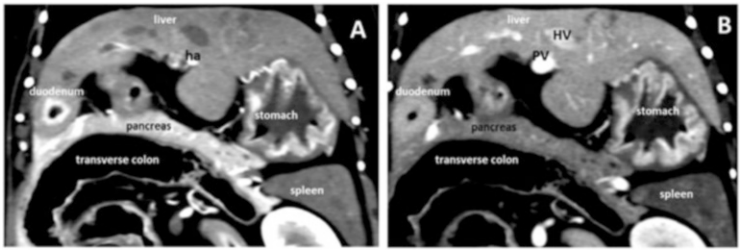

Fig. 3 Dorsal MPR views of the pancreas in a dog obtained in the pancreatic phase (**a**) and PVP (**b**). Note the difference in pancreatic parenchymal contrast enhancement between the images

injection of a small quantity of CM using the same flow rate as used for the main bolus may be problematic. Again, because of the high vascularity of the pancreatic parenchyma, pre-enhancement may result in suboptimal imaging and missed diagnosis due to the reduction of tumor conspicuity. The achievement of the appropriate timing for adequate contrast enhancement of the pancreas in each phase of scanning is more difficult and critical using faster MDCT scanners (64–320 MDCT and various generations of DSCT). With advanced, more rapid MDCT scanners, the bolus peak can be better utilized, but an additional scan delay must be introduced to not outrun the CM (scans reach a body region before the CM). Determination of this scan delay is critical and varies among scanners and scan protocols (in particular, scan speed and injection duration). The bolus-tracking technique is currently used routinely to adjust for variation in the cardiac circulation time (see the chapter "Basic Principles of MDCT Angiography" for further explanations). With an appropriate additional diagnostic delay for a rapid MDCT scanner, bolus tracking

may lead to major contrast enhancement in the pancreatic parenchyma and provide greater tumor conspicuity relative to the pancreas. With the recent advancement of dual-energy CT, two CT acquisitions can be performed at two different energy levels. The introduction of this scanner technology in veterinary practice may enable further advancement in pancreas disease assessment in dogs and cats (Figs. 4 and 5).

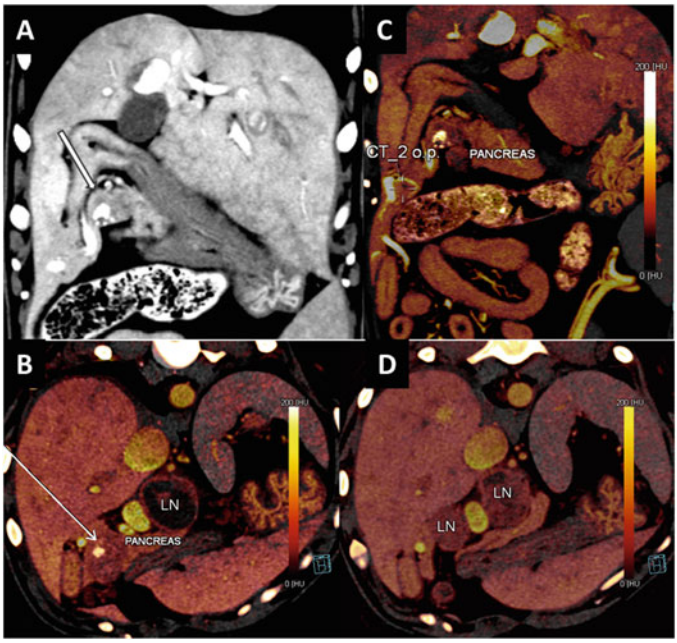

Fig. 4 Pancreatic carcinoma in a dog with hepatic lymph node metastasis (LN). (**a**) Dorsal MPR showing a mass in the pancreatic lobe that is iso-hypoattenuating to the surrounding parenchyma. (**b**) Color-coded iodine image. The *arrow* indicates a defined ovoid mass. Note the enlarged and inhomogeneous lymph node (LN). (**c**) The deviation of a pancreatic vessel in the left lobe helped to identify another small nodule. (**d**) Metastatic portal lymph nodes

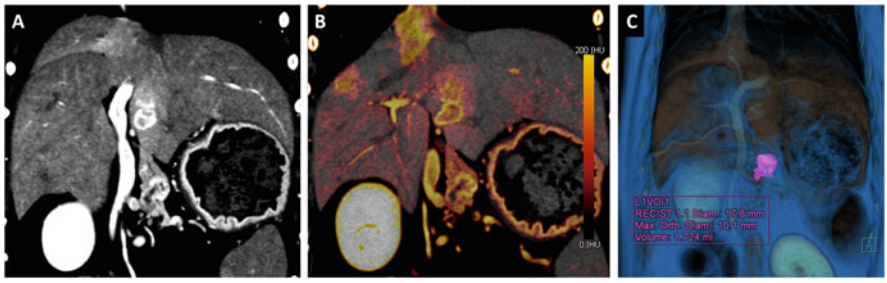

Fig. 5 Dorsal MPR views of the abdomen in a dog with pancreatic carcinoma metastasis to the liver. (**a**) PVP. (**b**) Color-coded iodine image. The pancreatic and hepatic lesions are more conspicuous and better defined, enabling more precise measurement. (**c**) Automatic identification and measurement of the pancreatic nodule

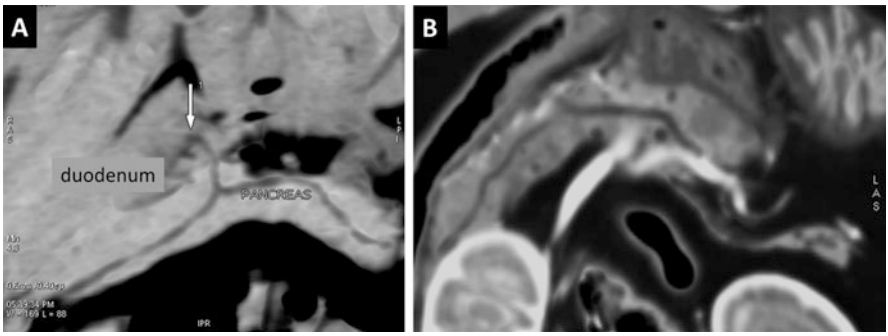

Fig. 6 (**a**) Dorsal MinIP (0.6/0.4 mm) image from a cat showing the pancreatic duct draining into the duodenum (*arrow*). (**b**) Dorsal MinIP of the pancreas in another cat with cystic changes due to chronic pancreatitis

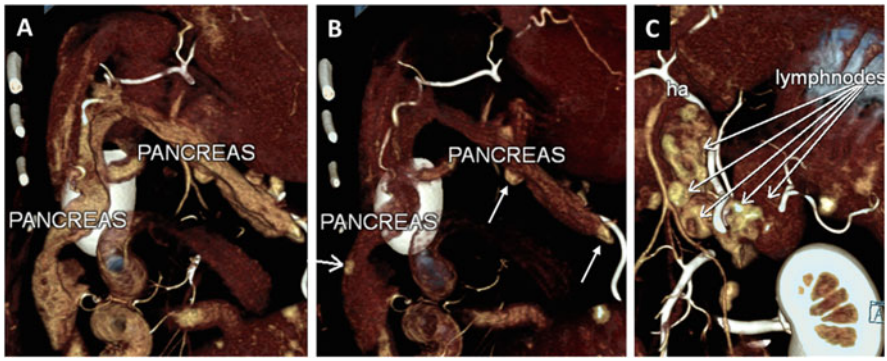

Fig. 7 3D VR of pancreatic carcinoma in a dog. (**a**) The whole pancreas is well visualized. (**b**) Note the small nodular lesions (*arrows*) in the pancreas (carcinoma). (**c**) Enlarged metastatic lymph nodes (portal and splenic)

Post-processing techniques, such as MPR (multiplanar), MIP (Maximum Intensity Projection), MinIP (Minimum Intensity Projection), and VR (Volume Rendering), can provide details about vascular and ductal involvement in pathological processes and should be used routinely to review datasets from multiphasic MDCT studies. In particular, MPR is essential for accurate interpretation of the relationships among the pancreas, duodenum, and common biliary duct. MinIP helps in identification of biliary duct and pancreatic cystic lesions (Figs. 6 and 7).

4 MDCT of Pancreatic Diseases

Dogs and cats can be affected by several diseases of the exocrine pancreas, including exocrine pancreatic insufficiency, pancreatic carcinoma, and pancreatitis.

4.1 Pancreatic Atrophy

Pancreatic acinar atrophy is the most important cause of exocrine pancreatic insufficiency in dogs. Pancreatic acinar atrophy is thought to be an immune-mediated condition in dogs that begins with lymphocytic pancreatitis (Fig. 8a, b). In this setting, pancreatic acinar atrophy may also be a sequela of chronic pancreatitis in dogs. End-stage chronic pancreatitis is considered to be the most common cause of pancreatic dysfunction in cats. Again, pancreatic atrophy may be observed in pancreatic neoplasia of the exocrine pancreas (Fig. 8c).

4.2 Pancreatitis

MDCT enables the evaluation of the entire pancreas and the identification of more pancreatic and extra-pancreatic abnormalities than with ultrasound. Studies of dogs and cats undergoing necropsy for a variety of reasons suggest that pancreatic lesions, especially those consistent with chronic pancreatitis, are much more common than previously thought. Common lesions seen on necropsy were pancreatic hyperplastic nodules, lymphocytic or neutrophilic inflammation, fibrosis, atrophy, pancreatic fat necrosis, pancreatic necrosis, and edema. All of these changes are potentially detectable in vivo using thin-slice, multiphase MDCT. In humans, CT with intravenous CM administration is used frequently to diagnose and stage pancreatitis and is considered to be a highly sensitive and specific method for the assessment of acute and chronic pancreatitis. Recommendations state that imaging of the pancreas should always be performed with the maximum amount of contrast at a maximum flow rate, as pancreatic necrosis can be difficult to detect. Early studies of the use of CT to examine pancreatitis in dogs and cats were discouraging, and CT was initially reported to be of limited utility in the assessment of

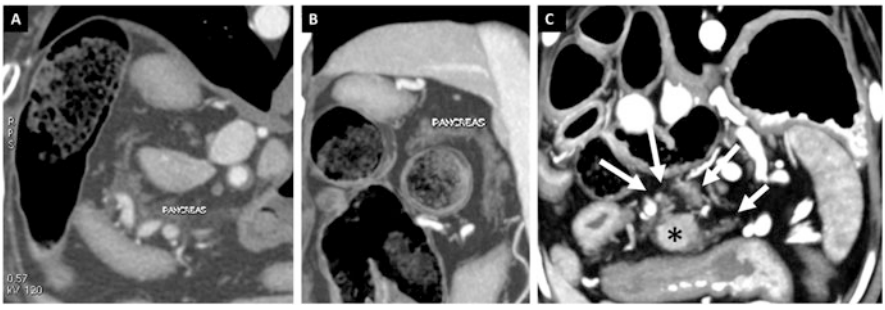

Fig. 8 Pancreatic atrophy. (**a**, **b**) Transverse and dorsal MPR views of a German shepherd with exocrine pancreatic insufficiency. (**c**) Transverse view of the abdomen in another German shepherd with pancreatic adenocarcinoma (*asterisk*) and atrophy of the surrounding pancreatic parenchyma (*arrows*)

inflammatory diseases of the pancreas. The use of older CT technologies, incorrect scan protocols (e.g., in terms of slice thickness), and inappropriate CM administration may explain the lack of visualization of pancreatic changes and even of the pancreas itself. The requirement for anesthesia in small animals may represent a limitation of the systematic use of CT in cases of suspected pancreatitis. However, advanced MDCT scanners permit more rapid examination in awake and sedated patients. Results of a recent study in which multiphase 16-MDCT was used in sedated dogs with suspected pancreatitis are encouraging in this sense. In this pilot work, most changes in pancreatic and peripancreatic tissues were detected in the delayed phase, obtained 2–3 min after CM injection; the arterial and venous phases did not add information. However, the timing of CM injection, which is critical for the optimization of pancreatic imaging, was not reported in the study.

Moderate enlargement of the pancreas, with rounded borders and a pseudonodular aspect; non-enhancing parenchyma; and the absence of peripancreatic peritoneal changes may suggest chronic pancreatitis. Acute pancreatitis has a similar appearance in dogs and cats, characterized by an enlarged pancreas with irregular margins; strongly enhanced parenchyma, peripancreatic peritoneal stranding, and increased opacification are early signs of inflammation (Figs. 9, 10, 11, and 12). Apart from alterations of the pancreas, MDCT should be used to assess the presence of extra-pancreatic findings, such as gallstones, biliary dilatation, venous thrombosis, aneurysm, and contiguous inflammatory involvement of the gastrointestinal tract (Figs. 13 and 14). Clinical parameters and morphological criteria, defined by MDCT, dictate the type of treatment that a patient needs.

4.3 Pancreatic Cyst, Pseudocyst, and Abscess

MDCT can be used to easily detect complications of acute pancreatitis, such as pseudocysts, abscesses (showing peripheral enhancement), and parenchymal

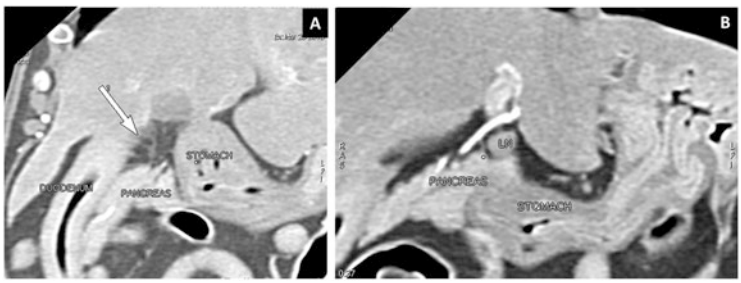

Fig. 9 Acute pancreatitis. MDCT examination of a dog with clinically suspected pancreatitis and uncertain ultrasound results. (**a**) Dorsal MPR view showing peripancreatic peritoneal stranding (*arrow*). (**b**) The lymph node at the pancreatic body shows moderate subjective enlargement

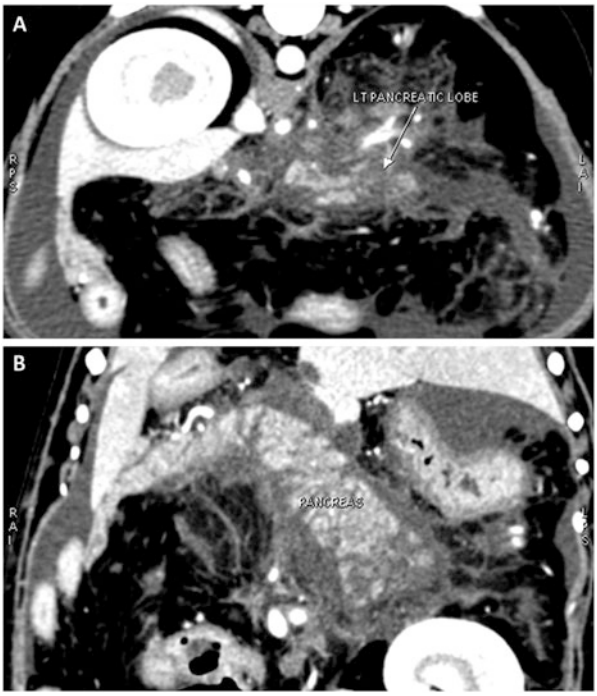

Fig. 10 Acute pancreatitis in a mongrel dog, particularly affecting the left lobe, which is enlarged and poorly defined with irregular margins. Note the peritoneal fluid and peripancreatic fat stranding

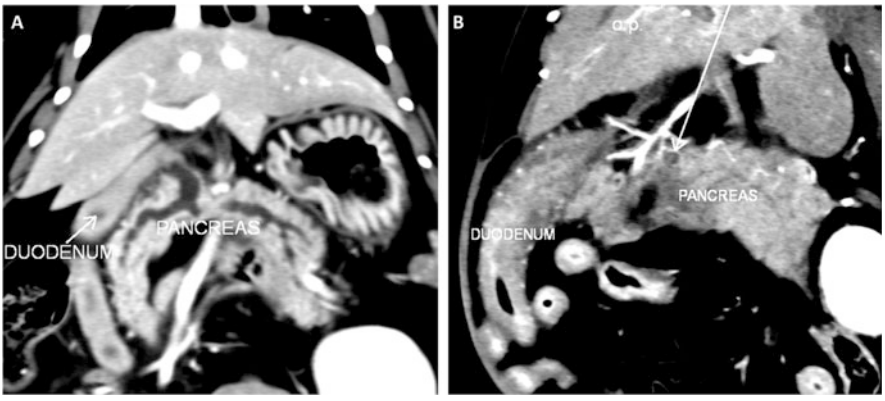

Fig. 11 Acute pancreatitis. (**a**) Dorsal MPR image of the pancreas in a cat with acute pancreatitis. The pancreas is enlarged and the parenchyma shows great enhancement. Note the pancreatic duct dilatation. (**b**) Dorsal MPR image from another cat with active pancreatitis. The pancreas is enlarged and inhomogeneous; the *arrow* indicates a small cystic change at the pancreatic body. Note the thickening of the duodenal wall with undefined margins

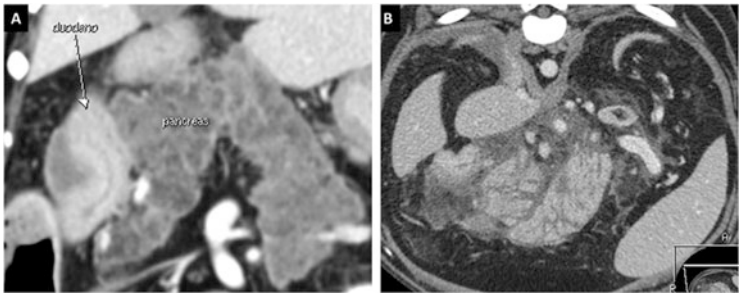

Fig. 12 (**a**) Dorsal MPR image of a dog with granulomatous pancreatitis. Note the duodenal involvement. (**b**) Transverse view from a dog with gangrenous pancreatitis. The pancreas is enlarged, edematous, and impacted at the center of the abdomen. Note the peritoneal thickening and stranding and the peripancreatic fluid

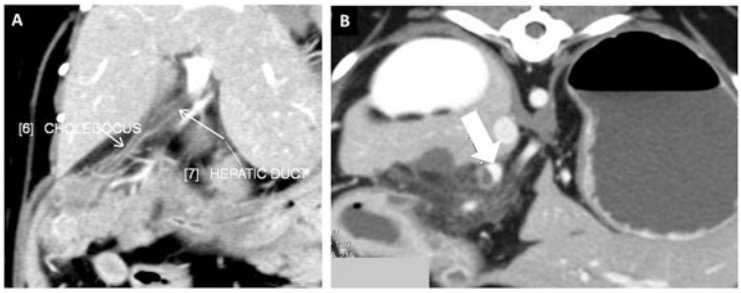

Fig. 13 Complication of pancreatitis. (**a**) Dorsal MPR image of a dog with active pancreatitis. Note the secondary involvement of the common biliary duct (choledochus) and hepatic biliary ducts. (**b**) Portal vein thrombosis (*arrow*) in a dog with active pancreatitis

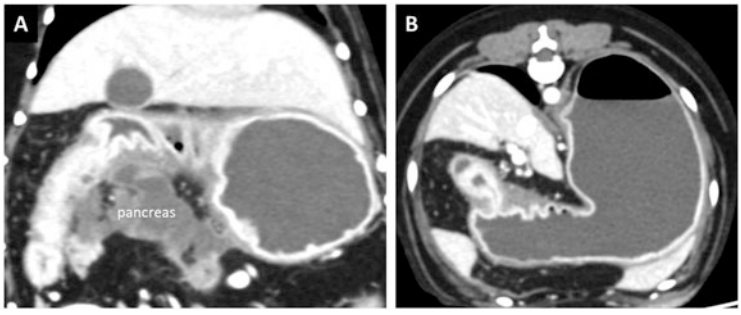

Fig. 14 Gastric outflow obstruction in a dog. (**a**) Dorsal MPR showing pancreatic abscessation and peritonitis. (**b**) Transverse view of the same dog showing pyloric stenosis and gastric dilatation (the stomach is distended by fluid and gas)

necrosis (hypoattenuating non-enhancing areas). Abscess are rare and are encountered in patients with chronic pancreatitis that fails to respond to medical therapy (Figs. 14 and 15). Recurrent cystic changes of the pancreas in cats are associated to chronic, active pancreatic inflammation (Figs. 6b and 16a, b). True pancreatic cysts (not communicating with pancreatic duct) are typically seen in cats with polycystic kidney diseases (PKD) (Fig. 16c).

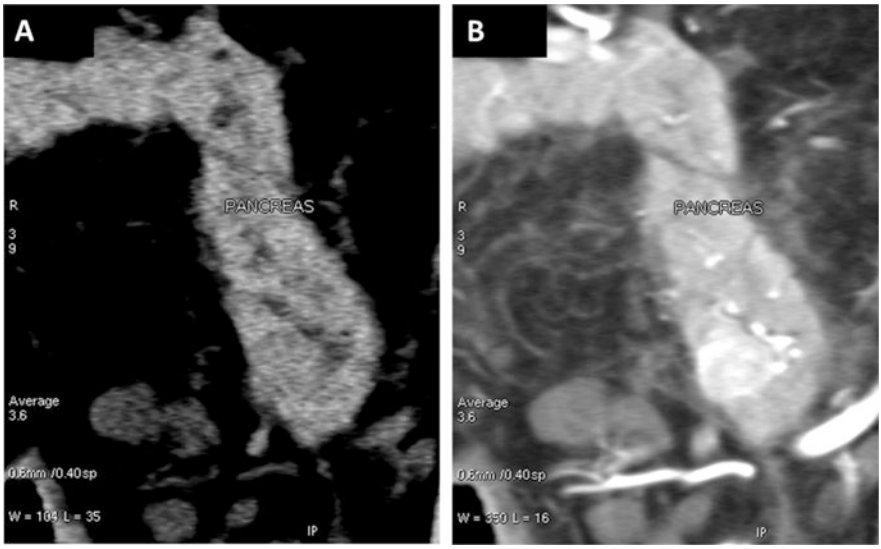

Fig. 15 Pancreatic abscess in a dog with active, chronic pancreatitis. (**a**, **b**) Pre- and post-contrast images of the left pancreatic lobe, which is enlarged and poorly marginated. A parenchymal lesion is iso-hypoattenuating to the surrounding parenchyma on the pre-contrast image and shows great enhancement after CM injection (abscess). In (**b**), note the peripancreatic peritoneal fluid

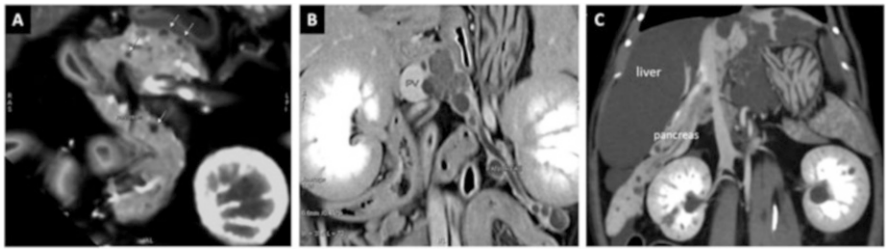

Fig. 16 Pancreatic cysts. (**a**) Pancreatic cysts in a cat with chronic pancreatitis. (**b**) Cystic changes and pancreatic duct dilatation in a cat with chronic pancreatitis. (**c**) Multiple pancreatic cysts in a Persian cat with PDK. Note the large hepatic cysts and multiple small renal cysts

4.4 Pancreatic Exocrine Neoplasia

Clinical distinction of pancreatic neoplasia from pancreatitis can be difficult or sometime impossible. Pancreatic imaging may aid diagnosis, although both conditions can coexist and cytological or histological examination is necessary to establish a final diagnosis. Small adenocarcinoma of the exocrine pancreas in dogs generally appears as a solitary mass, iso- to hypoattenuating to the pancreas, which is difficult to distinguish from the surrounding normal parenchyma. Indirect signs, such as mass effect on pancreatic parenchyma, with deviation of pancreatic vessels, pancreatic duct dilation, and atrophy of the parenchyma distal to the tumor, may be helpful for diagnosis of less obvious tumors. Tumor enlargement deforms the pancreatic profile and may result in the encasement or invasion of adjacent vasculature structures (e.g., pancreatic arteries and veins, portal vein, or splenic vein) (Figs. 3, 7, 17, 18, 19, and 20). Intrapancreatic splenic tissue has been described in dogs. This ectopic splenic tissue within the pancreatic parenchyma may mimic a hypervascular pancreatic neoplasm and should be considered in the differential diagnosis of non-secreting pancreatic tumors in dogs. Again, in the case of a malignant splenic mass (i.e., hemangiosarcoma), the pancreas should be assessed for potential metastasis.

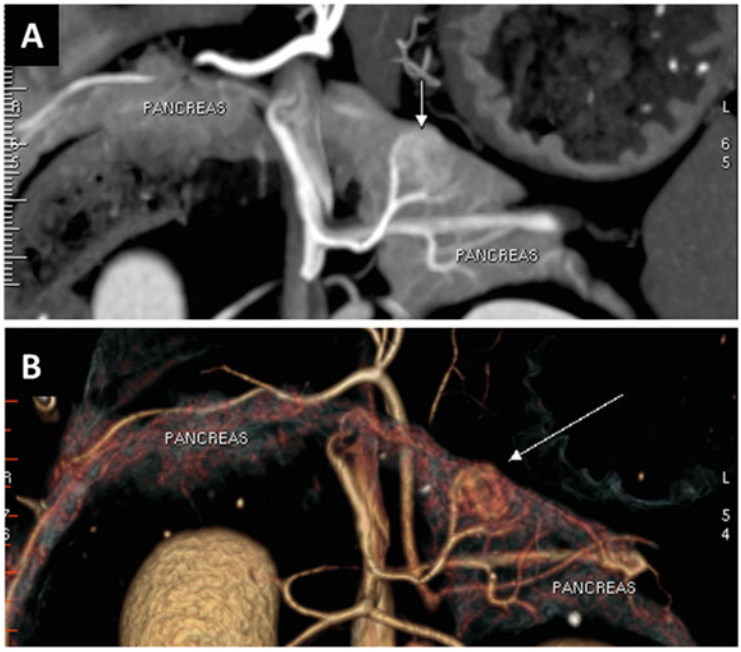

Fig. 17 Pancreatic carcinoma in a dog. (**a**, **b**) Thin-MIP and thin volume-rendered images of the pancreas (LAP) in a mongrel dog with pancreatic carcinoma of the left lobe, discovered incidentally during an MDCT examination performed for other reasons

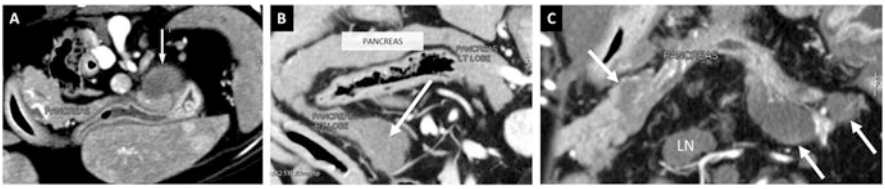

Fig. 18 Pancreatic carcinoma in dogs. (**a**) Transverse view from the PVP showing a rounded, hypovascular mass in the left pancreatic lobe (*arrow*). (**b**) Dorsal-oblique MPR view from the PVP of a dog with a mass in the left pancreatic lobe (*arrow*), which is iso-hypoattenuating to the surrounding pancreatic parenchyma. (**c**) Dorsal MPR image from a dog with pancreatic carcinoma metastasis to the liver. *Arrows* indicate multiple hypoattenuating hypovascular lesions. *LN* enlarged metastatic mesenteric lymph node

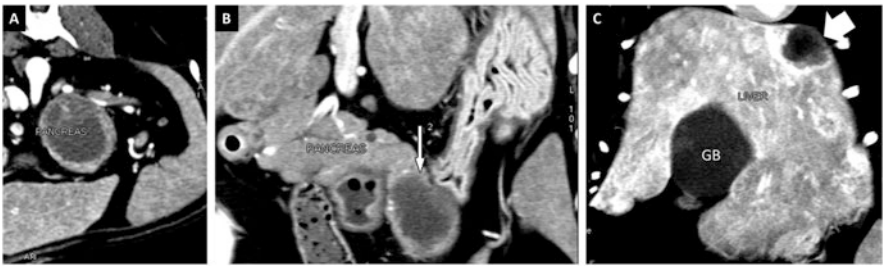

Fig. 19 Pancreatic carcinoma in a dog. (**a**) Transverse view showing a large hypoattenuating, hypovascular mass in the left pancreatic lobe. (**b**) Dorsal MPR view of the pancreatic body and the left lobe with a mass. (**c**) Dorsal MPR image of the liver (PVP) showing a metastatic mass (*arrow*) and diffuse heterogeneous parenchymal enhancement. *GB* gallbladder

Pancreatic malignant neoplasias, including primary and metastatic tumors, are rare in cats. Exocrine pancreatic adenocarcinoma, the most common malignant tumor in cats, can originate in the acinar cells or ductular epithelium and can have a nodular or diffuse presentation (Fig. 21). This tumor is aggressive, with a high rate of metastasis (mostly to the liver, lung, and small intestine) and a poor prognosis. In a recent work, 15% of cats with pancreatic carcinoma were diabetic, suggesting a link between these two diseases, as in people.

Benign tumors (i.e., adenomas) are subclinical in most cases. Many are encountered incidentally during CT examinations performed for other purposes. Adenoma is generally characterized by an encapsulated solitary mass with slow expansive growth. The examiner must remember that pancreatic nodular hyperplasia is much more common than neoplasia in older dogs and cats and may be found incidentally by CT. Hyperplastic changes generally appear as multiple small hypovascular nodules with no capsule.

Tumors of the endocrine pancreas are treated in the chapter entitled “MDCT of the Endocrine System.”

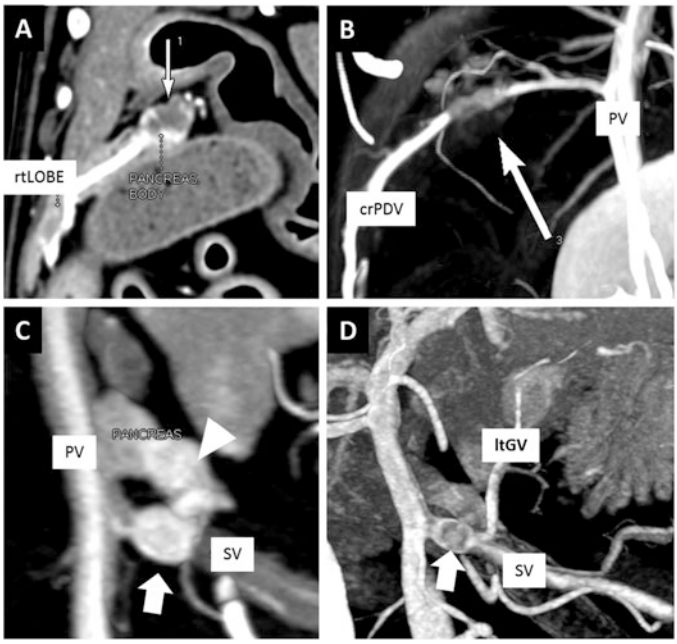

Fig. 20 Vascular involvement. (**a**) Pancreatic carcinoma of the pancreatic body (*arrow*), invading the cranial pancreatic duodenal vein (crPDV), in a dog. (**b**) Thin-MIP showing the site of vascular encasement and invasion by the mass. (**c**) Pancreatic carcinoma of the left lobe (*arrowhead*), invading the splenic vein (SV; *arrow*), in another dog. *PV* portal vein. (**d**) MIP of the portal system in the same dog as (**c**), showing the intravascular mass (*arrow*)

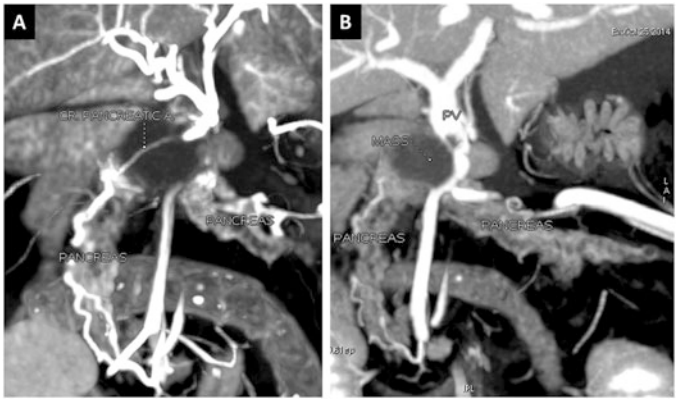

Fig. 21 Pancreatic carcinoma in a cat. (**a**) Dorsal MPR of the abdomen obtained in the HAP, showing a hypoattenuating hypovascular mass encasing the cranial pancreatic artery. (**b**) The same image in the PVP showing initial portal vein tumor invasion

Further Readings

Adrian AM, Twedt DC, Kraft SL, Marolf AJ. Computed tomographic angiography under sedation in the diagnosis of suspected canine pancreatitis: a pilot study. J Vet Intern Med. 2015;29 (1):97–103. doi:10.1111/jvim.12467.

Branter EM, Viviano KR. Multiple recurrent pancreatic cysts with associated pancreatic inflammation and atrophy in a cat. J Feline Med Surg. 2010;12(10):822–7. doi:10.1016/j.jfms.2010.06.005.

Cáceres AV, Zwingenberger AL, Hardam E, Lucena JM, Schwarz T. Helical computed tomographic angiography of the normal canine pancreas. Vet Radiol Ultrasound. 2006;47(3):270–8.

Choi SY, Choi HJ, Lee KJ, Lee YW. Establishment of optimal scan delay for multi-phase computed tomography using bolus-tracking technique in canine pancreas. J Vet Med Sci. 2015;77(9):1049–54. doi:10.1292/jvms.14-0693.

Choi SY, Lee I, Seo JW, Park HY, Choi HJ, Lee YW. Optimal scan delay depending on contrast material injection duration in abdominal multi-phase computed tomography of pancreas and liver in normal Beagle dogs. J Vet Sci. 2016;17(4):555–61.

Chu AJ, Lee JM, Lee YJ, Moon SK, Han JK, Choi BI. Dual-source, dual-energy multidetector CT for the evaluation of pancreatic tumours. Br J Radiol. 2012;85(1018):e891–8. doi:10.1259/bjr/26129418.

Fletcher JG, Wiersema MJ, Farrell MA, Fidler JL, Burgart LJ, Koyama T, Johnson CD, Stephens DH, Ward EM, Harmsen WS. Pancreatic malignancy: value of arterial, pancreatic, and hepatic phase imaging with multi-detector row CT. Radiology. 2003;229(1):81–90.

Forman MA, Marks SL, De Cock HE, Hergesell EJ, Wisner ER, Baker TW, Kass PH, Steiner JM, Williams DA. Evaluation of serum feline pancreatic lipase immunoreactivity and helical computed tomography versus conventional testing for the diagnosis of feline pancreatitis. J Vet Intern Med. 2004;18(6):807–15.

Head LL, Daniel GB, Tobias K, Morandi F, DeNovo RC, Donnell R. Evaluation of the feline pancreas using computed tomography and radiolabeled leukocytes. Vet Radiol Ultrasound. 2003;44(4):420–8.

Iseri T, Yamada K, Chijiwa K, Nishimura R, Matsunaga S, Fujiwara R, Sasaki N. Dynamic computed tomography of the pancreas in normal dogs and in a dog with pancreatic insulinoma. Vet Radiol Ultrasound. 2007;48(4):328–31.

Jaeger JQ, Mattoon JS, Bateman SW, Morandi F. Combined use of ultrasonography and contrast enhanced computed tomography to evaluate acute necrotizing pancreatitis in two dogs. Vet Radiol Ultrasound. 2003;44(1):72–9.

Kishimoto M, Tsuji Y, Katabami N, Shimizu J, Lee KJ, Iwasaki T, Miyake Y, Yazumi S, Chiba T, Yamada K. Measurement of canine pancreatic perfusion using dynamic computed tomography: influence of input-output vessels on deconvolution and maximum slope methods. Eur J Radiol. 2011;77(1):175–81. doi:10.1016/j.ejrad.2009.06.016.

Lidbury JA, Suchodolski JS. New advances in the diagnosis of canine and feline liver and pancreatic disease. Vet J. 2016;215:87–95. doi:10.1016/j.tvjl.2016.02.010.

Linderman MJ, Brodsky EM, de Lorimier LP, Clifford CA, Post GS. Feline exocrine pancreatic carcinoma: a retrospective study of 34 cases. Vet Comp Oncol. 2013;11(3):208–18. doi:10.1111/j.1476-5829.2012.00320.x.

Mai W, Cáceres AV. Dual-phase computed tomographic angiography in three dogs with pancreatic insulinoma. Vet Radiol Ultrasound. 2008;49(2):141–8.

Marolf AJ. Computed tomography and MRI of the hepatobiliary system and pancreas. Vet Clin North Am Small Anim Pract. 2016;46(3):481–97, vi. doi:10.1016/j.cvsm.2015.12.006.

Ramírez GA, Altimira J, García-González B, Vilafranca M. Intrapancreatic ectopic splenic tissue in dogs and cats. J Comp Pathol. 2013;148(4):361–4. doi:10.1016/j.jcpa.2012.08.006. Epub 2012 Oct 11

Seaman RL. Exocrine pancreatic neoplasia in the cat: a case series. J Am Anim Hosp Assoc. 2004;40(3):238–45.

The Urinary System

Giovanna Bertolini

1 Introduction

The diffusion of MDCT in veterinary practice has changed approaches to many urinary tract disorders, such as urolithiasis, renal masses, and mucosal abnormalities of the renal collecting system, ureters, and bladder. As MDCT has become more widely available, CT urography has begun to replace other imaging techniques, such as plain-film radiography and excretory urography, because it enables accurate depiction of the renal collecting systems through thinner-section imaging, more rapid scanning, improved longitudinal spatial resolution, and the consequent acquisition of high-quality reformatted multiplanar and 3D images. Moreover, qualitative and quantitative assessment of renal and excretory function is possible using dynamic CT and most advanced perfusion imaging techniques. One of the clinical applications of dual-energy (DE) CT is the spectral analysis of urinary calculi (see below in this chapter).

2 MDCT Imaging Strategies

MDCT imaging of the urinary system encompasses different scan protocols, depending on the clinical suspicion and the structures and functions to be assessed. The most frequent indications for MDCT examination of the urinary system in small animals are congenital ureteral anomalies, urolithiasis, suspected urinary tract disruption in trauma patients, and renal and urinary bladder cancer. As for many

G. Bertolini (✉)
San Marco Veterinary Clinic, Padua, Italy
e-mail: bertolini@sanmarcovet.it

G. Bertolini (ed.), *Body MDCT in Small Animals*, DOI 10.1007/978-3-319-46904-1_9

Fig. 1 Patient positioning for urinary system examination

other situations, MDCT examination of the urinary system requires scan individualization, due to significant differences among species and in animal size.

Patient positioning is particularly important for the examination of the urinary collecting system (ureters and urinary bladder). Patients should be examined in sternal recumbency with the pelvis elevated on a wedge with a 5°–10° angle (Fig. 1).

A pre-contrast, low-voltage scan should be always performed to detect mineralization, urolithiasis, or hemorrhage in the renal and collecting systems. This series should include the pelvis and perineal region, for complete evaluation of the urethra. A MDCT urographic technique targeting the imaging of the distal collecting system in non-pathological patients has been described recently. The bolus tracking technique, with the region of interest placed within the distal ureters to track their maximum opacification, has been adopted for the visualization of the ureterovesicular junction of normal dogs. This technique is not indicated for comprehensive renal or abdominal examination, and its applicability in patients with urinary tract illness should be tested.

For comprehensive evaluation of the kidneys and collecting system in a single examination, a multiphasic approach should be adopted to obtain various vascular phases and urogram-like series of excellent quality. CT-contrast medium (CM) normally used is uroangiographic, meaning that it is eliminated continuously through the urinary system. A single CM bolus (possibly followed by the same quantity of saline) can be injected for a combined three- or four-phase study with corticomedullary (angiographic), nephrographic (parenchymal), and excretory (early and late) phase series (Fig. 2).

Moreover, a multiphasic approach allows simultaneous evaluation of other organs for staging, in cases of cancer. Increasing the saline fluid supplement to the patient before and during the examination will help to distend the urinary bladder rapidly. The corticomedullary (or angiographic) phase of enhancement is

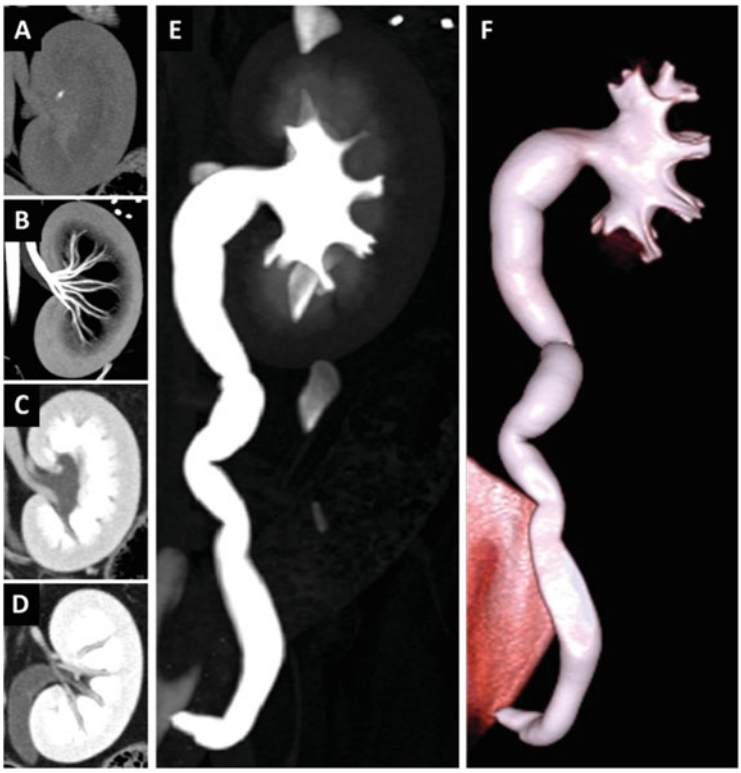

Fig. 2 MDCT uroangiography in a dog with urinary calculi and secondary ureteral and pyelic distension. (**a**–**d**) Dorsal views of the left kidney in the pre-contrast, corticomedullary or arterial (thin-slab MIP), nephrographic, and excretory phases. (**e**) Dorsal 10-mm-slab MIP obtained in the excretory phase. (**f**) VR of the same volume

useful for renal vascular evaluation. Preoperative knowledge of the renal vascular anatomy is important for selection of the appropriate feline renal donor and for partial nephrectomy. This phase is not optimal for the evaluation of small parenchymal lesions and not indispensable for the evaluation only of the collecting system. In the nephrographic (or venous or parenchymal) phase, the renal cortex and medulla are enhanced uniformly, and CM has not yet entered the renal collecting system. In cases of scanner limitation due to tube heating, this series can be restricted to the renal region. Nephrographic phase imaging has the greatest sensitivity in the detection of renal masses. The excretory (or pyelographic or urographic) phase generally occurs 5–20 min after CM administration. In this phase, while the intensity of the nephrogram declines, CM excretion results in opacification of the renal pelvis and ureters and, later, the urinary bladder. Partial bladder voiding (with gentle pressure or furosemide administration) with the patient positioned on the CT table leads to complete opacification of the urethra as well.

Alternatively, CT retrograde urethrography, with luminal distention by iodine CM, may be performed.

3 Normal Variants and Congenital Anomalies

Congenital renal anomalies and renal vasculature variants are commonly seen during MDCT examination and often discovered incidentally. However, certain types of anomaly and variant can cause clinical signs, and MDCT plays a pivotal role in their definitive diagnosis.

Unilateral or bilateral *renal agenesis* has been reported in dogs and cats and is often accompanied by other anomalies of the urinary and reproductive tracts, given their close developmental association. Therefore, the two systems must be evaluated thoroughly in these patients. In cases of unilateral renal agenesis, compensatory hypertrophy of the contralateral kidney, which appears larger than normal, is common. In unilateral renal agenesis, MDCT shows the absence of the kidney, renal vessels, and ipsilateral collecting system (Figs. 3 and 4). *Hypoplastic kidney* may result from developmental disorders and should be differentiated from acquired atrophy, in which the kidney is irregularly small and contracted (Fig. 5).

Variants of the renal vasculature are very common in mammals and have been described in dogs and cats. In most cases, these variants have no clinical

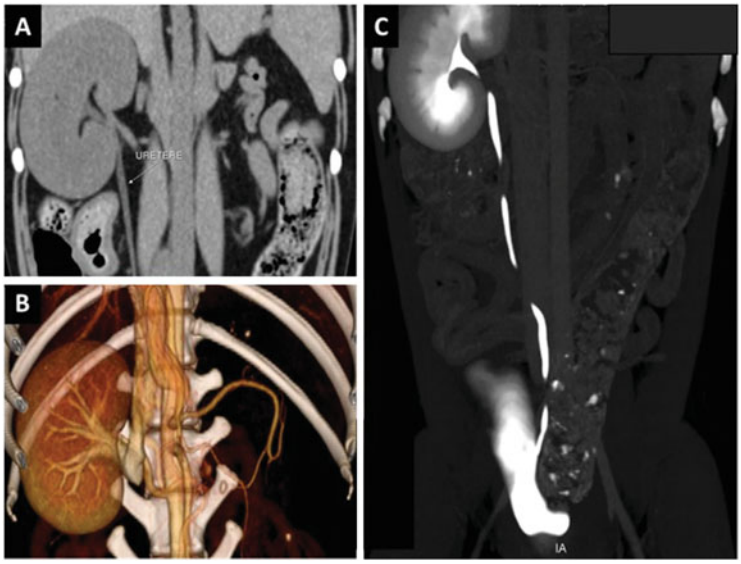

Fig. 3 Unilateral renal agenesis in a dog. (**a**) Pre-contrast image showing the right kidney and ipsilateral ureter represented normally. (**b**) Volume-rendered image showing moderate compensatory hypertrophy (subjectively enlarged) of the right kidney secondary to the absence of the left kidney. (**c**) Excretory-phase image showing the complete absence of the left kidney and ipsilateral ureter

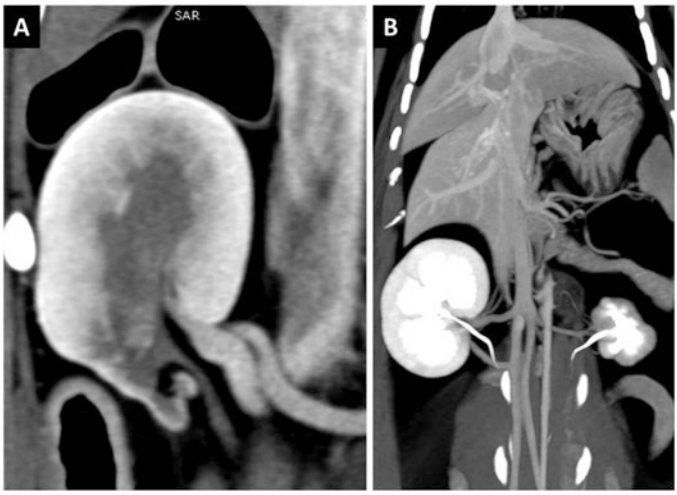

Fig. 4 (**a**) Congenital partial renal hypoplasia in a puppy. (**b**) Unilateral renal hypoplasia in a young rag doll cat

consequence, but knowledge of their existence may be relevant for the planning of surgery in the renal region. The renal artery commonly bifurcates into dorsal and ventral branches (variable in number), which supply the cranial and caudal portions of the kidney. The presence of double renal arteries at one or both sites is a frequent finding on MDCT images. The number of renal veins can also vary. In vivo CT studies have shown that such variation is more likely in the right kidney (Fig. 6). Congenital vascular anomalies of the prerenal and renal segments of the caudal vena cava can lead to the incarceration of one or both ureters. This anomaly is referred to as "retrocaval ureter" (or, more properly, preureteral vena cava) and can be seen with a normal right-sided vena cava or in association with a left-sided or duplicate vena cava (Figs. 7 and 8).

Excretory tract anomalies may involve one or more segments, from the renal pelvis to the urinary bladder, and the urethra. Normal ureters enhance rapidly (1–2 min) after intravenous CM injection and show multi-segmented opacification, reflecting their normal peristaltic activity. An *ectopic ureter (EU)* is the most common cause of urinary incontinence in female dogs and is probably the congenital defect seen most commonly on MDCT. EU has traditionally been considered to be rare in male dogs, but recent reports suggest that this diagnosis may be more common than previously suspected. EU in cats has been described rarely. Ureteral ectopia refers to the abnormal caudal migration of the ureteral bud, resulting in terminal ureteral opening at a site other than the bladder trigone. An *extramural EU* bypasses the bladder and opens directly into the urinary tract, distal to the trigone in the bladder neck or urethra, or directly into the vagina or vestibule. Most commonly, EUs enter the bladder wall at the level of the trigone, pass distally within the wall of the urethra (intramural EU), and then open in the urethra distal to the

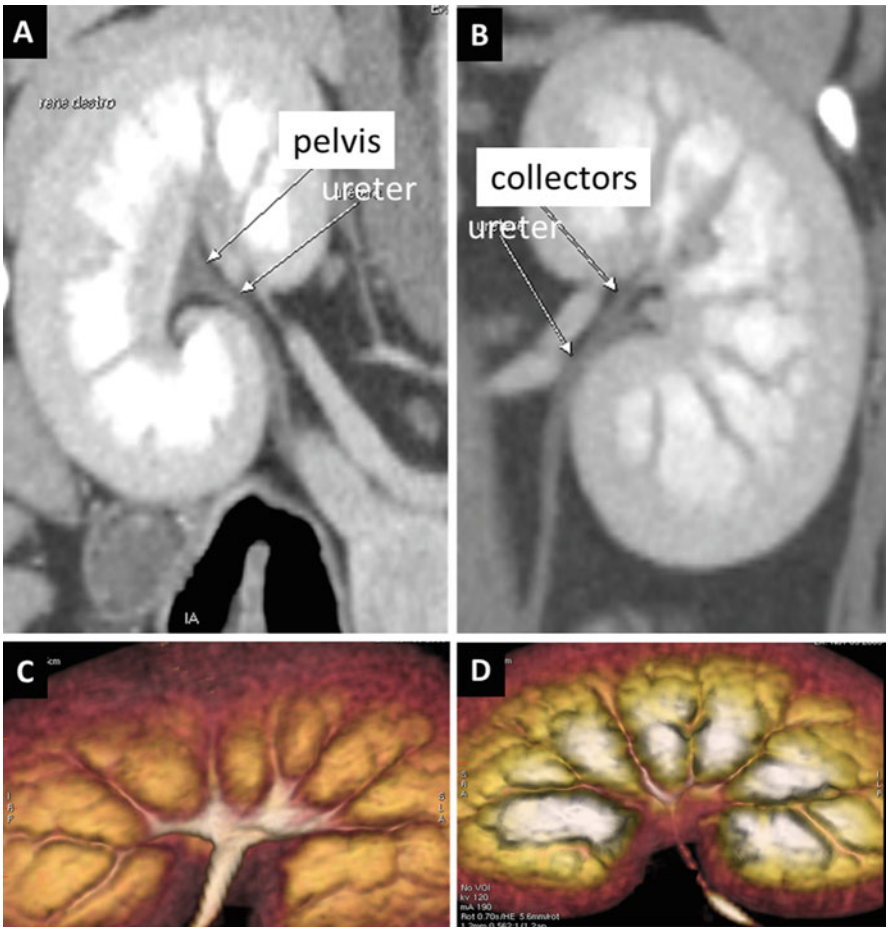

Fig. 5 (**a**, **b**) Dorsal MPR images from 16-MDCT urography in a dog with hematuria. (**a**) Image of the right kidney obtained in the nephrographic phase. Note the normal representation of the pelvis and ureter. (**b**) Image of the left kidney in the same dog. Note the absence of the pelvis. The collectors empty directly into the ureter. (**c**, **d**) Volume-rendered images of the same kidneys

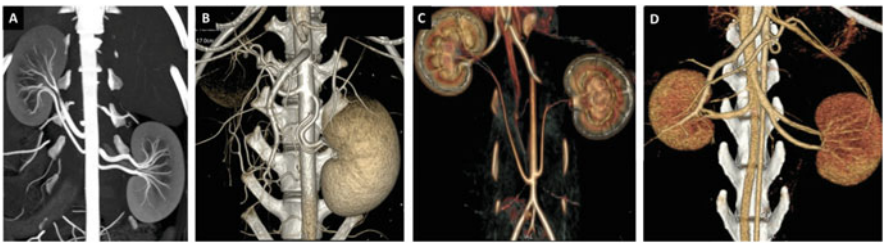

Fig. 6 Various renal variants in dogs and cats. (**a**) Bilateral duplication of the renal arteries in a dog. (**b**) Duplicated left renal artery and single right renal artery in a dog. (**c**) Ectopic caudal-sided renal arteries in a cat. (**d**) Duplication of the left renal vein in a cat

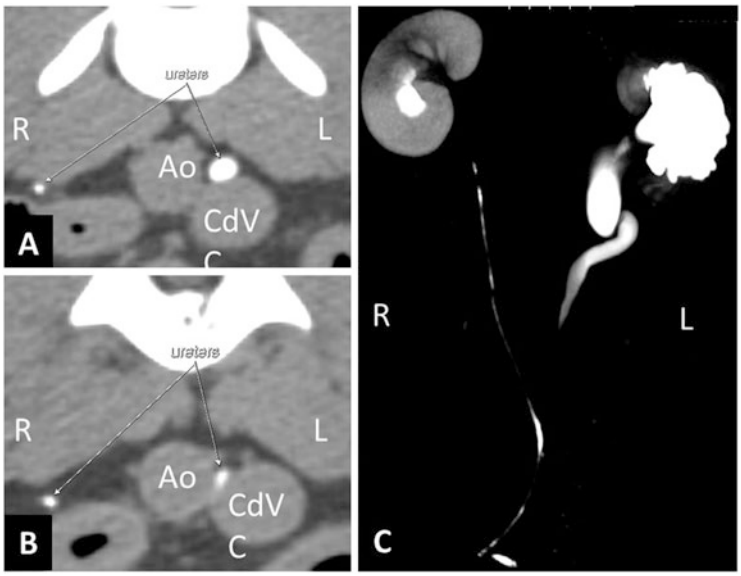

Fig. 7 Retrocaval ureter (preureteral vena cava) in a dog with the left prerenal segment of the caudal vena cava. (**a**) Transverse image showing the dilated left ureter just cranial to the point of stenosis, between the aorta and left vena cava (**b**). (**c**) MIP image obtained in the excretory phase showing the normal right ureter and dilated renal pelvis and ureter

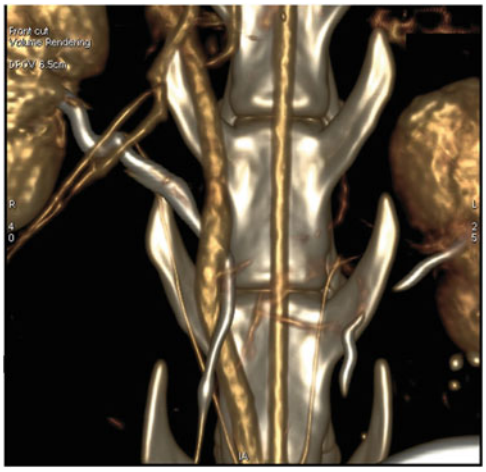

Fig. 8 Retrocaval ureter (preureteral vena cava) with a normal right-sided cava in a cat. Note the moderate distension of the right ureter compared with the contralateral structure

urethral sphincter (Fig. 9). In other cases, EUs terminate in the vagina, cervix, or uterus. Ipsilateral hydronephrosis and hydroureter are present. The ureter has a tortuous appearance and enhances late (5–30 min) after CM injection. Bilateral

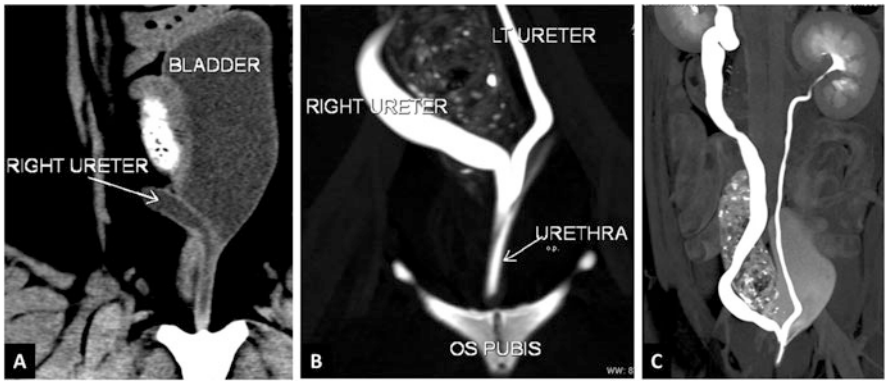

Fig. 9 Bilateral ureteral ectopia in a dog. Both ureters open directly into the urethra

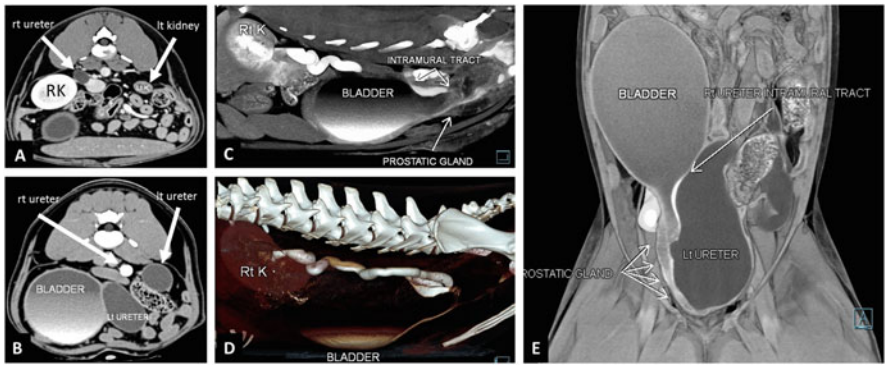

Fig. 10 Bilateral ureteral ectopia in a dog. (**a**) Transverse view of the abdomen. The left kidney is small and not normally perfused (renal hypoplasia). *RK* right kidney. (**b**) Transverse view of a more caudal region. Both ureters are enlarged. (**c**) Parasagittal MPR view showing the intramural tract at the neck of the urinary bladder, which opens into the prostatic segment of the urethra. (**d**) Volume-rendered image showing the tortuous aspect of the right ureter. (**e**) Dorsal thin volume-rendered image of the abdomen. The left urinary ureter shows noticeable enlargement and opens into the prostatic urethra

ectopia of the ureteral orifices has been reported to occur more frequently than does unilateral ectopia. Other urogenital anomalies, such as a short urethra, indistinct vesicourethral junction resulting in low urethral closure pressure, and vaginal and vestibular abnormalities, may coexist. Abnormal development of the kidney (single agenesis, renal hypoplasia, dysplasia) is encountered in some dogs with EU (Fig. 10). *Ureteroceles*, which are cystic dilatations of the submucosal portion of the distal ureter, may be present in dogs with EU or may be found alone (Fig. 11). They are classified into two types according to their location and that of the ureteral orifice: orthotopic or intravesical and ectopic. An orthotopic ureterocele has an orifice that communicates with the urinary bladder. Ectopic ureteroceles are associated with ectopic ureters and thus are located in the urethra or neck of the urinary bladder. Ureteroceles may be asymptomatic, but when enlarged they can cause

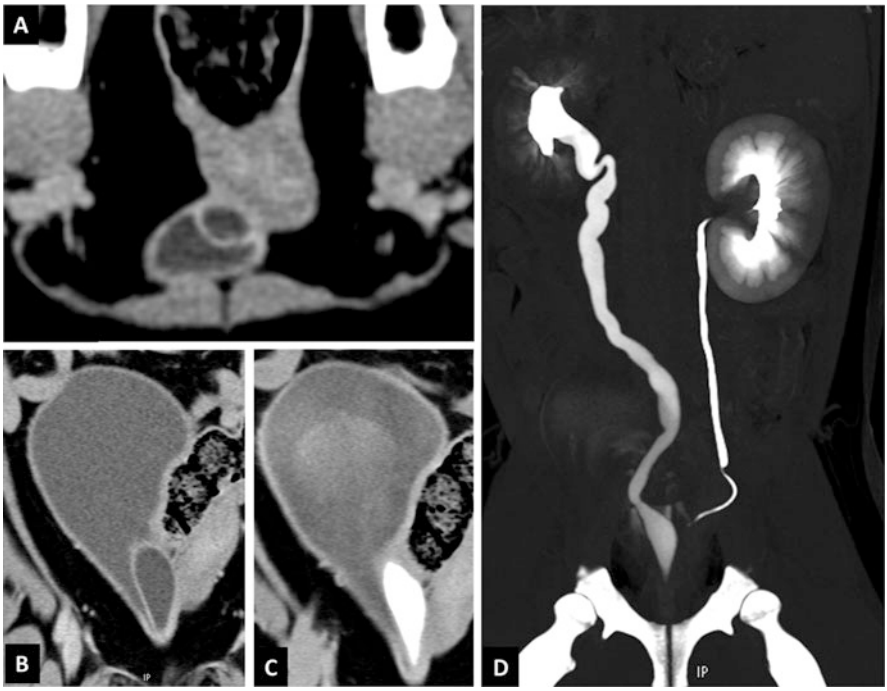

Fig. 11 Ureterocele in a dog with urinary incontinence. (**a**) Transverse view showing cystic dilatation of the submucosal portion of the right distal ureter. (**b**, **c**) Dorsal views obtained in the pre-contrast and excretory phases showing the ureterocele terminating into the neck of the bladder (ectopic). (**d**) MIP image obtained in the excretory phase showing right hydroureter and hydronephrosis. The left kidney and collecting system are represented normally

complications such as hydronephrosis, infection, lithiasis, and urinary incontinence.

Duplication of the urinary bladder or the urethra has been described in dogs. A second urethra can originate from the bladder, bladder neck, or prostatic urethra.

4 Urolithiasis

Urolithiasis is a common condition responsible for lower urinary tract disease in dogs and cats. Some uroliths produce no clinical sign and may be discovered incidentally during MDCT examination. A urolith may be defined as the aggregation of crystalline and matrix materials in one or more locations within the urinary tract. These entities are found most commonly in the urinary bladder (urocystolith) but can also be found in the urethra (urethrolith), ureters (ureterolith), and kidneys (nephrolith) (Fig. 12). Uroliths range in size from sand-like material to large individual stones, which may grow to fill the entire cavities in which they form.

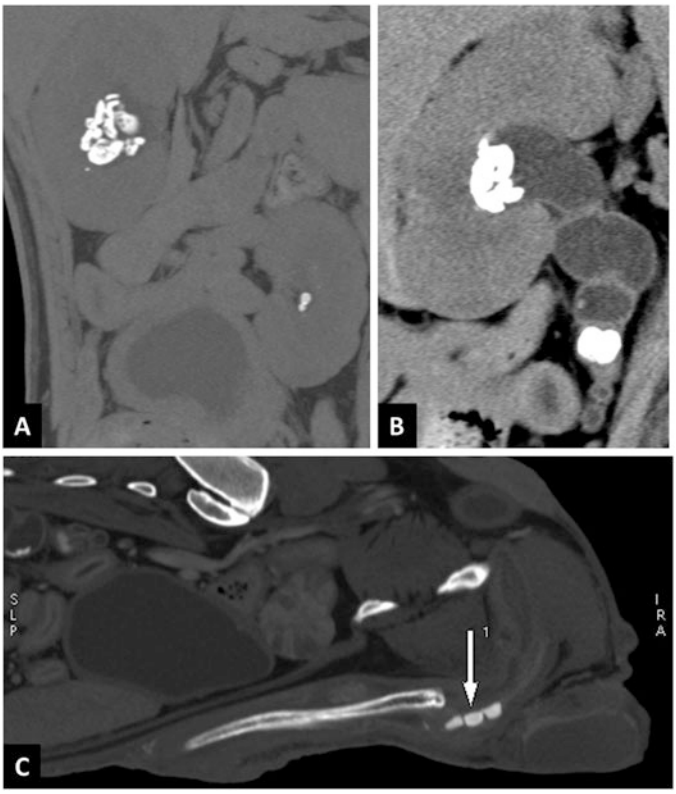

Fig. 12 Urinary calculi. (**a**) Pre-contrast image of a dog with bilateral nephroliths. (**b**) Pre-contrast image showing some nephroliths and a large ureterolith obstructing the ureter. (**c**) Sagittal view showing uroliths in the urethra peniena in a male dog

Uroliths that form in cats and dogs (and humans) can be grouped into four main mineral types: urate (ammonium urate, sodium urate, uric acid), cystine, magnesium ammonium phosphate (struvite), and calcium (calcium oxalate, calcium phosphate).

In most cases, the definitive diagnosis of urolithiasis requires MDCT examination of the entire length of the urinary tract to identify the presence of uroliths, determine whether they are in multiple locations, and identify any factor predisposing the patient to urolith formation, such as infection or neoplasia. MDCT is required for the planning of interventional or surgical therapy and in cases of complication, such as ureteral rupture. MDCT is particularly useful for ureterolith detection. Knowledge of the stone's location and its site of impaction in the ureter is very important for therapeutic management. Direct visualization of the stone in the ureteric lumen with proximal ureteral dilatation and normal caliber of the distal ureter is a common CT finding. Other secondary signs, such as perinephric fat stranding, periureteral edema, hydroureter, and hydronephrosis, aid the diagnosis of ureteral stones.

5 DECT Analysis of Urinary Calculi

MDCT can provide accurate submillimetric information on urolith location and size but is not a robust technique for the determination of urinary stone composition. As demonstrated by several studies in humans, CT cannot be used to predict the composition of urinary stones on the basis of differences in radiodensity and appearance.

Reliable and accurate characterization of urinary stone composition is now possible using DECT techniques. These methods utilize the attenuation difference produced by two different X-ray energy spectra to quantify urinary calculus composition while still providing the information attained with conventional CT. The basic principle is that two materials with similar attenuation values on CT but different chemical compositions can be distinguished from one another by analyzing their energy-dependent changes in attenuation. The degree of material separation (and thus the performance of the technique) depends on the spectral separation between high- and low-energy X-rays and accurate temporal registration and spatial correlation. Various CT vendors have developed different technical solutions. Most advanced MDCT scanners with single energy sources (X-ray tubes, e.g., Discovery CT 750 HD, GE Healthcare, Milwaukee, WI, USA) can switch rapidly (within $<$0.5 ms) from 80 to 140 kVp during the same tube rotation. DSCT scanners (e.g., SOMATOM Definition Flash and Force, Siemens Healthineers, Forchheim, Germany) have two X-ray tubes and two detector systems arranged at an angle of approximately 90°. DE-DSCT enables simultaneous acquisition of the same volume at different energy levels (100–140 and 150 kV) with a high degree of temporal resolution (see also Part I "MDCT technics and technology" for further description). It also allows for the use of different arrangements of tube current, which is important for the minimization of radiation exposure while maintaining optimal spectral separation (crucial for the determination of stone composition) and image quality (noise reduction). In the human radiology literature, the reported accuracy of DE-DSCT in distinguishing the composition of stones $\geq$3 mm is nearly 100%. No in vivo DECT study of urinary calculi in dogs and cats is currently available. Preliminary studies performed at our center using a second-generation DSCT scanner (SOMATOM Definition Flash) have yielded similar results in dogs and cats (Fig. 13). The generation of images based on changes in attenuation at different energy levels requires the use of dedicated post-processing software techniques and workstations for analysis. Post-processing techniques for DE-MDCT and DE-DSCT differ. In any case, in addition to anatomic and morphological characterization (based on attenuation values, homogeneity, volume), the software creates color-coded images using information from both energies (e.g., materials with behavior similar to calcium appear blue and those with behavior similar to urate appear red).

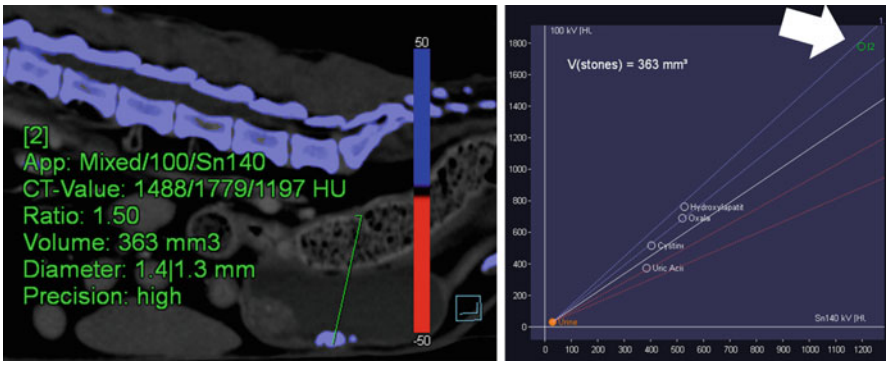

Fig. 13 DECT characterization of urinary calculi in a dog

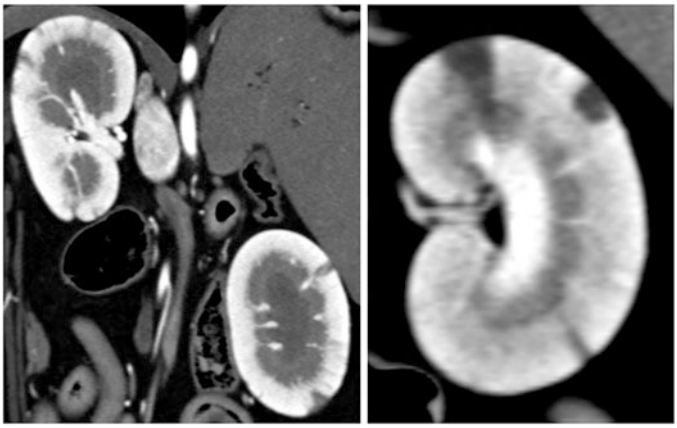

Fig. 14 Renal infarcts. Bilateral wedge-shaped infarcts in a dog

6 Renal Infarction

Renal infarction occurs in dogs and cats in a variety of clinical settings. Renal infarcts appear on MDCT as one or more focal, wedge-shaped parenchymal defects that involve the cortex and medulla, often with a typical triangular appearance (Fig. 14). They are best detected in the corticomedullary (or angiographic arterial) phase. In acute renal infarction, occluded renal artery branches may be identified in this vascular phase (Figs. 15 and 16). However, in most cases, small parenchymal arteries are affected and occlusion is thus difficult to detect. Acute renal infarction and acute pyelonephritis may have similar CT features, making them difficult to distinguish. However, most cases of acute renal infarction involve no perinephric

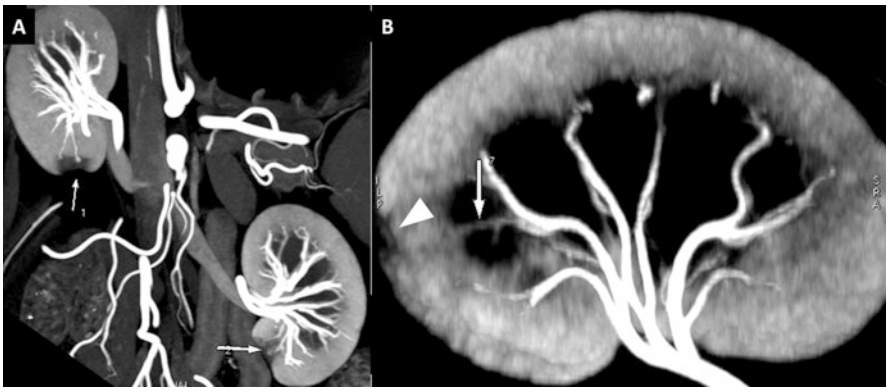

Fig. 15 (**a**) Acute bilateral renal infarcts (*arrow*) in a dog with hypercoagulable state. Angiographic (corticomedullary) phase. (**b**) *Arrow* indicates a thrombosed subsegmental artery. *Arrowhead* indicates the dependent infarcted area

Fig. 16 Renal infarction in a patient with metastatic lung carcinoma

tissue changes (i.e., fat stranding) or retroperitoneal effusion, which are visible in acute pyelonephritis. In humans, a thin rim of enhancing cortical tissue representing collateral vessel perfusion peripheral to the infarcted, unperfused area (the "cortical rim sign") is a key feature differentiating this condition from inflammatory disease. This sign is also sometime appreciable in dogs (Fig. 17).

Chronic renal infarcts are encountered more commonly in veterinary patients and can result in segmental parenchymal atrophy and changes in renal shape and contour (Fig. 18).

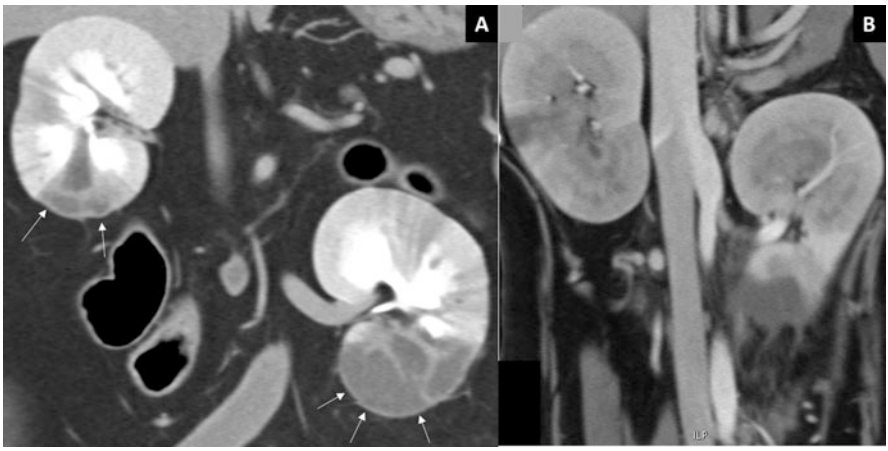

Fig. 17 (**a**) Bilateral renal infarction in a dog with metastatic prostatic carcinoma. Note the "cortical rim sign" (*arrows*) representing collateral vessel perfusion. (**b**) Acute pyelonephritis in a dog with systemic mycobacteriosis. Note the perinephric retroperitoneal effusion (at the caudal pole of the left kidney)

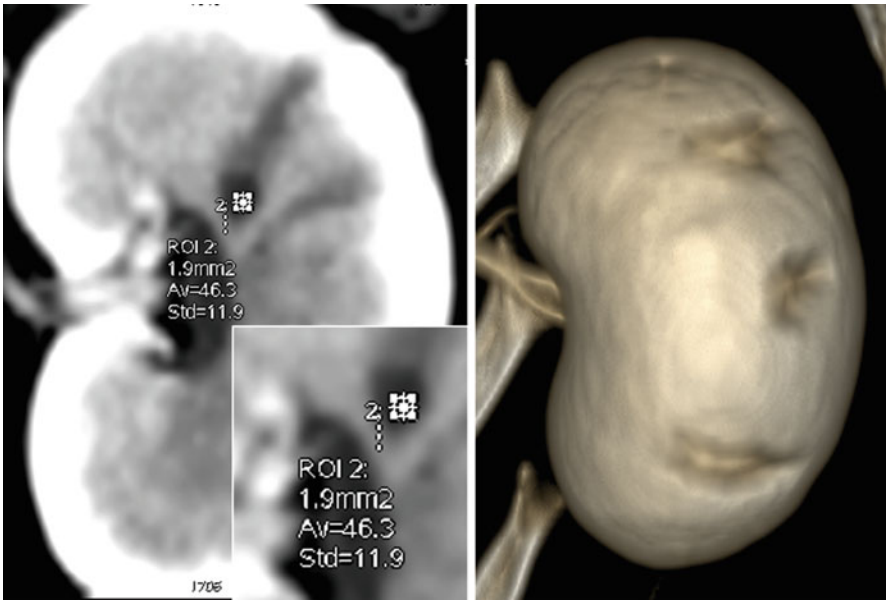

Fig. 18 Chronic renal infarcts in a dog (46.3 HU). 3D volume-rendered image shows changes in the renal surface

7 Renal Cysts

Renal cysts are encountered frequently on MDCT examination. They can be detected on pre-contrast images, but are best characterized in the nephrographic phase of enhancement (Fig. 19). Renal cysts may be congenital or acquired, solitary or multiple, and unilateral or bilateral. They can be small, located in the renal parenchyma, resulting in no change in renal size or shape. Larger cysts located in the outer renal cortex can protrude on the renal surface, resulting in overall renal shape distortion (Fig. 20).

In dogs, benign renal cysts are usually small, solitary, and detected incidentally during imaging evaluation. True cysts have epithelial cell membranes separating them from the surrounding tissue. On MDCT images, they appear to be composed

Fig. 19 Multiphasic examination of the kidney in a dog with a single cyst. Corticomedullary (**a**), nephrographic (**b**), and excretory (**c**) phases. The cyst is more conspicuous in the nephrographic phase

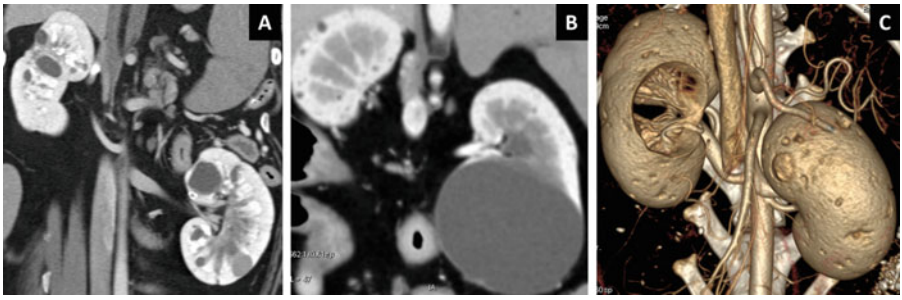

Fig. 20 Various examples of bilateral renal cysts in dogs. (**a**) Dorsal MPR image of a dog with multiple bilateral renal cystic changes. (**b**) Dorsal MPR from a dog with a large cyst at the caudal pole of the left kidney, protruding onto the renal surface. Note various other small cysts in both kidneys. (**c**) Volume-rendered image of a dog with multiple renal cysts, showing overall renal distortion

entirely of low-attenuation (0–20 HU) fluid, surrounded by thin smooth walls, with no enhancement after CM injection (Fig. 21). Renal pseudocysts have walls consisting of granulation and/or fibrous tissue as a result of inflammation and may show peripheral enhancement and inhomogeneous content that may be related to hemorrhage or cellular debris.

Congenital polycystic kidney disease is the most common inherited renal disease in cats. It has been described in Persian and Persian-cross cats. In affected cats, multiple cysts form in both kidneys and occasionally in the liver. Renal cysts arise from tubules and occur in the cortex and medulla. They can be detected incidentally in cats at any age and occur in various numbers, sizes, and distributions, as they form early in life and gradually become more numerous and larger. Autosomal polycystic renal disease has been reported also in bull terrier, Carin terrier, and

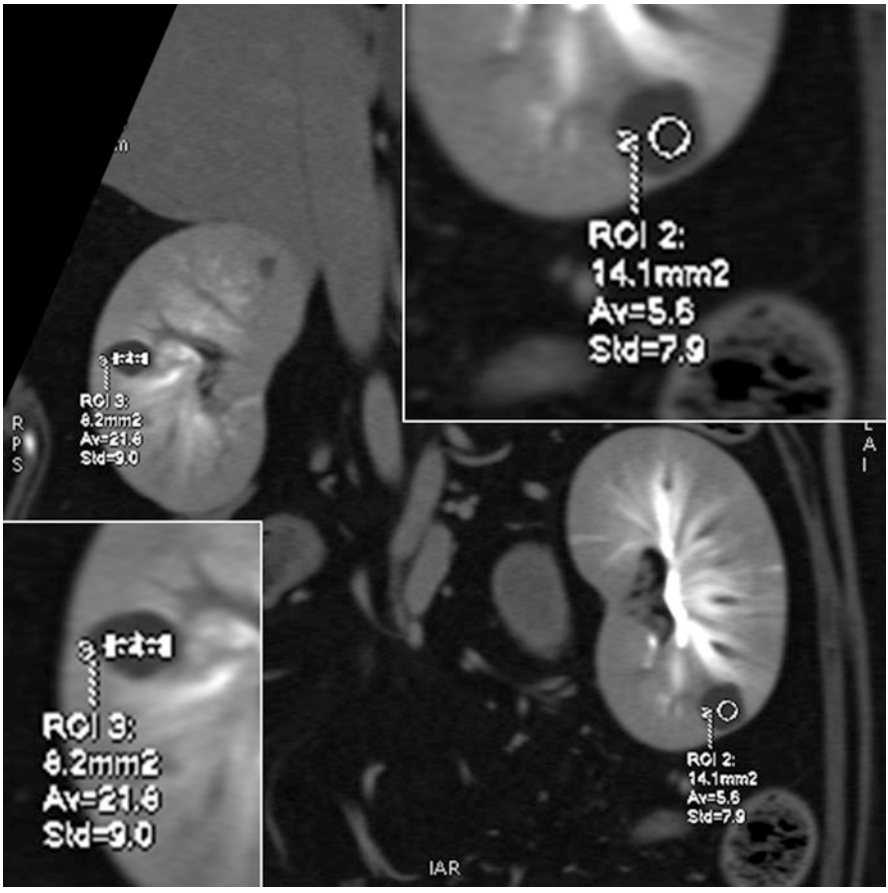

Fig. 21 Bilateral renal cysts in a dog. Post-contrast image (excretory phase). The lesions are hypoattenuating and not enhanced. The attenuation values of the cysts are 5.6 HU (*left*) and 21.8 HU (*right*)

West Highland white terrier dogs (Fig. 22). CT detection of malignant renal cysts in a German shepherd with hereditary renal multifocal cystadenocarcinoma has been described.

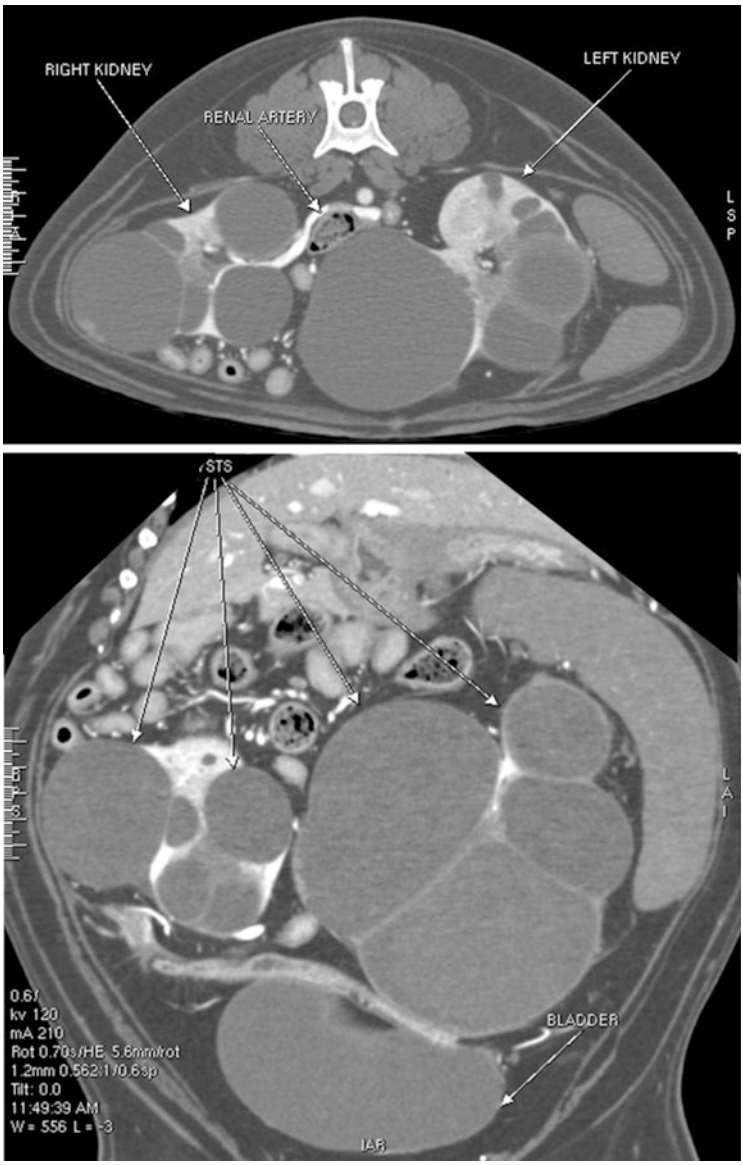

Fig. 22 Transverse and dorsal MPR views of the abdomen of an English bulldog with polycystic renal disease

8 Renal Masses

Primary tumors are rare in dogs and cats and are usually malignant. Metastatic tumors in the kidneys are also rare. Although most renal masses can be evaluated with ultrasound, CT is considered to be superior for the evaluation of relationships in complex lesions and is necessary for staging in oncology patients. All malignant primary renal tumors are associated with a significant risk of metastasis to other regions of the body. Whole-body MDCT can be used to detect regional and distant metastasis.

The most common renal tumors in dogs are carcinomas (including renal cell carcinoma, transitional cell carcinoma [TCC], and anaplastic carcinoma); lymphoma is the most common renal carcinoma in cats (Figs. 23, 24, 25, and 26). Renal lymphoma is encountered in dogs, but whether these cases represent primary or multicentric disease is difficult to determine. Renal cell and other carcinomas tend to be highly invasive into surrounding structures, including other organs and blood vessels (Fig. 27). Other primary renal tumors that can arise in the kidney are

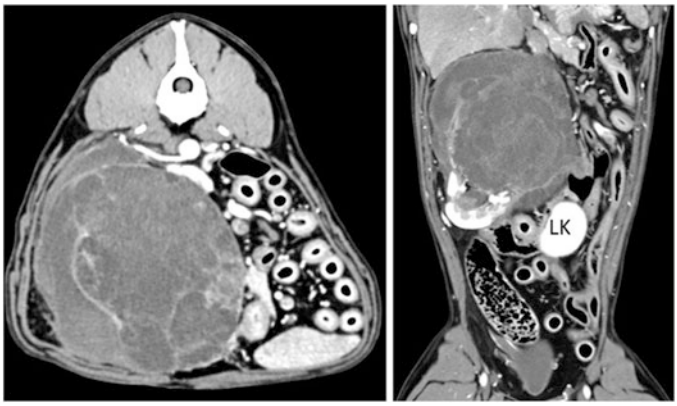

Fig. 23 Renal adenocarcinoma of the right kidney in a 10-year-old mongrel dog (transverse and dorsal MPR views from the HAP). *LK* left kidney

Fig. 24 TCC of the right kidney and ureter in an English bulldog. (**a**) Transverse view. (**b**) Dorsal MPR view. (**c**) Transverse section of the right ureter

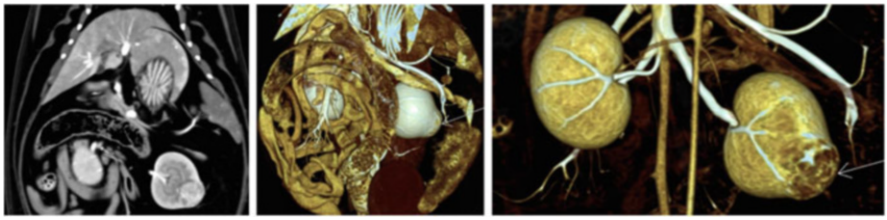

Fig. 25 Renal tubular carcinoma in a domestic shorthair cat. CT study for partial nephrectomy

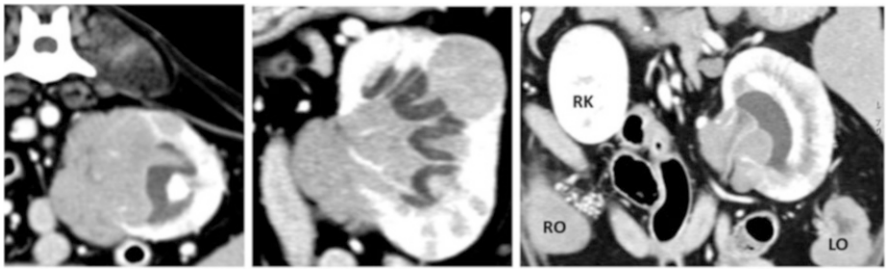

Fig. 26 T-cell lymphoma of the left kidney, also involving the ovaries, in a female mongrel dog. *RK* right kidney, *RO* right ovary, *LO* left ovary

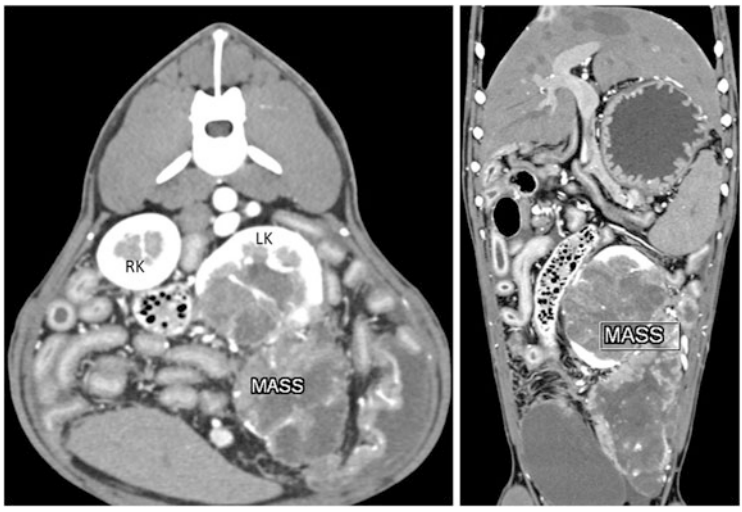

Fig. 27 Renal carcinoma of the left kidney, showing peritoneal involvement, in a dog

hemangiosarcoma, anaplastic sarcoma, and nephroblastoma. Metastatic renal cancer from other sites is more common than primary tumor (Figs. 28 and 29).

Renal tumors are generally seen in mature patients. Nephroblastoma, however, occurs most commonly in young dogs. This tumor arises from the embryonic

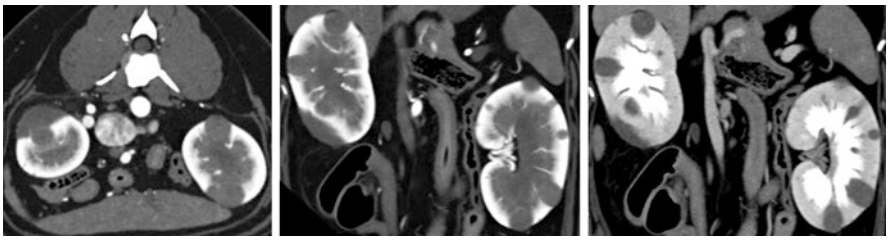

Fig. 28 Renal metastases of melanoma. Transverse view is from the angiographic phase. Dorsal MPRs are obtained in the angiographic and nephrographic phases

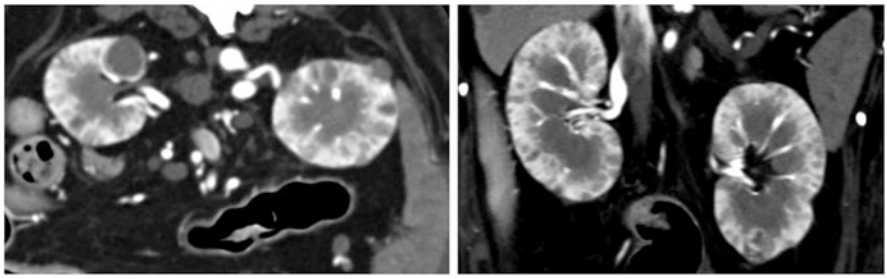

Fig. 29 Renal metastases of splenic hemangiosarcoma in a dog

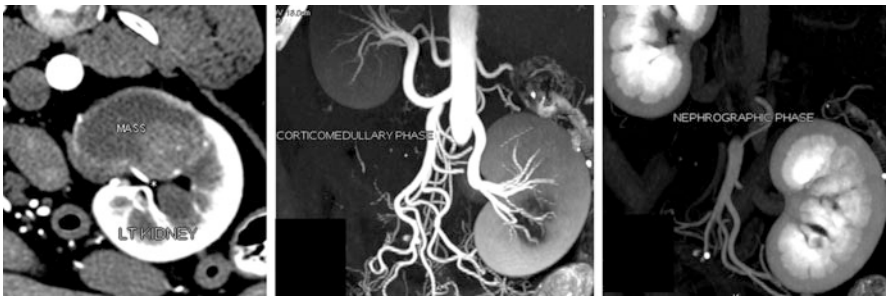

Fig. 30 Renal adenoma of the left kidney in a dog. The mass has well-defined margins and does not affect the renal vascular structures

remnants of the immature kidney and has been reported to involve the kidney and/or spinal cord. A hereditary syndrome of nodular dermatofibrosis associated with renal cystadenocarcinoma, and accompanied by uterine tumors in females, has been identified in German shepherds, golden retrievers, boxers, and mixed-breed dogs. The CT findings and gross pathology of cystadenocarcinoma in dogs are strongly correlated, as CT enables easy distinction of solid and cystic lesions within the renal parenchyma.

Benign renal tumors, such as adenoma or hemangiomas, are even rarely reported than malignant tumors (Figs. 30 and 31).

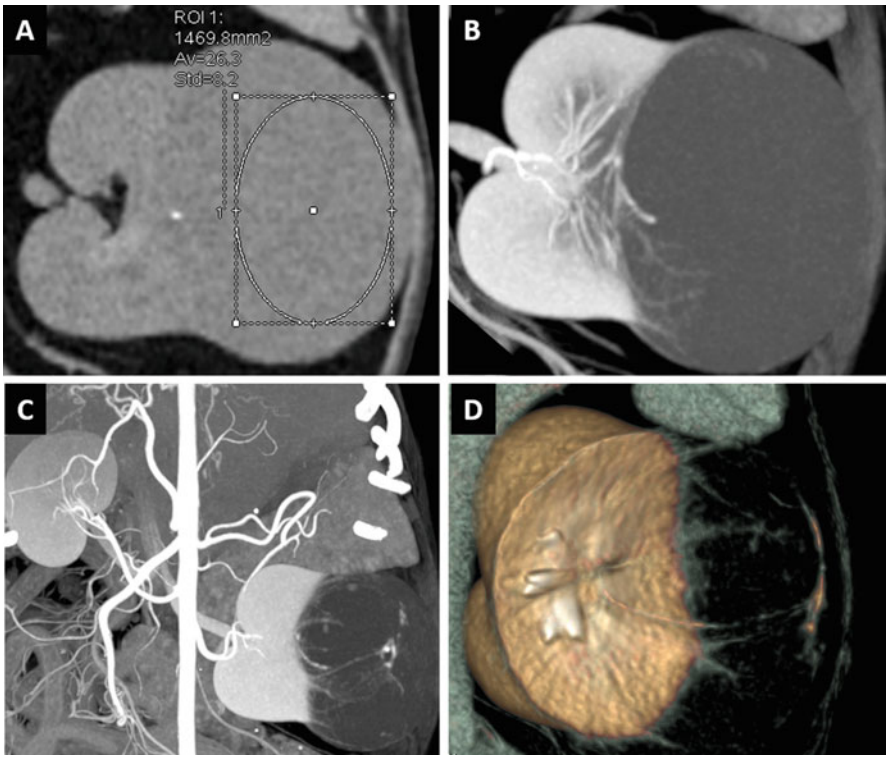

Fig. 31 Renal tubular adenoma in a beagle. (**a**) Pre-contrast image (26.3 HU). (**b**) Corticomedullary/angiographic phase image showing no enhancement of the mass. (**c**) Thin-MIP image from the same phase. Note the stretched capsular vessels. (**d**) Volume-rendered image showing compression of the renal parenchyma by the mass (not visible here)

9 Lower Urinary Tract Masses

Neoplasms of the ureters, bladder, and urethra are uncommon in dogs and rare in cats. Among primary malignant neoplasms of the lower urinary tract, TCC is diagnosed most frequently in both species. TCC is an aggressive solitary or multiple tumor that affects the urinary bladder. On CT, it may present as focal regions of bladder wall thickening, or as masses protruding into the bladder lumen (Figs. 32, 33, 34, 35, and 36). It often invades the urethra or ureters. Rarely, it involves the serosa of the bladder and infiltrates surrounding tissues. TCC can cause

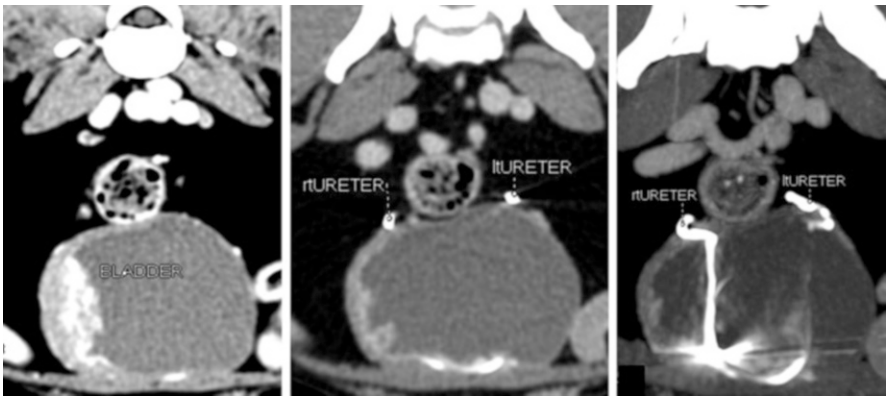

Fig. 32 Urinary bladder TCC (nonobstructing) in a dog

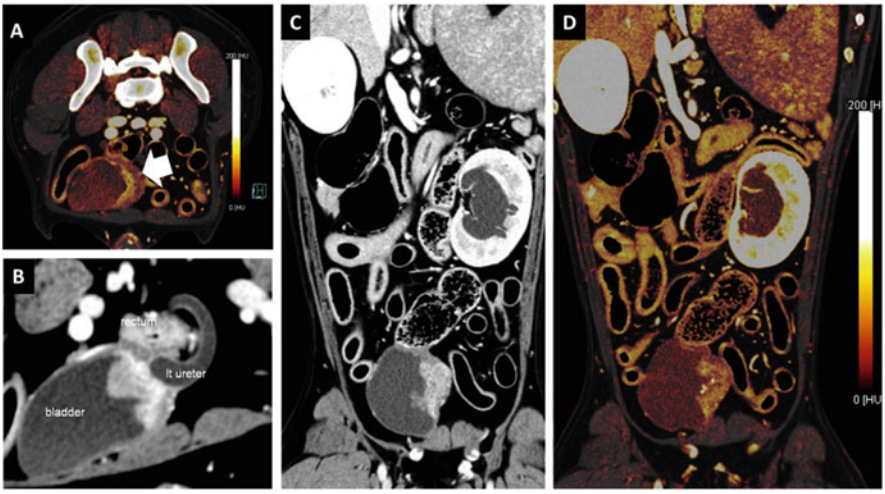

Fig. 33 Urinary bladder TCC in a dog, with partial obstruction of the left ureter and ipsilateral hydronephrosis. (**a**) Transverse view from a DE-DSCT examination. Note the cancer in the urinary bladder (*arrow*). (**b**) Transverse-oblique view showing left ureteral distension. (**c**, **d**) Routine and DE MPR images of the abdomen. Note the hydronephrosis (left kidney)

the chronic obstruction of urine flow with secondary hydronephrosis. It is highly invasive and metastasizes frequently, most commonly to the regional lymph nodes and lungs. Other reported sites of metastasis are the bones, liver, skeletal muscle, and spinal cord.

Other malignant tumor types described in the urinary bladder are squamous cell carcinoma, adenocarcinoma, fibrosarcoma, leiomyosarcoma, hemangiosarcoma,

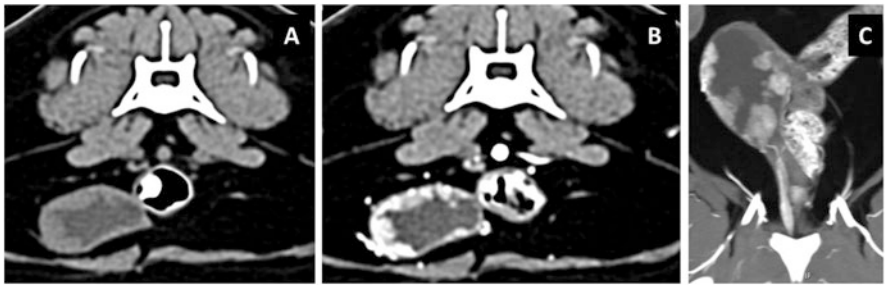

Fig. 34 TCC of the urinary bladder in a cat. (**a**) Pre-contrast transverse image. (**b**) Same image in an angiographic series. (**c**) Dorsal thin-MIP showing multiple polypoid lesions protruding into the bladder lumen

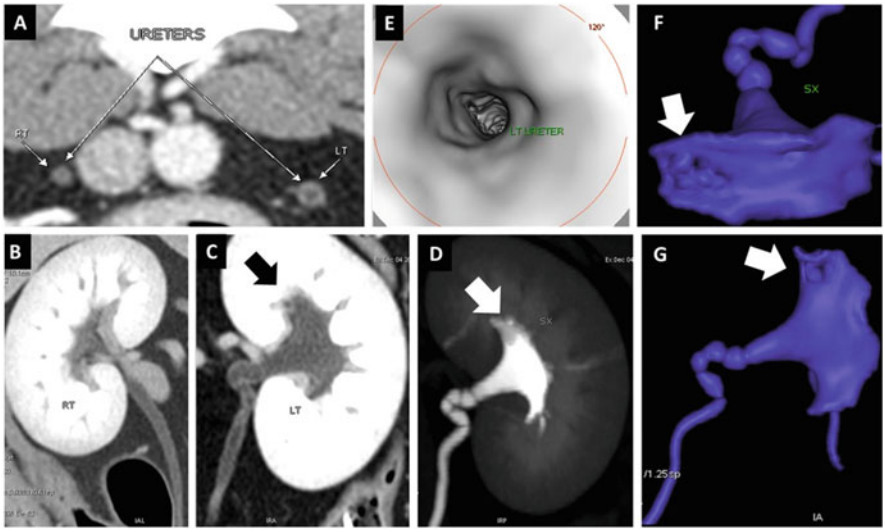

Fig. 35 TCC in a dog with chronic hematuria. (**a**) Transverse view. Note the thickening of the left ureter. (**b**) Dorsal MPR view of the normal right kidney and ureter. (**c**) Dorsal MPR image of the affected ureter and pelvis. Note the irregular margin of the renal pelvis (*arrow*). (**d**) Dorsal MIP image emphasizing the pelvic defect. (**e**) Endoluminal image through the left ureter, showing its irregular aspect. (**f**, **g**) Volume-rendered images of the renal pelvis and ureter

and rhabdomyosarcoma. Benign tumors reported in the urinary bladder are fibromas, leiomyomas, and papillomas. Finally, noncancerous mass-like growths, including those of pyogranulomatous or polypoid cystitis, may be encountered.

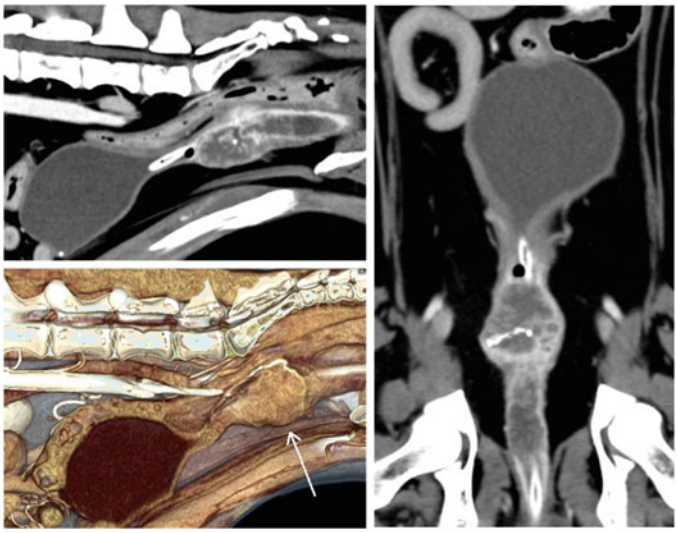

Fig. 36 TCC of the urethra in a castrated male dog

Further Readings

Agut A, Fernandez del Palacio MJ, Laredo FG, Murciano J, Bayon A, Soler M. Unilateral renal agenesis associated with additional congenital abnormalities of the urinary tract in a Pekingese bitch. J Small Anim Pract. 2002;43(1):32–5.

Alexander K, Ybarra N, del Castillo JR, Morin V, Gauvin D, Bichot S, Beauchamp G, Troncy E. Determination of glomerular filtration rate in anesthetized pigs by use of three-phase whole-kidney computed tomography and Patlak plot analysis. Am J Vet Res. 2008;69(11):1455–62. doi:10.2460/ajvr.69.11.1455.

Alexander K, Dunn M, Carmel EN, Lavoie JP, Del Castillo JR. Clinical application of Patlak plot CT-GFR in animals with upper urinary tract disease. Vet Radiol Ultrasound. 2010;51 (4):421–7.

Anders KJ, McLoughlin MA, Samii VF, Chew DJ, Cannizzo KL, Wood IC, Weisman DL. Ectopic ureters in male dogs: review of 16 clinical cases (1999-2007). J Am Anim Hosp Assoc. 2012;48(6):390–8. doi:10.5326/JAAHA-MS-5302. Epub 2012 Oct 1.

Bouma JL, Aronson LR, Keith DG, Saunders HM. Use of computed tomography renal angiography for screening feline renal transplant donors. Vet Radiol Ultrasound. 2003;44(6):636–41.

Brown PJ, Evans HK, Deen S, Whitbread TJ. Fibroepithelial polyps of the vagina in bitches: a histological and immunohistochemical study. J Comp Pathol. 2012;147(2–3):181–5. doi:10.1016/j.jcpa.2012.01.012. Epub 2012 Apr 18.

Bryan JN, Henry CJ, Turnquist SE, Tyler JW, Liptak JM, Rizzo SA, Sfiligoi G, Steinberg SJ, Smith AN, Jackson T. Primary renal neoplasia of dogs. J Vet Intern Med. 2006;20(5):1155–60.

Cáceres AV, Zwingenberger AL, Aronson LR, Mai W. Characterization of normal feline renal vascular anatomy with dual-phase CT angiography. Vet Radiol Ultrasound. 2008;49(4):350–6.

Carvallo FR, Wartluft AN, Melivilu RM. Unilateral uterine segmentary aplasia, papillary endometrial hyperplasia and ipsilateral renal agenesis in a cat. J Feline Med Surg. 2013;15 (4):349–52. doi:10.1177/1098612X12467786.

Chang J, Jung JH, Yoon J, Choi MC, Park JH, Seo KM, Jeong SM. Segmental aplasia of the uterine horn with ipsilateral renal agenesis in a cat. J Vet Med Sci. 2008;70(6):641–3.

Davidson AP, Westropp JL. Diagnosis and management of urinary ectopia. Vet Clin North Am Small Anim Pract. 2014;44(2):343–53. doi:10.1016/j.cvsm.2013.11.007.
Esterline ML, Biller DS, Sicard GK. Ureteral duplication in a dog. Vet Radiol Ultrasound. 2005;46(6):485–9.
Fujita A, Tsuboi M, Uchida K, Nishimura R. Complex malformations of the urogenital tract in a female dog: Gartner duct cyst, ipsilateral renal agenesis, and ipsilateral hydrometra. Jpn J Vet Res. 2016;64(2):147–52.
Granger LA, Armbrust LJ, Rankin DC, Ghering R, Bello NM, Alexander K. Estimation of glomerular filtration rate in healthy cats using single-slice dynamic CT and Patlak plot analysis. Vet Radiol Ultrasound. 2012;53(2):181–8. doi:10.1111/j.1740-8261.2011.01899.x.
Heng HG, Lowry JE, Boston S, Gabel C, Ehrhart N, Gulden SM. Smooth muscle neoplasia of the urinary bladder wall in three dogs. Vet Radiol Ultrasound. 2006;47(1):83–6.
Hoskins JD, Abdelbaki YZ, Root CR. Urinary bladder duplication in a dog. J Am Vet Med Assoc. 1982;181(6):603–4.
Mai W, Suran JN, Cáceres AV, Reetz JA. Comparison between bolus tracking and timing-bolus techniques for renal computed tomographic angiography in normal cats. Vet Radiol Ultrasound. 2013;54(4):343–50. doi:10.1111/vru.12029. Epub 2013 Mar 15.
Mansouri M, Aran S, Singh A, Kambadakone AR, Sahani DV, Lev MH, Abujudeh HH. Dual-energy computed tomography characterization of urinary calculi: basic principles, applications and concerns. Curr Probl Diagn Radiol. 2015;44(6):496–500. doi:10.1067/j.cpradiol.2015.04.003. Epub 2015 Apr 15.
Marques-Sampaio BP, Pereira-Sampaio MA, Henry RW, Favorito LA, Sampaio FJ. Dog kidney: anatomical relationships between intrarenal arteries and kidney collecting system. Anat Rec (Hoboken). 2007;290(8):1017–22.
Moe L, Lium B. Computed tomography of hereditary multifocal renal cystadenocarcinomas in German shepherd dogs. Vet Radiol Ultrasound. 1997;38(5):335–43.
Newman M, Landon B. Surgical treatment of a duplicated and ectopic ureter in a dog. J Small Anim Pract. 2014;55(9):475–8. doi:10.1111/jsap.12227.
O'Dell-Anderson KJ, Twardock R, Grimm JB, Grimm KA, Constable PD. Determination of glomerular filtration rate in dogs using contrast-enhanced computed tomography. Vet Radiol Ultrasound. 2006;47(2):127–35.
O'Handley P, Carrig CB, Walshaw R. Renal and ureteral duplication in a dog. J Am Vet Med Assoc. 1979;174(5):484–7.
Reichle JK, Peterson RA 2nd, Mahaffey MB, Schelling CG, Barthez PY. Ureteral fibroepithelial polyps in four dogs. Vet Radiol Ultrasound. 2003;44(4):433–7.
Reis RH, Tepe P. Variation in the pattern of renal vessels and their relation to the type of posterior vena cava in the dog (Canis familiaris). Am J Anat. 1956;99:1–15.
Rieck AF, Reis RH. Variations in the pattern of renal vessels and their relation to the type of posterior vena cava in the cat (Felis domestica). Am J Anat. 1953;93:457–74.
Rozear L, Tidwell AS. Evaluation of the ureter and ureterovesicular junction using helical computed tomographic excretory urography in healthy dogs. Vet Radiol Ultrasound. 2003;44(2):155–64.
Samii VF. Inverted contrast medium-urine layering in the canine urinary bladder on computed tomography. Vet Radiol Ultrasound. 2005;46(6):502–5.
Samii VF, McLoughlin MA, Mattoon JS, Drost WT, Chew DJ, DiBartola SP, Hoshaw-Woodard S. Digital fluoroscopic excretory urography, digital fluoroscopic urethrography, helical computed tomography, and cystoscopy in 24 dogs with suspected ureteral ectopia. J Vet Intern Med. 2004;18(3):271–81.
Secrest S, Britt L, Cook C. Imaging diagnosis-bilateral orthotopic ureteroceles in a dog. Vet Radiol Ultrasound. 2011;52(4):448–50. doi:10.1111/j.1740-8261.2011.01807.x. Epub 2011 Mar 29.
Secrest S, Essman S, Nagy J, Schultz L. Effects of furosemide on ureteral diameter and attenuation using computed tomographic excretory urography in normal dogs. Vet Radiol Ultrasound. 2013;54(1):17–24. doi:10.1111/j.1740-8261.2012.01985.x. Epub 2012 Sep 11.

Smith JS, Jerram RM, Walker AM, Warman CGA. Ectopic ureter and ureteroceles in dogs: Presentation, cause and diagnosis. Vet Radiol Ultrasound. 2004;4:303–9.
Stiffler KS, Stevenson MA, Mahaffey MB, Howerth EW, Barsanti JA. Intravesical ureterocele with concurrent renal dysfunction in a dog: a case report and proposed classification system. J Am Anim Hosp Assoc. 2002;38(1):33–9.
Taney KG, Moore KW, Carro T, Spencer C. Bilateral ectopic ureters in a male dog with unilateral renal agenesis. J Am Vet Med Assoc. 2003;223(6):817–20. 810
Tion MT, Dvorska J, Saganuwan SA. A review on urolithiasis in dogs and cats. Bulg J Vet Med. 2015;18(1):1–18. ISSN 1311-1477. doi:10.15547/bjvm.806.
Tyson R, Logsdon SA, Werre SR, Daniel GB. Estimation of feline renal volume using computed tomography and ultrasound. Vet Radiol Ultrasound. 2013;54(2):127–32. doi:10.1111/vru.12007. Epub 2012 Dec 20.
Wisenbaugh ES, Paden RG, Silva AC, Humphreys MR. Dual-energy vs conventional computed tomography in determining stone composition. Urology. 201483(6):1243–7. doi:10.1016/j.urology.2013.12.023. Epub 2014 Feb 16.
Yamazoe K, Ohashi F, Kadosawa T, Nishimura R, Sasaki N, Takeuchi A. Computed tomography on renal masses in dogs and cats. J Vet Med Sci. 1994;56(4):813–6.
Yates GH, Sanchez-Vazquez MJ, Dunlop MM. Bilateral renal agenesis in two cavalier King Charles spaniels. Vet Rec. 2007;160(19):672.

The Peritoneal Cavity, Retroperitoneum, and Abdominal Wall

Giovanna Bertolini

1 Introduction

The abdominal region is the large part of the body extending from the diaphragm to the pelvis. It includes the abdominal and pelvic cavities, bound by bone and muscle. The peritoneum is the largest and most complexly arranged serous membrane in the body. It forms the lining of the peritoneal cavity, which extends in abdominal cavity and contains the gastrointestinal tract; major abdominal organs, such as the liver, spleen, pancreas, urinary bladder, ovaries, and uterus; and many nerves, vessels, and lymph nodes. The peritoneum extends caudally in the pelvic cavity in males and females (as vaginal tunic and vaginal process, respectively). It is a serous membrane, divided into the parietal peritoneum, which covers the inner surface of the abdominal wall (the abdominal fascia) and the pelvic and scrotal cavities; the visceral peritoneum, which covers the abdominal, pelvic, and scrotal organs; and the connecting peritoneum, which extends between organs or between an organ and the parietal peritoneum, forming peritoneal folders that are divided into mesenteries, omenta, and ligaments. The purpose of the peritoneum is to provide a frictionless surface over which the viscera can move. It also serves as a site of fluid transport. A capillary film of serous fluid separates the parietal and visceral layers of the peritoneum from one another and lubricates the peritoneal surfaces. The retroperitoneal region extends dorsal to the peritoneal and pelvic cavities from the diaphragm to the pelvic inlet. It is bordered dorsally by the vertebrae and paraspinal muscles and laterally by the muscular abdominal and pelvic walls. The kidneys, ureters, and adrenal glands are considered to be retroperitoneal organs. The descending aorta, caudal vena cava, lumbar lymph nodes, cisterna chili, lymphatics, fat, and much of the abdominal wall musculature are also are also located in the

G. Bertolini (✉)
San Marco Veterinary Clinic, Padua, Italy
e-mail: bertolini@sanmarcovet.it

G. Bertolini (ed.), *Body MDCT in Small Animals*, DOI 10.1007/978-3-319-46904-1_10

retroperitoneum. The retroperitoneal cavity communicates cranially with the dorsocaudal mediastinum and caudally with the pelvic canal. Familiarity with these connections is important because diseases can spread easily among different body regions. MDCT studies performed with isotropic imaging and dorsal and sagittal reformation can fully delineate the peritoneal and retroperitoneal spaces and extent of diseases.

2 MDCT Imaging Strategies

The peritoneal and retroperitoneal spaces are normally included in abdominal MDCT examination. The scan range for such examination generally includes the diaphragmatic crura cranially and the pelvic outlet caudally, but not the perineal and scrotal regions. These regions must be included in examinations in cases of specific clinical indications (e.g., pelvic mass) or for comprehensive evaluation of the retroperitoneal space.

On MDCT, normal peritoneum appears as a fine, thin, and thus barely detectable structure. In humans, contrast-enhanced MDCT is the primary imaging modality for the assessment of peritoneal pathology. Early detection of peritoneal changes is essential for the management of several neoplastic and non-neoplastic conditions in veterinary patients. Contrast-enhanced MDCT scans with near-isotropic or isotropic resolution are necessary for fine evaluation of the abdominal cavity in dogs and cats. Most peritoneal and retroperitoneal pathological processes originate in the peritoneal and retroperitoneal organs. Therefore, a multiphasic approach (including the arterial phase and portal venous phase) provides adequate results in most instances. Performance of a third delayed series may be helpful for interpretation of pelvic pathological processes (e.g., prostatic, rectal, and vaginal diseases).

3 Disorders of the Peritoneum and Retroperitoneum

3.1 Inflammatory Peritoneal Disorders

Peritonitis is the inflammation of the peritoneal cavity. It may be primary or secondary and generalized (i.e., diffuse) or localized (i.e., involving a small portion of the peritoneum). Primary septic peritonitis may occur as the result of the hematogenous spread of microorganisms; the most common example is feline infectious peritonitis caused by coronavirus infection (Fig. 1). Secondary septic peritonitis in dogs and cats results from gastrointestinal rupture (perforation, rupture, and surgical dehiscence), intraabdominal (hepatic, pancreatic, splenic, and prostatic) abscess, pyometra rupture, and penetrating injury. Noninfectious secondary chemical peritonitis can be caused by contact of irritants with the peritoneum in

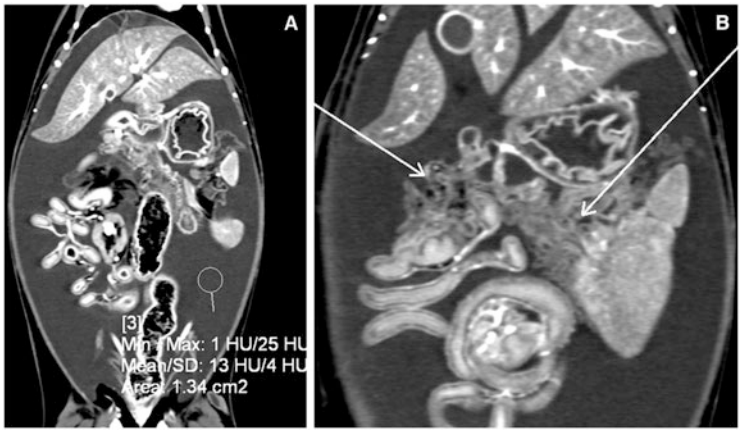

Fig. 1 Feline infectious peritonitis. (**a**) Dorsal MPR view of the abdomen in a cat. Note the large amount of free peritoneal fluid (13 HU). (**b**) *Arrow* indicates omental thickening and coarctation. Note the gastrointestinal wall edema

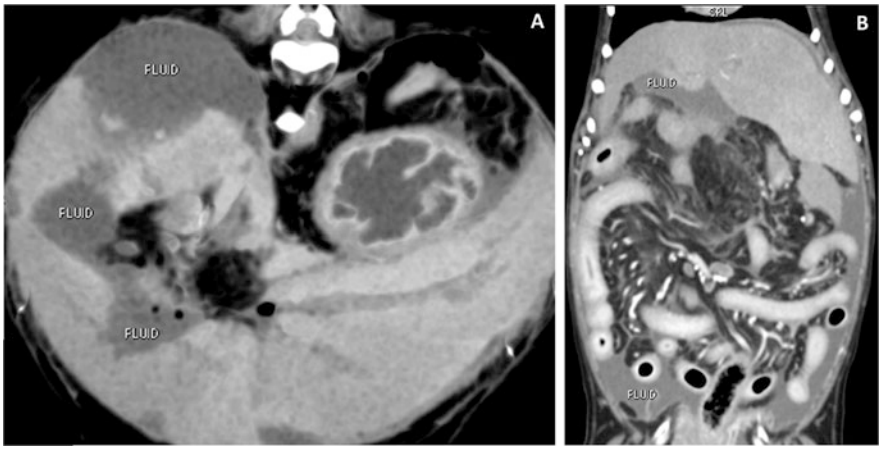

Fig. 2 Postoperative biliary peritonitis in a dog. (**a**) Transverse MinIP view of the liver showing bile collection (bilomas), a complication of recent biliary surgery. (**b**) Dorsal MPR view of the abdomen in the same dog, showing omental thickening in the cranial-middle abdomen and diffuse abdominal fluid

cases of urinary tract disruption (sterile uroabdomen); bile leakage caused by gallbladder rupture, hepatic torsion, or hepatobiliary surgical complication (bile peritonitis); and pancreatic disruption with leakage of exocrine pancreatic secretions (sterile bile peritonitis) (Figs. 2, 3, and 4).

Pathological involvement causes thickening of the peritoneal layers, which become easily noticeable. However, several acute and chronic peritoneal diseases have overlapping clinical and imaging features. In humans, three major patterns of

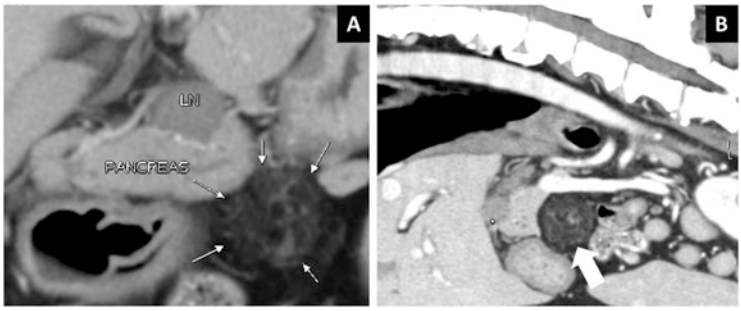

Fig. 3 Focal peritonitis in a dog with a history of recurrent pancreatitis. (**a**) Transverse view showing focal peripancreatic peritoneal thickening (*arrows*). Note the enlarged pancreatic lymph node (LN). (**b**) Sagittal view of the same dog showing focal increased peritoneal opacity and thickening (*arrow*)

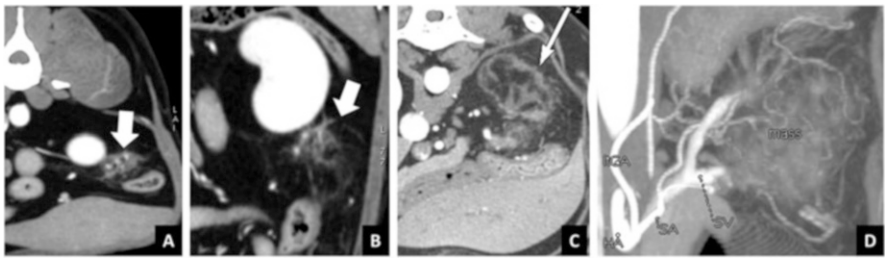

Fig. 4 Postoperative peritonitis. (**a**, **b**) Transverse views of a female dog obtained 3 weeks after ovariectomy. *Arrow* indicates focal thickening of the peritoneum at the site of the left ovary (focal peritonitis). (**c**, **d**) Transverse and dorsal MIP views of a dog obtained after splenectomy for splenic torsion. Note the omental thickening and infarction at the site of surgery

peritoneal thickening are possible: smooth regular (uniform thickness, smooth interface with omental fat), irregular (nonuniform thickening of focal segments, irregular interface with omental fat), and nodular (well-defined nodules of variable diameter with soft tissue attenuation). Although inflammatory and neoplastic conditions may have similar CT appearances, the patient's clinical history and the analysis of the CT peritoneal pattern together with associated ancillary findings aid interpretation and differential diagnosis. Smooth uniform thickening is the prevalent pattern in most cases of acute peritonitis. Granulomatous peritonitis can show a diffuse nodular pattern that may mimic a malignant condition (Fig. 5). Peritoneal/omental necrosis and steatites may form mass-like lesions, which could be confounded with malignancy (Figs. 6 and 7). These MDCT features, described in humans, are similar to those we find routinely in dogs and cats, and they have been reported on in recent veterinary studies.

Sclerosing encapsulating peritonitis is a condition of unknown etiology that causes intestinal obstruction, described rarely in dogs and cats. As described in humans, the canine and feline abdominal organs are encased in a thick

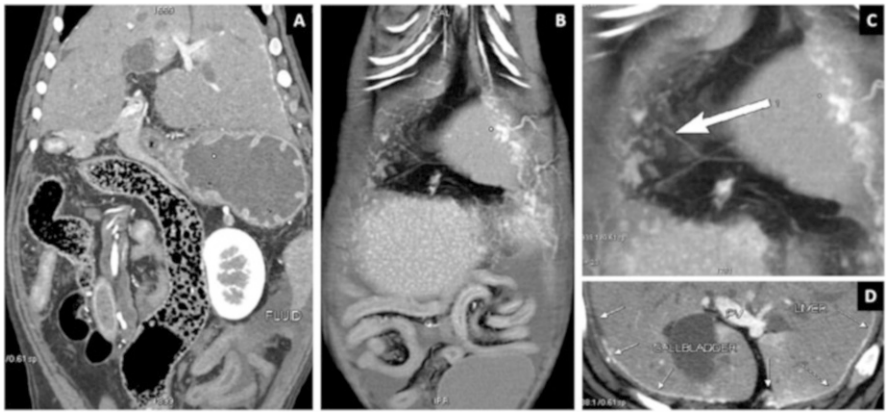

Fig. 5 Granulomatous peritonitis in a young Bernese dog. (**a**) Dorsal MPR view showing diffuse increased peritoneal/omental opacity. (**b**) Dorsal thin-average view through the ventral abdomen, showing peritoneal nodules that mimic a neoplastic condition. (**c**) Close-up view of (**b**), showing the peritoneal nodular pattern (*arrow*). (**d**) Transverse view from the same dog, showing thickening and enhancement of the parietal peritoneum

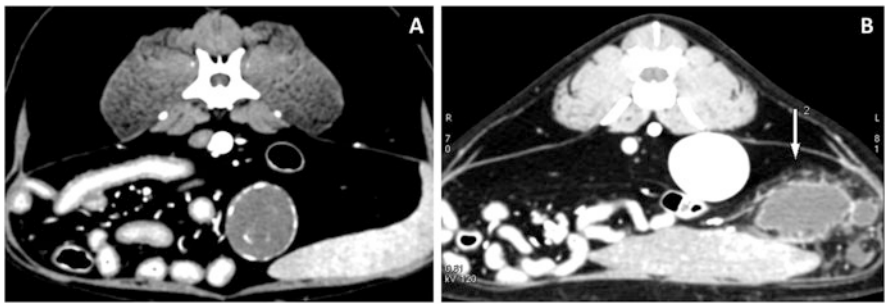

Fig. 6 (**a**) Peritoneal fat necrosis. Transverse view of the abdomen in a dog showing a well-defined, ovoid, non-enhancing mass with mineralized borders. (**b**) Transverse view of a cat showing a mass in the left middle peritoneal cavity that is hypoattenuating with great peripheral enhancement (*arrow*). Other smaller lesions (omental steatitis) are present in the same region

fibrocollagenous membrane in patients with this condition. Signs of gastrointestinal obstruction, distortion, and fixation, and peritoneal or mural calcification, may be seen (Fig. 8).

3.2 Neoplastic Peritoneal Diseases

Mesotheliomas originate from the cells covering the serosal cavities (pleura, pericardium, peritoneum, and tunica vaginalis). They are very uncommon in animals,

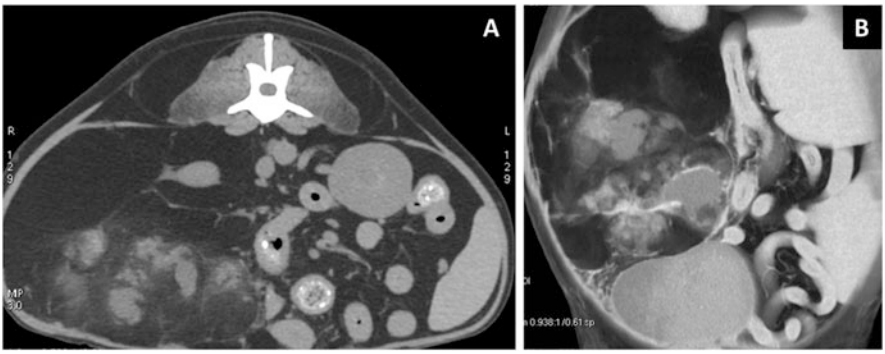

Fig. 7 Necrotic omental lipoma forming mass-like lesions in a dog. (**a**) Transverse view. (**b**) Dorsal MPR view showing the omental masses, which compress the surrounding peritoneal organs

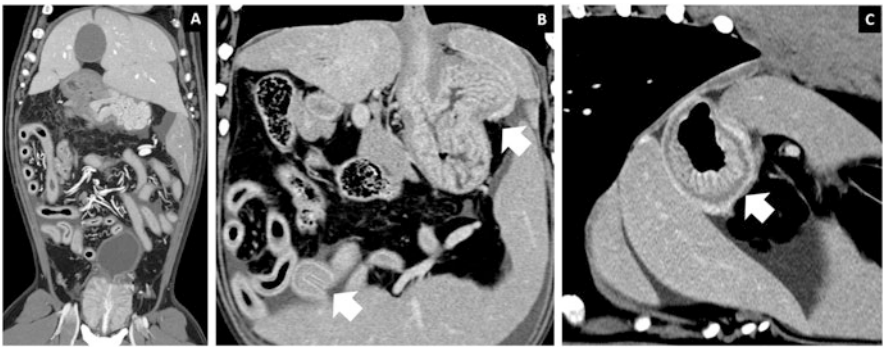

Fig. 8 Sclerosing peritonitis in a Labrador retriever. (**a**) Dorsal MPR view showing diffuse peritoneal/omental thickening. (**b**) Dorsal view in the same dog. Note the signs of gastrointestinal distortion and incarceration (*arrows*). (**c**) Parasagittal image showing a thick fibrocollagenous membrane encasing the stomach (*arrow*)

representing just 0.2% of all canine tumors. Mesotheliomas are usually malignant and may involve one or all cavities.

Peritoneal mesothelioma appears on MDCT images as irregular peritoneal thickening with the diffuse nodular pattern or coalescent, mass-like soft tissue within the omentum (omental caking), which enhances in post-contrast series (Fig. 9). MDCT is useful for the detection, characterization, and staging of, and biopsy guidance for, peritoneal nodules and masses. Peritoneal effusion is present in most cases. The amount of ascites is quite variable, ranging from massive, diffuse ascites to focal, small, loculated collections of fluid. Concomitant pleural mesothelioma, with or without pleural effusion, is possible. Mesothelioma may extend to the visceral peritoneal surfaces of the small bowel, encasing it. As a result, the small bowel is compacted and located in the center of the abdomen.

Malignant peritoneal mesothelioma is indistinguishable from carcinomatosis when the predominant imaging findings are multifocal peritoneal nodules and

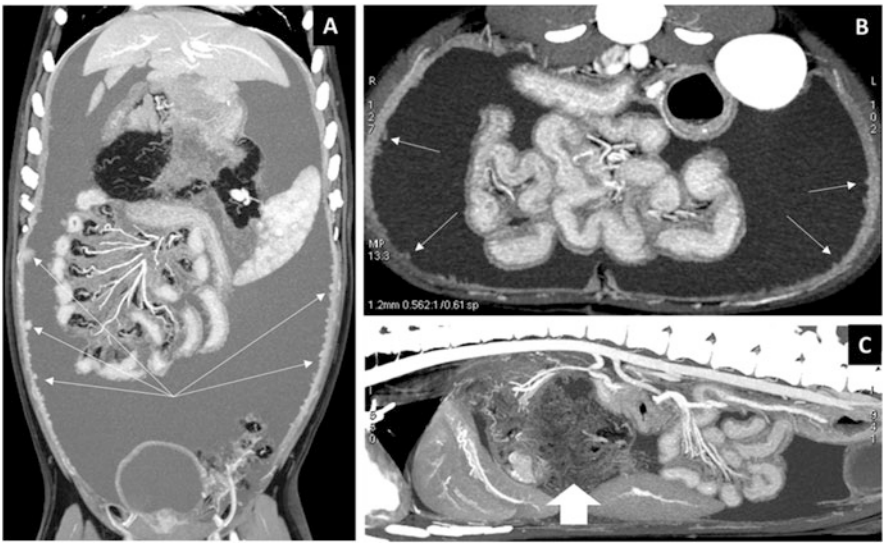

Fig. 9 (**a**) Peritoneal mesothelioma in a 9-year-old boxer. Note the large amount of free fluid in the peritoneal cavity. The small bowel is compacted and located in the center of the abdomen. *Arrows* indicate peritoneal nodules. (**b**, **c**) Transverse and sagittal thin-MIP views from another dog, showing free abdominal fluid, peritoneal thickening, and small bowel compaction. In (**c**), note the diffuse increased omental opacity and thickening (*arrow*)

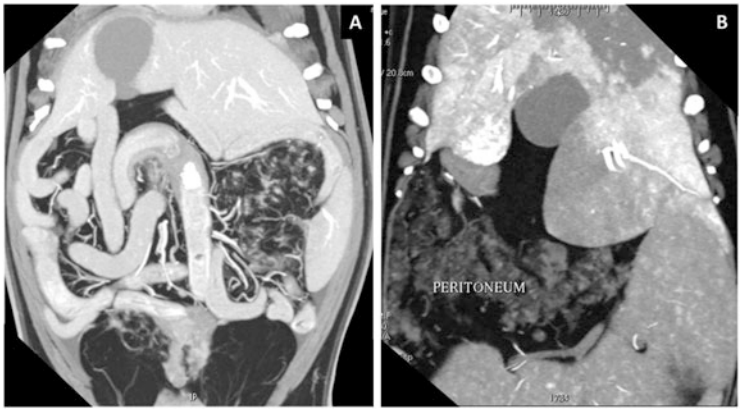

Fig. 10 Carcinomatosis in two different dogs. (**a**) Dorsal MPR view showing diffuse thickening of the omentum with the reticulonodular pattern in a dog with intestinal carcinoma. (**b**) Peritoneal thickening with nodular/micronodular lesions, which spare some peritoneal areas. Note the concomitant diffuse HPD

omental caking (Figs. 10 and 11). Ascites, peritoneal nodules and thickening, and omental nodules and masses are also the most common MDCT features of peritoneal carcinomatosis. Carcinomatosis refers to metastatic peritoneal diseases, especially those arising from carcinomas of the gastrointestinal tract and pancreas.

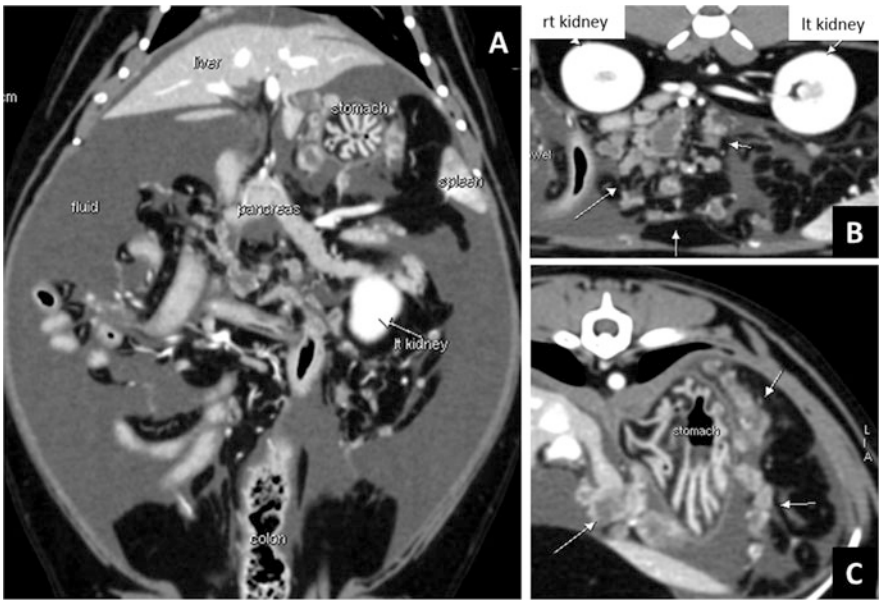

Fig. 11 Carcinomatosis in a cat. (**a**) Dorsal MPR view in a cat that had previously undergone enterectomy for intestinal carcinoma. Abundant free peritoneal fluid is present. The omentum is thickened and shows nodular aspects, which are better visible in **b** and **c** (*arrows*)

Intraperitoneal dissemination of tumor cells occurs by several mechanisms: intraperitoneal seeding, direct invasion, hematogenous dissemination, and lymphatic dissemination. Rupture of an abdominal hemangiosarcoma can cause widespread peritoneal seepage of blood with local implantation (Fig. 12).

3.3 Retroperitoneal Diseases

MDCT is an excellent tool for the evaluation of the retroperitoneal space. Fluid accumulation and masses in the retroperitoneal space are frequent indications for MDCT examination. Retroperitoneal fluid can occur in many benign and malignant conditions. In veterinary patients, most common retroperitoneal pathologies are caused by penetrating injuries, leading to hypaxial muscular hemorrhage, ureter rupture (see also the "The Body Trauma" chapter), or foreign body migration with abscess formation or phlegmon (Figs. 13 and 14).

Retroperitoneal tumors may be primary or secondary. Primary retroperitoneal masses originate in the retroperitoneum but outside of the major retroperitoneal organs. They derive from tissues contained in the retroperitoneal space (adipose, muscle, vessel, and nerve tissue), from embryonic remnants or heterotopies, from one or more embryonic layers (ectoderm, mesoderm, and/or endoderm), or from

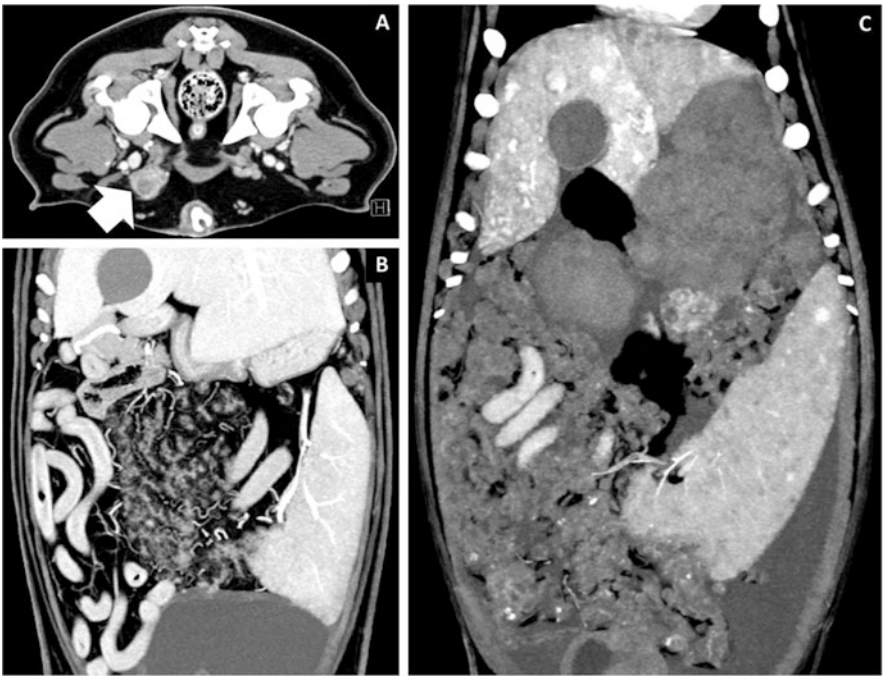

Fig. 12 (**a**) Transverse view of the pelvis in a dog with funicular infiltration (*arrow*) from testicular seminoma, which had recently been removed. (**b**) Dorsal MPR view from the same dog shows intraperitoneal seeding. (**c**) Dorsal MPR view of another dog with ruptured splenic hemangiosarcoma and peritoneal implantation

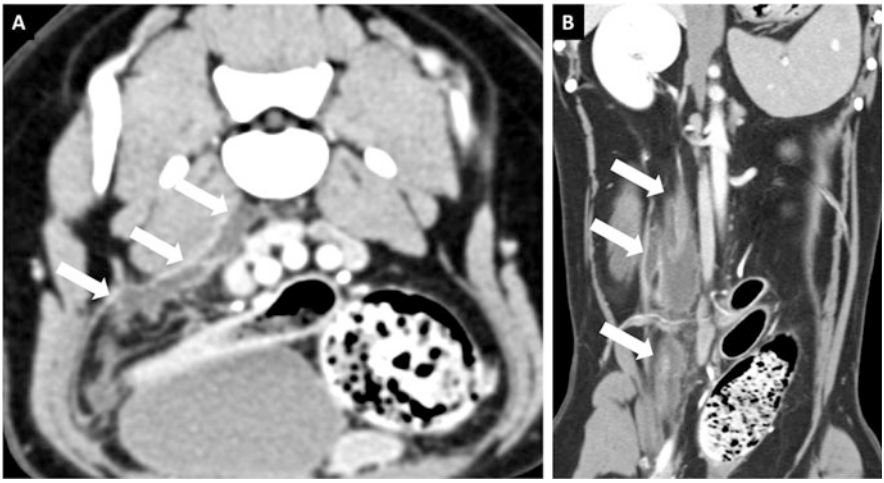

Fig. 13 Retroperitoneal phlegmon. (**a**, **b**) Transverse and dorsal MPR views of a dog with retroperitoneal unilateral effusion due to foreign body (not visible here) migration

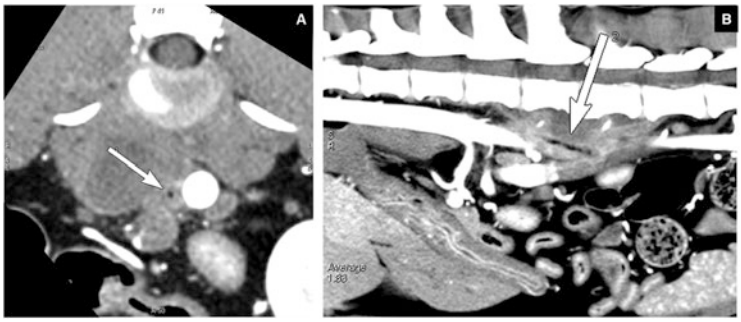

Fig. 14 Retroperitoneal abscess of the hypaxial muscles. (**a**) Transverse view showing muscular thickening and moderate hypoattenuation. Note the small air-containing lesion (*arrow*), better visible in the parasagittal view (**b**), consistent with a non-radiopaque (vegetal) foreign body

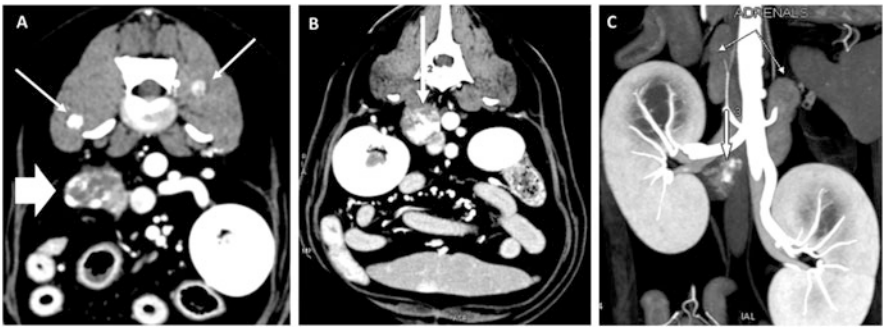

Fig. 15 Primary retroperitoneal neoplasia. (**a**) Transverse view from a dog with small retroperitoneal hemangiosarcoma (*large arrow*) and muscular metastasis (*arrows*). (**b**, **c**) Transverse and dorsal views from another dog with retroperitoneal aortic paraganglioma (*arrow*)

totipotent embryonic germs. In veterinary patients, retroperitoneal hemangiosarcoma is probably the most common primary retroperitoneal malignancy, and it is often associated with hemoretroperitoneum (Fig. 15a). Other primary retroperitoneal tumors described in dogs are extra-adrenal paraganglioma (aortic body tumor), extraskeletal mesenchymal chondrosarcoma, osteosarcoma, and teratoma (Figs. 15b, c and 16).

Secondary retroperitoneal tumors include tumors of the retroperitoneal organs (primary and metastatic adrenal, renal, and collecting system tumors), retroperitoneal lymph node metastasis (e.g., lumbar lymph node metastasis of testicular or anal sac cancer), and infiltrative neoplasias (e.g., lymphoma) (Figs. 17, 18, and 19).

Retroperitoneal hemorrhage commonly occurs with ruptured malignant masses (e.g., adrenal masses, sarcomas) (Fig. 20).

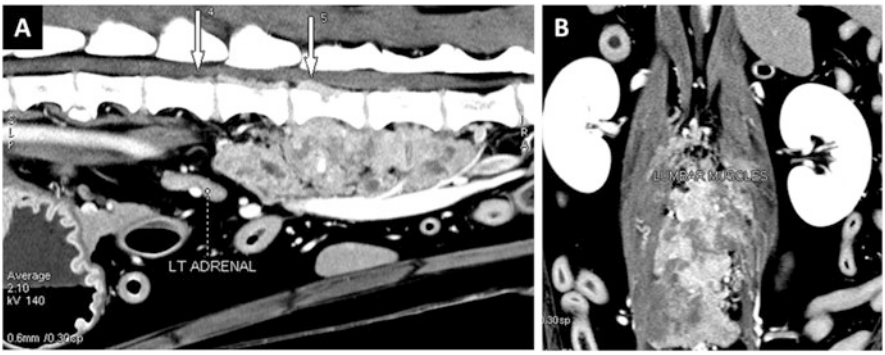

Fig. 16 Primary retroperitoneal neoplasia (neuroendocrine tumor). (**a**) Sagittal (thin-average) view of a dog with lumbar pain and paraparesis. Note the large and complex hypervascular retroperitoneal mass and enlarged vertebral sinuses (*arrows*). (**b**) Dorsal MPR view of the same dog, showing the mass extension and relationships to the hypaxial musculature

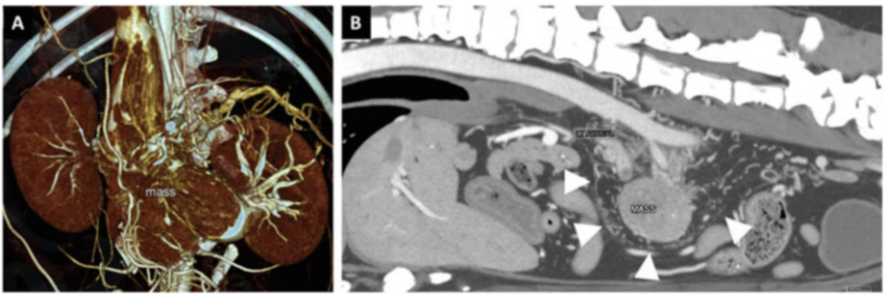

Fig. 17 Secondary retroperitoneal neoplasia. (**a**) VR of the retroperitoneal region in a dog, showing a huge left adrenal mass invading the caudal vena cava and renal veins. (**b**) Sagittal MPR view of the same dog, showing the adrenal mass in the retroperitoneal region surrounded by multiple vascular collaterals. Note the distinction between the retroperitoneal and peritoneal cavities (*arrowheads*)

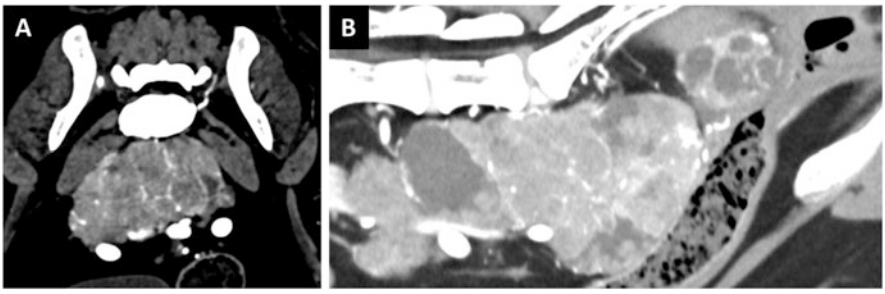

Fig. 18 Secondary retroperitoneal neoplasia. Lymph node metastasis (median sacral and iliac lymph nodes) of anal sac carcinoma in a dog. (**a**) Transverse view. (**b**) Sagittal view

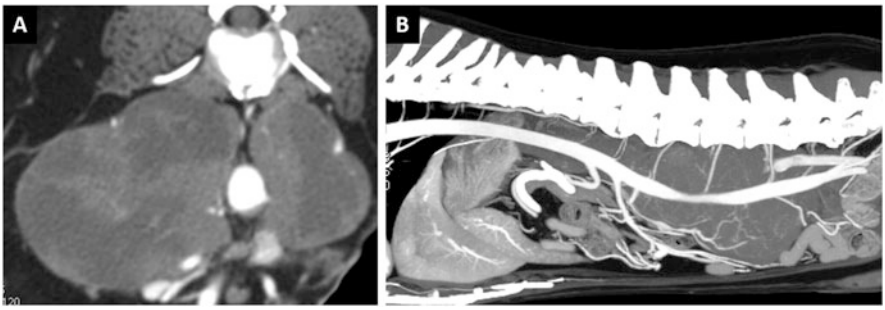

Fig. 19 Secondary retroperitoneal neoplasia. Lumbar lymph-node metastasis of seminoma in a dog. (**a**) Transverse view. (**b**) Thin-MIP sagittal view. Note the ventral displacement of the aorta and stretched lumbar arteries

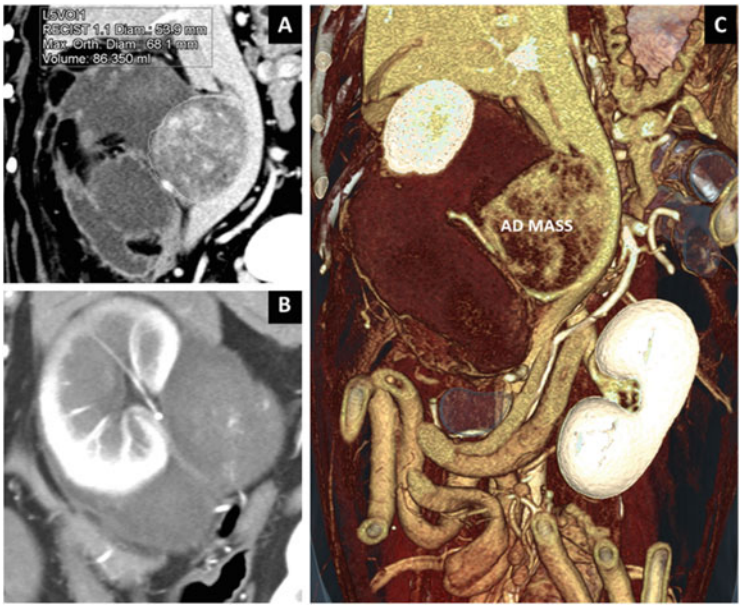

Fig. 20 Retroperitoneal hemorrhage due to large adrenal mass rupture in a dog. (**a**) Non-contrast image showing the large right adrenal mass, which compresses and deviates the caudal vena cava (not invaded). Note the retroperitoneal fluid collection surrounding the mass. (**b**) The hematoma encases the renal vasculature. (**c**) Volume-rendered image showing the right adrenal mass and large retroperitoneal hematoma

3.4 Large Abdominal Masses

The veterinary literature contains no studies on large and huge abdominal masses or the interpretation of MDCT images of such masses. However, MDCT is often required to characterize these masses and establish eligibility criteria for

resectability. Large abdominal masses may involve the abdominal wall and peritoneal or retroperitoneal cavity.

Cranially, the abdominal wall is composed of osseocartilaginous structures, including the sternum, ribs, and costal cartilages. Muscles and fascial layers compose the ventral and lateral abdominal walls. They support and protect the intraperitoneal content and extend to the retroperitoneal space. Masses of the abdominal wall may be subcutaneous or involve one or more deep structures.

Nonneoplastic and neoplastic conditions may affect the abdominal wall, and both types can require MDCT assessment. Nonneoplastic abdominal wall lesions include abscesses, phlegmonous lesions, and abdominal wall hernias (see below in this chapter). Tumor lesions include various benign (e.g., lipoma) and malignant (e.g., sarcoma) conditions.

MDCT is required for the assessment and staging of cutaneous and subcutaneous neoplastic lesions and for the presurgical assessment of large superficial masses. MDCT allows assessment of the boundaries of a mass, its vascularization, and possible deep tissue involvement. Patients with large lipomas and sarcomas are commonly evaluated using MDCT. Large masses involving osseocartilaginous structures or deep tissues of the abdominal wall require comprehensive MDCT evaluation to determine their characteristics before selecting a therapeutic approach (Figs. 21 and 22a).

Regarding cavitary abdominal masses, large peritoneal and retroperitoneal lipomas may be easily identified based on their CT characteristics (negative Hounsfield

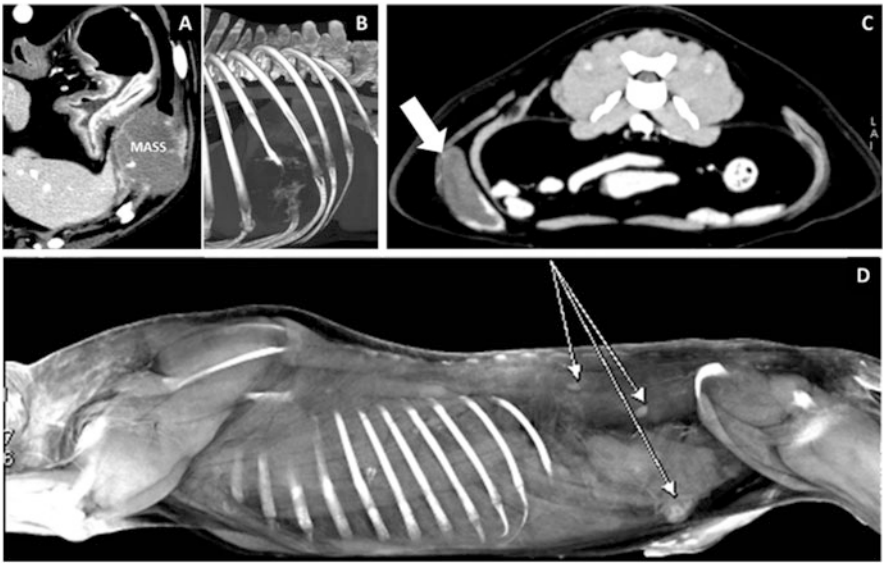

Fig. 21 (**a**, **b**) Transverse and 3D images of a dog with abdominal wall sarcoma (mass) involving the ninth rib (costochondral junction). (**c**) Transverse view from a cat with an abdominal wall mass (mastocytoma, *arrow*). (**d**) Volume-rendered image from a dog showing abdominal wall metastasis (*arrows*) of splenic hemangiosarcoma (not visible here)

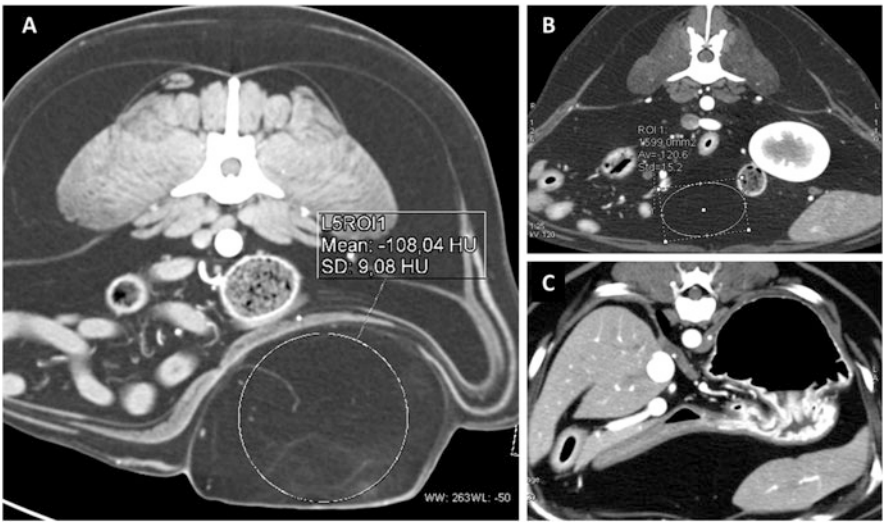

Fig. 22 (**a**) Large subcutaneous abdominal lipoma in a dog (−108 HU). (**b**, **c**) Pre- and post-contrast transverse views of the abdomen in a dog with peritoneal lipomatosis (−120.6 HU), which displaces the abdominal organs

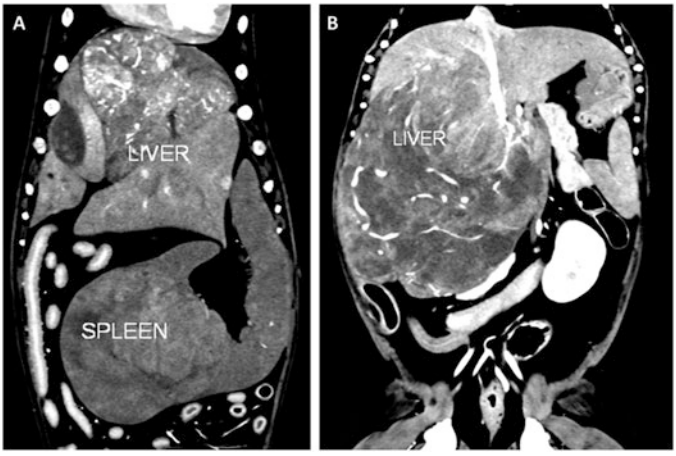

Fig. 23 Large abdominal masses (peritoneal cavity). (**a**) Large splenic and hepatic masses (hemangiosarcoma). In this case, the masses are completely inside the organ of origin and the interpretation is simple. (**b**) Large hepatic sarcoma. The mass is not completely inside the liver, but is clearly connected to it

Unit [HU] values) (Fig. 22b, c). The identification of the organ of origin of large masses can be easy when the mass is completely inside or clearly connected to it (Fig. 23). However, huge masses may occupy the majority of the abdominal cavity and show relationships with various organs. The role of MDCT in the assessment of

masses possibly requiring resection is to demonstrate the organ of origin (if any); establish whether the tumor extends beyond that organ, invading/infiltrating adjacent organs or tissues; identify any vascular encasement/invasion and the affected vessel; and identify any evidence of local or distant metastasis (Fig. 24). In addition, it demonstrates any important anatomical displacement that may be problematic during surgery.

The first step of MDCT assessment is to determine whether the mass is located in the peritoneal or retroperitoneal space. Assessment of the displacement of normal anatomic structures is useful. Dorsal or lateral displacement of retroperitoneal organs, such as the kidney and ureters, may suggest a peritoneal origin. In contrast, ventral displacement of retroperitoneal organs and ventral displacement or encasement of major vessels (aorta, caudal vena cava) or their branches strongly suggests that the tumor has arisen in the retroperitoneum (Figs. 25 and 26). CT signs of large abdominal masses described in humans may be helpful for the assessment of such

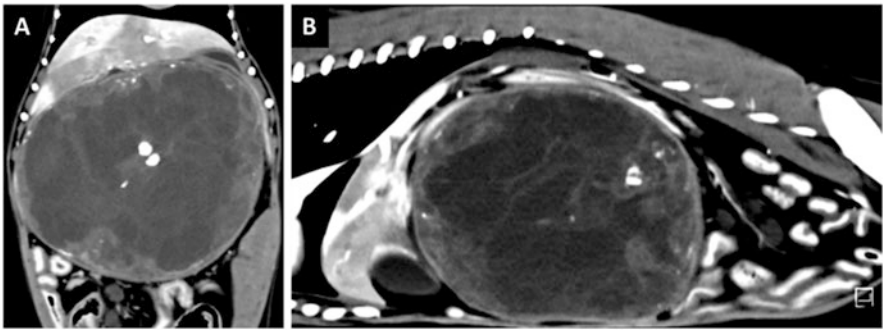

Fig. 24 Huge abdominal mass in a Dobermann Pinscherinscher. The mass occupies the majority of the abdominal cavity and has relationships to various peritoneal organs but shows no vascular or tissue connection with other peritoneal organs. The mass was surgically removed and the histopathological results indicated chronic, capsulated granulomatous peritonitis. (**a**) Dorsal view. (**b**) Sagittal view

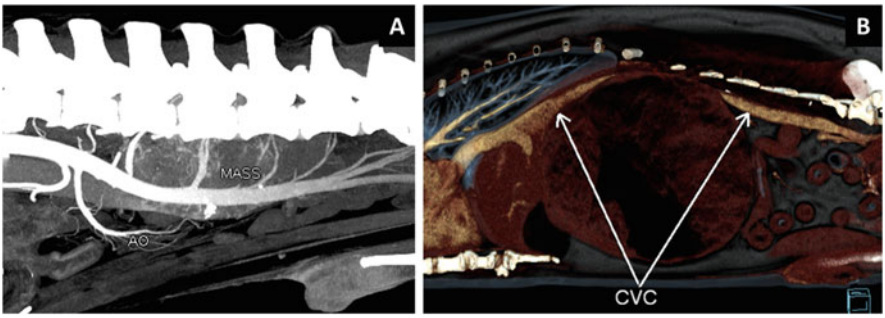

Fig. 25 (**a**) Abdominal masses located in the retroperitoneum may displace the vasculature ventrally. (**b**) Large peritoneal masses compress the vessels dorsally

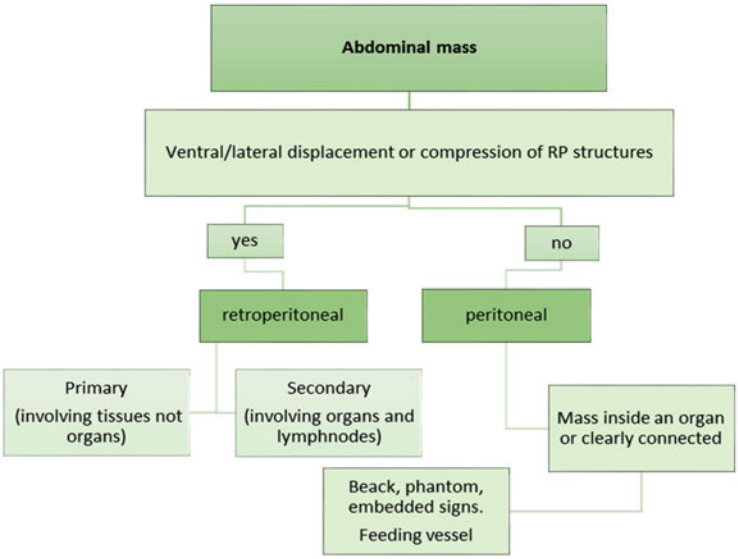

Fig. 26 Flowchart for abdominal mass identification (see the text for further details)

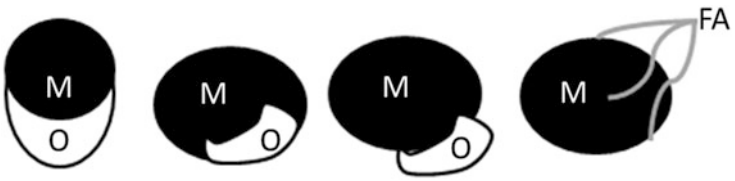

Fig. 27 CT signs indicating the possible origin of an abdominal mass. From *left to right*: beak sign, phantom sign, embedded sign, and feeding artery sign. *M* mass, *O* organ, *FA* feeding artery

masses in veterinary patients as well. These are the "beak sign," in which the mass causes the edge of an adjacent organ to become beak shaped, meaning that it arises from that organ; the "phantom organ sign," in which a small organ with a huge mass arising from it becomes undetectable; the "embedded organ sign," in which part of a hollow organ appears to be embedded in the tumor; and the "prominent feeding artery sign," which is particularly useful for the assessment of hypervascular lesions supplied by arteries that are sufficiently prominent to be visualized on CT (Figs. 27, 28, and 29).

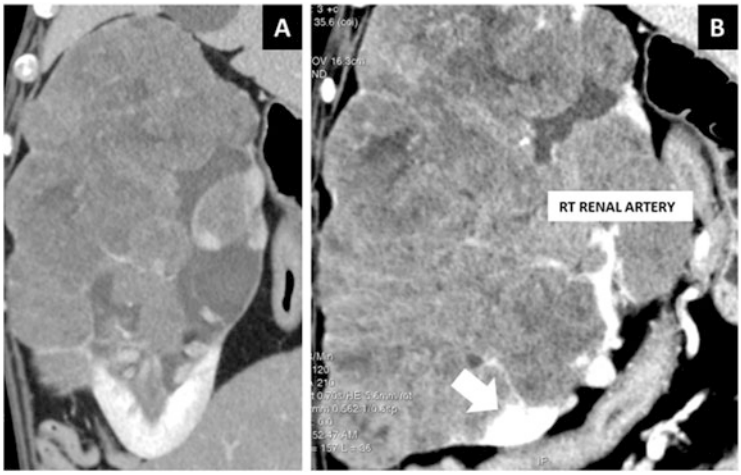

Fig. 28 (**a**) Large renal mass in a dog. Note the beak-shaped margins of the renal tissue, meaning that the mass arises from that organ. (**b**) Huge abdominal mass in another dog. The *arrow* indicates part of the normal renal tissue embedded in the tumoral tissue. The mass (renal carcinoma) also encases and invades the right renal artery

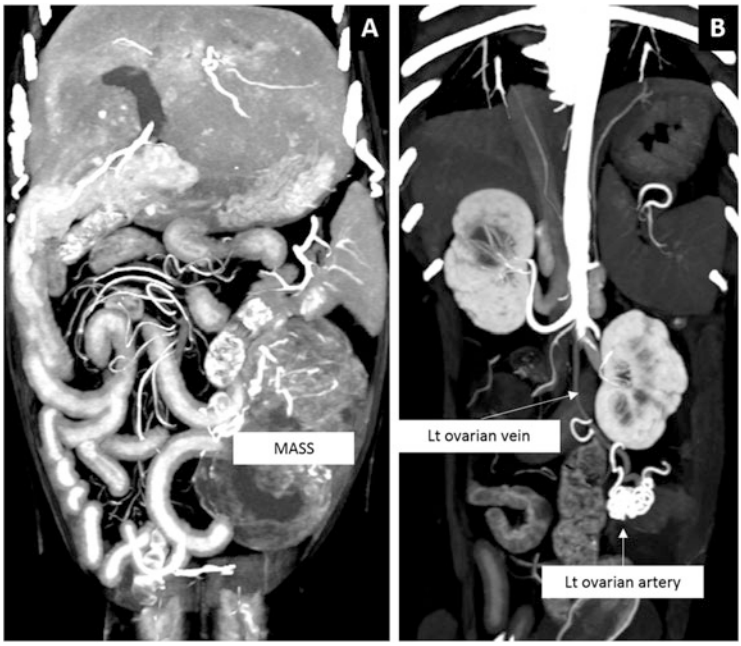

Fig. 29 Feeding artery (ovarian carcinoma). (**a**) Large left-sided abdominal mass in a female mongrel dog. (**b**) The mass is supplied by the left ovarian artery (in the arterial phase, the left ovarian vein is still not enhanced; see the text for supplementary explanation)

3.5 Abdominal Hernias

Abdominal hernias are protrusions of intra-abdominal contents through defects in the diaphragm or abdominal wall. Abdominal hernia types in small animals include diaphragmatic (hiatal hernia [HH], pleuroperitoneal, and peritoneopericardial), umbilical, and inguinal hernias. Internal abdominal hernias are reported rarely, but their occurrence is probably underestimated. Perineal hernias are encountered commonly in MDCT examinations performed to evaluate pelvic trauma or masses.

Diaphragmatic hernias include HH and pleuroperitoneal and peritoneopericardial hernias. HH is a congenital condition in which organs of the abdominal cavity herniate through the esophageal hiatus into the thoracic cavity (see the chapter entitled "The Mediastinum and Neck"). Pleuroperitoneal hernia is a defect in the dorsolateral diaphragm with the herniation of abdominal viscera into the thoracic cavity. Acquired pleuroperitoneal hernias are commonly observed after blunt trauma in dogs and cats. Such hernias associated with congenital conditions are rarely reported on because affected animals die shortly after birth.

Peritoneopericardial diaphragmatic hernia (PPDH) is the most frequently reported congenital pericardial anomaly in dogs and cats. PPDH occurs with improper development of the transverse septum (and rarely due to trauma in early life) and refers to persistent communication between the pericardial and peritoneal cavities, allowing abdominal contents to enter the pericardial cavity, while the pleural space remains intact (Fig. 30). The liver and gallbladder are herniated most frequently, followed by the small intestines, spleen, and stomach. PPDH may be diagnosed using first-level imaging techniques. However, MDCT can have a determinant role in the assessment of concomitant thoracic and abdominal congenital defects and embryonic variants in these subjects, which may change the therapeutic approach and prognosis.

Abdominal wall hernias include umbilical and inguinal hernias. Umbilical hernia is probably the most common type of hernia in dogs. It is commonly diagnosed clinically in puppies and seen incidentally on MDCT images acquired

Fig. 30 Peritoneopericardial diaphragmatic hernia in a puppy with concomitant complex cardiac anomaly (not shown here). (**a**, **b**) Dorsal and sagittal MPR views showing the stomach and small bowel dislocated in the pericardial sac

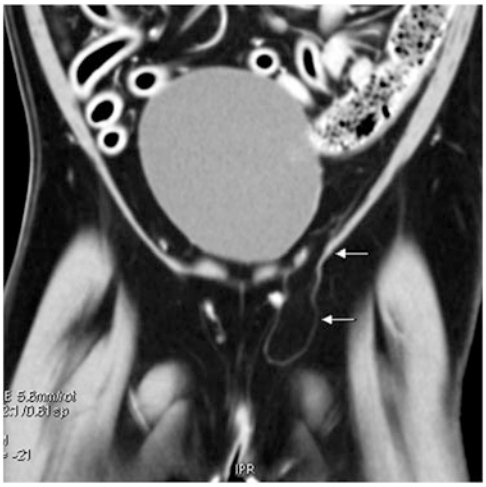

Fig. 31 Direct inguinal hernia in a young female dog. *Arrows* indicate the small sac containing omental fat

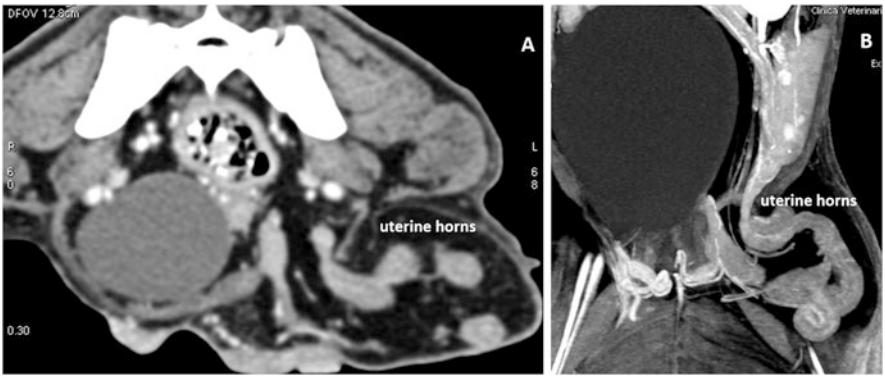

Fig. 32 Indirect inguinal herniation in a female dog with vaginal leiomyoma (not visible here). (**a**, **b**) Transverse and dorsal views showing the inguinal herniation of the uterine horns (uterine adenomyomatosis)

for other purposes. Inguinal hernias are subdivided into direct and indirect inguinal hernias. Direct inguinal hernia occurs when tissue protrudes through weakened or injured abdominal wall muscles, in a hernia sac formed by the parietal peritoneum. This kind of hernias is encountered commonly on MDCT examinations of patients with pelvic trauma and in non-traumatized dogs (Fig. 31). Indirect inguinal hernia is generally congenital and refers to the herniation of tissue into the inguinal canal through the deep inguinal ring in the tunica vaginalis. The organs most commonly

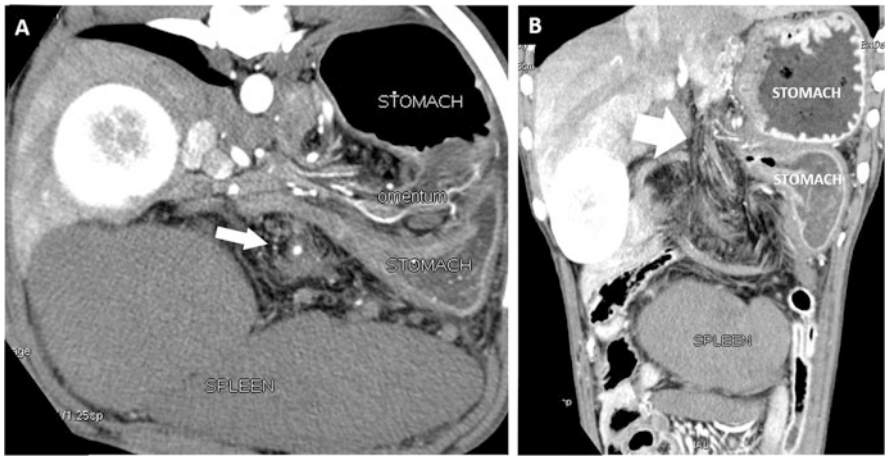

Fig. 33 Internal hernia in a dog with recurrent gastric dilatation. (**a**) Transverse view showing partial distension of the stomach with air-fluid level. The spleen is enlarged and hypoperfused. Note a "whirl sign" in the middle abdomen (*arrow*), consistent with omental torsion. (**b**) Dorsal thin-average view of the abdomen in the same dog, showing herniation through the foramen (*arrow*). Surgical findings confirmed the CT diagnosis

involved in inguinal hernia are the omentum, small intestine, bladder, and uterus (Fig. 32). They may become incarcerated or strangulated within the relatively narrow inguinal canal.

Internal abdominal hernia refers to protrusion of the viscera through the peritoneum or mesentery while remaining in the abdominal cavity. In humans, MDCT is considered to be the gold standard imaging technique for the diagnosis of these hernias. The most common presentation is acute intestinal obstruction of small bowel loops, which develops through normal or abnormal apertures, such as foramina or defects in the mesentery or visceral peritoneum. MDCT signs differ depending on the subtype of internal hernia. These hernias result in the abnormal positioning of the stomach and/or bowel loops, which show signs of obstruction or strangulation. High-quality MDCT images obtained using a multiphasic approach are necessary for the evaluation of the mesenteric vasculature, which can show engorgement, twisting, and stretching (Fig. 33). Volumetric datasets must be assessed thoroughly to exclude inflammatory and neoplastic gastrointestinal conditions. Thin-slab MIP and VR are helpful for accurate image interpretation, especially for evaluation of the course and patency of the mesenteric vasculature.

Perineal hernias differ from other hernias in that the displaced organs are not usually within a peritoneal sac. Perineal hernias form due to failure or weakening of the fascia and muscles of the perineum, which permits prolapse of abdominal or pelvic organs. This type of hernia has been described mostly in mature, male dogs. Perineal hernia is seen incidentally on MDCT or appears as a corollary sign of complex traumatic or neoplastic pelvic diseases. Perineal hernias usually involve herniated abdominal and pelvic canal contents, such as dilated rectum, prostate, urinary bladder, fat, omentum, and/or small intestine (Fig. 34).

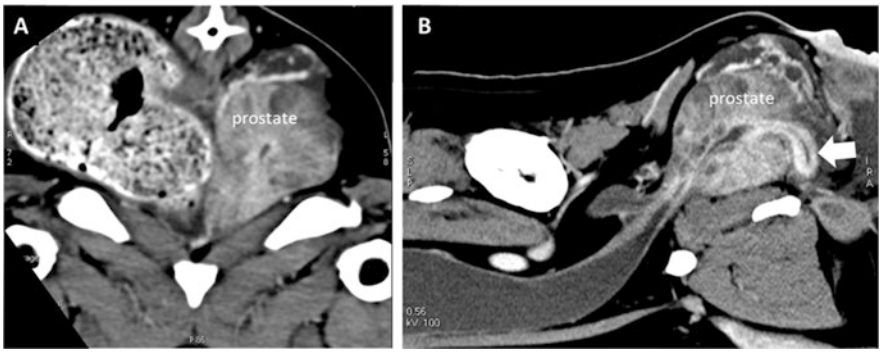

Fig. 34 Perineal hernia in a dog. (**a**) Transverse view of the pelvis showing dislocation of the prostate and rectum with feces. (**b**) Sagittal view from the same patient, showing caudal dislocation of the prostate and urethra (*arrow*)

Further Readings

Barfield DM, Tivers MS, Holahan M, Welch K, House A, Adamantos SE. Retrospective evaluation of recurrent secondary septic peritonitis in dogs (2000-2011): 41 cases. J Vet Emerg Crit Care (San Antonio). 2016;26(2):281–7. doi:10.1111/vec.12413.

Berezin A, Seltzer SE. Differential diagnosis of huge abdominal masses visualized on CT scans. Comput Radiol. 1984;8(2):95–9.

Culp WT, Holt DE. Septic peritonitis. Compend Contin Educ Vet. 2010;32(10):E1–14. quiz E15

Culp WT, Zeldis TE, Reese MS, Drobatz KJ. Primary bacterial peritonitis in dogs and cats: 24 cases (1990-2006). J Am Vet Med Assoc. 2009;234(7):906–13. doi:10.2460/javma.234.7.906.

DeGroot W, Giuffrida MA, Rubin J, Runge JJ, Zide A, Mayhew PD, Culp WT, Mankin KT, Amsellem PM, Petrukovich B, Ringwood PB, Case JB, Singh A. Primary splenic torsion in dogs: 102 cases (1992-2014). J Am Vet Med Assoc. 2016;248(6):661–8. doi:10.2460/javma.248.6.661.

Drost WT, Green EM, Zekas LJ, Aarnes TK, Su L. Having GG2. Comparison of computed tomography and abdominal radiography for detection of canine mechanical intestinal obstruction. Vet Radiol Ultrasound. 2016;57(4):366–75. doi:10.1111/vru.12353.

Filippone A, Cianci R, Pizzi AD, et al. CT findings in acute peritonitis: a pattern-based approach. Diagn Interv Radiol. 2015;21(6):435–40. doi:10.5152/dir.2015.15066.

Ilha MR, Styer EL. Extra-adrenal retroperitoneal paraganglioma in a dog. J Vet Diagn Invest. 2013;25(6):803–6. doi:10.1177/1040638713506579.

Liptak JM, Dernell WS, Ehrhart EJ, Rizzo SA, Rooney MB, Withrow SJ. Retroperitoneal sarcomas in dogs: 14 cases (1992-2002). J Am Vet Med Assoc. 2004;224(9):1471–7.

Llabrés-Díaz F. The retroperitoneum. Chapter 5. In: O'Brien R, Barr FJ, editors. BSAVA manual of canine and feline abdominal imaging. Gloucester: BSAVA Publications; 2009. p. 40–8.

Mayhew PD, Brockman DJ. Body cavity lipomas in six dogs. J Small Anim Pract. 2002;43(4):177–81.

Munday JS, Prahl A. Retroperitoneal extraskeletal mesenchymal chondrosarcoma in a dog. J Vet Diagn Invest. 2002;14(6):498–500.

Nagashima Y, Hoshi K, Tanaka R, Shibazaki A, Fujiwara K, Konno K, Machida N, Yamane Y. Ovarian and retroperitoneal teratomas in a dog. J Vet Med Sci. 2000;62(7):793–5.

Ragetly GR, Bennett RA, Ragetly CA. Septic peritonitis: etiology, pathophysiology, and diagnosis. Compend Contin Educ Vet. 2011;33(10):E1-6. quiz E7.
Santamarina G, Espino L, Vila M, Lopez M, Alemañ N, Suarez ML. Aortic thromboembolism and retroperitoneal hemorrhage associated with a pheochromocytoma in a dog. J Vet Intern Med. 2003;17(6):917–22.
Teixeira M, Gil F, Vazquez JM, Cardoso L, Arencibia A, Ramirez-Zarzosa G, Agut A. Helical computed tomographic anatomy of the canine abdomen. Vet J. 2007;174(1):133–8.
Waters DJ, Roy RG, Stone EA. A retrospective study of inguinal hernia in 35 dogs. Vet Surg. 1993;22(1):44–9.

Part IV
The Thorax

The Systemic Thoracic Vasculature

Giovanna Bertolini

1 Introduction

The thoracic vascularization includes systemic and pulmonary vessels. Systemic vessels (branches of the thoracic aorta) supply blood to extrapulmonary thoracic structures and supporting structures of the lungs. Systemic veins [cranial vena cava (CrVC) and azygos vein] drain the blood from the systemic arterial system. In the pulmonary circulation, arteries carry deoxygenated blood from the right ventricle of the heart to the lungs, and veins return oxygenated blood to the left atrium. MDCT offers an unprecedented opportunity for the in vivo study of the anatomy of the systemic and pulmonary vasculature of the thorax. CT studies are required for a wide range of congenital and acquired clinical conditions, including congenital vascular malformations and anomalous connections and thrombosis and vascular obstruction. CT is also used to evaluate the resectability of thoracic masses.

2 Thoracic Systemic Circulation

Parietal and visceral branches of the thoracic aorta (the thoracic segment of the descending aorta) supply blood to the neck, thoracic wall, thoracic spine, and intrathoracic organs. Parietal branches to the thorax are the dorsal intercostal, dorsal costoabdominal, and first two lumbar arteries. Visceral branches include bronchial arteries and the intrathoracic arterial blood supply to the esophagus from the bronchoesophageal artery (a branch of the aorta) and can vary in number and origin among subjects. The esophageal branches from the bronchoesophageal artery send

G. Bertolini (✉)
San Marco Veterinary Clinic, Padua, Italy
e-mail: bertolini@sanmarcovet.it

G. Bertolini (ed.), *Body MDCT in Small Animals*, DOI 10.1007/978-3-319-46904-1_11

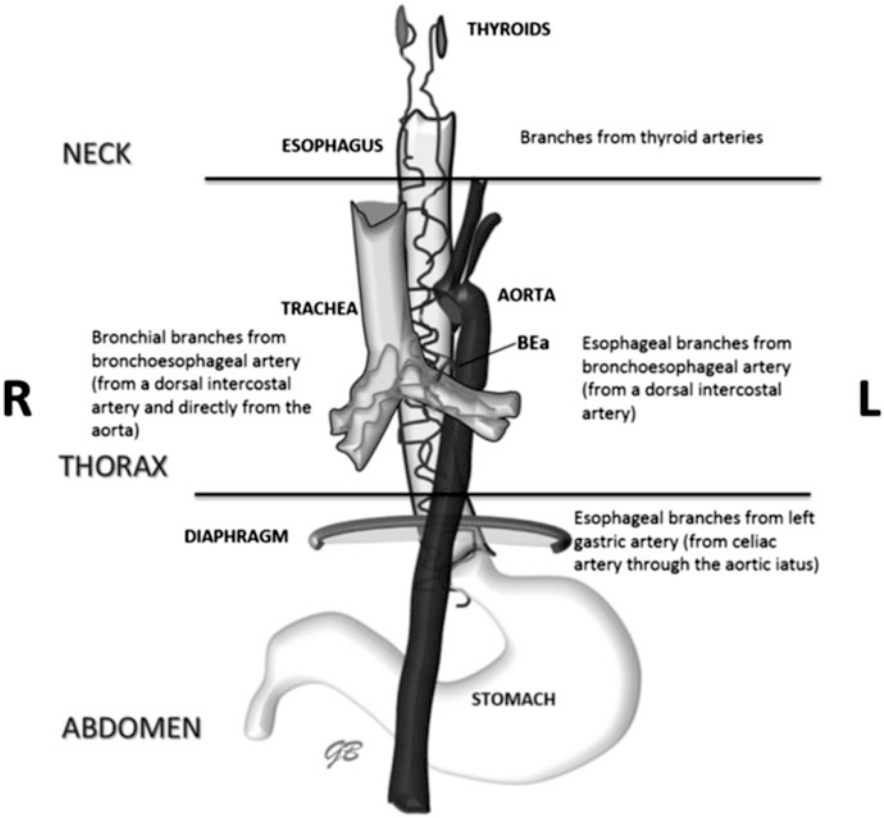

Fig. 1 Sources of arterial blood supply to the esophagus and bronchial system

ascending and descending (cranially and caudally, respectively) branches along the intrathoracic esophagus. They anastomose with each other, and the ascending esophageal arteries anastomose with esophageal branches on the caudal thyroid arteries; the descending branches anastomose with esophageal branches of the left gastric artery (Fig. 1). These connections are relevant to better understand some paraphysiological and pathological changes observed in contrast-enhanced MDCT examinations of the thorax. Capillary anastomoses exist between the bronchial and pulmonary circulations. Most bronchial and esophageal arteries have satellite veins that drain into the right azygos vein, which joins the CrVC before emptying into the right atrium. The CrVC forms by the confluence of the left and right brachiocephalic veins at the thoracic inlet. These veins receive venous blood from the head through the jugular veins before emptying into the CrVC.

2.1 Systemic Blood Supply to the Lung

The lungs have one of the largest blood supplies in the body. Their rich circulation is supplied via two separate vascular systems: the pulmonary and bronchial arteries. The pulmonary arteries carry deoxygenated blood at low pressure. They supply 99% of the blood flow to the lungs and participate in gas exchange at the alveolar capillary membrane (see chapter "The pulmonary vasculature"). The bronchial branches of the bronchoesophageal artery provide nourishment to the supporting structures of the lungs, including the pulmonary arteries. They carry oxygenated blood to the lungs at a pressure six times that of the pulmonary arteries but generally do not participate in gas exchange. The bronchial branches deliver blood primarily to the extra- and intrapulmonary airways (trachea and bronchial tree), bronchovascular bundles, nerves, supporting structures, regional lymph nodes, and visceral pleura. The pulmonary and bronchial arteries have rich and complex anastomoses at the capillary level.

3 MDCT Imaging Strategies

For complete evaluation of the thoracic vasculature, the scan range should extend from the neck (thyroid region) to the cranial abdomen. Visualization of the liver and abdominal vasculature is of value in cases involving bronchial arterial system hypertrophy or venous anomaly (e.g., interrupted caudal vena cava). In the author's experience, unenhanced scans are not useful for the evaluation of most vascular diseases. However, they may be useful for the simultaneous assessment of pulmonary or mediastinal pathology, and they should be obtained in such cases. The contrast-enhanced protocol depends on the clinical scenario and scanner available. For MDCTA of the thoracic vasculature, the same principles should be applied as for abdominal MDCTA. The goals are to optimize contrast medium (CM) delivery in the target vascular territory and to obtain isotropic or near-isotropic volume data. Factors related to patient characteristics (body weight and cardiac output), the injection protocol, and the scanner influence the degree of contrast enhancement. Optimal vascular enhancement for thoracic MDCTA requires rapid CM injection using a power injector system with a high flow rate (which varies according to patient size). Early CM distribution after peripheral intravenous administration differs among the heart and the systemic and pulmonary arteries and veins. For thoracic MDCTA, the delay between the start of CM injection and the initiation of scanning should be tailored based on the patient's characteristics using the bolus test or the bolus tracking technique. The ROI (region of interest) may be placed on different vascular structures, the aorta or the main pulmonary artery. Empiric timing or use of a standard scan delay may yield inconsistent results in veterinary patients. As a general principle, a larger CM volume with longer injection duration and, preferably, biphasic injection (with high initial and lower continuing flow

rates) should be used for slower MDCT scanners (<64 rows, requiring 20–50 s to cover the desired scan range at near-isotropic resolution) to achieve more favorable plateau-like arterial enhancement. For more rapid MDCT scanners (≥64 rows), a smaller amount of CM should be injected at a high iodine administration rate (i.e., high injection rate or high iodine concentration).

Comprehensive assessment of the thoracic aorta, for instance, in cases of suspected vascular rings, requires high-resolution (isotropic or near-isotropic) volumetric examination that enables clear delineation of the vascular and nonvascular mediastinal structures and compensates partially for pulsatile motion. Pulsatile artifacts are critical for the accurate diagnosis of aortic arch anomalies, especially in small patients. With slower scanners (with 2, 4, 8 and 16 rows), a half-scan interpolation reconstruction (50% overlap) algorithm for helical data can substantially clarify the difference between motion and intrinsic disease. With advanced (> 40 MDCT or DSCT) scanners, routine imaging of the thoracic aorta using electrocardiogram (ECG) gating is practical. The recent veterinary literature contains several descriptions of ECG-gated MDCT applications for the assessment of cardiac and extracardiac vascular anomalies in dogs and cats using advanced MDCT scanners with 40–64 or more rows. At our center, which is equipped currently with a second-generation 128-DSCT scanner, all CT examinations of patients with suspected or known aortic arch pathologies or other cardiovascular anomalies are now ECG gated or acquired in sub-second Flash spiral mode, resulting in the freezing of cardiovascular and respiratory motions. In our experience, a bolus test or bolus tracking is not required for consistent enhancement of the thoracic great venous vessels. Again, when assessment of the thoracic vasculature by thoracic-abdominal scanning is required as part of thoracic mass staging and characterization, biphasic acquisition using a unique high-rate CM injection (ideally followed by the same quantity of saline flush) can be performed. The first acquisition may include the neck, thorax, and cranial abdomen. The second scan includes the whole abdomen. When scanner technology permits, a third thoracic-abdominal series can be obtained as necessary. This approach enables the acquisition of excellent thoracic images and dual-phase evaluation of the liver in the same examination, with a single CM injection.

4 Anomalies of the Intrathoracic Systemic Arteries

4.1 Bronchoesophageal Artery Hypertrophy and Nonbronchial Artery Dilatation

In dogs, the bronchoesophageal artery usually originates from the right fifth intercostal artery, near the aorta. However, individual variation may exist, as reported in people and other mammals. Potential ectopic sites of origin include the inferior aortic arch, distal descending thoracic aorta, subclavian artery, brachiocephalic

trunk, internal mammary artery, and coronary arteries. The bronchial arteries play important roles in diseases affecting the airways and lung parenchyma. The bronchial circulation and other nonbronchial collateral vessels (e.g., intercostal, internal mammary, and inferior phrenic arteries) respond to chronic pulmonary ischemia and decreased pulmonary blood flow with hypertrophy or enlargement, in the effort to maintain blood flow to the affected lung and participate in gas exchange through systemic pulmonary arterial anastomoses that develop beyond the pulmonary artery obstruction. Bronchial branches, regardless of their origins, pass through the mediastinum to the hila, where they follow the course of the main bronchi and their branches. In contrast, nonbronchial systemic arteries do not enter the lung parenchyma through the hila and do not run parallel to the bronchi, but their presence can be suspected based on thin-section MDCT images showing thickening of the pleura and enhancement of tortuous arteries in the extrapleural fat. The imaging appearance of dilated bronchial and nonbronchial arteries should alert the radiologist to consider obstructive disorders affecting the pulmonary circulation and prompt the exclusion of related disorders, such as chronic infectious and/or inflammatory processes, chronic thromboembolic disease, and congenital cardiovascular anomalies of the thorax. In humans, normal bronchial arteries typically arise directly from the aorta and have diameters of <1.5 mm at the origin and 0.5 mm at the point of entry into a bronchopulmonary segment. A bronchial artery with a diameter >2 mm on a CT image is most likely abnormal and may be a source of hemoptysis. MDCT technology has been used to describe two distinct patterns of bronchoesophageal artery hypertrophy (BEAH) in dogs: congenital and acquired. The congenital vascular pattern includes an aberrant origin of the right bronchoesophageal artery (from the brachiocephalic trunk), the presence of a dense vascular network in the dorsal mediastinum, and the presence of a large vessel (5–7.2 mm diameter) arising from this network, describing a couple of loops and then clearly emptying into the proximal part of the left or right pulmonary artery through a small orifice (Figs. 2 and 3). This pattern may be the result of the persistence of the embryonic pulmonary–systemic connection, as hypothesized for patent ductus arteriosus (PDA). In the acquired pattern of BEAH, CT features in dogs are similar to those described for bronchial artery hypertrophy in humans. The bronchial branches are prominent; at the bronchial bifurcation, they continue their course along the bronchi, describing a tortuous path, and ultimately anastomose with the subsegmental pulmonary arteries (Figs. 4 and 5). These enlarged bronchial arteries may protrude into the bronchial lumen, as reported in humans. However, descriptions to date suggest that spontaneous rupture and hemoptysis do not occur in dogs. Differences in normal bronchial arterial blood supply, involving also the esophageal vasculature in dogs, may play a role in preventing the rupture of these enlarged vessels. The vast canine esophageal venous plexus may serve to decompress the arterial system, preventing vascular rupture and bleeding. Acquired patterns of BEAH are commonly seen on isotropic pulmonary MDCTA and high-quality contrast-enhanced MDCT examinations of the thorax. In the author's experience and in cases reported in the literature, the enlargement of bronchial arteries is a sequela of pulmonary embolism (e.g., dirofilariasis or angiostrongylosis).

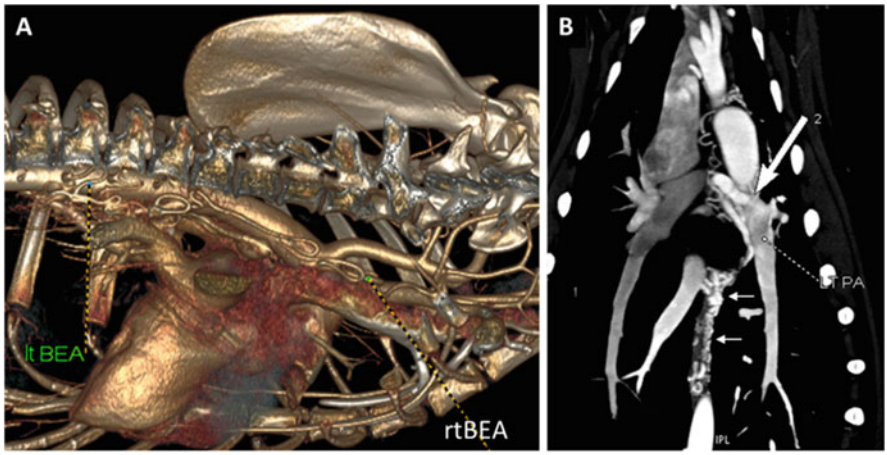

Fig. 2 BEAH with bronchial–pulmonary artery fistula (congenital pattern). (**a**) Left bronchoesophageal artery (ltBEA) from the aorta (through an intercostal artery) and right bronchoesophageal artery (rtBEA) from the brachiocephalic trunk. (**b**) Dorsal MPR of the same dog. *Arrow* indicates the bronchial left pulmonary artery (ltPA) fistula. Note the prominent tortuous esophageal vessels (*short arrows*)

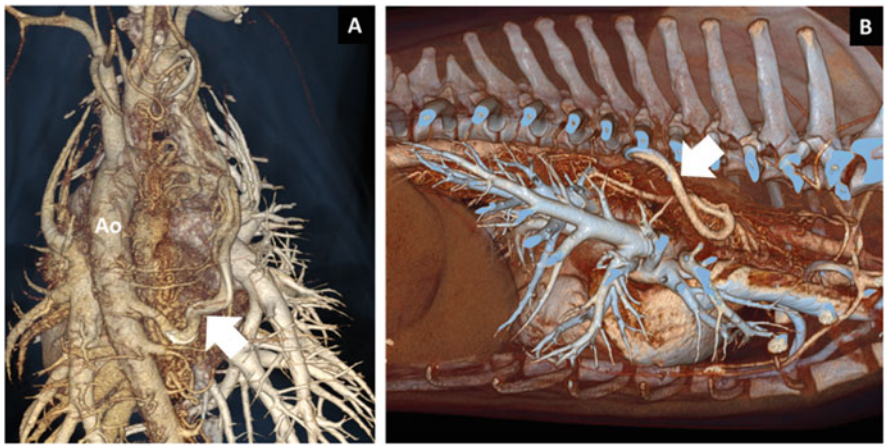

Fig. 3 BEAH with systemic pulmonary fistula (not visible here). (**a**) Dorsal view showing a larger bronchoesophageal artery arising directly from the aorta (Ao). Note the multiple small, tortuous esophageal vessels in the mediastinum. (**b**) VR of the same dog, again showing the course of the bronchoesophageal artery

4.2 Anomalies of the Aortic Arch and Its Branches

In mature mammals, the aortic arch is left sided and gives rise, in order, to the brachiocephalic trunk and the left subclavian artery. The brachiocephalic trunk gives rise, in order, the left and right common carotid arteries and the right

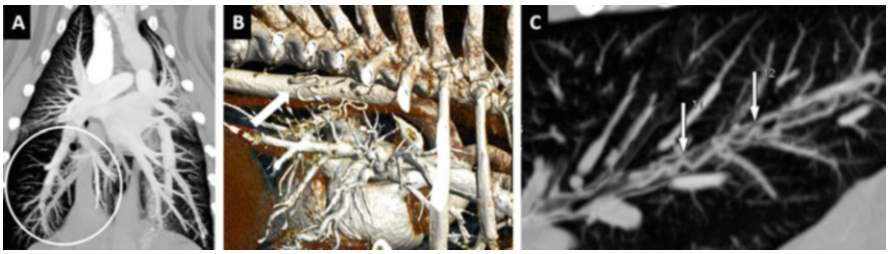

Fig. 4 Bronchial artery hypertrophy, acquired pattern (history of cardiopulmonary filariasis). (**a**) Dorsal thin-MIP view. The pulmonary vasculature of the right caudal lobe is less enhanced than the cranial and contralateral vasculature. *Arrow* indicates a moderately enlarged bronchial artery. (**b**) Thin-MIP view of the right caudal lobe in the same dog. *Arrows* indicate the prominent bronchial branches coursing along the bronchus

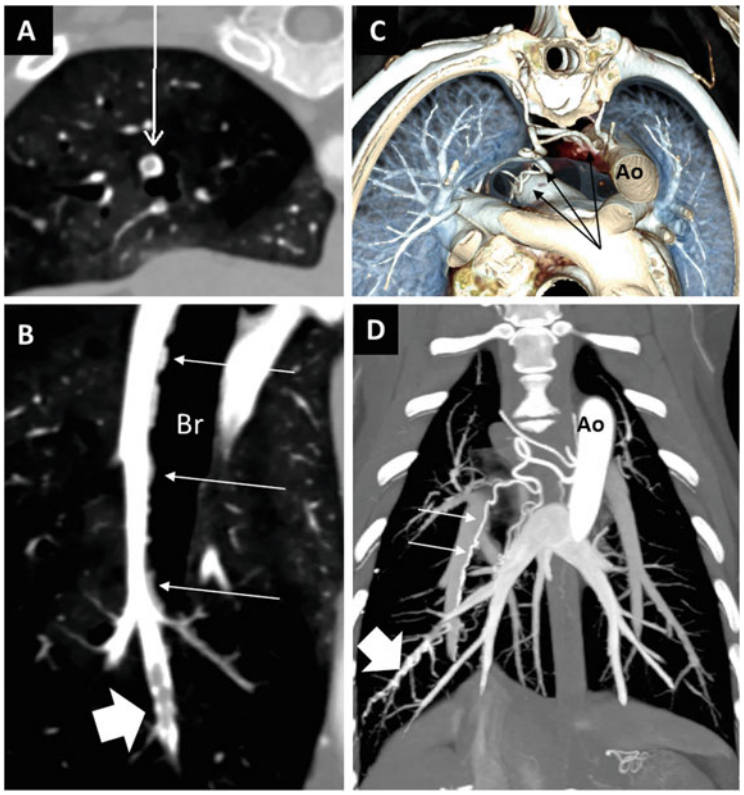

Fig. 5 Bronchial artery hypertrophy in a dog with pulmonary embolism (acquired pattern). (**a**) Transverse view showing a peripheral filling defect in a pulmonary vessel. (**b**) Dorsal MPR showing the filling defect (*arrow*). *Thin arrows* show the bronchial artery projecting into the bronchial lumen (Br). (**c**) Volume-rendered transverse cut of the thorax through the fourth to fifth ribs. Ao, descending aorta. *Arrows* indicate the bronchoesophageal artery arising from the aorta. (**d**) Dorsal thin-MIP showing the prominent bronchial branches from bronchoesophageal artery, coursing along the bronchi (*arrows*) and anastomosing with subsegmental pulmonary vessels (*large arrow*)

subclavian artery. A common bicarotid trunk is an uncommon anatomic variant, in which a single trunk arises from the brachiocephalic trunk directly and then divides into the two common carotid arteries. Any segment of the embryonic arch can regress or persist abnormally in an extensive array of aortic arch anomalies, known as vascular ring anomalies. They can remain asymptomatic or cause airway or esophageal compression and stenosis. Although considered to be rare, these anomalies are increasingly recognized with the diffusion of MDCT in veterinary practice. Coarctation of the aorta refers to a narrowing of the aortic lumen, which occurs in the segment of the aorta between the origin of the left subclavian artery and the insertion of the ductus arteriosus. It has been reported in a few dogs and one cat, where, as is the case with many congenital abnormalities, it has been associated with other anomalies, such as persistent right aortic arch (PRAA). Aortic hypoplasia, described in dogs, refers to the interruption of the aorta, which may be associated with coarctation and other congenital defects, such as PDA. Double aortic arches have been reported in dogs and cats. In this condition, the fourth aortic arches persist, encircling and constricting the esophagus and trachea. PRAA occurs when the right dorsal aorta remains patent and the left dorsal aorta regresses abnormally. Most vascular ring anomalies reported in dogs consist of PRAA and left-sided ligamentum arteriosum, with the heart base making up the ventral portion of the ring. The presence of an aberrant left subclavian artery is frequently reported in association with PRAA (i.e., in 33% of dogs with PRAA); in some cases, this artery takes a retroesophageal position, contributing to esophageal compression in dogs (Figs. 6 and 7). Commonly reported anomalies coexisting with vascular ring anomalies are PDA and persistent left CrVC. An aberrant left subclavian artery arising from a PDA has been described in a dog with PRAA. An aberrant right subclavian artery arises from the normally left-sided aortic arch, distal to the left

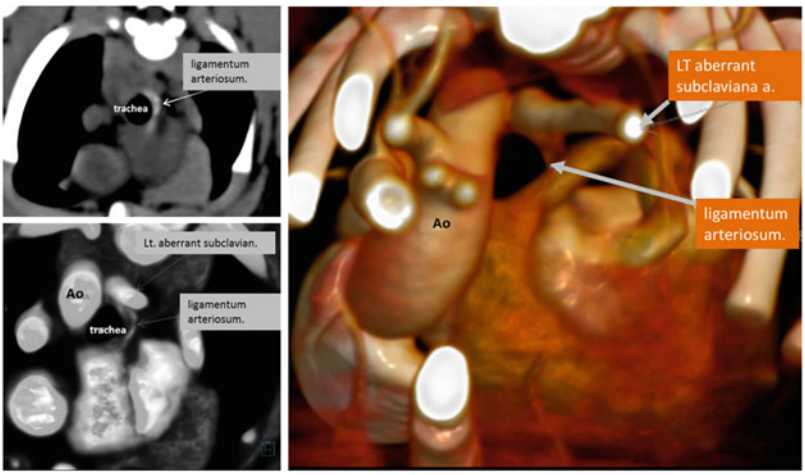

Fig. 6 PRAA, left retroesophageal subclavian artery and left-sided ligamentum arteriosum in a puppy with postprandial regurgitation

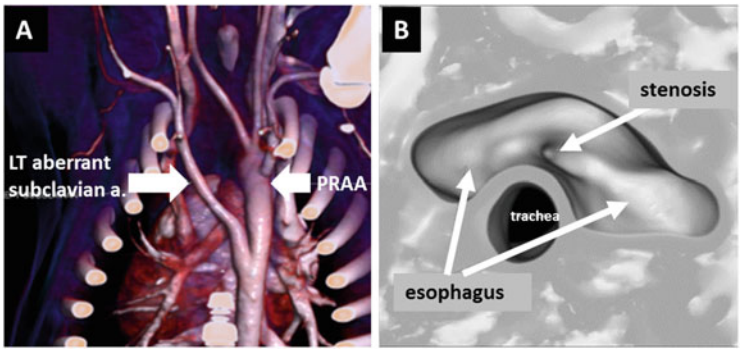

Fig. 7 PRAA and aberrant, retroesophageal, left subclavian artery. (**a**) Volume-rendered cut from the dorsal perspective. (**b**) 3D endoluminal view of the enlarged esophagus and the site of stenosis

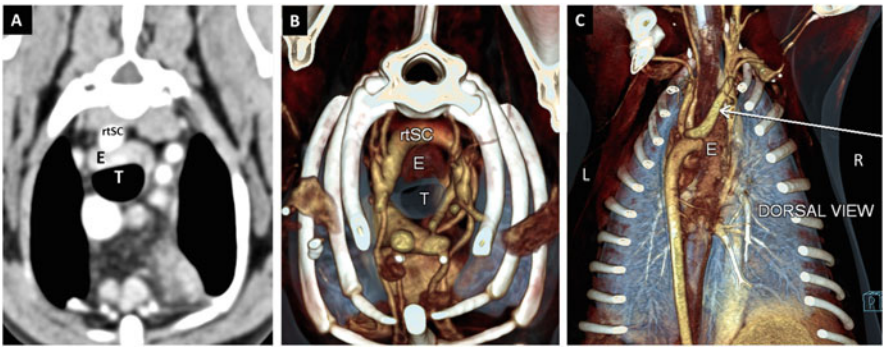

Fig. 8 Right aberrant subclavian artery in a dog with secondary aspiration pneumonia. (**a**) Transverse view at the thoracic inlet. *T* trachea, *E* esophagus, *rtC* right subclavian artery. (**b**) 3D volume-rendered transverse cut. (**c**) 3D volume-rendered dorsal cut. *Arrow* indicates the right aberrant subclavian artery

subclavian artery, or from a bisubclavian trunk. Crossing the mediastinal midline, the artery then passes to the right side, dorsal to the esophagus, constricting its dorsal aspect (Fig. 8). This finding may be incidental, but it has been reported in association with post-prandial regurgitation with secondary aspiration pneumonia in dogs.

5 Anomalies of the Intrathoracic Systemic Veins

The *jugular veins* drain the head and neck and enter the dorsal aspect of the brachiocephalic vein. Anomalies of the jugular veins described in the veterinary literature include the absence/agenesis of one or both jugular veins in cats and

primary congenital aneurysm in dogs (Fig. 9). These variants or anomalies are not of clinical significance (apart from the possibility of giant aneurysm rupture), but they may impact surgical and interventional endovascular treatment or be part of a complex of congenital vascular anomalies. In the mammalian embryo, venous return to the primitive heart occurs through the paired cranial and caudal cardinal veins. The left and right common cardinal veins empty into the transversely positioned sinus venosus, which subsequently develops into the right atrium. Most of the left cardinal system atrophies; only the left common cardinal vein persists, forming the coronary sinus. Incomplete atrophy of the left cranial cardinal vein leads to *persistence of the left CrVC* (Figs. 10 and 11). Two types of persistent left CrVC have been described in dogs and cats: a complete type, in which the non-atrophied left cranial cardinal vein retains its embryological connection with the coronary sinus; and an incomplete type, in which the distal portion of the persistent vein atrophies, whereas the proximal portion persists and receives the

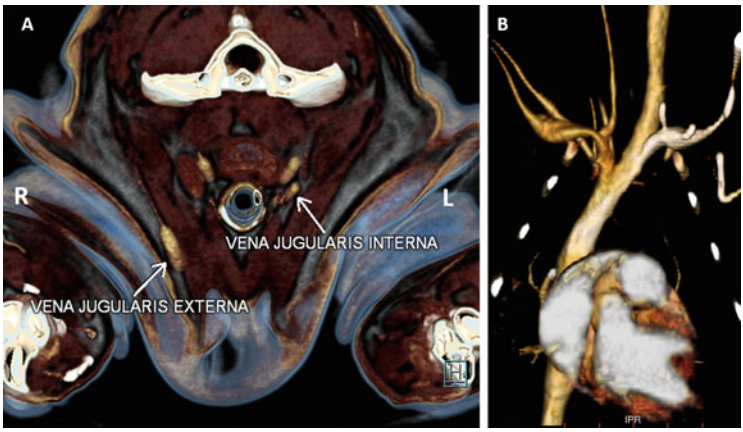

Fig. 9 Anomalies of the jugular veins. (**a**) Transverse cut of the neck in a dog with absent/hypoplastic right internal and left external jugular veins. (**b**) 3D VR from another dog with absent left internal and right external jugular veins

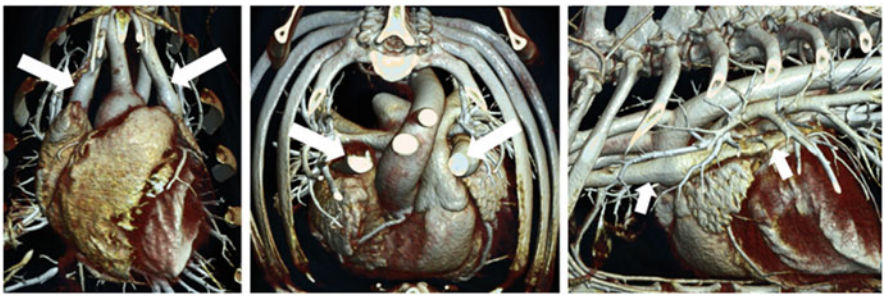

Fig. 10 Persistent left CrVC in an English bulldog (complete; see text for explanation)

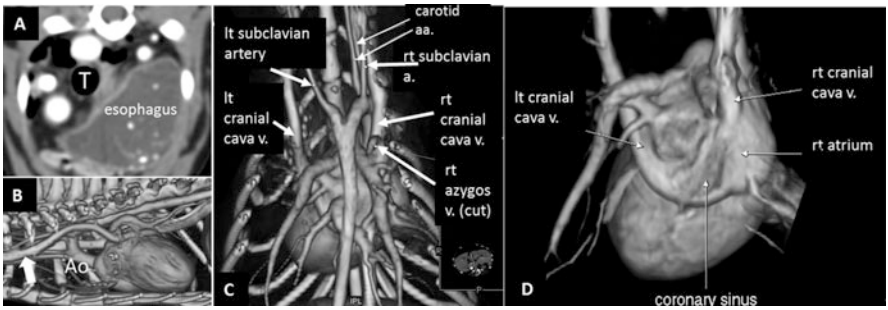

Fig. 11 16-MDCT image of the thoracic vasculature in a cat with PRAA, left aberrant subclavian artery, and duplication of the CrVC and caudal vena cava (not visible here). (**a**) Transverse view showing megaesophagus. *T* trachea. (**b**) VR of the thoracic cavity, *left view*. *Arrow* indicates the persistent left CrVC. (**c**) 3D volume-rendered dorsal cut. (**d**) Manual segmentation of the previous view. The ribs, aorta, and most pulmonary vessels have been removed. The non-atrophied left cranial cardinal vein retains its embryological connection with the coronary sinus

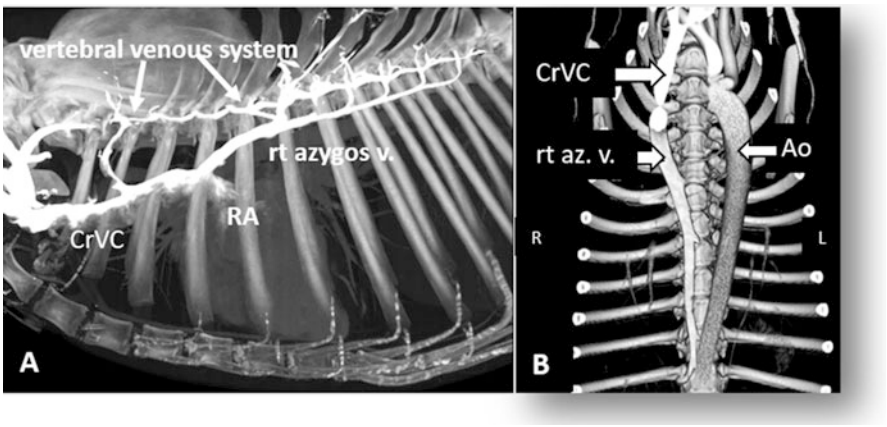

Fig. 12 Relationships among the CrVC, azygos vein, and vertebral venous system. *RA* right atrium. (**a**) Contrast-enhanced MIP image. (**b**) 3D VR of the dorsal mediastinum (*ventral view*). The heart, lung, and pulmonary vasculature have been removed

hemiazygos vein. Persistent left CrVC alone is often an incidental CT finding, but it has been reported to cause esophageal stenosis and secondary megaesophagus. Moreover, subjects with left persistent CrVC may have other severe cardiovascular defects and should be assessed thoroughly.

The *azygos system* (right azygos vein and hemizygous vein) is an important intermediary between the caudal and CrVCs via the internal vertebral venous system, which drains into the cranial vein (Fig. 12). In this setting, the azygos veins are systemic and involved in congenital and acquired portosystemic shunts. In patients with porto-azygos connections, the right azygos vein is enlarged and tortuous. Conspicuous enlargement of the right azygos vein may be encountered

also in azygos continuation of the caudal vena cava, a congenital anomaly. These congenital and acquired conditions are discussed extensively in the chapter entitled "MDCT of the abdominal vasculature." Moderate enlargement of the azygos vein may be seen in many other pathological conditions, such as obstruction or increased resistance in the CrVC, chronic obstruction of the caudal vena cava with collateral formation, diseases of the pericardium, and engorgement of the vertebral or esophageal venous plexi. Transient, slight enlargement of the right azygos vein and ipsilateral internal vertebral sinus is frequently observed in veterinary patients undergoing MDCT after high-rate CM injection via the cephalic vein, probably due to a temporary pressure increase in the CrVC.

The esophageal (submucosal) and periesophageal venous plexi drain the esophagus and are situated along its entire length. In the cranial part of the esophagus, the periesophageal venous plexus drains primarily into the CrVC via the bronchoesophageal and thyroid veins. Venous drainage of the middle part of the esophagus is largely into the azygos and hemiazygos veins and thereby into the CrVC. The veins of the caudal thoracic esophagus and abdominal esophagus drain into the azygos vein and accompany the esophageal branch of the left gastric artery, reaching the portal circulation by the splenic vein or directly by the portal vein (a tributary of the portal system). The latter is a possible hepatofugal pathway in cases of portal hypertension (PH). In several pathological conditions, MDCT of the thorax may reveal enlargement of these vessels, called *esophageal and paraesophageal varices*. Esophageal varices remain submucosal, whereas paraesophageal varices form a large mediastinal vascular nidus that enhances strongly after CM injection. Depending on the underlying cause, esophageal varices may be distinguished as "uphill" varices, which are commonly associated with PH and drain into the CrVC; and "downhill" varices, which form in cases of increase resistance or obstruction in the CrVC (Fig. 13). When the obstruction or resistance

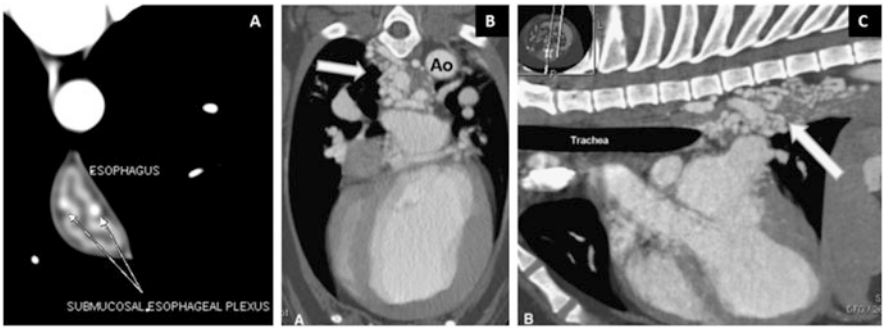

Fig. 13 Esophageal and paraesophageal varices. (**a**) Transverse view of the thoracic esophagus in a dog with PH. (**b**, **c**). Transverse and sagittal images from a dog with a congenital bronchial–pulmonary artery fistula (BEAH) and paraesophageal varices (*arrow*)

is proximal to the azygos veins, blood flows to the heart through mediastinal collaterals, and downhill varices are confined to the cranial esophagus. When the obstruction is below or involves the azygos vein, blood returns via the hemiazygos, esophageal, and portal veins and may be associated with varices extending throughout the entire esophagus. Both types of esophageal varices have been described and classified in small animals using MDCTA. Uphill varices have been described alone or in association with large abdominal acquired portosystemic shunts (APSS) in patients with PH. Downhill varices have been described in cases of BEAH, chronic CrVC compression, and tumoral invasion.

6 Acquired Conditions Affecting the Intrathoracic Systemic Vessels

Several acquired conditions may primary or secondarily involve the thoracic vasculature. Acquired conditions of the extracardiac arterial system, such as aortic dissections and aneurysms, are rarely reported in domestic animals. Aortic dissection has been documented in a cat with severe systemic hypertension using ECG-gated 64-MDCTA. Traumatic injuries may involve the thoracic vasculature (see the "The body trauma" chapter). Obstruction of the CrVC, jugular veins, or other thoracic veins may be caused by neoplastic invasion of the venous wall associated with intravascular neoplastic thrombosis or, more simply, by extrinsic pressure of a tumor mass against the relatively thin-walled CrVC. As obstruction is chronic, several venous collateral pathways usually develop, allowing blood to return to the right atrium (Figs. 14 and 15). The patterns of these pathways differ depending on the level of obstruction. Whatever its cause, obstruction of the CrVC causes elevated pressure in the veins draining into the CrVC and increased or reversed blood flow through the collateral vessels. The major collateral pathways are the vertebral–azygos–hemiazygos pathway and the internal and external mammary pathways. CT diagnosis is based on two important findings: a lack of or decrease in opacification of central venous structures distal to the obstruction site and intense opacification of collateral venous vessels. Despite these collateral pathways, venous pressure is elevated in the upper compartment when obstruction of the CrVC persists and CrVC syndrome ensues. Whole-body MDCT discloses the cause and site of increased resistance or obstruction of the CrVC, the collateral pathways, and the constellation of possible complications. Depending on the anatomic location of the thrombus, thrombosis of the CrVC can lead to increased lymphatic outflow from the thoracic duct into the venous system. Thoracic duct patterns vary greatly, but the duct always empties into the systemic circulation at the jugulocaval angle. Thrombosis at this level has been associated with chylothorax in dogs and cats (Fig. 16).

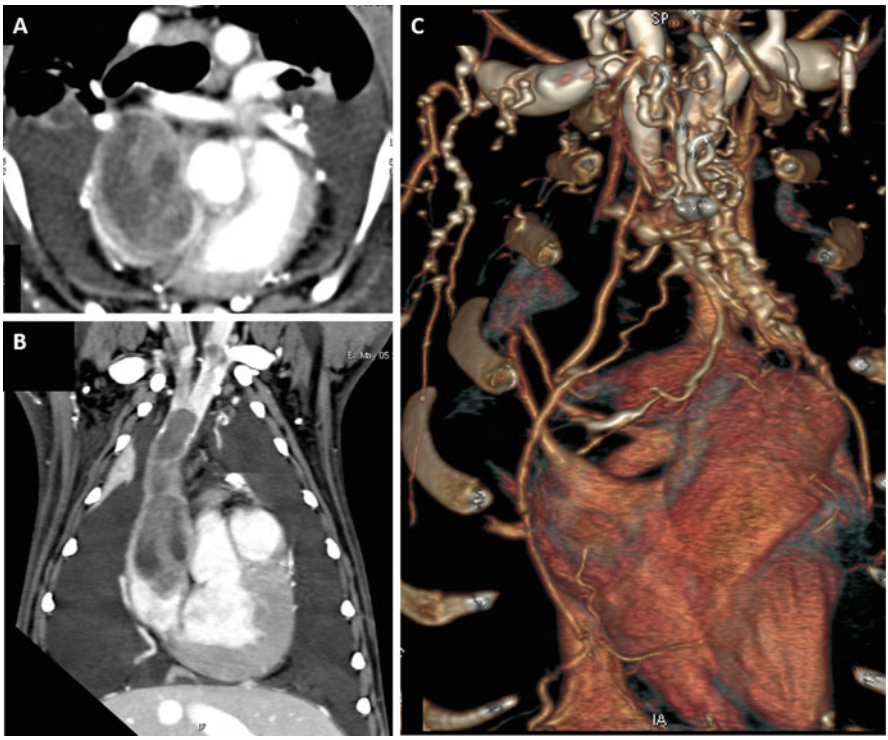

Fig. 14 Right atrial mass invading the CrVC. (**a**) Transverse view. (**b**) Dorsal MPR view. Note the abundant bilateral pleural effusion. (**c**) VR showing multiple collaterals with 'string of beads' pattern, bypassing the obstructed cava

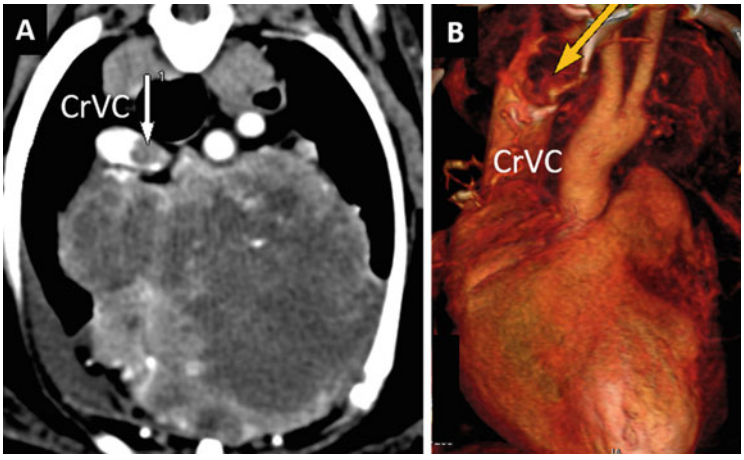

Fig. 15 (**a**) Mediastinal mass (thymic carcinoma) with CrVC invasion (*arrow*). (**b**) VR showing the invaded CrVC and initial collaterals (*thin arrow*)

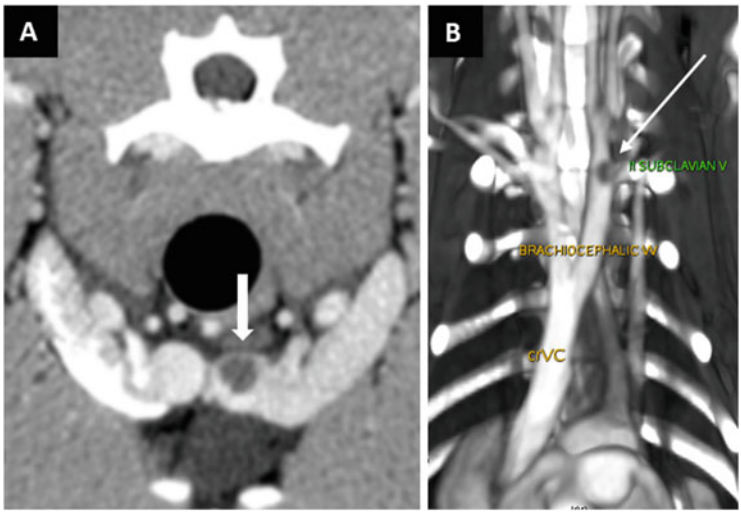

Fig. 16 Thrombosis at the jugulocaval angle and chylothorax. (**a**) Transverse view in a dog. (**b**) Dorsal MIP image of a cat. *Arrow* indicates the thrombosis

Further Readings

Bertolini G. Acquired portal collateral circulation in the dog and cat. Vet Radiol Ultrasound. 2010;5:25–33.

Bertolini G, Zotti A. Imaging diagnosis: absence of the left external and both internal jugular veins in a cat. Vet Radiol Ultrasound. 2006;47:468–9.

Bertolini G, De Lorenzi D, Ledda G, Caldin M. Esophageal varices due to a probable arteriovenous communication in a dog. J Vet Intern Med. 2007;21:1392–5.

Bezuidenhout AJ. Unusual anomalies of the arteries at the base of the heart in a dog. J S Afr Vet Assoc. 1992;63:32–5.

Bottorff B, Sisson DD. Hypoplastic aberrant left subclavian artery in a dog with a persistent right aortic arch. J Vet Cardiol. 2012;14(2):381–5. doi:10.1016/j.jvc.2012.01.013.

Buchanan JW. Persistent left cranial vena cava in dogs: angiocardiography, significance, and co-existing anomalies. J Am Vet Radiol Soc. 1963;4:1–8.

Du Plessis CJ, Keller N, Joubert KE. Symmetrical double aortic arch in a beagle puppy. J Small Anim Pract. 2006;47:31–4. doi:10.1111/j.1748-5827.2006.00009.x.

Heaney AM, Bulmer BJ. Cor triatriatum sinister and persistent left cranial vena cava in a kitten. J Vet Intern Med. 2004;18(6):895–8.

Henjes CR, Nolte I, Wefstaedt P. Multidetector-row computed tomography of thoracic aortic anomalies in dogs and cats: patent ductus arteriosus and vascular rings. BMC Vet Res. 2011;7:57.

Joly H, D'Anjou M-A, Huneault L. Imaging diagnosis – CT angiography of a rare vascular ring anomaly in a dog. Vet Radiol Ultrasound. 2007;49:42–6.

Larcher T, Abadie J, Roux FA, Deschamps JY, Wyers M. Persistent left cranial vena cava causing oesophageal obstruction and consequent megaoesophagus in a dog. J Comp Pathol. 2006;135 (2–3):150-2. Epub 2006 Sep 6.

Lawler LP, Corl FM, Fishman EK. Multi-detector row and volume-rendered CT of the normal and accessory flow pathways of the thoracic systemic and pulmonary veins. Radiographics 22 Spec No:S45–S60. 2002.

Leach SB, Fine DM, Schutrumpf RJ 3rd, Britt LG, Durham HE, Christiansen K. Coil embolization of an aorticopulmonary fistula in a dog. J Vet Cardiol. 2010;12:211–6.
Ledda G, Caldin M, Mezzalira G, Bertolini G. Multidetector-row computed tomography patterns of bronchoesphageal artery hypertrophy and systemic-to-pulmonary fistula in dogs. Vet Radiol Ultrasound. 2015;56(4):347-58. doi:10.1111/vru.12247. Epub 2015 Mar 9.
LeRoux A, Granger LA, Reynolds C, Gaschen L. Computed tomography features of bronchial and non-bronchial collateral arterial circulation development in a dog diagnosed with multiple chronic pulmonary thrombi. J Vet Cardiol. 2013;15:283–7.
Liu SK, Yarns DA, Carmichael JA, Tashjian RJ. Pulmonary collateral circulation in canine dirofilariasis. Am J Vet Res. 1969;30:1723–35.
Malik R, Bellenger CR, Hunt GB, Church DB, Allan GS. Aberrant bronchoesphageal artery mimicking patent ductus arteriosus in a dog. J Am Anim Hosp Assoc. 1994;30:162–4.
Markovic LE, Kellihan HB, Roldán-Alzate A, Drees R, Bjorling DE, Francois CJ. Advanced multimodality imaging of an anomalous vessel between the ascending aorta and main pulmonary artery in a dog. J Vet Cardiol. 2014;16:59–65.
Miller R, Wilson C, Wray J, Jakovljevic S, Tappin S. Adult-onset regurgitation in a dog with an aberrant right subclavian artery: a CT angiographic study. Vet Rec Case Rep. 2015;3:e000138. doi:10.1136/vetreccr-2014-000138.
Pownder S, Scrivani PV. Non-selective computed tomography angiography of a vascular ring anomaly in a dog. J Vet Cardiol. 2008;10:125–8. doi:10.1016/j.jvc.2008.09.003.
Robinson NA, Armíen AG. Tubular hypoplasia of the aorta and right atrioventricular valve dysplasia in a Bulldog. J Vet Diagn Invest. 2010;22(4):667–70.
Routh CE, Hagen RU, Else RW, Strachan FA, Yool DA. Imaging diagnosis—congenital venous aneurysm of the left external jugular vein. Vet Radiol Ultrasound. 2009;50(5):506–8.
Salmeri KR, Bellah JR, Ackerman N, Homer B. Unilateral congenital aneurysm of the jugular, linguofacial, and maxillary veins in a dog. J Am Vet Med Assoc. 1991;198(4):651–4.
Scollan K, D S. Multi-detector computed tomography of an aortic dissection in a cat. J Vet Cardiol. 2014;16(1):67–72. doi:10.1016/j.jvc.2013.11.002.
Singh A, Brisson BA. Chylothorax associated with thrombosis of the cranial vena cava. Can Vet J. 2010;51(8):847–52.
Specchi S, Olive J, Auriemma E, Blond L. Anatomic variations of feline internal and external jugular veins. Vet Radiol Ultrasound. 2012;53(4):367–70. doi:10.1111/j.1740-8261.2012.01936.x.
Vianna ML, Krahwinkel DJ. Double aortic arch in a dog. J Am Vet Med Assoc. 2004;225:1222–4. doi:10.2460/javma.2004.225.1222.
Walker CM, Rosado-de-Christenson ML, Martínez-Jiménez S, Kunin JR, Wible BC. Bronchial arteries: anatomy, function, hypertrophy, and anomalies. Radiographics. 2015;35(1):32–49. doi:10.1148/rg.351140089.
White RN, Burton CA, Hale JS. Vascular ring anomaly with coarctation of the aorta in a cat. J Small Anim Pract. 2003;44(7):330–4.
Yamane T, Awazu T, Fujii Y, et al. Aberrant branch of the bronchoesophageal artery resembling patent ductus arteriosus in a dog. J Vet Med Sci. 2001;63:819–22.
Yoon H-Y, Jeong S. Surgical correction of an aberrant right subclavian artery in a dog. Can Vet J. 2011;52(10):1115–8.

The Pulmonary Vasculature

Randi Drees

1 Introduction

Pulmonary angiography (PA) using computed tomography (CT) aims to highlight the anatomy of the pulmonary vessels by timing the acquisition of the CT scan with the presence of the contrast medium in the pulmonary vessels. CTPA is specifically useful to evaluate for intravascular alterations such as pulmonary thromboembolism (PTE). Scan protocols are aimed to provide high-resolution images of the thorax to resolve the anatomy of the pulmonary vessels, further allowing for assessment of changes in the pulmonary parenchyma, which can often support diagnosis of PTE.

2 MDCT Imaging Strategies

Sedation or general anesthesia is generally needed to enable safe positioning of the patient on the CT couch during image acquisition and allow for injection of the contrast bolus without inducing patient motion. Decision for general anesthesia or sedation is to be made based on the presentation of the individual patient; general anesthesia will allow for better respiration control compared to sedation only. Respiratory control can be achieved manually or medically. Respiration control is essential for avoiding respiratory motion that may reduce the diagnostic quality of the CTPA exam.

Newer CT units may be equipped with respiratory gating capabilities, though a panting patient will still remain challenging to examine. Ideally, sedation or

R. Drees (✉)
Royal Veterinary College, University of London, London, UK
e-mail: rdrees@rvc.ac.uk

G. Bertolini (ed.), *Body MDCT in Small Animals*, DOI 10.1007/978-3-319-46904-1_12

anesthesia is induced just prior to the CT scan; this will help to avoid atelectasis that can make visibility of the pulmonary vessels challenging. Patients should be kept in sternal recumbency prior and during the scan for the same purpose.

Fan beam CT scanners are preferentially used to for the acquisition of CTPA exams. The acquisition time in cone beam CT scanners does usually not allow for motion-free images as well as accurate scan timing to the bolus arrival and duration of bolus persistence in the pulmonary vessels of interest, which can make image interpretation challenging.

The scan field should ideally include the cranial to the caudal extent of the lungs. The display field of view (DFOV) should be set to include the lungs. Increasing the DFOV beyond the patient anatomy of interest will reduce resolution along the *x*/*y* -plane, and smaller lesions may then be difficult to detect. Tube voltage setting of 100–120 kVp and tube current setting of 200 mA are commonly used. Helical scan mode is to be used for all CTPA exams. Tube rotation time, slice collimation, and pitch will need to be adjusted along with the contrast bolus volume and injection parameters to allow for optimal coverage of the selected area. Tube rotation time is ideally kept low ($\leq$1 s). Detector pitch values of $\leq$1.4 are desirable. For single detector row CT (SDCT) units, slice width of 2–3 mm should be used for patients under $<$10 kg; 3 to maximal 5 mm slice width may be used for patients $>$10 kg. For multi-detector row CT (MDCT) units, slice collimation and slice reconstruction thickness should aim for 0.625–1.25 mm for patients $<$10 kg and 1.25–3 mm for patients $>$10 kg. A medium frequency spatial reconstruction kernel is used to generate the diagnostic images for the CTPA exam. An additional high frequency reconstruction kernel may be acquired for evaluating the pulmonary parenchyma.

Ideally the contrast medium (CM) arrives through the cranial vena cava to the heart; a saphenous catheter is commonly used to inject the contrast medium unless a jugular catheter is present. Specific catheterization of the right ventricle is not necessary. Iodinated contrast medium is used for CTPA exams; ionic or nonionic products can be used. The CM dose or volume is determined by the length of the exam, i.e., the duration of contrast enhancement needed to highlight the pulmonary vessels, predominantly arteries, for the duration of the scan. The scan duration will heavily depend on the specifications of the scanner and the size of the patient: SDCT units will require a longer scan time compared to high-end MDCT or dual-source MDCT units for a given patient length. The standard contrast medium dose of 600–800 mgI/kg (commonly 2 ml/kg) will serve as a good starting point, though 400 mgI/kg has been reported as a sufficient dose. Especially in smaller patients, where bolus volume can be very low, mild increase of the bolus volume in combination with prolonging injection duration can help to achieve adequate vascular opacification. A saline flush can be used to advance the tail of the CM bolus into the central blood volume and also flush the tubing and may help to avoid streak artifact. A power injector should be used for all CTPA exams: this allows for

quick and precisely timed bolus delivery. Injection pressure of 300 PSI is usually not to be exceeded. The start of the scan will need to be timed to the arrival of the CM in the pulmonary vessels. Time of arrival of the contrast bolus is determined by injection speed and volume, though also patient factors such as heart rate and blood pressure play a role. Test bolus or bolus-tracking methods can be used to plan the individual patients' CTPA scan, though a generic scan delay of 4–6 s post-injection may deliver an adequate exam. Contrast bolus arrival times of 4–6 s for the main pulmonary artery and 5 s for the right pulmonary artery have been reported.

Soft tissue window width (~400 HU) and level (~40 HU) are used to review the images acquired using the medium frequency spatial reconstruction kernel. While the basic evaluation of the study relies on the acquired transverse images, standard multiplanar reconstructions (MPRs) or curved MPRs can be very helpful to outline specific structures. Minimum intensity projections (MinIPs) can be very helpful to detect subtle lung changes related to PTE. Specific vessel tracking software is available for human applications and has not been verified for veterinary studies.

3 Normal CT Anatomy

3.1 Pulmonary Arteries

The main pulmonary artery (MPA) arises from the right ventricular outflow tract (RVOT) with a small bulbous dilation just proximal to the pulmonic valves (Fig. 1). The valve leaflets may be seen as a thin filling defect in the lumen of the RVOT, especially when using cardiac gating to acquire the images during diastole. The

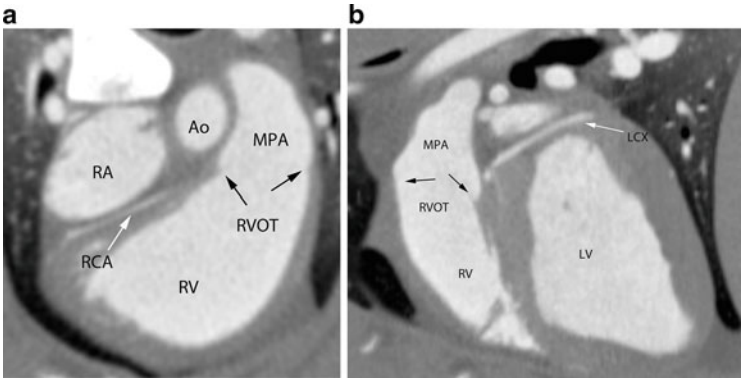

Fig. 1 The main pulmonary artery (MPA) arises from the right ventricular outflow tract (RVOT), depicted in transverse plane (**a**) and oblique sagittal plane (**b**). The pulmonic valves may be seen as small filling defects just ventral to the small bulbous dilation at the base of the MPA (*black arrows*). Also depicted are the right ventricle (RV), right atrium (RA), aorta (Ao), right coronary artery (RCA), left circumflex coronary artery (LCX), and left ventricle (LV)

main pulmonary artery to aortic diameter ratio (MPA:Ao) as used in echocardiography with upper limit of 0.98 cannot be fully translated to CTPA exams: inspiratory phase CTPA exams result in higher MPA:Ao ratio compared to expiratory phase CTPA exams and inspiratory CTPA exams constantly overestimated the MPA:Ao when comparing to echocardiography; a mean ratio of 1.108 with a standard deviation of 0.125 has been reported instead (Fig. 2).

The MPA branches into the left and right main pulmonary artery (LPA and RPA). The LPA has a fairly straight course caudally, whereas the RPA crosses along the heart base, ventral to the trachea, and may have a focal indentation where it crosses ventral to the trachea and right main stem bronchus (Fig. 3). The lobar

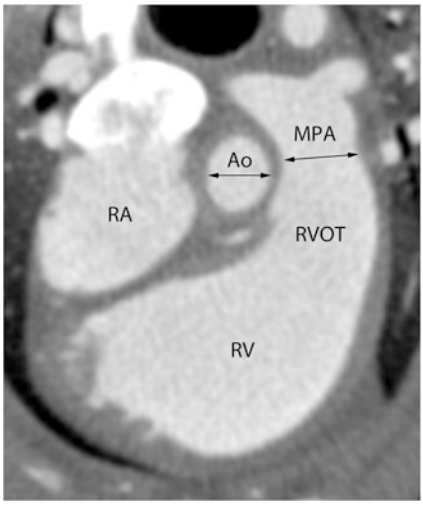

Fig. 2 The main pulmonary artery to aorta ratio (MPA:Ao) ratio can be estimated from a transverse plane image, though the values used in echocardiography cannot be fully translated. Main pulmonary artery (MPA), right ventricular outflow tract (RVOT), right ventricle (RV), right atrium (RA), aorta (Ao)

Fig. 3 The main pulmonary artery (MPA) branches into the left and right pulmonary artery (LPA, RPA). The right pulmonary artery shows a normal mild narrowing where it passes ventral to the trachea and right main stem bronchus (*black arrow*). Right ventricular outflow tract (RVOT), right ventricle (RV), aorta (Ao)

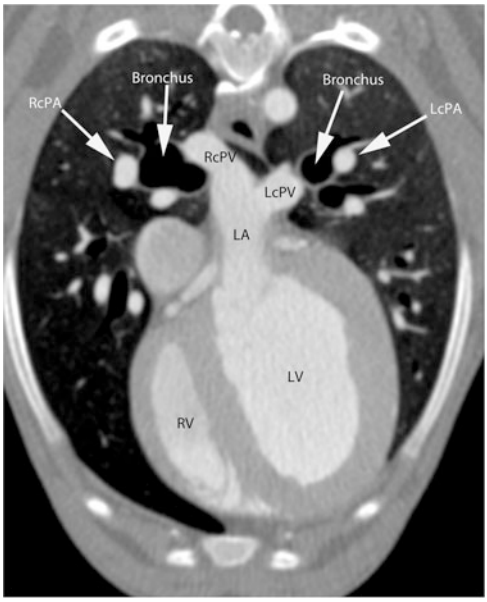

Fig. 4 The lobar pulmonary arteries can be seen laterally and dorsally to the respective bronchus; the veins are medial to the respective bronchus. Right and left caudal pulmonary artery (RcPA, LcPA), right and left caudal pulmonary vein (RcPV, LcPV), left atrium (LA), left ventricle (LV), right ventricle (RV)

arteries further branch along the lobar tree and can be followed laterally or dorsally to the bronchi (Fig. 4). The number of subsegmental lobar branches seen on CTPA exam is significantly associated with the reconstructed slice width used, slices reconstructed at 0.625 mm giving the best definition of the sublobar branches.

3.2 Pulmonary Veins

The pulmonary veins can be followed medially or ventrally along the lobar bronchi and show more individual variants in number compared to the pulmonary arteries. The veins of the right cranial and middle lobe as well as the right caudal and accessory lobes form one trunk each that drains into the right side of the left atrium; the left lobar veins are commonly seen to drain individually into the dorsal aspect of the left atrium (Fig. 5).

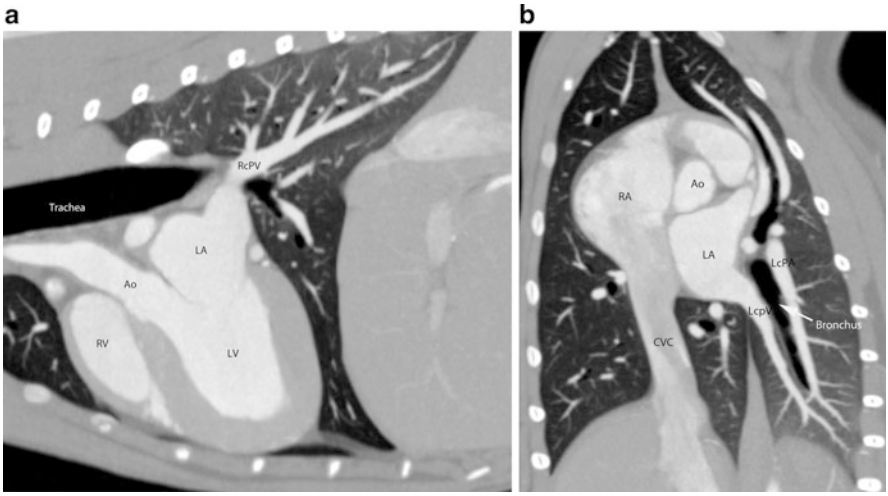

Fig. 5 The pulmonary veins drain into the left atrium: (**a**) shows the right caudal pulmonary vein (RcPV) draining into the right dorsal aspect of the left atrium (LA), (**b**) shows the left caudal pulmonary vein (LcPV) draining into the left side of the left atrium. Left ventricle (LV), right ventricle (RV), right atrium (RA), aorta (Ao), left caudal pulmonary artery (LcPA), caudal vena cava (CVC)

4 Pulmonary Vascular Diseases

4.1 Pulmonic Stenosis

Pulmonic stenosis (PS) at the level of the RVOT or proximal main pulmonary artery has been described as one of the most common congenital heart defects, and valvular, sub- and supravalvular locations can be identified, valvular lesions accounting for the most common form. Downstream from the stenotic lesion, turbulences usually cause a distinct dilation of the pulmonary artery that is well depicted on CT exams (Fig. 6). The stenotic area itself can usually also be appreciated, whereas exact determination of the location of the stenosis in relation to the valvular level may be more difficult to establish. Special care should be paid to the anatomy of the coronary arteries when evaluating these scans, since aberrant coronary anatomy may need be taken into consideration on following ballooning procedures. Stenosis of a peripheral pulmonary artery has also been described.

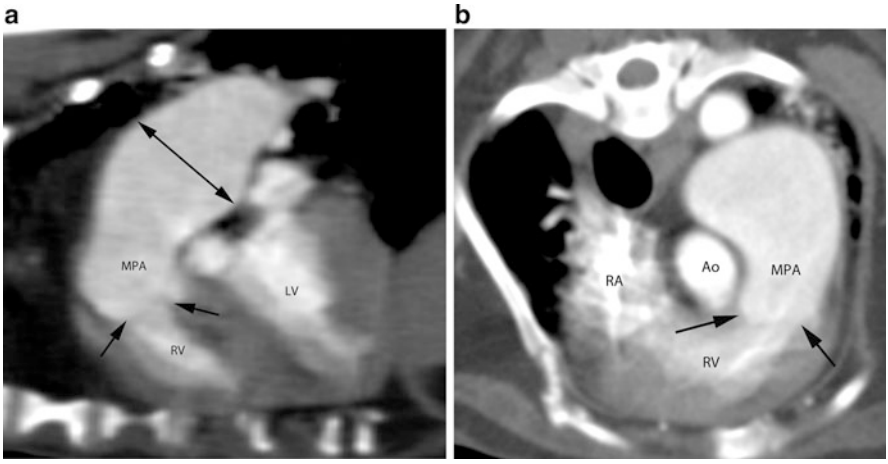

Fig. 6 Pulmonic stenosis at the level of the valve (*arrows*) in a 1-year-old Bulldog, oblique sagittal (**a**) and transverse plane (**b**). Note the marked poststenotic dilation (*double headed arrow*, oblique sagittal image **a**) of the main pulmonary artery (MPA). Subjectively the MPA:Ao ratio is enlarged. Right ventricle (RV), right atrium (RA), left ventricle (LV)

4.2 Pulmonary Thromboembolism

An obstruction of the pulmonary artery or its branches by a thrombus is described as pulmonary thromboembolism (PTE) and can cause significant morbidity and mortality. Patients with hypercoagulable state are predisposed to form thromboembolism, and this may affect specifically patients with immune-mediated hemolytic anemia, cancer patients, patients with systemic infectious or inflammatory conditions as well as trauma, or postsurgical patients.

In CTPA exams, PTE may appear as a full occlusion of the lumen of a pulmonary artery, central or peripheral luminal filling defect (Fig. 7). Further, abrupt tapering of a pulmonary artery can be indicative of a thrombus. Irregularities along the luminal outline of the pulmonary arteries, differing opacification between contralateral vessels (i.e., comparing left to right caudal pulmonary artery), or multifocal alveolar pattern with no probable differential diagnosis have been used as criteria for suspected thromboembolism. The detection of subsegmental PTE using CTPA can be challenging using traditional MDCT units and may be improved by the use of dual-energy CT units (see the chapter “The Lung and Airways”).

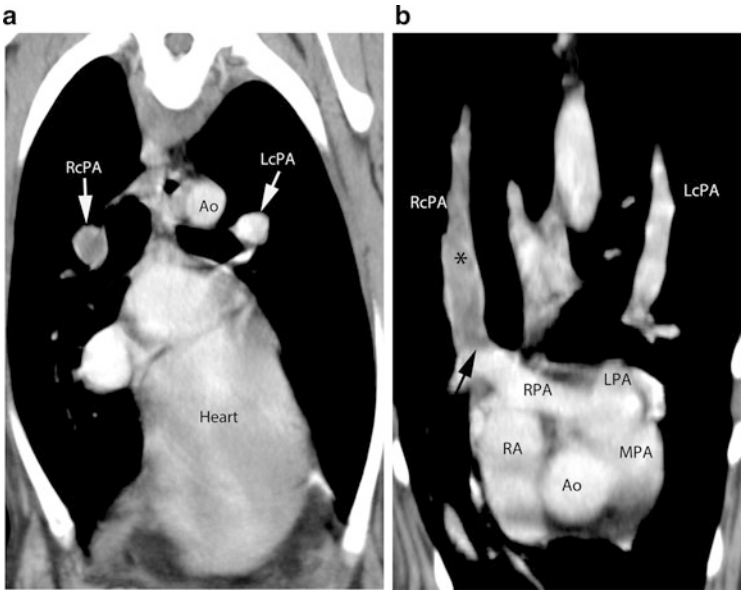

Fig. 7 Pulmonary thromboembolism (PTE) of the right caudal pulmonary artery (RcPA), transverse (**a**) and oblique dorsal plane (**b**) image. Note the contrast filling defect (*arrow* and *asterisk*, oblique dorsal plane image) compared to the left caudal pulmonary artery (LcPA) that shows normal contrast filling. Aorta (Ao), right atrium (RA), right pulmonary artery (RPA), left pulmonary artery (LPA), main pulmonary artery (MPA)

4.3 Pulmonary Hypertension and Dirofilariasis

Pulmonary hypertension itself cannot be assessed using CTPA but depends on echocardiography or catheter exams, though the enlargement of the pulmonary arteries in absence of a stenotic lesions may be appreciated in relation to the pulmonary veins. Pulmonary fibrosis is seen most commonly in terrier breeds, and attention may be paid to the size of the pulmonary arteries to support the otherwise fairly nonspecific CT diagnosis of pulmonary parenchymal disease. Dirofilaria immitis infection occurs in tropical, subtropical, and warm temperate areas and causes immune-mediated pulmonary artery changes that may be seen as thickening of the arterial wall (often a microscopic diagnosis), increased diameter and tortuosity of the vessels, as well as perivascular infiltrates. PTE may be caused in addition to the immature adult worms causing filling defects in the pulmonary arteries.

Further Reading

Drees R, Frydrychowicz A, Keuler NS, Reeder SB, Johnson R. Pulmonary angiography with 64-multidetector-row computed tomography in normal dogs. Vet Radiol Ultrasound. 2011;52 (4):362–7.

Fujii Y, Ishikawa T, Sunahara H, Sugimoto K, Kanai E, Kayanuma H, Mishina M, Aoki T. Partial anomalous pulmonary venous connection in 2 Miniature Schnauzers. J Vet Intern Med. 2014;28(2):678–81.

Goggs R, Chan DL, Benigni L, Hirst C, Kellett-Gregory L, Fuentes VL. Comparison of computed tomography pulmonary angiography and point-of-care tests for pulmonary thromboembolism diagnosis in dogs. J Small Anim Pract. 2014;55(4):190–7.

Granger LA, Pariaut R, Vila J, Coulter CE, Rademacher N, Queiroz-Williams P. Computed tomographic measurement of the main pulmonary artery to aortic diameter ratio in healthy dogs: a comparison to echocardiographically derived ratios. Vet Radiol Ultrasound. 2016;57 (4):376–86.

Habing A, Coelho JC, Nelson N, Brown A, Beal M, Kinns J. Pulmonary angiography using 16 slice multidetector computed tomography in normal dogs. Vet Radiol Ultrasound. 2011;52 (2):173–8.

Kang MH, Park HM. Evaluation of autologous blood clot subsegmental pulmonary thromboembolism in minimally invasive experimental canine model. Int J Exp Pathol. 2013;94(5):329–35.

Ledda G, Caldin M, Mezzalira G, Bertolini G. Multidetector-row computed tomography patterns of bronchoesphageal artery hypertrophy and systemic-to-pulmonary fistula in dogs. Vet Radiol Ultrasound. 2015;56(4):347–58.

Lee CM, Kim JH, Kang MH, Eom KD, Park HM. Unusual congenital pulmonary anomaly with presumed left lung hypoplasia in a young dog. J Small Anim Pract. 2014;55(5):274–7.

Locatelli C, Spalla I, Domenech O, Sala E, Brambilla PG, Bussadori C. Pulmonic stenosis in dogs: survival and risk factors in a retrospective cohort of patients. J Small Anim Pract. 2013;54 (9):445–52.

Macgregor JM, Winter MD, Keating J, Tidwell AS, Brown DJ. Peripheral pulmonary artery stenosis in a four-month-old west highland white terrier. Vet Radiol Ultrasound. 2006;47 (4):345–50.

Makara M, Dennler M, Kuehn K, Kalchofner K, Kircher P. Effect of contrast medium injection duration on peak enhancement and time to peak enhancement of canine pulmonary arteries. Vet Radiol Ultrasound. 2011;52(6):605–10.

Markovic LE, Kellihan HB, Roldán-Alzate A, Drees R, Bjorling DE, Francois CJ. Advanced multimodality imaging of an anomalous vessel between the ascending aorta and main pulmonary artery in a dog. J Vet Cardiol. 2014;16(1):59–65.

Seiler GS, Nolan TJ, Withnall E, Reynolds C, Lok JB, Sleeper MM. Computed tomographic changes associated with the prepatent and early patent phase of dirofilariasis in an experimentally infected dog. Vet Radiol Ultrasound. 2010;51(2):136–40.

Takahashi A, Yamada K, Kishimoto M, Shimizu J, Maeda R. Computed tomography (CT) observation of pulmonary emboli caused by long-term administration of ivermectin in dogs experimentally infected with heartworms. Vet Parasitol. 2008;155(3–4):242–8.

Tang CX, Zhang LJ, Han ZH, Zhou CS, Krazinski AW, Silverman JR, Schoepf UJ, Lu GM. Dual-energy CT based vascular iodine analysis improves sensitivity for peripheral pulmonary artery thrombus detection: an experimental study in canines. Eur J Radiol. 2013;82(12):2270–8.

The Lung and Airways

Giovanna Bertolini

1 Introduction

CT is superior to other imaging techniques for the study of lung diseases, as it can provide excellent anatomic detail of various structures. A variety of clinical conditions require comprehensive evaluation of the lungs. CT examination is generally required in patients with pulmonary masses or nodules, airway diseases, and respiratory signs with uncertain radiographic signs. In addition, oncological staging and the evaluation of thoracic trauma typically include CT assessment of the lung. Current MDCT scanners enable the acquisition of isotropic ($x = y = z$) data throughout the entire thorax in a single breath hold (apnea), permitting visualization of the image dataset in any plane with the same resolution. This capability further improves the diagnostic power of CT for diseases affecting the pulmonary parenchyma and small airways, and it provides detailed information about pulmonary masses and airway and vascular diseases. Advances in CT technology have transformed the imaging of the lung, an organ whose dynamic nature demands rapid acquisition and whose complex anatomy demands isotropic resolution for the distinction of fine anatomic detail and true 3D analysis. With the maximization of spatial resolution in any plane, MDCT findings frequently correlate closely with pathological findings, thereby narrowing differential diagnoses and guiding decisions regarding the most appropriate further investigation.

G. Bertolini (✉)
San Marco Veterinary Clinic, Padua, Italy
e-mail: bertolini@sanmarcovet.it

G. Bertolini (ed.), *Body MDCT in Small Animals*, DOI 10.1007/978-3-319-46904-1_13

2 MDCT Imaging Strategies

Patients undergoing thoracic CT under sedation or anesthesia should be maintained in sternal recumbency during the induction and maintenance of anesthesia and the performance of all scans. Lung atelectasis develops rapidly in unconscious animals, and it may obscure some parenchymal changes and affect image quality. Lateral and dorsal recumbency should be avoided, with the exception of patients with trauma, which are generally scanned in lateral recumbency until spinal injury has been excluded (see "The Body Trauma").

Substantial differences in scan protocols, image quality, and interpretation of results exist among technologies used for thoracic imaging in small animals. The development of an appropriate CT protocol requires careful review of the relevant patient history and clinical indications, as well as evaluation of the patient's clinical condition at the time of the examination. The ideal protocol maximizes the diagnostic power of CT while minimizing patient risk. In general, *high resolution computed tomography (HRCT)* data are indispensable for the morphological assessment of parenchymal lung and small airway diseases in dogs and cats, as in humans. The main objectives of HRCT in this setting are to detect, characterize, and determine the extent of diseases that involve the lung parenchyma and small airways. HRCT techniques for the assessment of interstitial lung diseases using conventional and helical CT scanners have been described in the veterinary literature. HRCT classically combines acquisition and reconstruction parameters (axial/incremental mode, high mAs, narrow collimation, and sharp reconstruction algorithm) to maximize anatomic detail. Parameter choices reflect equipment availability and clinical indication. With *axial or incremental HRCT*, in-plane (*x*-*y*) images are obtained at 5–10-mm intervals throughout the lungs, with slices (1.5–2.5-mm thickness) acquired during the expiratory pause to minimize movement artifacts. This HRCT protocol can be used also with two-slice CT and first-generation MDCT scanners. The resulting anisotropic data can be interpreted only in the axial (*x*-*y*) plane. With advanced MDCT scanners (with 16 or more rows), the thorax can be surveyed in a single breath hold (apnea) with narrow, near-isotropic collimation and a narrow reconstruction interval. With the advent of 64-MDCT scanners, spiral isotropic or *volumetric HRCT* of the whole lung can be performed in a few seconds. Volumetric HRCT datasets can be reviewed in any spatial plane, as the image quality is equivalent in all planes, which facilitates the evaluation and interpretation of the distribution of diffuse parenchymal and small airway diseases. The most recently developed MDCT scanners enable the routine performance of volumetric HRCT of the thorax for lung evaluation using different reconstruction parameters, for simultaneous assessment of the parenchyma, small airways, bronchial and vascular trees, and extrapulmonary structures. In this setting, full evaluation of the lung requires pre- and post-contrast series. CM administration is not necessary for primary evaluation of the lung parenchyma and small airways, and intrapulmonary contrast may obscure subtle pulmonary findings. Contrast-enhanced series are required for the assessment of the pulmonary vasculature (see

the chapter "The Pulmonary Vessels") and the qualitative and quantitative assessment of lung perfusion and extrapulmonary structures.

As with most other clinical applications, MDCT of the lungs, particularly high-resolution parenchymal and small airway assessment, requires anesthesia. This requirement may constitute a limitation in patients with severe pulmonary diseases. HRCT scan protocols for humans, particularly those used for the assessment of small airway disease, include inspiratory and expiratory series. Obviously, this approach is not possible in veterinary patients. The author's personal observations suggest that CT series obtained in mechanically ventilated patients at the time of apnea in expansion, followed by expiratory apnea, aid the detection of air entrapment.

16-MDCT evaluation of upper airway obstruction in awake veterinary patients using a restraining device but no chemical restraint has been described. However, volumetric datasets obtained for awake dogs and cats are of little or no use for the evaluation of the parenchyma and vascular structures, due to the presence of motion and respiratory artifacts. Moreover, the restraint of awake patients (even for a few seconds) may be extremely stressful and may worsen their respiratory conditions. Volumetric HRCT (with no or minimal artifacts) can now be performed in awake patients using the most advanced MDCT or DSCT scanners. For instance, a 320-MDCT scanner enables volumetric axial scanning of a 16-cm-long range (50-cm field of view) in a single 0.35-s rotation. A contiguous step-and-shoot protocol can be used to widen the scan range. To date, no report has described the use of a 320-MDCT scanner for veterinary patients. In our center, we installed in 2014 a second-generation DSCT scanner that permits the performance of spiral HRCT in "flash mode." The flash spiral scan mode combines a scan speed of 458 mm/s and a temporal resolution of 75 ms, reducing the thoracic HRCT examination time to 0.4–1.5 s. Our protocol includes a 0.6-mm slice thickness, 0.3-mm reconstruction interval, and double reconstruction algorithm for simultaneous lung and soft tissue assessment in awake patients.

Independent of the manner of data acquisition, display parameters, especially window width and level, have crucial effects on the ability to accurately interpret lung CT data. Interstitial and small airway diseases may lead to subtle changes. The low contrast difference between a subtle change in lung attenuation and the normal lung parenchyma may be missed when the assessment is performed using inappropriate window settings. Typical software preset values for lung evaluation in humans (1500 HU window width, −700 HU window level) are useful as starting settings for most veterinary patients. However, as for other anatomic regions, the selection of an appropriate lung window does not equate to the use of fixed window values. For instance, a narrow lung window setting may increase the contrast difference between the normal lung and lower-attenuation areas and is needed for the evaluation of pulmonary embolism.

The modern approach to volumetric lung MDCT includes simultaneous evaluation of 2D MPRs and 3D post-processed volumetric (MIP, MinIP, volume-rendered, and endoluminal) images. In particular, MPRs in standard (transverse, sagittal, dorsal) and multioblique planes aid the complete visualization of

longitudinal structures, such as bronchovascular bundles, and their relationships with surrounding parenchymal structures. MIP views enable rapid assessment of small hyperattenuating lesions, such as micronodules and lung nodules, and determination of their distribution in the lung parenchyma. Intuitively, MinIP views are very useful for the rapid detection and evaluation of low-attenuation focal and diffuse lung lesions, such as pulmonary bullae and blebs, and emphysematous areas of the lung. Thin-slab MinIP can also be used for the detection of early high-density changes in the lung parenchyma, such as subtle or small ground-glass opacities. VR techniques are much more useful in the comprehensive evaluation of pulmonary and extrapulmonary vessels and presurgical assessment of lung tumors.

3 MDCT Signs of Parenchymal Disease

A basic understanding of the pulmonary anatomy of veterinary patients is required for accurate interpretation of lung CT data. The parenchymal anatomy may be divided broadly into the pulmonary gas exchange units and the pulmonary interstitium. As the interstitium differs among species, some HRCT patterns described in humans are not similar in veterinary patients. On the other hand, several CT patterns are not typically observed in veterinary patients due to technological limitations or inappropriate CT protocols and review strategies. With the use of common (particularly non-isotropic) image acquisition parameters, CT signs are not associated with the microscopic distribution of disease below the level of the pulmonary acinus.

HRCT findings correlate closely with pathological findings, but they are often nonspecific. However, the combination of various HRCT findings, together with their anatomic distribution, can suggest the most likely diagnosis. When detected early, these findings can often be used to predict the cause and pathophysiological mechanism of lung disease and to guide selection of the most appropriate further diagnostic testing (e.g., bronchoalveolar lavage or lung biopsy). As for radiological data, the interpretation of HRCT data for the lung is based on the recognition and description of pathological patterns. Mixed patterns are encountered commonly in veterinary patients, especially those with chronic respiratory conditions. Knowledge of the basic physiopathological mechanisms of lung disease and subsequent CT changes is necessary for the accurate interpretation of findings for primary and secondary lesions of the lung.

3.1 Pattern-Based Approach to MD-HRCT Data

Lung patterns may be divided roughly into high-attenuation and low-attenuation categories. The attenuation of the normal lung is approximately −900 to −700 HU. High-attenuation patterns include situations of increased opacity, mainly in cases of

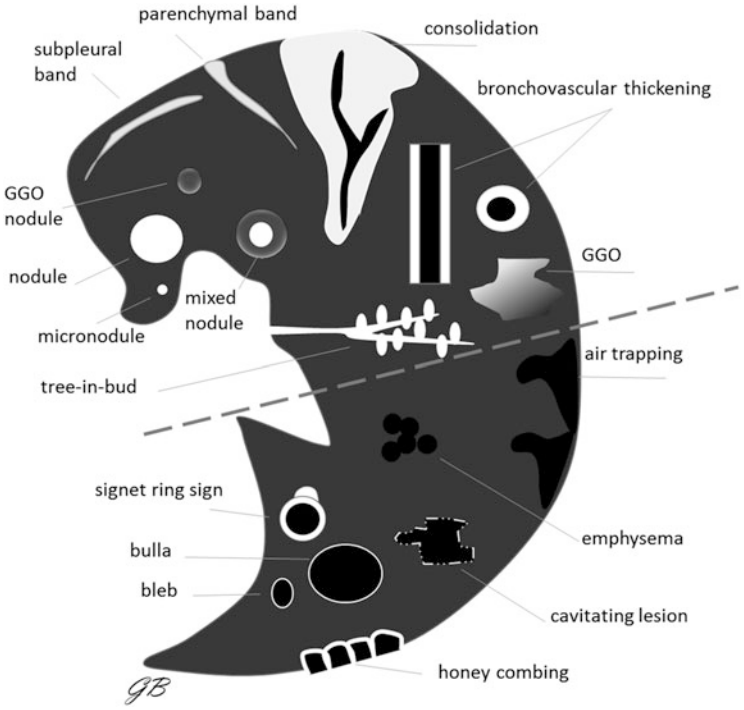

Fig. 1 Drawing summarizing the hyper- and hypoattenuating CT patterns

diminished aeration (e.g., consolidation) of the lung. In contrast, low-attenuation patterns involve hypoattenuation to the normal lung, indicating increased air content (e.g., pulmonary emphysema) (Fig. 1).

3.1.1 High-Attenuation Patterns

High-attenuation patterns are characterized by diffuse or focal areas of increased attenuation in the lung parenchyma. Conditions associated with these patterns include nodules, linear opacities, ground-glass opacities, lung consolidation, and lung collapse.

Nodules

Lung nodules and micronodules are often detected in veterinary patients using volumetric MDCT datasets with high spatial resolution. Pulmonary nodules appear as well- or poorly defined rounded or irregular opacities in the lung parenchyma. They are usually characterized further with respect to size, shape, border definition, density, number, and location. Several studies have compared the sensitivities of CT and radiology in the detection of lung nodules, but no study has described the HRCT assessment of lung nodules in small animals. In humans, nodules are

customarily classified as small (<1 cm) or large (1–3 cm) (Fig. 2). Nodules are also detectable by standard lung CT evaluation in veterinary patients. On HRCT images, micronodules appear as discrete, small, round, focal opacities in the lung parenchyma with dimensions <3–5 mm (Fig. 3). Micronodules distributed sparsely are encountered frequently in HRCT examination of the lung in dogs and cats. They are difficult to interpret and too small to be sampled. In older dogs, mineralized small nodules (generally <3 mm) in the lung are likely to represent a benign condition (i.e., pulmonary osseous metaplasia) (Fig. 4). However, in older oncological patients, benign osseous metaplasia and lung metastasis can coexist. In these patients, pulmonary micronodules should be considered to represent potential metastasis, possibly indicating further CT examination. The growth of a nodule raises the clinical suspicion of its malignancy. In the micronodular lung pattern, multiple pulmonary micronodules are usually distributed randomly in the

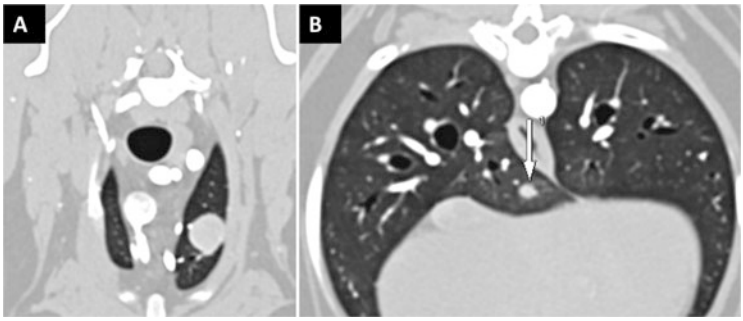

Fig. 2 (**a**) Lung nodule (metastatic melanoma) in the cranial left lobe in a dog. (**b**) Small nodule in the accessory lobe (*arrow*) in the same patient

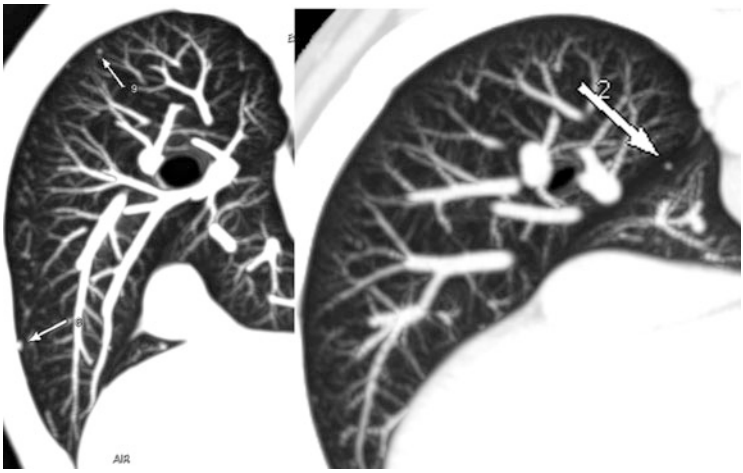

Fig. 3 Sparse micronodules in two canine oncological patients that underwent CT for staging (mammary carcinoma and anal sac adenocarcinoma)

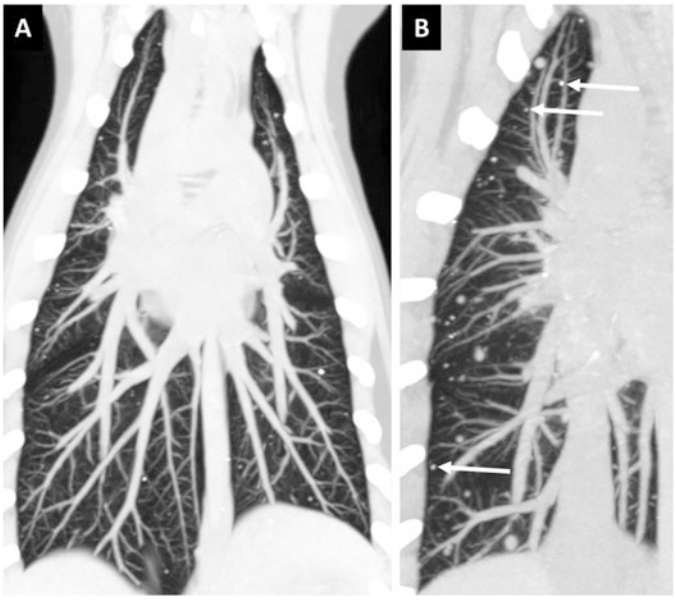

Fig. 4 Benign lung micronodules (pulmonary osseous metaplasia) in a 10-year-old beagle

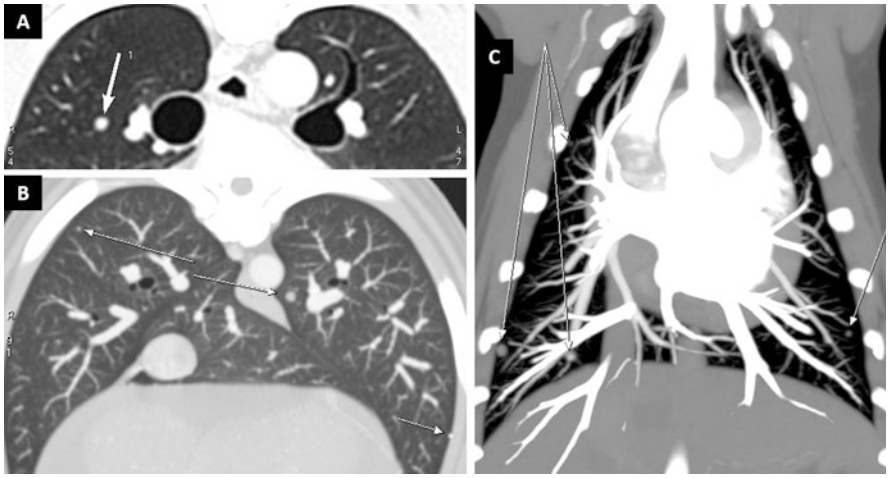

Fig. 5 (**a**) A small lung nodule in a dog with thyroid carcinoma (suspected metastasis). (**b**) Initial metastases of splenic hemangiosarcoma in a dog and concomitant subpleural pulmonary osseous metaplasia (*left lobe*, ventral). (**c**) Dorsal MIP image from a dog with lung metastasis of mammary carcinoma

pulmonary interstitium and may represent initial lung metastasis (Figs. 5, 6, and 7). Centrilobular micronodules with a linear branching appearance may form a "tree-in-bud" pattern, well described in humans and also seen in veterinary patients, particularly cats. This pattern may be encountered in a number of endo- and

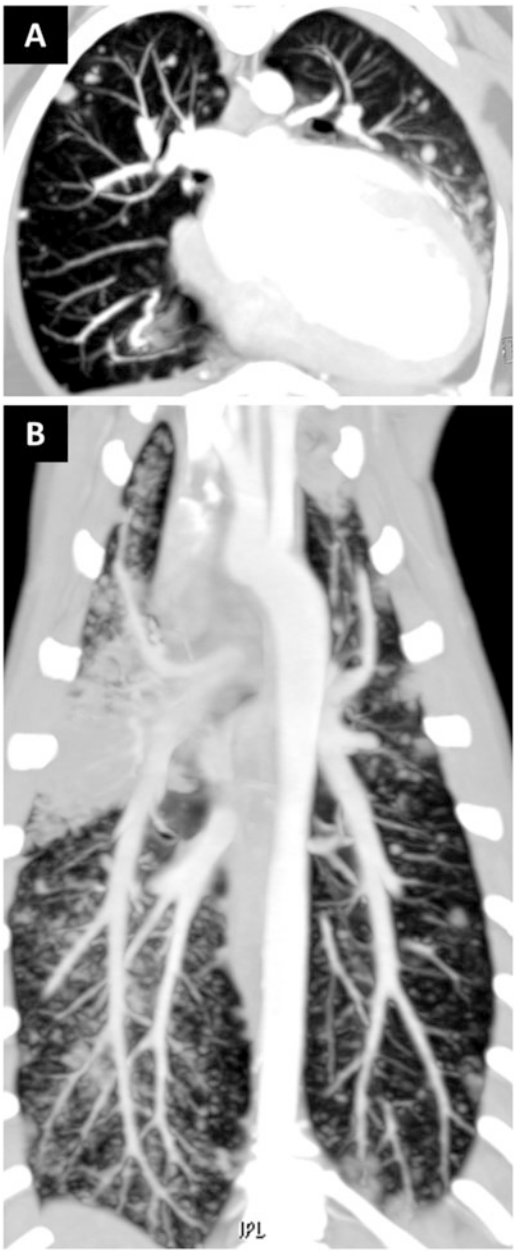

Fig. 6 Lung metastases. (**a**) Metastasis of splenic hemangiosarcoma in a dog. Numerous small nodules show a random distribution (hematogenous metastases). (**b**) Metastatic pulmonary dissemination of primary lung carcinoma. The right middle lobe and apex of the left cranial lobe are consolidated, and diffuse ill-defined (ground-glass) nodules and multiple small, well-defined nodules are present

peribronchiolar disorders. It reflects impaction of the centrilobular bronchus with mucous, pus, or fluid, resulting in dilation of the bronchus, associated with peribronchiolar inflammation (Fig. 8).

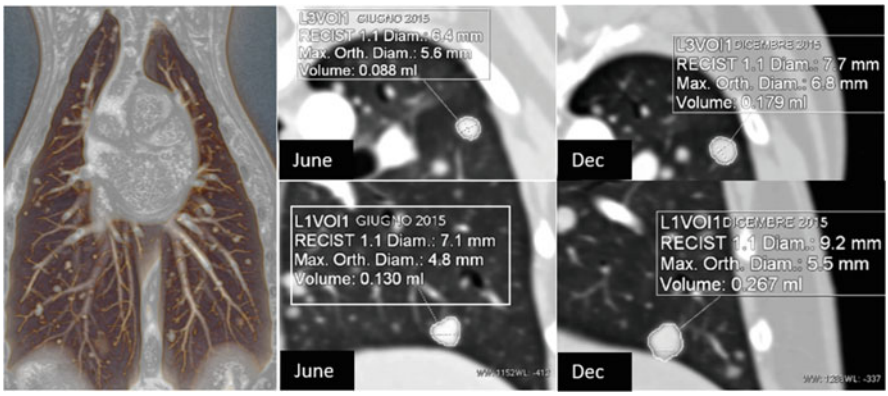

Fig. 7 Evaluation of lung nodule volume growth in a dog with metastases of adrenal carcinoma. CT monitoring for the assessment of tumor response to chemotherapy

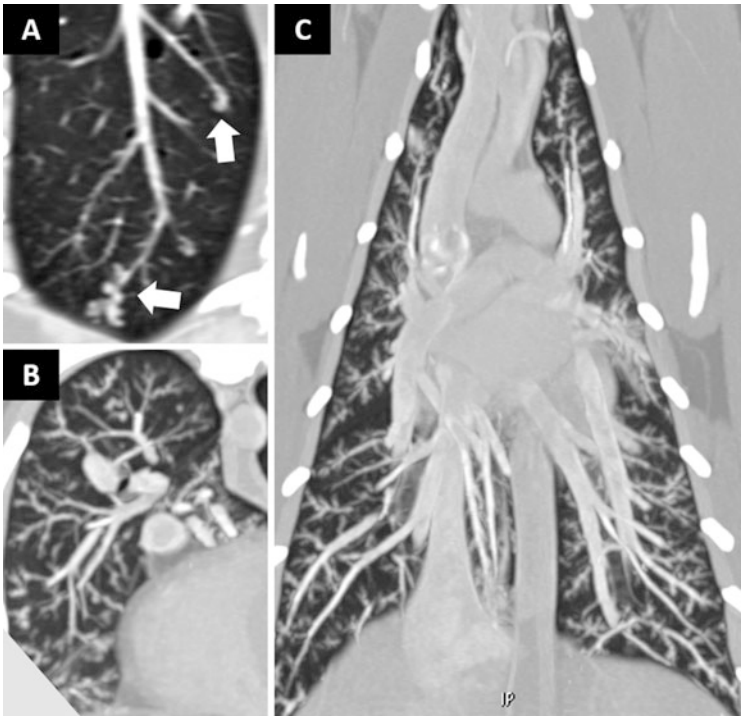

Fig. 8 The "tree-in-bud" pattern. (**a**) Linear branching pattern of centrilobular nodules in a dog with thyroid carcinoma. (**b**, **c**) Transverse and dorsal views of a cat with oral squamous cell carcinoma and a diffuse "tree-in-bud" pattern. Bronchoalveolar lavage fluid/cell analysis resulted in the diagnosis of severe nonspecific chronic pneumonia (with mixed lymphocytic/granulocytic/macrophagic components). Thin MIP facilitates detection of this pattern

Linear Opacities

Linear opacities form a broad subgroup of high-attenuation patterns suggesting thickening of the pulmonary interstitium. Peripheral, subpleural, and peribronchovascular interstitial thickening is seen commonly in veterinary patients with a variety of conditions. A reticular pattern has been described in dogs with chronic interstitial lung diseases (e.g., idiopathic lung fibrosis in West Highland White Terriers) and infiltrative lung metastasis of carcinoma (with a lymphatic-perilymphatic distribution) in dogs and cats (Fig. 9).

Ground-Glass Opacities

Ground-glass opacities (GGO) appear as diffuse or focal areas of increased lung parenchyma attenuation, with preservation of the bronchial and vascular margins. Thus, GGO are less dense than pulmonary consolidation, in which bronchovascular bundles are obscured. The basic mechanism underlying GGO is the partial displacement of air from the alveoli. Interstitial and alveolar diseases may produce ground-glass opacities. Causes include partial or complete filling of the alveolar space with fluid or cells; increased alveolar wall thickness due to the proliferation of pneumocytes, neoplastic infiltration, or expanded interstitium; increased capillary blood volume due to increased flow or reduced drainage; or a combination of two or more of these mechanisms. Thus, differential diagnoses of GGO may include inflammatory diseases, alveolar hemorrhage, and/or infiltrative neoplastic diseases (Figs. 10, 11, and 12). The interpretation of these opacities may thus be difficult and depend on the patient's history (acute vs. chronic respiratory signs), the actual presenting signs, and clinical suspicion. Bronchoalveolar lavage may be indicated in patients with diffuse ground-glass opacities and respiratory signs.

Ground-glass nodules are nonsolid entities with hazy increased attenuation. Mixed nodules have solid cores and ill-defined borders. These nodules have been reported in patients with pulmonary fibrosis (interstitial thickening), infiltrative

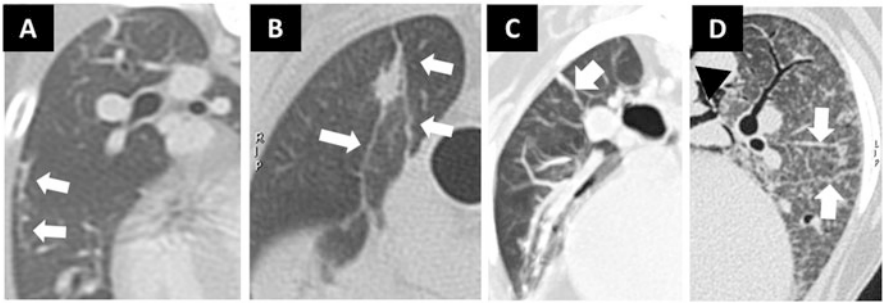

Fig. 9 Linear opacity. (**a**) Subpleural thickening (nonspecific mixed inflammation) in a cat. (**b**) Parenchymal bands in a West Highland White Terrier with septic pleuritis and chronic interstitial lung disease, consistent with pulmonary fibrosis (confirmed by histopathology). (**c**) Another West Highland White Terrier with chronic interstitial lung disease. *Arrow* indicates a thick parenchymal band reflecting the thickened interstitium. (**d**) Diffuse interstitial thickening in an American Staffordshire Terrier. Note the parenchymal bands and diffuse reticular pattern. *Arrowhead* indicates the pneumomediastinum

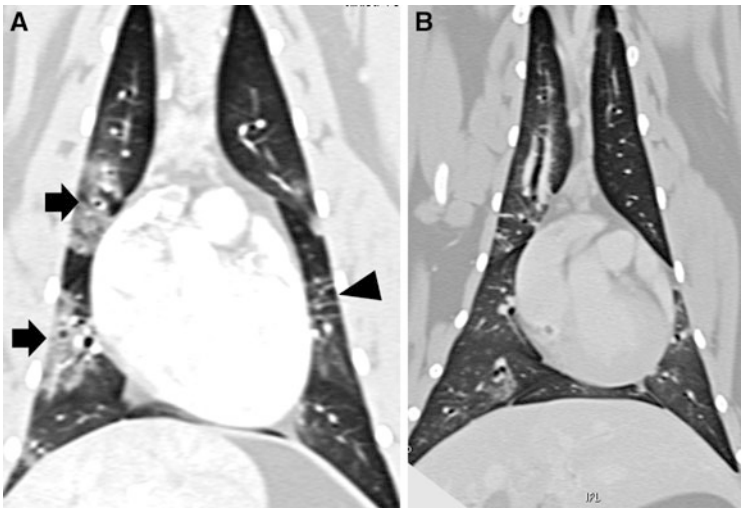

Fig. 10 High-attenuation interstitial patterns in cats. (**a**) *Arrows* indicate pulmonary areas of ground-glass opacity (vascular and bronchial structures are still visible). *Arrowhead* indicates parenchymal bands. (**b**) *Arrow* indicates a small ground-glass area. Note the peribronchovascular interstitial thickening (*circle*)

Fig. 11 Ground-glass opacity in dogs with lymphoma. (**a**) Dorsal MinIP shows ground-glass areas in the right cranial and middle lobes (*arrow*). (**b**) Dorsal MPR from another dog with B-cell lymphoma. Note the overall increased opacity, particularly evident in the caudal left lobe

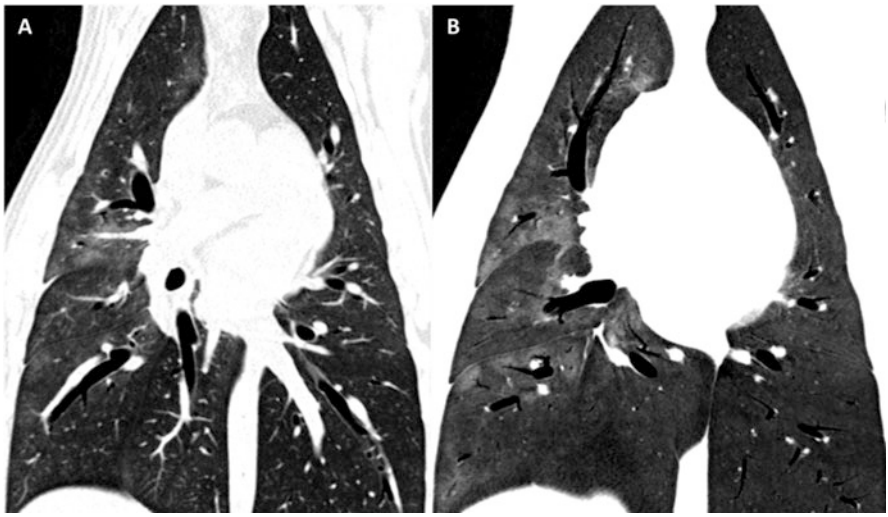

Fig. 12 Diffuse areas of ground-glass opacity in the right lung in a Labrador Retriever with anticoagulant poisoning. (**a**) Dorsal MPR. (**b**) Same volume examined with thin MinIP, which facilitates the detection of ground-glass areas (alveolar hemorrhage)

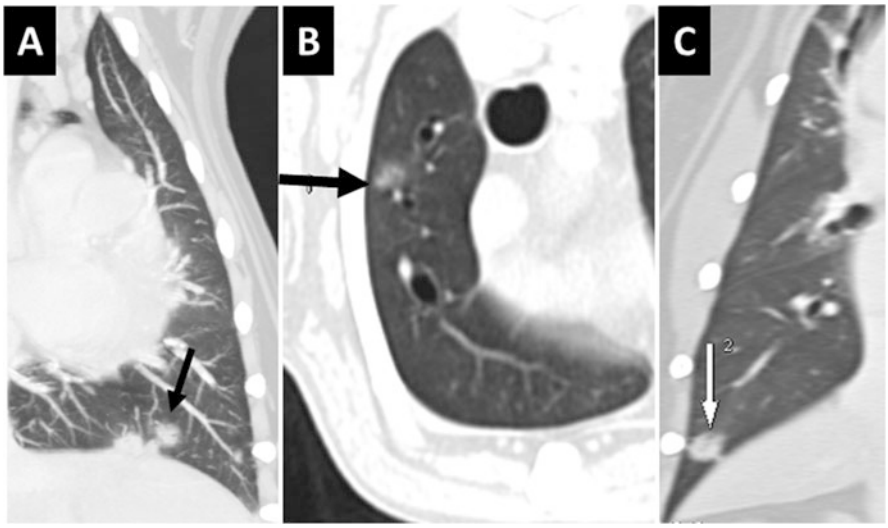

Fig. 13 (**a**) Ground-glass nodules in a dog with histiocytic sarcoma. (**b**) Ground-glass nodule in a dog with metastatic splenic hemangiosarcoma. (**c**) Ground-glass nodule in a dog with Evans syndrome (focal hemorrhage)

neoplastic conditions (i.e., lymphoma), initial metastasis of carcinomas and osteosarcomas, and metastatic hemangiosarcoma (Figs. 13, 14, and 15). A circular area of ground-glass attenuation surrounding a pulmonary nodule or mass is called the "halo sign." In humans, it has been described in several malignant and

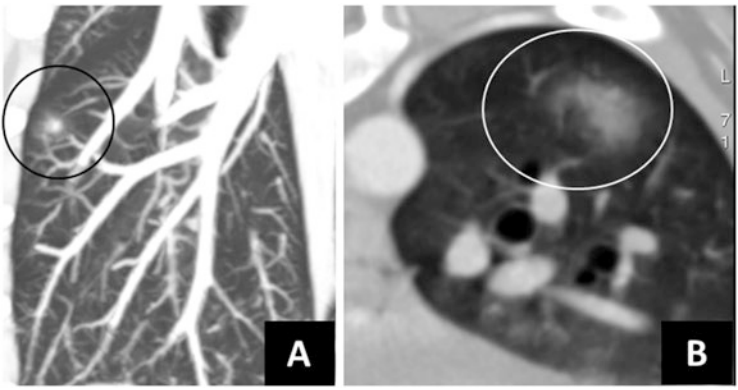

Fig. 14 Mixed nodules with solid cores and ill-defined borders (metastatic hemangiosarcoma)

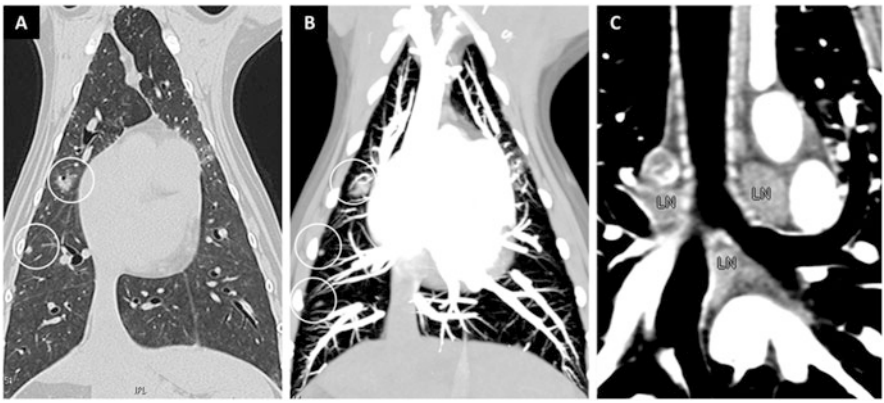

Fig. 15 (**a**) Ground-glass nodules in a dog with pneumonia. (**b**) Ground-glass nodules are detected more easily using thin MIP. (**c**) Tracheobronchial lymph node enlargement

nonmalignant conditions, and outer ground-glass attenuation generally represents hemorrhage or inflammatory infiltration. The halo sign has been described in a series of dogs with neoplastic lung nodules and histologically corresponds to neoplastic extension, necrosis, and/or fibrosis. The "reversed halo sign" is a focal, rounded area of ground-glass attenuation surrounded by a more or less complete ring of consolidation. It has been described in dogs and represents necrosis and/or hemorrhage in neoplastic nodules (Fig. 16).

Pulmonary Infarction

Pulmonary infarction results from the occlusion of a feeding pulmonary artery by an embolus or other obliterative vascular disease. Infarction typically appears as a triangular area of increased opacity, with the base located adjacent to the pleura and the apex directed toward the pulmonary hilum (Fig. 17). The hyperattenuating area represents local parenchymal hemorrhage that might evolve to necrosis, but tissue

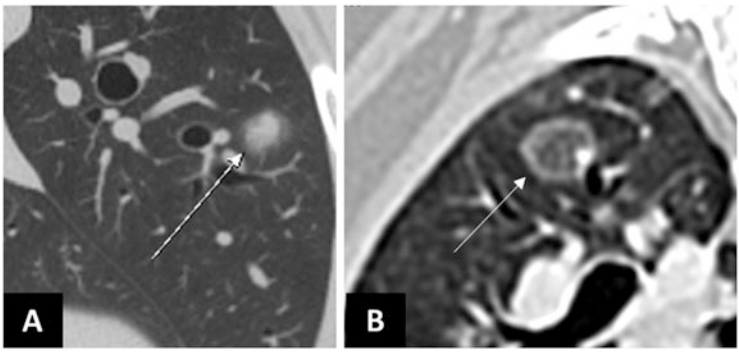

Fig. 16 Halo and reversed halo signs (see the text for further explanation)

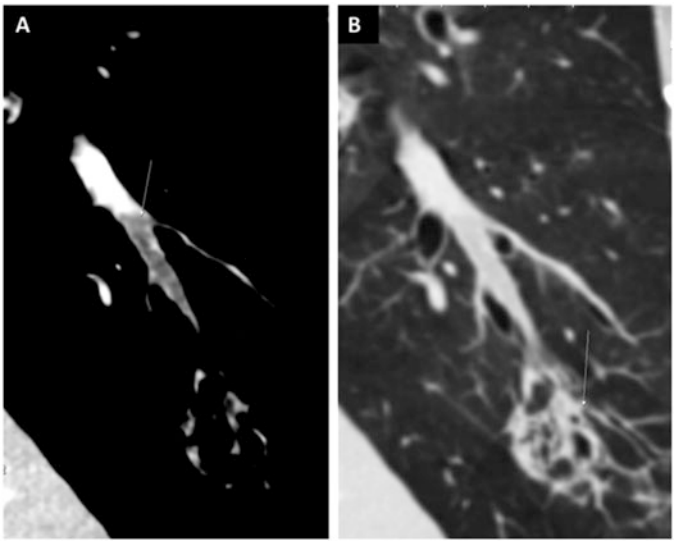

Fig. 17 Pulmonary infarction. (**a**) Pulmonary thrombosis. (**b**) Infarction of the dependent area of the lung

viability is maintained by the bronchial arterial blood supply (although accompanied by segmental bronchial artery hypertrophy).

Pulmonary Consolidation

The degree of lung attenuation distinguishes ground-glass opacity from consolidation. Consolidation appears as a homogeneous increase in pulmonary parenchymal attenuation that obscures the margins of vessels and airway walls (Fig. 18). Air bronchograms may be seen with consolidation and generally indicate that the bronchial lumen is not involved in the disease process. Large areas of pulmonary consolidation can be detected easily on radiographs and standard CT images of the

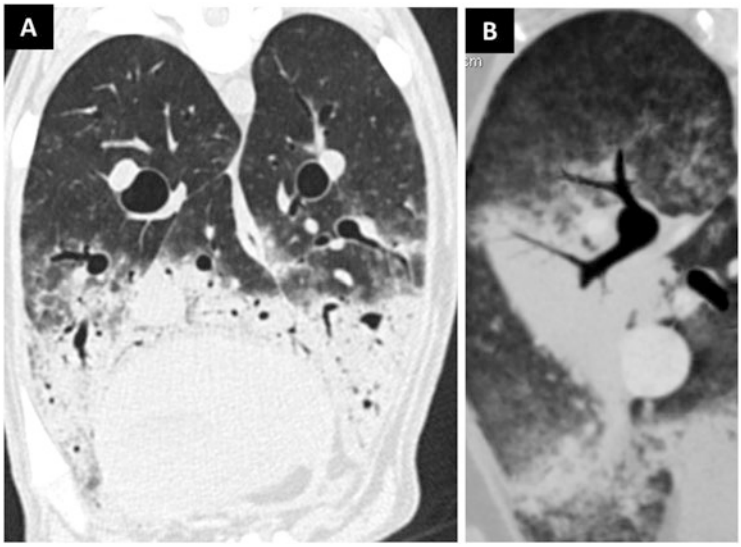

Fig. 18 Lobar consolidation. (**a**) Bacterial pneumonia in a dog. The ventral areas of the lungs show increased opacity, with bronchovascular obscuration. (**b**) Air bronchogram

lung; HRCT adds no further information. However, HRCT examination may result in the detection of initial or small areas of consolidation, which may influence decision-making about subsequent diagnostic and therapeutic procedures.

Pulmonary Atelectasis

Atelectasis refers to reduced ventilation of all or part of the lung, which results in reduced volume and increased attenuation in the affected portion. Atelectasis can be observed easily by standard CT of the lung, and HRCT does not add information. However, HRCT may disclose small airway or parenchymal lesions that can accompany atelectasis, thus aiding causative diagnosis. Depending on the underlying pathogenetic mechanism, different types of atelectasis may be recognized. Broadly, passive and active mechanisms lead to atelectasis of different causes. Non-pathological passive atelectasis of the peripheral lung is observed frequently in patients that undergo CT in aesthesia (positional atelectasis). As discussed previously, patients should be positioned in sternal recumbency after the induction of anesthesia (ideally directly on the CT table, with immediate positioning) to minimize this form of atelectasis. Passive atelectasis can occur in the presence of pleural effusion or pneumothorax (Fig. 19). The term "pulmonary collapse" is often used interchangeably, but it should be reserved to refer to complete lobar atelectasis. In this context, bronchial structures within the collapsed lung may be visible and must be differentiated from lung consolidation. Passive atelectasis can also occur when a thoracic mass compresses the lung parenchyma. Other causes of pulmonary atelectasis include alveolar adhesion in cases of acute respiratory distress syndrome or surfactant deficiency, rarely reported in small animals. Finally, areas of atelectasis

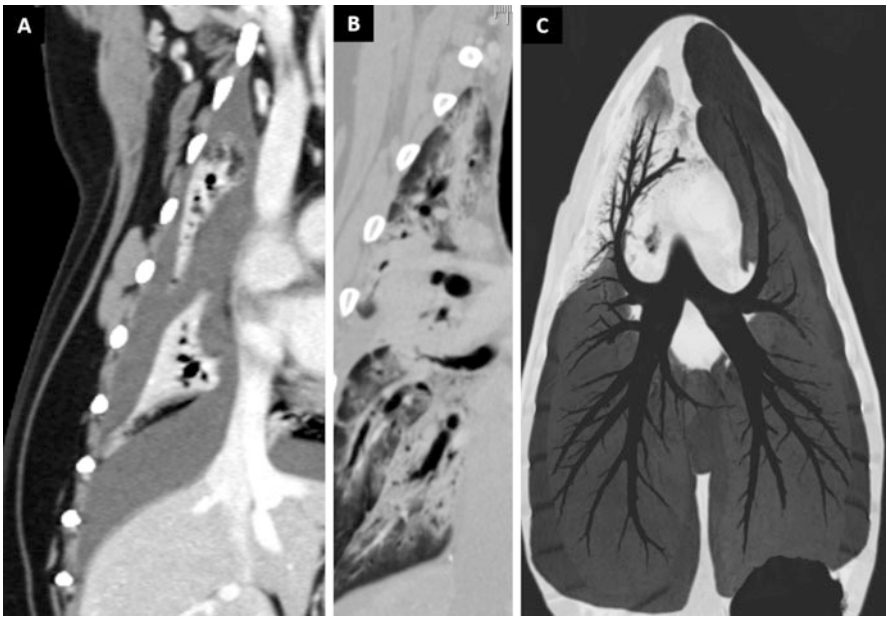

Fig. 19 (**a**, **b**) Pulmonary atelectasis in dogs with pleural effusion (passive atelectasis). (**c**) MinIP from a dog with right cranial lobar collapse. The bronchial structures within the collapsed lung are visible

may result from cicatrization or retraction following spontaneous or iatrogenic pleuropulmonary injuries. Focal atelectasis may mimic a lung tumor, as in the case of "round atelectasis," a form of peripheral alveolar collapse that develops as a result of pleural diseases. In round atelectasis, well described in humans, a rounded collapsed lung is associated with invaginated fibrotic pleura and thickened and fibrotic interlobular septa, assuming a mass-like appearance. Distorted vessels assume a curvilinear disposition as they converge on the mass-like lesion (the "comet tail sign") (Fig. 20). The atelectatic lung shows homogeneous enhancement in post-contrast series and can be mistaken for lung cancer.

3.1.2 Low-Attenuation Patterns

Low-attenuation patterns form a broad category including all conditions showing low attenuation of the lung parenchyma due to increased aeration.

Air Trapping

Air trapping is the retention of air in the lung distal to an obstruction. It has been described in dogs with severe interstitial lung diseases, but it can be observed also in other clinical circumstances, such as bronchial collapse (bronchomalacia). Air trapping is ideally assessed in the end-expiratory phase, when the lung is normally

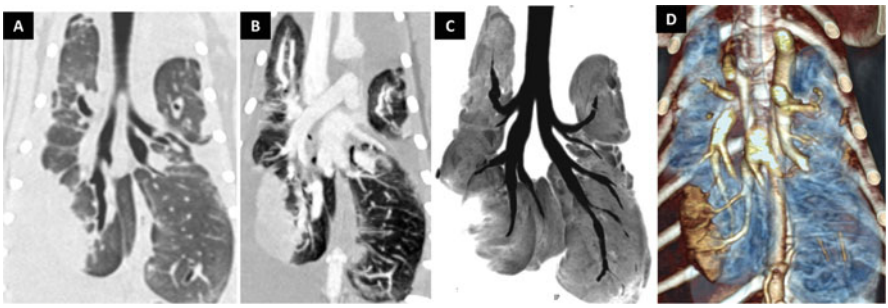

Fig. 20 Round atelectasis in a cat with chylothorax. Pre-contrast (**a**), post-contrast (**b**), and MinIP (**c**) dorsal views of the thorax showing a mass-like lesion at the caudal lung lobe. (**d**) Volume-rendered image clearly shows the "comet tail sign." Histopathological examination of rounded atelectasis revealed no tumor cell

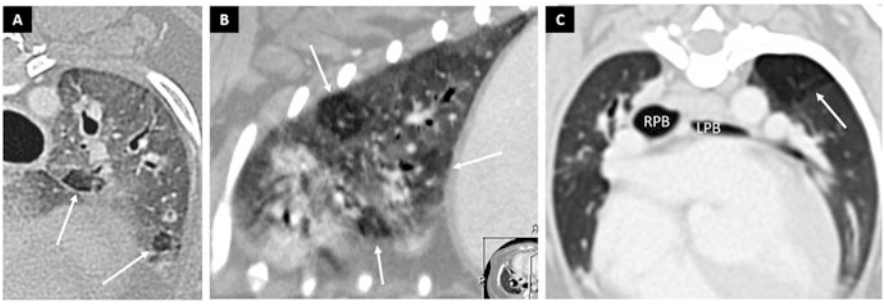

Fig. 21 (**a**, **b**) Transverse and parasagittal views from a West Highland White Terrier with severe chronic interstitial pneumonia (pulmonary fibrosis). *Arrows* indicate areas of air trapping. (**c**) Air trapping (*arrow*) in a dog with bronchial stenosis. *RPB* right principal bronchus, *LPB* left principal bronchus

less aerated and expanded. Areas of air trapping are hyperlucent and show no volume reduction (Fig. 21). As mentioned previously in this chapter, the author's experience suggests that air trapping is detected more easily in expiratory apnea after pulmonary expansion in mechanically ventilated patients.

Honeycombing

Honeycombing refers to the appearance of destroyed and fibrotic lung tissue containing numerous small cystic airspaces with thick fibrous walls. It represents the late stages of various lung diseases, including chronic interstitial diseases (e.g., canine idiopathic fibrosis). It appears as cystic-like lesions of comparable diameters with well-defined walls, which are usually subpleural in distribution (Fig. 22).

Pulmonary Bullae and Blebs

Pulmonary bullae are focal regions of emphysema in the pulmonary parenchyma with no discernible wall (they may be contained by connective tissue). They are caused by the disruption of the intra-alveolar septa and subsequent accumulation of air in the lung tissue. Blebs are characterized by the accumulation of air within the

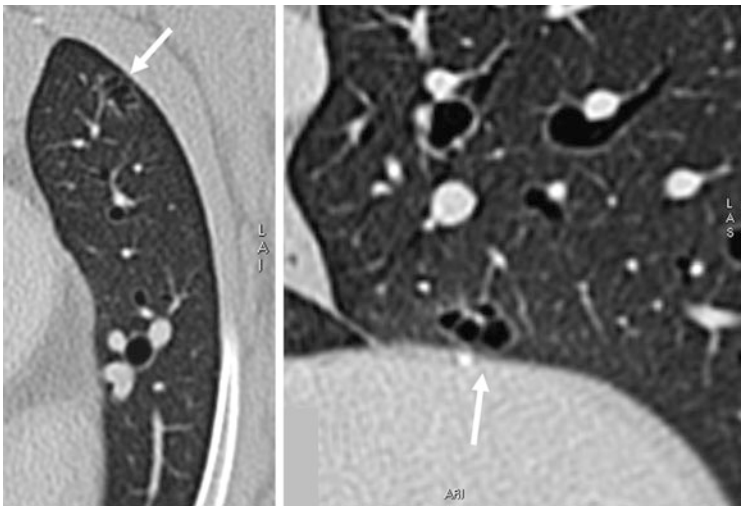

Fig. 22 Honeycombing (*arrows*) in dogs. Cystic airspaces with thick fibrous walls in the subpleural areas

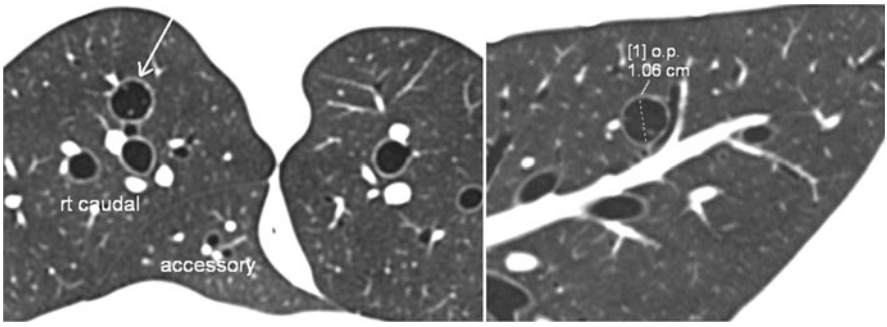

Fig. 23 Incidentally discovered pulmonary bulla in a dog

layers of the visceral pleura and are visible in the peripheral regions of the lung. The sizes of bullae and blebs can be variable. They may be found incidentally during MDCT examination of the lung for various reasons but are associated most often with spontaneous pneumothorax in dogs (Figs. 23, 24, and 25). The veterinary literature contains a few studies comparing the sensitivities of CT and radiology for the detection of pulmonary bullae and blebs in patients with spontaneous pneumothorax; results have been inconsistent. CT is certainly more powerful than radiography for the detection of these entities, but not all of them are identified readily on thoracic CT examination. In practice, blebs may be difficult to visualize and distinguish from surrounding pleural air in patients with abundant pneumothorax. Moreover, ruptured blebs or bullae may appear as small areas of consolidation and could be difficult to distinguish from surrounding collapsed lung tissue (passive atelectasis), which is observed consistently in patients with pneumothorax. In the

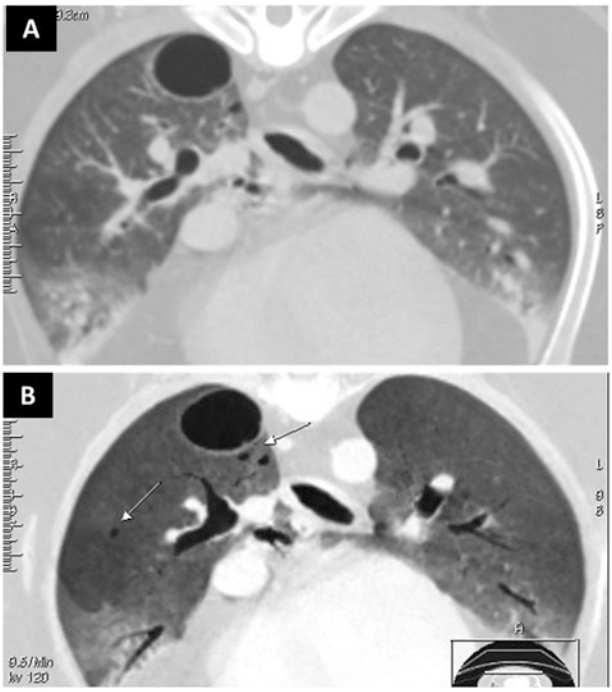

Fig. 24 (**a**) Transverse view from a dog with an incidentally discovered subpleural pulmonary bulla. (**b**) Same image analyzed with MinIP shows multiple other small pulmonary air-containing lesions (*arrows*)

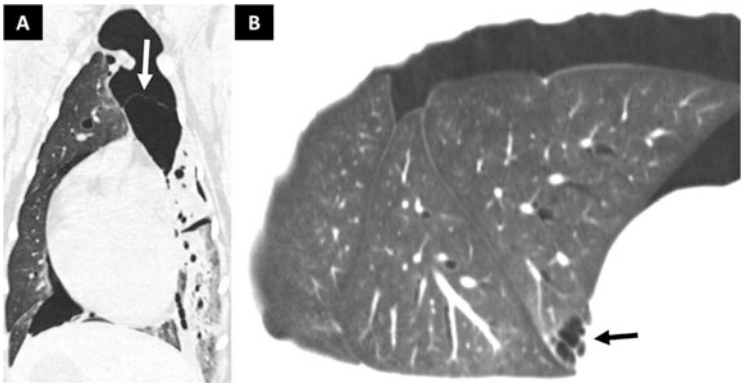

Fig. 25 Pulmonary bulla and blebs (*arrows*) in a dog with spontaneous pneumothorax. Note the left lung passive atelectasis

author's past experience with 16-MDCTscanner and in cases reported in the literature, a collapsed lung and motion artifacts (i.e., respiratory, heartbeat) strongly affect image quality and, thereby, the diagnostic power of CT examinations of the lung in these patients. Our approach to patients with spontaneous pneumothorax with that scanner includes an initial scan of the anesthetized, non-ventilated patient for general assessment of the lung and pleural space (quantification and exclusion of other causes of pneumothorax), followed by thin-slice series obtained after thoracentesis and lung expansion with the patient still on the CT table (Fig. 26).

Cavitating Lesions

Other low-attenuation focal lesions include cyst-like forms containing air or small quantities of fluid. This category includes benign lesions (e.g., focal bronchiectasis, bronchial cyst, abscess) and cavitary malignant tumors/nodules (i.e., carcinoma). Other CT signs (e.g., concomitant solid nodular lesions, pleural effusion, enlarged lymph nodes) are generally present, aiding interpretation (Figs. 27 and 28).

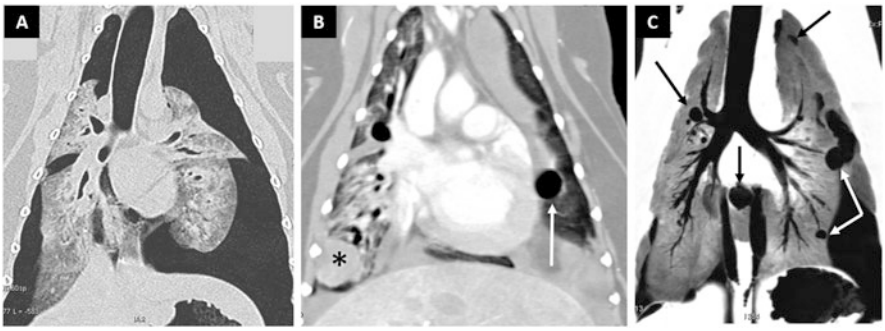

Fig. 26 Same volume in different series of a CT study of a dog with pneumothorax and pulmonary carcinoma. (**a**) The first series (lung kernel) shows bilateral pneumothorax and diffuse lung atelectasis. (**b**) The post-contrast series (soft-tissue kernel) obtained after thoracentesis and lung expansion shows a pulmonary bulla (*arrow*) and a mass in the right caudal lobe (*asterisk*). (**c**) MinIP shows multiple air-containing pulmonary lesions (*arrows*)

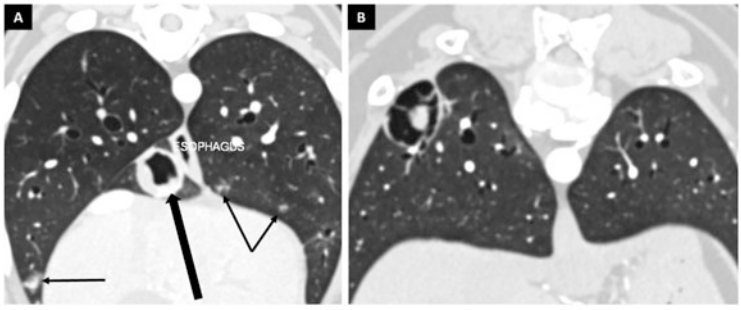

Fig. 27 (**a**) Air-containing lesion of the accessory lobe (pulmonary carcinoma). Note the presence of several ground-glass nodules (possible metastases) in other lung lobes. (**b**) Irregular cavitating lesion with a central solid nodule in a dog with metastatic soft tissue sarcoma

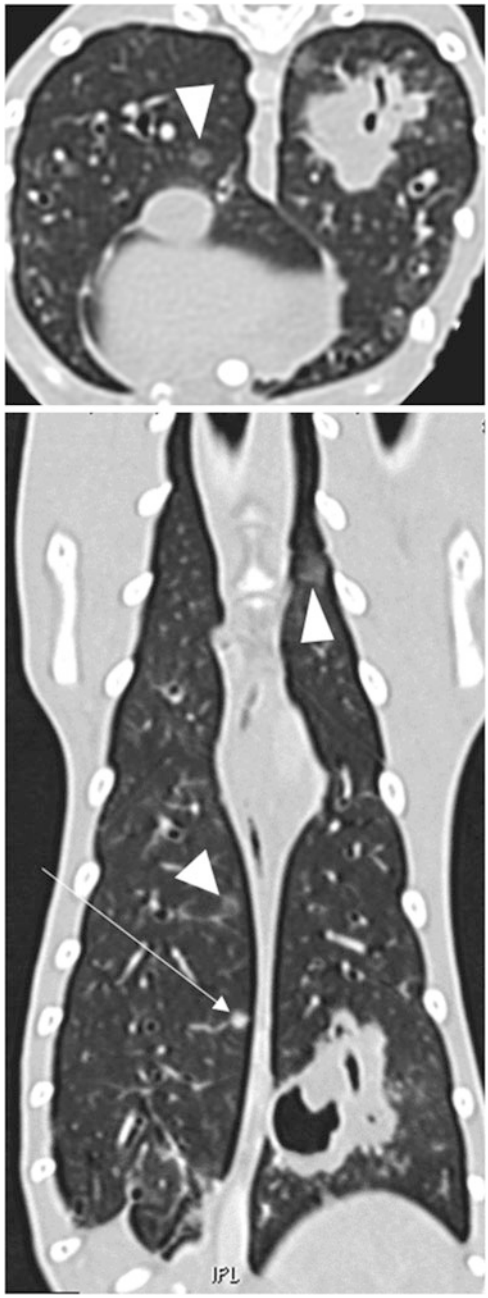

Fig. 28 Metastatic osteosarcoma in a cat. Note the cavitary lung lesion in the caudal left lobe. Overall peribronchovascular interstitial thickening, metastatic micronodules (*arrow*), and ground-glass nodules (*arrowhead*) are present

Emphysema

Emphysema is characterized by the permanent enlargement of airspaces distal to the terminal bronchiole with the destruction of alveolar walls (not visible on CT). In humans, description of the CT appearance of emphysema is based on its

distribution within secondary pulmonary lobules. No CT subclassification of lung emphysema in dogs or cats has been reported to date. However, several types of emphysema have been described and are easily recognizable on CT. In general, the CT appearance of emphysema consists of focal areas or regions of low attenuation, usually with no visible wall (in contrast to honeycombing). Vesicular emphysema of the affected lobe has been described in dogs with lung torsion (Figs. 29 and 46). Bullous emphysema is characterized by sharply demarcated, air-containing spaces (parenchymal bullae) in the lung parenchyma. They are often large and confluent, sometimes assuming a cavernous appearance (Fig. 30). Bullous emphysema is one of the many causes of spontaneous pneumothorax in dogs (Fig. 30). Lobar emphysema involves one lobe entirely. One or more lobar bronchiole can be obliterated, and the lobe is expanded, with a mediastinal contralateral shift. This condition has been reported in young Chow Chows, Jack Russell Terriers, Pekingese, Pomeranians, Shih Tzu, and Springer Spaniels. It may be congenital or acquired in nature. Acquired conditions reported in dogs include anomalies of the bronchial cartilage, causing collapse in the expiratory phase (air entrapment mechanism) (Figs. 31 and 32). Pulmonary interstitial emphysema (PIE) refers to the presence of air in the perivascular interstitium and lymphatics (Fig. 33). PIE is commonly described in humans as a consequence of the rupture of overdistended alveoli following barotrauma in preterm infants treated with mechanical ventilation or continuous positive airway pressure. Spontaneous PIE is described rarely in adult human patients. It was first described in a ventilated dog with severe pneumopathy that underwent 16-MD-HRCT. HRCT can be used to detect PIE in veterinary patients with pneumomediastinum, as the two conditions are physiopathologically linked (see Sect. 3 in chapter "The Mediastinum and Neck").

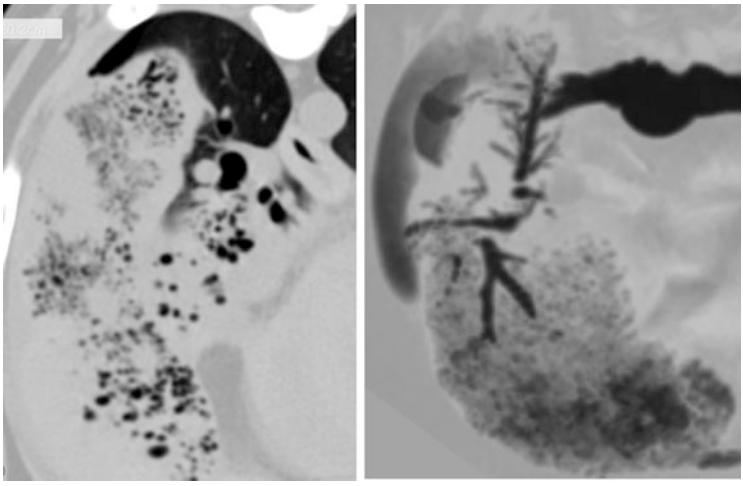

Fig. 29 Vesicular emphysema in lung lobe torsion in dogs

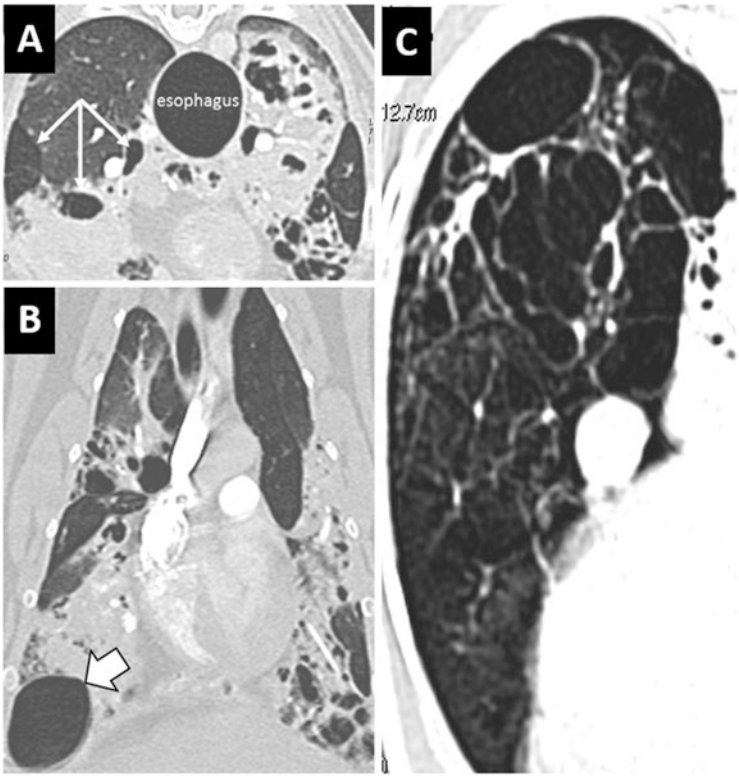

Fig. 30 Bullous emphysema in a cat with end-stage pulmonary fibrosis. Cystic changes of the lung parenchyma (*large arrow*) and areas of air trapping (*arrows*) are visible. The esophagus is noticeably enlarged. (**b**) Bullous emphysemal destruction (of undetermined cause) in a young dog

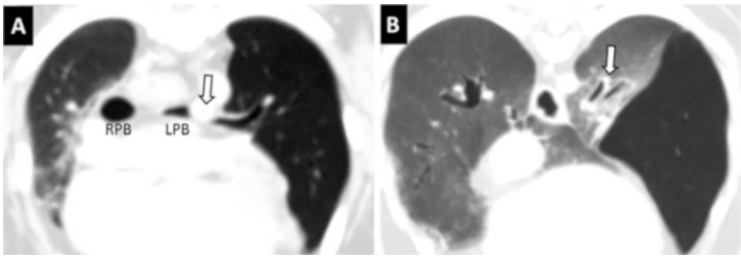

Fig. 31 (**a**) Lobar emphysema involving the left cranial lobe in a pug with left bronchial stenosis (*arrow*). *RPB* right principal bronchus, *LPB* left principal bronchus. (**b**) The *arrow* indicates stenotic subsegmental left bronchi. Note the hyperlucent dependent lobe

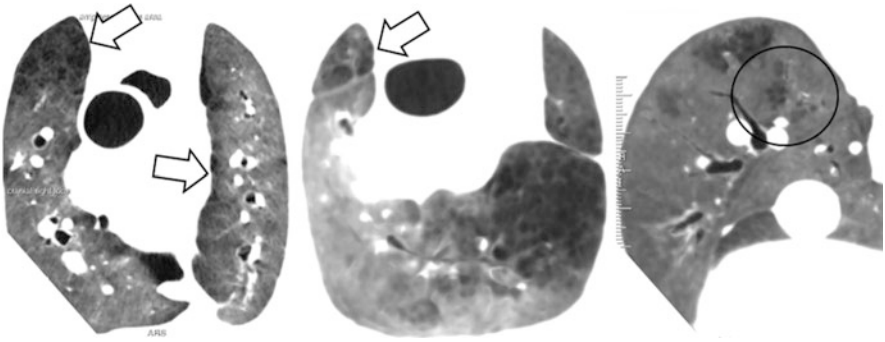

Fig. 32 Pulmonary emphysema in dogs, resembling paraseptal (*large arrow*) and centrilobular emphysema in humans

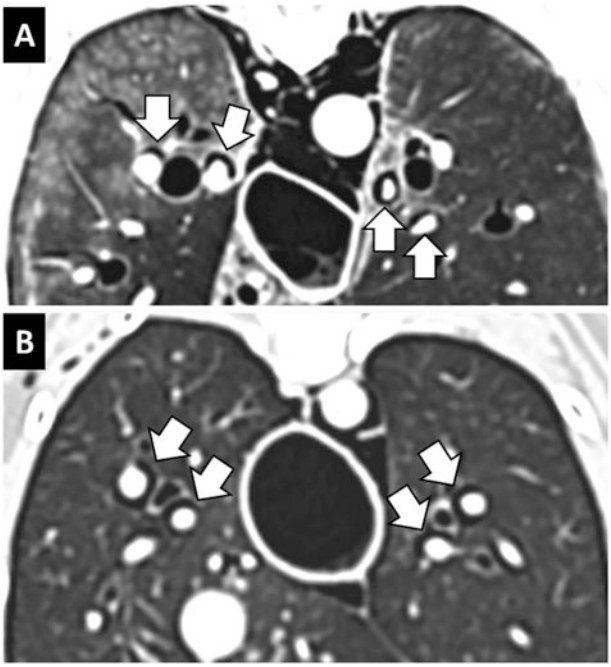

Fig. 33 Pulmonary interstitial emphysema and pneumomediastinum in a dog (**a**) and a cat (**b**) with severe pneumonia

3.1.3 Mosaic Pattern

The mosaic pattern is characterized by variable lung attenuation, which results in the heterogeneous appearance of the parenchyma. It may be found in several conditions but most commonly occurs in obstructive small airway diseases,

occlusive vascular diseases, and diffuse parenchymal diseases. Thus, a heterogeneous lung pattern on HRCT should prompt evaluation of the small airways (to detect bronchiolar and alveolo-interstitial patterns), assessment of the pulmonary vasculature (to determine the size and morphology of central and peripheral pulmonary arteries), and/or thorough assessment of the parenchyma (to detect areas of ground-glass opacity).

Chronic pulmonary embolism creates a mosaic pattern in the lung due to the redistribution of blood flow (Fig. 34). In humans and small animals, perfusion defects are not obvious on contrast-enhanced CT images. Dual-energy CT of the lung, based on the spectral differentiation of iodine, is technically feasible and can display pulmonary perfusion, aiding the identification of perfusion defects.

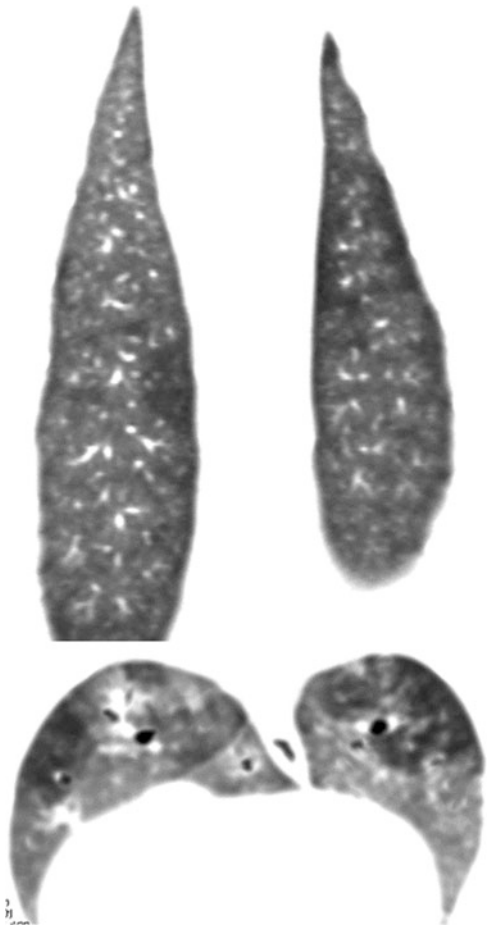

Fig. 34 Mosaic pattern in a cat with feline asthma

3.2 Dual-Energy and Lung Perfusion

Pulmonary CTA enables the visualization of pulmonary embolism in the majority of cases. However, small peripheral emboli may remain unnoticed, or their impacts on lung perfusion may remain unclear. Whereas pulmonary CTA provides only morphological information and does not allow direct assessment of the effects of thromboembolic clots on lung perfusion, dual-energy CTA simultaneously provides functional and morphological information that might be clinically useful for patient management. Pulmonary perfusion imaging in small animals is currently performed using lung scintigraphy, which has several practical and interpretative

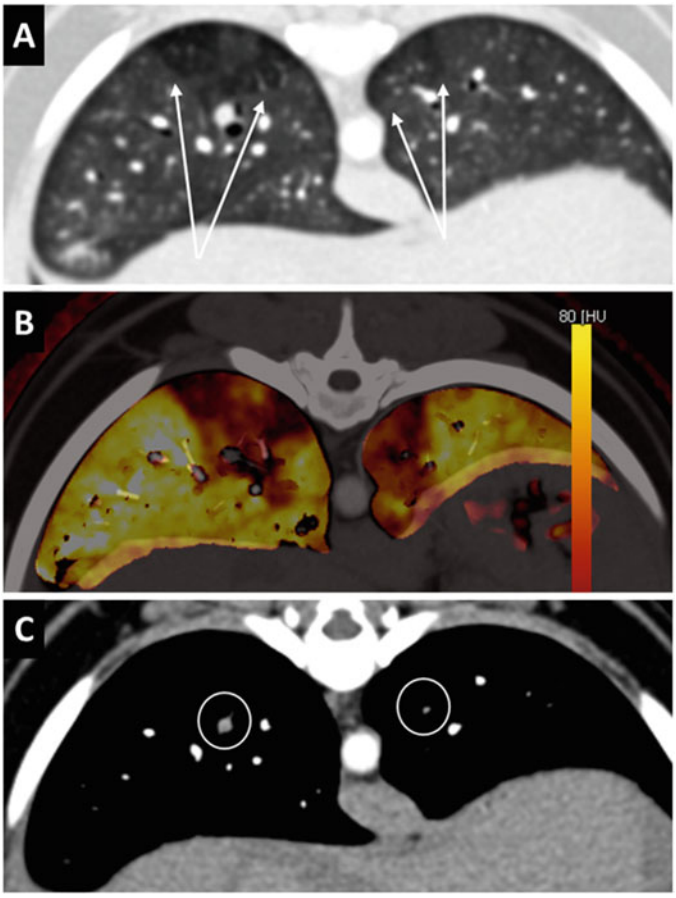

Fig. 35 DE-DSCT study of pulmonary embolism in a dog. (**a**) Post-contrast transverse view showing the mosaic pattern at the periphery of the lung (*arrows*). (**b**) Color-coded map of lung perfusion at the same level. Note the subsegmental perfusion defects. (**c**) Image obtained with a narrow window at the same level shows hypoperfused subsegmental vessels (pulmonary embolism)

limitations. In people and in experimental animal models, dual-energy CTA perfusion imaging showed good agreement with scintigraphic findings. The basic principle of dual-energy CT is material decomposition based on attenuation differences at different energy levels. Soft tissue, air, and iodine comprise the three-component system analyzed in the lung. The density of iodine CM is stronger at lower voltage than at higher voltage, whereas this effect is negligible for the other elements (air and soft tissue). Therefore, this peculiar X-ray absorption characteristic makes selective iodine mapping (corresponding to lung perfusion) possible. Most recent generations of single-source (single X-ray tube) MDCT scanners can be used to acquire dual-energy data by ultrafast switching between 140 kVp and 80 kVp. Most recent (second- and third-generation) DSCT scanners have double tube-detector systems (DE-DSCT) that enable the simultaneous acquisition of high-quality data at different energy levels (generally 140 kVp and 100 kVp). Dedicated software can be used to obtain virtual non-contrast images, color-coded MPRs, and specific measurements from original datasets. Color-coded images from normal lung show symmetrical and homogenous iodine distribution (normal lung perfusion) (see the Chapter 1 in Section 1 'Technics and technology'). Local triangular perfusion defects are signs of pulmonary embolism. In our 2-year experience with a second-generation DSCT scanner, results of dual-energy DSCTA examination of canine pulmonary embolism and other disorders affecting the lung parenchyma in small animals have been promising, similar to those described in people (Fig. 35).

4 Lung Tumors

One of the most common indications for thoracic CT examination in dogs and cats is the characterization and staging of lung tumors. Several primary and secondary neoplastic processes may involve the lungs. Lung masses and nodules may be found in the setting of a systemic neoplastic process (e.g., lymphoma or histiocytic sarcoma) and in cases of lung metastasis from a primary neoplasia outside the lung, via the bloodstream or lymphatic system or by direct extension to the lung (e.g., mammary carcinoma or thoracic wall sarcoma) (Fig. 36).

Primary pulmonary neoplasias are classified based on cell origin, cell morphology, and/or anatomic location. The most common primary lung tumors in small animals are adenocarcinoma, adenosquamous carcinoma, squamous cell carcinoma, and tumors of bronchial origin, including bronchial gland carcinoma. Reported prevalences of different tumor types vary among studies, but the literature shows agreement that certain carcinoma subtypes are the most frequently encountered lung tumors in dogs and cats. In dogs, primary lung tumors (adenocarcinoma, bronchoalveolar carcinoma) are located most commonly in the right caudal lobe. They are typically solitary, solid masses with well-defined margins and inhomogeneous enhancement after CM injection; they show hyper- and hypoattenuating areas due to variable blood supply to different parts of the tumor (Figs. 37 and

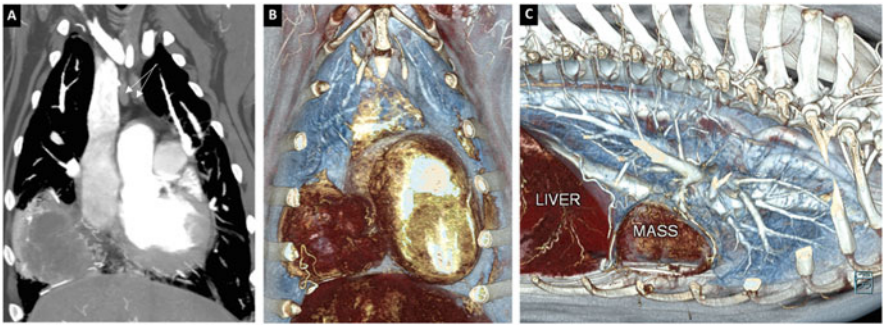

Fig. 36 Histiocytic sarcoma in a Bernese Mountain Dog. (**a**) Dorsal MPR image shows a large inhomogeneous mass in the right middle lobe. The mass does not include the pulmonary vasculature or bronchial structures. *Arrows* indicate mediastinal lymph nodes. (**b**, **c**) Volume-rendered images showing the relationships of the mass to other intrathoracic structures

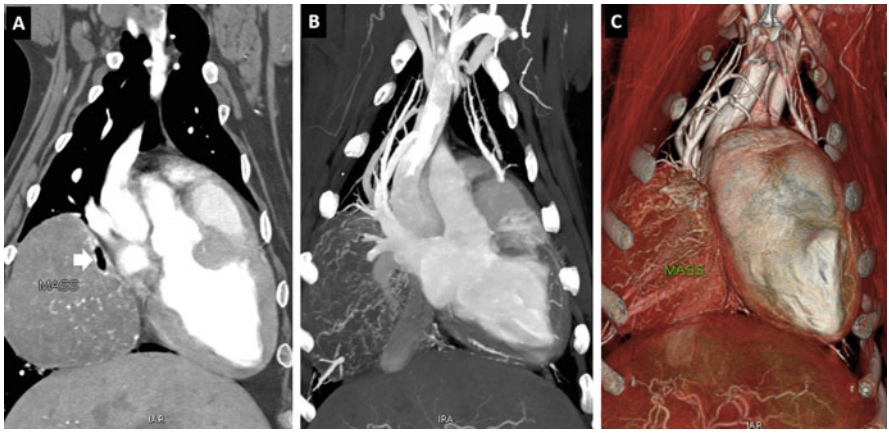

Fig. 37 Pulmonary adenocarcinoma of the caudal right lobe in a dog. (**a**) Dorsal MPR image showing the large mass with the positive bronchus sign (*arrow*). (**b**) Thin-MIP image showing neovascularization of the mass. (**c**) Volume-rendered image showing compression of the heart by the mass

38). Hypoattenuating areas generally represent necrosis, edema, or collection of mucus. Mineral foci may be detected inside a mass and are better appreciated on pre-contrast images. Some large masses have pseudocavities containing air and/or fluid, which may result from the involvement of small bronchial structures or the presence of cystic spaces in the neoplastic tissue. The thoracic lymph nodes, particularly the cranial mediastinal and tracheobronchial nodes, which drain various structures of the lung parenchyma, should be assessed thoroughly. The sensitivity of CT for the detection of lymph node involvement depends strongly on image quality, and thin-slice volumetric CT is required for the detection and

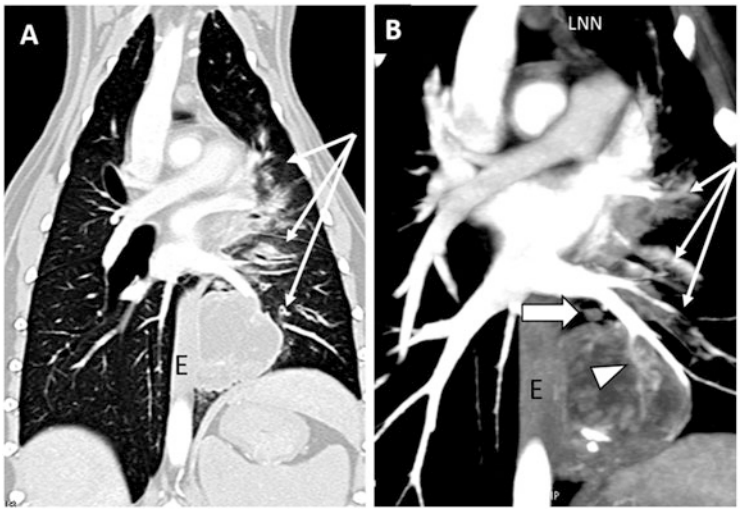

Fig. 38 (**a**) Pulmonary carcinoma in a mongrel dog with cough. Note the large mass of the left caudal lobe. *Arrow* indicates perilesional peribronchovascular interstitial thickening, which also affects the vascular hilum in the cranial lobe. E, esophagus. (**b**) Thin-MIP image with better visualization of perivascular thickening (*thin arrows*). Note the "angiogram sign" (*arrowhead*) and some mineralization within the mass. A satellite nodular lesion (*large arrow*) is present. LNN, mediastinal lymph nodes. Necropsy and histopathological evaluation confirmed metastatic carcinoma

characterization of various lymphatic structures, particularly for the tracheobronchial lymph nodes, which can be difficult to assess.

In cats, primary pulmonary neoplasia is uncommon; its reported prevalence at necropsy is 0.69–0.75%. Adenocarcinoma is the most frequently diagnosed lung tumor type in cats, and it generally has a poor prognosis. Tumors of bronchial origin, adenosquamous cell carcinomas, and squamous cell carcinomas are reported less commonly. As in dogs, primary lung tumors in cats appear on CT as well-defined masses, but they have irregular margins in most cases. Intratumoral mineral foci and gas-containing tumoral lesions have also been reported in cats (Fig. 28). In both species, large masses may cause bronchial compression or invasion. Primary lung tumors in dogs and cats may show the "angiogram sign" on contrast-enhanced images. This CT sign results from the normal enhancement of the pulmonary vessels within the low-attenuating consolidated lung parenchyma and may help to determine if a mass is pulmonary or not. It was first reported in humans with bronchoalveolar carcinoma and was considered to be indicative of that tumor type. However, several other neoplastic and nonneoplastic airspace-filling diseases, such as lymphoma and pneumonia, may show the angiogram sign (Fig. 39). Clinical information and concomitant pulmonary (e.g., nodular pattern, halo sign, areas of ground-glass opacity) and extrapulmonary (lymphadenopathy, pleural effusion) CT signs may aid the interpretation of this important CT sign.

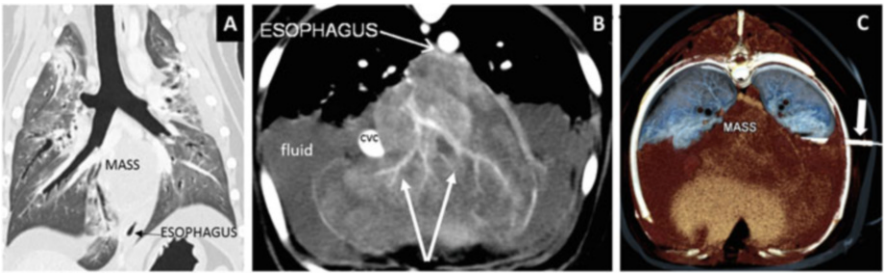

Fig. 39 Large intrathoracic mass in a Cocker Spaniel. (**a**) Dorsal MPR image of the thorax. The mass shows relationships to pulmonary and mediastinal structures. (**b**) Transverse view of the mass. *Arrows* indicate the "angiogram sign," suggesting the pulmonary origin (ventral part of the accessory lobe) of the mass. (**c**) Volume-rendered cut plane showing CT-guided fine-needle aspiration of the mass (*arrow*). Histopathology (after lobectomy) confirmed bronchoalveolar cell carcinoma

5 MDCT Signs of Airway Diseases

The use of MDCT for the assessment of primary, nonneoplastic laryngeal and tracheal obstructive conditions (e.g., laryngeal paralysis, tracheal hypoplasia, tracheal or bronchial collapse) in awake or sedated patients using 3D VR and endoluminal techniques (i.e., virtual endoscopy) has been proposed. Endoscopy is required for the dynamic evaluation of airway collapse, assessment of the respiratory mucosa, and biopsy. Therefore, the two examination techniques should be combined. Airway injury is a common reason for MDCT examination in the setting of polytrauma evaluation (see the chapter "The Body Trauma"). However, MDCT of the airways is performed most commonly to evaluate neoplastic diseases involving the larynx, trachea, and bronchi.

5.1 Airway Collapse

Airway collapse can affect the cervical trachea, intrathoracic trachea, or bronchial wall, diffusely or in a single segment. Tracheal collapse results from the softening of the tracheal cartilage. It is characterized by dorsoventral flattening of the tracheal rings and prolapse of the tracheal membrane into the lumen. When the principal bronchi are also involved, the condition is termed tracheobronchomalacia. Bronchomalacia refers to the narrowing and loss of luminal dimensions only in the intrathoracic airways, large bronchi, and small airways supported by cartilage. Bronchial collapse is a common finding in brachiocephalic dog breeds (Figs. 31, 40, 41, and 42). Stenosis most commonly affects the left cranial bronchi in these dogs, which may explain the predisposition of pugs and similar breeds to torsion of the left cranial lung lobe.

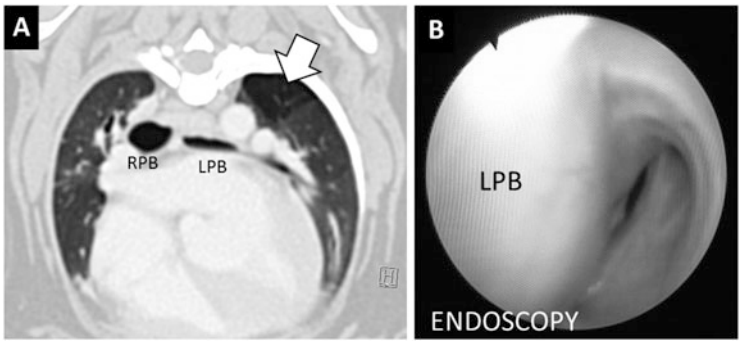

Fig. 40 Left principal bronchus collapse in a pug. (**a**) Transverse view. Note the difference in size between the right principal bronchus (RPB) and left principal bronchus (LPB), which is flattened (in the dorsoventral direction). *Arrow* indicates a hypoattenuating area of air trapping. (**b**) Image of the LPB from endoscopic evaluation (true endoscopy)

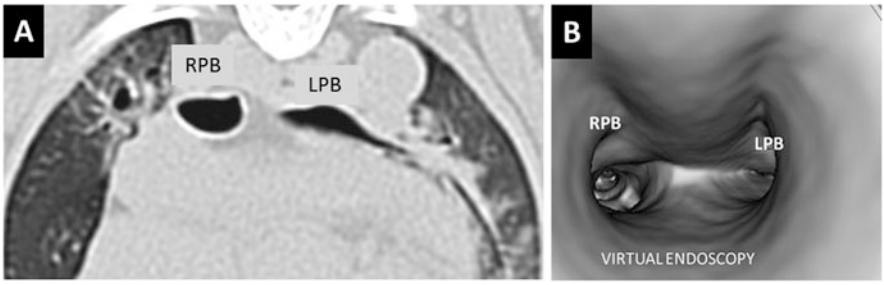

Fig. 41 (**a**) Transverse view from a pug showing bronchial stenosis. (**b**) Endoluminal imaging (virtual endoscopy)

Bronchial collapse has been correlated with laryngeal collapse. Elective tests for these conditions include radiology, fluoroscopy, and endoscopy, which enable the simultaneous assessment of primary nasopharyngeal malformation in brachycephalic breeds. CT is generally required for other reasons, including the assessment of pulmonary complications, in these patients.

5.2 Airway Stenosis

Airway stenosis refers to the narrowing of the tracheal and/or bronchial lumen and can occur with several intrinsic and extrinsic conditions. *Intrinsic causes of stenosis* include benign and malignant conditions primarily involving the trachea and bronchi. In inflammatory bronchial and rare congenital conditions, the airways

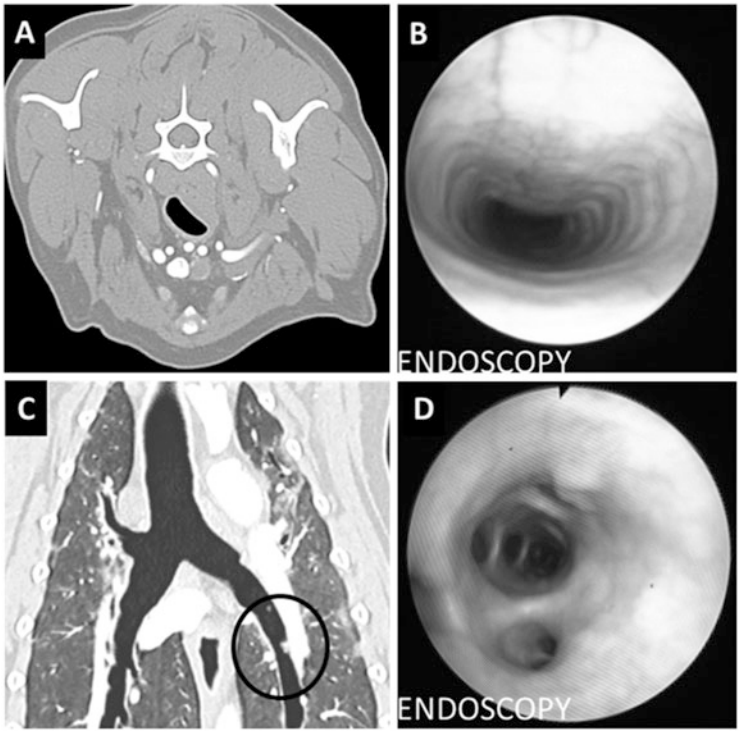

Fig. 42 (**a**) Moderate tracheal collapse and chronic bronchopathy in a mongrel dog. (**b**) Endoscopic image of the trachea (true endoscopy). (**c**) Dorsal MPR of the thorax. Note the projection of some hyperplastic nodules into the bronchial lumen (*circle*). (**d**) Endoscopic image from the same subsegmental left bronchus

may appear to be filled with mucoid secretions (mucus plugging or impaction), which can lead to various degrees of bronchial stenosis (Figs. 43 and 44).

Primary neoplasias of the airways are rare and may appear as segmental thickening of the bronchial wall or as a mass projecting into the lumen, leading to partial or complete obstruction. *Extrinsic stenosis* of the airways can be seen with several benign and malignant conditions affecting structures of the neck (e.g., abscess, large thyroid tumor) or the mediastinum (e.g., cranial mediastinal masses, such as thymic tumor). Upon enlargement, a primary pulmonary neoplasia may compress the bronchial structures.

Lung lobe torsion (LLT) leads to bronchial obstruction because of twisting of a lung lobe around its bronchovascular pedicle. The etiology of LLT is unknown, but increasing lung mobility due to pleural effusion, atelectasis, or thoracic surgery is a possible contributing mechanism. Deep-chest breeds seem to be predisposed, but a Pug dog is overrepresented in several works. CT angiography is an effective noninvasive method for confirming the correct diagnosis. MinIP, MIP, and volume-rendered images can unequivocally show features of stenosis or occlusion

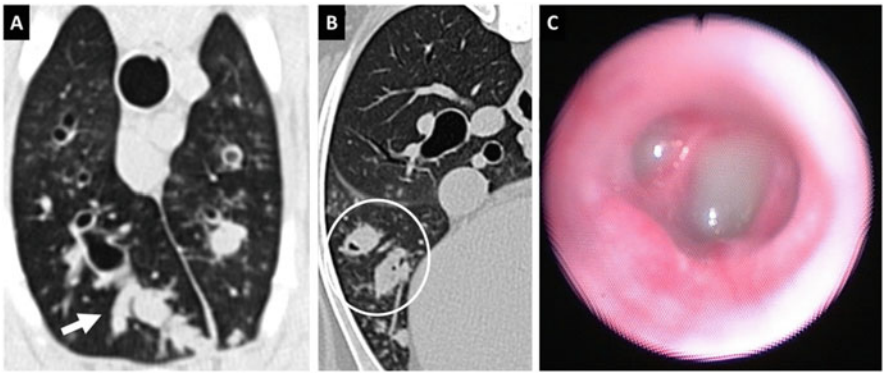

Fig. 43 Mucoid impactions in a dog with septic bronchitis. (**a**) Transverse view. *Arrow* indicates the bronchocele with mucus inspissated in the bronchi (finger-in-glove sign). (**b**) Mucus plugging of the subsegmental bronchi (*circle*). (**c**) Image from endoscopy showing dense mucus in the bronchial lumen

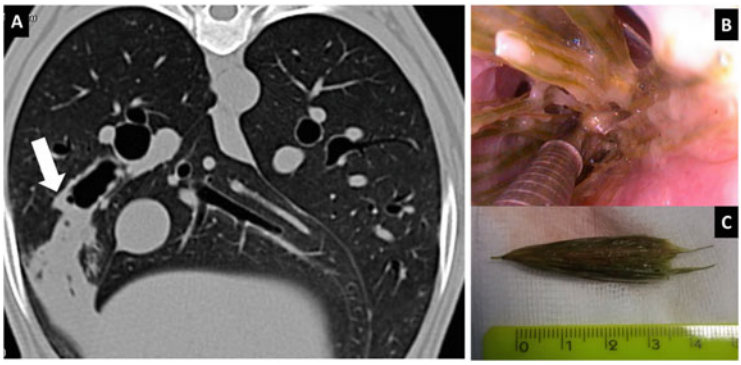

Fig. 44 Segmental mucoid impaction in a dog with a vegetal bronchial foreign body. (**a**) Transverse view. *Arrow* shows the segmental bronchiectasis. Ventrally, the bronchus is filled with mucoid secretions. (**b**) Image of bronchoscopic retrieval of the foreign body. (**c**) The foreign body

of bronchovascular structures (Fig. 45). The twisted lobe may contain trapped gas, which appeared as a vesicular gas pattern (Figs. 29 and 46).

5.3 Bronchial Diseases

Bronchial diseases such as bronchitis, bronchiectasis, and bronchomalacia are encountered frequently in small animals. All of these diseases are associated with changes in the bronchial diameter. Subjective qualitative evaluation of bronchial size and appearance on CT images is usually performed as part of routine thoracic

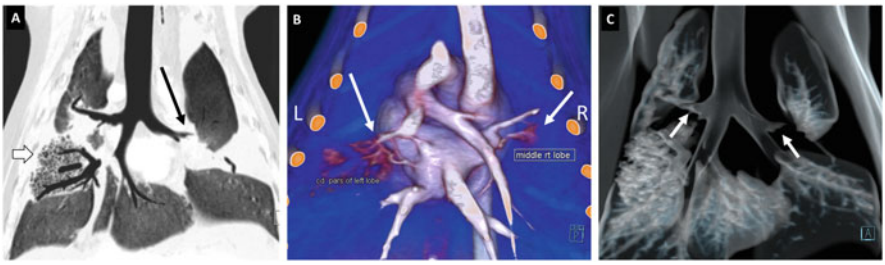

Fig. 45 Bilateral lobar torsion in a 3-kg Maltese dog. (**a**) Dorsal thin-MinIP image. *Large arrow* shows vesicular emphysema in the right middle lobe. *Thin arrow* indicates the interrupted segmental bronchus to the caudal part of the left cranial lobe. (**b**) Volume-rendered dorsal image showing vascular torsion. (**c**) Volume-rendered image of the air-containing structures showing interrupted bronchi (*arrows*)

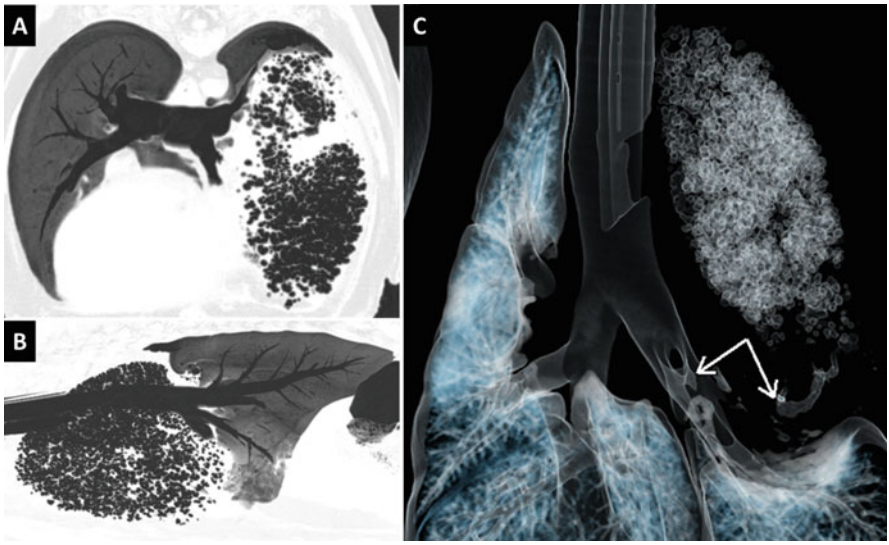

Fig. 46 Vesicular emphysematous pattern in a dog with left cranial lung lobe torsion. (**a**, **b**) Transverse and sagittal MinIP views. (**c**) VR. *Arrows* show the segmental bronchial interruption

CT assessment. However, in patients with suspected bronchopulmonary conditions, the quantitative assessment of bronchial size is now recommended. No range of absolute measurements of normal bronchial diameter has been established for humans or animals. However, the diameter of a bronchial lumen may be compared with that of the corresponding pulmonary artery and expressed as a bronchoarterial (BA) ratio. One or more sites that are convenient for tangential visualization of the bronchus and artery may be chosen for measurement, even when the use of multioblique MPRs showing true transverse planes across the structures would be more accurate. BA ratios of 0.8–2.0 have been reported in normal dogs, and the value of 2.0 has been suggested as a threshold to differentiate normal from

abnormal bronchi in this species. Differences exist among breeds; the mean BA ratio for healthy brachycephalic dogs (1.08 ± 0.10) is lower than that for healthy non-brachycephalic dogs (1.50 ± 0.06). A mean BA ratio of 0.71 ± 0.1 was identified for cats, which suggests that an upper threshold of 0.91 can be used to differentiate normal from abnormal bronchi in this species.

The BA ratio can increase or decrease in various situations. *An increase in the BA ratio* may be observed with any condition that causes bronchiectasis. The term "bronchiectasis" refers to chronic and irreversible, segmental or diffuse, abnormal dilatation of the bronchial tree following the loss of bronchial wall structural integrity (Figs. 47, 48, and 49). It is a rare condition in dogs, with a reported prevalence of 0.05–0.08%. Certain canine breeds, including the American Cocker Spaniel, West Highland White Terrier, Poodle, Siberian Husky, and Springer Spaniel, seem to be predisposed to the development of bronchiectasis. This condition is a sequela of many congenital and acquired disorders, including infection, presence of a foreign body, neoplasia, immunodeficiency, and primary ciliary dyskinesia. Again, it has been associated with tracheal collapse and bronchomalacia in dogs. Three macroscopic morphological CT patterns have been described in veterinary patients: cylindrical (the most common form in dogs and cats), saccular, and cystic. The varicose pattern (dilatation of the bronchi with circumferential constrictions, resulting in a "beaded" appearance), described in humans, has not been reported in dogs and cats. In the cylindrical pattern, one or more of the largest, thick-walled bronchi show uniform dilatation and loss of distal tapering. Saccular bronchiectasis affects primarily the intermediate-sized bronchi, which assume a

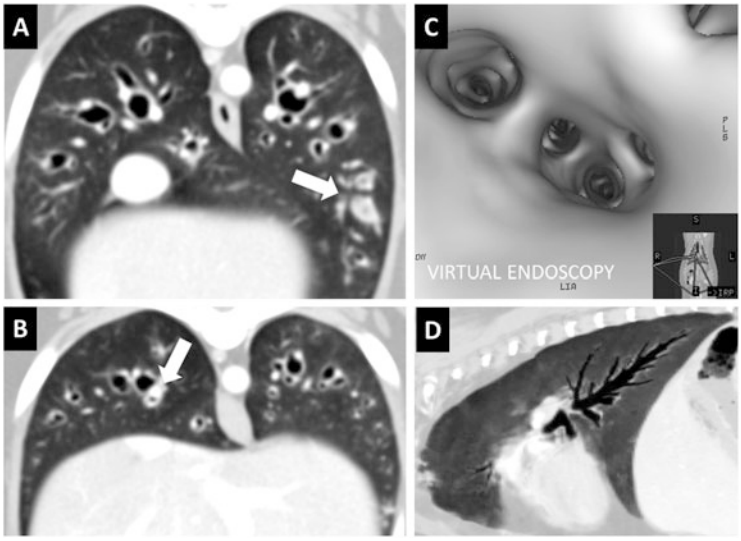

Fig. 47 Cylindrical bronchiectasis in a Cocker Spaniel with chronic chough. (**a**, **b**) Transverse sections showing moderate diffuse bronchial dilatation and bronchial wall thickening. *Arrow* indicates mucus plugging within the subsegmental bronchi

Fig. 48 Bronchiectasis in a mongrel dog with a history of bronchopulmonary infection (*Dirofilaria immitis* and angiostrongylosis). Note the beaded, widened bronchi with irregular contours. This aspect is similar to that of varicose bronchiectasis in humans. Subsegmental ventral bronchi show mucus impaction (*circle*)

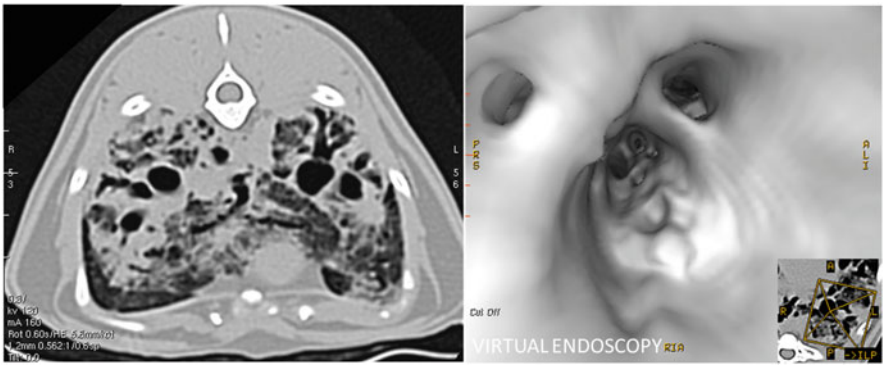

Fig. 49 Diffuse bronchial dilatation in a cat with severe septic bronchopneumonia

"grape cluster" appearance due to circumscribed sacculation of the bronchial walls at their terminal ends. Cystic bronchiectasis, the end stage of the saccular pattern, involves the terminal bronchi. Bronchiectasis is often accompanied by mucoid impaction and small airway abnormalities. The affected bronchial segments show bronchial wall thickening, which leads to an increased BA ratio. Increased BA ratios due to bronchial wall thickening may be observed also in patients with chronic inflammatory diseases of the bronchial tree (*chronic bronchitis*). Other causes of increased BA ratio include *chronic feline asthma (*when the bronchial wall thickens) and diminished pulmonary vessel diameters, as in *chronic pulmonary embolism*. As stated previously, *a decrease of the BA ratio* is normally found in brachycephalic dogs but can also be detected with any condition causing bronchoconstriction.

Further Readings

Aarsvold S, Reetz JA, Reichle JK, Jones ID, Lamb CR, Evola MG, Keyerleber MA, Marolf AJ. Computed tomographic findings in 57 cats with primary pulmonary neoplasia. Vet Radiol Ultrasound. 2015;56(3):272–7. doi:10.1111/vru.12240. Epub 2015 Jan 21.

Alexander K, Joly H, Blond L, D'Anjou MA, Nadeau MÈ, Olive J, Beauchamp G. A comparison of computed tomography, computed radiography, and film-screen radiography for the detection of canine pulmonary nodules. Vet Radiol Ultrasound. 2012;53(3):258–65. doi:10.1111/j.1740-8261.2012.01924.x. Epub 2012 Mar 14.

Ballegeer EA, Adams WM, Dubielzig RR, et al. Computed tomography characteristics of canine tracheobronchial lymph node metastasis. Vet Radiol Ultrasound. 2010;51:397–403.

Cannon MS, Wisner ER, Johnson LR, Kass PH. Computed tomography bronchial lumen to pulmonary artery diameter ratio in dogs without clinical pulmonary disease. Vet Radiol Ultrasound. 2009;50(6):622–4.

Cannon MS, Johnson LR, Pesavento PA, Kass PH, Wisner ER. Quantitative and qualitative computed tomographic characteristics of bronchiectasis in 12 dogs. Vet Radiol Ultrasound. 2013;54(4):351–7. doi:10.1111/vru.12036. Epub 2013 Apr 12.

Dungworth DL, Hauser B, Hahn FF, et al. Histological classification of tumors of the respiratory system of domestic animals. Washington, DC: Armed Forces Institute of Pathology in cooperation with the American Registry of Pathology and the World Health Organization Collaborating Center for Worldwide Reference on Comparative Oncology; 1999.

Eberle N, Fork M, von Babo V, Nolte I, Simon D. Comparison of examination of thoracic radiographs and thoracic computed tomography in dogs with appendicular osteosarcoma. Vet Comp Oncol. 20119(2):131–40. doi:10.1111/j.1476-5829.2010.00241.x. Epub 2010 Aug 30.

Goldfinch N, Argyle DJ. Feline lung-digit syndrome: unusual metastatic patterns of primary lung tumours in cats. J Feline Med Surg. 2012;14(3):202–8. doi:10.1177/1098612X12439267.

Hawkins EC, Basseches J, Berry CR, Stebbins ME, Ferris KK. Demographic, clinical, and radiographic features of bronchiectasis in dogs: 316 cases (1988-2000). J Am Vet Med Assoc. 2003;223(11):1628–35.

JJ A, Weisman DL, Stefanacci JD, Palmisano MP. Use of computed tomography for evaluation of lung lesions associated with spontaneous pneumothorax in dogs: 12 cases (1999-2002). J Am Vet Med Assoc. 2006;228(5):733–7.

Johnson EG, Wisner ER. Advances in respiratory imaging. Vet Clin North Am Small Anim Pract. 2007;37(5):879–900, vi.

Johnson VS, Ramsey IK, Thompson H, Cave TA, Barr FJ, Rudorf H, Williams A, Sullivan M. Thoracic high-resolution computed tomography in the diagnosis of metastatic carcinoma. J Small Anim Pract. 2004;45(3):134–43.

Johnson VS, Corcoran BM, Wotton PR, Schwarz T, Sullivan M. Thoracic high-resolution computed tomographic findings in dogs with canine idiopathic pulmonary fibrosis. J Small Anim Pract. 2005;46(8):381–8.

Kim J, Kwon SY, Cena R, Park S, Oh J, Oui H, Cho KO, Min JJ, Choi J. CT and PET-CT of a dog with multiple pulmonary adenocarcinoma. J Vet Med Sci. 2014;76(4):615–20. Epub 2013 Dec 31.

Lipscomb VJ, Hardie RJ, Dubielzig RR. Spontaneous pneumothorax caused by pulmonary blebs and bullae in 12 dogs. J Am Anim Hosp Assoc. 2003;39(5):435–45.

Marolf A, Blaik M, Specht A. A retrospective study of the relationship between tracheal collapse and bronchiectasis in dogs. Vet Radiol Ultrasound. 2007;48(3):199–203.

Marolf AJ, Gibbons DS, Podell BK, Park RD. Computed tomographic appearance of primary lung tumors in dogs. Vet Radiol Ultrasound. 2011;52(2):168–72. doi:10.1111/j.1740-8261.2010.01759.x.

Mesquita L, Lam R, Lamb CR, McConnell JF. Computed tomographic findings in 15 dogs with eosinophilic bronchopneumopathy. Vet Radiol Ultrasound. 2015;56(1):33–9. doi:10.1111/vru.12187.

Morandi F, Mattoon JS, Lakritz J, Turk JR, Wisner ER. Correlation of helical and incremental high-resolution thin-section computed tomographic imaging with histomorphometric quantitative evaluation of lungs in dogs. Am J Vet Res. 2003;64(7):935–44.

Morandi F, Mattoon JS, Lakritz J, Turk JR, Jaeger JQ, Wisner ER. Correlation of helical and incremental high-resolution thin-section computed tomographic and histomorphometric quantitative evaluation of an acute inflammatory response of lungs in dogs. Am J Vet Res. 2004;65(8):1114–23.

Nemanic S, London CA, Wisner ER. Comparison of thoracic radiographs and single breath-hold helical CT for detection of pulmonary nodules in dogs with metastatic neoplasia. J Vet Intern Med. 2006;20(3):508–15.

Nunley J, Sutton J, Culp W, Wilson D, Coleman K, Demianiuk R, Schechter A, Moore G, Donovan T, Schwartz P. Primary pulmonary neoplasia in cats: assessment of computed tomography findings and survival. J Small Anim Pract. 2015;56(11):651–6. doi:10.1111/jsap.12401.

Otoni CC, Rahal SC, Vulcano LC, Ribeiro SM, Hette K, Giordano T, Doiche DP, Amorim RL. Survey radiography and computerized tomography imaging of the thorax in female dogs with mammary tumors. Acta Vet Scand. 2010;52:20. doi:10.1186/1751-0147-52-20.

Paoloni MC, Adams WM, Dubielzig RR, et al. Comparison of results of computed tomography and radiography with histopathologic findings in tracheobronchial lymph nodes in dogs with primary lung tumors: 14 cases (1999–2002). J Am Vet Med Assoc. 2006;228:1718–22.

Reetz JA, Caceres AV, Suran JN, Oura TJ, Zwingenberger AL, Mai W. Sensitivity, positive predictive value, and interobserver variability of computed tomography in the diagnosis of bullae associated with spontaneous pneumothorax in dogs: 19 cases (2003-2012). J Am Vet Med Assoc. 2013;243(2):244–51. doi:10.2460/javma.243.2.244.

Reid LE, Dillon AR, Hathcock JT, Brown LA, Tillson M, Wooldridge AA. High-resolution computed tomography bronchial lumen to pulmonary artery diameter ratio in anesthetized ventilated cats with normal lungs. Vet Radiol Ultrasound. 2012;53(1):34–7. doi:10.1111/j.1740-8261.2011.01870.x.

Schultz RM, Zwingenberger A. Radiographic, computed tomographic, and ultrasonographic findings with migrating intrathoracic grass awns in dogs and cats. Vet Radiol Ultrasound. 2008;49(3):249–55.

Schultz RM, Peters J, Zwingenberger A. Radiography, computed tomography and virtual bronchoscopy in four dogs and two cats with lung lobe torsion. J Small Anim Pract. 2009;50(7):360–3. doi:10.1111/j.1748-5827.2009.00728.x.

Scrivani PV, Thompson MS, Dykes NL, Holmes NL, Southard TL, Gerdin JA, Bezuidenhout AJ. Relationships among subgross anatomy, computed tomography, and histologic findings in dogs with disease localized to the pulmonary acini. Vet Radiol Ultrasound. 2012;53(1):1–10. doi:10.1111/j.1740-8261.2011.01881.x.

Secrest S, Sakamoto K. Halo and reverse halo signs in canine pulmonary computed tomography. Vet Radiol Ultrasound. 2014;55(3):272–7. doi:10.1111/vru.12132.

Seiler G, Schwarz T, Vignoli M, Rodriguez D. Computed tomographic features of lung lobe torsion. Vet Radiol Ultrasound. 2008;49(6):504–8.

Stadler K, O'Brien R. Computed tomography of nonanesthetized cats with upper airway obstruction. Vet Radiol Ultrasound. 2013;54(3):231–6. doi:10.1111/vru.12019.

Stadler K, Hartman S, Matheson J, O'Brien R. Computed tomographic imaging of dogs with primary laryngeal or tracheal airway obstruction. Vet Radiol Ultrasound. 2011;52(4):377–84. doi:10.1111/j.1740-8261.2011.01816.x.

Szabo D, Sutherland-Smith J, Barton B, Rozanski EA, Taeymans O. Accuracy of a computed tomography bronchial wall thickness to pulmonary artery diameter ratio for assessing bronchial wall thickening in dogs. Vet Radiol Ultrasound. 2015;56(3):264–71. doi:10.1111/vru.12216.

Tang CX, Zhang LJ, Han ZH, Zhou CS, Krazinski AW, Silverman JR, Schoepf UJ, Dual-energy LGM. CT based vascular iodine analysis improves sensitivity for peripheral pulmonary artery thrombus detection: an experimental study in canines. Eur J Radiol. 2013;82(12):2270–8. doi:10.1016/j.ejrad.2013.06.021.

Tsai S, Sutherland-Smith J, Burgess K, Ruthazer R, Sato A. Imaging characteristics of intrathoracic histiocytic sarcoma in dogs. Vet Radiol Ultrasound. 2012;53(1):21–7. doi:10.1111/j.1740-8261.2011.01863.x.

Won S, Lee A, Choi J, Choi M, Yoon J. Computed tomographic bronchioarterial ratio for brachycephalic dogs without pulmonary disease. J Vet Sci. 2015;16(2):221–4.

Yamamoto T, Kent MS, Wisner ER, Johnson LR, Stern JA, Qi L, Fujita Y, Boone JM. Single-energy computed tomography-based pulmonary perfusion imaging: Proof-of-principle in a canine model. Med Phys. 2016;43(7):3998. doi:10.1118/1.4953188.

Yun S, Lee H, Lim J, Lee K, Jang K, Shiwa N, Kwon Y. Congenital lobar emphysema concurrent with pneumothorax and pneumomediastinum in a dog. J Vet Med Sci. 2016;78(5):909–12. doi:10.1292/jvms.15-0362.

The Mediastinum and Neck

Giovanna Bertolini

1 Introduction

The mediastinum is a space that lies along the midline of the thorax between the lung pleurae, extending from the thoracic inlet to the diaphragm. Although divided academically into cranial, middle, caudal, and ventral or dorsal compartments, it is actually a single space in which fluid and air/gas move freely, and it can be affected by benign and malignant conditions. The mediastinum itself is customarily evaluated during thoracic MDCT examination. As a result of embryological development, however, an anatomical continuum exists between the mediastinum and the neck in mammals. Several structures, such as the thyroid, trachea, and esophagus, may be affected by various conditions, indicating the need for simultaneous assessment of these two body compartments. Moreover, spaces between the organs of the neck communicate directly with the mediastinum, creating a conduit for the extension of a variety of pathological processes. For this reason, the neck and mediastinum are treated together here.

2 MDCT Imaging Strategies

As is standard, the choice of acquisition strategy and protocol depends on clinical suspicion and the scanner technology available. Imaging of the neck is particularly challenging in veterinary patients because a large number of cervical structures with similar tissue densities exist in a small space and due to the presence of a tracheal tube for anesthesia. The tracheal tube renders the evaluation of the larynx

G. Bertolini (✉)
San Marco Veterinary Clinic, Padua, Italy
e-mail: bertolini@sanmarcovet.it

G. Bertolini (ed.), *Body MDCT in Small Animals*, DOI 10.1007/978-3-319-46904-1_14

and cervical trachea difficult. The use of a 16-MDCT scanner for the simultaneous assessment of extra- and intrathoracic primary airway obstructive diseases in awake dogs and cats has been proposed. Results may be inconsistent due to artifacts, caused mainly by motion in awake subjects, and rescanning is often necessary to obtain better-quality images. An alternative approach, used in our center, to achieve high-quality scanning of the larynx and cervical trachea, involves the use of a laryngeal mask instead of a tracheal tube (Fig. 1). This approach allows optimal assessment of suspected laryngeal or tracheal injuries in patients with pneumomediastinum (PM). It is also useful for the evaluation of cervical masses, as it enables the acquisition of images without artifacts or anatomical distortion. Cranial cervical masses should be examined with the patient's mouth open, which allows for better evaluation of the pharyngeal region. Proper patient positioning is crucial in MDCT evaluation of the neck. The use of dorsal and sternal recumbency for dogs and cats has been reported. For both of these positions, the most important aspect is the caudal positioning of the forelimbs to avoid CT beam-hardening artifacts. For simultaneous assessment of the mediastinum and for tumor staging, additional scans should be performed with the patient's forelimbs positioned cranially, for the same reason (Fig. 2). Further scanogram is generally not necessary.

A pre-contrast series is important for the detection of benign and malignant mineralization (e.g., sialolithiasis, mineralization of a thyroid mass). A pre-contrast series of the neck and thorax is also required in patients with PM. When laryngeal or tracheal injury is excluded, HRCT of the lung could provide useful information about the possible cause of PM (see below in the next section of this chapter). The choice of contrast-enhanced scan protocol depends on the underlying pathology. When a mediastinal or cervical mass is known or suspected, a multiphase approach is useful for its characterization. Major artifacts occurring during scanning of the mediastinum are related to the patient's heart-beat and aorta pulsation (especially in large patients); streak artifacts are produced by the accumulation of contrast medium (CM) in the brachiocephalic vein and

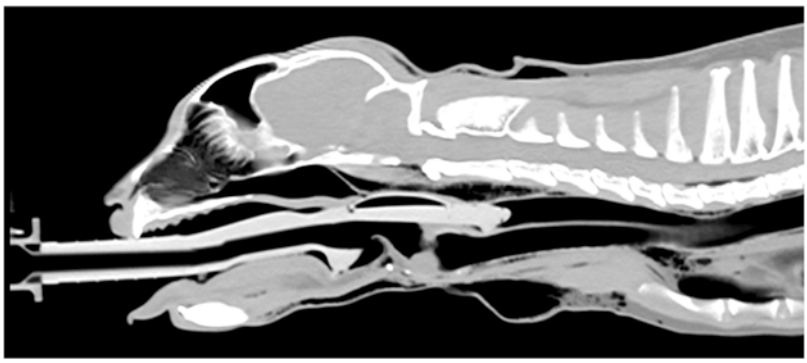

Fig. 1 The image shows the laryngeal mask in a cat with PM and pneumoderma

Fig. 2 Suggested positioning of the patient for CT evaluation of the neck and mediastinum

cranial vena cava (CrVC) (when injection is through the cephalic vein) and obscure the surrounding structures. The physiological movement of the heart and great vessels can cause blurring and double imaging of the other mediastinal structures. With a very rapid scanner, the mediastinum can be scanned during cardiac diastole within a single heartbeat, which significantly reduces the effects of cardiac motion. ECG-gated examination is also possible. Possible strategies for slower scanners include acquisition with thin collimation and overlapping reconstruction. Streak artifacts can be reduced with one or more of the following expedients: use of less (or less concentrated) CM; use of a slower injection rate; and dilution of CM (for single syringe injector systems) or, preferably, use of a saline bolus of the same quantity immediately after CM injection (for dual-barrel injector systems).

The choice of viewing strategy for an MDCT cervico-mediastinal dataset depends on the suspected underlying pathology. A systematic approach includes the lung window (width, 1500 HU; center, −700/800 HU) and mediastinal window (width, 400 HU; center, 40 HU), followed by further modulation using window widths and levels falling between these values, for simultaneous assessment of all

parenchyma, vessels, soft tissues, and air-containing structures of the neck and mediastinum, as well as free air/gas and/or fluid.

MPR and VR from the volume dataset may aid the evaluation of cervical and mediastinal mass extension and relationships with surrounding vascular structures. This approach is particularly useful for surgical planning. Thin-slab MinIP images are extremely useful for the detection of small quantities of free air in cases of PM.

3 Pneumomediastinum and Pneumopericardium

MDCT is the main modality used for the evaluation of suspected PM. Ectopic air can be depicted on radiographs, but small quantities may be overlooked. In contrast, CT is highly sensitive in the detection of small amounts of normal and abnormal air/gas accumulation. However, severe motion artifacts on CT images may make the differentiation of small quantities of PM from medial pneumothorax difficult. After the confirmation of PM, determination of its cause is critical. In a case of blunt or penetrating trauma, secondary PM may have an obvious cause, such as an airway or esophageal injury, which can be detected using CT alone or in combination with endoscopy (see the "The Body Trauma" chapter). Primary or spontaneous PM may develop in non-traumatized patients. Many preexisting predisposing conditions and precipitating factors for spontaneous PM have been identified in humans; they all share a unique pathogenetic mechanism known as the Macklin effect. This effect involves alveolar rupture with air dissecting along the peribronchovascular interstitial sheaths, interlobular septa, and visceral pleura and into the mediastinum. The air then travels along tissue planes and can distribute cranially to the neck, head, and even the forelimbs or caudally in the abdominal region, resulting in subcutaneous emphysema. This mechanism has been well demonstrated in a series of experiments on cats and other animals, and it has also been documented as a spontaneous pathology in dogs (Figs. 3, 4, and 5). The CT feature indicative of the Macklin effect in humans, as well as in dogs and cats, is the presence of free air collection around the bronchi or vasculature (PIE), dissecting the bronchovascular sheaths and spreading into the pulmonary hilum. These signs are usually absent in cases of PM secondary to large airway or esophageal rupture (and without lung parenchyma damage). The Macklin effect, PIE, and spontaneous PM are present in cases of an increased pressure gradient between the air-filled alveoli and the surrounding interstitium. Several structural lung diseases, including severe pneumopathy, bronchiectasis, respiratory distress syndromes, and barotrauma (including prolonged mechanical ventilation in patients

Fig. 3 PM and PIE in a dog with severe pneumonia (*Leptospira interrogans*)

with severe pneumopathy), may predispose patients to the development of PM. Therefore, upon the detection of PIE, the examiner should thoroughly assess the lung parenchyma, looking particularly for evidence of small airway/interstitial disease. In a study involving more than 45 cats with radiographic diagnoses of PM, 69% of cats had PM secondary to obvious inciting causes, such as positive pressure ventilation, trauma, and tracheal foreign bodies. Spontaneous PM was diagnosed in 31% of cases, and the underlying causes remained unknown. Pneumoderma was present in 74% of cats with secondary PM and in 50% of cats with spontaneous PM. Pneumothorax and pleural effusion may coexist in cases of secondary PM.

Tension PM results from the persistent entry of air into the mediastinal space via a one-way valve mechanism, increasing the air pressure in this compartment. It has been described in a dog with a caudal cervical penetration wound, which acted as a one-way valve allowing air to enter, but not to exit, the cranial mediastinum. Tension PM is a life-threatening condition, as increasing compartmental pressure can impair venous return and cardiac function; immediate surgical intervention is necessary to decompress the mediastinum (Fig. 6).

Pneumopericardium (PP) has been described rarely in dogs and cats. Reported causes of PP in humans are similar to those described for PM; they include alveolar rupture, barotrauma, and blunt chest trauma. Cardiac intervention and esophageal

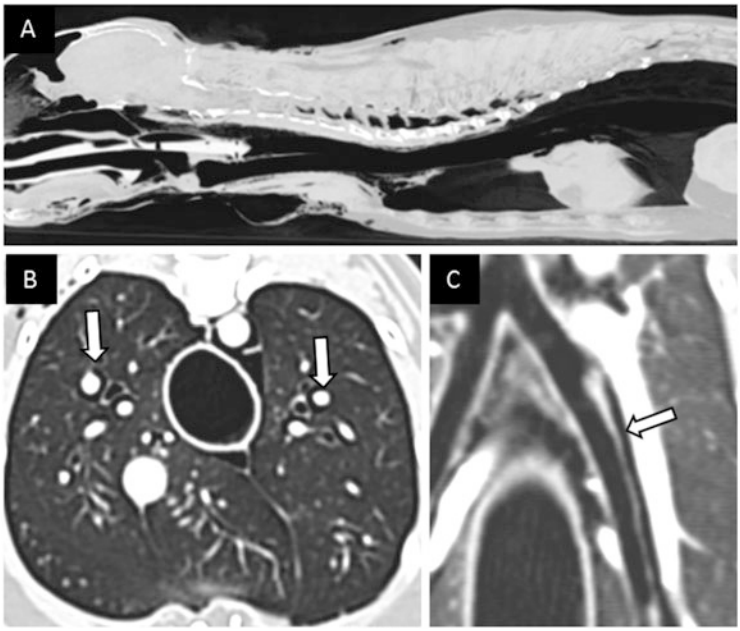

Fig. 4 PM and PIE in a cat with pneumonia. (**a**) Sagittal MinIP view showing the PM (dorsal mediastinum) and pneumoderma (ventral neck). (**b**) Transverse view of the lung. Note the enlarged esophagus surrounded by mediastinal air. *Arrows* show air in the interstitium around the pulmonary vessels. (**c**) Dorsal-oblique MPR. *Arrows* indicate the air coursing in the peribronchovascular interstitium

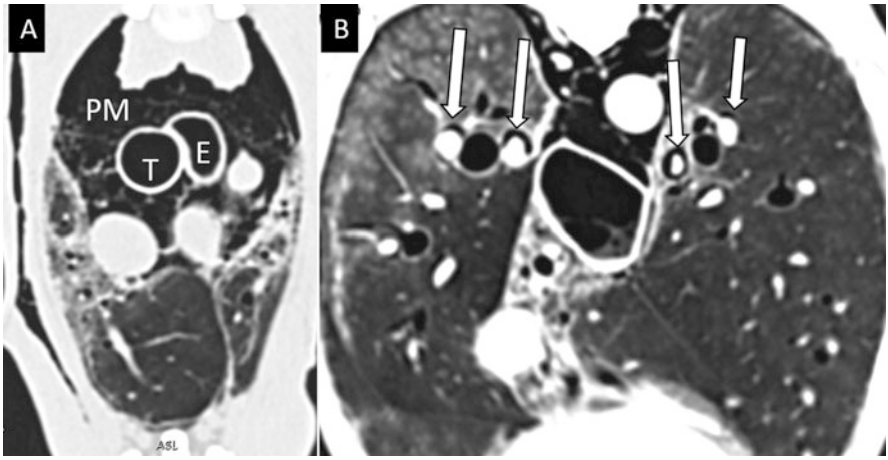

Fig. 5 PM and PIE in a dog with chronic pleuropneumonia. (**a**) Great vessels are displaced ventrally by the air, but are not compressed. T. trachea and E. esophagus are not compressed by the PM. (**b**) *Arrows* indicate the air in the interstitium around the pulmonary vessels (PIE)

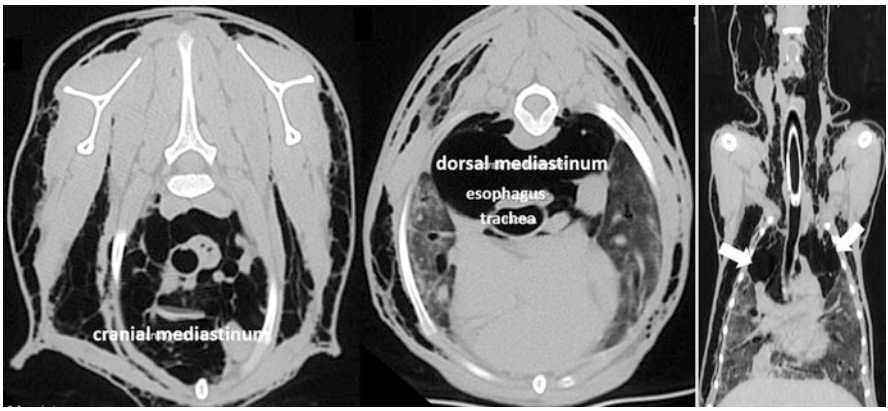

Fig. 6 Tension PM in a mongrel dog. There is large amount of air in the cranial and dorsal mediastinum with severe compression of great vessels, trachea, and esophagus. Note also fascial and subcutaneous air. The dog underwent immediate surgical intervention for draining the air and was discharged well after few days. The cause of tension PM was not identified

or gastric perforation may also cause PP. Spontaneous PP is characterized by the presence of pericardial gas in the absence of an iatrogenic or traumatic cause. In six cases reported in the veterinary literature to date, causes of PP were bronchopulmonary diseases, blunt trauma, and barotrauma due to positive pressure ventilation.

4 Vascular Diseases of the Neck and Mediastinum

Most mediastinal masses seen on thoracic images are of solid tumor origin. Aortic arch anomalies are located in the mediastinum and are easily recognized. However, some vascular lesions may present as mediastinal masses, and they should be considered in the differential diagnosis of the latter. Adequate contrast-enhanced CT series should be obtained to discover their vascular nature. Mediastinal vascular mass-like lesions include venous collaterals from the azygous or vertebral veins, in cases of CrVC obstruction, and esophageal varices that reform in cases of CrVC or, more commonly, portal hypertension; esophageal varices may also accompany the congenital form of bronchial artery hypertrophy (Fig. 7). For a more extensive description of these vascular diseases, see the chapter entitled “The Systemic Thoracic Vasculature.”

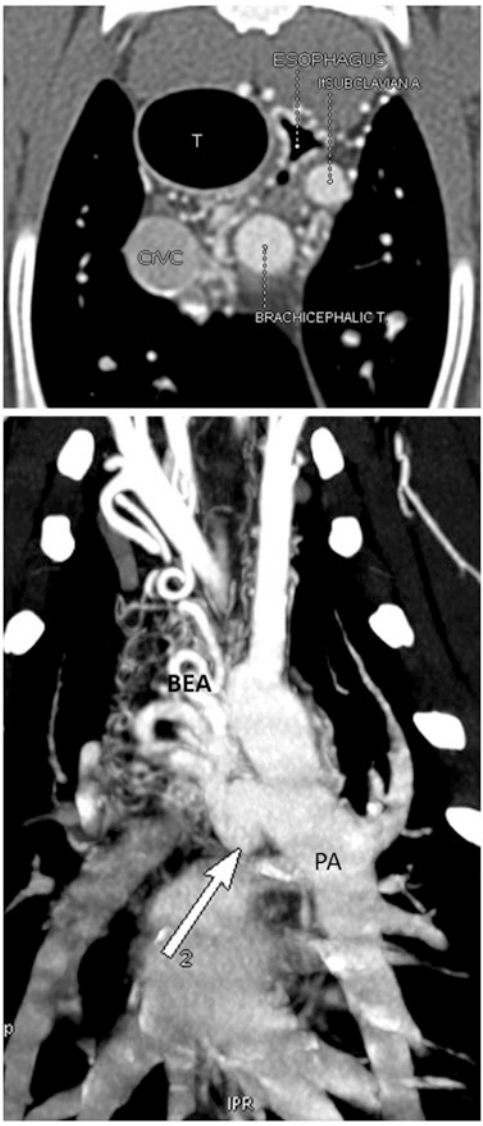

Fig. 7 Mediastinal collaterals in a dog with congenital bronchoesophageal artery (BEA) hypertrophy with bronchial to pulmonary artery fistula (*arrow*)

5 Mediastinal Mass Lesions

Mediastinal masses occur in dogs and cats and are encountered most frequently in the cranial mediastinum. CT plays a role in mass definition and the staging of local and distant malignant metastases. Benign and malignant lesions may form from any structure in the mediastinal space, and the determination of a diagnosis based on imaging alone may be difficult.

Mediastinal cysts have been described in dogs and cats. They include a variety of entities that may have similar imaging appearances. They can occur in any area of the mediastinum but are seen most frequently in the cranial mediastinum. The category of mediastinal cysts includes congenital cysts, such as bronchogenic, thymic, pericardial, and esophageal cysts, originating from the endoderms of the third and fourth embryonic pharyngeal pouches (branchial cysts). In general, mediastinal cysts appear on MDCT as well-marginated round lesions that contain homogeneous, non-enhancing fluid and may have variable dimensions (Figs. 8 and 9). Although most congenital cysts are benign, they can become large and compress other mediastinal structures, requiring intervention. Otherwise, they are discovered incidentally during MDCT examinations performed for other purposes. Importantly, many mediastinal tumors (e.g., thymoma) undergo cystic transformation and may have CT characteristics similar to those of congenital formations; the clinical signs, however, differ (Fig. 10). Among acquired cysts, parasitic lesions and abscesses may occur in the mediastinum. The patient's history and clinical signs aid imaging-based diagnosis (Fig. 11).

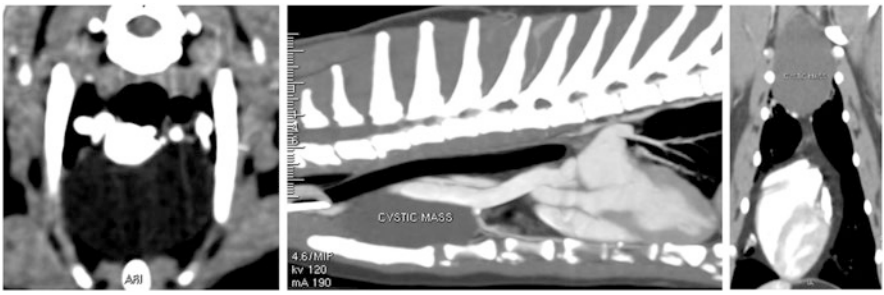

Fig. 8 Mediastinal cyst incidentally discovered in a Siamese cat. Transverse, sagittal, and dorsal views showing a large homogeneous, hypoattenuating, non-enhancing cystic lesion in the cranial mediastinum

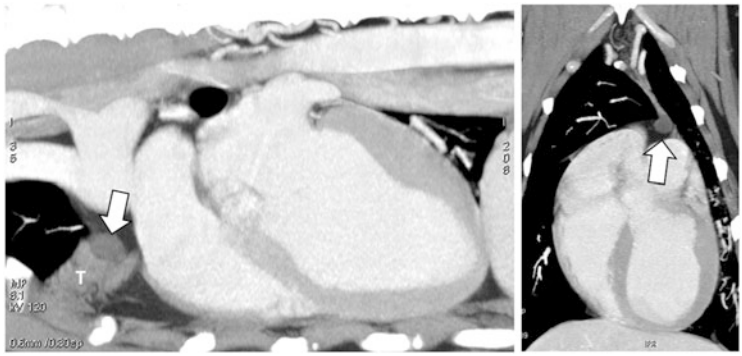

Fig. 9 Sagittal and dorsal MPRs of a dog. *Arrows* show a small, round, cystic lesion arising from thymic tissue (T). Incidental finding

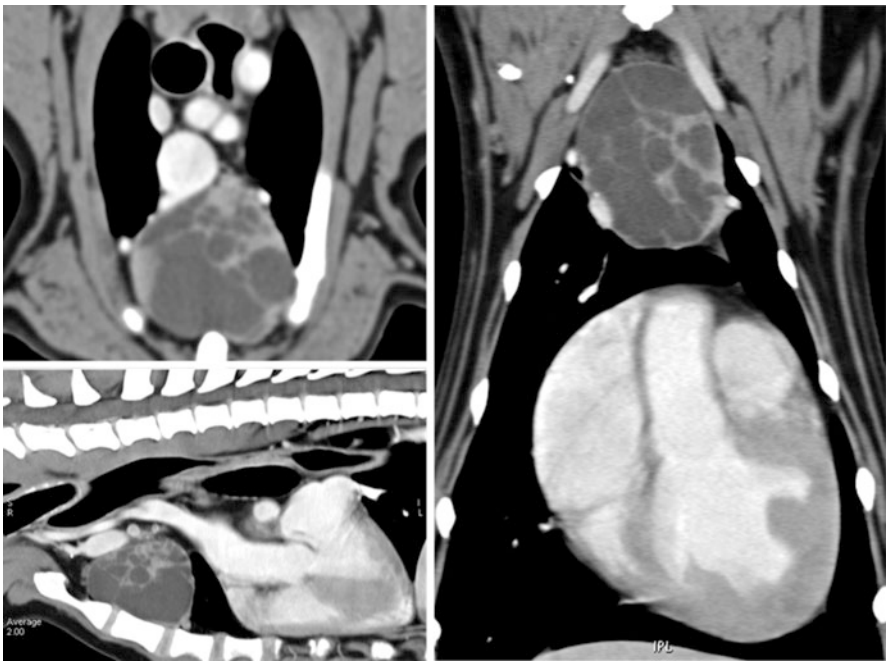

Fig. 10 Transverse, sagittal, and dorsal views showing cystic changes of a thymoma in a dog

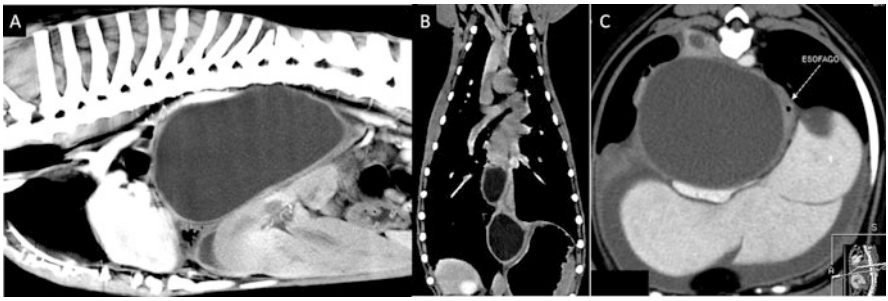

Fig. 11 Cystic-like masses in the caudal mediastinum. (**a**, **b**) are abscesses in two different dogs. (**c**) Paraesophageal cyst in a dog with Spirocerca lupi infection. Note the abdominal fluid in case **a** (*arrows*) and **c**, because of the compression of the mass on the posthepatic segment of the caudal vena cava (Budd-Chiari-like syndrome)

Solid masses in the cranial mediastinum are frequently seen in dogs and cats, and the majority of these lesions are malignant. However, with the increasing use of advanced MDCT scanners that enable the routine acquisition of near-isotropic and true isotropic volumes, incidental benign lesions are increasingly being detected.

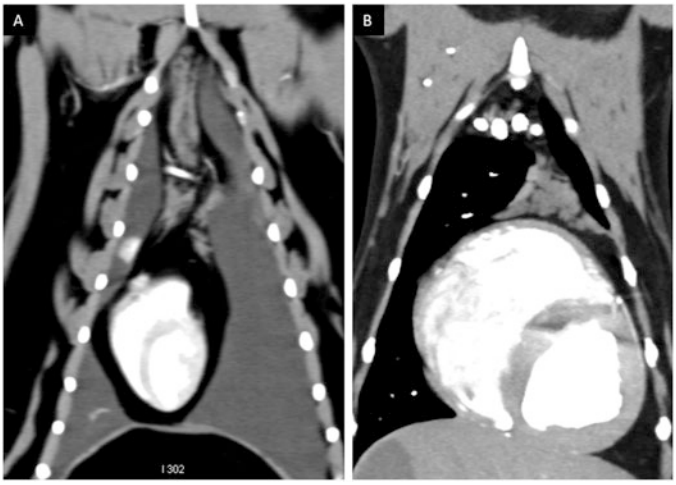

Fig. 12 (**a**) Thymic hyperplasia (pathologically proved) in a 4-year-old cat with pleural effusion and suspected thymic mass. (**b**) Rebound thymic hyperplasia in a dog underwent CT examination for staging for anal sac carcinoma

Thymic lymphoid hyperplasia has been described in dogs and cats, alone or associated with other benign and malignant conditions of the thymus (Fig. 12a). On MDCT images, enlargement of the thymus is frequently seen in adults and mature patients. Two types of thymic hyperplasia have been described in humans: thymic lymphoid follicular hyperplasia (similar to that seen in dogs and cats), associated with a variety of autoimmune diseases; and the so-called "rebound hyperplasia" of the thymus, seen in patients who have experienced particularly stressful conditions, such as chemotherapy, corticosteroid therapy, or radiotherapy. In these cases, the thymus is larger than expected in an adult patient but usually retains its normal shape. In the author's experience, this MDCT feature is also very common in veterinary patients and might have similar significance (Fig. 12b).

Benign mediastinal widening is associated most commonly with diffuse lipomatosis, which is typically seen in obese patients and dogs with Cushing's disease. In this condition, the adipose tissue can be distinguished easily with CT based on its typically negative attenuation values. Mediastinal lipoma has also been reported in dogs. Although benign, these conditions may lead to compression of the heart and great vessels or cause atelectasis of the cranial lung lobes due to compression. The differential diagnosis should include thymolipomas, which have been reported in dogs. Thymolipomas may appear almost entirely fatty, with some areas of inhomogeneous soft tissue density representing thymic tissue.

Thymoma and *lymphoma* are the most common mediastinal neoplasias described in veterinary patients, but other malignancies, including ectopic thyroid, parathyroid, neurogenic, and heart-base tumors, may be encountered (Figs. 13, 14, 15, 16, and 17). Moreover, lymph node enlargement can occur in

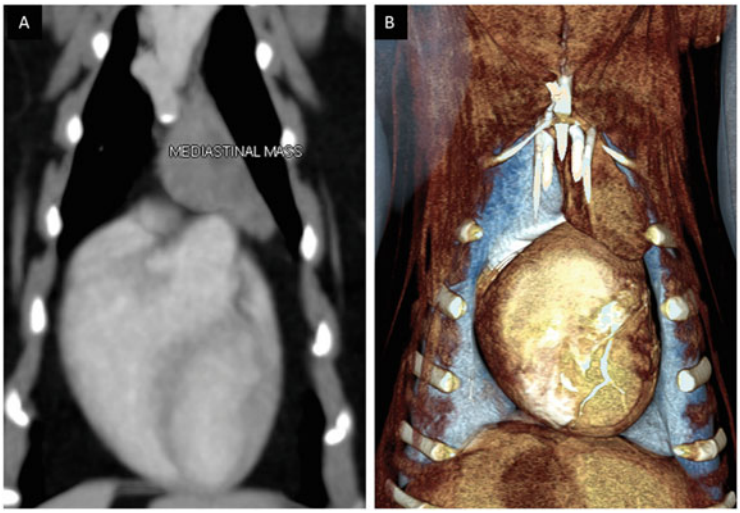

Fig. 13 (**a**) Thymoma in a cat. (**b**) Thymic T-cell lymphoma in a dog

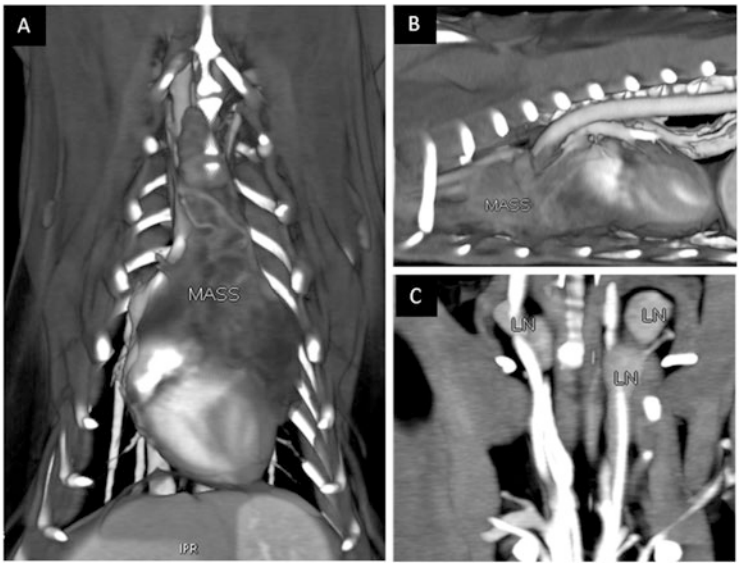

Fig. 14 Thymoma in a cat. (**a**) VR of the thorax showing a large mediastinal mass. (**b**) VR left lateral view of the mediastinum in same cat. (**c**) Dorsal MPR of the neck, showing the enlargement of the deep cervical lymph nodes

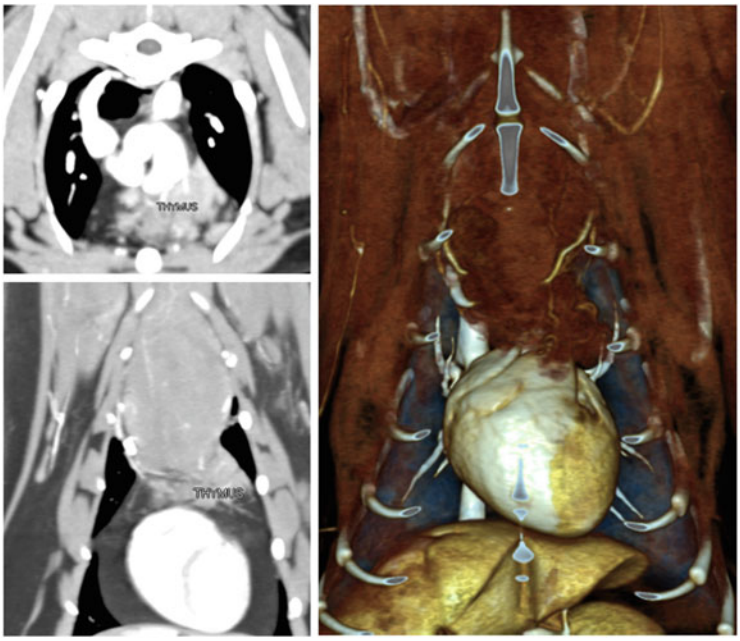

Fig. 15 Thymic T-cell lymphoma in a cat

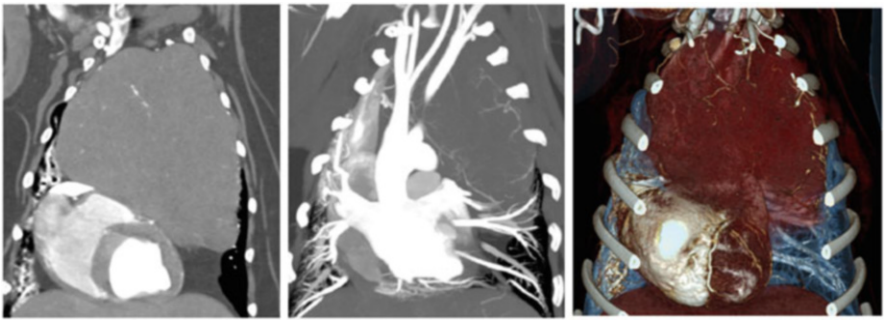

Fig. 16 Dorsal MPR, MIP, and VR of the thorax in a dog with large thymoma that compresses the heart and other mediastinal structures (without invasion)

many nonneoplastic and neoplastic metastatic conditions. Cranial mediastinal tumors can invade vascular structures, such as the aortic root, subclavian vessels, CrVC, internal thoracic vessels, and axillary veins. The cava may show severe narrowing or an intraluminal opacification defect (Figs. 17 and 18). Collaterals

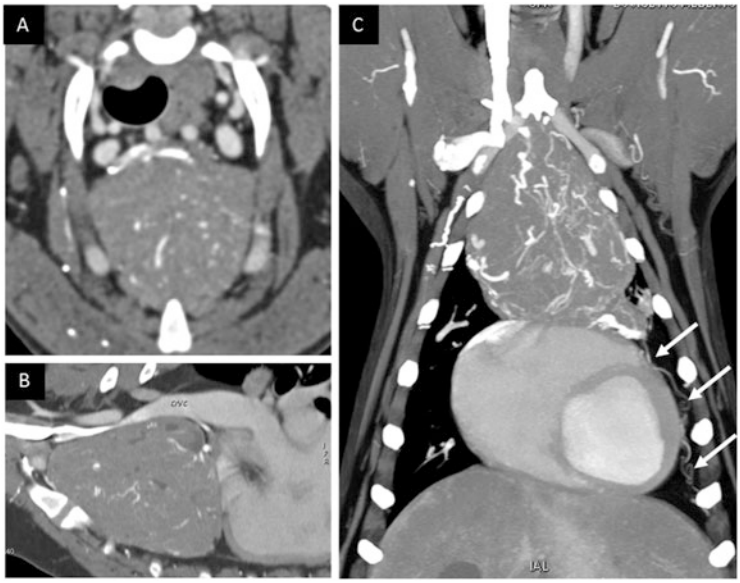

Fig. 17 Thymic carcinoma in a dog. (**a**) Transverse view showing a large mass in the cranial mediastinum. (**b**) Sagittal view. The mass compresses the cranial vena cava (CrVC). Note the stasis of the contrast medium in the CrVC. (**c**) Dorsal thin MIP of the thorax. The mass is highly vascularized. There are some collateral vessels (*arrows*), due to the chronic compression of the CrVC (not invaded)

Fig. 18 Thymic carcinoma invading the cranial vena cava in two dogs with cranial cava syndrome

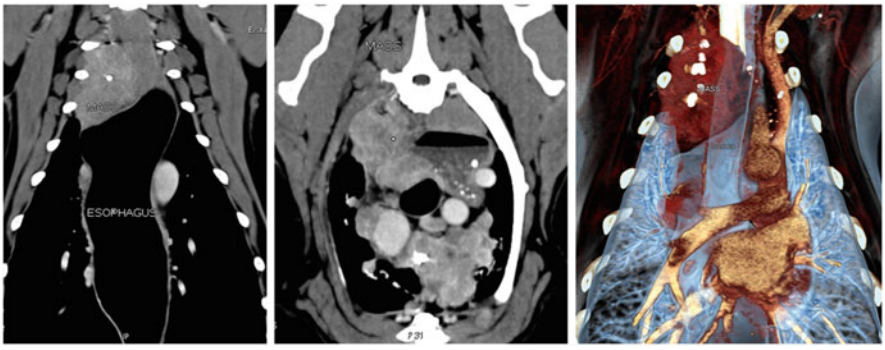

Fig. 19 Mediastinal mass and megaesophagus in a dog with relapse of thoracic spinal paraganglioma. The mass invades the dorsal and cranial mediastinum, encasing the vascular structures and involving the mediastinal lymph nodes

may develop in cases of chronic obstruction of the CrVC to maintain venous drainage to the heart. Transverse CT images enable the evaluation of changes in vascular shape and can reveal invasion, but MPR from a near-isotropic dataset provides invaluable information about the level and degree of obstruction and the length of the affected caval segment and is extremely useful for surgical planning.

Studies of the correlation between CT and surgical findings have yielded inconsistent results. In a retrospective study of JPEG and DICOM images of CT studies conducted in dogs with mediastinal masses, contrast-enhanced CT was not sensitive for the preoperative prediction of vascular invasion of cranial mediastinal masses. However, the scan protocol, CM injection protocol, and dataset review strategies together determine the sensitivity of an imaging method and the results obtained. Adequate opacification of the CrVC with no streak artifact is essential for the assessment of vascular involvement.

Finally, masses arising from the spine or digestive tract may invade the cranial, dorsal, and caudal mediastinum and should not be considered to be true mediastinal masses. However, independently of their nature, lesions that develop in these mediastinal areas can have severe clinical consequences (Fig. 19). Compression of the posthepatic segment of the caudal vena cava by a mass can cause posthepatic PH. A plethora of other MDCT signs, including hepatomegaly, ascites, varices, and other portal collaterals (Budd-Chiari-like syndrome), may be detected on CT (Figs. 11 and 20).

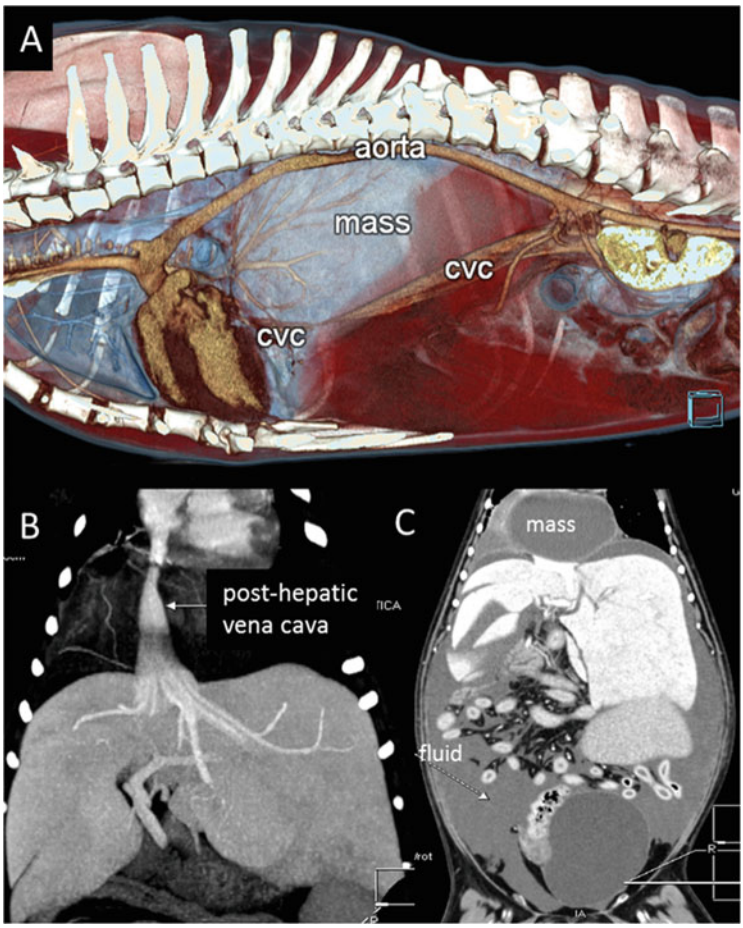

Fig. 20 (**a**) Posthepatic caudal vena cava (CVC) compression due to caudal mediastinal cystic mass in a dog. (**b**) Compression of the posthepatic segment of the caudal vena cava. (**c**) Secondary signs of CVC compression: hepatomegaly, ascites (Budd-Chiari-like syndrome)

6 Pathological Conditions of the Neck

Due to the complex anatomy of the neck and the large number of structures present in this restricted anatomic space, comprehensive knowledge of regional anatomy and recognition of common patterns of disease presentation on CT images can aid image-based diagnosis of conditions affecting this region. The superficial and deep layers of the cervical fascia define spaces within which are located specific structures of the neck. Some spaces are continuous with the cranial base, and others are continuous with the cranial mediastinum. Fascial layers tend to limit the diffusion of a pathological process within a given compartment. Based on this concept, CT

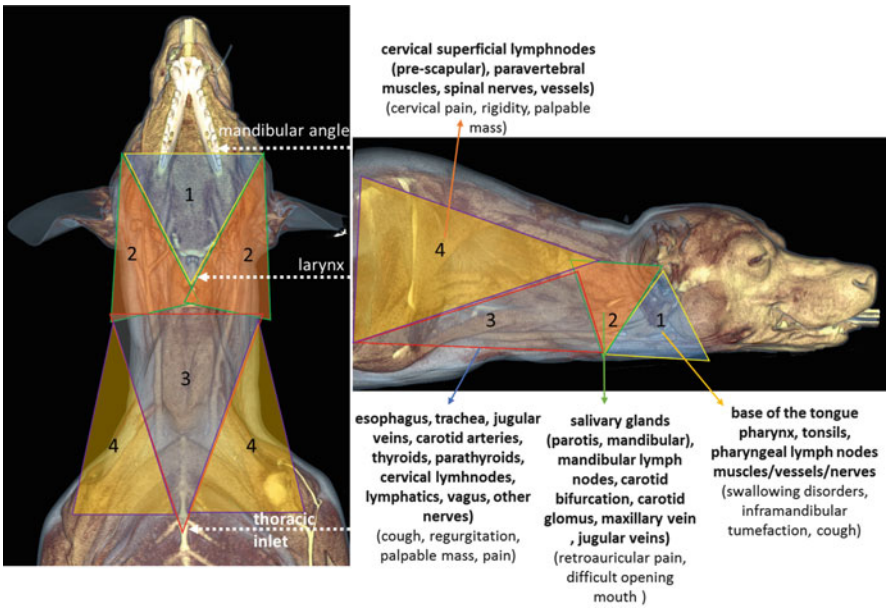

Fig. 21 Schematic representation of cervical subregions (anatomic-functional approach). (**a**) Ventral view of the head and neck. (1) Unpaired cranial subregion extending from the mandibular angle to the laryngeal region. (2) Paired, lateral cranial, retroauricular subregions. (3) Unpaired median subregion (visceral neck). (4) Paired lateral caudal, prescapular subregions. (**b**) Right lateral view of the head and neck. Major anatomic structures included in each subregion are reported

evaluation of the neck is anatomy based, using the fascia as a landmark, in humans. This approach facilitates the understanding and interpretation of cross-sectional images in such a complex region. No similar approach has been described in the veterinary CT literature. In the author's personal view, an anatomic-functional approach combining clinical and CT signs greatly aids interpretation and enables accurate diagnosis in most cases (Fig. 21). Masses primary involving structures in each subregion of the neck are associated with specific clinical signs and are attributable to a limited number of structures.

Masses of the median cranial subregion of the neck (throat) include pharyngeal and laryngeal lesions. The pharynx has three subdivisions: the oropharynx and nasopharynx, which pertain to the oral cavity and proximal respiratory airways, respectively, and thus are not usually included in neck CT examinations, and the laryngopharynx. Tonsillar squamous cell carcinoma (TSCC) is the most common tumor encountered in the oropharynx of both dogs and cats, but other tumor types are possible (Figs. 22, 23, 24, and 25). Laryngopharyngeal and laryngeal masses can be accompanied by a variety of clinical signs, such as cough, dysphagia, and changes in vocalization. Benign lesions in this area include cystic and cystic-like lesions, such as abscesses. Malignancies are rarely reported in small animals; they

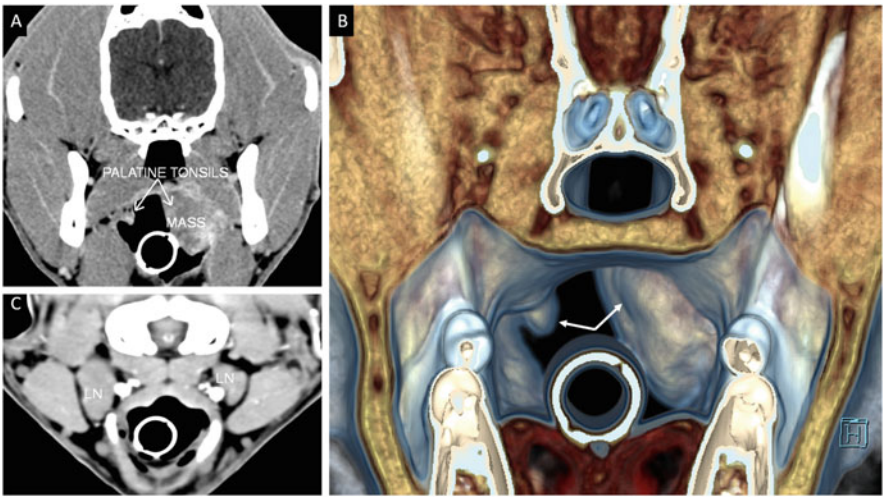

Fig. 22 (**a**) Tonsillar lymphosarcoma in a dog. (**a**) Transverse view showing a left-sided tonsillar mass and prominent right palatine tonsil. (**b**) Volume rendered image showing the tonsils (*arrows*). (**c**) Medial retropharyngeal lymph nodes (LN)

include squamous cell carcinoma, adenocarcinoma, sarcoma, melanoma, and lymphoma (Fig. 26). Even rarer are primary cartilaginous laryngeal and ectopic thyroid tumors. They are accompanied by unilateral or bilateral median pharyngeal lymph node enlargement in most cases, and they may involve the hyoid (Fig. 27).

Masses in the lateral aspect of the most cranial region of the neck are generally palpable and are often accompanied by pain when opening the mouth and dysphagia. They may develop in cases of severe middle ear disease, salivary gland disease, lymph node enlargement, and carotid body tumor. Several articles have described the CT features of masses in the lateral neck regions. CT is an excellent tool for the evaluation of the salivary glands in patients with sialolithiasis, salivary mucocele, adenitis, or salivary gland malignancy. Salivary mucocele (or sialocele) may arise for various salivary glands or may occur bilaterally and is clinically classified in cervical mucocele, sublingual, pharyngeal, and zygomatic mucocele. CT can easily detect sialoliths in patients with mucocele. In case of large salivary mucocele, it may be difficult to detect the communication between the cystic collection and the salivary gland. Commonly, the salivary mucocele involves more than one gland (Figs. 28 and 29). Differential diagnosis of salivary mucocele should include salivary abscess and salivary malignancy with cystic changes (Fig. 30).

A recent paper described the CT and MRI features of carotid body paragangliomas (PGs) in dogs. PGs are slow growing, usually benign neoplasms that arise from extraadrenal paraganglionic tissue derived from neural crest cells. They are associated closely with the autonomic (parasympathetic) nervous system and are often located near vascular and nervous structures. In humans, PGs of the head and neck region may be located in four primary sites: the carotid bifurcation

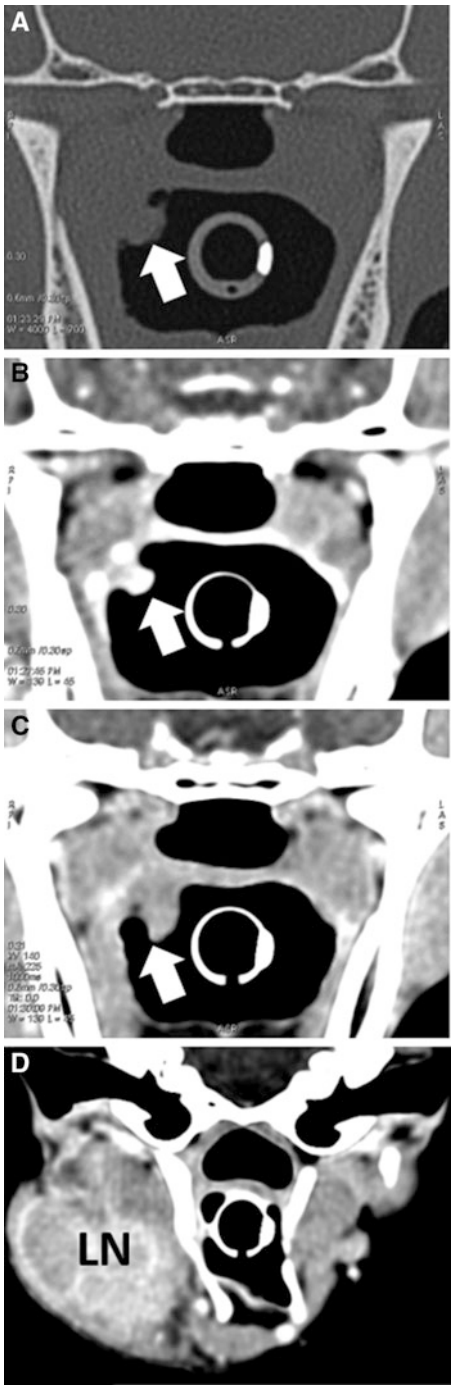

Fig. 23 Unilateral tonsillar squamous cell carcinoma (TSSC) in a dog. (**a**) Pre-contrast. (**b**) Arterial phase. (**c**) Venous phase. (**d**) Regional lymph node metastasis (LN, right median retropharyngeal lymph node)

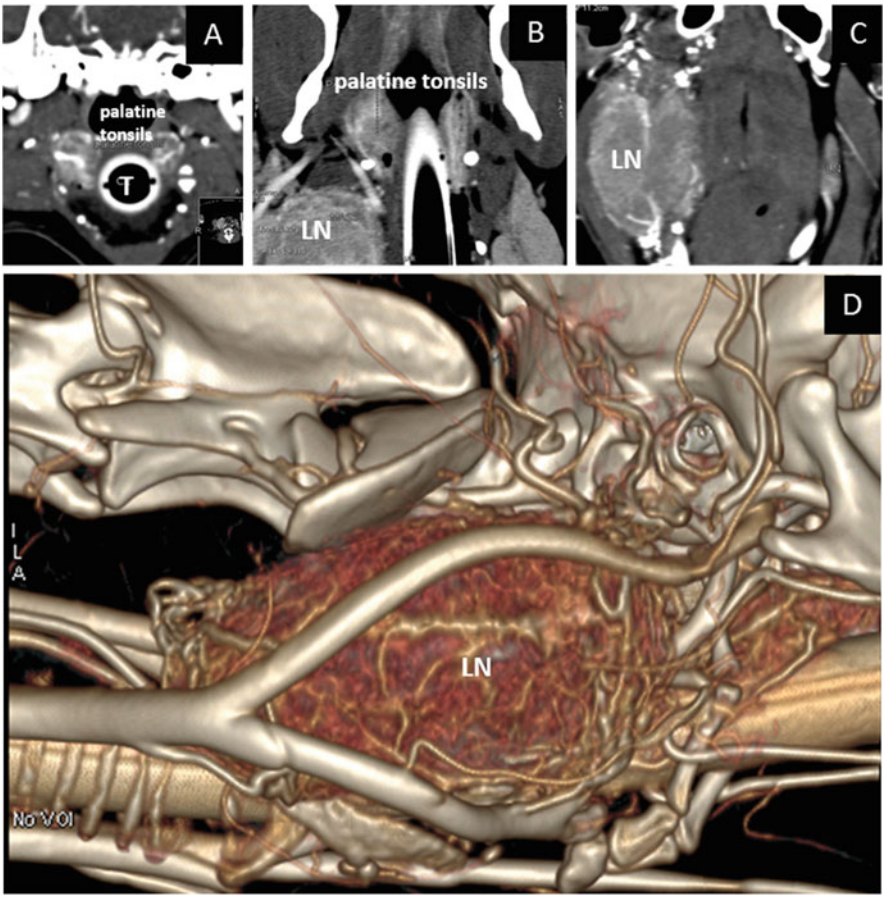

Fig. 24 Tonsillar carcinoma in a dog (palpable mass in right retroauricular region). (**a**) Transverse view showing enlargement of both palatine tonsils. (**b**) Dorsal MPR showing the palatine tonsils and enlarged median retropharyngeal lymph node (LN). The contralateral lymph node has normal characteristics. (**c**) Dorsal MPR showing the lymph node mass. (**d**) Right lateral VR of the lymph node mass. Histopathology confirmed the TSCC of the right tonsil and its lymph node metastasis. The left tonsil resulted hyperplastic

(carotid PG or carotid body tumor), the jugular bulb (jugular PG), the tympanic plexus (tympanic PG), and the vagal ganglia (vagal PG). The first three tumor types have been described in dogs, but heart-base PG and chemodectoma are more common in this species (Fig. 31). Due to their benign and nonsecreting nature, PGs are often diagnosed when they have enlarged to a degree that they compress local tissues, generating clinical signs. In the author's experience, however, small PGs can be found incidentally during MDCT examination performed for other purposes. Moreover, the detection of multiple PGs in the mediastinum, neck, and skull base of the same patient is not uncommon. This presentation is well

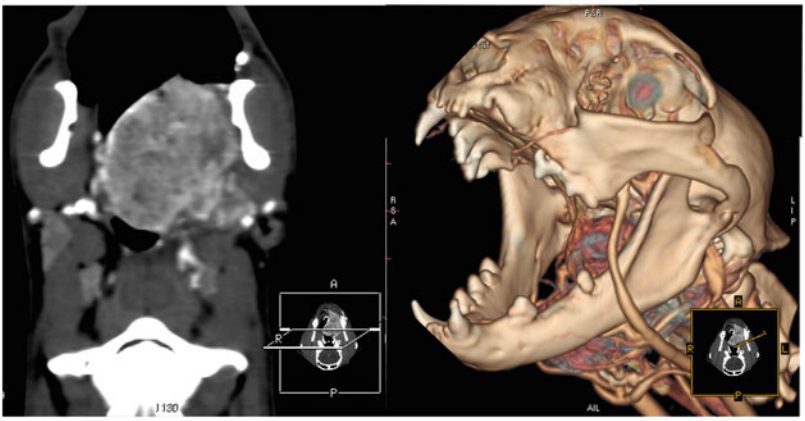

Fig. 25 Left tonsillar squamous cell carcinoma (TSCC) in a cat

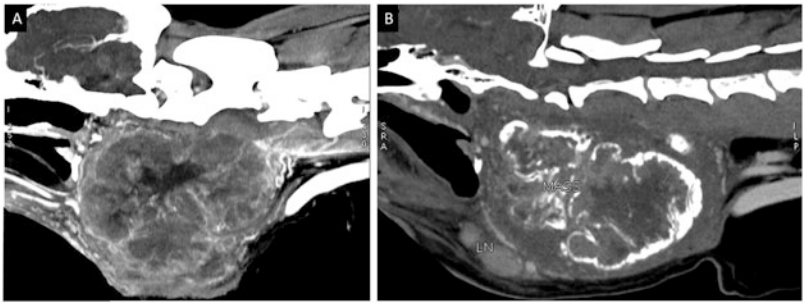

Fig. 26 Laryngeal tumors in dogs. (**a**) Metastatic melanoma. (**b**) Primary chondrosarcoma. LN, median pharyngeal lymph node

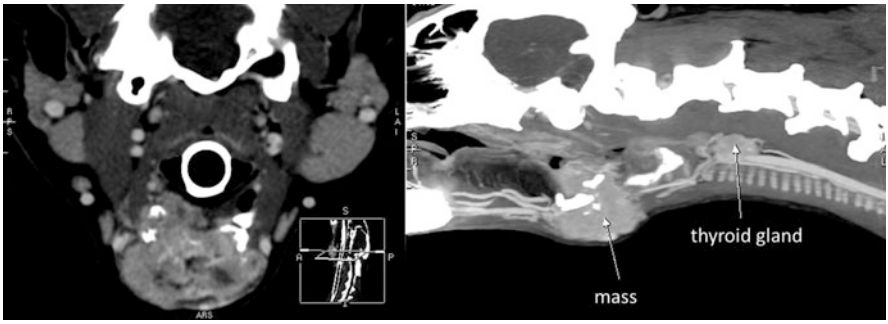

Fig. 27 Ectopic thyroid carcinoma in a dog involving the hyoid bone

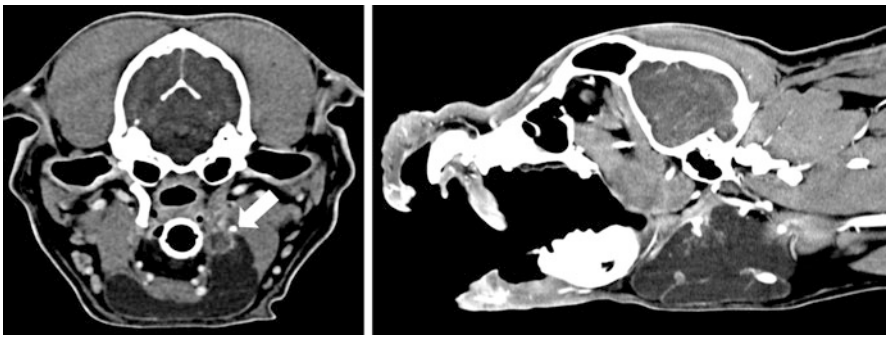

Fig. 28 Salivary mucocele and sialolithiasis (*arrow*) in a dog with cervical fluctuant mass (sialocele of the left mandibular gland)

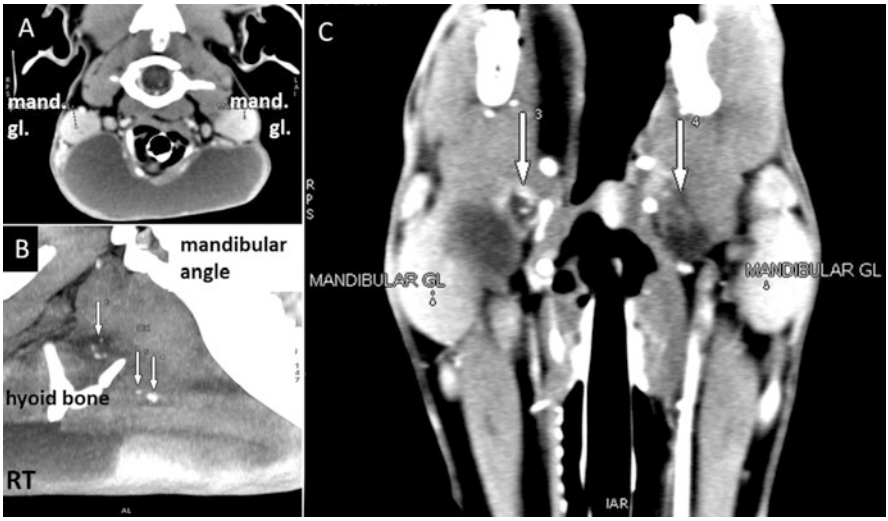

Fig. 29 Sublingual mucocele in a Maltese dog with sialolithiasis. (**a**) Transverse view showing a large fluctuant, inframandibular mass. Mandibular glands are normally represented. (**b**) Right parasagittal view showing several sialoliths along the mandibular salivary duct. (**c**) Dorsal MPR. *Arrows* indicate mandibular salivary ducts ectasia. There is a sialolith in the right duct. Sublingual salivary glands and both mandibular glands were removed. Histopathology examination revealed sialoadenitis of sublingual glands and normal mandibular glands

documented in humans, in whom multicentric tumors occur in 10–20% of cases. Independently of their location, PGs are homogeneous and iso- to hypoattenuating to surrounding muscles on pre-contrast images. Mineralization may be present. In post-contrast series, they generally show strong and heterogeneous enhancement in the early phases. Very large carotid body tumors may be difficult to distinguish from large thyroid malignancies. In the author's experience, thin-collimated scans

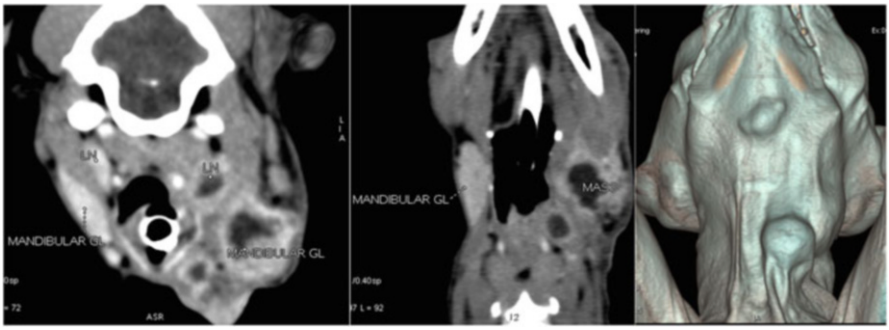

Fig. 30 Salivary gland carcinoma in a cat. Transverse, dorsal MPRs, and ventral view of volume rendering of the head and neck. Note the mass of the left mandibular gland, having a central fluid collection. The left median retropharyngeal lymph node has similar characteristics as well as the ipsilateral mandibular lymph node

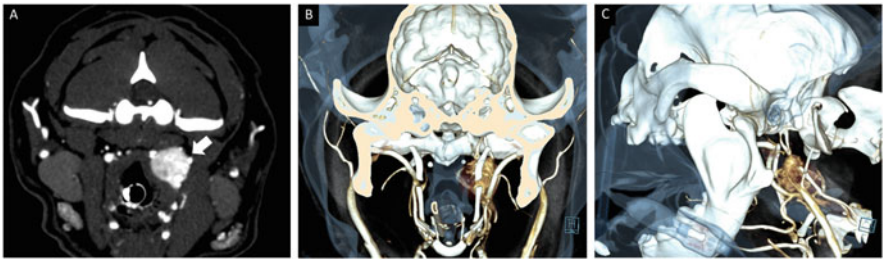

Fig. 31 Carotid body tumor (extraadrenal paraganglioma) in a dog with pain when opening the mouth

of the neck obtained during the arterial phase enable identification of the tumoral feeding artery in most cases, as well as distinction of the thyroid gland from a carotid body tumor.

Thyroid and parathyroid masses are the most commonly detected masses in the middle cervical region. They are described in "The Endocrine System" chapter. Other malignant and nonmalignant, inflammatory conditions may affect this region (Fig. 32).

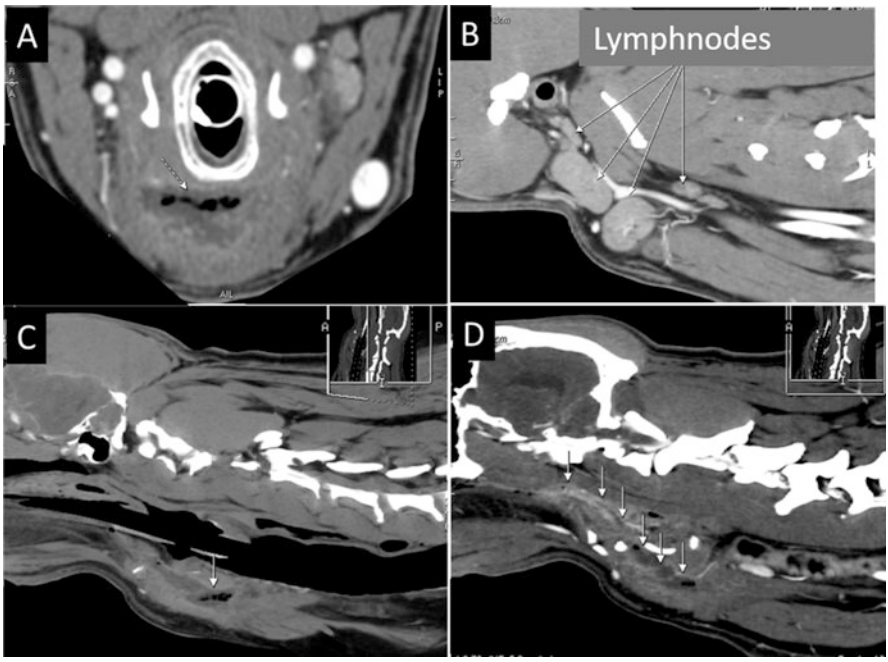

Fig. 32 Retropharyngeal phlegmon and reactive lymphadenopathy in a dog (foreign body migration). (**a**) Transverse view showing some air surrounded by fluid in the ventral cervical region. (**b**) Retropharyngeal and mandibular lymph node enlargement (left parasagittal view). (**c**, **d**) are MinIP and MPR sagittal views showing pathway taken by the foreign body

7 Tracheal and Esophageal Diseases

Given the extent of these structures in the neck and thorax, comprehensive evaluation requires the simultaneous examination of these two regions. Traumatic injuries, primary obstructive diseases (e.g., tracheal collapse, stenosis), inflammatory changes, exogenous compression (see also the "The body trauma" and "The Lung and Airways" chapters), and masses may affect the cervical or intrathoracic trachea (Fig. 33). Primary intratracheal neoplasia is uncommon in dogs and cats; this category includes benign tumors, such as chondroma, osteochondroma, leiomyoma, and ecchondroma/osteochondromal dysplasia in younger dogs (Fig. 34). Malignant conditions include lymphoma, chondrosarcoma, and squamous cell carcinoma. Bronchoscopy is the preferred evaluation method because it allows direct visualization, sampling for cytological and histological analyses, and prompt intervention in cases of respiratory compromise. However, MDCT has a primary role in staging in these patients.

Conditions involving the esophagus include traumatic injury, megaesophagus, herniation, stenosis and stricture, inflammatory changes, pseudocystic lesions, exogenous compression, and tumors. Traumatic injuries of the esophagus are

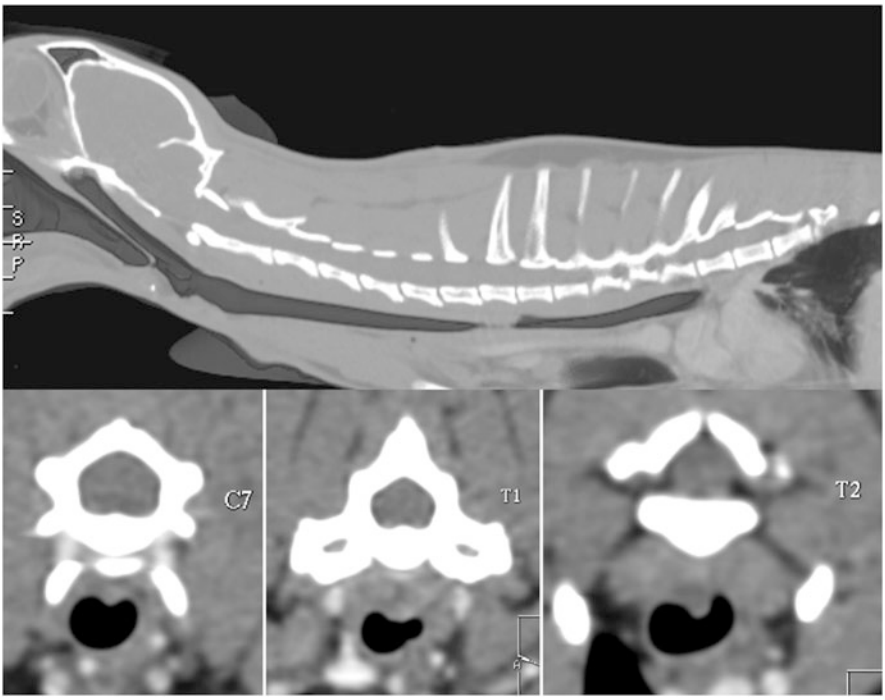

Fig. 33 Segmental tracheal stenosis in a 6-month-old cat (congenital tracheal stenosis)

described in the chapter entitled "The Body Trauma." Moderate distention of the entire esophagus is commonly seen in anesthetized patients undergoing MDCT examination and should not be confused with other conditions leading to esophageal distention. Megaesophagus refers to the loss of esophageal tone and motility, often resulting in diffuse dilation and clinical signs of regurgitation. It can be congenital or acquired. Certain canine breeds (e.g., Great Dane, Irish Setter, Labrador Retriever, German Shepherd, Shar Pei, Fox Terrier) have been suggested to have familiar predisposition to congenital diffuse megaesophagus. Acquired megaesophagus may occur in dogs and cats. The detection of megaesophagus should prompt further investigation to identify potential causes. Megaesophagus may be secondary to peripheral neuropathies, laryngeal paralysis, severe esophagitis, and chronic or recurrent gastric dilatation, as well as many other local and systemic conditions (Figs. 19 and 34). Although hypothyroidism has been cited as a potential cause of megaesophagus, data supporting this association are lacking. Segmental megaesophagus can be caused by vascular rings (see the chapter entitled "The Systemic Thoracic Vasculature"), foreign bodies, and masses. The role of MDCT in the evaluation of canine and feline megaesophagus is to rule out obstructive, inflammatory, and neoplastic diseases or to diagnose vascular rings.

Hernia of the esophageal hiatus, or hiatal hernia (HH), is characterized by the herniation of part of the stomach or abdominal esophagus through the esophageal

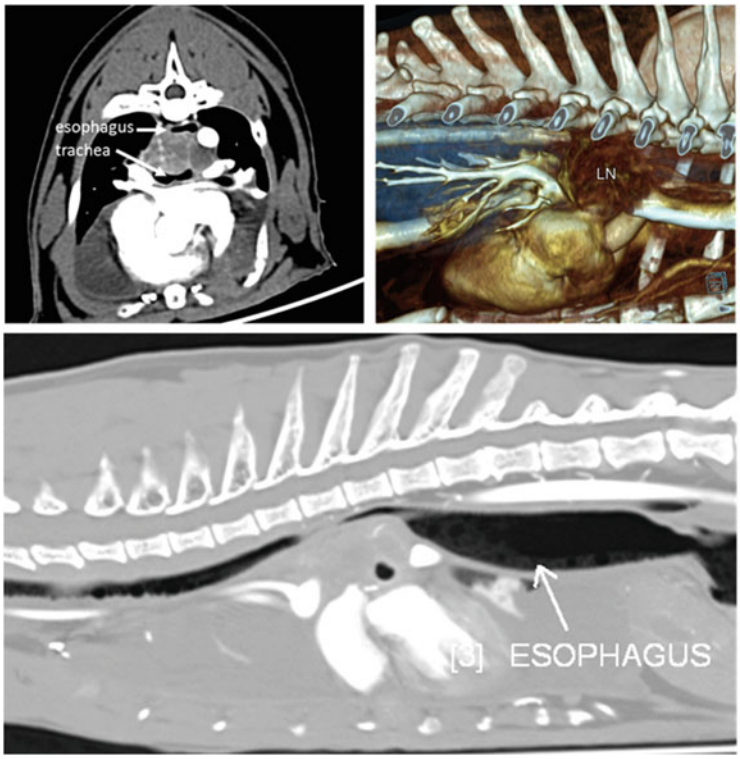

Fig. 34 Tracheal and esophageal compression in a cat with metastatic pulmonary carcinoma and chylothorax. LN are enlarged tracheobronchial lymph nodes

hiatus into the thoracic cavity. Sliding HH refers to dynamic and intermittent prolapse of the distal part of the esophagus, the gastroesophageal junction, and part of the stomach through the esophageal hiatus. This type of HH occurs more frequently than other types in companion animals and is the most common type of HH described in cats (Fig. 35). Paraesophageal hernia refers to the prolapse of the fundic region of the stomach into the thoracic cavity alongside the thoracic esophagus (the hiatus remains in normal position). It has been described in a few dogs and one cat. Other organs (e.g., stomach, liver) or portions thereof may herniate through the esophageal hiatus (Figs. 35 and 36).

Cystic-like lesions of the esophagus may be encountered during MDCT examination. They include rare congenital diseases, such as duplication cyst, and, more commonly, acquired conditions. The latter include esophageal cysts caused by *Spirocerca lupi* infestation, abscess, and cystic neoplasia (Figs. 11 and 20). Sarcoma is the most common esophageal cancer reported in dogs. An association between Spirocerca lupi infestation and esophageal sarcoma has been reported in dogs. Other primary esophageal tumors, including leiomyoma, leiomyosarcoma, squamous cell carcinoma, and lymphoma, are rare in dogs and cats.

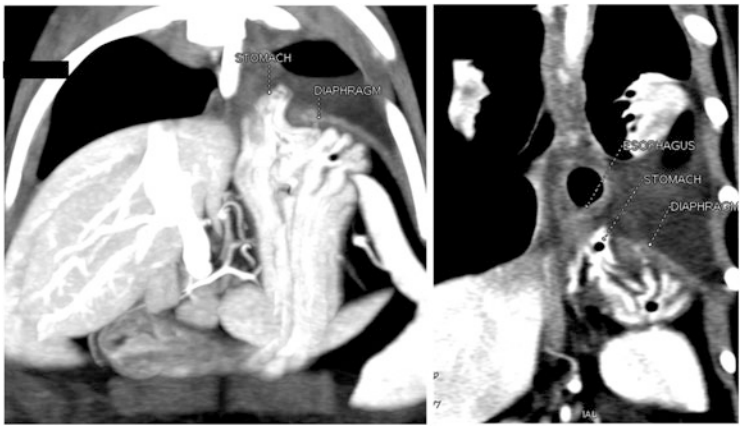

Fig. 35 Sliding HH in a cat with sclerosing pleuritis and chylothorax

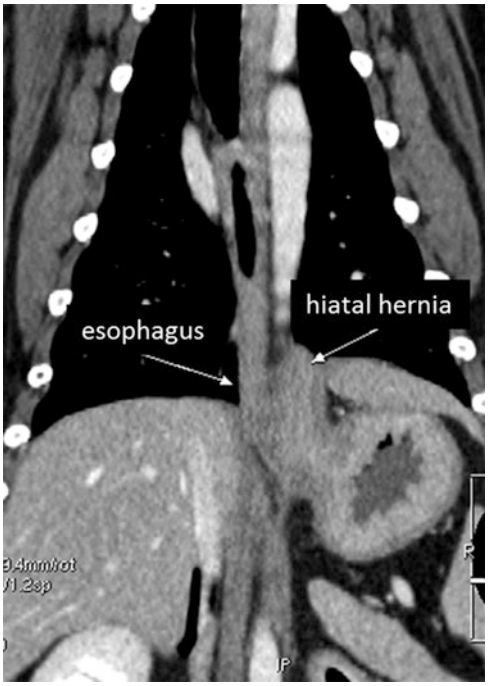

Fig. 36 Paraesophageal hiatal hernia in a dog with chronic enteritis and ileus

Further Readings

Agut A, Talavera J, Buendia A, Anson A, Santarelli G, Gomez S. Imaging diagnosis-spontaneous pneumomediastinum secondary to primary pulmonary pathology in a dalmatian dog. Vet Radiol Ultrasound. 2015;56(5):E54–7. doi:10.1111/vru.12223. Epub 2014 Nov 12.

Bertolini G, Stefanello C, Caldin M. Imaging diagnosis—pulmonary interstitial emphysema in a dog. Vet Radiol Ultrasound. 2009;50(1):80–2.

Borgonovo S, Rocchi PM, Raiano V, Diana D, Greci V. Spontaneous pneumopericardium in a dog with bronchopulmonary disease complicated by pyothorax and pneumothorax. Can Vet J. 2014;55(12):1186–91.

Brown DC, Holt D. Subcutaneous emphysema, pneumothorax, pneumomediastinum, and pneumopericardium associated with positive-pressure ventilation in a cat. J Am Vet Med Assoc. 1995;206(7):997–9.

Carozzi G, Zotti A, Alberti M, Rossi F. Computed tomographic features of pharyngeal neoplasia in 25 dogs. Vet Radiol Ultrasound. 2015;56(6):628–37. doi:10.1111/vru.12278. Epub 2015 Jul 14.

Gabor LJ, Walshaw R. Esophageal duplication cyst in a dog. Vet Pathol. 2008;45(1):61–2. doi:10.1354/vp.45-1-61.

Greci V, Baio A, Bibbiani L, Caggiano E, Borgonovo S, Olivero D, Rocchi PM, Raiano V. Pneumopericardium, pneumomediastinum, pneumothorax and pneumoretroperitoneum complicating pulmonary metastatic carcinoma in a cat. J Small Anim Pract. 2015;56(11):679–83. doi:10.1111/jsap.12366. Epub 2015 May 11.

Macklin CC. Transport of air along sheaths of pulmonic blood vessels from alveoli to mediastinum: clinical implications. Arch Intern Med. 1939;64:913–26.

Mai W, Seiler GS, Lindl-Bylicki BJ, Zwingenberger AL. CT and MRI features of carotid body paragangliomas in 16 dogs. Vet Radiol Ultrasound. 2015;56(4):374–83. doi:10.1111/vru.12254. Epub 2015 Apr 5.

Morini M, Bettini G, Diana A, Spadari A, Casadio Tozzi A, Santi M, Romagnoli N, Scarpa F, Mandrioli L. Thymofibrolipoma in two dogs. J Comp Pathol. 2009;141(1):74–7. doi:10.1016/j.jcpa.2009.03.001. Epub 2009 May 7.

Nemanic S, Hollars K, Nelson NC, Bobe G. Combination of computed tomographic imaging characteristics of medial retropharyngeal lymph nodes and nasal passages aids discrimination between rhinitis and neoplasia in cats. Vet Radiol Ultrasound. 2015;56(6):617–27. doi:10.1111/vru.12279. Epub 2015 Jul 20.

Oliveira CR, Mitchell MA, O'Brien RT. Thoracic computed tomography in feline patients without use of chemical restraint. Vet Radiol Ultrasound. 2011;52(4):368–76. doi:10.1111/j.1740-8261.2011.01814.x. Epub 2011 Mar 29.

Prather AB, Berry CR, Thrall DE. Use of radiography in combination with computed tomography for the assessment of noncardiac thoracic disease in the dog and cat. Vet Radiol Ultrasound. 2005;46(2):114–21.

Ramírez GA, Spattini G, Altimira J, García B, Vilafranca M. Clinical and histopathological features of a thymolipoma in a dog. J Vet Diagn Invest. 2008;20(3):360–4.

Ramírez GA, Altimira J, Vilafranca M. Cartilaginous tumors of the larynx and trachea in the dog: literature review and 10 additional cases (1995-2014). Vet Pathol. 2015;52(6):1019–26. doi:10.1177/0300985815579997. Epub 2015 Apr 16.

Rossi F, Caleri E, Bacci B, Drees R, Groth A, Hammond G, Vignoli M, Schwarz T. Computed tomographic features of basihyoid ectopic thyroid carcinoma in dogs. Vet Radiol Ultrasound. 2013;54(6):575–81. doi:10.1111/vru.12060. Epub 2013 Jun 23.

Rudloff E, Crowe DT Jr, Kirby R, Mammato B. Suspected tension pneumomediastinum in a dog: a case report. J Vet Emerg Crit Care. 1996;6:103–7.

Scherrer W, Kyles A, Samii V, Hardie E, Kass P, Gregory C. Computed tomographic assessment of vascular invasion and resectability of mediastinal masses in dogs and a cat. N Z Vet J. 2008;56(6):330–3. doi:10.1080/00480169.2008.36855.

Taeymans O, Penninck DG, Peters RM. Comparison between clinical, ultrasound, CT, MRI, and pathology findings in dogs presented for suspected thyroid carcinoma. Vet Radiol Ultrasound. 2013;54(1):61–70. doi:10.1111/j.1740-8261.2012.01966.x. Epub 2012 Sep 18.

Taylor SS, Harvey AM, Barr FJ, Moore AH, Day MJ. Laryngeal disease in cats: a retrospective study of 35 cases. J Feline Med Surg. 2009;11(12):954–62. doi:10.1016/j.jfms.2009.04.007. Epub 2009 Jun 17.

Thomas EK, Syring RS. Pneumomediastinum in cats: 45 cases (2000-2010). J Vet Emerg Crit Care (San Antonio). 2013;23(4):429–35. doi:10.1111/vec.12069. Epub 2013 Jul 15.

Tobias JR, Cullen JM. Thymofibrolipoma in a labrador retriever. Vet Pathol. 2014;51(4):816–9. doi:10.1177/0300985813502816. Epub 2013 Sep 10.

Yoon J, Feeney DA, Cronk DE, Anderson KL, Ziegler LE. Computed tomographic evaluation of canine and feline mediastinal masses in 14 patients. Vet Radiol Ultrasound. 2004;45(6):542–6.

Zekas LJ, Crawford JT, O'Brien RT. Computed tomography-guided fine-needle aspirate and tissue-core biopsy of intrathoracic lesions in thirty dogs and cats. Vet Radiol Ultrasound. 2005;46(3):200–4.

The Pleurae, Thoracic Wall, and Diaphragm

Giovanna Bertolini

1 Introduction

The thoracic wall, pleurae, and diaphragm enclose the lung and are interconnected. The pleura has parietal and visceral layers. Anatomically, the parietal pleura may be subdivided into costal, mediastinal, and diaphragmatic pleura. The costal pleura firmly adheres to the medial surface of the ribs and intercostal muscles; the mediastinal pleura forms the wall of the mediastinal space; the diaphragmatic pleura is the portion of the parietal pleura that covers the diaphragm. The visceral pleura covers the lung surface and fissures. Systemic thoracic vessels carry blood to and from the parietal pleura. The visceral pleura is nourished and drained by the pulmonary circulation. On either side of the body, the parietal and visceral pleura form a complete sac or pleural cavity. Each pleural cavity is an essential virtual cavity (sometimes communicating with its counterpart) that contains a capillary film of fluid, which is not normally appreciable in multiple detector computed tomography (MDCT) images.

2 MDCT Imaging Strategies

A thoracic computed tomography (CT) examination encompasses the thoracic wall, pleura, and diaphragm. The accumulation of air or fluid in the pleural cavity is easily detected on MDCT images, and a standard protocol may be adopted. When the scanner permits, an initial CT scan should be obtained for stable patients before any thoracic drainage and/or mechanical ventilation, to assess the status quo. At our

G. Bertolini (✉)
San Marco Veterinary Clinic, Padua, Italy
e-mail: bertolini@sanmarcovet.it

G. Bertolini (ed.), *Body MDCT in Small Animals*, DOI 10.1007/978-3-319-46904-1_15

center, patients are usually scanned initially while they are awake, using a second-generation 128-dual-source CT scanner with the Flash modality, which allows for sub-second volumetric (isotropic) thoracic image acquisition. The same is possible with most advanced MDCT scanners (e.g., 256-320-MDCT). When pleural disease is suspected, CT and contrast medium protocols should be adapted to achieve the best results. The optimal imaging strategies are similar to those described for thoracic cavity and lung assessment. Thorough assessment of the pleura for minor changes, such as pleural tags, small nodules, or diffuse thickening, may require high-resolution computed tomography (HRCT) evaluation of the thorax. Pre-contrast scans of the pleura are helpful for the identification of mineralization and small pleural blebs. In inflammatory and neoplastic changes to the pleura, early post-contrast series can better delineate pleural thickening, nodules, and increased vascularity. A late series is particularly useful for characterizing pleural thickening, distinguishing between pleural layers and fluid, and identifying small quantities of pleural fluid in the pleural cavity.

This approach can also be adopted in patients with thoracic wall neoplasia. In such cases, early post-contrast series allow for the identification of neoplastic vasculature and real extension of the mass, which are essential for planning a therapeutic approach (surgical resection or palliative therapies, such as radiotherapy, transarterial embolization, or chemoembolization). Late-phase imaging is essential for further characterization of the mass, particularly to identify the optimal site for biopsy. Moreover, late-phase CT imaging can help the clinician to assess pleural involvement of a thoracic wall mass.

3 Diseases of the Pleura and Pleural Space

Common conditions affecting the pleura and pleural space in dogs and cats include the accumulation of air (pneumothorax) or fluid (pleural effusion) in the pleural space. Inflammatory and neoplastic processes can involve the pleura and are often associated with pleural effusion. CT scanning is excellent at detecting small amounts of both air and fluid and can often be used to identify the underlying intrathoracic causes.

3.1 Pneumothorax

Pneumothorax refers to the presence of air in the pleural space, between the parietal and visceral pleura. Pneumothorax is customarily divided into “open pneumothorax,” when air enters the pleural space through a defect in the thoracic wall, resulting in communication of the pleural space with the atmosphere, and “closed pneumothorax,” in which there is no defect in the thoracic wall, and air enters the pleural space due to lung or large airway injuries. In our patients, open

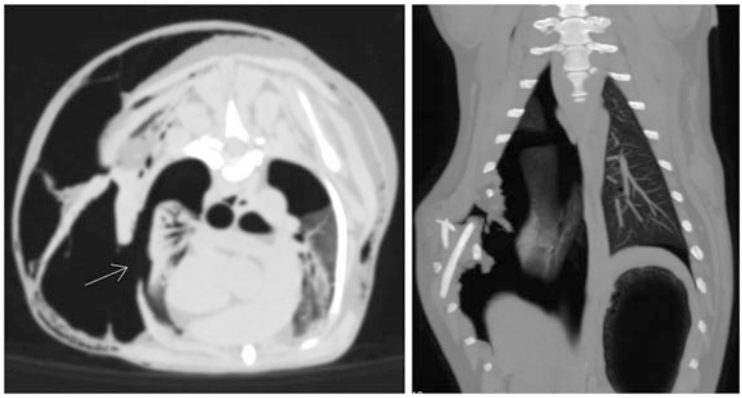

Fig. 1 Tension pneumothorax in dogs with penetrating trauma of the thoracic wall (bite wounds)

pneumothorax is typically caused by penetrating injuries, while closed pneumothorax may be caused by blunt trauma or spontaneous rupture of superficial pulmonary bullae or pleural blebs. Tension pneumothorax is a rare life-threatening condition in which air accumulates within the pleural space via a one-way-valve effect allowing air to enter, but not to leave, the pleural space, resulting in severe compromise to both the cardiovascular and respiratory systems (Fig. 1). Pneumothorax, hemothorax, and diaphragmatic hernia are the three acute trauma-associated pleural space diseases that occur most commonly in our patients. Thoracic wall, pleural, and diaphragmatic injuries have been examined in the chapter on "The Body Trauma." Other information is provided in the chapter on "The Lung and Airways," particularly regarding pleural blebs.

3.2 Pleural Effusions

Pleural effusion is a common clinical finding with many potential causes. Forces that promote the development of pleural effusion include an increase in capillary hydrostatic pressure, a decrease in capillary colloid osmotic pressure (transudate), and an increase in permeability of the microvascular circulation (exudate). The main cause of transudates is usually congestive heart failure, whereas exudates usually form due to inflammatory or neoplastic processes. The lymphatic system is responsible for draining fluid formed within the pleural space. Obstruction, disruption, and decreased efficacy of the lymphatic drainage system can also result in exudative effusions.

CT is frequently used to assess patients with pleural effusion associated with various pleural or pulmonary diseases. The total protein and number of cells in transudate is low; therefore, the fluid is generally homogeneous, and its CT-attenuation values range from 0 to 30 HU. On the contrary, exudates contain

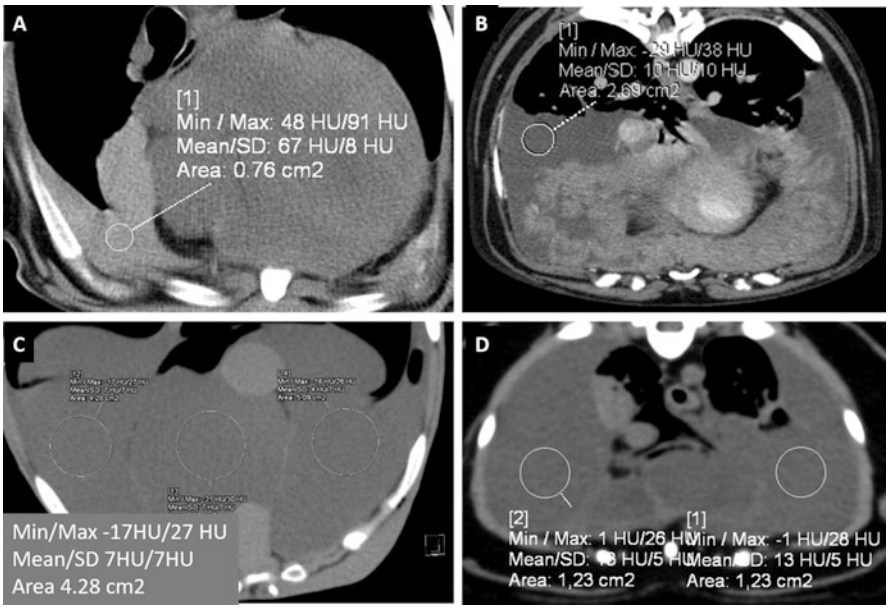

Fig. 2 Pleural effusion. (**a**) Hemothorax in dog (rodenticide poisoning). (**b**) Pyothorax in a dog with septic pleuritis. (**c**, **d**) Chylothorax in a dog and a cat

high levels of cells, protein, and other substances; thus, the fluid may exhibit a heterogeneous aspect in association with a wider range of CT-attenuation values. Measurements should be performed preferably in post-contrast series, so as to avoid including pleura or a collapsed lung lobe in the region of interest. In general, CT cannot distinguish among various pleural fluids based on CT numbers alone (Fig. 2).

Hemothorax

Among our patients, several causes of hemothorax are observed, including trauma, coagulopathies, neoplasia, lung-lobe torsion, and infectious causes. Disorders of either primary or secondary hemostasis can lead to hemothorax, with anticoagulant rodenticide intoxication being the most frequent coagulation disturbance encountered in clinical practice. Thoracic wall, pleural, and lung tumors can also cause hemothorax in extrapleural or pleural space (e.g., hemangiosarcoma, mesothelioma, metastatic carcinoma, osteosarcoma, and pulmonary carcinoma (Figs. 3 and 4). Other causes of hemothorax include lung lobe torsion, as well as parasitic and nonparasitic infectious causes (e.g., angiostrongylosis, spirocercosis). CT findings in hemothorax include heterogeneously attenuating pleural fluid with variable HU values. A recent hemorrhage may have an attenuation value ranging from 40 to 60 HU. As the hemorrhagic pleural effusion begins to clot, attenuation values may rise and loculations develop within the pleural fluid; fibrin mass-like formations may appear as well. These pleural pseudotumors can be distinguished from pleural-based masses by their high attenuation on unenhanced CT scans.

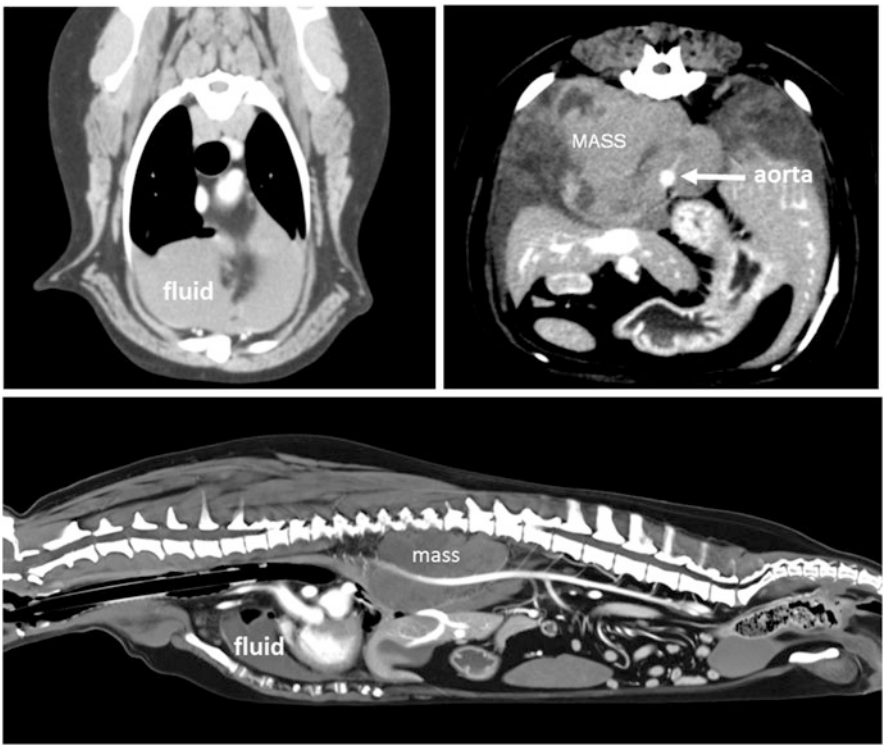

Fig. 3 Hemothorax in a mongrel dog with sarcoma in the dorsal mediastinum (retrocrural space)

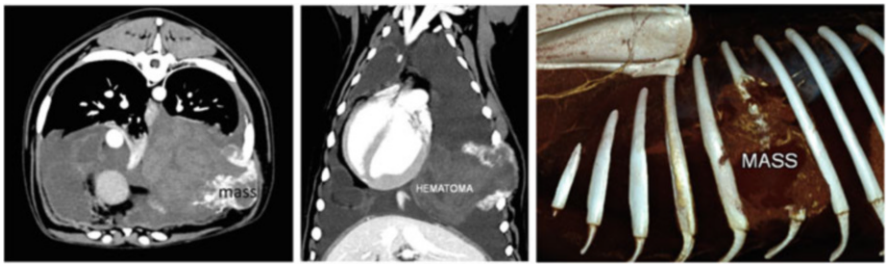

Fig. 4 Hemothorax and hematoma in the pleural cavity of a dog with ruptured hemangiosarcoma involving the left seventh rib

Pyothorax

Pyothorax is the accumulation of exudate within the thoracic cavity. The main cause of pyothorax is the presence of an infectious agent within the thoracic cavity, resulting in an inflammatory response and fluid accumulation in the pleural space. Many possible routes of infection have been identified in small animals, including foreign material, penetrating injuries, hematogenous spread, esophageal

perforation, parasitic migration, previous thoracocentesis or thoracic surgery, progression of discospondylitis, and neoplasia with abscess formation (Figs. 5 and 6). In cats, pyothorax can be caused by parapneumonic spread, foreign-body migration, and penetrating thoracic wounds. Concomitant signs of pleuritis are seen on CT images. The pleura is irregularly thickened and strongly enhanced in post-contrast series (Fig. 5).

In dogs, the most common cause is plant material or a migrating grass awn. The usefulness of CT for diagnosis and presurgical evaluation in these cases has been reported in recent studies. Vegetal foreign bodies are difficult to see in CT images. When detected, grass seeds are reported to appear as foci of soft-tissue attenuation in air-containing structures, as elongated gas-containing foci in soft tissues or as slightly hyperattenuating foci within soft tissues. Moreover, CT images may also reveal secondary signs, such as soft-tissue inflammation, cavitary lesions or tracts, pleural thickening, pulmonary consolidation, and soft-tissue thoracic wall thickening, which can be used to estimate the position of a foreign body in cases when it cannot be visualized directly (Fig. 7) This may allow for ultrasonography-guided retrieval of the foreign body or surgical approach.

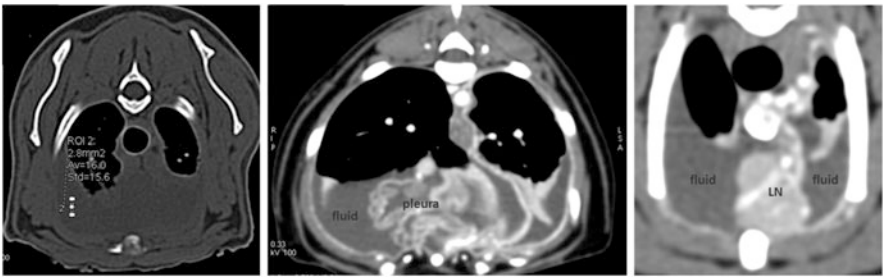

Fig. 5 Pyothorax in cats with concomitant septic pleuritis. Note the sternal lymph node enlargement (LN)

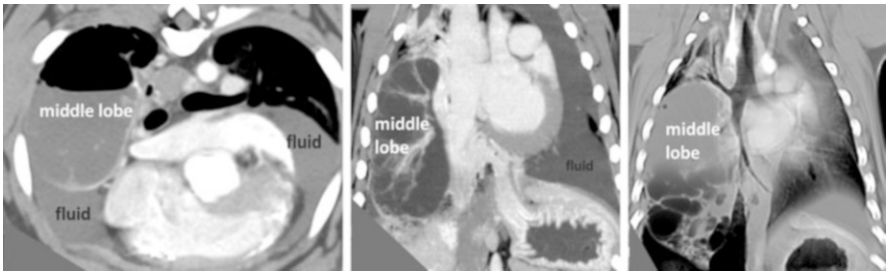

Fig. 6 Pyothorax in a dog with an abscess in the right lung lobe. Note the concomitant pneumothorax

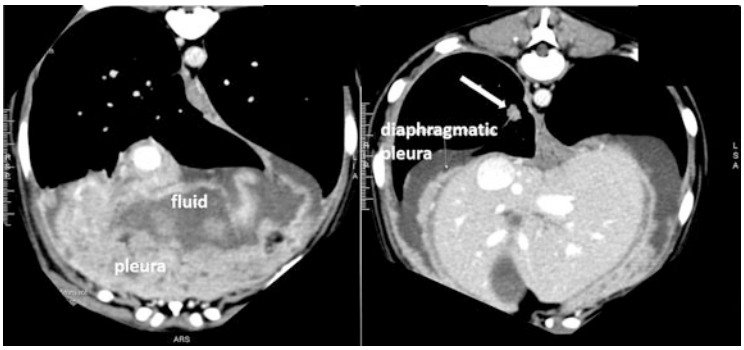

Fig. 7 Septic pleuritis and pyothorax in a dog due to migrating grass awn

Chylothorax

Chylothorax is an accumulation of lymph within the pleural cavity. Traumatic chylothorax is reported in small animals, and CT is often required for investigating a possible disruption of the thoracic duct or one of its major divisions. However, patients with thoracic duct rupture are unlikely to develop significant pleural effusion and are not commonly seen (Fig. 8). Most commonly, chylothorax results from impaired or obstructed lymphatic drainage. Because of the inflammatory nature of chyle, chronic effusion increases the risk for the development of pleuritis and pericarditis. Chylothorax can result from abnormalities of the lymphatic vessels, abnormal organ position (e.g., peritoneal-pericardial diaphragmatic hernia, or lung-lobe torsion), increased venous hydrostatic pressure at the level of the right heart, venous thrombosis at the outlet of the thoracic duct, or any other factor obstructing the lymphatic drainage (e.g., large mediastinal masses). In most instances, the cause remains obscure (idiopathic chylothorax) (Fig. 9). Various studies in the veterinary literature report that CT is the ideal technique for visualization of the thoracic duct. More branches of the thoracic duct can be identified with CT than with radiography. Diluted iodinate contrast medium is injected directly into one or more lymph nodes. The choice of popliteal, medial iliac, or mesenteric lymph nodes (ultrasound guided) depends on lymph node size and the skill and comfort levels of the operator. Personal experience suggests that MDCT lymphangiography may be frustrating, and the contrast medium may not progress into the lymphatics in diseased patients as well as reported in normal dogs and cats.

3.3 Pleural Thickening and Masses

Diseases of the pleura can be broadly classified as benign or malignant. High-quality MDCT data can detect even slight pleural changes. In addition, MDCT serves as a guide for further diagnostic and therapeutic steps (thoracoscopy or thoracotomy). As said before, a comprehensive evaluation of the pleura requires

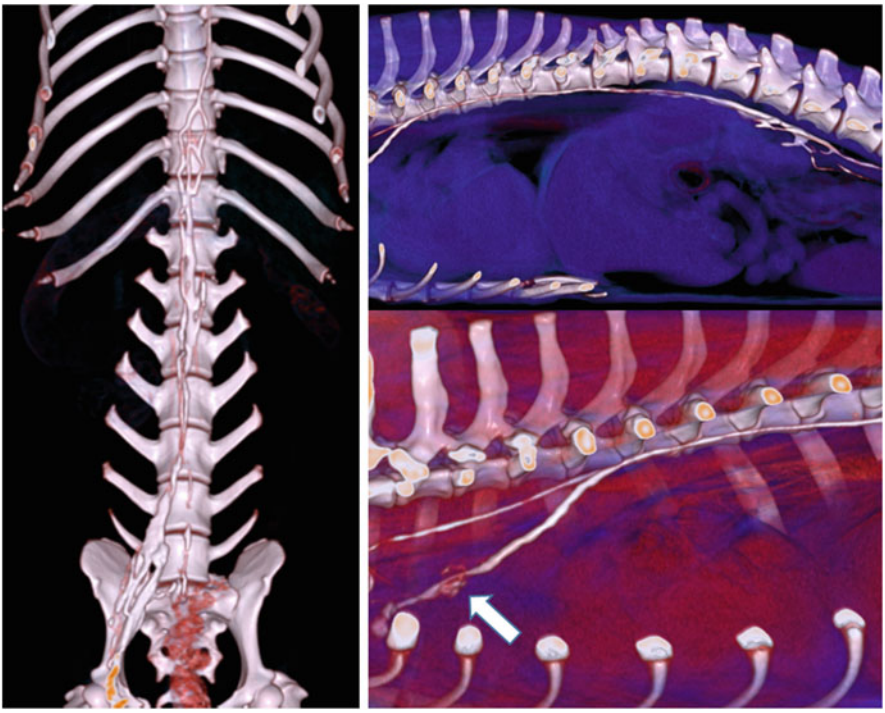

Fig. 8 MDCT lymphangiography from the popliteal lymph nodes in a dachshund with chylothorax diagnosed 7 days after blunt trauma. *Arrow* indicates a site of lymph leakage in the cranial mediastinum

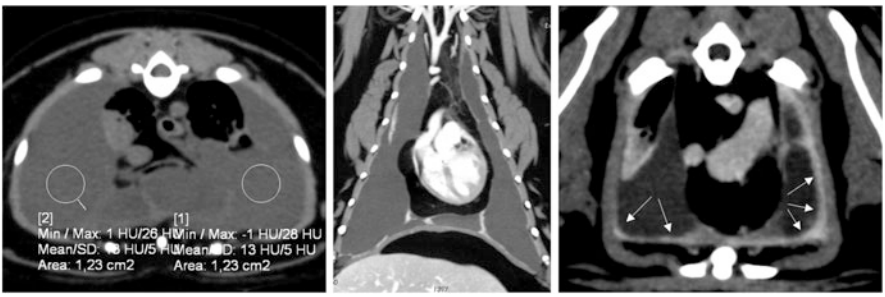

Fig. 9 Fibrosing pleuritis in a cat with idiopathic chylothorax

thin-collimated, contrast-enhanced series for the identification of diffuse or focal pleural thickening and small pleural nodules, which are not detectable on pre-contrast images. The inflamed pleura (pleuritis) is thickened and folded, sometime assuming a mass-like appearance (Figs. 5, 7, and 10). In pleuritis, the pleura shows substantial early enhancement after the injection of contrast medium, with prominent vessels on the pleural surface. Depending on the underlying cause,

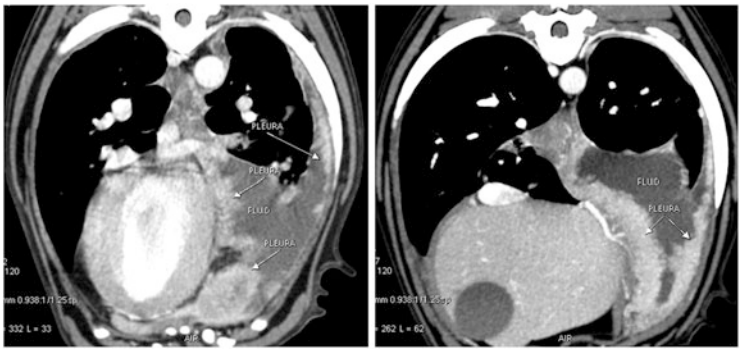

Fig. 10 Septic pleuritis in a dog, involving the left hemithorax. The pleurae are thickened and show a mass-like appearance. The migration of a foreign body was suspected but not proven. The dog recovered completely with medical treatment

Fig. 11 Pneumothorax and effusion in a cat with pleural mesothelioma. (**a**) Thin-MinIP image showing passive atelectasis of the left lung due to pneumothorax (*arrow*). (**b**). Transverse view showing pleural fluid (transudate) and diffuse pleural thickening. (**c**) Dorsal thin-MIP image

various types of exudates can be present (pyothorax, chylothorax, etc.). Small nodules and thickening of the pleura may be seen in either benign or malignant conditions, such as in pleural mesothelioma or carcinomatosis (Figs. 11, 12, 13, 14, and 15). Most common primary tumors of the pleura are mesotheliomas: low-grade malignancies originating from mesothelial cells covering the coelomic cavities

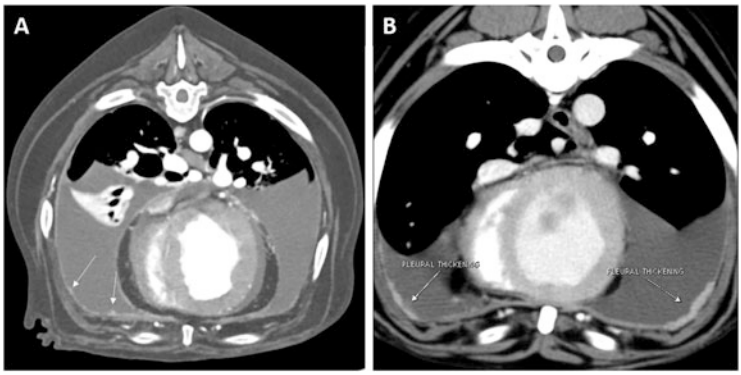

Fig. 12 Pleural mesothelioma in two dogs. (**a**) Note the irregular thickening of the pleurae (*arrows*). (**b**) Plaque-like pleural lesions

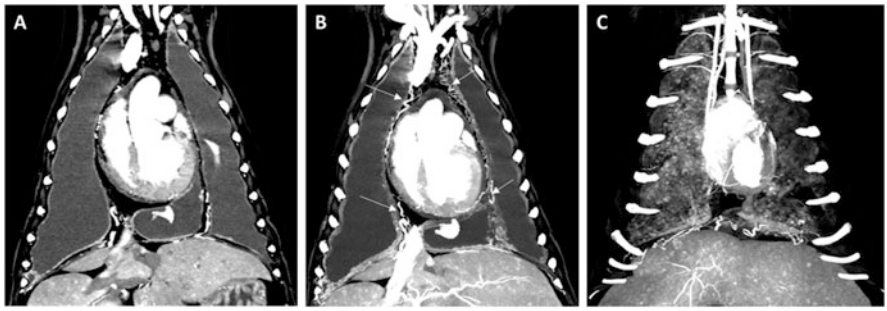

Fig. 13 Pleural mesothelioma in a dog. (**a**) Note the abundant bilateral pleural effusion. (**b**) The pleurae are thickened and show great vascularization (*arrows*). (**c**) Thin-MIP view of the pleurae shows a diffuse, miliary pattern

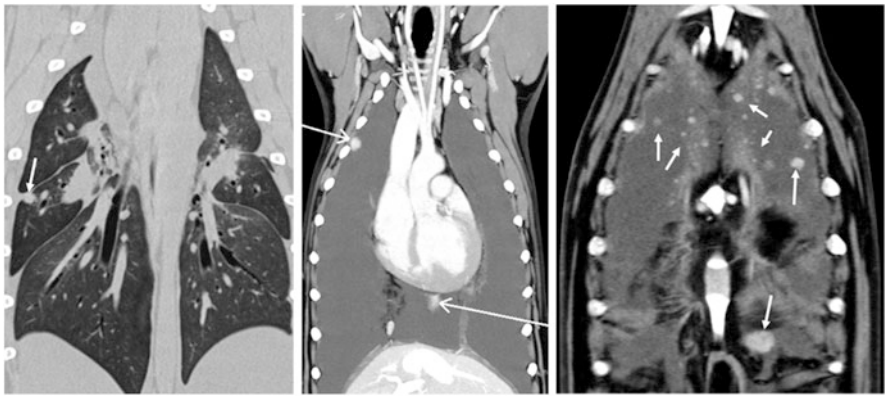

Fig. 14 Pleural mesothelioma in a dog. Note various pleural visceral and parietal nodules (*arrows*), pleural effusion, and diffuse pleural thickening

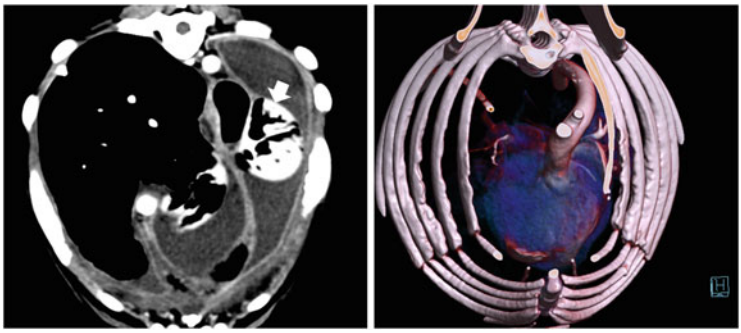

Fig. 15 Pleural mesothelioma in a cat. Note the left lung collapse, hyperinsufflation of the contralateral lobes, and mediastinal shift. Pleural effusion and diffuse pleural thickening are present. Note the rib remodeling

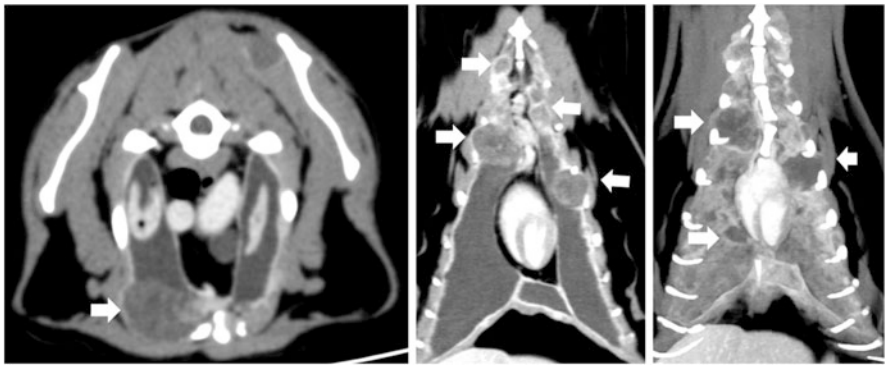

Fig. 16 Pleural metastasis of infrascapular "feline injection-site sarcomas" (not visible here). Bilateral pleural effusion (note the apical passive lung atelectasis), diffuse pleural thickening, and multiple nodular lesions of the pleurae (metastases of fibrosarcoma; *arrows*) are present

(including pericardium, pleura, peritoneum, and vaginal tunic). These tumors can have a localized or diffused distribution and may present as multiple to coalescing nodularity or broad-based plaque-like pleural masses. Differentiation of pleural mesothelioma from metastatic carcinoma is difficult; however, clinical data and associated findings seen on MDCT, such as pulmonary lesions, extrathoracic neoplasia, and lymph node enlargement, may facilitate the imaging diagnosis (Figs. 16 and 17).

In cats, pleural tags have been reported in association with primary lung tumors. Similar to that reported in humans, these tags may have neoplastic or nonneoplastic significance. Thus, they should not be interpreted univocally as metastatic spread.

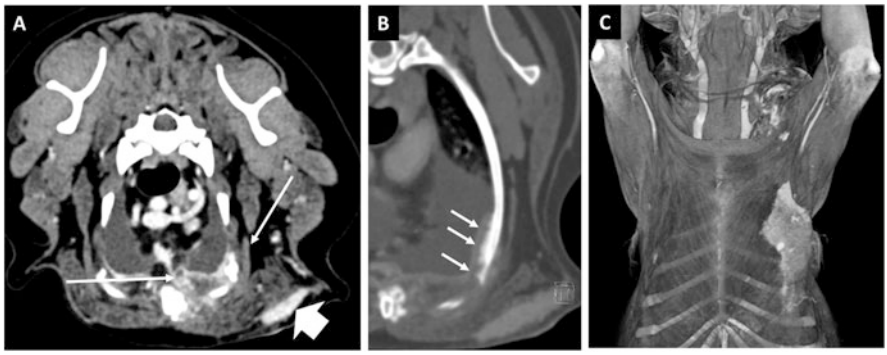

Fig. 17 Mammary carcinoma in a dog with secondary pleural involvement. (**a**) *Large arrow* indicates the mammary neoplasia. Note the pleural effusion and pleural thickening, with loss of extrapleural fat planes (*arrows*) in the area under the mass. (**b**) *Arrows* indicate the parietal pleura and rib involvement. (**c**) VR of the thoracic wall showing the mammary tumor

4 Diseases of the Thoracic Wall and Diaphragm

The thoracic wall is formed by several bony and soft-tissue structures. An extrapleural space lies between the parietal pleura and the thoracic wall. Thoracic, extrapleural effects may arise from any structures of the thoracic wall, such as extrapleural fat, ribs, intercostal muscles, and neurovascular bundles. Expanding lesions of the pleura typically do not cause the erosion of ribs or involve soft tissues of the thoracic wall. In contrast, extrapleural neoplasias frequently involve bony structures (rib, sternum), fat, muscles, nerves, and vessels of the wall, projecting inward to the thoracic cavity with possible secondary involvement of the pleura. Extrapleural benign soft-tissue mass lipoma is the most frequently encountered fatty soft-tissue tumor of the thoracic wall. Although benign in nature, many lipomas of the thoracic wall are deep seated and involve deep intermuscular or muscular layers, impairing thoracic expansion or compressing intrathoracic structures (Figs. 18 and 19). They are easily distinguished in CT by their hypoattenuating (negative CT number) and non-enhancing appearance. Among our patients, chondromas and benign bony tumors are seen on occasion, but malignant tumors of the thoracic wall are more common. Malignant neoplasias of the thoracic wall in dogs and cats include osteosarcoma, chondrosarcoma, soft-tissue sarcoma, subcutaneous hemangiosarcoma, and peripheral nerve tumors. Extrapleural thoracic hemorrhage and hematoma are commonly associated with thoracic wall sarcoma in dogs (Figs. 4, 20, and 21).

The diaphragm is a large, dome-shaped, musculotendinous structure located at the caudal-most part of the pleural cavity that divides the thoracic cavity from the abdominal cavity and the primary muscle of ventilation. The diaphragm is interconnected with the thoracic wall and neoplastic condition of this latter may also involve the diaphragm (Fig. 22).

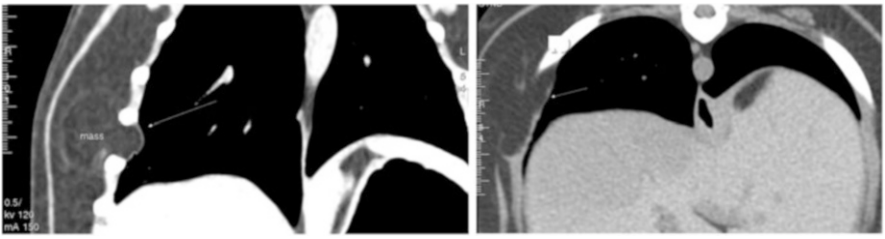

Fig. 18 Small thoracic wall lipoma in a dog with pleural involvement

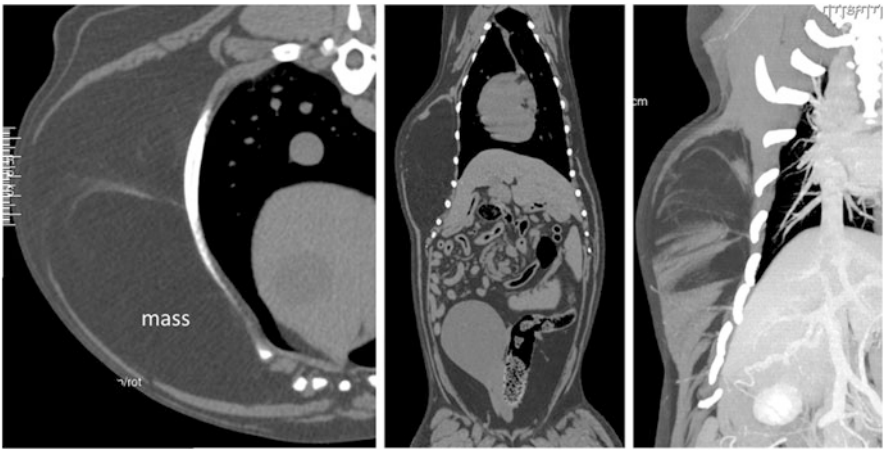

Fig. 19 Large thoracic wall lipoma in a dog. The mass compresses the ribs and stretches the muscles

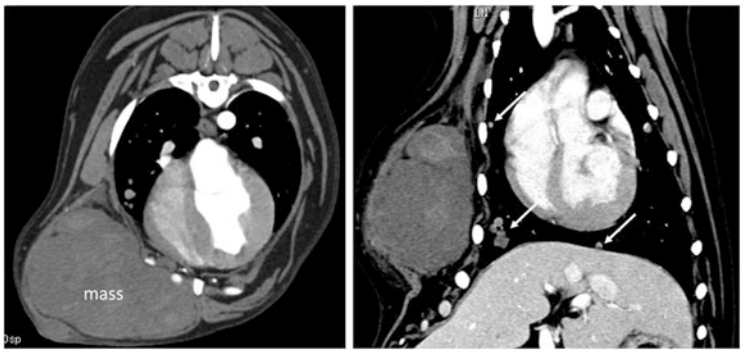

Fig. 20 Hemangiosarcoma of the thoracic wall in a dog. The mass compresses the thoracic cage. *Arrows* indicate metastatic pulmonary lesions

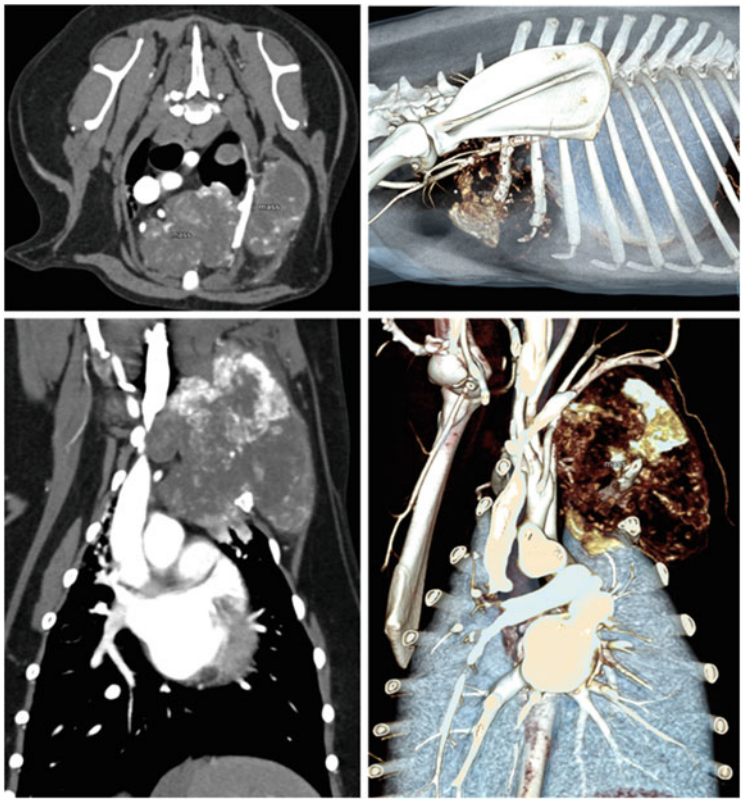

Fig. 21 Chondrosarcoma of the thoracic wall in a dog. The mass projects inward to the thoracic cavity, involving the pleura, lung, and cranial mediastinal lymph nodes

Several congenital and acquired diaphragmatic functional and structural defects are described in dogs and cats. Dysfunction of the diaphragm can be classified as paralysis, weakness, or eventration and appears as partial cranial displacement or flattened diaphragmatic cupola. Congenital eventration is the result of incomplete muscularization of part or the entire membranous diaphragm during fetal life. Imaging differentiation among these dysfunctional congenital conditions is difficult; CT may help to diagnose the acquired forms that may be secondary to trauma, inflammation, or neoplastic invasion of the phrenic nerve.

Structural defects of the diaphragm are easily assessed and best characterized on MDCT images. In the author's opinion, the dorsal and sagittal planes from thin-section MDCT data are better suited to examination of the diaphragm and its relationships with thoracic and abdominal structures.

The diaphragm develops in early embryonic life and comprises four components: the transverse septum, pleuroperitoneal folds, esophageal mesentery, and muscular body wall. The transverse septum becomes the central tendinous part of the diaphragm. Incomplete development of this part leads to peritoneal-pericardial

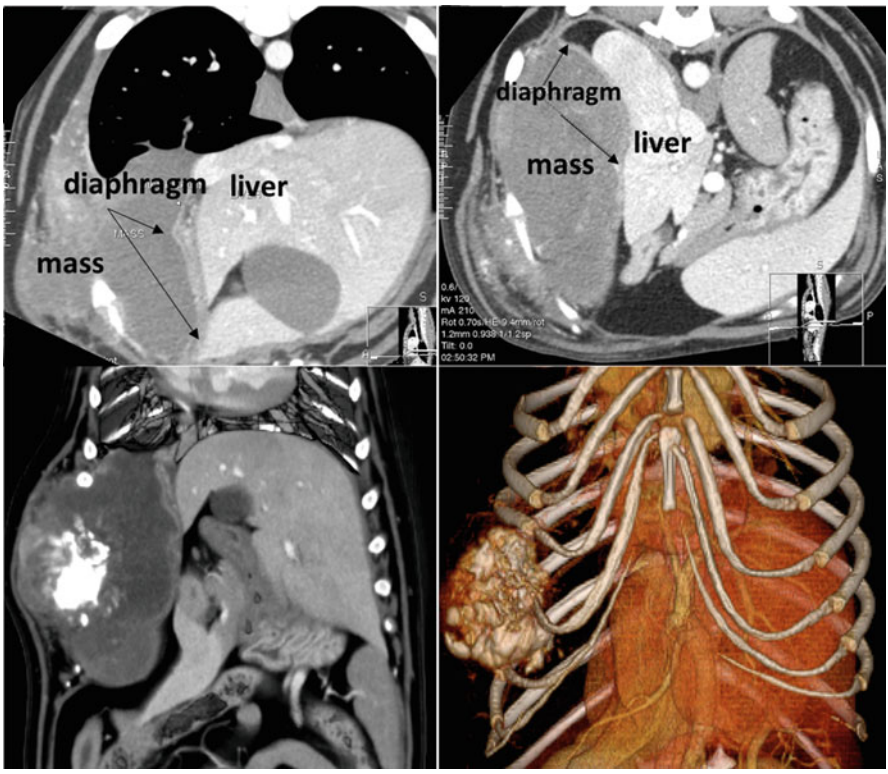

Fig. 22 Thoracic wall osteosarcoma in a dog, involving the right 10th and 11th ribs. The mass projects into the thoracic cavity, involving the diaphragm (*arrows*)

diaphragmatic hernia, with migration of the abdominal organs and viscera into the pericardial sac. This congenital hernia is easily detected on CT images and is often accompanied by other congenital anomalies of the thoracic and abdominal structures (Fig. 23). Various other congenital or trauma-induced conditions may lead to diaphragmatic ruptures, with herniation of some abdominal organs, such as the stomach and liver, into the thoracic cavity (Fig. 24). CT appearance in these cases may vary, depending on the underlying causes and herniated structures (see also chapter on "The Body Trauma"). Diaphragmatic hernias can also occur through three physiological diaphragmatic apertures, the aortic hiatus, the esophageal hiatus, and the caval foramen, which are difficult to assess using radiology alone. See also the chapter on "The Mediastinum and Neck." Caval foramen hernia is rarely reported in dogs and has recently been described using MDCT. Caval foramen hernia is likely underestimated in our patients, because of radiological misdiagnosis as an intrathoracic lesion (e.g., accessory lung lobe mass), caudal mediastinal mass, or diaphragmatic eventration.

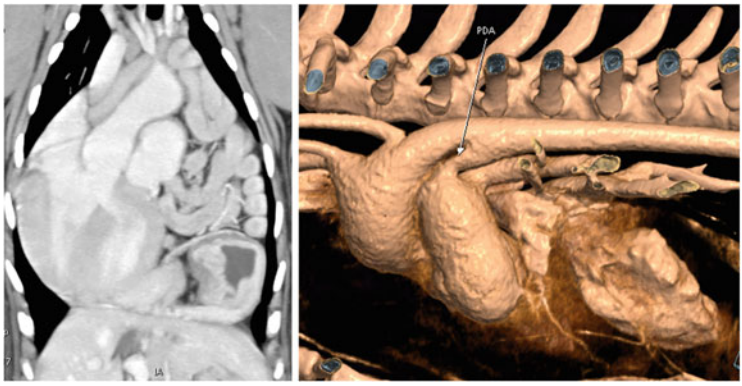

Fig. 23 Peritoneo-pericardial diaphragmatic hernia (PPDH) in a puppy with concomitant PDA (patent ductus arteriosus). The stomach and small bowel are dislocated into the pericardial sac

Fig. 24 Traumatic diaphragmatic rupture in a dog (*arrow*)

Further Readings

Ayres, C.J., Treharne, D.F. (1978) Eventration of the diaphragm in a Great Dane. Aust Vet Pract. ISSN: 0310-138X

Dhein CR, Rawlings CA, Rosin E, Losonsky JM, Chambers JN. Esophageal hiatal hernia and eventration of the diaphragm with resultant gastroesophageal reflux. J Am Anim Hosp Assoc. 1980;16:517–22.

Echandi RL, Morandi F, Newman SJ, Holford A. Imaging diagnosis – canine mesothelioma. Vet Radiol Ultrasound. 2007;48:243–5.

Johnson EG, Wisner ER, Kyles A, et al. Computed tomographic lymphography of the thoracic duct by mesenteric lymph node injection. Vet Surg. 2009;38:361–7.

Jones JC, Ober CP. Computed tomographic diagnosis of non-gastrointestinal foreign bodies in dogs. J Am Anim Hosp Assoc. 2007;43(2):99–111.
Kim M, Lee H, Lee N, et al. Ultrasound-guided mesenteric lymph node iohexol injection for thoracic duct computed tomographic lymphography in cats. Vet Radiol Ultrasound. 2011; 52(3):302–5.
Kim J, Kim S, Jo J, Lee S, Eom K. Radiographic and computed tomographic features of caval foramen hernias of the liver in 7 dogs: mimicking lung nodules. J Vet Med Sci. 2016;78(11):1693–7. doi:10.1292/jvms.16-0161.
Kirkby KA, Bright RM, Owen HD. Paraoesophageal hiatal hernia and megaoesophagus in a three-week-old Alaskan malamute. J Small Anim Pract. 2005;46(8):402–5.
Millward IR, Kirberger RM, Thompson PN. Comparative popliteal and mesenteric computed tomography lymphangiography of the canine thoracic duct. Vet Radiol Ultrasound. 2011; 52(3):295–301.
Raj V, Kirke R, Bankart MJ, Entwisle JJ. Multidetector CT imaging of pleura: comparison of two contrast infusion protocols. Br J Radiol. 2011;84(1005):796–9. doi:10.1259/bjr/55980445.
Reetz JA, Buza EL, Krick EL. CT features of pleural masses and nodules. Vet Radiol Ultrasound. 2012;53(2):121–7. doi:10.1111/j.1740-8261.2011.01883.x.
Schultz RM, Zwingenberger A. Radiographic, computed tomographic, and ultrasonographic findings with migrating intrathoracic grass awns in dogs and cats. Vet Radiol Ultrasound. 2008; 49(3):249–55.
Singh A, Brisson B, Nykamp S. Idiopathic chylothorax: pathophysiology, diagnosis and thoracic duct imaging. Compend Contin Educ Vet. 2012;34(8):E2.
Stillion JR, Letendre JA. A clinical review of the pathophysiology, diagnosis, and treatment of pyothorax in dogs and cats. J Vet Emerg Crit Care (San Antonio). 2015;25(1):113–29. doi:10.1111/vec.12274. Epub 2015 Jan 13.
Swinbourne F, Baines EA, Baines SJ, et al. Computed tomographic findings in canine pyothorax and correlation with findings at exploratory thoracotomy. J Small Anim Pract. 2011;52:203–8.
Vansteenkiste DP, Lee KC, Lamb CR. Computed tomographic findings in 44 dogs and 10 cats with grass seed foreign bodies. J Small Anim Pract. 2014;55(11):579–84. doi:10.1111/jsap.12278. Epub 2014 Oct 7.
Zoia A, Drigo M. Diagnostic value of Light's criteria and albumin gradient in classifying the pathophysiology of pleural effusion formation in cats. J Feline Med Surg. 2016;18(8):666–72. doi:10.1177/1098612X15592170. Epub 2015 Jun 26.
Zoia A, Drigo M, Caldin MA. new approach to pleural effusion in dogs: markers for distinguishing transudates from exudates. J Vet Intern Med. 2011;25:1505.

Part V
The Heart

Cardiac CT Angiography

Randi Drees

As the heart is constantly moving during the cardiac cycle, acquisition of motion-free images using standard fan-beam computed tomography (CT) units can be challenging. Cardiac computed tomographic angiography (CCTA) has been introduced into veterinary medicine with the event of ECG-gating capabilities on multidetector row CT (MDCT) units that allow for capturing the heart either in the moment of least motion during end diastole or recording the cardiac cycle synchronized with an ECG recording. While basic assessment of the cardiac, pericardial, and coronary anatomy may be performed on non-ECG-gated CCTA studies, measuring functional or morphological parameters necessitates CCTA exams performed using ECG-gating.

1 Cardiac CT Angiography Imaging Strategies

Sedation or general anesthesia is required to safely position the patient on the CT couch during the CCTA exam and contrast bolus injection. While there is no distinct recommendation for positioning the patient in dorsal or ventral recumbency when assessing the heart, ventral recumbency usually allows for better ventilation and therefore easier respiration control and may be preferred.

If ECG leads are used for cardiac gating, these can either be placed on the paws or the thoracic wall after regional clipping of the fur. The recommended heart rate using 64-MDCT units for EKG-gated CCTA exams is at or below 65 bpm in humans, which is difficult to achieve in veterinary patients. Successful CCTA exams have been performed with much higher heart rates in dogs. This likely

R. Drees (✉)
Royal Veterinary College, University of London, London, UK
e-mail: rdrees@rvc.ac.uk

G. Bertolini (ed.), *Body MDCT in Small Animals*, DOI 10.1007/978-3-319-46904-1_16

relates to the fact that with increased heart rate the excursions of the cardiac muscle are smaller and overall less motion is introduced. Several protocols have been tested and found applicable in canine CCTA exams. Vasodilators have not shown significant effect to improve visibility of the coronary arteries. Sedation and anesthetic protocols tailored to the individual patient's needs are recommended; introducing a regular physiologic heart rate in the lower range may be beneficial. Respiratory control remains essential for avoiding respiratory motion on the CCTA exams and can be achieved manually or medically. Patients in heart failure may need to be carefully evaluated if the rapid injection of the contrast bolus can be tolerated.

The CCTA exam will be timed to the presence of the contrast bolus in the vascular bed of interest. Levophase exams will highlight the left atrium, ventricle, coronary arteries, and aorta; dextrophase exams will highlight the right atrium, ventricle, and pulmonary artery. So-called triple-rule-out exams will show all four chambers, coronary arteries as well as the aorta and pulmonary arteries and veins opacified (Fig. 1). Choice of exam type is to be made based on the clinical question to be answered; dextro- or levophase exams are especially helpful when demonstrating left-to-right or right-to-left shunting, while triple-rule-out exams give an excellent overview over the entire anatomy of the heart, coronary arteries, as well as the aorta and its branches and the pulmonary vessels. Timing the start of the scan with the arrival of the contrast bolus in the desired vascular bed can be achieved with automated bolus tracking or test bolus. Scan delay from end of the cine scan for bolus tracking to start of the diagnostic scan needs to be taken into consideration when planning region of interest placement for bolus tracking as well as the slightly different geometry of the test bolus compared to the diagnostic contrast bolus.

Ionic or nonionic iodinated contrast media can be used for CCTA exams. A power injector should be utilized for all CCTA exams to ensure adequate delivery of contrast medium; injection pressures are usually set not to exceed 300 PSI. To ensure the delivery of a tight bolus, use of a saline chaser may be helpful using a

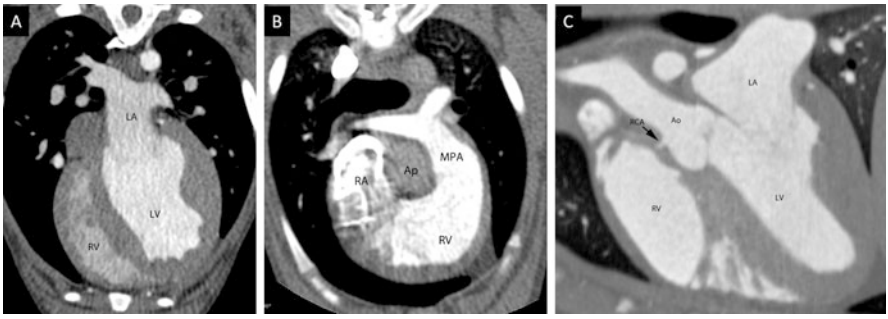

Fig. 1 The exam can be tailored to highlight the specific vascular bed of interest: the levophase highlights the left atrium (LA), left ventricle (LV), aorta (Ao), and coronary arteries (**a**, transverse plane); the dextrophase highlights the right atrium (RA), right ventricle (RV), and pulmonary arterial tree (**b**, transverse plane); the triple-rule-out exam combines the two phases and highlights all of the abovementioned structures with contrast during the exam (**c**, sagittal image). Main pulmonary artery (MPA), right coronary artery (RCA)

dual barrel power injector. Contrast bolus volume depends on the duration of the scan and the standard dose of contrast medium at 600–800 mgI/kg (usually 2 ml/kg) can be used as a starting orientation. For prolonged injection, protocols such as the triple-rule-out studies, diluted bolus design, or slower injection rates may be helpful to achieve adequate opacification keeping possible volume overload as a complication in mind.

The scan will be timed to the presence of the contrast bolus in the vascular bed of interest; in addition, it may be performed in relation to the phase of the ECG of the patient. Non-ECG-gated CCTA exams rely on a little bit of luck to catch the heart at the time of least motion during diastole. A lower heart rate will result in a longer diastolic phase, increasing the chances of luck a little further. Where mild motion may be acceptable to diagnose larger lesions such as heart base masses, small anatomical structures such as the coronary arteries may no longer be visible if the heart is moving during image acquisition. A strategy to still being able to resolve these small structures without ECG-gating software available on the given CT scanner may be to repeat the scan over the heart 2–3 times immediately and subsequently after calculated bolus arrival time, alternating scan direction to avoid delay times due to gantry translation (Fig. 2). On review, the scan with least motion is usually sufficient to resolve the anatomy of the small structures. This technique is performed at the expense of increased radiation dose to the patient, and the phase of the cardiac cycle during image acquisition cannot be correlated to the ECG.

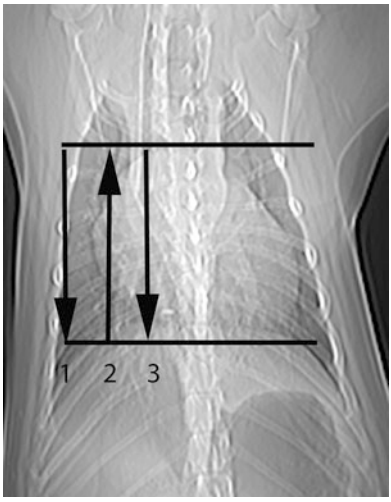

Fig. 2 Without ECG-gating software, the phase of image acquisition cannot be linked to the ECG of the patient; the phase of the cardiac cycle displayed on the image cannot be reliably identified or predicted. To gain an overview of the anatomy, the heart needs to be imaged at the time of least motion during end diastole. Since this cannto be pedicted without ECG gating, two to three sequential scans (1,2,3) can be planned with opposing scan direction (*arrows*) to minimize gantry translation time, and with a little bit of luck one of the series will show the heart in end diastole so that anatomy can be evaluated

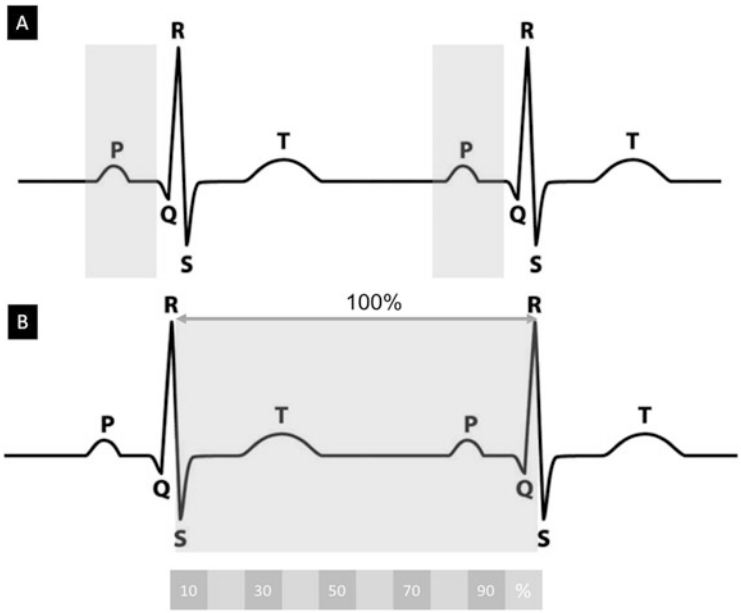

Fig. 3 With prospective gating, (**a**) a predefined phase of the cardiac cycle, usually end diastole (shaded area in A), will be acquired on the images. Retrospective gating (**b**) acquires images of the entire cardiac cycle (shaded area in B) that can then be reconstructed at user-defined intervals (%) of the cardiac cycles. The entire R–R interval is determined as 100% of the cycle

ECG-gating software can be applied prospectively or retrospectively (Fig. 3). For prospectively ECG-gated CCTA exams, the image acquisition will be performed triggered by the ECG in the end-diastolic period, recording a snapshot of the cardiac cycle that is of excellent use to evaluate the anatomy of the heart and coronary arteries. Retrospectively ECG-gated CCTA exams record the entire cardiac cycle that can then be retrospectively segmented according to the simultaneously recorded ECG. The entire cardiac cycle is set as 100% from R–R wave; usually 5–10% segments of the cardiac cycle are constructed that allow to observe the motion of the heart during the cardiac cycle. Retrospectively ECG-gated exams deliver a higher dose of radiation to the patient compared to prospectively gated exams, and allow for functional and anatomical evaluation of the heart.

Scan length should include the most cranial to most caudal extent of the heart taking into consideration possible excursions of the heart during the cardiac cycle. Setting the display field of view (DFOV) around the heart increases resolution in the *x*/*y*-plane, helping especially to resolve the small coronary vessels. For standard MDCT units, tube voltage settings of 100–120 kVp and tube current settings of 200 mA may be adequate; units equipped with ECG-gating will commonly modulate the radiation according to the cardiac cycle. Helical exams are to be used on conventional MDCT units, where high-end MDCT units with cardiac gating may enable single rotation volume acquisitions. In conventional MDCT units, tube rotation time should be set as low as possible ($\leq$1 s) in combination with a low

detector pitch ($\leq$1.4), higher-end MDCT units enabled for ECG-gating may adjust these parameters based on the heart rate. Slice width collimation and reconstruction slice thickness should ideally be low at 0.625–1.25 mm. A medium frequency spatial reconstruction kernel is used to generate the diagnostic images.

Soft tissue window width (~400 HU) and level (~40 HU) are commonly used to review the images; slightly wider window width settings may be helpful with high bolus density. The basic evaluation of the study is performed on the acquired transverse plane images, yet the use of multiplanar reconstructions (MPRs) is very helpful to understand and evaluate the anatomy and necessary to construct image planes similar to those used in echocardiography to allow for quantitative planar and volumetric evaluation. Maximum intensity projections (MIPs) can be very helpful to highlight small structures such as the coronary arteries. Specific vessel tracking software for the coronary arteries is available for human applications and may be applied in veterinary patients, difficulties can arise due to the relatively small size of the vessels. Automated segmentation software for quantitative functional evaluation is also based on human anatomy and needs to be verified for use in veterinary patients.

2 Normal Cardiac CT Angiography (CCTA)

2.1 The Heart

The contrast filled lumen of the left and right ventricle and atrium are well delineated from the cardiac muscle including the interventricular and interatrial septum on CCTA exams acquired with ECG-gating. The papillary muscles and the trabeculae of the free right ventricular wall are easily appreciated. The atrioventricular valves may be depicted as thin linear filling defects in normal patients, though this usually necessitates an ECG-gated CCTA exam (Fig. 4).

2.2 Functional Evaluation of the Heart

The functional evaluation of the heart requires a retrospectively ECG-gated exam. The end-diastolic and end-systolic phases are determined and used for evaluation. Image planes are aligned using MPRs similarly to the planes used in echocardiography to acquire the standard planar and volumetric measurements. Alternatively, dedicated software may aid in autocontouring and obtaining the measurements needed for evaluation. These software applications are currently only available for human applications, recognition of the slightly differing anatomy of the veterinary patients may need to be tested.

For the volumetric measurements, usually the short axis plane is used generated via an MPR; regions of interest can be (semi)automatically or manually drawn

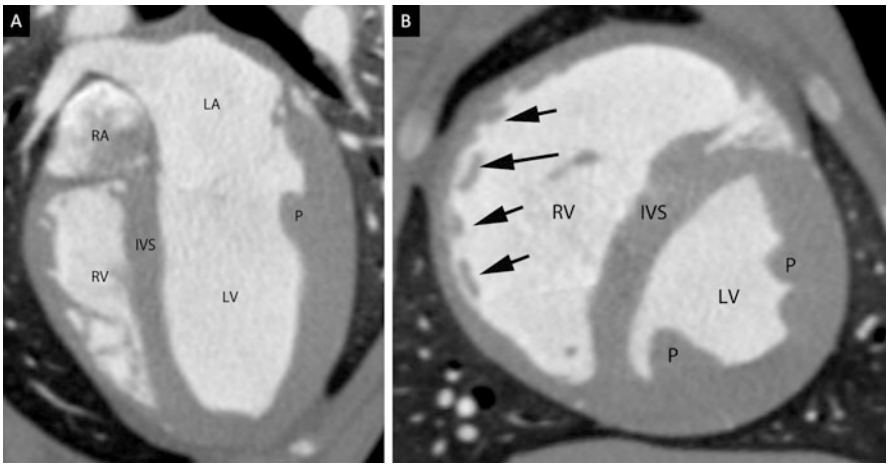

Fig. 4 ECG-gated exam of the heart shown in the diastolic phase in transverse (**a**) and short axis plane (**b**). The chambers of the heart as well as the cardiac muscle are easily evaluated: right atrium (RA), right ventricle (RV), left atrium (LA), left ventricle (LV), interventricular septum (IVS), papillary muscle (P), trabeculae of the right ventricular wall (*arrow heads*)

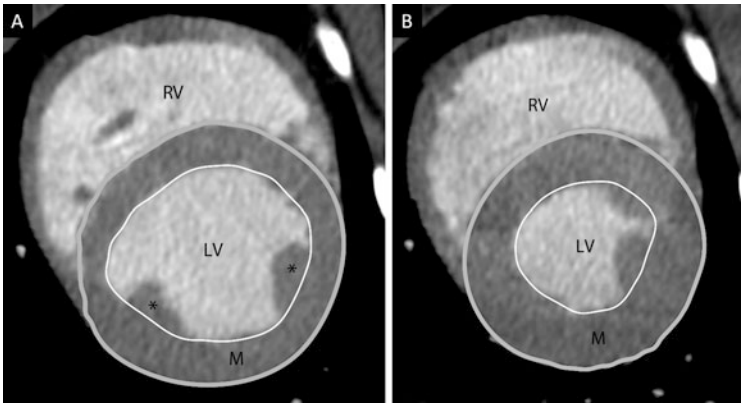

Fig. 5 For volumetric evaluation of the left ventricle (LV), a short axis plane is reconstructed, and the endocardial (*thin white line*) and epicardial (*thick light gray line*) border are traced in end diastole (**a**) and (**b**) on all images including the left ventricle from the cardiac apex to the annulus. The created volume volumes are further used to calculate the left ventricular functional volumetric parameters. The papillary muscles are included in the ventricular volume in this example. Right ventricle (RV), myocardium (M), papillary muscles (*asterisk*)

along the endocardial and epicardial border of the left ventricle including the cardiac apex to the level of the annulus. Where greater than 25% of the annulus is located in the imaging plane, the basal border of the ventricle is drawn, and images with >25% annulus in the imaging plane are excluded from the analysis. The papillary muscles can be included or excluded in the ventricular volume, though no consensus has been reached for the evaluation in dogs or cats (Fig. 5).

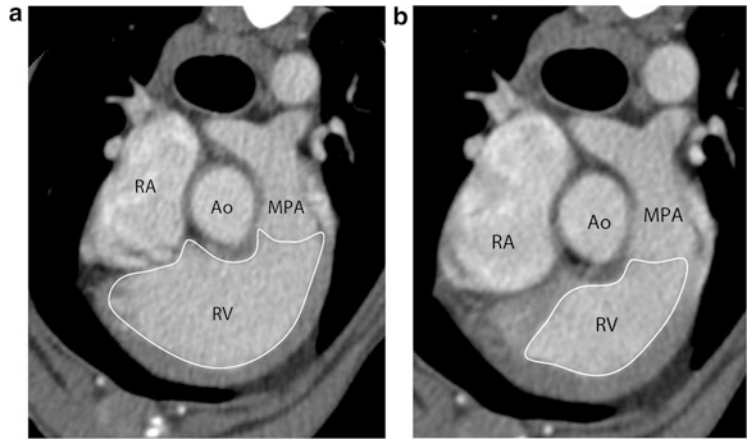

Fig. 6 For volumetric evaluation of the right ventricle (RV), the transverse plane images are commonly used. Using the tricuspid and pulmonic annulus as borders, the endocardial margin of the right ventricle is traced (*white line*) in diastole (**a**) and systole (**b**) on all images showing the right ventricle. The created volumes are used to calculate the functional volumetric right ventricular parameters. Right atrium (RA), main pulmonary artery (MPA), aorta (Ao)

For the right ventricle, transverse plane images are considered more consistent compared to the short axis plane for manual or (semi)automated placing of the regions of interest along the endocardial borders of the right ventricle. The tricuspid and pulmonic annulus mark the borders of the ventricular volume included in the analysis. Papillary muscles and trabeculae can be included with the ventricular volume for consistency (Fig. 6). The endocardial surface of the right ventricle is more irregular than the left and slightly more difficult to trace.

The following volumetric variables can be calculated form the regions of interest placed using the Simpson method:

- Left ventricular end-diastolic and end-systolic volume (LVEDV and LVESV)
- Left ventricular end-diastolic and end-systolic epicardial volume (epiEDV and epiESV)
- Left ventricular stroke volume (LVSV = LVEDV − LVESV)
- Left ventricular ejection fraction (LVEF % = LVSV/LVEDV × 100).

- Right ventricular end-diastolic volume (RVEDV)
- Right ventricular end-systolic volume (RVESV)
- Right ventricular stroke volume (RVSV = RVEDV − RVESV)
- Right ventricular ejection fraction (RVEF % = RVSV/RVESV × 100)

To verify alignment of the regions of interest drawn between the end-systolic and end-diastolic phase, usually maximally 5–10% variability between the measurements for left ventricular end-diastolic and end-systolic myocardial mass (LVmassD and LVmassS) is acceptable within one patient.

For the planar measurement several different imaging planes are generated as MPRs used in end diastole or end systole.

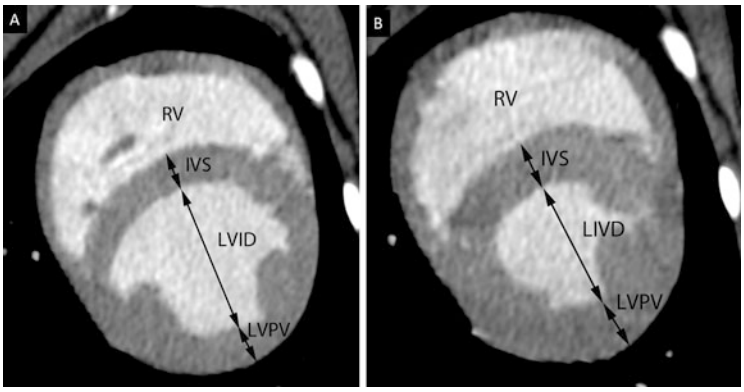

Fig. 7 The short axis view of the left ventricle (LV) is used in diastole (**a**) and systole (**b**) to measure the interventricular septum thickness, left ventricular internal diameter (LVID), and left ventricular posterior wall thickness (LVPW). Right ventricle (RV)

The short axis view, that is aligned similar to the right parasternal short axis view as utilized in echocardiography, is used to measure following parameters (Fig. 7).

- End-diastolic and end-systolic interventricular wall thickness (IVSd, IVSd)
- End-diastolic and end-systolic left ventricular posterior wall thickness (LVPWd, LVPWs)
- End-diastolic and end-systolic left ventricular internal diameter (LVIDd, LVIDs)

Fractional shortening (FS%) is calculated from these variables: $FS = [LVIDd - LVIDs])/LVIDd \times 100$.

The approximate three-chamber view, aligned similar to the parasternal long axis view utilized in echocardiography, is used to measure the end-systolic left atrial diameter and aortic annulus diameter just prior to opening of the mitral valves and while the aortic valves are open and to measure the end-diastolic mitral annulus diameter while the mitral valves are open. The left atrium diameter can also be measured using a short axis plane at the level of the aortic cusps (Fig. 8). The left atrium/aorta ratio (La/Ao ratio) is calculated from these variables.

The approximate four-chamber view can be used to measure the mitral annulus in a further plane (Fig. 9).

2.3 The Coronary Vessels

The aortic cusps can usually be seen on ECG-gated CCTA exams as small linear filling defects in at the base of the aorta (Fig. 10). The left coronary artery (LCA) arises from the left side of the base of the aorta, just downstream to the left semilunar valve (Fig. 11). The left coronary artery is a very short vessel that immediately branches into the left septal (LS), paraconal interventricular (LPIV),

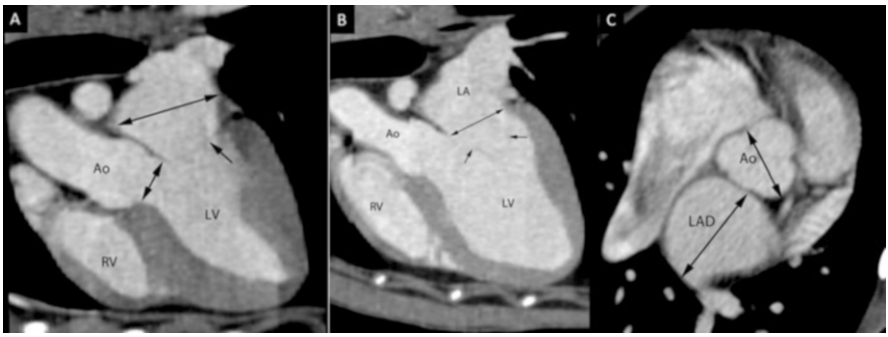

Fig. 8 The approximate three-chamber view (**a**) in end systole is used to measure the aortic annulus (*small double-headed arrow*) and the left atrial diameter (*long double-headed arrow*, **a**), while the mitral valves (*arrow*) are closed. The same view is used in end diastole (**b**) to measure the mitral annulus (*double-headed arrow*, **b**), while the mitral valves (*arrows*) are open. The left atrial diameter (LAD, **c**) can also be estimated using a short axis plane (**c**) at the level of the root of the aorta (Ao), aligned similar to the right parasternal short axis view used in echocardiography, determining the LA:Ao ratio. Right ventricle (RV)

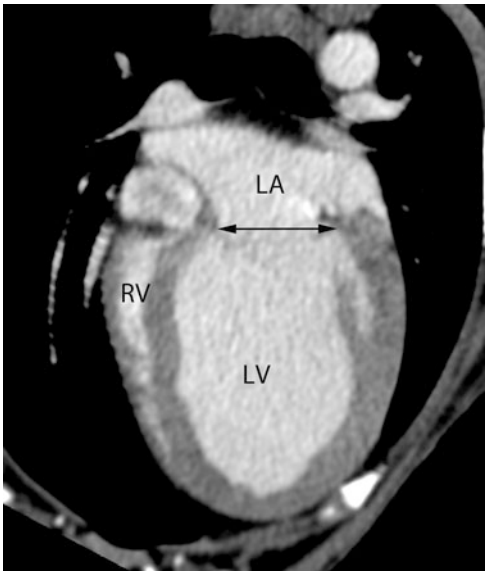

Fig. 9 The approximate four-chamber view can be used to obtain the mitral annulus diameter (*double-headed arrow*) in an additional plane. Right ventricle (RV), left atrium (LA), left ventricle (LV)

and circumflex (LCX) branch. A distinct left coronary artery is not seen in all dogs, the CCTA anatomy has not been determined in cats to date. The septal branch is commonly the smallest branch in dogs that dives into the septum shortly after its origin. It may be of variable origin, for example, origin directly of the aorta or one of the other left coronary artery branches have been reported. The paraconal

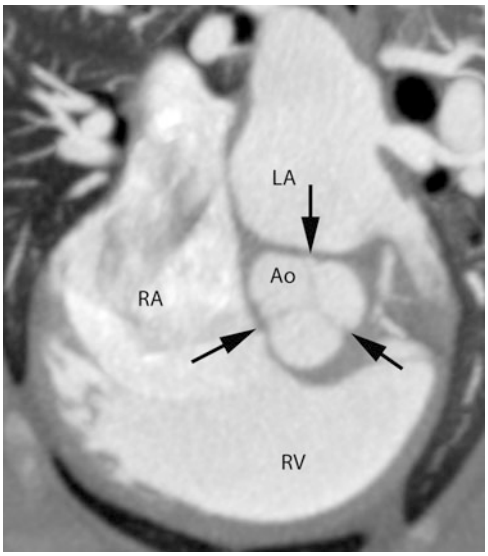

Fig. 10 Oblique short axis plane of the heart to display the base of the aorta (Ao), showing the aortic cusps (*arrows*) as small filling defects. Right atrium (RA), right ventricle (RV), left atrium (LA)

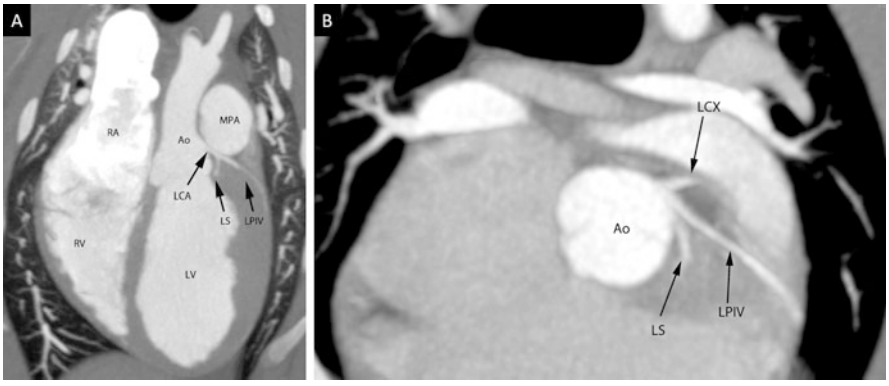

Fig. 11 Oblique transverse plane of the left ventricular outflow tract (**a**) of a dog showing the left coronary artery (LCA) arising just proximal to the left semilunar valve. The left paraconal interventricular (LPIV) and the small left septal (LS) branch can be seen. Left ventricle (LV), aorta (Ao), right atrium (RA), right ventricle (RV), main pulmonary artery (MPA). The oblique short axis plane (**b**) shows all three branches of the left coronary artery; in this dog the main coronary artery was not seen as a distinct vessel. A MIP has been applied to highlight the small coronary vessels. Aorta (Ao), left septal branch (LS), left paraconal interventricular branch (LPIV), left circumflex (LCX) branch

interventricular branch runs initially fairly straight ventrally before it turns along the interventricular grove. It can usually be followed to the apical region. The circumflex branch is often of similar size as the LPIV and turns immediately caudally from its origin to follow the coronary grove. It can often be traced to the

Fig. 12 The right coronary artery (RCA) braches from the cranial aspect of the aorta (Ao) just proximal to the right semilunar valve and can be seen in the coronary grove. Right atrium (RA), right ventricle (RV)

right side of the heart. Especially from the LPIV and LCX smaller diverging coronary artery branches may be seen.

The right coronary artery branches from the cranial aspect of the aorta just downstream to the right semilunar valve (Fig. 12). The vessel is smaller than the LCA and similar or slightly smaller compared to the LPIV and LCX. It curves to the right and cranioventrally along the coronary grove.

Evaluation of the coronary arteries is usually best performed in the mid to late diastolic period (70–95% interval) since the motion of the heart is least and the vessels are well perfused at the time. The CCTA appearance of coronary arteries in cats has not been described at this time.

The cardiac veins have not been specifically described using CCTA in dogs or cats, though the coronary sinus is easily seen ventrally and parallel to the LCX branch in the coronary grove.

3 Heart Diseases

3.1 Congenital Cardiac Defects

A variety of congenital defects can be present and be further evaluated using CCTA exams. Depending on their physiological effect, these may also be detected as additional findings especially when evaluating breeds prone to congenital cardiac alterations such as the brachycephalic population.

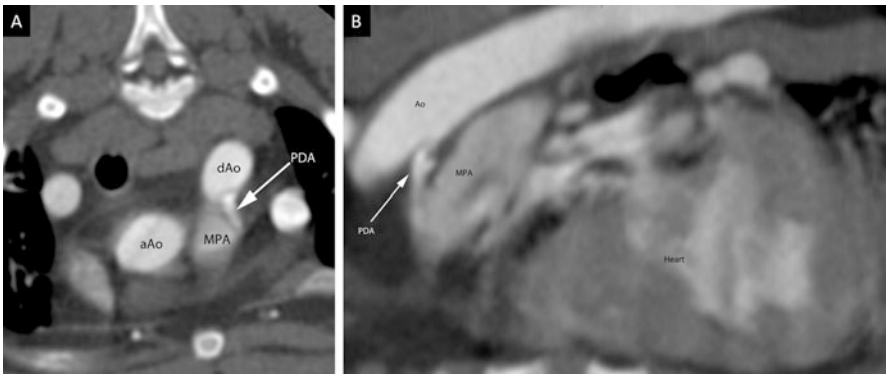

Fig. 13 A very small persistent ductus arteriosus (PDA) connects the descending aorta (dAo) to the main pulmonary artery (MPA) in a 9-month-old Labrador, shown in transverse (**a**) and sagittal (**b**) plane and 3D rendering (**c**) of a non-ECG gated CCTA exam. Ascending aorta (aAo)

Persistent Ductus Arteriosus (PDA)

The PDA represents a short vessel connecting the pulmonary artery to the aorta which fails to close at birth (Fig. 13). Shunting occurs usually from left to right along the pressure gradient between aorta and pulmonary artery and causes volume overload in the pulmonary circulation that may lead to left atrial enlargement and left heart failure. In addition, the turbulences caused at the site of the shunting vessel may produce characteristic dilations in the pulmonary artery and aorta. Right to left shunting occurs in case of reverse of the pressure gradient, which may be given in the case of primary pulmonary hypertension or further complex cardiac defects. The shunting vessel and the focal bulges in the pulmonary artery and aorta are usually seen also on non-ECG gated exams, since there is limited motion due to the heart in this region. Lobar pulmonary arterial and venous dilation has not been specifically described using CCTA.

Pulmonic Stenosis PS

Pulmonic stenosis at the valvular, sub-, or supravalvular level will introduce secondary right- ventricular hypertrophy that may be appreciated on CCTA exams, though ECG-gated CCTA exams are needed for exact analysis. The area of stenosis may be seen on the ECG-gated CCTA exam, though exact determination of the level of the stenosis with regards to the valvular level may be challenging since the valves cannot be always clearly distinguished, different to the echocardiographic exam. The post stenotic bulge in the pulmonary artery is easily appreciated also on exams performed without ECG-gating.

Aortic Stenosis AS

Aortic stenosis can also be seen at the valvular, sub-, supravalvular level, and secondary left ventricular hypertrophy will develop depending on the severity of the stenosis. An ECG-gated CCTA exam is needed for determination of ventricular

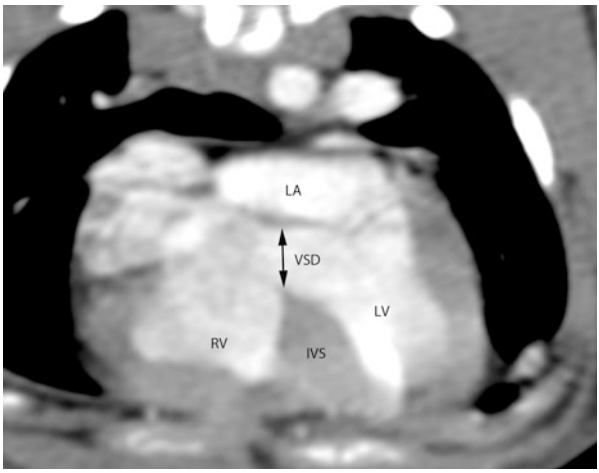

Fig. 14 Ventricular septal defect (VSD) in the perimembranous region of the interventricular septum in a dog. The exam was acquired using a 16MDCT unit without ECG-gating; therefore, the anatomy is slightly blurred, though the defect can be depicted. Left atrium (LA), left ventricle (LV), right ventricle (RV), interventricular septum (IVS)

functional and planar variables. The post stenotic bulge in the aorta is easily appreciated also on non-ECG-gated exams; detecting the exact location of the level of the stenosis with regards to the valvular level may be difficult since the valves may not be clearly depticted as seen on on the echocardiography exam; though an ECG-gated exam will be helpful to delineate the regional anatomy.

Ventricular Septal Defects VSD

Ventricular septal defects are most commonly found in the perimembranous region of the interventricular septum, adjacent to the right and noncoronary aortic valve cusps and the cranioseptal tricuspid valve commissure (Fig. 14). Further locations along the muscular wall or just beneath the aortic and pulmonic valve may be seen. Especially for small defects, a levophase exam may be essential to demonstrate shunting of contrast medium into the non-contrast filled right side of the heart. While defects may be visilbe on a non-ECG-gated exam, exact anatomical delineation is desirable using an ECG-gated CCTA exam. Secondary changes to the right ventricular volume and pulmonary arteries due to volume overload in case of left-to-right shunting may be detected using ECG-gated CCTA exams.

Atrial Septal Defects ASD

Atrial septal defects may be of limited clinical significance depending on the size and shunt direction and can occasionally even be detected incidentally non-ECG gated on CCTA exams.

Tetralogy of Fallot TOF

Tetralogy of Fallot presents a combination of defects: pulmonic stenosis and secondary right ventricular hypertrophy, ventricular septal defect, and variable transposition of the aorta, leading to decreased blood flow to the lungs secondary cyanotic symptoms. ECG-gated CCTA exams are most helpful to outline and quantify the given alterations to the cardiac function and anatomy.

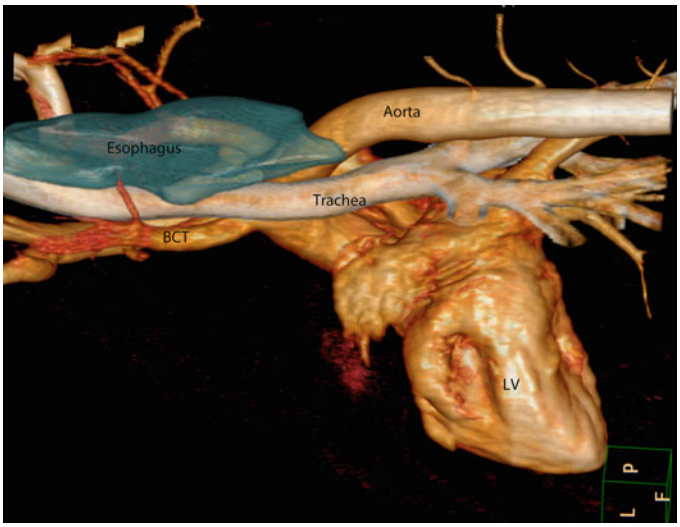

Fig. 15 3D rendering of the triple-rule-out exam of a patient with a persistent right aortic arch, viewed from the *left*. The dilated esophagus cranial to the stenosis is displayed in *light blue*

Ring Anomalies

Persistent right aortic arch is the most common ring anomaly seen; the right aortic arch passes dorsal to the esophagus and trachea and causes a focal esophageal stenosis that is clinically represented with regurgitation and difficulties in swallowing (Fig. 15). CCTA exams are helpful to determine the vessels and structures involved, and non-ECG-gated exams can be quite helpful here since there is limited influence due to cardiac motion in this region.

AV Valvular Dysplasia or Stenosis

Valvular dysplasias are characterized by insufficient ability of closure between the atrium and ventricle allowing regurgitation of blood from the ventricle to the atrium, whereas stenotic valvulopathies obstruct blood flow from the atrium into the ventricle. Unless there is thickening of the valves or a ring constriction is present, the valvular changes may be difficult to specifically detect on the CCTA exam. Secondary changes of atrial enlargement and venous congestion may be appreciated.

Cor Triatriatum Dexter

A fibrous membrane is dividing the right atrium into two chambers, where the proximal chamber receives venous blood from the cranial and caudal vena cava and the distal chamber connects to the atrioventricular junction and the tricuspid valve. Depending on the perforation of the membrane, congestive heart failure may occur. The atrial enlargement may be well depicted whereas the membrane can be very small and difficult to spot on CCTA exams. ECG-gated exams are preferred for evaluation of this condition.

3.2 Coronary Arteries

3.2.1 Aberrant Coronary Artery Anatomy

Aberrant coronary artery anatomy may become clinically significant especially if entrapment of other vessels occurs. This is most commonly seen with the R2A type aberrant coronary artery, where the left and right coronary artery arise from a common trunk at the right aortic sinus and the left coronary artery wraps cranially around the pulmonary artery (Fig. 16). This can be seen in combination with pulmonic stenosis and needs to be taken into consideration when attempting balloon dilation of PS. Though small, the proximal portion of the coronary arteries can be depicted using non-ECG-gated studies, though ECG-gated studies are preferred for evaluation.

3.2.2 Stensosis of Coronary Arteries

Stenotic disease of coronary vessels has to date not been evaluated using CCTA in veterinary patients.

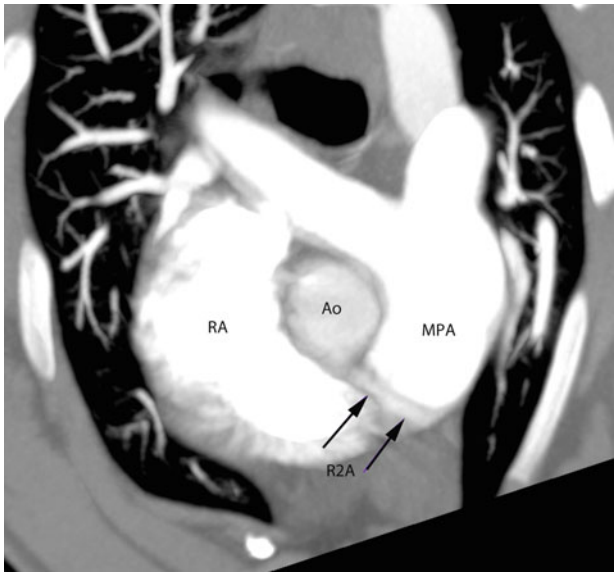

Fig. 16 Six-month-old bulldog puppy with pulmonic stenosis and an aberrant coronary artery cranially wrapping around the main pulmonary artery, R2A conformation. The example shown was acquired on a 16MDCT unit without ECG-cardiac gating. Aorta (Ao), main pulmonary artery (MPA), right atrium (RA)

3.3 Pericardial Effusion

A CCTA study is not necessarily required to determine the presence of pericardial effusion, the pericardial space is to be evaluated on any cardiac exam. Pericardial fluid is usually slightly hypoattenuating to the myocardium; this is better distinguished on post-contrast exams (Fig. 17). The pericardial sac may show mild thickening or contrast enhancement depending on the duration and nature of the effusion.

3.4 Cardiac or Heart Base Neoplasia

Primary cardiac neoplasia is rare, though heart base tumors such as chemodectomas may interfere with the cardiac anatomy and necessitate assessment for possible surgical removal (Fig. 18). An overview can often be gained using non-ECG-gated CCTA studies. Right atrial hemangiosarcomas can be difficult to detect in the curved architecture of the right atrium; differentiating intraluminal lesions from lesions invading the cardiac muscle is very challenging. ECG-gated CCTA studies are preferred in these cases due to the increased anatomical depiction, enabling better diagnostic and planning ability.

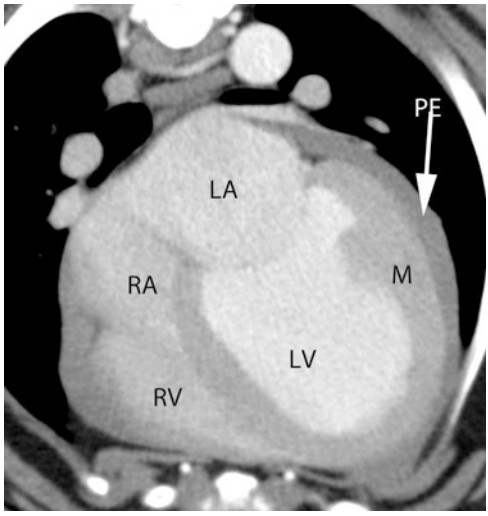

Fig. 17 Pericardial effusion (PE) in a 13-year-old collie with heart base tumor (not depicted). The pericardial fluid is slightly hypoattenuating compared to the myocardium (M). Right atrium (RA), right ventricle (RV), left atrium (LA), left ventricle (LV)

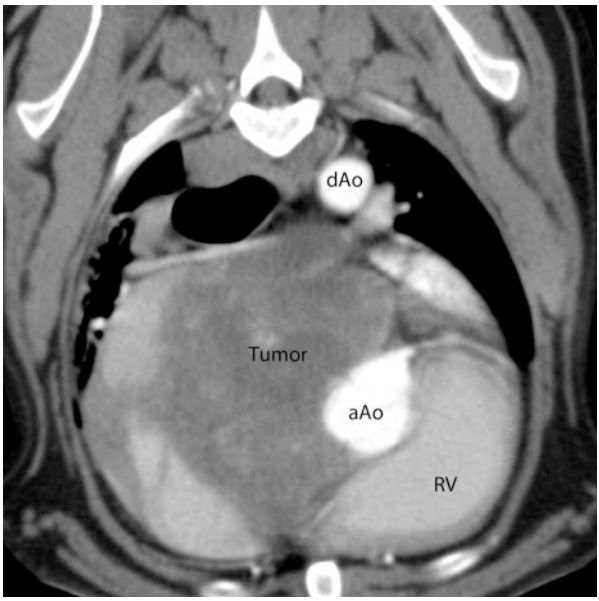

Fig. 18 A large chemodectoma (tumor) was present adjacent to the ascending aorta (aAo), deviating the cardiac anatomy abaxially. Right ventricle (RV), descending aorta (Ao)

Further Reading

Drees R, Frydrychowicz A, Reeder SB, Pinkerton ME, Johnson R. 64-multidetector computed tomographic angiography of the canine coronary arteries. Vet Radiol Ultrasound. 2011;52 (5):507–15.

Drees R, François CJ, Saunders JH. Invited review-Computed tomographic angiography (CTA) of the thoracic cardiovascular system in companion animals. Vet Radiol Ultrasound. 2014;55 (3):229–40.

Drees R, Johnson RA, Pinkerton M, Del Rio AM, Saunders JH, François CJ. Effects of two different anesthetic protocols on 64-MDCT coronary angiography in dogs. Vet Radiol Ultrasound. 2015a;56(1):46–54.

Drees R, Johnson RA, Stepien RL, Munoz Del Rio A, Saunders JH, François CJ. Quantitative planar and volumetric cardiac measurements using 64 MDCT and 3T MRI vs. Standard 2d and m-mode echocardiography: does anesthetic protocol matter? Vet Radiol Ultrasound. 2015b;56 (6):638–57.

Laborda-Vidal P, Maddox TW, Navarro-Cubas X, Dukes-McEwan J, McConnell JF. Comparison between echocardiographic and non-ECG-gated CT measurements in dogs. Vet Rec. 2015;176 (13):335.

Park N, Lee M, Lee A, Lee S, Lee S, Song S, Jung J, Eom K. Comparative study of cardiac anatomic measurements obtained by echocardiography and dual-source computed tomography. J Vet Med Sci. 2012;74(12):1597–602.

Rutherford L, Stell A, Smith K, Kulendra N. Hemothorax in three dogs with intrathoracic extracardiac hemangiosarcoma. J Am Anim Hosp Assoc. 2016;52:325–9.

Scollan KF, Bottorff B, Stieger-Vanegas S, Nemanic S, Sisson D. Use of multidetector computed tomography in the assessment of dogs with pericardial effusion. J Vet Intern Med. 2015;29 (1):79–87.

Sieslack AK, Dziallas P, Nolte I, Wefstaedt P. Comparative assessment of left ventricular function variables determined via cardiac computed tomography and cardiac magnetic resonance imaging in dogs. Am J Vet Res. 2013;74(7):990–8.

Sieslack AK, Dziallas P, Nolte I, Wefstaedt P, Hungerbühler SO. Quantification of right ventricular volume in dogs: a comparative study between three-dimensional echocardiography and computed tomography with the reference method magnetic resonance imaging. BMC Vet Res. 2014;10:242.

Cardiac DSCT

Giovanna Bertolini

As described extensively in the first chapter of this book, DSCT is a technology that involves the simultaneous use of two X-ray tubes and two corresponding detector arrays mounted at orthogonal orientations in the gantry. This scanner design significantly improves the hardware-based temporal resolution of the CT system, which is highly relevant in cardiac imaging. Unlike previous generations of MDCT scanners, the temporal resolution in DSCT is independent of the patient's heart rate because data from only a single cardiac cycle contribute to the reconstruction of one image. In most recent DSCT scanners, the temporal resolution has been reduced to 66 ms at 0.25-s rotation time by combining data from the two detectors. Similar temporal resolution values (<100 ms) can be achieved in single-source systems by employing the multisegmental reconstruction technique, in which data from multiple heart cycles contribute to an image. Therefore, the temporal resolution depends strongly on heart rate and rotation time. Combining data from the two measurement systems provides not only high temporal resolution but also very high scan speeds. The maximum pitch for single-source MDCT is usually about 1.5. DSCT can be operated at more than twice this value (3.4 for 128-slice DSCT and 3.2 for 192-slice DSCT, resulting in maximum scan speeds of 458 mm/s and 737 mm/s, respectively; see the section "MCDT Techniques and Technology"). These improvements have a tremendous impact on cardiac CT applications in small animals. Motion artifacts occur frequently in non-ECG-gated cardiac imaging with high heart and respiratory rates. In veterinary patients, slight motion may be acceptable for the visualization of larger lesions, such as heart-base masses, but small anatomical structures such as the coronary arteries may not be visible and small lesions may be missed or misinterpreted. In our experience, cardiac imaging

G. Bertolini (✉)
San Marco Veterinary Clinic, Padua, Italy
e-mail: bertolini@sanmarcovet.it

G. Bertolini (ed.), *Body MDCT in Small Animals*, DOI 10.1007/978-3-319-46904-1_17

with a 64-slice CT or DSCT scanner has adjunctive diagnostic value compared with other techniques (i.e., trans-thoracic and trans-esophageal echocardiography) in small animals. The temporal resolution of earlier technology, such as 16-MDCT scanners, is insufficient (Figs. 1 and 2).

The advanced scanning options of DSCT devices, such as high-pitch scanning and short rotation times, strongly improve the diagnostic value of non-ECG-gated

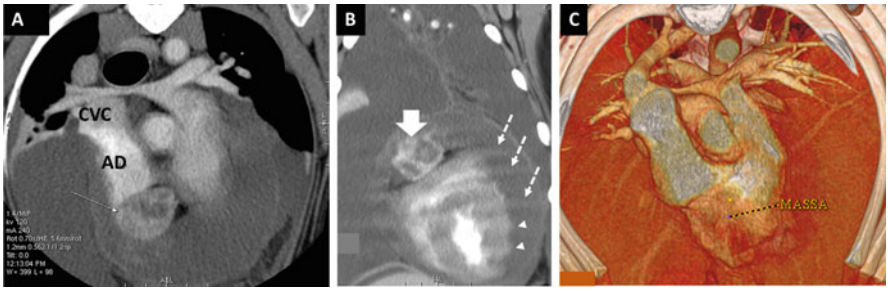

Fig. 1 Non-ECG-gated cardiac evaluation performed with a 16-MDCT scanner (Lightspeed 16; GE Medical Systems) in a boxer with a cardiac mass (hemangiosarcoma) and pericardial and pleural effusion. (**a**) The mass (*arrow*) is well discernible from surrounding fluid and normal tissues. The margins of the cardiac structures, however, are poorly defined. (**b**) On a dorsal MPR, motion artifacts due to the heartbeat are evident (*arrows*) and also affect the ventricular margin (*arrowheads*). *Large arrow* shows the mass. (**c**) VR from the same volume dataset

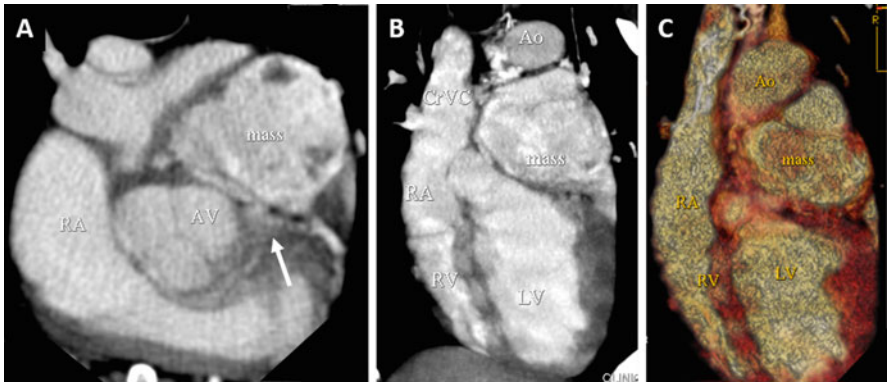

Fig. 2 Non-ECG-gated 16-MDCT examination of a dogue de Bordeaux with a heart-base tumor (chemodectoma). (**a**) Transverse view. (**b**) Dorsal MPR view. (**c**) Volume-rendered segmentation. The mass is easily detected, but several artifacts affect the images and obscure some anatomic details [i.e., the origin and proximal segments of the coronary vessels (*arrow*)]

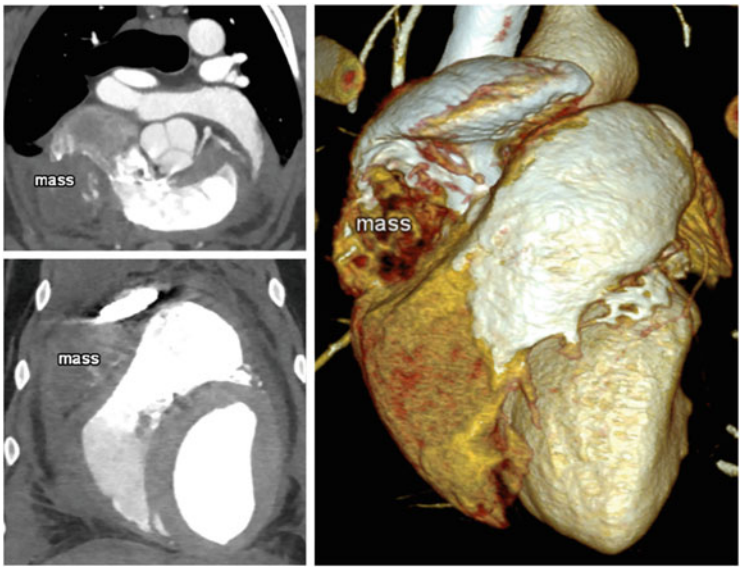

Fig. 3 Non-ECG-gated, 128-DSCT, high-pitch evaluation (Flash mode, Somatom Definition Flash; Siemens Healthcare) for cardiac evaluation and tumor staging in a golden retriever with a right atrial mass and bicavitary effusion (after pericardiocentesis). Motion blurring is minimal. There are few streaking artifacts due to nonuniform contrast enhancement of the right atrium

examinations. Non-ECG-gated acquisition is more rapid than ECG-gated acquisition and thus results in the occurrence of fewer motion artifacts. Using DSCT, a patient's body can be scanned in about 1 s (or less); thus, respiratory artifacts are minimal, even in awake patients (Fig. 3). When greater morphological detail is required (e.g., coronary visualization to search for a possible anatomical variant), or for functional and perfusion cardiac CT studies, ECG-gated protocols are recommended (Fig. 4). DSCT enables more rapid volume coverage in both modes of cardiac imaging: retrospective gating and prospective triggering (see also the chapter "Cardiac MDCT"). At our center, patients are positioned on the CT table in sternal recumbency with ECG leads placed on the paws (Fig. 5). CT protocols differ according to the anatomic structures imaged, the purposes of the study, and the pathology evaluated. CT imaging techniques for congenital heart disease are not the same as those for acquired heart disease, which generally require

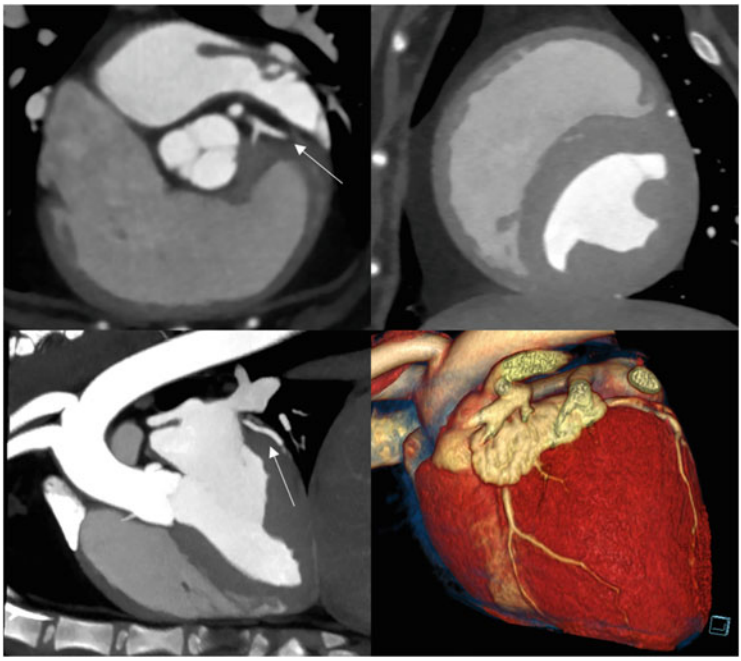

Fig. 4 ECG-gated cardiac 128-DSCT in a normal dog "freezes" the heart (various MPR planes and VR of the volume datasets). The margins of the cardiac chambers are well defined, and the CM is distributed uniformly. The appearance of the anatomy is highly detailed. See, for instance, the well-defined coronary vessels (*arrows*) on a 3D volume-rendered image

combined scans for tumor staging and/or the assessment of concurrent diseases (Figs. 3 and 6).

To date, retrospective ECG-gated cardiac DSCT has been used as a reference-standard modality to compare the CT measurement of left ventricle volume in healthy dogs with that obtained by two echocardiographic methods (the modified Simpson and Teichholz methods). DSCT has been reported to be a highly accurate diagnostic modality for congenital heart diseases in pediatric patients, obviating the need for invasive modalities. Besides its noninvasive nature, DSCT can simul-

Fig. 5 Patient positioning for ECG-gated DSCT. The ECG system is integrated into the CT table and synchronized automatically. ECG data are reported in real time on a monitor at the top of the gantry and simultaneously on the monitor of the CT console (not visible here)

taneously provide detailed anatomic information about the heart and other mediastinal structures, the lungs, and the intraabdominal organs. Similar applications are possible in veterinary patients with congenital cardiac defects (Figs. 7 and 8). At our center, a second-generation DSCT scanner is used to perform retrospective ECG-gated studies in patients with suspected or known cardiac congenital defects for further characterization and pre-interventional planning.

DSCT dramatically improves the feasibility of cardiac CT in veterinary patients and has the potential to significantly impact the diagnosis and management of cardiovascular diseases in the near future.

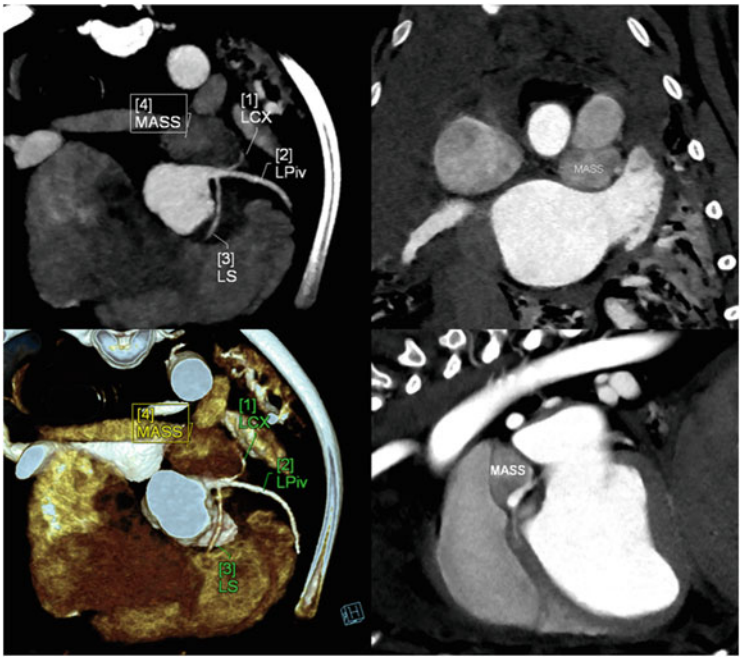

Fig. 6 ECG-gated cardiac 128-DSCT study in a 25-kg Shar Pei with a heart-base tumor and bicavitary effusion (after pericardiocentesis)

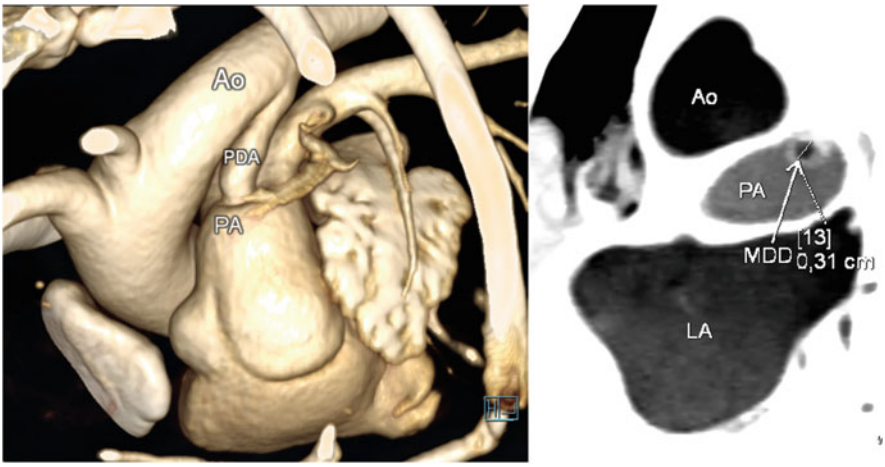

Fig. 7 ECG-gated DSCT cardiac study in a 4-kg Maltese dog with patent ductus arteriosus (PDA). *Ao* aorta, *PA* pulmonary artery

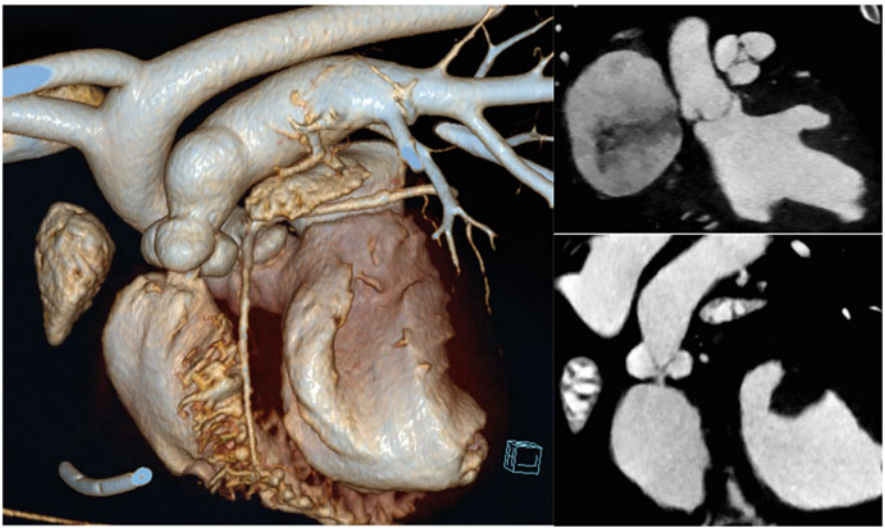

Fig. 8 ECG-gated DSCT cardiac study in a boxer with pulmonary stenosis

Further Readings

Hausmann P, Stenger A, Dittrich S, Cesnjevar R, Rüffer A, Hammon M, Uder M, Rompel O, Glöckler M. Application of dual-source-computed tomography in pediatric cardiology in children within the first year of life. Röfo. 2016;188(2):179–87. doi:10.1055/s-0041-108912.

Ihlenburg S, Rompel O, Rueffer A, Purbojo A, Cesnjevar R, Dittrich S, Gloeckler M. Dual source computed tomography in patients with congenital heart disease. Thorac Cardiovasc Surg. 2014;62(3):203–10. doi:10.1055/s-0033-1349791.

Lee M, Park N, Lee S, Lee A, Jung J, Kim Y, Ko S, Kim H, Jeong S, Eom K. Comparison of echocardiography with dual-source computed tomography for assessment of left ventricular volume in healthy Beagles. Am J Vet Res. 2013;74(1):62–9. doi:10.2460/ajvr.74.1.62.

Nakagawa M, Ozawa Y, Nomura N, Inukai S, Tsubokura S, Sakurai K, Shimohira M, Ogawa M, Shibamoto Y. Utility of dual source CT with ECG-triggered high-pitch spiral acquisition (Flash Spiral Cardio mode) to evaluate morphological features of ventricles in children with complex congenital heart defects. Jpn J Radiol. 2016;34(4):284–91. doi:10.1007/s11604-016-0522-x.

Sedaghat F, Pouraliakbar H, Motevalli M, Karimi MA, Armand S. Comparison of diagnostic accuracy of dual-source CT and conventional angiography in detecting congenital heart diseases. Pol J Radiol. 2014;79:164–8. doi:10.12659/PJR.890732.

Sun Z, Xu W, Huang S, Chen Y, Guo X, Shi Z. Dual-source computed tomography evaluation of children with congenital pulmonary valve stenosis. Iran J Radiol. 2016;13(2):e34399.

Part VI
The Endocrine System

MDCT of Hyperadrenocorticism

Giovanna Bertolini

1 Introduction

Hyperadrenocorticism (HAC) or Cushing syndrome is a complex endocrine syndrome in dogs, which occurs in subjects chronically exposed to inappropriately high levels of cortisol. HAC has two major forms: (1) adrenocorticotropic-dependent hyperadrenocorticism (ADHAC), associated with pituitary tumors [also known as pituitary-dependent hyperadrenocorticism (PDH) or Cushing disease] or, rarely, caused by the ectopic secretion of adrenocorticotropic hormone (ACTH), and (2) adrenocorticotropic-independent hyperadrenocorticism (AIHAC), triggered mostly by adrenocortical tumors, adenoma, and carcinoma and, rarely, by ectopic hormone receptors. Accurate differentiation between ADHAC and AIHAC is of great importance because treatment options and prognoses differ. Spontaneous HAC is rare in cats; fewer than 100 cases have been described in the peer-reviewed veterinary literature. Description of CT features of HAC in cats is limited to pituitary assessment in seven cases.

The suspicion of such a complex endocrine disorder is based on the patient's history, clinical signs, and laboratory results. However, direct depiction of changes in the involved anatomical structures is essential for the final diagnosis or exclusion of HAC. MDCT offers unparalleled opportunities for the simultaneous assessment of the hypophysis and adrenal glands. Moreover, MDCT may help to disclose an ectopic tumor secreting ACTH and is essential for the evaluation of complications related to endocrine syndrome, such as thrombosis, vascular invasion, adrenal mass rupture, steroid-induced hepatopathy, and intracranial complications (stroke, pituitary apoplexy, brain compression by a large pituitary tumor).

G. Bertolini (✉)
San Marco Veterinary Clinic, Padua, Italy
e-mail: bertolini@sanmarcovet.it

G. Bertolini (ed.), *Body MDCT in Small Animals*, DOI 10.1007/978-3-319-46904-1_18

2 MDCT Imaging Strategies

The scan protocol for HAC should include at minimum the evaluation of the neurocranium and abdomen, for simultaneous assessment of the pituitary and adrenal glands. When a secreting adrenal gland tumor is suspected, additional thoracic scans are recommended for staging.

When designing the MDCT examination protocol, one should prioritize the suspected tumor site, based on previous clinical evaluation and abdominal ultrasound examination. Strategies for the acquisition of high-quality contrast-enhanced images of the whole body using a single CM injection include the following: (1) In the case of suspected PDH, examination of the neurocranium must be prioritized. At our center, the HAC protocol includes unenhanced scanning of the neurocranium, which is essential for the evaluation of possible tumor mineralization or hemorrhage. Immediately after CM injection, we obtain an early enhanced series of the brain and then perform a whole-body scan. A late brain series is also performed. This four-series MDCT protocol enables the acquisition of images with great diagnostic value for the optimal evaluation of the pituitary gland during early and late enhancement. (2) In the case of a suspected or known adrenal mass, the abdomen must be prioritized. After unenhanced scanning of the adrenal region, dual- or tri-phase examination of the abdomen is advisable for evaluation of the characteristics of the mass and possible vascular or tissue invasion. This information is essential for surgical planning and prognosis. The thorax should be scanned early after CM injection for the assessment of possible lung metastasis and pulmonary thromboembolism, which cannot be detected in a late phase. Inclusion of the thorax in the first phase of the dual-phase examination may be an option. Due to the tube heating that occurs with some MDCT scanners (those with 4, 8, and 16 rows), the thorax and cranial and mid-abdominal regions (obviously including the renal-adrenal region) could be included, with the portal phase including the whole abdomen, when the acquisition of only a single vascular phase is possible due to scanner limitations or, for another reason, a single hepatic venous phase is preferred, as it can provide information about the vascular invasion of the phrenico-abdominal region, renal vein, and/or caudal vena cava. These compromises are not necessary when using a more advanced scanner ($\geq$64 rows). Our center currently has a second-generation DSCT scanner, which enables the acquisition of two vascular phases of the neurocranium and thorax and tri-phase scanning of the abdomen using a single CM injection.

The analysis of MDCT images of a patient with HAC should systematically include: (1) evaluation of the appearance of the involved glands (pituitary and adrenal), (2) estimation of the gland dimensions (pituitary/brain ratio, 2D or volumetric measurement of the adrenal glands), (3) evaluation of the pattern of enhancement (pituitary flush; vascularity and enhancement in adrenal masses), (4) assessment of local tumor invasion (vascular and tissue invasion in pituitary and adrenal tumors), and (5) assessment of secondary lesions of HAC in other

organs (e.g., steroid-induced hepatopathy, adrenal mass rupture, thromboembolism, and pituitary apoplexy).

3 MDCT of Pituitary-Dependent Hyperadrenocorticism

Dogs with PDH usually present bilateral and symmetrical enlargement of the adrenal glands, due to chronic exposure to high levels of ACTH from the pituitary gland. CT is traditionally used to evaluate the pituitary gland in canine PDH. Evaluation of the neurocranium is beyond the scope of this book and thus is not treated in depth here. Pituitary micro- and macroadenomas, as well as possible intracranial complications, can be detected easily on MDCT images (Fig. 1).

Studies conducted in our center using a 16-MDCT scanner have involved CT-based quantification of the adrenal glands in normal dogs and those with PDH. *CT attenuation values* of glands were measured by placing circular/ovoid ROIs on unenhanced images of all glands. The ROIs included one-half to two-thirds of the area of the adrenal gland, excluding the gland edges, to minimize partial volume effects and to exclude adjacent periadrenal fat (Fig. 2). The mean (±standard deviation) unenhanced attenuation values of the left and right adrenal glands in normal dogs were 36.0 ± 5.3 HU (range, 22.0–42.0 HU) and 34.3 ± 7.0 HU (range, 20.4–48.6 HU), respectively. The mean attenuation values of the left and right adrenal gland in dogs with HAC were 33 ± 9.1 and 33 ± 8.0 HU, respectively. These studies showed an overlap of adrenal gland attenuation values

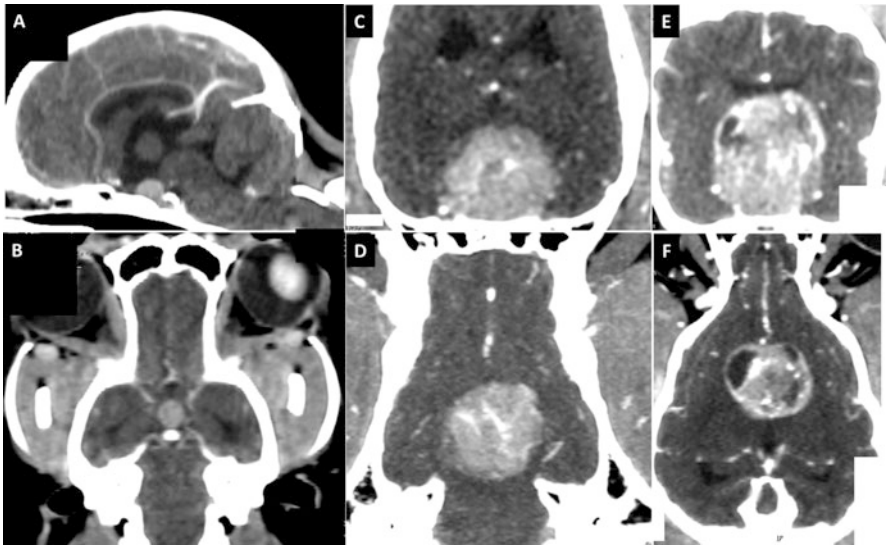

Fig. 1 Sagittal and dorsal MPR views of the brain in dogs with PDH. (**a**, **b**) Pituitary microadenoma (noninvasive). (**c**, **d**) Invasive pituitary adenoma. (**e**, **f**) Pituitary adenocarcinoma

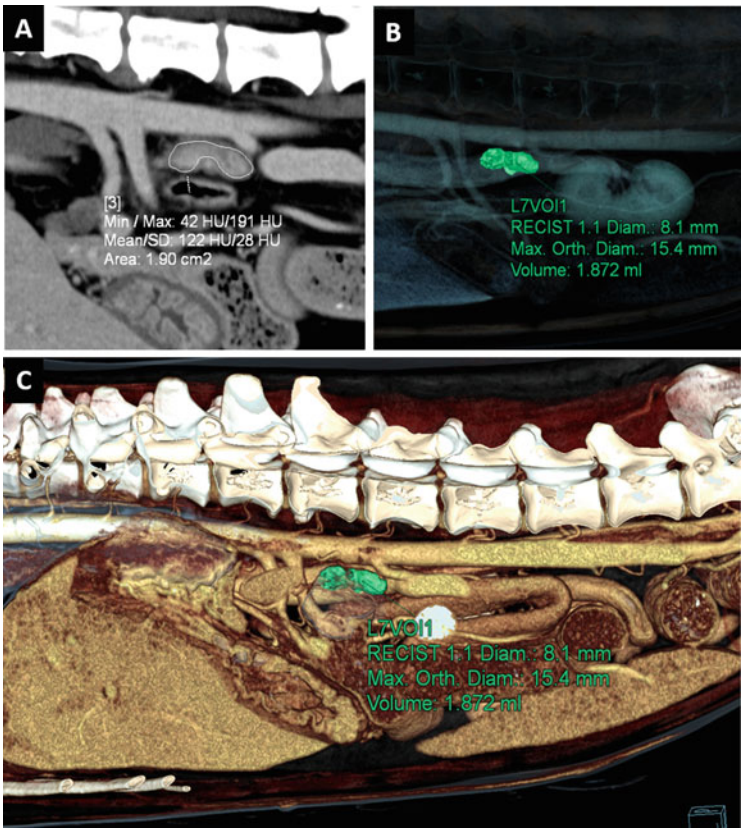

Fig. 2 Adrenal gland CT quantification. (**a**) Measurement of the attenuation value. The ROI is placed manually in the sagittal plane over the left adrenal gland, avoiding inclusion of the phrenico-abdominal vein. The software calculates the attenuation value of each voxel within the selected area and gives mean, minimum, and maximum values and a standard deviation. The latter reflects tissue homogeneity. (**b**) Results from adrenal volume measurement using an automatic software technique based on Response Evaluation Criteria in Solid Tumors 1.1. (**c**) VR showing the measured gland in its normal site

between normal dogs and dogs with PDH, which prevents differentiation of normal and affected dogs using adrenal attenuation values. However, when measuring X-ray attenuation, the equipment's software automatically calculates the attenuation value of each voxel within an ROI and displays the mean and standard deviation, with the standard deviation reflecting the degree of homogeneity within the ROI. The differences in standard deviation between the normal and affected populations may reflect differences in adrenal tissue homogeneity.

2D or 3D measurement using MDCT technology has been proposed for the determination of adrenal gland size. Transverse images alone may lead to miscalculations of maximum diameter and length of the glands. Instead, MPRs from near-isotropic or isotropic data allow optimal visualization of the glands and more

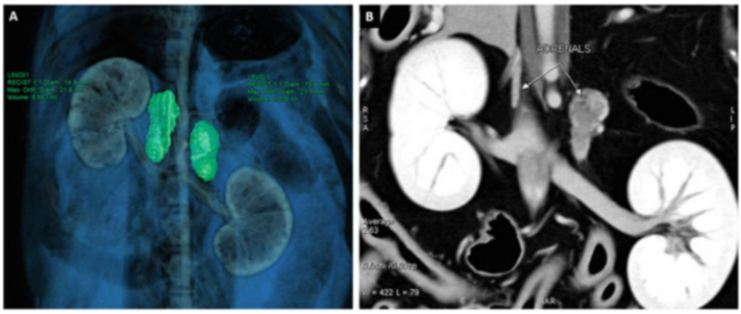

Fig. 3 (**a**) Symmetrical adrenal gland enlargement in a dog with PDH. (**b**) Adrenal gland asymmetry

accurate 2D measurements (Fig. 2b, c). The adrenal volume is usually larger in dogs with HAC than in normal dogs. The mean CT volumes of the left and right adrenal glands in normal dogs, as determined in a study we conducted at our center, were 0.60 (0.20–0.95) cm^3 and 0.55 (0.22–1.01) cm^3, respectively. In another study, we determined that the mean CT volumes of the adrenal gland in dogs with HAC were 1.60 cm^3 (0.35–2.85) in patients with microadenoma and 2.88 cm^3 (1.2–4.48) in those with macroadenoma. Symmetrical enlargement of the adrenal glands is traditionally considered to constitute evidence of ADHAC, whereas asymmetry is considered to suggest AIHAC (Fig. 3). However, MDCT studies (and those using other imaging modalities) published to date have shown consistent overlap in the 2D and 3D dimensions of these glands between the two forms of HAC.

A study conducted over 64 dogs tested the performance of maximum diameter CT measurements and derived ratios using both cross-sectional and reformatted images for distinguishing between AIHAC and ADHAC. Maximum adrenal gland diameter ratio appeared to be the most useful parameter (rather than the absolute size of the glands), particularly when this ratio was calculated from reformatted images. An adrenal diameter ratio on reformatted images >2.08 is highly suggestive of AIHAC.

4 MDCT of Secreting Adrenocortical Tumors

Primary adrenocortical neoplasms producing cortisol cause signs of pituitary-independent HAC in dogs. Adrenal adenoma and adenocarcinoma occur with similar frequencies. Although some CT signs may reflect their biological behavior and pathological characteristics, CT alone cannot be used to distinguish adrenal tumor type. A mass with a regular shape, no invasion of the adjacent tissues or vessels, and thin peripheral enhancement after CM injection is suggestive of benign behavior. An irregularly shaped mass with an inhomogeneous appearance and multiple hypo- or hypervascular foci is more likely to be malignant. Importantly,

MDCT and surgical features of these masses show excellent agreement. Thin-section volume data acquired in an appropriate vascular venous phase are necessary to distinguish the early signs of venous adhesion and wall invasion (Fig. 4). Thin-section transverse images and 3D volume-rendered images are helpful in distinguishing the loss of the thin adipose cleavage plane between the neoplasm and the vessel and irregular vascular wall surfaces, respectively. Invasion of the caudal vena cava and/or renal veins may be due to intravascular migration of the neoplasia through the phrenico-abdominal vein or directly by the mass through the vascular wall. On post-contrast images, an inhomogeneously enhanced endoluminal tumor thrombus can be distinguished from a hematic thrombus, which does not enhance (Figs. 5 and 6). Invasion of other adjacent tissues (hypaxial and epaxial muscles or diaphragmatic pillars) can be detected easily on MDCT.

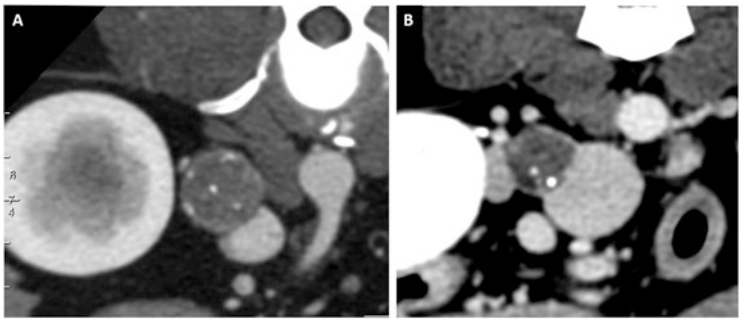

Fig. 4 (**a**) Noninvasive adrenal tumor. Note some mineralization within the mass. The caudal vena cava is compressed but not invaded. Note the loss of the thin adipose cleavage plane between the neoplasm and the vessel (*arrow*). (**b**) Adrenal tumor with vascular wall invasion. Note the mineralization within the mass

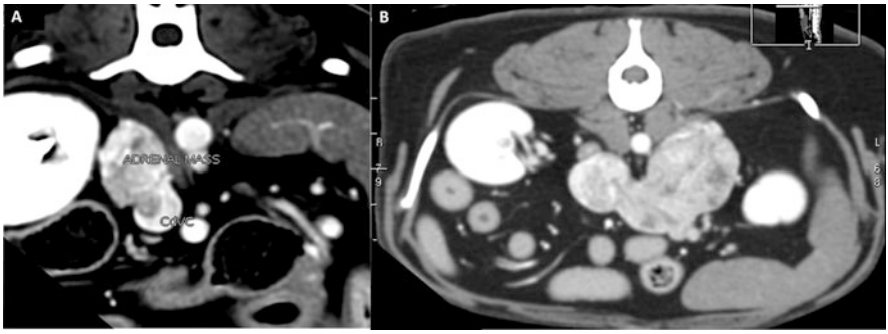

Fig. 5 (**a**) Right adrenal mass with caudal vena cava invasion. (**b**) Left adrenal mass invading the caudal vena cava. In both cases, cava invasion is through the phrenico-abdominal veins

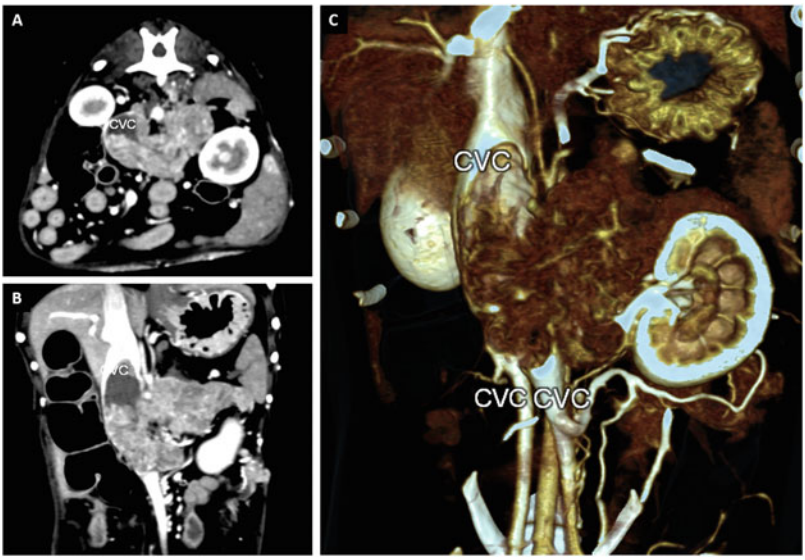

Fig. 6 (**a**) Transverse view of an invasive left adrenal mass. (**b**) Dorsal view. The mass invades the caudal vena cava through the phrenico-abdominal vein. The endoluminal tumor thrombus can be easily distinguished from a hematic, non-enhancing thrombus. (**c**) VR showing the mass extending into the caudal vena cava and left renal vein. The mass also extends dorsally and laterally through the cranial abdominal vein. Note the duplication of the caudal vena cava

5 MDCT of Complications of Hyperadrenocorticism

Dystrophic mineralization commonly occurs in association with canine HAC. Mineralization in these patients is likely due to the protein catabolic actions of cortisol, which lead to calcium and phosphorus deposition in the organic matrix of the abnormal protein, despite normal calcium and phosphorus concentrations in the serum. Mineralization is detected easily on non-contrast MDCT images as calcinosis cutis and mineralization of the tracheal rings, bronchial walls, kidneys, gastric mucosa, liver, skeletal muscle, and branches of the abdominal aorta (Fig. 7).

Metabolic changes in patients with HAC are responsible for diffuse osteopenia, which is most noticeable in the vertebrae. Qualitative and quantitative assessments of bone density can be performed using CT. A recent work revealed a significant difference in bone mineral density of the vertebrae in normal dogs and dogs with PDH.

Abdominal Complications

Hepatomegaly due to steroid-induced vacuolar hepatopathy is a constant abdominal feature in patients with HAC. The liver is enlarged and inhomogeneous. Glycogen accumulation may lead to increased attenuation values (normal value, 59.58 ± 3.34 HU). In multiphasic MDCT studies, patients with steroid-induced hepatopathy may show a diffuse pattern with inhomogeneous parenchymal enhancement in the PVP.

In some patients, MDCT reveals a focal pattern with one or more nodular lesions. Steroid-induced hepatopathy can result in the development of large hepatic masses. The presence of diffuse or focal lesions can lead to hepatic rupture and subcapsular effusion (Fig. 8). Thrombosis of the portal vein or hepatic veins may be detected in patients with HAC, due to the hypercoagulable state (see also the chapter "The Liver").

Dogs with HAC appear to be more prone to the development of gallbladder mucocele, characterized by mucus-filled distention of the gallbladder with associated gallbladder dysfunction. MDCT features of gallbladder mucocele have not been reported. However, the same patterns seen on ultrasound are easy to recognize on thin-section multiphasic MDCT examinations of patients with HAC or other predisposing conditions (e.g., hyperlipidemia/hypercholesterolemia of other causes or due to breed predisposition in miniature schnauzers, cocker spaniels, and Shetland sheepdogs) (Fig. 8a). Gallbladder mucocele can have serious clinical consequences, such as gallbladder ischemia and necrosis, which can lead to gallbladder rupture and bile peritonitis. Mucin produced in the gallbladder can enter and obstruct the extrahepatic biliary ducts, causing progressive distension of the biliary

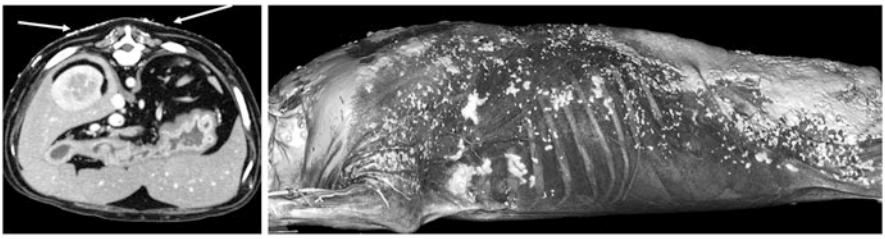

Fig. 7 Calcinosis cutis in a dog with HAC

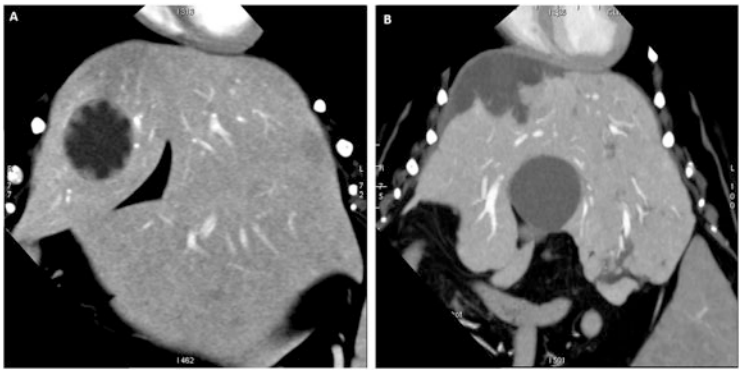

Fig. 8 (**a**) Dorsal MPR of the liver in a dog with PDH, hepatomegaly, and gallbladder mucocele. (**b**) Dorsal MPR from another dog with PDH and severe steroid-induced hepatopathy, with laceration of the hepatic parenchyma and effusion

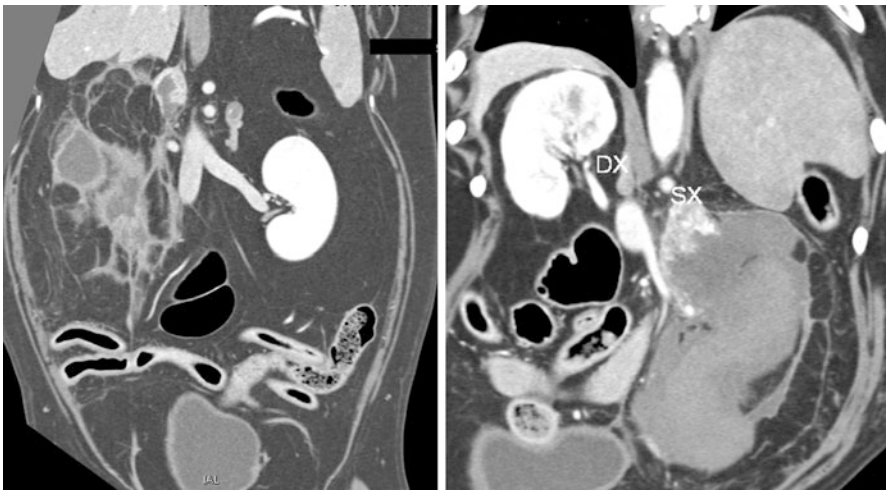

Fig. 9 Retroperitoneal effusion and hematoma due to adrenal gland tumor rupture in two different dogs

tree and predisposing patients to cholecystitis (see also the chapter "The Gallbladder and Biliary System").

Retroperitoneal effusion may be observed in cases of adrenal gland tumor rupture. MDCT is generally performed in these patients for staging and presurgical assessment (Fig. 9). Pre-contrast imaging (with 40–70 HU) can show the sentinel clot sign within a large hematoma. Thin-section multiphasic MDCT can be used to clearly distinguish the glandular tissue from the retroperitoneal hematoma (see also the chapter "The Peritoneal Cavity, the Retroperitoneum, and Abdominal Wall").

Thoracic Complications

Patients with HAC are at high risk of thrombosis, due mainly to glucocorticoid-induced hypercoagulability. Thromboembolism can occur in any vascular district, but the lung is considered to be the most common site. Contrast-enhanced MDCT of the thorax can show one or more filling defects in the pulmonary vessels (Figs. 10 and 11). Pulmonary MDCTA can reveal even small defects in the peripheral pulmonary vessels. In acute embolism, the dependent area of pulmonary parenchyma may show increased opacity due to pulmonary infarction. Lung perfusion studies in these patients can provide high-resolution angiographic images of the pulmonary arteries while enabling the assessment of lung perfusion defects caused by pulmonary embolism.

Intracranial Complications

Patients with neurological signs and HAC should undergo whole-body MDCT examination, with the prioritization of brain assessment. Pre- and post-contrast series of the brain should be performed before body series to detect changes in the pituitary and brain tissue. At our center, these neurological patients are examined

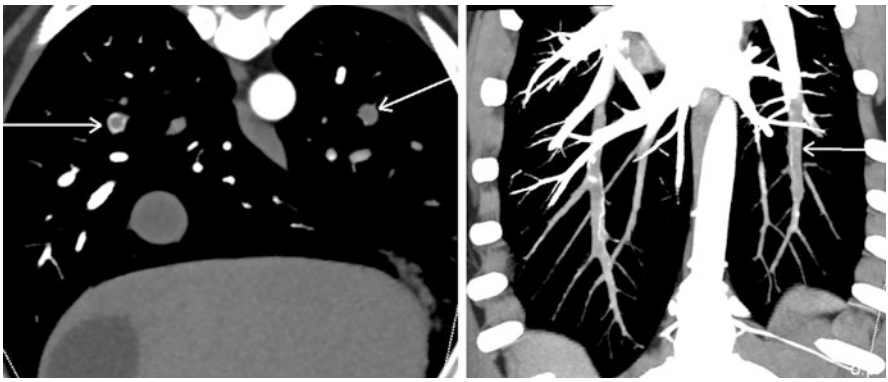

Fig. 10 Peripheral pulmonary embolism in a dog with HAC. Transverse and dorsal thin-MIP views showing the filling defects in the pulmonary vessels

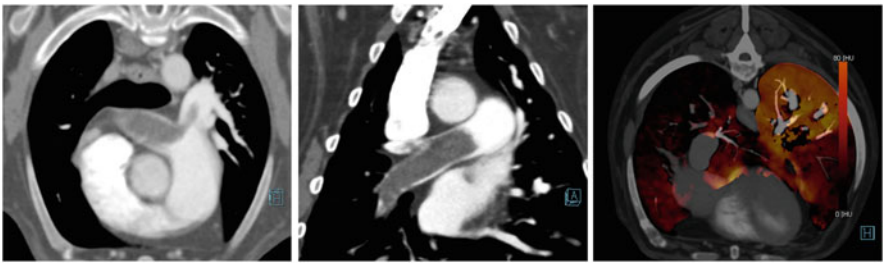

Fig. 11 Pulmonary thrombosis in a dog with HAC. Note the large filling defect in pulmonary vessels in the angiographic series and the resultant parenchymal hypoperfusion (DE-DSCT lung perfusion analysis)

first using non-contrast series, followed by CT brain perfusion and angiographic series.

In a few patients with PDH, pituitary masses become large and may compress or invade the hypothalamus or other adjacent structures (macrotumor syndrome). Most patients with HAC presenting neurological signs have experienced stroke that occludes one or more cerebral arteries or causes intracranial hemorrhage (ischemic or hemorrhagic stroke) (Figs. 12 and 13).

Pituitary apoplexy is a rare neurological syndrome that can occur in patients with HAC. It is caused by hemorrhagic or non-hemorrhagic necrosis of the pituitary gland, which produces several sudden and severe neurological signs. To date, this condition has been described in a few dogs and one cat. Sudden enlargement of the gland may cause an extreme and rapid rise in intrasellar pressure, which produces areas of focal necrosis and impaired delivery of hypothalamic hormones to the pituitary gland. Moreover, the enlarged mass can compress structures adjacent to the sella. Non-contrast MDCT series are essential for the characterization of infarction or hemorrhage in symptomatic patients and aid in the definitive diagnosis of this life-threatening condition (Fig. 14).

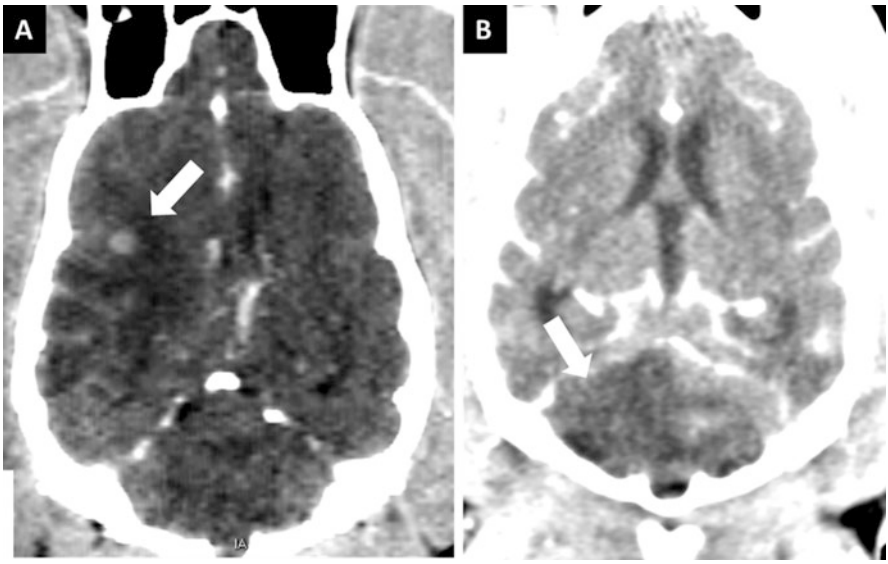

Fig. 12 (**a**) Brain hemorrhage in a dog with HAC. Note the surrounding large hypoattenuating area (perilesional edema). (**b**) Right cerebellar ischemic stroke in a dog with HAC

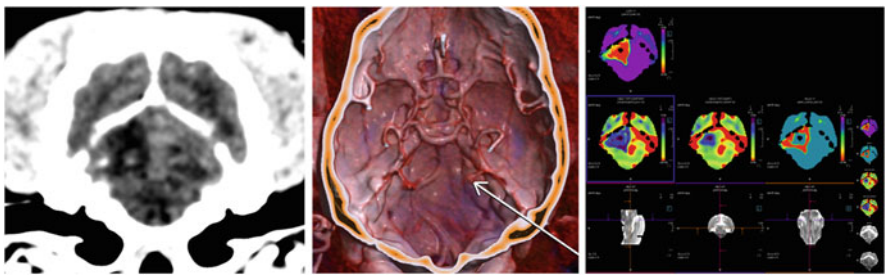

Fig. 13 CT morphological and perfusion study in a dog with HAC and cerebellar ischemic stroke

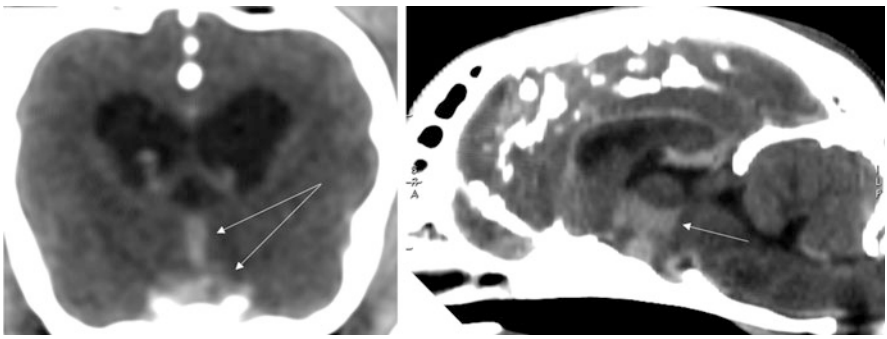

Fig. 14 Pituitary hemorrhage in a dog with known PDH and sudden neurological signs. The hypophysis is poorly defined and surrounded by hyperattenuating fluid, extending dorsally into the third ventricle

Further Readings

Auriemma E, Barthez PY, van der Vlugt-Meijer RH, Voorhout G, Meij BP. Computed tomography and low-field magnetic resonance imaging of the pituitary gland in dogs with pituitary-dependent hyperadrenocorticism: 11 cases (2001–2003). J Am Vet Med Assoc. 2009;235(4): 409–14. doi:10.2460/javma.235.4.409.

Beltran E, Dennis R, Foote A, De Risio L, Matiasek L. Imaging diagnosis: pituitary apoplexy in a cat. Vet Radiol Ultrasound. 2012;53(4):417–9. doi: 10.1111/j.1740-8261.2012.01933.x. Epub 2012 May 1.

Bertolini G, Furlanello T, De Lorenzi D, Caldin M. Computed tomographic quantification of canine adrenal gland volume and attenuation. Vet Radiol Ultrasound. 2006;47(5):444–8.

Bertolini G, Rossetti E, Caldin M. Pituitary apoplexy-like disease in 4 dogs. J Vet Intern Med. 2007;21(6):1251–7.

Bertolini G, Borsetto A, Furlanello T, Caldin M. Multidetector CT attenuation values of the liver in canine pituitary dependent hyperadrenocorticism. Vet Radiol Ultrasound. 2008a; 49(2):196–219.

Bertolini G, Furlanello T, Drigo M, Caldin M. Computed tomographic adrenal gland quantification in canine adrenocorticotroph hormone-dependent hyperadrenocorticism. Vet Radiol Ultrasound. 2008b;49(5):449–53.

Diaz-Espiñeira MM, Mol JA, van den Ingh TS, van der Vlugt-Meijer RH, Rijnberk A, Kooistra HS. Functional and morphological changes in the adenohypophysis of dogs with induced primary hypothyroidism: loss of TSH hypersecretion, hyper-somatotropism, hypoprolactinemia, and pituitary enlargement with transdifferen-tiation. Domest Anim Endocrinol. 2008;35(1):98–111. doi:10.1016/j.domaniend.2008.03.001. Epub 2008 Mar 31

Galac S, Kooistra HS, Voorhout G, van den Ingh TS, Mol JA, van den Berg G, Meij BP. Hyperadrenocorticism in a dog due to ectopic secretion of adrenocorticotropic hormone. Domest Anim Endocrinol. 2005;28(3):338–48. Epub 2005 Jan 11.

Gregori T, Mantis P, Benigni L, Priestnall SL, Lamb CR. Comparison of computed tomographic and pathologic findings in 17 dogs with primary adrenal neoplasia. Vet Radiol Ultrasound. 2015;56(2):153–9. doi:10.1111/vru.12209. Epub 2014 Aug 19.

Lee D, Lee Y, Choi W, Chang J, Kang JH, Na KJ, Chang DW, Quantitative CT. assessment of bone mineral density in dogs with hyperadrenocorticism. J Vet Sci. 2015;16(4):531–42. doi:10.4142/jvs.2015.16.4.531.

Liotta A, Cavrenne R, Peeters D, Manens J, Bolen G. CT scan features of presumptive haemorrhagic stroke in a dog with cushing's disease. Case Rep Vet Med. 2014;2014:1.

Love NE, Fisher P, Hudson L. The computed tomographic enhancement pattern of the normal canine pituitary gland. Vet Radiol Ultrasound. 2000;41(6):507–10.

Paul AE, Lenard Z, Mansfield CS. Computed tomography diagnosis of eight dogs with brain infarction. Aust Vet J. 2010;88(10):374–80. doi:10.1111/j.1751-0813.2010.00629.x.

Pollard RE, Reilly CM, Uerling MR, Wood FD, Feldman EC. Cross-sectional imag-ing characteristics of pituitary adenomas, invasive adenomas and adenocarci-nomas in dogs: 33 cases (1988–2006). J Vet Intern Med. 2010;24(1):160–5. doi:10.1111/j.1939-1676.2009.0414.x.

Respess M, O'Toole TE, Taeymans O, Rogers CL, Johnston A, Webster CR. Portal vein thrombosis in 33 dogs: 1998–2011. J Vet Intern Med. 2012;26(2):230–7. doi:10.1111/j.1939-1676.2012.00893.x. Epub 2012 Feb 28.

Rodríguez Piñeiro MI, de Fornel-Thibaud P, Benchekroun G, Garnier F, Maurey-Guenec C, Delisle F, Rosenberg D. Use of computed tomography adrenal gland measurement for differentiating ACTH dependence from ACTH independence in 64 dogs with hyperadenocorticism. J Vet Intern Med. 2011;25(5):1066–74. doi:10.1111/j.1939-1676.2011.0773.x. Epub 2011 Aug 16.

Schultz RM, Wisner ER, Johnson EG, MacLeod JS. Contrast-enhanced computed tomography as a preoperative indicator of vascular invasion from adrenal mass-es in dogs. Vet Radiol Ultrasound. 2009;50(6):625–9.

Teshima T, Hara Y, Taoda T, Koyama H, Takahashi K, Nezu Y, Harada Y, Yogo T, Nishida K, Osamura RY, Teramoto A, Tagawa M. Cushing's disease compli-cated with thrombosis in a dog. J Vet Med Sci. 2008;70(5):487–91.

Valentin SY, Cortright CC, Nelson RW, Pressler BM, Rosenberg D, Moore GE, Scott-Moncrieff JC. Clinical findings, diagnostic test results, and treatment out-come in cats with spontaneous hyperadrenocorticism: 30 cases. J Vet Intern Med. 2014;28(2):481–7. doi:10.1111/jvim.12298. Epub 2014 Jan 16.

van der Vlugt-Meijer RH, Voorhout G, Meij BP. Imaging of the pituitary gland in dogs with pituitary-dependent hyperadrenocorticism. Mol Cell Endocrinol. 2002;197(1-2):81–7.

van der Vlugt-Meijer RH, Meij BP, van den Ingh TS, Rijnberk A, Voorhout G. Dynamic computed tomography of the pituitary gland in dogs with pituitary-dependent hyperadrenocorticism. J Vet Intern Med. 2003;17(6):773–80.

van der Vlugt-Meijer RH, Meij BP, Voorhout G. Intraobserver and interobserver agreement, reproducibility, and accuracy of computed tomographic measure-ments of pituitary gland dimensions in healthy dogs. Am J Vet Res. 2006;67(10):1750–5.

Whittemore JC, Preston CA, Kyles AE, Hardie EM, Feldman EC. Nontraumatic rupture of an adrenal gland tumor causing intra-abdominal or retroperitoneal hemorrhage in four dogs. J Am Vet Med Assoc. 2001;219(3):324, 329–33.

Wood FD, Pollard RE, Uerling MR, Feldman EC. Diagnostic imaging findings and endocrine test results in dogs with pituitary-dependent hyperadrenocorticism that did or did not have neurologic abnormalities: 157 cases (1989–2005). J Am Vet Med Assoc. 2007;231(7):1081–5.

MDCT of Thyroid and Parathyroid Glands

Giovanna Bertolini

1 Introduction

The thyroid gland consists of two elongated lobes located on both dorsolateral aspects of the cranial portion of the trachea, medial to the common carotid arteries. A thin isthmus is seen rarely in normal dogs and may become more evident when involved in thyroid malignancy. On non-contrast images, the gland is generally hyperattenuating compared with the surrounding muscle because of its iodine content. It enhances dramatically due to its vascularity after CM administration, as it is largely supplied from the cranial and caudal thyroid arteries and branches of the common carotids (Fig. 1).

2 Hypothyroidism

The thyroid gland has a mean pre-contrast CT attenuation value of 107.5 HU in dogs and 123 HU in cats. Variation in the attenuation value may reflect pathological changes of the gland and its iodine level. Variation in appearance and decreased attenuation values have been reported in humans with diffuse thyroiditis and hypothyroidism. Similar CT features may be detected in dogs but have not been described. Functional hypothyroidism may result from immune-mediated lymphocytic thyroiditis or idiopathic gland tissue atrophy, with loss of thyroid parenchyma and replacement by adipose tissue. Thus, common observations in MDCT of hypothyroid dogs include enlargement of the gland in cases of thyroiditis or reduction in the sizes of both lobes due to gland atrophy (Fig. 2). Moreover, on

G. Bertolini (✉)
San Marco Veterinary Clinic, Padua, Italy
e-mail: bertolini@sanmarcovet.it

G. Bertolini (ed.), *Body MDCT in Small Animals*, DOI 10.1007/978-3-319-46904-1_19

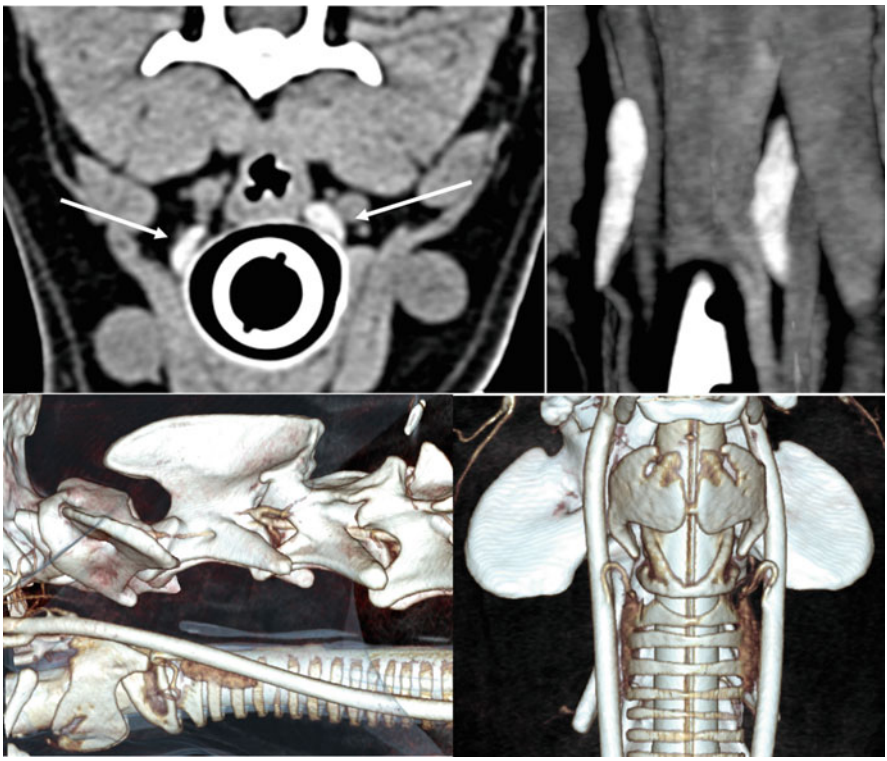

Fig. 1 Normal thyroid gland in a dog as they appear on pre-contrast thin-slice MDCT and post-contrast volume-rendered images

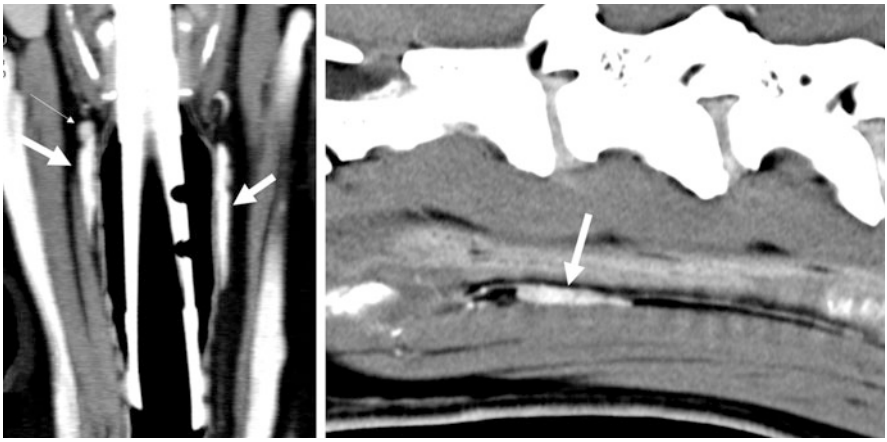

Fig. 2 Dorsal and parasagittal MPRs in a dog with hypothyroidism. *Thin arrow* in the dorsal image shows the external parathyroid gland, just cranial to the right thyroid lobe. The left lobe measures 0.18 cm^3 and the right lobe measures 0.03 cm^3 (normal ranges, 0.22–0.78 cm^3 and 0.22–0.87 cm^3, respectively)

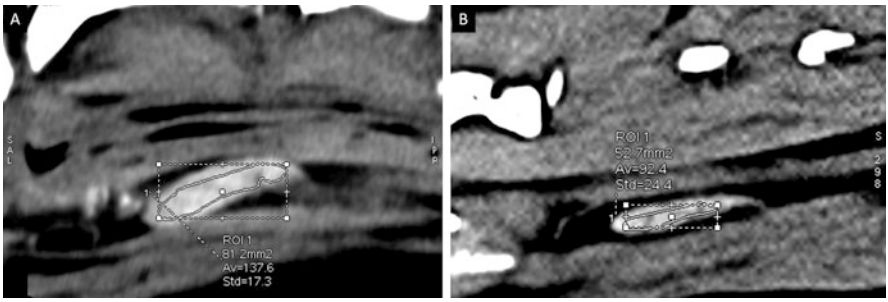

Fig. 3 Sagittal sections of the left thyroid lobe in a euthyroid dog (**a**) and in a dog with hypothyroidism (**b**). In patients with hypothyroidism, the thyroid has a lower mean attenuation value and higher standard deviation calculated within the ROI, reflecting diminished iodine content and internal tissue inhomogeneity

direct scans, the gland has a decreased attenuation value due to diminished iodine content and increased content in adipose tissue and shows moderate inhomogeneous enhancement on post-contrast images (Fig. 3).

3 Thyroid Masses

Unilateral or bilateral functional thyroid hyperplastic nodules or adenomas are frequently encountered in older cats that undergo MDCT for other reasons (Fig. 4). MDCT is used for the staging of thyroid cancer in dogs. It enables the evaluation of regional lymphadenopathy, vascular invasion, locoregional extension of the tumor (particularly involving the trachea and esophagus), and spread of disease into the mediastinum, as well as the detection of pulmonary and hepatic metastases.

About 60% of dogs with thyroid tumors have normal thyroid function: 30% are hypothyroid and 10% are hyperthyroid. Thyroid adenocarcinoma accounts for about 90% of clinically detected thyroid masses in dogs. Most malignant masses are large and palpable and isoattenuating to the adjacent ventral cervical musculature on pre-contrast images. They may show hypoattenuating areas, pseudocystic lesions, and mineralization. Characteristics of contrast enhancement may overlap considerably between benign and malignant masses, preventing distinction based on imaging alone. However, some MDCT features, such as intratumoral vascularization and vascular and tissue invasiveness, strongly suggest malignancy (Figs. 5 and 6).

Incidental, non-palpable thyroid tumors have been described recently in dogs, based on ultrasound or MDCT examination. Small benign and malignant thyroid

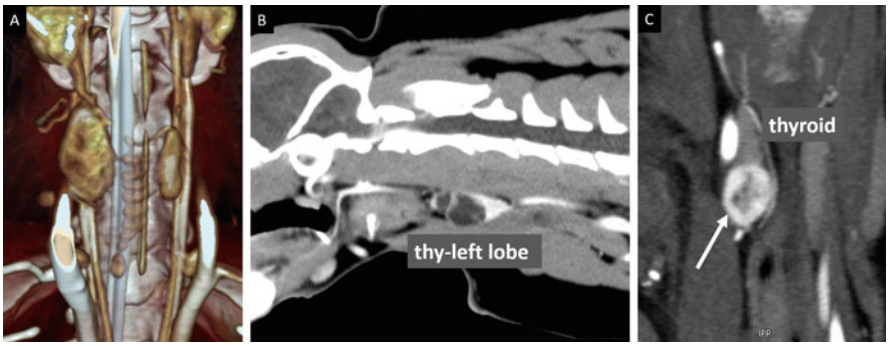

Fig. 4 (**a**) Bilateral hyperplastic thyroid nodules in an elderly cat. (**b**) Left thyroid lobe of a cat with thyroid adenoma. (**c**) Follicular hyperplastic nodule at the caudal pole of the right thyroid lobe

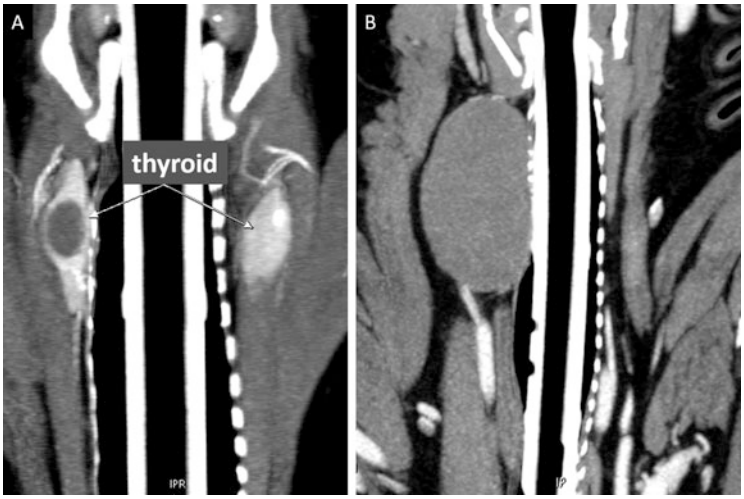

Fig. 5 Thyroid adenoma in dogs. (**a**) Both thyroid lobes are moderately enlarged. Note the hypoattenuating, hypovascular thyroid nodule in the right lobe, discovered incidentally. (**b**) Large hypoattenuating, hypovascular mass of the right thyroid lobe

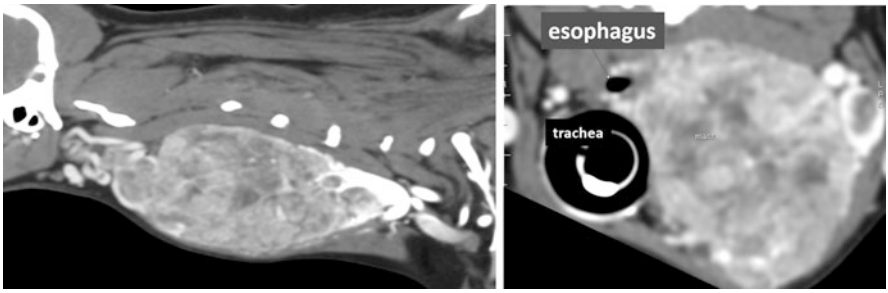

Fig. 6 Sagittal and transverse views of a large thyroid carcinoma, with vascular invasion and esophageal and tracheal wall infiltration, in a dog

lesions may go unnoticed on physical examination and be found incidentally on whole-body MDCT examination performed for other reasons. In a study we published recently, the overall prevalence of thyroid tumors in 4520 dogs examined by MDCT was 2.12% (0.76% incidentalomas). More than 70% of these incidentally discovered thyroid tumors were carcinomas (Figs. 7 and 8).

The examiner must remember that ectopic thyroid tissue can be present from the base of the tongue to the thorax. During embryological development, the main mass of the developing thyroid migrates from the primitive pharynx along a midline descent to its final eutopic location. Failure of the thyroid primordium to descend fully leads to the development of lingual or sublingual ectopic thyroid tissue, whereas descent beyond its normal craniocervical location results in ectopic cranial mediastinal and/or heart-base thyroid tissue (Fig. 9). Ectopic tissue can be subject to the same pathological processes as normal eutopic thyroid tissue, such as inflammation, hyperplasia, and tumorigenesis. In dogs, ectopic thyroid tumors have been described cranial to the eutopic thyroid gland in sublingual locations or involving

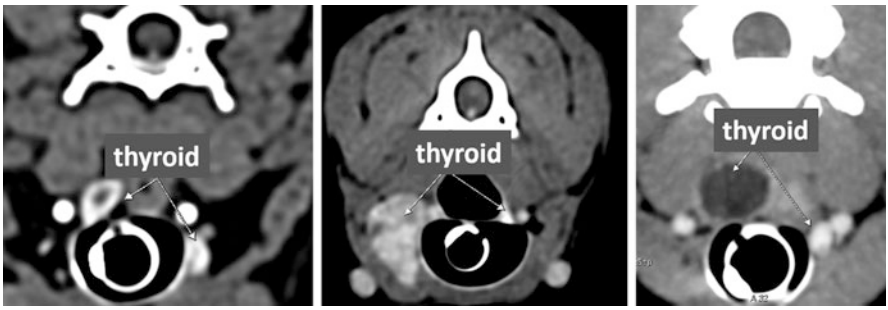

Fig. 7 Thyroid incidentaloma. Incidental, non-palpable thyroid carcinoma in three dogs, showing different characteristics

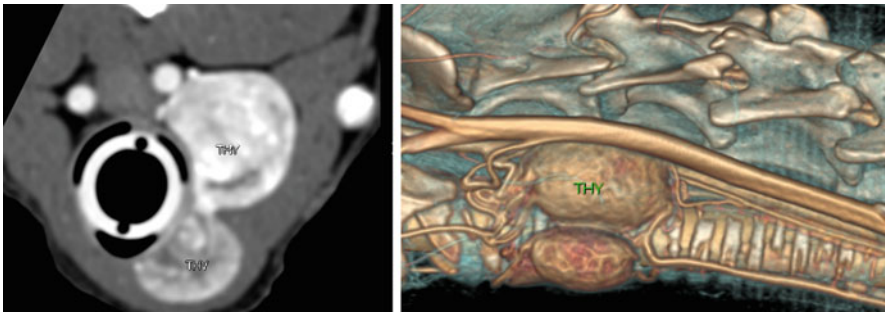

Fig. 8 Thyroid incidentaloma (carcinoma) in a dog. Transverse volume-rendered image showing a bilobed inhomogeneous mass

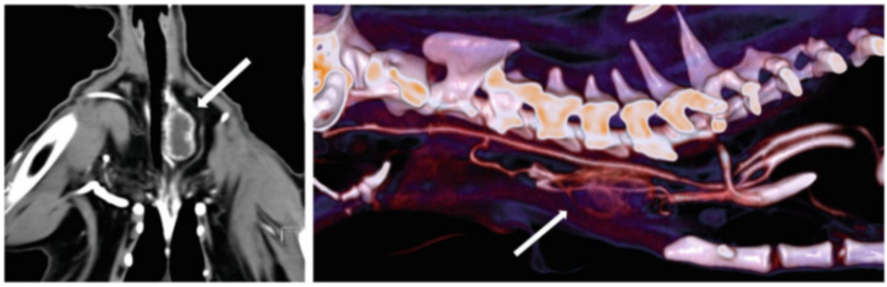

Fig. 9 Ectopic thyroid nodule in a cat with hyperthyroidism

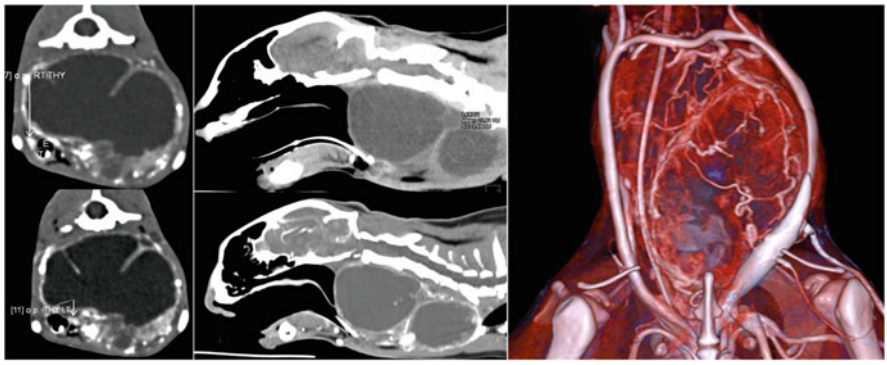

Fig. 10 Thyroglossal duct squamous cell carcinoma in a cat

the hyoid apparatus, or caudal to the normal gland, along the cervical region or in the cranial mediastinum. The ectopic location of these thyroid tumors reflects the embryological origin and migration of thyroid tissue. Lesions arising from cystic remnants of the thyroglossal duct are rarely reported in dogs and cats. Thyroglossal duct tumors may be clinically indistinguishable from a benign thyroglossal duct cyst. The preoperative diagnosis of carcinoma can have important implications for surgical planning and postoperative treatment. In these patients, documenting a normal thyroid gland is important because an ectopic thyroid gland may mimic a thyroglossal duct cyst clinically (Fig. 10).

4 Parathyroid Tumors

Anatomically, the parathyroids are related closely to the thyroid gland. In general, there are external parathyroids that are close to the thyroid surface and internal parathyroids, embedded in the thyroid tissue. Substantial variations exist in number

and location of the parathyroids. On thin-section MDCT images, external parathyroids are detected easily just craniomedial or medial to each thyroid lobe (Fig. 11). Internal parathyroids are located toward the caudal pole of the thyroid lobe and appear as one or more hypoattenuating areas embedded in the thyroid tissue. Parathyroid adenomas and carcinomas usually affect single glands and are grossly similar in appearance. The other parathyroid glands are normal, atrophied, or not grossly visible. Most commonly, primary hyperparathyroidism in dogs develops as a result of a solitary parathyroid gland adenoma (73–86%); less commonly, it is caused by hyperplasia of one or more glands (11–16%), and, rarely, it is the result of parathyroid adenocarcinoma (3–11%). In humans, multiphasic (4D) MDCT examination of the parathyroid is the method of choice for the assessment of parathyroid adenoma. The key difference between CT and 4D MDCT is that the latter is used to obtain additional information about the parathyroid lesion from scans conducted in two or more contrast-enhanced phases. Parathyroid adenomas show low attenuation on non-contrast images, intense enhancement in the arterial phase, and washout of contrast in the delayed phase (Figs. 12 and 13). Ectopic parathyroid tumors are rarely reported in dogs (Fig. 14).

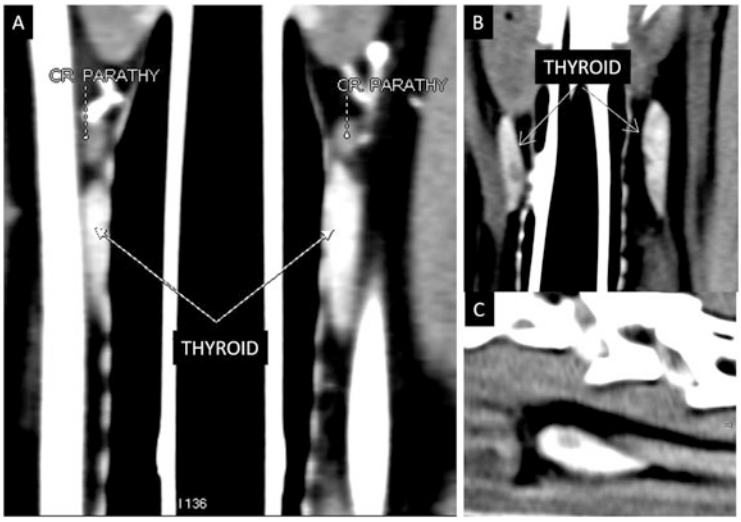

Fig. 11 CT appearance of the parathyroid gland. (**a**) Dorsal MPR showing the external parathyroid glands as they usually appear. (**b**) Internal parathyroids may be seen as hypoattenuating areas at the caudal pole of the thyroid gland. (**c**) Parathyroid (hypoattenuating area at the cranial pole of the thyroid lobe) in a cat

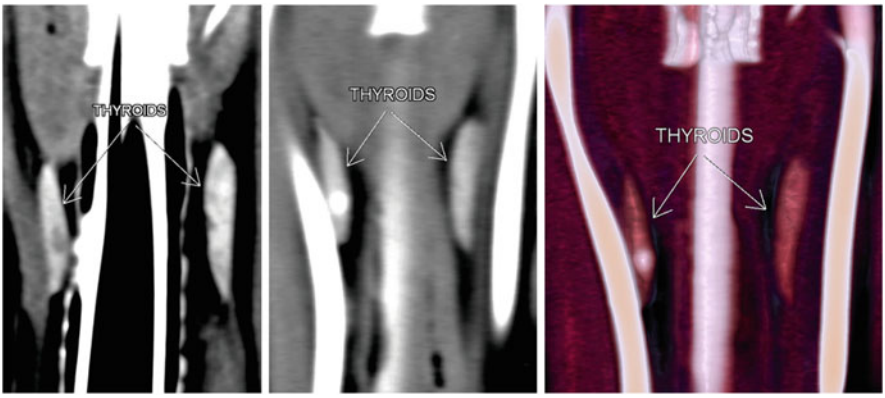

Fig. 12 Parathyroid nodule in a dog with primary hyperparathyroidism (pre-contrast and 2D and 3D arterial phase images)

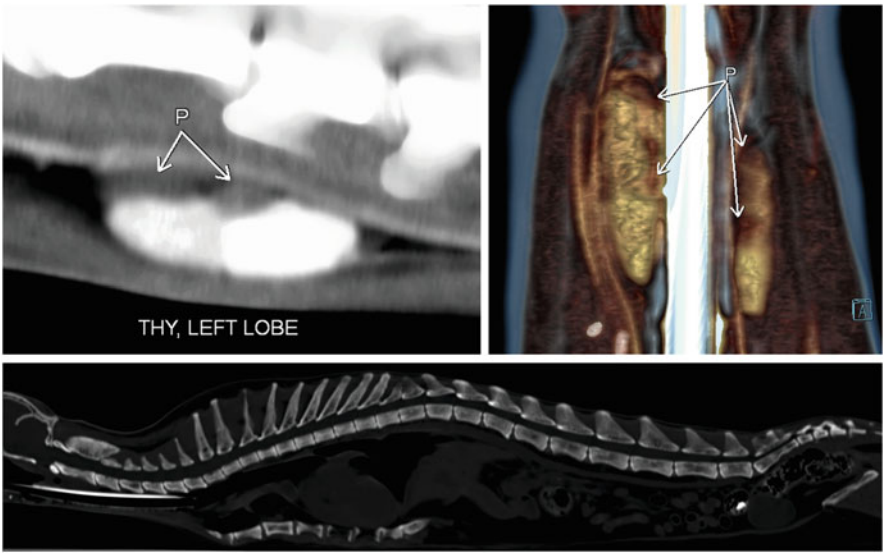

Fig. 13 Multiple parathyroid nodules (adenomas) in a cat with primary hyperparathyroidism and diffuse bone loss

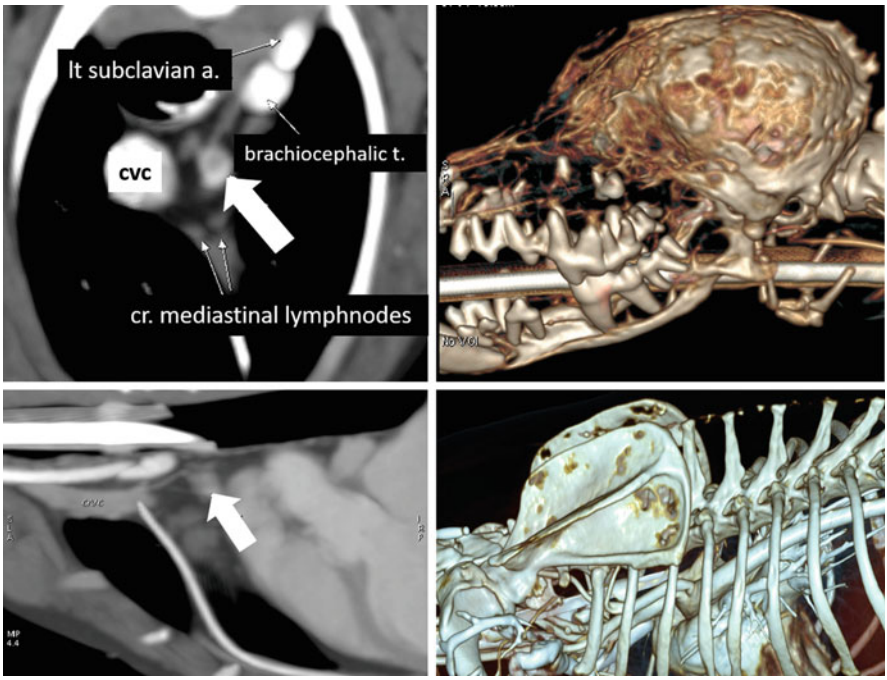

Fig. 14 Ectopic parathyroid carcinoma in the cranial mediastinum (*arrow*) in a dog with primary hyperparathyroidism and diffuse bone loss

Further Readings

Bertolini G, Drigo M, Angeloni L, Caldin M (2017) Incidental and nonincidental canine thyroid tumors assessed by multidetector row computed tomography: a single-centre cross sectional study in 4520 dogs. Vet Radiol Ultrasound. doi:10.1111/vru.12477

Deitz K, Gilmour L, Wilke V, Riedesel E. Computed tomographic appearance of canine thyroid tumours. J Small Anim Pract. 2014;55:323–9.

Gear RNA, Neiger R, Skelly BJS, Herrtage ME. Primary hyperparathyroidism in 29 dogs: diagnosis, treatment, outcome and associated renal failure. J Small Anim Pract. 2005;46:10–6.

Moorer JD, Breshears MA, Dugat DR. Thyroglossal duct carcinoma in a cat. J Am Anim Hosp Assoc. 2016;52(4):251–5. doi:10.5326/JAAHA-MS-6266. Epub 2016 Jun 3

Rodgers SE, Hunter GJ, Hamberg LM et al (2006) Improved preoperative planning for directed parathyroidectomy with 4-dimensional computed tomography. Surgery 140(6):932–940; discussion 940–941

Taeymans O, Dennis R, Saunders JH. Magnetic resonance imaging of the normal canine thyroid gland. Vet Radiol Ultrasound. 2008a;49:238–42.

Taeymans O, Schwarz T, Duchateau L, Barberet V, Gielen I, Haskins M, Van Bree H, Saunders JH. Computed tomographic features of the normal canine thyroid gland. Vet Radiol Ultrasound. 2008b;49:13–9.

Taeymans O, Penninck DG, Peters RM. Comparison between clinical, ultrasound, CT, MRI, and pathology findings in dogs presented for suspected thyroid carcinoma. Vet Radiol Ultrasound. 2013;54:61–70.

MDCT of the Endocrine Pancreas

Giovanna Bertolini

1 Introduction

Pancreatic endocrine tumors arise from endocrine tissue of the islets of Langerhans (embedded in the exocrine tissue) and are usually malignant in small animals. Insulinoma and gastrinoma are the most common endocrine tumors in dogs. Insulinomas, functional insulin-secreting tumors arising from pancreatic β cells, are the most common endocrine pancreatic tumors described in dogs. Visualization of a pancreatic mass lesion is essential for definitive diagnosis and treatment. The use of dual- and tri-phase MDCT has been described for the identification of pancreatic insulinomas in dogs and for surgical planning. In contrast to other imaging techniques, CT enables thorough assessment of the entire pancreas. Because insulinomas are usually hypervascular and the pancreas is perfused exclusively by the arterial system, scanning during the arterial phase has been suggested to increase the contrast between the tumor and normal pancreas.

2 Endocrine Pancreas Tumors

In humans, multiphasic thin-slice MDCT is considered to be the first-line imaging examination for tumor detection and staging, surgical planning, and follow-up in patients with pancreatic endocrine tumors. Insulinomas in humans appear as iso- to hyperattenuating lesions in pre-contrast series and show mostly hypervascular enhancement in the early arterial phase, typically with a homogeneous hyperattenuating appearance in the late arterial and venous phases. Definitive

G. Bertolini (✉)
San Marco Veterinary Clinic, Padua, Italy
e-mail: bertolini@sanmarcovet.it

G. Bertolini (ed.), *Body MDCT in Small Animals*, DOI 10.1007/978-3-319-46904-1_20

conclusions about the features of canine insulinoma on multiphasic CT cannot be drawn, due to the small number of cases described in the veterinary literature to date and differences in CT protocols used in these cases. Initial descriptions based on dual-phase examinations indicated that insulinomas appear as hypervascular lesions that enhance strongly in the (late) arterial phase. Tri-phase MDCT examination of insulinomas in nine dogs showed inconsistent features, with some lesions showing more conspicuous enhancement in the PVP (portal venous phase), pancreatic phase, or the later phase (see the chapter "The Pancreas" for further information of scanning technique) (Fig. 1). Importantly, in all published studies, multiphasic CT findings regarding mass and metastasis size and location were similar to surgical findings. Malignant insulinomas commonly metastasize to the lymph nodes and liver. MDCT is essential for the assessment of metastases and tumoral vascular invasion. Insulinoma of the body or right lobe of the pancreas tends to invade the pancreatico-duodenal vein, whereas that of the left pancreatic lobe may invade the splenic vein (Figs. 2 and 3).

Gastrinoma is a rare neuroendocrine tumor that usually arises as a result of malignant transformation of somatostatin-secreting delta cells of the endocrine pancreas to gastrin-producing cells. The diagnosis of gastrinoma is based on the demonstration of low gastric pH and concurrently high gastrin levels. Unlike

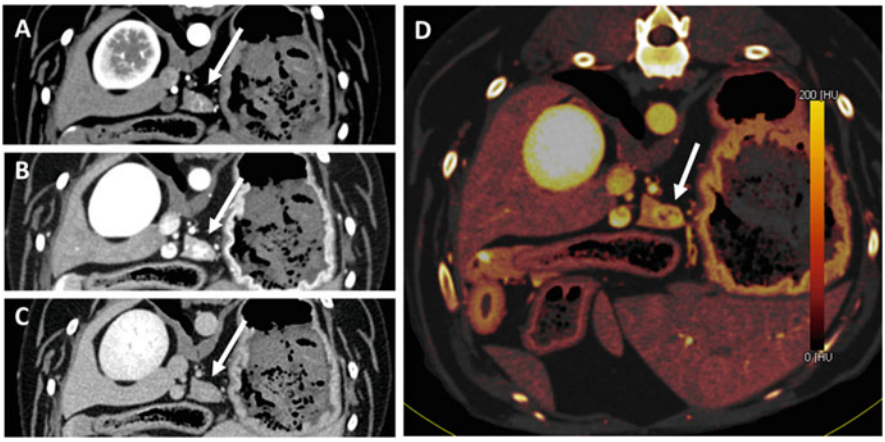

Fig. 1 (**a–c**) Transverse views from the arterial phase, PVP, and EP in a dog with small pancreatic insulinoma at the pancreatic body (*arrow*). (**d**) *Color-coded* iodine image from DE PVP datasets. The pancreatic nodule is more conspicuous, its margins are more defined, and its heterogeneous characteristics are more evident

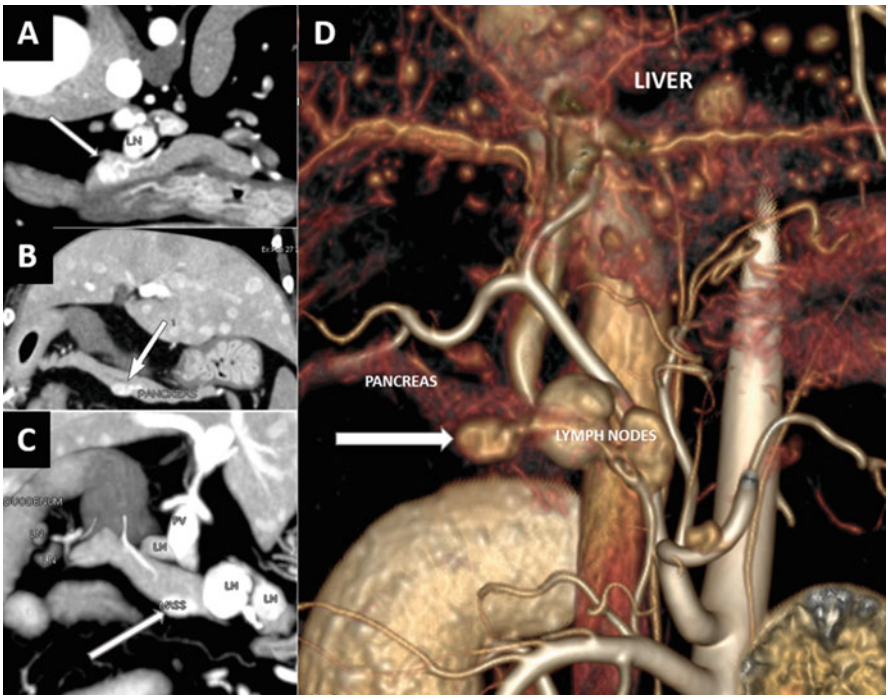

Fig. 2 Pancreatic insulinoma in a dog. (**a**) Transverse view showing a hypervascular nodule in the pancreatic body (*arrow*). Note the enlarged and strongly enhanced pancreatic lymph node (LN). (**b**) Transverse view in the same dog, showing another small hypervascular nodule in the left pancreatic lobe (*arrow*). (**c**) Thin-MIP image showing the small nodule in the left pancreatic lobe (*arrow*) and enlarged peripancreatic lymph nodes (LN; duodenal, pancreatic, and splenic). The splenic and pancreatic lymph nodes are enhanced to the same degree as the pancreatic mass. *PV* portal vein. (**d**) Volume-rendered image showing the left pancreatic nodule, metastatic lymph nodes, and multiple hypervascular nodules (metastases) in the liver parenchyma

insulinomas, gastrinomas are usually multiple and are often located extra-pancreatically. In humans, the lesions are isodense to normal pancreatic tissue on non-contrast CT images and are often hypervascular; thus, they may be visible on arterial-phase CT and angiography. To date, the CT features of gastrinoma in dogs have not been described. At our center, gastrinomas in two dogs that underwent MDCT showed isoattenuation in pre-contrast series and hypovascularity after CM administration (Fig. 4).

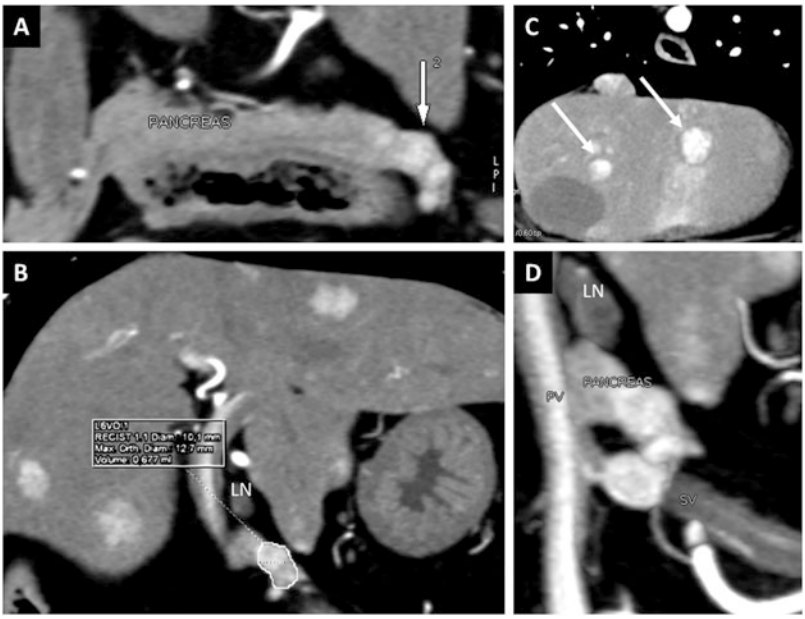

Fig. 3 Metastatic insulinoma of the left lobe (**a**, **b**) in a dog with hepatic metastases (**c**) and splenic vascular invasion (**d**)

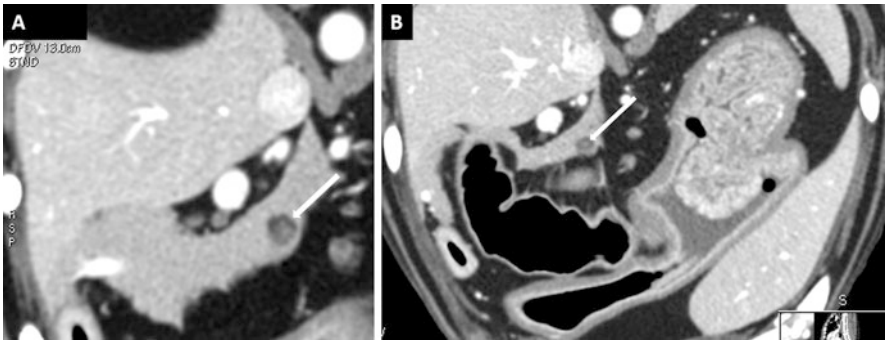

Fig. 4 Pancreatic gastrinoma in a dog with melena and hematemesis, suspicious for a gastric tumor. (**a**) An inhomogeneous hypoattenuating nodule (*arrow*) is present in the body of the pancreas. (**b**) Note the rugal fold hypertrophy, resembling a gastric mass

Further Readings

Fukushima K, Fujiwara R, Yamamoto K, et al. Characterization of triple-phase computed tomography in dogs with pancreatic insulinoma. J Vet Med Sci. 2015;77(12):1549–53. doi:10.1292/jvms.15-0077.

Iseri T, Yamada K, Chijiwa K, Nishimura R, Matsunaga S, Fujiwara R, et al. Dynamic computed tomography of the pancreas in normal dogs and in a dog with pancreatic insulinoma. Vet Radiol Ultrasound. 2007;48(4):328–31.

Kishimoto M, Tsuji Y, Katabami N, Shimizu J, Lee KJ, Iwasaki T, et al. Measurement of canine pancreatic perfusion using dynamic computed tomography: influence of input-output vessels on deconvolution and maximum slope methods. Eur J Radiol. 2011;77(1):175–81. doi:10.1016/j.ejrad.2009.06.016.

Lidbury JA, Suchodolski JS. New advances in the diagnosis of canine and feline liver and pancreatic disease. Vet J. 2016;215:87–95. doi:10.1016/j.tvjl.2016.02.010.

Mai W, Cáceres AV. Dual-phase computed tomographic angiography in three dogs with pancreatic insulinoma. Vet Radiol Ultrasound. 2008;49(2):141–8.

Marolf AJ. Computed tomography and MRI of the hepatobiliary system and pancreas. Vet Clin North Am Small Anim Pract. 2016;46(3):481–97, vi. doi:10.1016/j.cvsm.2015.12.006

Robben JH, Pollak YW, Kirpensteijn J, Boroffka SA, van den Ingh TS, Teske E, et al. Comparison of ultrasonography, computed tomography, and single-photon emission computed tomography for the detection and localization of canine insulinoma. J Vet Intern Med. 2005;19(1):15–22.

Part VII
MDCT of Body Trauma

The Body Trauma

Giovanna Bertolini

1 Introduction

Body trauma occurs commonly in small animal patients. According to their underlying cause, injuries are classified as blunt or penetrating. Blunt trauma is reported more frequently, and common causes include being hit by a car, falling from a height, interactions between large and small dogs, and human–animal interactions. Penetrating injuries are less frequent in small animals. Extensive body trauma often results in life-threatening injuries that must be identified rapidly to enable immediate implementation of the appropriate treatment.

Workup of the blunt trauma patient has evolved with the advent of MDCT in veterinary practice. The combined value of MDCT, 3D reformatting, and VR has been well documented in various instances in dogs and cats. Major MDCT applications described in the veterinary literature to date are related to spinal and musculoskeletal injuries and sacropelvic trauma. In these cases, MDCT can provide information on complex bone fractures and accompanying injuries, such as those affecting the urinary tract and bladder (Fig. 1).

As most trauma patients have simultaneous injuries to several anatomic regions or organs, whole-body MDCT examination is always advisable. MDCT can rapidly detect active bleeding, vascular rupture, diaphragmatic rupture, and parenchymal injuries. In cases of thoracic trauma, MDCT is a very sensitive imaging technique that reveals tracheobronchial injuries, pulmonary contusion, and small pneumothorax, which may remain occult on radiographs.

G. Bertolini (✉)
San Marco Veterinary Clinic, Padua, Italy
e-mail: bertolini@sanmarcovet.it

G. Bertolini (ed.), *Body MDCT in Small Animals*, DOI 10.1007/978-3-319-46904-1_21

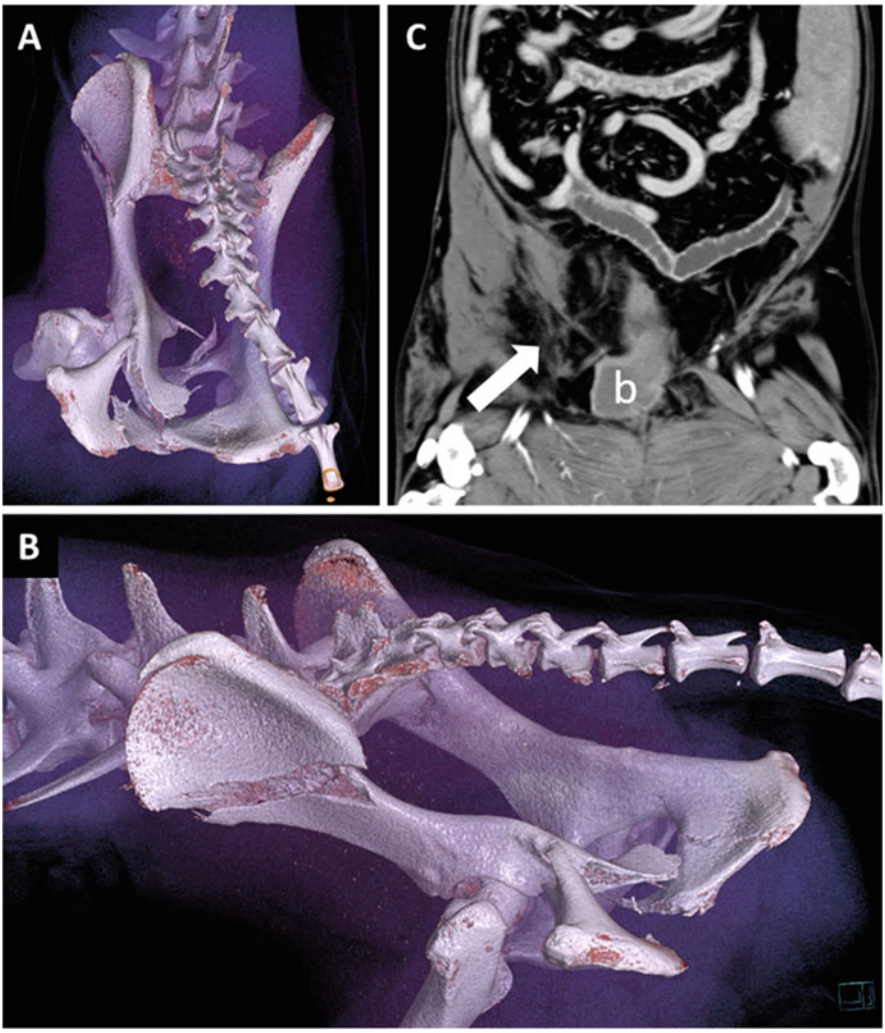

Fig. 1 (**A**, **B**) Volume-rendered images of a traumatized dog with multiple fractures. (**C**) *Arrow* shows the abdominal wall rupture with urinary bladder (b) herniation

2 MDCT Imaging Strategies

Optimization of the MDCT technique for multiple trauma requires consideration of several aspects pertaining to the positioning of the patient, use of sedation or anesthesia, and image acquisition and interpretation. No standardized MDCT protocol has been developed for small animal trauma. An ideal trauma protocol would maximize the detection of important body injuries while minimizing patient risks. Some expedients may be useful in cases of non-anesthetizable patients with trauma. The

use of tools (e.g., foam wedges and bands) or commercial devices enables the scanning of awake canine and feline patients. Particular caution should be taken when positioning trauma patients in cases of suspected spinal trauma. These patients should be scanned in lateral recumbency while remaining on a radiotransparent stretcher. In some situations, a thoracic, abdominal, or whole-body MDCT examination (depending on the scanner available) of an awake traumatized patient can be completed in a single respiratory cycle. Voluntary breath holding is not possible in veterinary patients as it is in conscious adult human patients. With MDCT scanners, increasing the image acquisition speed can minimize voluntary (respiratory) and involuntary (e.g., due to intestinal peristalsis or cardiac heartbeat) physiological motion artifacts. However, because of the need to perform reformatting in other planes, the highest *z*-axis resolution should be used. The ability to achieve this goal depends on the scanner technology available. A combination of high pitch (1.5) and relatively high initial collimation (2.5–3 mm) is generally recommended when using first-generation (4-, 8-, and 16-) MDCT scanners. However, the use of thick-slice images results in multiplanar and 3D reconstructions of limited diagnostic value, especially in small patients and in cases of subtle lesions. A typical artifact deriving from high-pitch and larger-collimation scans is the stair-step artifact. It is highlighted in 2D MPR and 3D volume-rendered images of straight structures with oblique main axes relative to the longitudinal *z*-axes of the scans (e.g., appendicular bones or major abdominal vessels). Stair-step artifacts can be reduced by using smaller collimation and overlapping reconstruction while retaining a high pitch value. The following parameters are recommended for 16-MDCT scanners when examining awake/sedated patients, to improve temporal and spatial resolution: helical mode, 0.5-s tube rotation, 0.9–1.3 pitch, 2.5-mm slice thickness, and 50% overlap (1.2 reconstruction thickness). With such a high-pitch scan protocol, a high (230–325) mAs should be used to increase the signal-to-noise ratio when scanning the abdomen. Lower exposure parameter values may be used for the examination of the thorax, an area with less radiation absorption and greater contrast between single structures. For instance, the kilovolt value can be reduced to 80–100, and the mAs value can be decreased to 60–80, which may help to conserve tube power for further scans.

In our experience, data on soft tissue lesions and minor skeletal lesions obtained from awake polypnoeic/dyspnoeic patients (e.g., those with rib fractures, pneumothorax, or massive pulmonary contusions) with a 16-MDCT scanner are poorly interpretable or uninterpretable, even when a high-pitch scan protocol is adopted (Fig. 2). With 16-MDCT, excellent image quality can be obtained with sedated, hemodynamically stable, traumatized patients using the following scan parameters: helical mode, 16 detectors enrolled, 0.7-s tube rotation, 0.98:1 pitch, 1.25-mm slice thickness, and 50% overlap (0.6 reconstruction interval).

Most modern MDCT and DSCT scanners can be used to perform imaging of the head, spine, thorax, abdomen, pelvis, and appendicular skeleton with submillimetric isotropic voxel resolution in a single examination that takes a few seconds, providing rapid and detailed information about organ and tissue injuries (Fig. 3) (see Part I ‘MDCT technics and technology’ for extensive explanation). Thousands

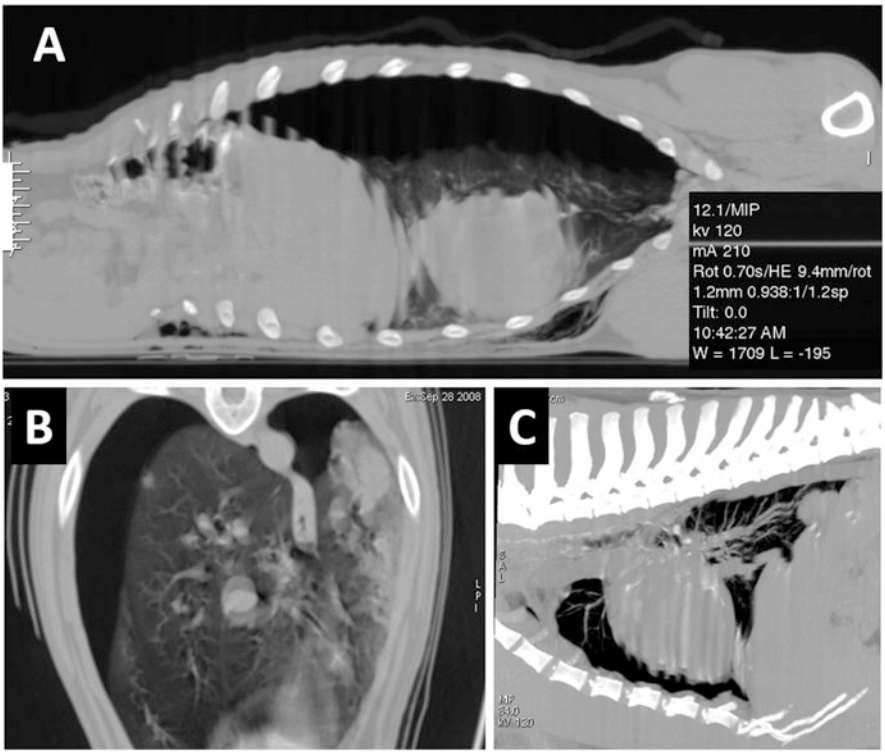

Fig. 2 (**a**) 16-MDCT image of the thorax in a 4-year-old corso dog with pneumothorax and rib fractures due to blunt trauma (the patient was hit by a car). The patient was scanned in the right decubitus in spontaneous ventilation, using 0.938 pitch, 0.7-s rotation time, and 1.2-mm slice thickness. (**b**) Transverse image of the thorax in a 7-year-old dog with severe thoracic trauma. Respiratory movements affect the image quality. (**c**) 10-mm-thick slab sagittal MIP of the same dog

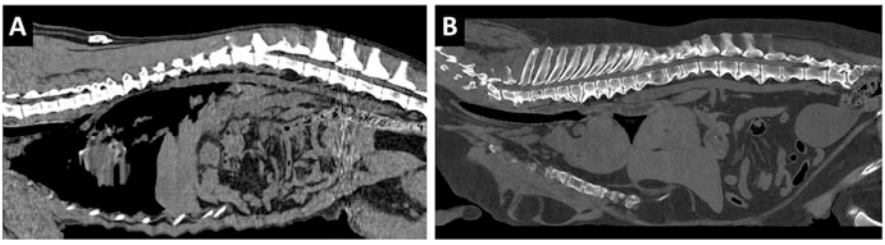

Fig. 3 Comparison of 16-MDCT (**a**) and 128-DSCT (**b**) whole-body examinations in awake traumatized dogs

of images are produced for each series and must be interpreted quickly and systematically to minimize missed traumatic lesions. Dedicated workstations and software are necessary for 2D and 3D post-processing of this large amount of data, and radiologists should be able to perform and interpret oblique, multi-oblique, and

3D-rendered segmentations to understand complex anatomy (especially in patients that are not well positioned) and pathological changes of trauma.

In acute trauma, the full extent of a patient's injuries is usually not readily apparent at the time of admission. Thus, the clinician cannot determine whether a whole-body MDCT examination with pre- and post-contrast sequences, rather than the examination of specific anatomic regions, should be performed. Because of the high rate of injuries missed by radiography and initial clinical evaluation on admission, and given the potential for delayed diagnosis, whole-body MDCT examinations are performed routinely at our center in cases of severe trauma. The trauma protocol at our center includes direct scanning for active hemorrhage detection (in awake or intubated non-ventilated patients). The decision to also perform post-contrast whole-body MDCT, MDCTA, or MDCT urography in hemodynamically stable patients is made on the basis of several findings raising the likelihood of vascular, parenchymal, or collecting system injuries and ultimately lies with the emergency critical care and surgical teams. While radiologists review the whole-body MDCT data acquired, secondary triage and additional diagnostic and therapeutic procedures (e.g., fluid collection, blood gas analysis, bandaging, and/or thoracic drainage) are performed with the patient still on the CT table (Fig. 4).

Basic interpretation strategies include appropriate windowing through the volume. Lung windows may be helpful for evaluation of the entire thorax (to detect even a small pneumothorax) and also the abdomen and pelvis, to enable easy identification of free air in the peritoneum and retroperitoneum. Narrowing of the soft tissue or mediastinal window enables the identification of even a small amount of free fluid in the pleural, peritoneal, or retroperitoneal space. The analysis of free fluid (HU measurement) on pre-contrast images may be useful for identification of its nature. In cases of hyperattenuating effusion or clotting, MDCTA can be used to identify arterial bleeding or active extravasation and may be very helpful in selecting the appropriate therapeutic approach (surgical ligation or noninvasive selective embolization). Other strategies that improve image interpretation include retro-reconstruction with a reduced field of view and the use of different reconstruction algorithms for different anatomic regions.

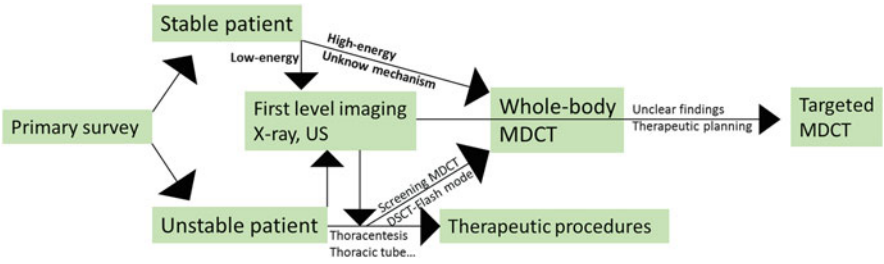

Fig. 4 Flowchart showing the combined diagnostic/therapeutic approach to traumatized patients adopted at our center (low, high energy refers to the trauma mechanism)

3 MDCT of Thoracic Trauma

MDCT is an excellent tool for the assessment of all thoracic compartments and reveals changes that cannot be detected with other imaging methods. Low-energy trauma is generally assessed using thoracic radiology and ultrasound. In these cases, MDCT is required secondarily in the presence of unclear findings or worsening of the patient. MDCT should be always performed in cases of trauma with an unknown mechanism and in those of high-energy injury, such as blunt trauma. Blunt injuries of the thorax involve three principal mechanisms—direct impact, compression, and deceleration—which are often combined in the same traumatized patient. These mechanisms are responsible for the presence of different CT signs. Penetrating injuries of the thorax occur with less frequency than does blunt trauma, but they can result in immediately life-threatening problems when major vascular structures are damaged. The thoracic wall, pleura, diaphragm, and lung parenchyma are injured most commonly. Mediastinal structures, the heart, and the airways are damaged less commonly.

3.1 Injuries of the Thoracic Wall, Pleura, and Diaphragm

Rib fractures are encountered commonly in thoracic blunt trauma. Thoracic wall damage from penetrating injuries (e.g., bite wounds) often includes thoracic musculature laceration and lesions of the pleural space and lung parenchyma (Figs. 5, 6, and 7). Rib fractures invariably result in severe pain and hyperventilation, which make the acquisition of diagnostic images from unsedated and non-anesthetized patients using first-generation MDCT scanners difficult. Rib fractures may have serious impacts on adjacent thoracic or abdominal parenchyma. An internally displaced fractured rib can puncture and lacerate the lung parenchyma. The fracture of several consecutive ribs at two or more sites may create thoracic wall instability accompanied by changes in intrapleural pressure and paradoxical thoracic wall movement (flail chest). MDCT, along with other imaging modalities, is not necessary for flail chest diagnosis. However, it can be used to simultaneously assess the number of fractured ribs and concurrent thoracic and abdominal injuries, thereby providing essential information for therapeutic intervention.

Pneumothorax (air within the pleural space) is the most common trauma-associated pleural space disease in small animals. It can result from lung, tracheal, esophageal, or penetrating injury (Figs. 6, 7, and 8). MDCT can be used to easily detect pneumothorax and identify even small expression, which is difficult to see on radiographs. Importantly, pneumothorax can enlarge during positive-pressure ventilation in anesthetized patients. Thus, we should assume that all traumatized patients undergoing MDCT may have a pneumothorax (even when it is not detected on radiographs). In our center, we routinely perform initial unenhanced evaluations of non-intubated, non-ventilated patients to assess the pleural space before

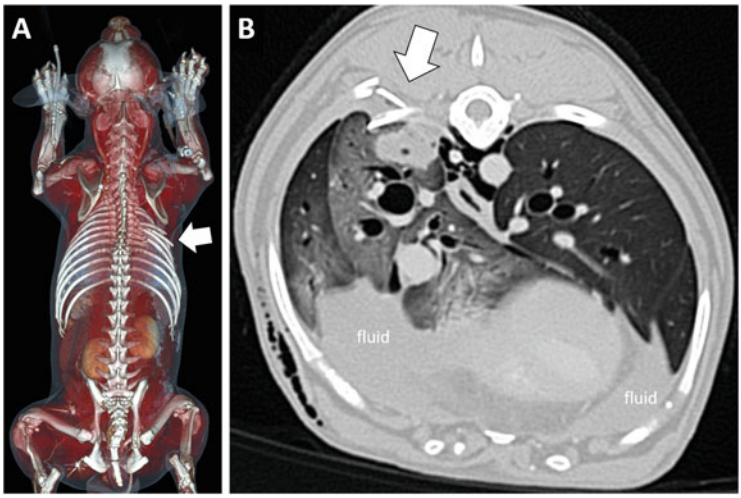

Fig. 5 (**a**) Penetrating thoracic injuries (*arrow*) in a mongrel dog (volume rendering). (**b**) Transverse view showing internally displaced fractured ribs that puncture and lacerate the lung parenchyma. Note the increased lung opacity (ground-glass opacity and consolidation), reflecting pulmonary contusion, and hemorrhage. Note also the pneumomediastinum and small amount of pneumothorax

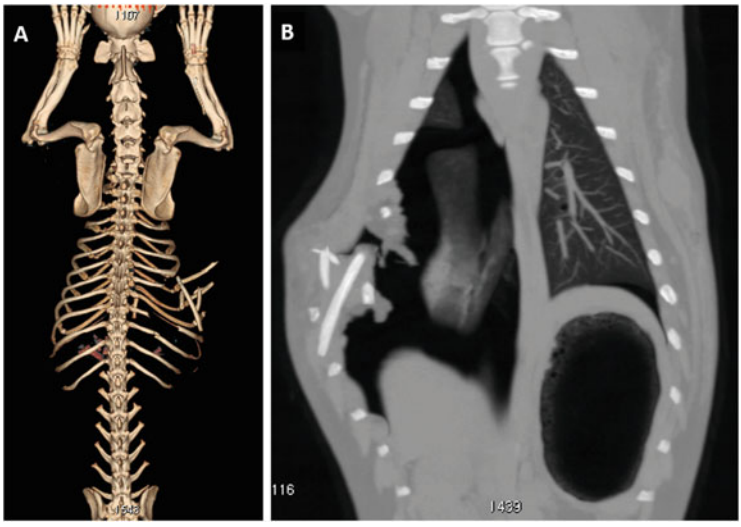

Fig. 6 3D volume-rendered image (from the dorsal perspective) of a traumatized dachshund with a penetrating injury (bite wound). The thoracic wall is lacerated and pneumothorax is present, with passive lung atelectasis

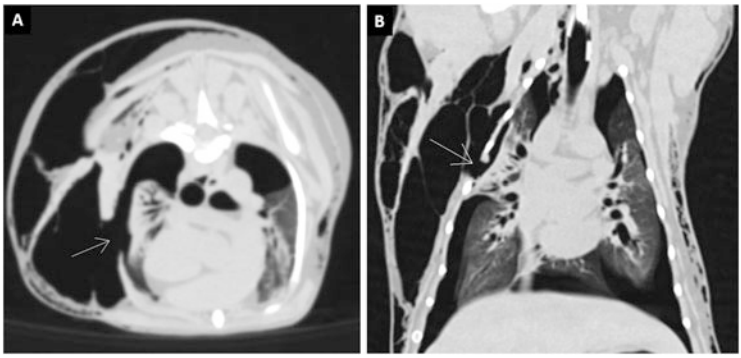

Fig. 7 Pneumothorax and pneumoderma due to thoracic wall laceration (bit wound)

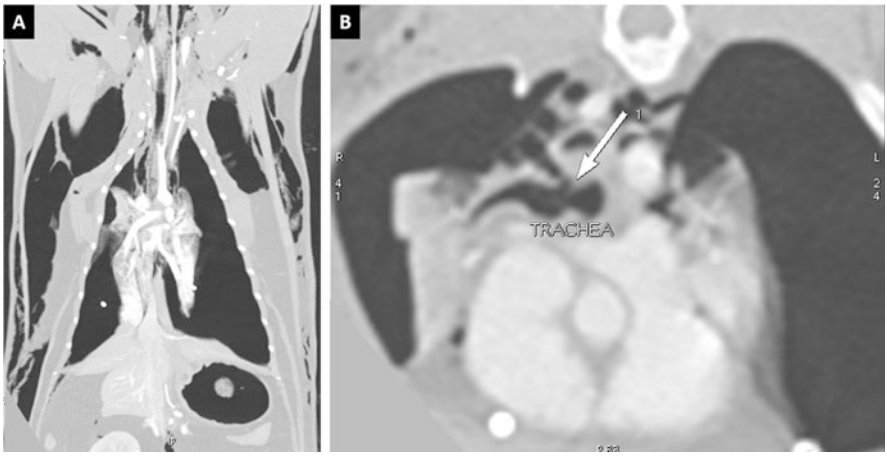

Fig. 8 Pneumothorax, pneumomediastinum, and pneumoderma in a cat due to a fall from a height. (**a**) Note the lung atelectasis. (**b**) Transverse view showing perforation at the tracheobronchial junction

performing any other procedures. This initial rapid evaluation provides information about the presence of pneumothorax and its possible pathogenetic mechanism (i.e., closed, open, or tension). Closed pneumothorax results from lung or mediastinal injuries, whereas open pneumothorax results from penetrating injuries. The cause of pneumothorax and concurrent injuries (e.g., rib fracture, thoracic wall laceration, or lung laceration) is easily identified with MDCT examination. Tension pneumothorax results from airway or lung injuries associated with one-way accumulation of air within the pleural space, and it is a clinical emergency. As the intrapleural pressure rises, the mediastinal structures are compressed, decreasing the venous return to the heart and leading to serious hemodynamic impairment. MDCT images

show hyperexpansion of one hemithorax, ipsilateral diaphragm flattening, and contralateral mediastinal shift.

Hemothorax (accumulation of blood in the pleural space) may result from injury of the thoracic wall, diaphragm, lung, or mediastinal structures. MDCT can be used to confirm the presence of hemothorax when the attenuation of the pleural fluid is 30–40 HU. MDCT should be used to determine the cause of hemothorax. Bleeding into the pleural cavity is caused most commonly by laceration of the pulmonary parenchyma and pleural injury (Fig. 5). Alternatively, it can result from injury to the vessels of the thoracic wall, pulmonary vessels, great vessels, or the heart. Thus, a post-contrast series should be performed to opacify these key anatomic structures to exclude minor injuries with active bleeding.

Diaphragmatic rupture is an uncommon complication of major trauma that may be identified by an acute rise in intra-abdominal pressure resulting from a high-energy impact with major energy dissipation directed cranially toward the diaphragm (Figs. 9 and 10). Penetrating injuries that lacerate the diaphragmatic insertion in the thoracicoabdominal wall can also cause diaphragmatic rupture. Early diagnosis of even a small diaphragmatic rupture is important. Direct CT signs of diaphragmatic rupture include discontinuity of the diaphragm with thickening at the edge of the defect. Indirect signs of diaphragmatic rupture include intrathoracic dislocation of the abdominal viscera and mesenteric structures. Complications related to abdominal viscera displacement in the thoracic cavity through the lacerated diaphragm may result in respiratory compromise due to the impairment of lung inflation. Visceral incarceration may lead to strangulation and perforation or other major complications (Fig. 11).

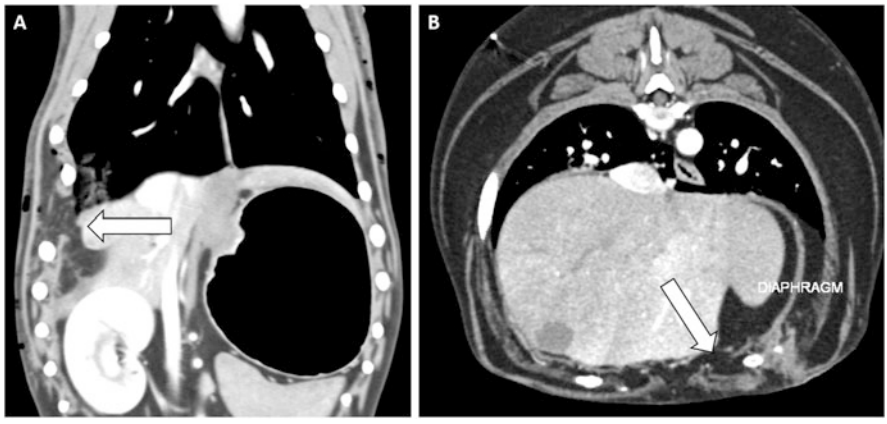

Fig. 9 Diaphragmatic traumatic rupture in dogs. (**a**) Dorsal MPR image of a dog with rupture of the pars costalis of the diaphragm (*arrow*), following a bite wound. (**b**) Transverse view of a dog with pars sternalis diaphragmatic rupture due to blunt trauma

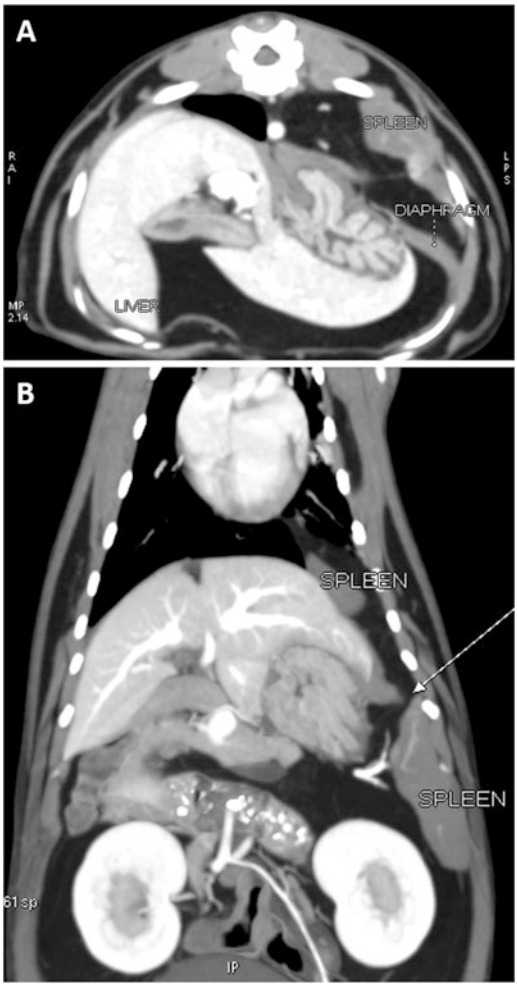

Fig. 10 Diaphragmatic rupture in a cat due to blunt trauma (*arrow*), with dislocation of the spleen in the thoracic cavity

3.2 Mediastinal Injuries

Pneumomediastinum (PM) refers to the accumulation of air in the mediastinal space. Blunt and penetrating trauma can cause pneumomediastinum. MDCT can reveal even a small amount of mediastinal air, not detected by radiography. The presence of pneumomediastinum should prompt assessment to determine the underlying cause. The rupture of air-containing structures of the mediastinum (i.e., larynx, trachea, and esophagus) is the most obvious cause of free air in the mediastinal space. Injuries of the throat, trachea, and esophagus are generally assessed definitively with endoscopic examination but may be first encountered on MDCT examination during comprehensive evaluation for polytrauma (Figs. 5, 8, and 12). In cases of cervical wounds

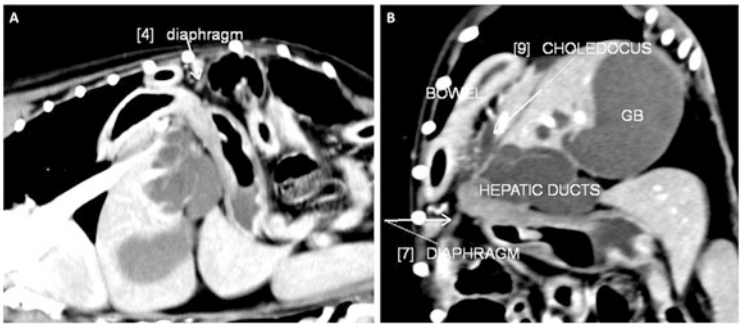

Fig. 11 Chronic diaphragmatic rupture in a pinscher with a history of trauma several months previously. (**a**) Parasagittal image showing a small diaphragmatic rupture, with passage of the duodenum, choledochus, and pars of the pancreas into the thoracic cavity. Note the distension of the gallbladder and hepatic duct due to strangulation. (**b**) Dorsal view

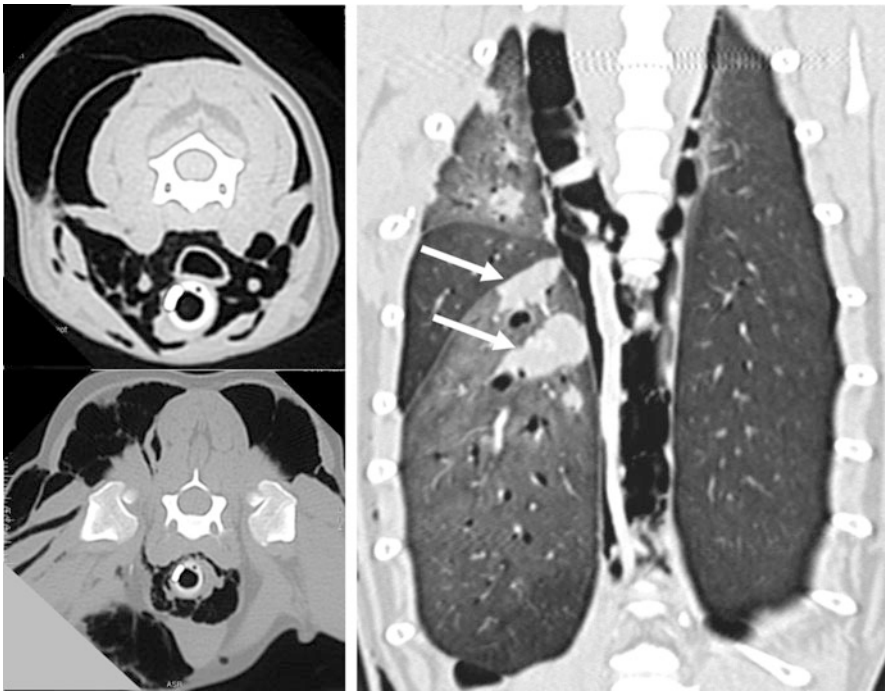

Fig. 12 Air along the airway and vascular structures of the neck and in the mediastinum in a traumatized dog. *Arrows* on the dorsal MPR image indicate pulmonary consolidation due to severe thoracic trauma (contusion, hemorrhage)

(evident on clinical evaluation), air can track along the airway and vascular structures of the neck back into the mediastinum.

Injuries of the cervical and thoracic esophagus are rare. Esophageal rupture can be confirmed by leakage of iodinate contrast medium (administered by gavage using a flexible tube) into the mediastinum. Tracheal trauma can be difficult to assess with MDCT. Linear tracheal trauma is generally perpendicular to the cartilage rings. The examination of transverse and thin-slice MPR images and 3D visualization of the trachea using virtual bronchoscopy or another volume-rendering technique may aid detection of the rupture site. The use of MinIP may help to identify the leakage of air into the area surrounding the tracheal defect. Tracheal avulsion is reported more commonly in cats than in dogs and is thought to occur due to rapid and extreme hyperextension of the head and neck. Avulsion is seen most commonly in the thorax. In tracheal laceration, air leaks continuously through a tracheal rupture, dissecting into fascial planes and leading to concurrent subcutaneous emphysema (pneumoderma). When the rupture involves a bronchus (tracheobronchial laceration), pneumothorax also occurs (Figs. 8, 13, and 14). Alveolar rupture from lung injuries can cause pneumomediastinum. Air from ruptured alveoli distributes along the interstitium into the mediastinum. In the author's experience, this condition is observed more frequently than are tracheobronchial and esophageal rupture. Streaks of air surrounding and paralleling the bronchovascular bundles associated with pneumomediastinum may be observed on CT (for further description, see the chapter "The Lung and Airways"). Injuries of the heart and great vessels of the mediastinum are rare but serious complications of thoracic trauma. They include pericardial effusion, myocardial contusion, and arterial and venous lacerations associated with mediastinal hematoma and hemothorax.

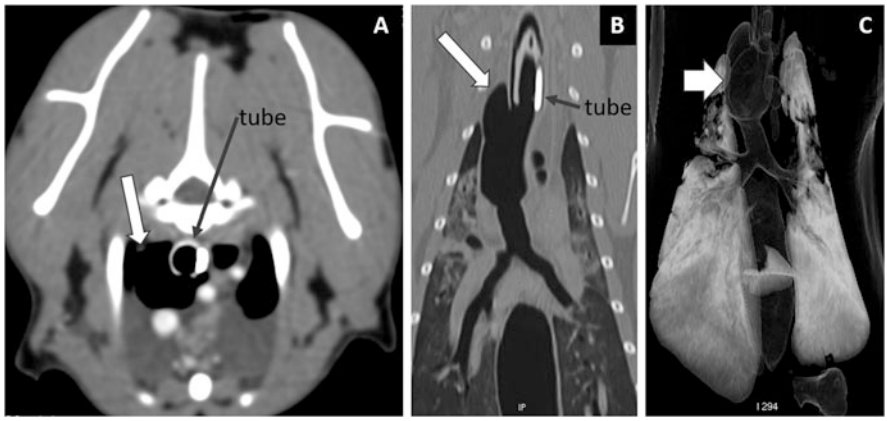

Fig. 13 Intrathoracic tracheal avulsion in a cat following blunt trauma. (**a**) Transverse view showing free air around the trachea. (**b**, **c**) Dorsal MPR and volume-rendered images show discontinuity of the tracheal silhouette (*arrows*)

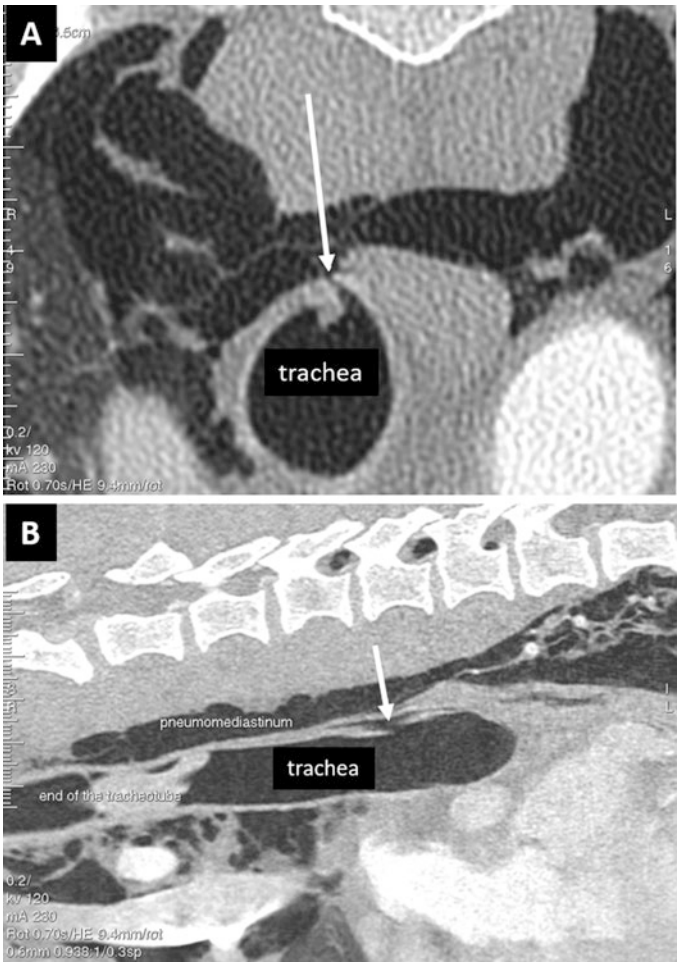

Fig. 14 (**a**, **b**) Transverse and sagittal MPRs of a dog with a recent history (7 days previously) of blunt trauma and recent onset of severe dyspnea. The dog shows pneumomediastinum due to tracheal rupture (*arrows*)

3.3 Lung Parenchyma Injuries

Pulmonary contusion is the most common injury identified after blunt chest trauma in small animals. The main mechanism is compression and tearing of the lung parenchyma at the impact site, which result in focal alveolocapillary injuries with no significant parenchymal damage, but ultimately leading to alveolar collapse and lung consolidation. This damage occurs at the time of injury, but it may be undetectable on thoracic radiographs in the initial hours after trauma and may worsen over the first 1–2 days. CT is very sensitive to contusion and can reveal pulmonary contusion immediately after trauma. Moreover, it enables contusion

quantification, which is important in the determination of further treatment. Importantly, when CT is performed immediately after trauma, further progression of the findings must be taken into account. On MDCT images, pulmonary contusions appear as areas of ground-glass opacity, often beneath the impact site (but countercoup may be present), when damage is limited to the interstitial alveolar structures. Most serious injuries lead to pulmonary consolidation, which may reveal small air bronchograms when the bronchioles are not filled with blood (Figs. 5, 12, and 15). In high-energy impact, pulmonary contusion may be found surrounding areas of lung laceration.

Pulmonary laceration is caused by higher-energy blunt trauma than is contusion. It results from a mechanical shear or puncture that disrupts the parenchyma, creating a cleavage plane within the lung. Different CT patterns of lung laceration

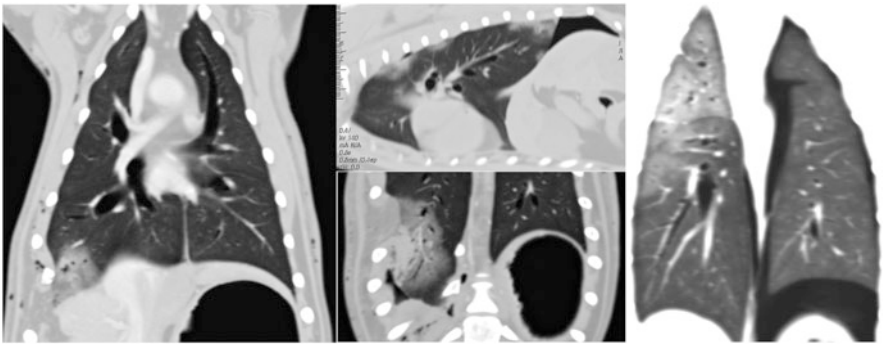

Fig. 15 Pulmonary contusion with ground-glass opacity and consolidation beneath the impact site (pneumothorax is also present)

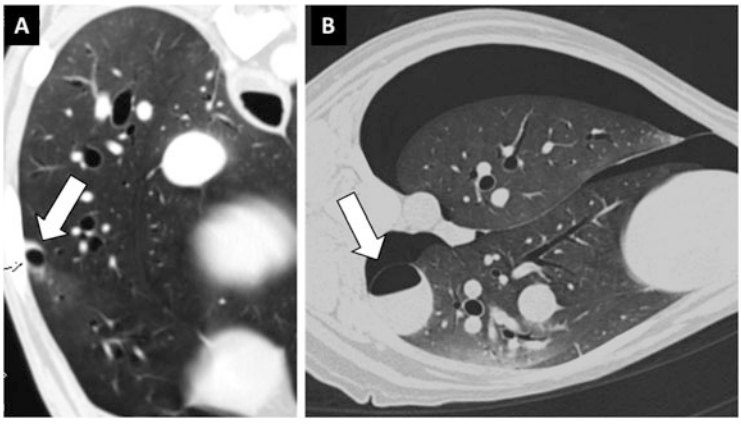

Fig. 16 Lung laceration in dogs. (**a**) Transverse view in a dog with blunt trauma. The *arrow* shows a small subpleural lung laceration surrounded by increased-opacity lung tissue. (**b**) Transverse view of the thorax obtained in an awake patient (flash modality) scanned in right lateral recumbency. The *arrows* indicate a large lung laceration filled partially with blood (air-fluid level)

are possible according to the mechanism of injury and location within the lung. Rib penetration injuries lead to increased lung opacity and consolidation (Figs. 5 and 7). CT of pulmonary parenchyma lacerations due to high-energy trauma shows single or multiple round or oval cavities, instead of the linear appearance typically seen in other solid organs. Because of the normal pulmonary elastic recoil, lung tissues surrounding a laceration pull back from it. The traumatic cavity may be filled with air and/or blood (Fig. 16).

4 MDCT of Abdominal Trauma

MDCT is an excellent imaging modality for evaluation of the abdomen in hemodynamically stable traumatized patients. It can provide essential anatomic and physiological information required to choose the appropriate management of intra-abdominal injuries and to select patients that require urgent surgical intervention. As for thoracic trauma, compression and deceleration forces can cause abdominal injuries in blunt trauma cases. Other mechanisms include penetrating injuries and falling from a height, a common cause of trauma in feline patients. The mechanism of trauma influences the likelihood that individual abdominal organs are injured. Peritoneal and retroperitoneal structures, the diaphragm, and body wall constituents all can be damaged by blunt or penetrating trauma.

4.1 Free Abdominal Fluid

Initially, the abdomen should be assessed using a soft tissue window to identify possible free abdominal fluid. The fluid may or may not be immediately evident. In these cases, the dependent portions of the abdomen should be analyzed thoroughly to detect even small quantities of free fluid.

When peritoneal or retroperitoneal fluid is identified, individual organs must be scrutinized for possible rupture and active hemorrhage. Intraperitoneal fluids of traumatic cause include blood from parenchymal, bowel, or mesenteric injury, bowel contents, bile from a ruptured gallbladder, and/or biliary tree or urine from a ruptured bladder. Fluid location is extremely helpful in identifying the site of bleeding. With parenchymal injuries, initial bleeding occurs adjacent to the affected organ. Thus, careful review of the parenchymal margins may reveal subtle lacerations accompanied by peri-parenchymal free fluid (Figs. 17 and 18). With bowel injuries, initial bleeding into the interloop space occurs. Small collection of free fluid can be observed without evidence of major organ injury. Occult small parenchymal fractures or bowel injuries may be hypothesized, and the patient should be monitored for 24–48 h by ultrasound or CT examination. The simultaneous presence of free extraluminal gas in the peritoneal cavity strongly suggests rupture of

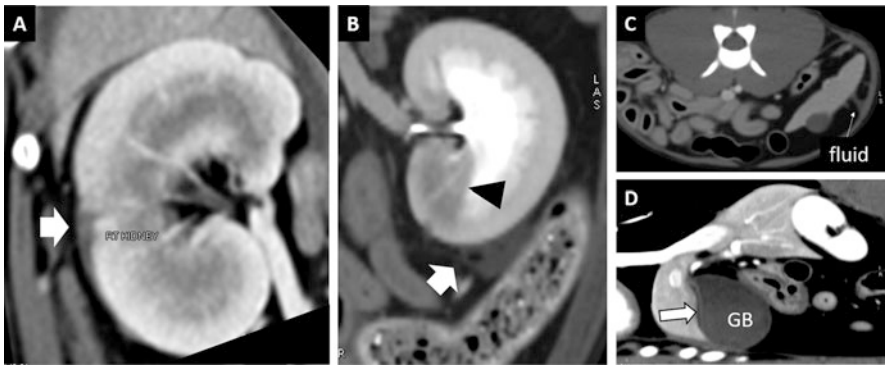

Fig. 17 (**a**) A small amount of fluid in the subcapsular area of the right kidney of a dog after trauma. (**b**) A small amount of retroperitoneal fluid (*arrow*) in a traumatized dog. Note the infarcted renal area (*arrowhead*). (**c**) A small amount of fluid in the splenic area in a traumatized cat. A small splenic subcapsular hematoma is also present. (**d**) Parasagittal image of a traumatized dog. Note the small amount of free fluid around the gallbladder (GB)

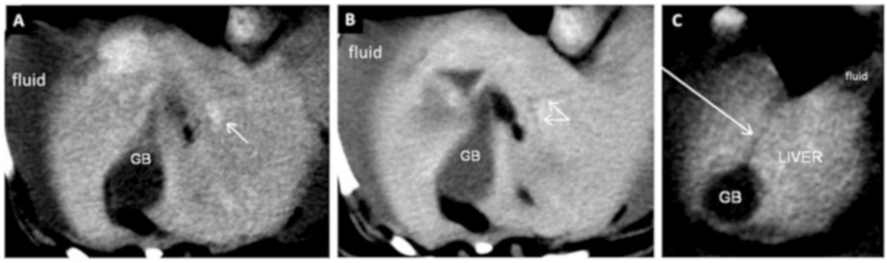

Fig. 18 Pre-contrast images of dogs with hepatic trauma and hemoabdomen (fluid). (**a**) Transverse view showing small hyperattenuating areas (hemorrhage). (**b**, **c**) Transverse views of two other dogs showing thin hypoattenuating parenchymal lines, consistent with hepatic lacerations

the gastrointestinal tract. However, the absence of free gas does not exclude the possibility of injury to the bowel wall, which should be assessed carefully to avoid overlooking a lesion, especially in a case of penetrating trauma.

CT characteristics may aid the identification of possible sources of large amounts of free fluid. Different attenuation values can distinguish hypoproteic fluids, such as ascites (<15 HU), from hemoperitoneum (~40 HU). In some cases, however, distinguishing the origin of lower-attenuating fluids, ascites, bile, or urine from the bladder or excretory rupture may be difficult. Perihepatic and perisplenic fluids are generally blood. Perirenal and retroperitoneal free fluids may be blood or urine. A delayed series is essential to detect the escape of contrast medium into the fluid collection; this can require several minutes, depending on the site and size of the rupture (Figs. 19 and 20). In our center, the protocol for patients with known or suspected ureteral or urinary bladder rupture involves descending MDCT urography for opacification of the urinary collecting system and detection

Fig. 19 Urinary bladder rupture in a dog after blunt trauma. (**a**) Note the thin laceration in the bladder wall and perivesical fluid (uroabdomen). (**b**) Image obtained at the same level during the excretory phase. Note that the CM is free in the pelvic cavity. (**c**) Dorsal MIP image obtained in the excretory phase showing the escape of CM in the retroperitoneal cavity through the ruptured bladder

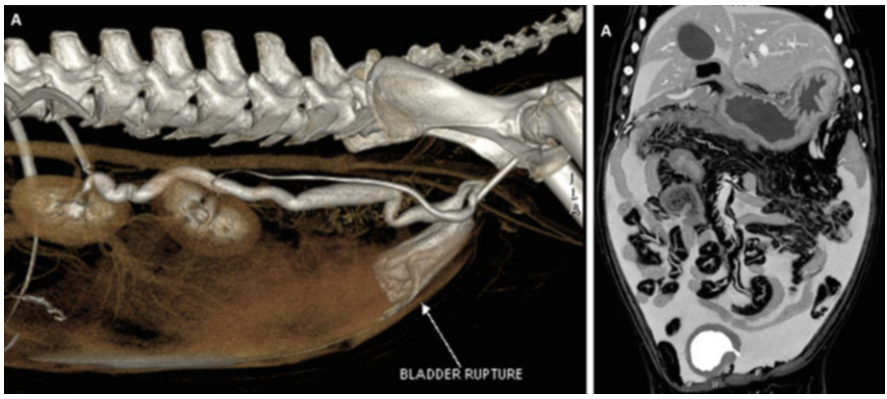

Fig. 20 Rupture of the urinary bladder and uroabdomen in a dog. (**a**) VR of the excretory phase showing the ruptured urinary bladder. Note the enlargement of the right ureter. (**b**) The remaining urinary bladder has a thickened wall. The CM diffuses from the bladder to the peritoneal cavity (uroperitoneum)

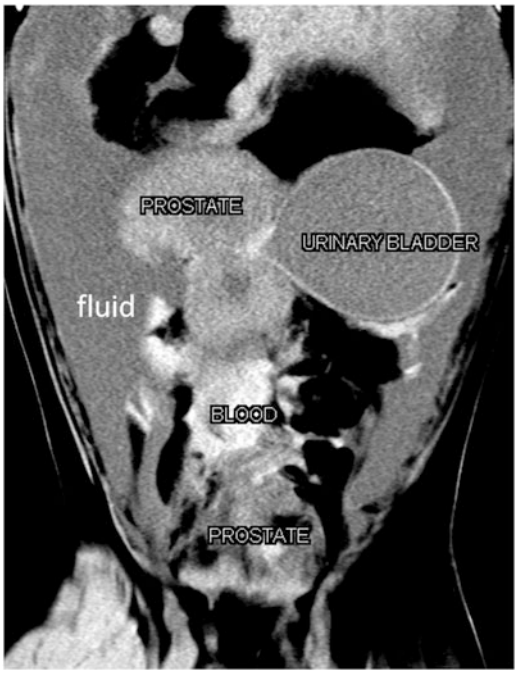

Fig. 21 Dorsal pre-contrast MPR of the caudal abdomen in a dog after severe pelvic trauma. The prostate gland and prostatic tract of the urethra are ruptured and dislocated cranially, with active perilesional hemorrhage (blood) and uroperitoneum (fluid)

of the injury site. CT cystography with retrograde bladder filling can also be performed in cases of suspected ureterovesical rupture.

Clotted blood can be observed adjacent to the source of bleeding (sentinel clot sign) and may have higher attenuation (40–70 HU) (Fig. 21). The acquisition of different vascular phases facilitates differentiation between active venous and active arterial hemorrhages, which is important in the setting of blunt trauma. In the radiology literature, active arterial hemorrhage is defined as being evidenced by extravascular regions with high attenuation, similar to or greater than that of the aorta, on arterial-phase images. Areas of active arterial hemorrhage are expected to increase in size and remain of higher attenuation than the aorta on portal venous-phase and delayed-phase images.

Extravascular high-attenuating areas that are identified on the portal venous phase or later, and are not evident on arterial-phase images acquired earlier, are generally of venous origin. In severe trauma with injury to both compartments, these two patterns can coexist. The acquisition of a single venous phase is not sufficient for differentiation between the two hemorrhage types unless the vessel of origin is readily identified. The identification of active bleeding in traumatized patients is important because it is associated with vascular or important parenchymal injury. Thus, when initial evaluation raises the suspicion of active bleeding (due to the presence of free fluid and/or the sentinel clot sign), contrast medium injection should be used to search for the site of extravasation. In our center, a multiphase approach including arterial and portal venous phases is used in

hemodynamically stable patients to try to distinguish the source of bleeding (artery or vein) and to assess whether the extravasation is contained or active. Active extravasation should appear as a jet of contrast medium into the adjacent hematoma in vascular phases (the timing of scanning is crucial for identification). A third delayed series may be helpful to confirm the extravasation, as the hematoma will have increased in size and/or density.

4.2 Injuries of the Abdominal Wall and Parenchyma

Abdominal wall injuries resulting from penetrating trauma, as in the case of large–small dog interactions, are usually obvious. The key role of MDCT in the assessment of penetrating trauma of the abdominal wall is to recognize possible associated intra-abdominal injuries, particularly of those the bowel and mesentery. Bowel wall thickening, abnormal bowel enhancement, mesenteric infiltration, stranding, or hematoma may indicate mesenteric/bowel injuries mandating surgical exploration (Figs. 1 and 22). Moreover, bowel and mesenteric fat can herniate through abdominal wall defects, with the risks of obstruction and strangulation.

Blunt and penetrating trauma can cause injuries of major abdominal parenchyma. MDCT can be used to easily detect direct and indirect signs of parenchymal damage, with simultaneous exclusion of surgical lesions, such as pancreatic and intestinal lesions. Traumatic injuries of solid parenchyma most often affect the spleen or liver. Direct signs of *splenic injury* include intraparenchymal or subcapsular hematoma and laceration (fracture) with capsular tear. These injuries appear as hypoattenuating linear or lacunar lesions and are detected more easily in post-contrast series (Fig. 23).

Hepatic contusion appears on contrast-enhanced MDCT images as a poorly marginated, low-attenuation area compared with the surrounding, normally enhancing, hepatic parenchyma. Hepatic lacerations appear as well-defined, linear lesions of low attenuation within the normally enhancing liver parenchyma and often present a branching pattern. Variable degrees of hemoperitoneum accompany these lesions, depending on their number and location within the parenchyma. Severe hepatic trauma may cause bile leaks that appear as low-density free fluid collection, isoattenuating to the bile (Figs. 18 and 24).

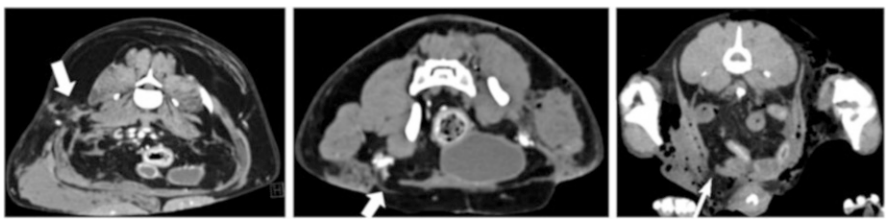

Fig. 22 Examples of traumatic abdominal wall laceration (*arrows*)

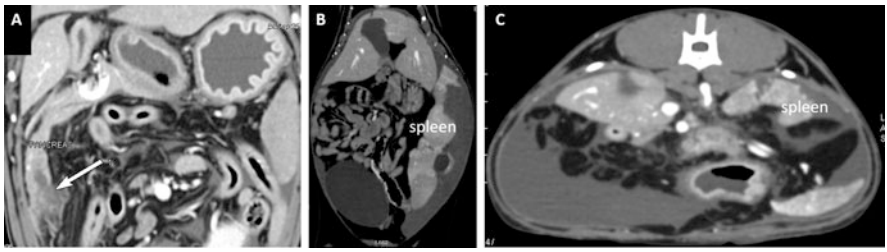

Fig. 23 (**a**) Dorsal MPR in a dog after severe blunt trauma. The *arrow* shows rupture of the right pancreatic lobe. (**b**) Dorsal MPR view of the abdomen in a traumatized cat with rupture of the spleen and perilesional fluid accumulation (hemoabdomen). (**c**) Transverse view in a traumatized dog with abundant hemoabdomen due to hepatic and splenic rupture

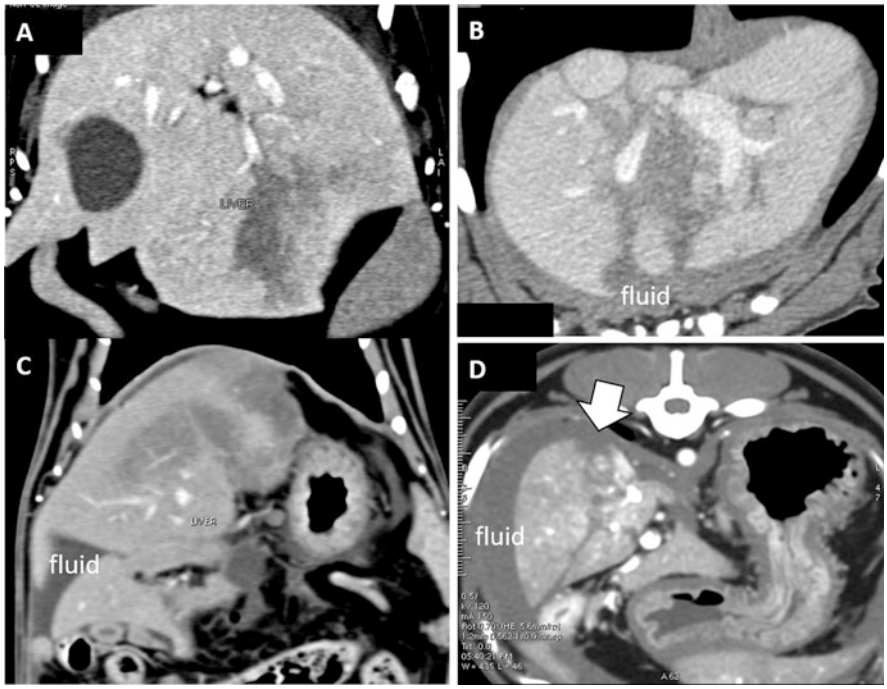

Fig. 24 (**a**, **b**) Liver contusion in dogs after blunt trauma. Note the hypoattenuating areas of the liver parenchyma and perihepatic fluid (hemoabdomen). (**c**) Posttraumatic bile peritonitis in a cat. (**d**) Severe abdominal trauma in a dog, with hepatic laceration (*arrow*) and perihepatic effusion (hemoabdomen)

MDCT enables the precise delineation of *renal injuries* in dogs and cats. As mentioned previously, in our center, patients with suspected urinary system trauma are evaluated using a multiphasic approach, including delayed series for the assessment of collecting pathways. In the arterial (corticomedullary) phase, MDCT can

reveal renal contusions and lacerations. Contusions appear as hypoattenuating, ill-defined areas within the renal parenchyma. Lacerations are linear hypoattenuating fractures accompanied by perinephric blood or subcapsular hematoma. Focal renal infarcts can be seen on renal poles (for stretching or thrombosed small arterioles) (Figs. 17 and 25). Urine leakage is indicated by low-density retroperitoneal or peritoneal fluid (depending on the site of rupture) in the pre-contrast and early post-contrast (arterial) phases. Delayed series show the escape of contrast medium from the damaged collecting system.

The veterinary literature contains descriptions of the advantages of MDCT in cases of pelvic trauma, as it can provide detailed information about complex bone fractures. In the author's experience, MDCT is also valuable for the evaluation of damage to the pelvic structures and soft tissues in dogs and cats with pelvic injury due to blunt trauma. Scanners with 64 or more rows have unprecedentedly short acquisition times. This feature allows for the tailoring of complex multiphasic tests in which pelvic and aortoiliac CTA are combined into a single comprehensive examination for simultaneous evaluation of the bone, muscles, and vessels, as well as the pelvic structures (e.g., urinary bladder, prostate, and urethra) (Fig. 26).

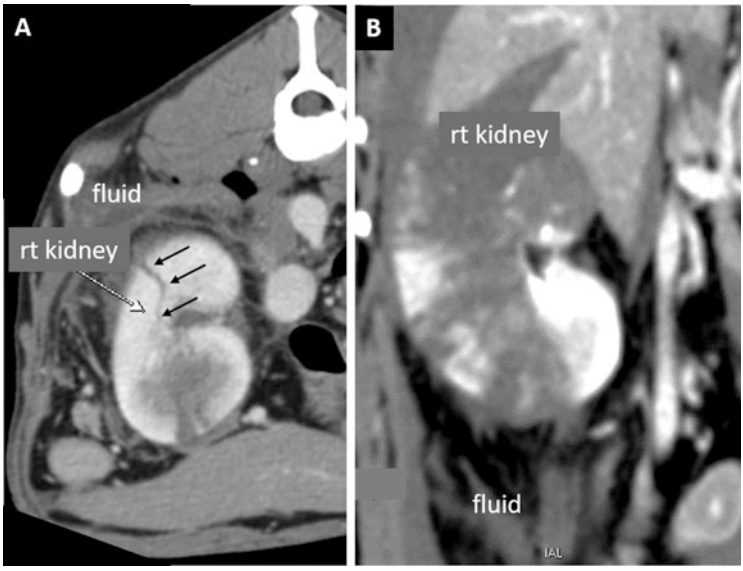

Fig. 25 (**a**) Transverse view of the abdomen in a dog after blunt trauma. The parenchyma of the right kidney shows a thin hypoattenuating line (*arrows*), consistent with renal laceration. In the ventral area of the kidney, there are a couple of triangular hypoattenuating areas of infarction. (**b**) Note the retroperitoneal perirenal fluid (*arrow*)

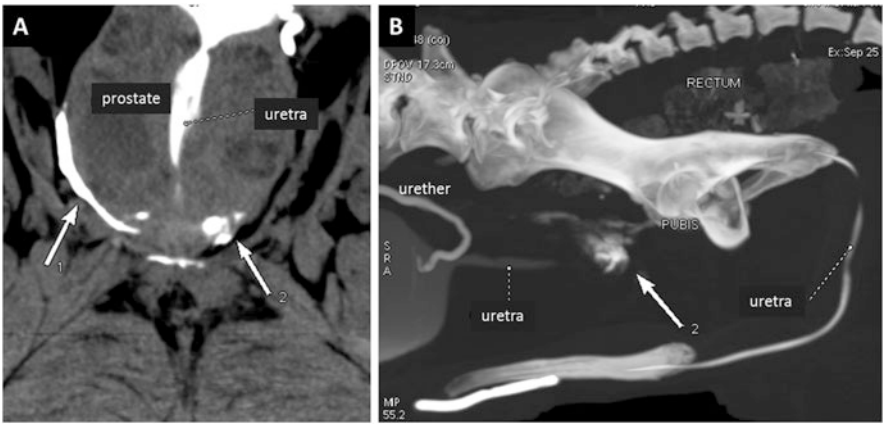

Fig. 26 Rupture of the intraprostatic segment of the urethra of a dog with severe pelvic trauma. (**a**) Dorsal MPR image of the pelvis obtained in the excretory phase, showing partial enhancement of the intraprostatic urethra and the presence of free CM in the periprostatic area (*arrows*). (**b**) Thick-MIP obtained in the same phase showing the interrupted urethra with CM escape

Further Readings

Fields EL, Robertson ID, Brown JC Jr. Optimization of contrast-enhanced multidetector abdominal computed tomography in sedated canine patients. Vet Radiol Ultrasound. 2012;53(5): 507–12. doi:10.1111/j.1740-8261.2012.01950.x.

Hoffberg JE, Koenigshof AM, Guiot LP. Retrospective evaluation of concurrent intra-abdominal injuries in dogs with traumatic pelvic fractures: 83 cases (2008–2013). J Vet Emerg Crit Care (San Antonio). 2016;26(2):288–94. doi:10.1111/vec.12430. Epub 2016 Jan 11.

Liang T, McLaughlin P, Arepalli CD, Louis LJ, Bilawich AM, Mayo J, Nicolaou S. Dual-source CT in blunt trauma patients: elimination of diaphragmatic motion using high-pitch spiral technique. Emerg Radiol 2016;23(2):127–32. doi:10.1007/s10140-015-1365-y. Epub 2015 Dec 4.

Nishino M, Kubo T, Kataoka ML, Raptopoulos V, Hatabu H. Coronal reformations of the chest on 64-row multi-detector row CT: evaluation of image quality in comparison with 16-, 8- and 4-row multi-detector row CT. Eur J Radiol. 2006;59(2):231–7. Epub 2006 Mar 29.

Oliveira CR, Mitchell MA, O'Brien RT. Thoracic computed tomography in feline patients without use of chemical restraint. Vet Radiol Ultrasound. 2011;52(4):368–76. doi:10.1111/j.1740-261.2011.01814.x.

Ricciardi M. Usefulness of multidetector computed tomography in the evaluation of spinal neuromusculoskeletal injuries. Vet Comp Orthop Traumatol. 2016;29(1):1–13. doi:10.3415/VCOT-15-05-0082.

Shanaman MM, Hartman SK, O'Brien RT. Feasibility for using dual-phase contrast-enhanced multi-detector helical computed tomography to evaluate awake and sedated dogs with acute abdominal signs. Vet Radiol Ultrasound. 2012;53(6):605–12. doi:10.1111/j.1740-8261.2012.01973.x.

Specchi S, Auriemma E, Morabito S, Ferri F, Zini E, Piola V, Pey P, Rossi F. Evaluation of the computed tomographic "sentinel clot sign" to identify bleeding abdominal organs in dogs with hemoabdomen. Vet Radiol Ultrasound. 2016. doi:10.1111/vru.12439. Epub ahead of print.

Stieger-Vanegas SM, Senthirajah SK, Nemanic S, Baltzer W, Warnock J, Bobe G. Evaluation of the diagnostic accuracy of four-view radiography and conventional computed tomography

analysing sacral and pelvic fractures in dogs. Vet Comp Orthop Traumatol. 2015a;28(3): 155–63. doi:10.3415/VCOT-14-06-0096.

Stieger-Vanegas SM, Senthirajah SK, Nemanic S, Baltzer W, Warnock J, Hollars K, Lee SS, Bobe G. Evaluation of the diagnostic accuracy of conventional 2-dimensional and 3-dimensional computed tomography for assessing canine sacral and pelvic fractures by radiologists, orthopedic surgeons, and veterinary medical students. Vet Surg. 2015b;44(6):694–703. doi:10.1111/j.1532-950X.2014.12313.x.

Index

G. Bertolini (ed.), *Body MDCT in Small Animals*, DOI 10.1007/978-3-319-46904-1